Experiments in Beauty

A Habilitationsschrift
submitted to the Faculty of Science
at University of Zürich

Olaf Steinkamp
Physik-Institut der Universität Zürich

September 4, 2015

Als ik zou willen dat je het begreep, had ik het wel beter uitgelegd.

— Johan Cruijff

Contents

Chapter 1

Introduction

> We must continue to seek the origin of the *CP* symmetry violation by all means at our disposal. We know that improvements in detector technology and quality of accelerators will permit even more sensitive experiments in the coming decades. We are hopeful, then, that at some epoch, perhaps distant, this cryptic message from nature will be deciphered.
>
> — James W. Cronin, Rev. Mod. Phys. **53** (1981) 373.

This work has grown out of a lecture course on the experimental aspects of Flavour Physics that I have had the pleasure to teach at the beautiful Irchel Campus of Universität Zürich and — in abbreviated from — at the 2013 CHIPP PhD Winter School, surrounded by the possibly even more spectacular setting of Eiger, Mönch and Jungfrau. Flavour physics, in its most general definition, concerns itself with the properties and interactions of the three fermion families of the Standard Model of particle physics. It covers a vast field of topics, from efforts to reach a better understanding of neutrino masses in the sub-eV regime to precision measurements that could reveal indirect evidence for the existence of hitherto unknown heavy particles at the TeV scale and beyond. I will concentrate here on the specific aspect of Flavour Physics that has kept me entertained in my own research for almost 20 years now, namely the study of flavour-changing interactions and *CP* violating phenomena in the mixing and decays of beauty quarks. Even within this restriction, it is impossible to do justice to all the exciting measurements and results that have been published over the last years and I apologize for the choices I had to make. Also, my upbringing as a hardcore experimental physicist will shine through again and again.

After a brief introduction, the stage will be set in Chapter 2 which gives a short historical overview, highlighting the landmark achievements that have led to our basic understanding of Flavour Physics in the quark sector. Chapter 3 is a short excursion to introduce the formalism and phenomenology of particle-antiparticle mixing in the neutral meson system and to discuss the sources of *CP* violation in the Standard Model. The main players will be introduced in Chapter 4 in the form of the experiments that have shaped the field of Flavour Physics in the heavy quark sector over the past fifteen years — the two B-meson factories, BaBar and Belle, which provided a wealth of beautiful results on *CP* violating phenomena in the $B^0\overline{B}^0$ and B^+B^- systems and established the Cabibbo-Kobayashi-Maskawa mechanism of the Standard Model as the dominant source of flavour-changing interactions in the quark sector; the experiments CDF and D0 at the Tevatron, which provided a first glimpse into the system of B_s^0 and $\overline{B}_s^0$ mesons; and, finally, the LHCb experiment at the LHC, which is now probing the Standard Model by confronting its predictions with precision measurements in decays of all types of b hadrons. The plot of the story unfolds in Chapter 5, in which measurements are described of the sides and angles of the Unitarity Triangle that can be derived from the Cabibbo-Kobayashi-Maskawa model of flavour-changing interactions and allows to test the internal consistency of this model. The results of these measurements have established the

validity of the model, but cannot exclude possible sub-dominant contributions from "New Physics" beyond the Standard Model. The story therefore enters a new phase in Chapter 6, which concentrates on precision measurements of *CP* violating phenomena in the $B_s^0\overline{B}_s^0$ system and of observables in certain rare decays of B_s^0 and B^0 mesons. These measurements provide good sensitivity to possible contributions from physics beyond the Standard Model. Except for a couple of small deviations, which will need to be investigated further, results of these measurements are so far in excellent agreement with Standard Model predictions and the by now 40 year old Standard Model of particle physics still stands tall at the beginning of 2015. The Large Hadron Collider is foreseen to resume its operation in the middle of 2015 and the LHCb collaboration hope to treble or even quadruple the size of their data samples over the coming three to four years. At the same time, a new Super-B factory, Belle II, is under construction in Japan and the LHCb collaboration is working on a comprehensive upgrade of their experiment, which should allow them to accumulate significantly larger event samples and improve the sensitivity to key observables by large factors. Chapter 7 gives a very brief glimpse into this next chapter in the story of heavy-quark Flavour Physics — and concludes this work.

This text was compiled over the course of roughly a year, from early 2014 till early 2015 and uses results published by the end of 2014. Quoted averages and combinations of results are based on the 2014 edition of the Review of Particle Physics [1], on the work of the Heavy Flavour Averaging Group published in December 2014 [2] and on the Standard-Model fit by the CKM-fitter group [3] using results presented up to the CKM 2014 conference in early September 2014. When figures were extracted from original publications, references are given in the captions. No copyright infringements are intended. The plots shown in Figure 4.22 were prepared by Christian Elsasser. All Feynman diagrams were produced using the FeynMF package as implemented in the Feynman Diagram Library at `http://www.physik.uzh.ch/~che/FeynDiag/`.

1.1 Flavour Physics

The field of Flavour Physics concerns itself with the properties and interactions of the three fermion families of the Standard Model of particle physics. Many of these properties have been measured, some to amazing precision, but very fundamental questions remain unanswered.

- Without at least three lepton families, there would be no known source of *CP* violation that could generate a matter-antimatter asymmetry in the universe and for all we know today, we would not exist. But why do fermions occur in families and why are there three of them? Could there actually be more than three families?

- The Higgs or BEH mechanism explains how fermions can acquire mass in the Standard Model, but it does not explain the values of the measured masses. Can the observed mass hierarchies between the three families be explained by an underlying theory?

- Similarly, flavour mixing between the families is observed to exhibit a clear hierarchical pattern. Does this pattern point to an underlying theory?

- The *CP* violating effects measured in the quark sector seem to be too small by many orders of magnitude to explain the apparent matter-antimatter asymmetry that we observe in the universe. We seem to need additional sources of *CP* violation. What are they?

An important guiding principle in Flavour Physics is provided by fundamental discrete symmetries and by their breaking:

- Charge conjugation (C), parity (P) and time reversal (T);

- The combined symmetries *CP* and *CPT*;
- Baryon number;
- Lepton number and lepton flavour.

Flavour being a conserved quantum number in strong and electromagnetic interactions, Flavour Physics concerns itself mainly with properties of the weak interaction. A good understanding of the effects of strong interaction is, however, often required in order to extract the interesting observables from measurements.

The field of Flavour Physics is readily divided into three distinct subfields — the neutrino sector, charged leptons, and the quark sector — by the theoretical questions that are addressed, by the phenomenology of the processes that are studied and, consequently, by the experimental techniques that are employed. A very brief summary of current issues in the neutrino and charged lepton sectors is given in the next section, before we turn to the main topic of this article, Flavour Physics in the quark sector.

1.2 Neutrino sector and charged leptons

The possibility that lepton family number conservation might be violated through flavour oscillations in the neutrino sector was first suggested in 1969 by Gribov and Pontecorvo [4] as a possible explanation for the apparent deficit in the observed flux of solar neutrinos on Earth. Neutrino oscillations have now been firmly established by a number of large-scale experiments using solar, atmospheric, reactor and accelerator neutrinos. For a comprehensive review, see e.g. the section on "Neutrino Mass, Mixing, and Oscillations" in the Review of Particle Physics [1]. The main goals of experiments in the neutrino sector today are

- to obtain more precise measurements of the mixing parameters, in particular of the small mixing angle θ_{13}, and to explore the prospects for *CP* violating asymmetries in the neutrino sector;
- to resolve the still unknown mass hierarchy and to obtain better constraints on the absolute mass scale for neutrinos;
- to resolve the nature of neutrinos as Dirac or Majorana particles.

The first set of goals is being pursued at existing or proposed long-baseline neutrino observatories, such as T2K, MINOS and NOvA and the Daya Bay and RENO reactor neutrino experiments. The hypothesis of neutrinos being Majorana particles is being tested by searching for neutrino-less double beta ($0\nu\beta\beta$) decays. About a dozen large-scale projects are under construction or have been proposed to search for these decays. For a recent review of the status and prospects of these searches, see e.g. Ref. [5].

Transitions violating lepton flavour in the charged lepton sector occur naturally in the Standard Model if the mass differences between the three neutrino species are non-zero as implied by the observation of neutrino oscillations. However, these transitions are suppressed by the fourth power of the ratio between the neutrino mass differences and the W boson mass and are therefore extremely small. For example, the Standard Model branching fraction for the decay $\mu \to e\gamma$ is predicted to be of the order of 10^{-54}, many orders of magnitude below the reach of experiments. However, lepton flavour violating amplitudes can be significantly enhanced in New Physics scenarios. Searches for lepton flavour violating transitions in radiative muon decays $\mu^\pm \to e^\pm\gamma$ and $\mu^\pm \to e^+e^-e^\pm$ are pursued at high-intensity muon beams at the PSI in Switzerland; an alternative approach is to search for $\mu^- \to e^-$ transitions of muons captured in muonic atoms. Such searches have also been performed at PSI, new experiments are under development at Fermilab in the United States and at J-PARC in Japan. Searches

for lepton flavour violating τ lepton decays have been performed at the B factories BaBar and Belle and are now being pursued at LHCb. Another topic in the charged lepton sector that is related to flavour physics is the precise determination of the anomalous magnetic moment of the muon. The most precise results were achieved at BNL in the United States and currently show a discrepancy of around 2.5 to 3.5 standard deviation from Standard Model calculations. Measurements as well as theoretical calculations involve a large number of subtle corrections and the interpretation of the observed discrepancy has been inconclusive for many years now. For a slightly more comprehensive overview of the field of flavour physics in the charged lepton sector, see for example Ref. [6].

1.3 Quark sector

The Cabibbo-Kobayashi-Maskawa model provides a consistent and by now well tested description of flavour-changing interactions in the quark sector. It is the main goal of Flavour Physics today, to probe this model by confronting its precise predictions with similarly precise measurements and hopefully discover discrepancies that will point the way towards the New Physics that is believed to be lurking behind the Standard Model of particle physics. Of particular interest are observables for which Standard Model predictions are precise and potential contributions from New Physics can be significant. This is the case for a number of *CP* violating observables in the mixing and decay of B^0 and B_s^0 mesons and for branching fractions and angular observables in rare B^0 and B_s^0 meson decays.

In the Standard Model, flavour-changing transitions in the quark sector are parametrized by the unitary Cabibbo-Kobayashi-Maskawa (CKM) quark mixing matrix

$$V_{ij} \;=\; V_{\rm CKM} \;=\; \begin{pmatrix} V_{ud} & V_{us} & V_{ub} \\ V_{cd} & V_{cs} & V_{cb} \\ V_{td} & V_{ts} & V_{tb} \end{pmatrix}$$

in the effective charged current Lagrangian

$$L_{\rm cc} \;=\; -\frac{g}{\sqrt{2}}\,\overline{u}_i\,\gamma^\mu\,(1-\gamma_5)\,V_{ij}\,d_j\,W_\mu^+ \;+\; \text{h.c.}\;,$$

where W_μ^+ describes the W boson field, u_i the up-type and d_j the down-type quark currents, g is the universal weak coupling constant and γ^μ are the usual Dirac matrices, with $\gamma^5 \equiv i\gamma^0\gamma^1\gamma^2\gamma^3$ defining the $V-A$ character of the weak interaction.

A single complex phase in this CKM matrix is the only known source in the Standard Model of all *CP* violating phenomena. The precise study of these phenomena therefore permits to test the consistency of the model. For three quark families, the CKM matrix contains nine complex and therefore 18 real numbers. The requirement of unitarity

$$V_{\rm CKM}\,{V_{\rm CKM}}^\dagger \;=\; {V_{\rm CKM}}^\dagger\,V_{\rm CKM} \;=\; 1$$

imposes nine constraints. Another five of the parameters are absorbed by unobservable ("unphysical") phases between the quark fields, due to the fact that the Lagrangian is invariant under simultaneous transformations of the type

$$u_i \to e^{i\phi_i}u_i \;\;;\;\; d_j \to e^{i\phi_j}d_j \;\;;\;\; V_{ij} \to e^{i(\phi_i-\phi_j)}V_{ij}\;.$$

Therefore, the 3×3 CKM matrix is fully described by $18-9-5=4$ independent real parameters. Only three of these can be absorbed by rotation angles, the fourth free parameter introduces a complex phase amongst the elements of the CKM matrix.

This phase enters with opposite sign in the amplitudes for charge-conjugated processes and a *CP* violating asymmetry can be generated by interference effects in processes in which at

least two amplitudes with different CKM phase contribute. This phase appears with opposite signs in the amplitudes of charge-conjugated processes. If at least two amplitudes with different CKM phase contribute to the same process, interference effects between these amplitudes can cause the charge-conjugated processes to occur at different rate, generating a *CP* violating asymmetry. The mechanisms at work will be discussed in detail in Section 3.3.

The values of the CKM matrix elements are not predicted by the Standard Model and have to be measured by experiments. The measured magnitudes exhibit a clear hierarchy, with the diagonal elements being close to unity, while mixing between the first and second family is of the order λ, mixing between the second and third family of the order λ^2, and mixing between the first and third family of the order λ^3, where $\lambda \approx 0.23$ is the sine of the Cabibbo mixing angle θ_C. The latest Standard Model fit results yield [1]:

$$|V_{\mathrm{CKM}}| = \begin{pmatrix} 0.97425 \pm 0.00022 & 0.2252 \pm 0.0009 & 0.00389 \pm 0.00044 \\ 0.2230 \pm 0.0011 & 1.023 \pm 0.036 & 0.0406 \pm 0.0013 \\ 0.0084 \pm 0.0006 & 0.0387 \pm 0.0021 & 0.88 \pm 0.07 \end{pmatrix}.$$

This hierarchy is reflected in the often used Wolfenstein parametrization [7], which expands the elements of the CKM matrix in terms of λ and assigns the complex phase to the smallest elements, V_{ub} and V_{td}. Approximating the expansion to order λ^3, the Wolfenstein parametrization yields

$$V_{\mathrm{CKM}} = \begin{pmatrix} 1-\lambda^2/2 & \lambda & A\lambda^3(\rho - i\eta) \\ -\lambda & 1-\lambda^2/2 & A\lambda^2 \\ A\lambda^3(1-\rho-i\eta) & -A\lambda^2 & 1 \end{pmatrix} + O\left(\lambda^5\right).$$

Unitarity of the CKM matrix imposes three normalization conditions and six orthogonality conditions. The latter,

$$\begin{array}{rcrcrcll} V_{ud}V_{cd}^* & + & V_{us}V_{cs}^* & + & V_{ub}V_{cb}^* & = & 0 & (\lambda, \lambda, \lambda^5) \\ V_{ud}V_{td}^* & + & V_{us}V_{ts}^* & + & V_{ub}V_{tb}^* & = & 0 & (\lambda^3, \lambda^3, \lambda^3) \\ V_{cd}V_{td}^* & + & V_{cs}V_{ts}^* & + & V_{cb}V_{tb}^* & = & 0 & (\lambda^4, \lambda^2, \lambda^2) \\ V_{ud}V_{us}^* & + & V_{cd}V_{cs}^* & + & V_{td}V_{ts}^* & = & 0 & (\lambda, \lambda, \lambda^5) \\ V_{ud}V_{ub}^* & + & V_{cd}V_{cb}^* & + & V_{td}V_{tb}^* & = & 0 & (\lambda^3, \lambda^3, \lambda^3) \\ V_{us}V_{ub}^* & + & V_{cs}V_{cb}^* & + & V_{ts}V_{tb}^* & = & 0 & (\lambda^4, \lambda^2, \lambda^2)\ , \end{array}$$

can be conveniently described as triangles in the complex plane as illustrated in Figure 1.1.

Careful inspection shows that all six triangles have the same area, which can be taken as a measure for the amount of *CP* violation in the Standard Model [9]. However, the shape of the triangles differs significantly. Noted next to each of the triangular relations above is the order

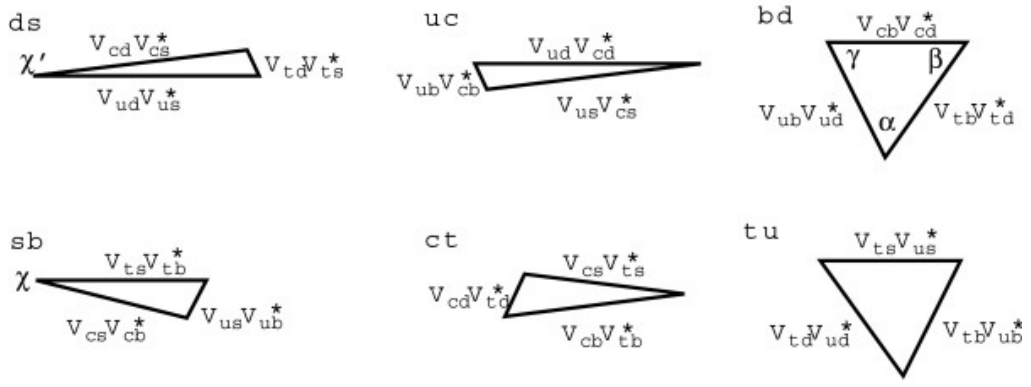

Figure 1.1: Illustration of the six orthogonality conditions of the CKM matrix as triangles in the complex plane. The triangle usually referred to as "The Unitarity Triangle" is that depicted in the top right. Note that the triangles are not drawn to scale (illustration from [8]).

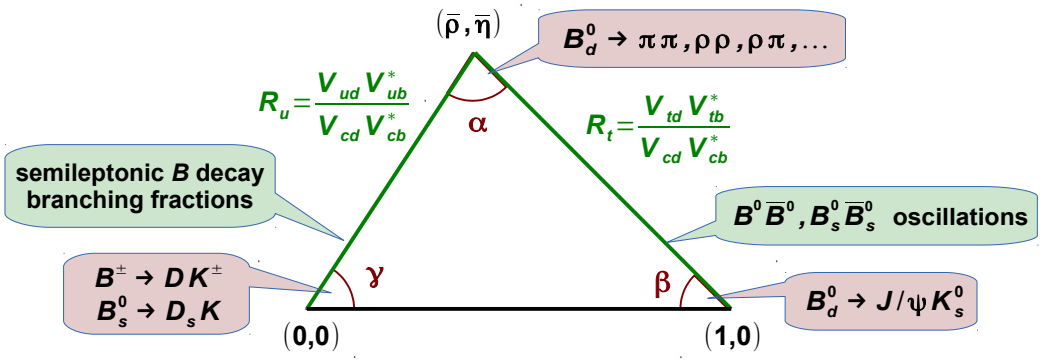

Figure 1.2: Sketch of the normalized Unitarity Triangle, indicating some of the processes that can be employed to measure the angles α, β and γ, and the lengths of the sides, $|R_u|$ and $|R_t|$.

in λ for each of the three terms in the sum. For two of the six relations, all three terms are of the same order in λ, leading to triangles with three sides that are approximately equal in length. The other four triangles are "squashed", with one side that is much shorter than the other two. The two non-squashed triangles are obtained by combining the first and the third row, or the first and the third column of the matrix, respectively. The second of these triangles is usually referred to as "The Unitarity Triangle". In fact, the two triangles are identical in the Wolfenstein parametrization to order λ^3, but not when the Wolfenstein parametrization is expanded to include terms of the order λ^5. The small difference has been negligible compared to the measurement precision achieved in previous experiments but starts to become relevant at the precision expected from the LHCb experiment.

The standard version of the Unitarity Triangle is obtained by normalizing bythe side $V_{cd}V_{cb}^*$, which is real in the Wolfenstein parametrization, such that one of the three sides points from the origin, $(0,0)$, of the complex plane to the point $(1,0)$ along the real axis. The apex of the triangle is then given by $\overline{\rho} + i\overline{\eta} \equiv (1 - \lambda^2/2)(\rho + i\eta)$, with the Wolfenstein parameters λ, ρ and η. In this form, the Unitarity triangle provides a powerful concept for testing the CKM picture of CP violation, since its three angles as well as the lengths of its two sides are directly related to measurable quantities. The most relevant processes are indicated in Figure 1.2.

> A short remark on notations: Kobayashi and Maskawa in their original publication denoted the three angles as ϕ_1, ϕ_2 and ϕ_3, and the Belle collaboration follows that original notation. In most other publications, however, the angles are referred to as β, α and γ and this notation will also be employed here. The two sides will be referred to as R_u and R_t after the up-type quark involved in the relevant CKM matrix elements.

As can be seen from Figure 1.2, measurements in the neutral, charged and strange B meson systems are of particular relevance for the determination of the Unitarity Triangle. The rich phenomenology of the B mesons systems combined with the ability to derive relatively precise theoretical predictions allow to peform overconstraint determinations of all parameters and to test the internal consistency of the CKM picture of flavour-changing interactions and CP violation in the quark sector.

Measurements of the Unitarity Triangle parameters have been performed at the two B factories, BaBar at SLAC and Belle at KEK, the two general-purpose experiments CDF and D0 at the Tevatron and, more recently, at the LHCb experiment at the LHC. The experiments will be described in Chapter 4. BaBar and Belle were dedicated experiments at dedicated, high-intensity e^+e^- colliders that had been constructed with the explicit goal to produce large samples of $B^0\overline{B}^0$ and B^+B^- pairs via resonant $b\bar{b}$ production at the $\Upsilon(4S)$ resonance. Unfortunately, e^+e^- B factories do not give access to the $B_s^0\overline{B}_s^0$ system, since B_s^0 mesons are

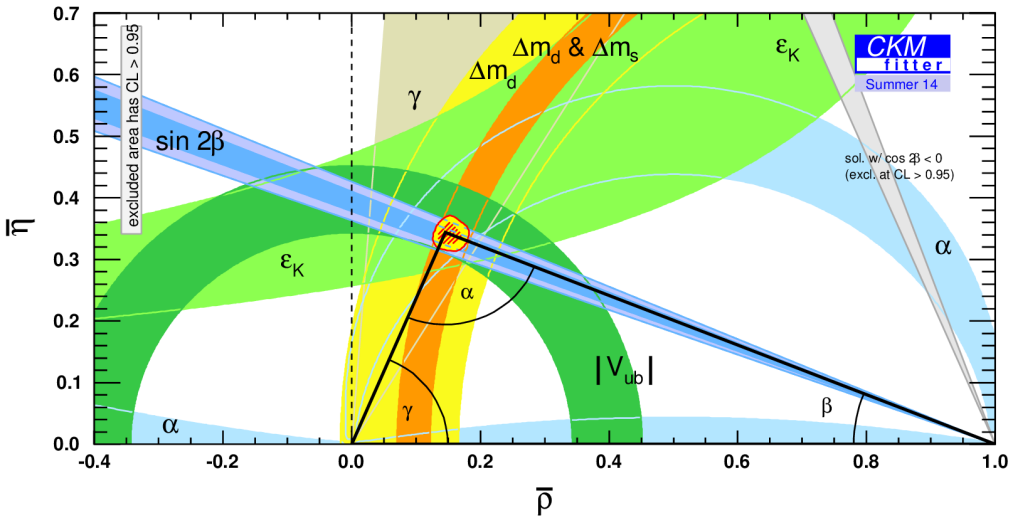

Figure 1.3: Result of a global Standard-Model fit of Unitarity Triangle parameters as compiled by the CKMfitter group [3] including results presented up to the CKM 2014 conference in September 2014. The red hashed area corresponds to 68% confidence region for the apex of the triangle.

too heavy to be produced in $\Upsilon(4S)$ decays. An intial exploration of the $B_s^0\overline{B}_s^0$ system was the privilege of the CDF and D0 experiments at the Tevatron, Fermilab's $p\overline{p}$ collider operating at a collision energy of of 1.96 TeV. Both CDF and D0 were designed as general-purpose detectors and their mail goal was to study top quark properties and to search for the Higgs boson and new heavy particles predicted by extentions of the Standard Model. However, exploiting the large $b\bar{b}$ production cross section in high-energy hadron-hadron collisions, both experiments also pursued an active B physics programme. While they could not compete in precision with the B factories in the neutral and charged B meson systems, they had unique potential in the B_s^0 system. Both B factories as well as the Tevatron have been terminated a few years ago and it is now the LHCb experiment at CERN's Large Hadron Collider that continues to explore the field, challenging the Standard Model by confronting its predictions with more and more precise measurements. As its name indicates, studying the physcis of b hadrons is the main goal of the LHCb experiment. The dedicated design and layout of the detector, in combination with the even larger $b\bar{b}$ production cross section at the LHC collision energies of initially 7, then 8 and hopefully soon 13 TeV, allow the experiment in many measurements to improve on the precision reached at the earlier experiments.

The measurements themselves will be described in Chapter 5. The results obtained so far are in good agreement with Standard Model predictions. The impressive level of consistency in the determination of the parameters of the Unitarity Triangle is illustrated by the most recent Standard Model fit by the CKMfitter group [3] shown in Figure 1.3. The current level of precision of the measurements still allows for sub-dominant contributions from "New Physics" beyond the Standard Model at a level of 10-20%. It is the goal of the LHCb experiment and the planned Super-B factory, Belle II, to search for such sub-dominant effects. These searches are pursued along two general lines:

- Improve the precison in the measurement of CKM parameters and search for inconsistencies in the overconstrained determination of the CKM triangle. Special attention is on the CKM angle γ, which is at present the least well measured parameter of the CKM triangle.

- Perform precision measurements of processes that are dominated by diagrams involving internal loops of virtual particles, such as the box and penguin diagrams illustrated in Figure 1.4. Most extensions of the Standard Model predict the existence of new, heavy

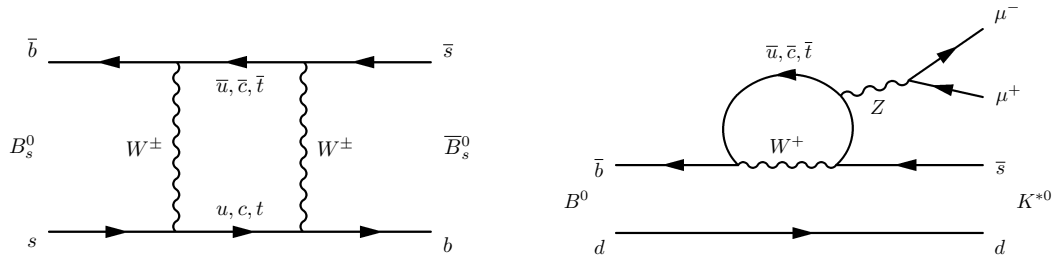

Figure 1.4: Examples of Standard Model loop diagrams: (left) one of the box diagrams mediating $B_s^0 - \overline{B}_s^0$ mixing and (right) the penguin diagram describing the FCNC decay $B^0 \to K^{*0}\mu^+\mu^-$.

particles, which can appear in the virtual loops and modify the value of observables with respect to Standard Model predictions. Of particular interest are observables that are predicted with good precision to be small in the Standard Model, because the relative effect of possible contributions from New Physics can then be large. Prominent examples are the *CP* violating phase ϕ_s in $B_s^0 - \overline{B}_s^0$ mixing and observables in rare Flavour-Changing Neutral Current decays of B^0 and B_s^0 mesons.

Examples of measurements that fall into the second category of searches for New Physics will be discussed in Chapter 6.

Chapter 2

Setting the Stage: A Historical Overview

> The discovery triggered an intense international experimental effort. It also provoked many theoretical speculations which in turn stimulated a variety of experiments.
>
> — James W. Cronin, Nobel lecture, 8 December 1980

This chapter presents a brief historical overview of quark flavour physics in the 20^{th} century, concentrating on some of the major milestones: the introduction of the concepts of strong isospin in 1932 and of strangeness in 1953, the introduction of the Cabibbo mixing angle in 1963; the development of the quark model in the early 1960's; the discoveries of parity violation in 1953 and of *CP* violation in 1964; the postulation by Sakharov, in 1967, of *CP* violation as one of three necessary conditions for the existence of matter in the universe; the proposition of the GIM mechanism in 1970, predicting a fourth quark, and of the CKM mechanism in 1972, postulating a third family of quarks; the discovery of the charm quark in 1974; the first observations of the beauty quark in 1977 and of the top quark in 1994; the first observation of $B^0\overline{B}^0$ mixing in 1987; and, finally, the first significant observations of direct *CP* violation in the $K^0\overline{K}^0$ System and of *CP* violation in the $B^0\overline{B}^0$ system in 2001. More recent measurements in the B and B_s^0 meson systems will be discussed in detail in subsequent chapters.

2.1 Isospin (1932)

The concept of quarks as constituents of mesons and baryons was developed in the early 1960's and started to gain acceptance in the particle physics community only in 1974, when the J/ψ resonance was discovered and interpreted as a bound $c\bar{c}$ state (more about this below). The history of quark flavour physics, however, can be said to begin in 1932 with a paper by Heisenberg in which he investigated the structure of atomic nuclei [10]. Heisenberg noted that the masses of the constituents of the atomic nucleus (neutrons and protons) were almost equal, and so were the forces between pairs of them. He therefore considered protons and neutrons to be different states of the same particle. To distinguish them, he introduced a discrete variable, to which he assigned the value $+1$ for neutrons and the value -1 for protons. The similarity of the forces between all pairs of nucleons implied that the Hamiltonian describing these forces had to be invariant under transformations of this variable. The transformation properties of this variable are those of a spin and Wigner, in a later paper [11], coined the expression "isotopic spin" for this variable, which was later abbreviated to "isospin". The assigned isospin values were also adjusted to exploit better the analogy to a spin: proton and neutron were assigned to an isospin doublet with isospin $I = 1/2$, where the projection $I_z = +1/2$ corresponds to the proton and the projection $I_z = -1/2$ corresponds to the neutron. Similarly, charged and

Table 2.1: Isospin assignment and valence quark content for nucleons and pions.

	p	n	π^+	π^0	π^-
(I, I_z)	(1/2, +1/2)	(1/2, -1/2)	(1, +1)	(1, 0)	(1, -1)
quark content	$\|\, uud \,\rangle$	$\|\, udd \,\rangle$	$\|\, u\overline{d} \,\rangle$	$\frac{1}{\sqrt{2}} \|\, u\overline{u} + d\overline{d} \,\rangle$	$\|\, \overline{u}d \,\rangle$

neutral pions were assigned to an isospin triplet with isospin $I = 1$ and the projections $I_z = +1$, 0 and -1 corresponding to the π^+, π^0 and π^-, respectively.

In today's language, $I_z = +1/2$ corresponds to an up quark (u) or an anti-down quark ($\overline{d}$), $I_z = -1/2$ corresponds to a down quark (d) or an anti-up quark ($\overline{u}$). The isospin of mesons and baryons is obtained by summing over their u and d valence quarks (see Tab. 2.1).

Although isospin is not an exact symmetry, it has been rather successful as a working concept. The reason why it works so well is that the masses of the up quark and the down quark are very similar and much smaller than the QCD scale parameter, i.e. $m_u \approx m_d \ll \Lambda_{\mathrm{QCD}} \approx 200$ MeV.

2.2 Strangeness (1953)

In 1947, new unstable types of particles where discovered in two cloud-chamber photographs of cosmic ray showers [12]. These particles came later to be known as kaons and Λ^0 baryons. As larger numbers of events were observed in various experiments, it became apparent that these new particles were "strangely" behaved: they were copiously produced, with production cross sections typical of strong interactions, but had long lifetimes of a few times 10^{-10} s, which are typical for weakly decaying particles. Pais [13] suggested that this behaviour could be explained by a selection rule that allowed a strong interaction only in processes in which an even number of these strange particles was involved. If an odd number of such strange particles was involved in a process, the interaction could proceed only via the weak force. These particles could then be produced in pairs through the strong interaction — a feature that was later verified experimentally and came to be known as "associated production" — but could decay individually only through the weak interaction. Gell-Mann [14], expanding on Pais' ideas, and independently Nakano and Nishijima [15, 16], introduced a new quantum

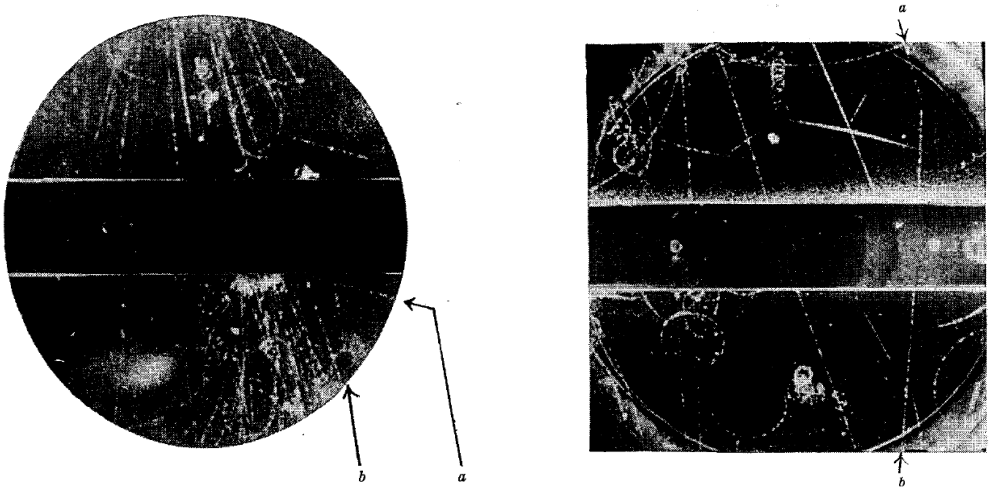

Figure 2.1: First cloud chamber pictures of the (left) neutral and (right) charged long-lived particles discovered in 1947 by Rochester and Butler. The relevant trajectories are marked "a" and "b" (from [12]).

number — which later came to be known as "strangeness" — that had to be conserved in strong interactions but could be violated in weak interactions.

In today's language, one negative unit in strangeness corresponds to a strange quark (s) and one positive unit in strangeness corresponds to an anti-strange quark ($\overline{s}$). Associated production of strange particles is the creation of an $s\overline{s}$ pair in strong interaction and the decay of a strange particle is due to a weak $s \to u\,W^-$ transition.

2.3 Parity violation (1956)

A puzzling experimental observation related to strange particles was the measurement of two spin-0 states — dubbed θ^+ and τ^+ — that had "closely identical" [17] masses and lifetimes, indicating that they were in fact one and the same particle. However, the θ^+ decayed into two pions, while the τ^+ decayed into three pions. Since both the θ^+ and the pion are spin-0 particles, the two pions from the θ^+ decay had to be produced with relative angular momentum $L_{\pi\pi} = 0$ to conserve angular momentum in the decay. The parity P of the final state is $P = (-1)^L = +1$. The θ^+ therefore had to have even parity, if parity was conserved in the decay. For similar arguments, the three pions from the τ^+ decay had to be produced in an overall P odd state, indicating odd parity for the τ^+. These experimental facts led Lee and Yang to question [17] the hypothesis of parity conservation in weak interactions. Surveying existing literature they found convincing experimental evidence that demonstrated parity conservation in strong and electromagnetic interactions, but not a single measurement that proved parity was conserved in the weak interaction.

Lee and Yang went on to suggest two possible experiments that would put their hypothesis to the test: the measurement of the angular distribution of electrons from the β decay of polarized ^{60}Co and the measurement of the angular distribution between muons and electrons from the decay $\pi \to \mu\,\nu_\mu$ followed by $\mu \to e\,\nu_e\,\nu_\mu$.

In the first type of experiment, $^{60}_{27}\mathrm{Co} \to {}^{60}_{28}\mathrm{Ni}^\star + e^- + \overline{\nu}_e$ is a Gamow-Teller transition in which the spin of the nucleus changes by one unit (from spin-5 for the ^{60}Co nucleus to spin-4 for the excited ^{60}Ni* nucleus). To satisfy angular momentum conservation, the spins of the final-state electron and neutrino therefore must both point in the direction of the spin of the decaying ^{60}Co nucleus. Electrons emitted in the direction parallel to the spin of the decaying ^{60}Co nucleus therefore have their spin $\vec{\sigma}$ and momentum $\vec{p}$ pointing in the same direction, i.e. $\vec{\sigma} \cdot \vec{p} > 0$ while electrons emitted in the opposite direction have their spin and momentum pointing in opposite directions, i.e. $\vec{\sigma} \cdot \vec{p} < 0$. Momentum being a vector and angular momentum being an axial vector, their scalar product changes sign under the parity transformation. If parity is conserved in weak decays, $\vec{\sigma} \cdot \vec{p}$ therefore has to be zero on average and the angular distribution of electrons has to be up-down symmetric with respect to the spin direction of the polarized ^{60}Co source. In the second type of experiment, analogous arguments show that the angular distribution between muons and electrons must be forward-backward symmetric if parity is conserved in the two subsequent weak decays.

Both experiments were carried out soon after [18–20] and found large asymmetries, demonstrating that parity (as well as the charge conjugation and time reversal symmetries) are in fact violated in these weak decays. As an example, the result of the ^{60}Co β-decay experiment is shown in Figure 2.2. These observations triggered Salam [21], Landau [22] and Lee and Yang [23] to speculate about the nature of the neutrino: if neutrinos are massless, they can be described by a single two-component field, one for a left-handed neutrino and the other for a right-handed antineutrino. This description of neutrinos was in accordance with experimental observations and would automatically lead to a maximal violation of parity, charge conjugation and time reversal symmetry in β decays involving neutrinos. Feynman and Gell-Mann [24] pointed out that this mechanism alone cannot explain parity violation in processes that do not involve neutrinos, such as the orginal "$\theta - \tau$ puzzle" that had led Lee and Yang

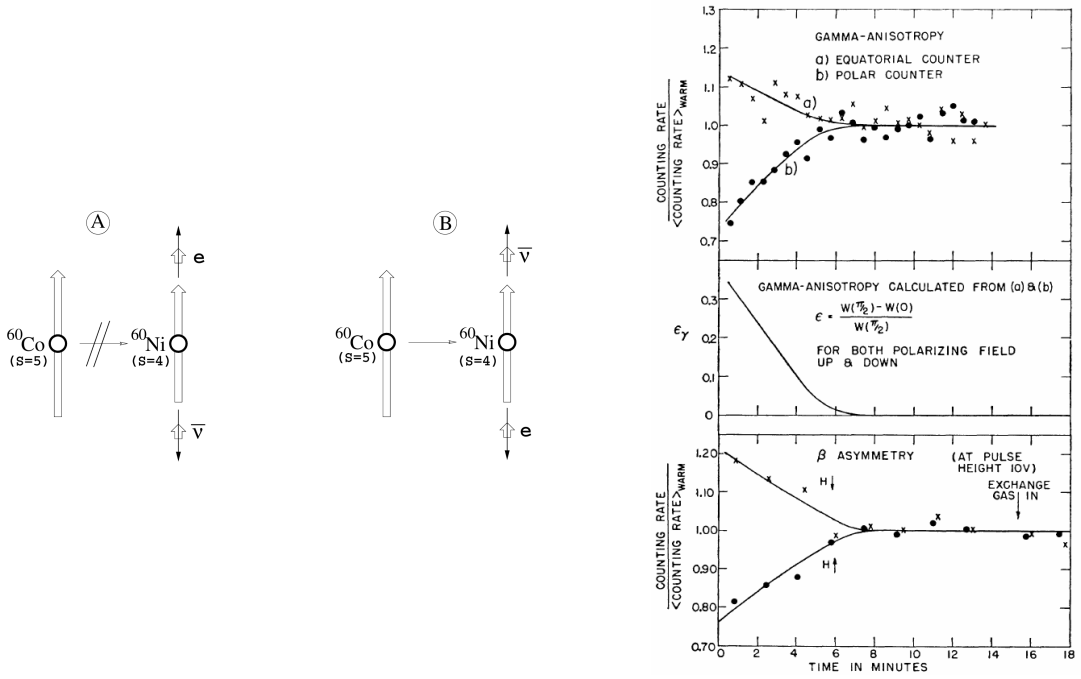

Figure 2.2: Observation of parity violation in nuclear β decay: the panels on the left illustrate the spin configurations in the β decay that are (A) forbidden and (B) allowed if parity is maximally violated and only right-handed antineutrinos participate in the weak interaction. The panels on the right show the result of the experiment by Wu *et al.*. Here, the lower panel shows the measured anisotropy of electrons from the β decay of the ^{60}Co nuclei, for two polarities of the source polarization. A clear asymmetry is observed, which decreases as a function of time, as the polarization of the source decays away. The source polarization is monitored as a function of time by measuring the anisotropy of γ-ray emission from the decay of the excited ^{60}Ni* daughter nucleus, as shown in the upper and middle panels (from [18]).

to question parity conservation in the first place. Feynman and Gell-Mann went on to propose that the weak interaction was due to equal amounts of vector and axial vector coupling and coupled to the chirality projection $\frac{1+i\gamma_5}{2}|\,\Psi\,\rangle$ for all fermions $|\,\Psi\,\rangle$ entering the interaction. Here, $\gamma_5 = \gamma_0\,\gamma_1\,\gamma_2\,\gamma_3$ and the γ_i are the usual Dirac matrices. As a consequence, parity and charge conjugation are then maximally violated in weak interactions.

2.4 Cabibbo Angle (1963)

Another puzzling observation with regard to strange particles was their branching fraction in semileptonic decays, which was measured to be much smaller than that for similar decays of non-strange particles. This seemed at variance with the assumption of a universal coupling constant for all weak decays. To resolve the discrepancy, Cabibbo proposed [25] in 1963 that the total charged weak current, J_μ, could actually consist of a linear combination of a strangeness conserving part, $J_\mu^{(0)}$, and a strangeness changing part, $J_\mu^{(1)}$. Since the squared sum of the two contributions had to preserve unity, he expressed the linear combinations in terms of a mixing angle θ as

$$J_\mu \;\equiv\; \cos\theta\; J_\mu^{(0)} \;+\; \sin\theta\; J_\mu^{(1)}$$

Comparing existing measurements of the branching fractions for the decays $K^+ \to \mu^+\nu_\mu$ and $\pi^+ \to \mu^+\nu_\mu$, and taking into account the apprpriate phase-space factors,

$$\frac{\Gamma(K^+ \to \mu^+\nu_\mu\,)}{\Gamma(\pi^+ \to \mu^+\nu_\mu)} \;=\; \frac{\sin^2\theta}{\cos^2\theta} \;\times\; \frac{(m_K(1-m_\mu^2/m_K^2))^2}{(m_\pi(1-m_\mu^2/m_\pi))^2}\;,$$

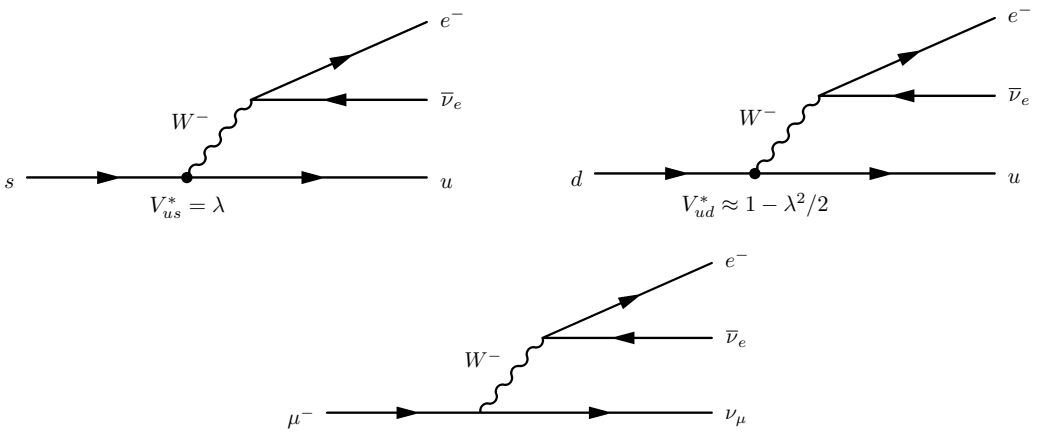

Figure 2.3: Feynman diagrams for the decays (top left) $s \to u e^- \overline{\nu}_\mathrm{e}$, (top right) $d \to u e^- \overline{\nu}_\mathrm{e}$ and (bottom) $\mu^- \to \nu_\mu e^- \overline{\nu}_\mathrm{e}$.

Cabibbo estimated the value of the mixing angle to $\theta \approx 0.257$ rad. From a similar comparison of the observed branching fractions for $K^+ \to \pi^0\, e^+\, \nu$ and $\pi^+ \to \pi^0\, e^+\, \nu$ he obtained the consistent result $\theta \approx 0.26$ rad. Moreover, Cabibbo's hypothesis could explain why observed decay rates in nuclear β-decays appeared to be slightly smaller than expected from the assumption of a universal weak coupling constant. Using Cabibbo's hypothesis, the decay $n \to p e^- \overline{\nu}_\mathrm{e}$ is mediated by the strangeness-conserving part of the current and its rate is therefore reduced by a factor $\cos^2\theta$.

The mixing angle has come to be known as the Cabibbo angle, θ_C, and its sine is equal to the parameter λ in the Wolfenstein parametrization of the Unitarity Triangle. The current world average [1] of its value is $\sin\theta_C = (0.2252 \pm 0.0009)$ rad, not far from Cabibbo's initial estimates. The underlying processes in terms of the quark language are illustrated in Figure 2.3, where the weak interaction couples to a linear combination of the down-type quarks,

$$| d' \rangle \;=\; \cos\theta_C \,| d \rangle \;+\; \sin\theta_C \,| s \rangle \;.$$

2.5 *CP* violation (1964)

The $V - A$ character of weak interactions implies that both parity, P, and charge conjugation, C, are maximally violated in these interactions. However, Landau [22] and Okun [26] soon realized that symmetry was still preserved under the combined transformation $C \times P$, as illustrated by the naive sketch shown in Figure 2.4. Feynman, in one of his famous lectures [27], expressed his relief as follows:

> "Therefore, at long last, it is really true that right and left symmetry is still maintained ... instead of two rules in our list of symmetries, two of these rules go together to make a new rule, which says that matter to the right is symmetrical to antimatter to the left."

One year after the Feynman lectures were published, a small violation of the *CP* symmetry was observed in the weak decay of neutral kaons to two pions. In order to understand this measurement, it is necessary to very briefly introduce the phenomenology of the neutral kaon system. A more comprehensive discussion of particle-antiparticle mixing in the system of neutral kaons and other neutral meson-antimeson systems will be given in Chapter 3.1.

The only quantum number that distinguishes a neutral kaon from a neutral antikaon is strangeness. Since strangeness is not conserved in weak interactions, $K^0 - \overline{K}^0$ transitions can

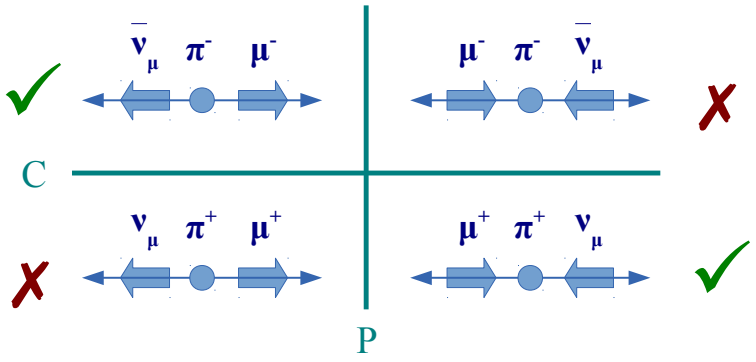

Figure 2.4: Illustration of P and C violation and CP invariance in $\pi \to \mu\nu_\mu$ decays. Thin, long, solid arrows indicate the momenta of the final-state particles while the shorter, thick, shaded arrows indicate their spin. The parity operator transforms the diagrams on the left to those on the right, while charge conjugation transforms diagrams in the top row to those in the bottom row. The CP related processes shown in the top left and bottom right are allowed and happen with the same rate, those shown in the top right and bottom left are forbidden.

$$K^0 \leftrightarrow \left\{ \begin{array}{c} 2\pi \\ 3\pi \end{array} \right\} \leftrightarrow \overline{K}^0$$

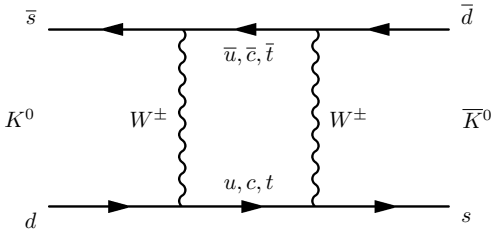

Figure 2.5: $K^0 - \overline{K}^0$ mixing through (left) multi-pion intermediate states accessible to both K^0 and $\overline{K}^0$ and (right) box diagrams with the exchange of two $W^\pm$ bosons and quark-antiquark intermediate states (right).

occur through processes that are mediated by the weak interaction. In the language of the 1960's, such processes involve real or virtual intermediate states of pions that are accessible to both K^0 and $\overline{K}^0$ as illustrated in the left panel in Figure 2.5. In today's language, they inolve box diagrams with an exchange of two W bosons as shown in the right panel in Figure 2.5.

Gell-Mann and Pais [28] realized that $K^0 - \overline{K}^0$ mixing can lead to the existence of two neutral kaon states with different decay modes and very different lifetimes. Since kaons and antikaons can mix, they have to be described as a coupled system

$$|\,\Psi\,\rangle \;=\; a \cdot |\,K^0\,\rangle \;+\; b \cdot |\,\overline{K}^0\,\rangle$$

and it is possible to define states $|\,K_1^0\,\rangle$ and $|\,K_2^0\,\rangle$ that are eigenstates of the CP operator,

$$\begin{aligned} |\,K_1^0\,\rangle &= \tfrac{1}{\sqrt{2}} \cdot \Big(|\,K^0\,\rangle + |\,\overline{K}^0\,\rangle \Big) \qquad \text{with} \qquad CP\,|\,K_1^0\,\rangle = +|\,K_1^0\,\rangle\,, \\ |\,K_2^0\,\rangle &= \tfrac{1}{\sqrt{2}} \cdot \Big(|\,K^0\,\rangle - |\,\overline{K}^0\,\rangle \Big) \qquad \text{with} \qquad CP\,|\,K_2^0\,\rangle = -|\,K_2^0\,\rangle\,. \end{aligned}$$

If CP is conserved in weak interactions[1], the CP eigenstates are also eigenstates of the weak interaction, meaning that K_1^0 and K_2^0 are the particles that will be observed in weak decays.

[1] In fact, Gell-Mann and Pais [28] based their argument on charge conjugation invariance; Lee, Oehme and Yang [29] pointed out that this assumption was not justified in weak interactions and derived a phenomenology of neutral kaon decays using the CPT theorem. They realized that the two weak eigenstates do not necessarily have to be orthogonal to each other. The discovery of CP violation in the neutral kaon system demonstrated later that this is indeed not the case.

The by far dominant decay mode for neutral kaons is that to two pions. Kaons and pions being pseudoscalar particles with internal spin $J = 0$, angular momentum conservation implies that the two pions must be produced in this decay with relative angular momentum $L = 0$ and with $CP\,|\,\pi\pi\,\rangle = -1^L = +1$. Therefore, the final state in this decay is a *CP*-even eigenstate and only the *CP*-even state K_1^0 can decay into two pions if *CP* symmetry is concerved in the weak interaction. The *CP* odd state K_2^0 can only decay into three pions or in semileptonic decays to $\pi e \nu_{\mathrm{e}}$ or $\pi \mu \nu_{\mu}$. All these decays are, however, significantly suppressed. The decay into three pions is phase-space suppressed since the masses of three pions add up to almost that of the kaon, while the semileptonic decays to $\pi e \nu_{\mathrm{e}}$ and $\pi \mu \nu_{\mu}$ are suppressed by parity violation. This is easiest seen in the pion rest frame, in which the momenta of the charged lepton and the (anti-)neutrino point into opposite directions. Due to the conservation of angular momentum in the decay, their spins have to be opposite as well, i.e. they are produced in one of the two "forbidden" configurations shown in Figure 2.4. Putting all these arguments together, Gell-Mann and Pais argued that the neutral kaon system should have a short-lived component, the K_1^0, that decayed to two pions and a component with a much longer lifetime, the K_2^0, that decayed into three pions and semileptonically. The long-lived neutral kaon predicted by Gell-Mann and Pais was soon after discovered by Lederman and collaborators [30] and its lifetime was subsequently measured to be more than 500 times that of the short-lived neutral kaon.

The large difference in lifetimes allows to isolate a pure beam of K_2^0 particles. A beam of neutral kaons can be produced by shooting a beam of pions or protons into a solid target. Associated production of $s\overline{s}$ pairs leads to the generation of similar numbers of of K^0ăand $\overline{K}^0$ mesons, corresponding to a roughly equal admixture of the K_1^0 and K_2^0 components. Due to the large difference in the lifetimes τ_1 and τ_2 of the K_1^0 and K_2^0, however, the fraction of the K_1^0 component in the beam will decrease rapidly and for times $t \gg \tau_1$ an almost pure K_2^0 state will remain. To quantify this statement, by letting a neutal kaon beam travel in vacuum for twenty K_1^0 lifetimes, the K_1^0 component will have reduced to $e^{-20\,\tau_1} \approx 2 \times 10^{-9}$ of its initial intensity, while the intensity of the K_2^0 component will remain at $e^{-20\,\tau_1/\tau_2} \approx 96\%$ of its initial value.

As was first realized by Pais and Piccioni [31], an additional complication appears if interactions in nuclear matter are taken into consideration. By definition, the *CP* eigenstates K_1^0 and K_2^0 are equal admixtures of K^0 and $\overline{K}^0$. However, K^0 and $\overline{K}^0$ have different strong interaction cross sections with nuclear matter. For example, processes like $\overline{K}^0 + p \to \Lambda^0 + \pi^+$ or $\overline{K}^0 + n \to \Lambda^0 + \pi^0$ are possible while the K^0 can only undergo charge exchange processes like $K^0 + p \to K^+ + n$. In the language of quarks, this is due to the fact that the $\overline{K}^0$ contains a $\overline{d}$ quark that can annihilate with the d valence quarks present in nuclear matter, while there is no equivalent process for the K^0, which contains a d quark. Therefore, when a K_2^0 beam traverses nuclear matter, the $\overline{K}^0$ component will be absorbed faster than the K^0 component. This corresponds to the regeneration of a K_1^0 component in the beam, as is most easily seen by considering an extreme scenario in which the $\overline{K}^0$ component is completely absorbed due to nuclear interactions. What is left then is a pure K^0 component with

$$|\,K^0\,\rangle \;= \frac{1}{\sqrt{2}} \cdot (|\,K_1\,\rangle \;+\; |\,K_2\,\rangle) \;.$$

This effect has become known as "regeneration" and was first observed by Muller, Good *et al.* [32, 33]. They generated a beam of neutral kaons by impinging a π^- beam on a hydrogen target, let the K_1^0 component decay away and passed the remaining K_2^0 beam through a regenerator plate embedded in a large bubble chamber. As illustrated in Figure 2.6, they found clear evidence for two-body decays just downstream of the regenerator plates, demonstrating the regeneration of a K_1^0 component.

A beam of K_2^0 particles was also employed in the famous experiment by Christenson, Cronin, Fitch and Turlay [34], in which they discovered *CP* violation in the neutral kaon system. Neutral kaons were produced in collisions of 30 GeV protons in an internal Be target

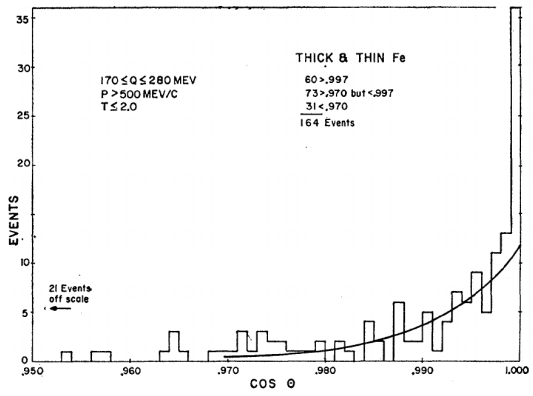

Figure 2.6: Distribution of $\cos\theta$, where θ is the angle between the direction of the incoming kaon beam and the vector sum of the reconstructed momenta of the two daughter particles, for two-prong events that occured within two K_1^0 lifetimes after the regenerator plate and for which energy conservation was fulfilled under the $K^0 \to \pi^+\pi^-$ hypothesis. The angle θ should be zero for two-body decays due to momentum conservation, but it will in general be different from zero for multi-body decays. The observed excess of events at $\cos\theta \approx 1$ (for which both energy and momentum are conserved) is proof for decays into two charged pions and demonstrates K_1^0 regeneration in the plates (from [33]).

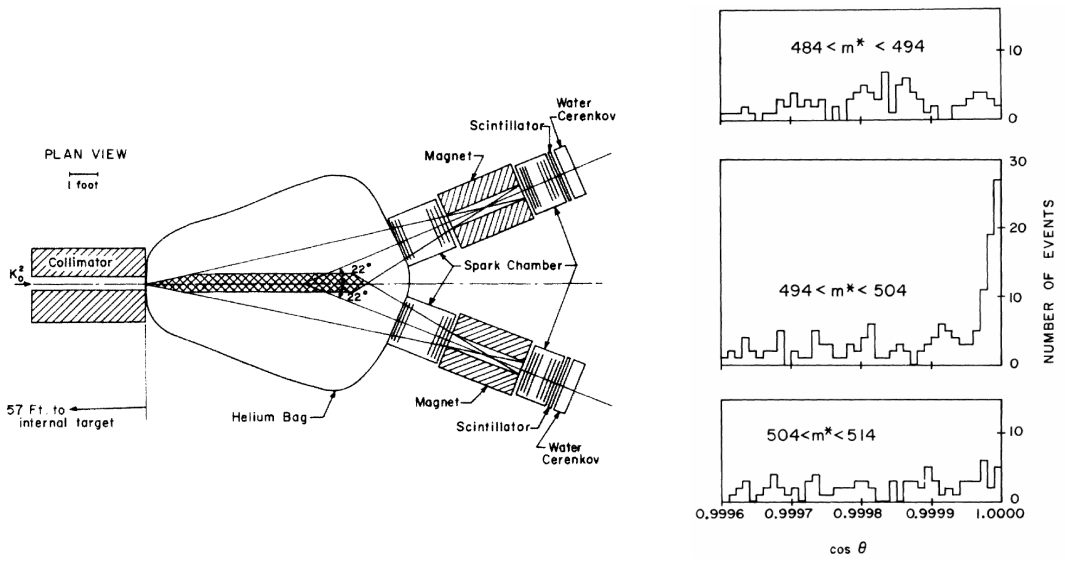

Figure 2.7: Discovery of *CP* violation by the observation of 2-body decays of the long-lived neutral kaon. A sketch of the experimental setup is shown on the left, the result of the measurement in terms of the variable cos *theta* on the right. Here, the middle panel shows the distribution of $\cos\theta$ for candidates with dipion invariant mass close to the mass of the K^0 meson, while the upper and lower panels show the distributions for dipion candidates with invariant mass above and below the K^0 mass, respectively. For further details see the main text (from [34]).

at the Brookhaven AGS and the K_1^0 component was left to decay away in a 57 ft long vacuum transfer line between the target and the decay volume watched by the detector. A sketch of the decay volume and the detector is shown in Figure 2.7. The decay volume was embedded in a large Helium bag to minimize K_1^0 generation and the detector consisted of a two-arm dipole magnet spectrometer to measure the directions and momenta of two charged pions. Candidates were characterized in terms of two discriminating variables, namely the invariant mass of the pair of pions and the angle θ between the sum of their reconstructed momenta and the direction of the incoming kaon beam. Due to momentum conservation in the decay, the angle θ should be zero for true two-body decays, while it will in general be different from zero for multi-body decays. The result of the measurement is also shown in Figure 2.7. For

dipion candidates with invariant mass above or below the kaon mass, the distribution in $\cos\theta$ is indeed flat as expected for a sample of two pions from multibody decays. For candidates with invariant mass close to the mass of the kaon, however, a clear excess is seen at $\cos\theta \approx 1$. For these candidates, both energy conservation and momentum conservation are fulfilled, i.e. they establish a signal of *CP* violating decays to two charged pions in the K_2^0 beam. Various sources of potential background were studied, but none was identified that could fake the observed signal. In particular, potential background from K_1^0 regeneration in the Helium gas was calculated to be a factor of 10^6 too small to account for the observed effect. As a cross-check, data were also collected with a regenerator plate inserted at different positions within the decay volume. It was found that the signal candidates from the main measurement and reconstructed two-body decays from the regenerated K_1^0 component in the control sample looked alike in all relevant aspects. From the observed excess of 45 ± 9 events, Christenson, Cronin, Fitch and Turlay calculated the relative branching fraction for the *CP* violating decay to $\pi^+\pi^-$ to be $\mathrm{BF}\,(K_2^0 \to \pi^+\pi^-)/\,\mathrm{BF}\,(K_2^0 \to \text{all charged modes}) = (2.0 \pm 0.4) \times 10^{-3}$.

If *CP* is violated in the neutral kaon system, the weak eigenstates are not identical to the eigenstates of the *CP* operator. The names K_S^0 and K_L^0 were subsequently introduced for the short-lived and long-lived eigenstates, to distinguish them from the *CP* eigenstates K_1^0 and K_2^0, with

$$\begin{aligned} K_L^0 &\equiv \frac{1}{\sqrt{1+|\varepsilon|^2}}\,(K_2^0 + \varepsilon \cdot K_1^0) \\ K_S^0 &\equiv \frac{1}{\sqrt{1+|\varepsilon|^2}}\,(K_1^0 - \varepsilon \cdot K_2^0)\ . \end{aligned}$$

Christenson, Cronin, Fitch and Turlay derived $|\varepsilon| \approx 2.3 \times 10^{-3}$ from their measurement, close to today's world average [1] of $|\varepsilon| = (2.228 \pm 0.011) \times 10^{-3}$, obtained from a fit to available $K \to \pi\pi$ data.

An important proof that the observed effect was indeed due to *CP* violating decays of the long-lived neutral kaon was the observation of an interference with the *CP* allowed decays to two charged pions of short-lived kaons. To demonstrate this interference, a measurement of the decay rate to two charged pions was performed [35, 36] in a beam of long-lived neutral kaons passing through a diffuse beryllium regenerator of variable density. In the presence of a regenerator, the kaon state is

$$|\,\Psi\,\rangle = |\,K_2^0\,\rangle + (\varepsilon + A_r)\,|\,K_1^0\,\rangle,$$

where A_r is the coherent regeneration amplitude. The expected decay rate to two charged pions is proportional to

$$|\varepsilon + A_r|^2 \;=\; |\varepsilon|^2 \;+\; |A_r|^2 \;+\; 2\,|\varepsilon|\,|A_r|\cos\alpha\ ,$$

where α is the phase difference between ε and A_r. A sizeable interference effect can be obtained by tuning the regenerator density such that $A_r \approx \varepsilon$. The measured $\pi^+\pi^-$ rate as a function of the regenerator density is shown in Figure 2.8. A fit to the data shows $\cos\theta = 1.00 \pm 0.21$, i.e. full constructive interference between the two amplitudes.

Soon after its discovery in decays of the long lived neutral kaon into two charged pions, *CP* violation in the neutral kaon system was also observed in the decay into two neutral pions [37, 38] and by the measurement of a non-vanishing charge asymmetry

$$\delta_\ell \;\equiv\; \frac{\Gamma(K_L^0 \to \pi^-\ell^+\nu_\ell) \;-\; \Gamma(K_L^0 \to \pi^+\ell^-\overline{\nu}_\ell)}{\Gamma(K_L^0 \to \pi^-\ell^+\nu_\ell) \;+\; \Gamma(K_L^0 \to \pi^+\ell^-\overline{\nu}_\ell)} \qquad (\ell^\pm \;\in\; e^\pm, \mu^\pm)$$

in semileptonic decays to electrons [39] and to muons [40]. By definition, the K_2^0 is an equal admixture of K^0 and $\overline{K}^0$ and, as illustrated in Figure 2.9, the K^0 component decays to negative

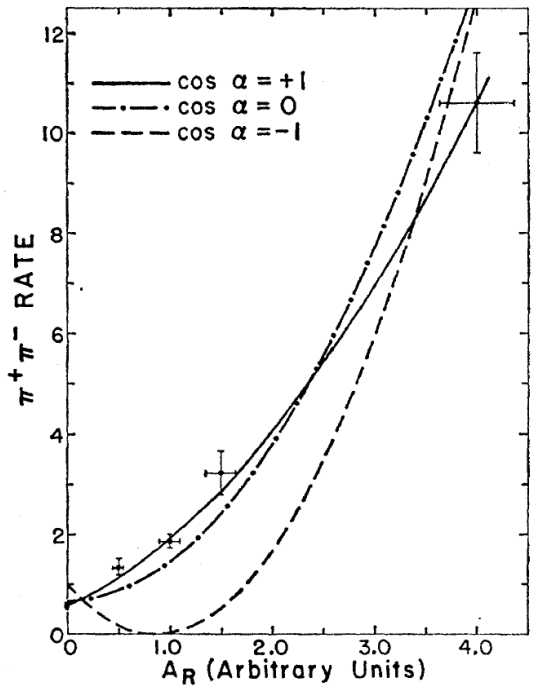

Figure 2.8: Observed $\pi^+\pi^-$ rate as a function of the coherent regeneration amplitude A_r. The curves show the best fit to the data for three hypotheses for the interference angle α. Only the curve for $\cos\alpha = 1$ agrees well with the data (from [36]).

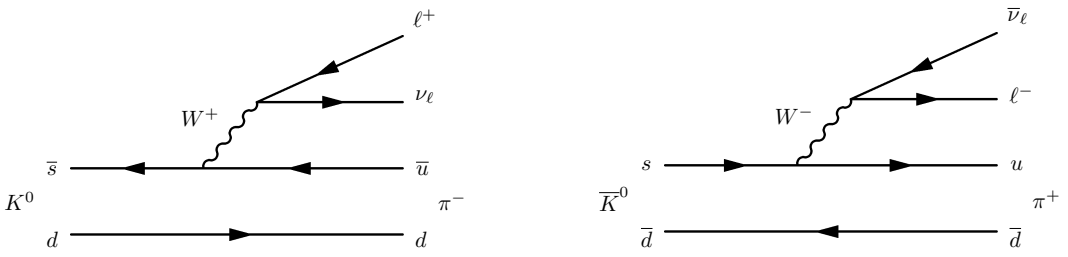

Figure 2.9: Feynman diagrams for the semileptonic decays of (left) K^0 and (right) $\overline{K}^0$.

leptons while the $\overline{K}^0$ component decays to positive leptons. If the K_L^0 were identical to the K_2^0, one would therefore expect equal numbers of semileptonic decays to negative and positive leptons. Both measurements showed an excess of positive leptons, confirming that the K_L^0 is not identical to the K_2^0.

That the laws of nature should not be invariant under the *CP* symmetry initially left the particle physics community in shock. However, in 1967 Sakharov [41] pointed out that *CP* violation (together with baryon number violation and thermal non-equilibrium) is in fact a necessary ingredient for the creation of a matter dominated universe from the matter-antimatter symmetric initial state that is postulated if the universe was born out of pure energy in a Big Bang. Today, the Standard Model naturally incorporates *CP* violation in weak interactions via the complex phase in the CKM quark-mixing matrix. However, the effect seems to be more than nine orders of magnitude too small to explain the amount of matter observed in the universe. This discrepancy is one of the great outstanding problems of fundamental physics today.

2.6 GIM mechanism (1970)

In an attempt to classify the plethora of new mesons and baryons discovered in cosmic rays and in experiments at the new particle accelerators, Gell-Mann [42] and Zweig [43] had derived in 1964 what came to be known as the quark model[2]. According to their model, all known mesons and baryons could be described as composite $(q\overline{q})$ and (qqq) states, respectively, with three types of quarks q: up (u), down (d) and strange (s). Cabibbo had shown that the weak interaction then coupled to a linear combination $d' = \cos\theta_C \cdot d + \sin\theta_C \cdot s$ of the down and strange quark. The simplest renormalizable theory of the weak interaction was then considered to be described by a Lagrangian

$$L_W \;=\; g\, W_\lambda\, J^\lambda \;+\; \text{h.c.}$$

with the weak current

$$J^\lambda \;=\; \overline{\nu}_{\rm e} \cdot \gamma^\lambda (1-\gamma_5) \cdot e^- \;+\; \overline{\nu}_\mu \cdot \gamma^\lambda (1-\gamma_5) \cdot \mu^- \;+\; \overline{u} \cdot \gamma^\lambda (1-\gamma_5) \cdot d' \;,$$

a single, electrically charged, massive intermediate vector boson, W, and a coupling constant g given by

$$\frac{G_F}{\sqrt{2}} \;=\; \frac{g^2}{m_W^2} \;,$$

where G_F is the Fermi constant and m_W is the mass of the intermediate vector boson. However, it seemed difficult to reconcile this theory with certain observed features of flavour-changing interactions between quarks. One of these features was the small splitting between the masses of the K_S^0 and K_L^0 states in the neutral kaon system, which pointed to a strong suppression of so-called $\Delta S = 2$ amplitudes that change the strangeness by two units. The $\Delta S = \Delta Q$ rule reflected the strong suppression of flavour-changing neutral hadronic current processes such as $K^+ \to \pi^+ \ell^+ \ell^-$ or $K_L^0 \to \mu^+ \mu^-$. For example, the branching fraction for the decay $K_L^0 \to \mu^+ \mu^-$ had been measured to be of the order of 10^{-7}, while that for the corresponding charged current decay $K^+ \to \mu^+ \nu_\mu$ is about 63.5%.

Glashow, Iliopoulos and Maiani postulated [46] in 1970 that these observed features could be explained by the introduction of a fourth quark, which they dubbed "charm" (c). In extention of Cabibbo's concept, the weak interaction would couple to the up and charm quarks and to a linear combination of the down and strange quarks,

$$(\, d' \,,\, s' \,) \;\equiv\; C_H \begin{pmatrix} d \\ s \end{pmatrix} \;=\; \begin{pmatrix} \cos\theta_C & \sin\theta_C \\ -\sin\theta_C & \cos\theta_C \end{pmatrix} \begin{pmatrix} d \\ s \end{pmatrix} \;.$$

Since the mixing matrix C_H is unitary, i.e. $C_H^\dagger C_H = 1$, the neutral hadronic current then becomes

$$\begin{aligned} J_{NC}^\lambda \;&=\; \left(\overline{d}' \,,\, \overline{s}' \right) \, \gamma^\lambda \, (1+\gamma_5) \begin{pmatrix} d' \\ s' \end{pmatrix} \\ &=\; \left(\overline{d} \,,\, \overline{s} \right) \, C_H^\dagger \, \gamma^\lambda \, (1+\gamma_5) \, C_H \begin{pmatrix} d \\ s \end{pmatrix} \\ &=\; \left(\overline{d} \,,\, \overline{s} \right) \, \gamma^\lambda \, (1+\gamma_5) \begin{pmatrix} d \\ s \end{pmatrix} \\ &=\; \overline{d} \, \gamma^\lambda \, (1+\gamma_5) \; d \;+\; \overline{s} \, \gamma^\lambda \, (1+\gamma_5) \; s \end{aligned}$$

and flavour-changing neutral hadronic currents cancel naturally. Complete cancelation occurs for the case of massless quarks, in practice the cancellation is almost complete since the mass

[2] An earlier version was the so-called "eightfold way", developed by Gell-Mann [44] and Ne'eman [45].

differences between the quarks are small compared to the mass of the vector boson that mediates the weak interaction. Flavour changing neutral hadronic currents as well as $\Delta S = 2$ transitions can occur at higher order but are suppressed by the smallness of the weak coupling constant. Their study is one of the most important aspects in quark flavour physics today as will be discussed in Chapter 6.

Already in 1961, Glashow had postulated [47] a renormalizable theory of the electroweak interaction of leptons, which was based on the gauge group $SU(2) \otimes U(1)$. As well as the two charged W bosons, his model contained two neutral vector bosons, one massive, now known as the Z or Z^0, and the other massless, the photon, In their 1970 paper [46], Glashow, Iliopoulos and Maiani pointed out that the additional quark proposed by them created a symmetry between the quark sector and the lepton sector and proposed to extend Glashow's electroweak theory to the quark sector. They also pointed out that the introduction of a neutral vector boson did not change the cancellation in neutral currents described above.

2.7 CKM mechanism (1972)

In 1971, Weinberg discussed several physical processes that were known to suffer from divergences in "conventional models" considered at the time and demonstrated that these processes were free of divergences in the proposed renormalizable $SU(2)_L \otimes U(1)$ model of electro-weak interactions [48]. Following Glashow, Iliopoulos and Maiani, he also introduce a fourth quark to explain the suppression of flavour-changing neutral hadronic currents.

One year later, Kobayashi and Maskawa published their now famous paper [49] in which they explored various mechanisms by which *CP* violation could be encorporated in the model proposed by Weinberg. Observing that the model with two left-handed quark doublets,

$$\begin{pmatrix} u \\ d \end{pmatrix} , \begin{pmatrix} c \\ s \end{pmatrix}$$

cannot encorporate *CP* violation since the 2×2 mixing matrix that couples the two doublets

$$U = \begin{pmatrix} \cos\theta_C & \sin\theta_C \\ -\sin\theta_C & \cos\theta_C \end{pmatrix}$$

has only one free parameter (the mixing angle θ_C) and is therefore real. Kobayashi and Maskawa went on to propose an "interesting model of *CP*-violation", namely that there could be a sextuplet of quarks, decomposed into three left-handed $SU(2)$ doublets and six right-handed $SU(2)$ singlets. As already discussed here in Section 1.3, not all complex phases of the unitary 3×3 mixing matrix can then be absorbed into the phase convention and *CP* violation effects can occur through the interference of different components of the current with different complex phases. An attractive feature of the model was that *CP* violation effects at the lowest order appear only in non-leptonic $\Delta S \neq 0$ processes and in semileptonic decays of strange mesons, in accordance with experimental observations.

Kobayashi and Maskawa's paper was published two years before the discovery of the charm quark confirmed the existence of two quark doublets and initially it went mostly unnoticed. It was the discovery of the bottom quark in 1977 that finally drew the attention of the community to their work and the "CKM mechanism" — so named to honour the earlier work by Cabibbo — then quickly gained popularity.

2.8 Charm quark (1974)

By the summer of 1974, essentially all ingredients of what is known today as the Standard Model of particle physics had been developed and a coherent picture started to gradually

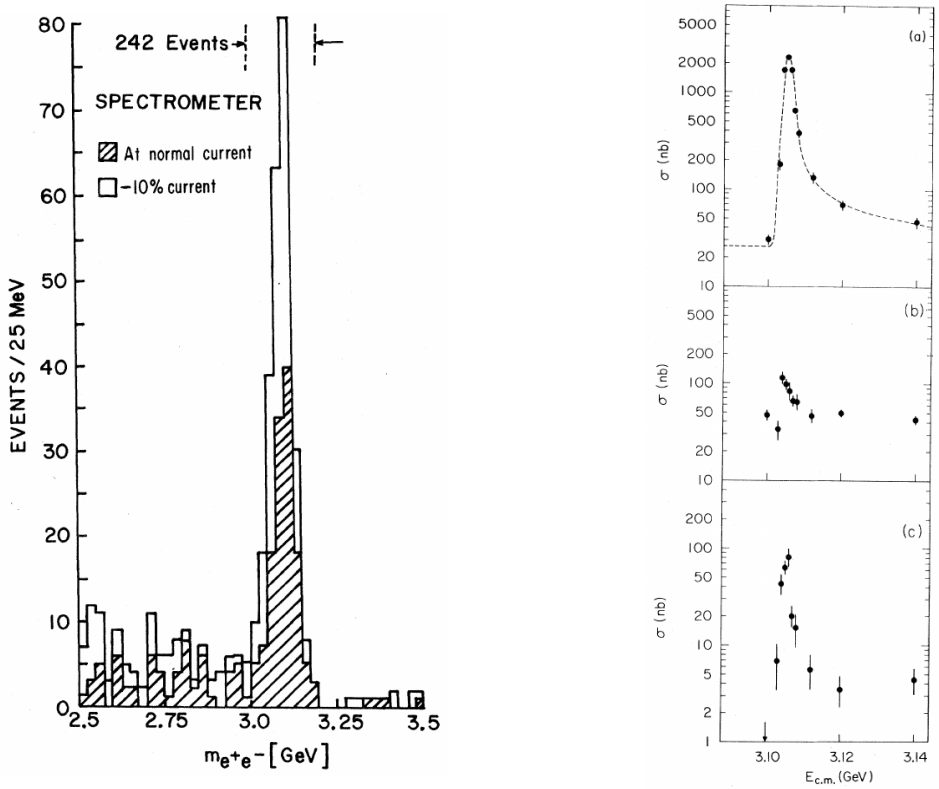

Figure 2.10: Discovery of (left) the ψ at BNL and (right) the J at SLAC. The panel on the left shows the e^+e^- invariant mass spectrum in e^+e^-X events produced in proton collisions on a beryllium target. The panels on the right show the measured cross section to (top) e^+e^-, (middle) $\mu^+\mu^-$ and (bottom) $\pi^+\pi^-$ or K^+K^- pairs as a function of the center of mass energy of the e^+e^- collision (from [50] and [51], respectively).

emerge. Searches for the charm were ongoing, the favoured method being to look for "open charm", i.e. particles composed of a charm quark and lighter quarks. Then, in November 1974, a narrow resonance with a mass of about 3.1 GeV was discovered simultaneously in the invariant-mass spectrum of e^+e^- pairs produced in the reaction $p + \mathrm{Be} \to e^+e^- + X$ at BNL [50] and in the e^+e^- interaction cross section at SLAC [51]. The signals observed in the two measurements are shown in Figure 2.10. The BNL group called this resonance "J" and the SLAC group named it "ψ".

The observation of the J/ψ was quickly confirmed by measurements at Frascati [53] and DESY [54]. The measured width of the signal was in all cases compatible with the experimental resolution. From a fit to the measured branching fractions to e^+e^-, $\mu^+\mu^-$ and hadrons, the SLAC group computed a total decay width of about (69 ± 15) keV [52], corresponding to a lifetime of about 10^{-20} s. Since the resonance was produced in e^+e^- collisions, its spin-parity could be inferred to be $J^{PC} = 1^{--}$. This was confirmed by the SLAC group in measurements of the interference between the resonant and non-resonant production of $\mu^+\mu^-$ pairs, and by the measurement of the angular distributions in the e^+e^- and $\mu^+\mu^-$ final states [52] as illustrated in Figure 2.11. About two weeks after the discovery of the J/ψ, the SLAC group also reported the observation of a second narrow resonance at 3.7 GeV [55].

Their narrow width meant that these resonances could not be excited states of lighter hadrons. Such excited states would decay through strong or electromagnetic processes, resulting in much shorter lifetimes and larger decay widths. The interpretation of the J/ψ and the resonance at 3.7 GeV as the $(1s)$ and $(2s)$-states in the spectrum of bound $c\bar{c}$ states was first proposed in Refs. [56] and [57], respectively. Additional bound $c\bar{c}$ states were predicted in Refs. [57] and [58] and several of these were observed soon after, confirming this interpretation.

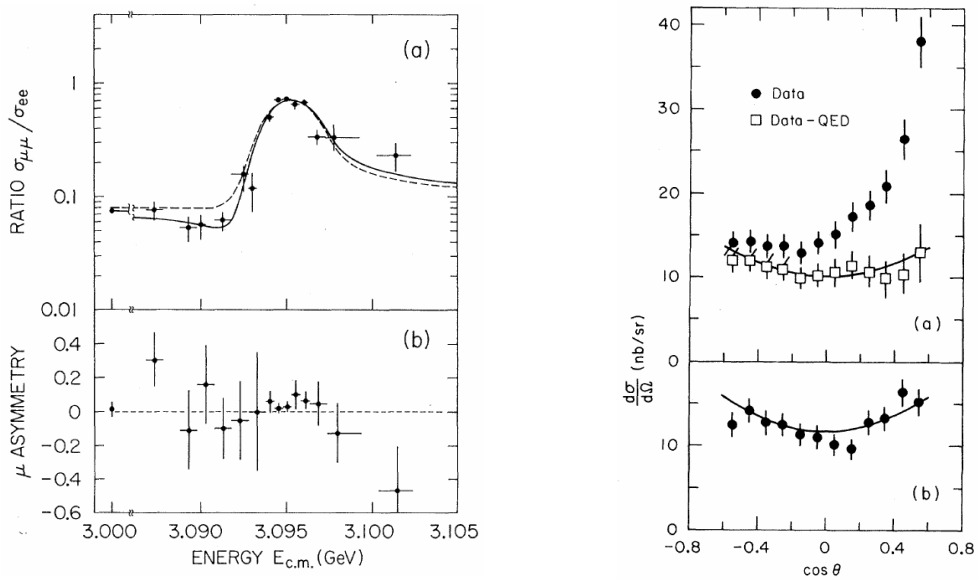

Figure 2.11: Direct determination of the spin-parity of the J/ψ at SLAC. The upper left panel shows the ratio of the $\mu^+\mu^-$ and e^+e^- yields as a function of the e^+e^- annihilation energy. The solid curve indicates the expected behaviour for a $J^{PC} = 1^{--}$ state, the dip just below the resonance being due to the interference with non-resonant $e^+e^- \to \mu^+\mu^-$ production, while the dashed line indicates the behaviour expected in case of no interference. The two panels on the right show the observed angular distributions of (top) e^+e^- and (bottom) $\mu^+\mu^-$ pairs from J/ψ decays, overlayed with the $\cos^2\theta$ dependence expected for the decay of a $J = 1$ resonance (from [52]).

Almost two years after the discovery of the J/ψ, the first observation of open charm was finally reported by the SLAC group [59]. Studying the invariant-mass spectra of $K\pi\pi$ candidatesm, they observed a narrow resonance at a mass of 1876 MeV/c^2 in the final state $K^{\mp}\pi^{\pm}\pi^{\pm}$ but not in the final state $K^{\pm}\pi^+\pi^-$, a signature that was expected for the decay of a charmed meson. The result of the measurement is shown in Figure 2.12 together with the Feynman diagramm for the decay.

Around the same time, the τ lepton was discovered with a very similar mass and it became clear that it was the similar signature of tau decays that had made it so difficult to clearly identify decays of charmed mesons.

The discovery of the J/ψ and its interpretation as a $c\bar{c}$ resonance caused a paradigm shift in particle physics. Over the next few years, quarks became generally accepted as a physical reality and the Standard Model as the theory that described their interactions.

2.9 Bottom or beauty quark (1977)

About three years after the discovery of the J/ψ resonance, a broad enhancement at a mass around 9.5 GeV/c^2 was observed in the invariant-mass spectrum of $\mu^+\mu^-$ pairs produced via the reaction $p + (\mathrm{Cu,Pt}) \to \mu^+\mu^- + \mathrm{X}$ in a 400 GeV proton beam at Fermilab [60]. The measurement is shown in Figure 2.13. The observation was quickly interpreted as a bound state of a new quark and its antiquark [61], which was later named beauty or bottom. With a three-fold increase in the size of the analyzed data set, the structure could be resolved into two narrow resonances, with a hint for a possible contribution from a third resonance [62].

The three resonances were originally named Υ, Υ' and Υ'', but are today referred to by the notation $\Upsilon(1S)$, $\Upsilon(2S)$ and $\Upsilon(3S)$, reflecting their respective positions in the spectrum of $b\bar{b}$ resonances. The Υ and Υ' were soon after confirmed in e^+e^- collisions at DESY [66–69], while the Υ'' was confirmed by the Fermilab experiment two years later [63].

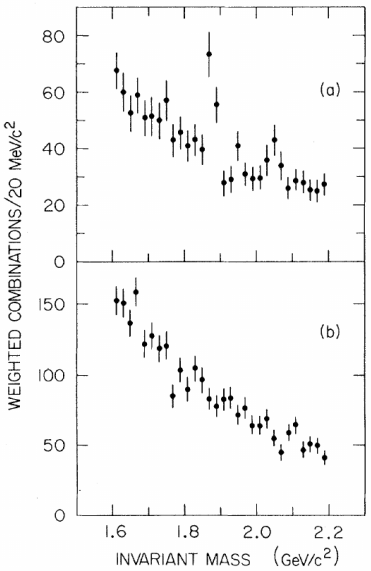

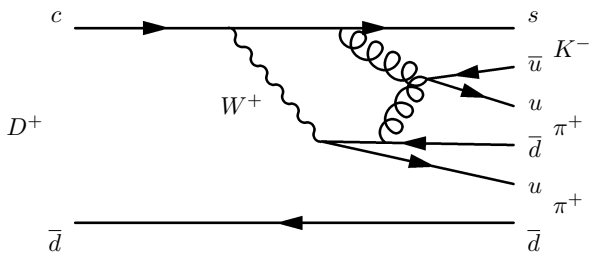

Figure 2.12: Discovery of the $D^{\pm}$ meson at SLAC. The upper left panel shows the observed signal in the $K^{\mp}\pi^{\pm}\pi^{\pm}$ invariant mass spectrum, while the lower left panel demonstrates the absence of a signal in the final state $K^{\pm}\pi^{+}\pi^{-}$, characteristic for the decay of a charmed meson (from [59]). The corresponding Feynman diagram for the decay $D^{\pm} \to K^{\mp}\pi^{\pm}\pi^{\pm}$ is shown on the right.

The fourth radial excitation, $\Upsilon(4S)$, was discovered in 1980 by the CLEO collaboration in a measurement the hadronic excitation function in e^+e^- annihilations [64] . The mass of this resonance was found to be 10.55 GeV and its total decay width was determined to be about 20 MeV. The large witdh suggested that the $\Upsilon(4S)$ could decay via the strong interaction, i.e. that its mass had to lie above the production threshold for pairs of b flavoured mesons. Evidence for the production of B mesons at the $\Upsilon(4S)$ was reported by CLEO in 1981 [70] , followed by the observation , in 1983, of the exclusive decays $B \to D^{(*)}\pi$ and $B \to D^{(*)}\pi\pi$ [65] .

After the discoveries of the b quark and the τ lepton, it was pretty much taken for granted that a sixth quark, the top, had to exist to complete the third quark doublet. First indication that the mass of the top quark had to be much larger than those of the other quarks came from the observation of strong $B^0\overline{B}^0$ mixing, as described in the next section. Standard-Model fits to electroweak precision measurements, such as those of the decay width of the Z boson and the Weinberg angle $\sin\theta_W$ at LEP and SLC, then permitted to derive the mass of the top quark to within about 20 GeV/c^2 uncertainty[3]. The first direct observation of the top quark was announced in 1995 by the CDF [71] and D0 [72] collaborations at the Tevatron at Fermilab. The measured mass was in good agreement with the prediction from electroweak fits. Today's world average is $m_t = (\,173.21 \pm 0.51\,(\text{stat}) \pm 0.71\,(\text{syst})\,)$ GeV/c^2 [1]. As the top quark decays essentially to 100% to W^+b, it does not play a significant role in flavour physics. Studies of top quark decays are, however, an important topic in electroweak physics.

2.10 $B^0-\overline{B}^0$ mixing (1987)

In analogy to particle-antiparticle mixing in the neutral kaon system, $B^0-\overline{B}^0$ transitions can occur via box diagrams as those shown in Figure 2.16. However, though the processes responsible for $B^0-\overline{B}^0$ mixing are analogous to those for $K^0-\overline{K}^0$ mixing — compare the diagrams shown in Figure 2.16 with that shown in 2.5 — the phenomenology in the two systems is very

[3]The last prediction from electroweak fits prior to the announcement of direct evidence was presented at the Moriond conference in March 1994 as $m_t = (174 \pm 11\,(\text{stat})\,^{+17}_{-19}\,(\text{syst}))$ GeV/c^2.

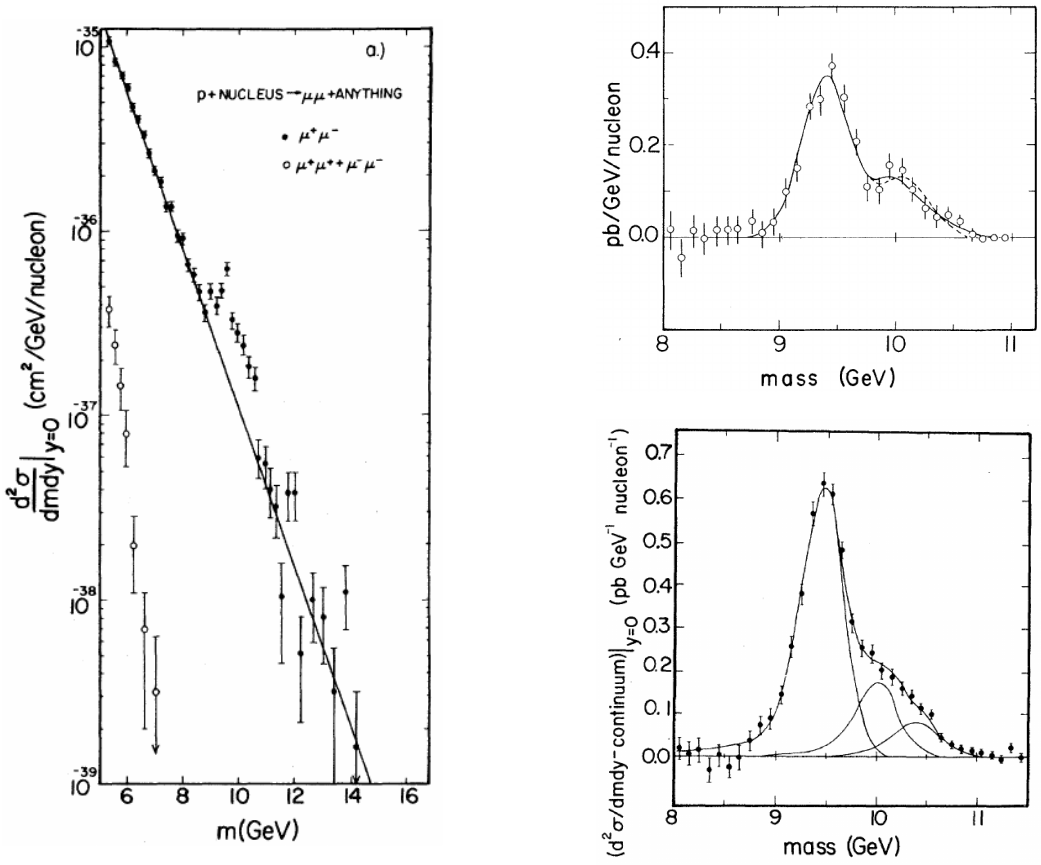

Figure 2.13: Discovery of the Υ resonances at Fermilab: (left) the initial observation of a broad enhancement in the $\mu^+\mu^-$ invariant mass spectrum; (top right) the signal exscess over the fitted continuum background from a three times larger data sample, the two lines showing fits assuming two (solid line) or three (dashed line) narrow resonances; (bottom right) the confirmation of the Υ'' (from [60], [62] and [63], respectively).

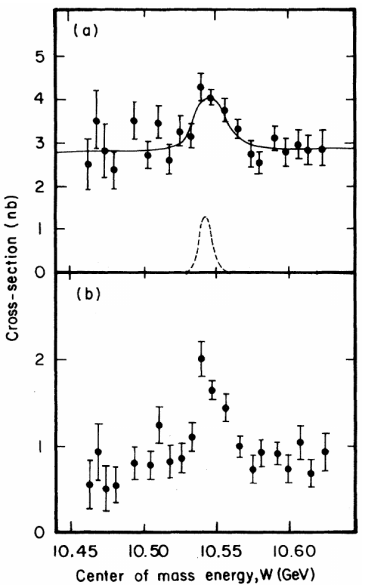

Figure 2.14: Discovery of the $\Upsilon(4S)$ resonance at CLEO (from [64]).

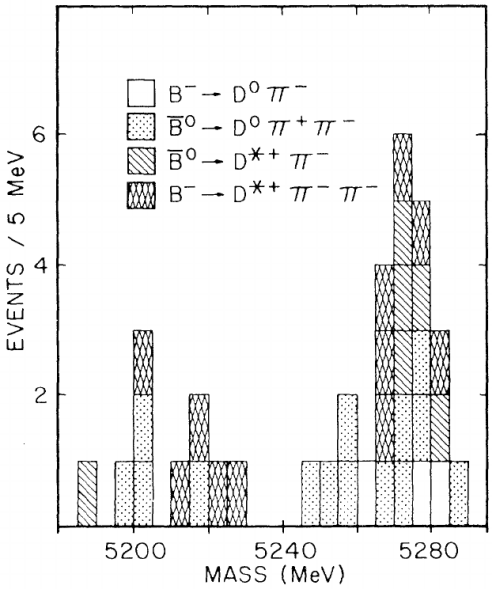

Figure 2.15: First observation of B mesons at CLEO (from [65]).

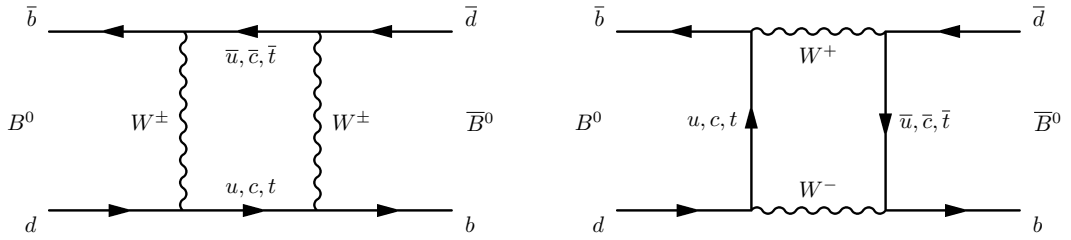

Figure 2.16: $B^0-\overline{B}^0$ mixing through box diagrams with the exchange of two $W^\pm$ bosons via (left) quark-antiquark intermediate states and (right) two virtual $W^\pm$ bosons in the intermediate state.

different. Due to the larger mass of the B^0 meson, there are many decay modes for both weak eigenstates and the difference of their lifetimes is negligibly small compared to the average. Therefore, unlike in the $K^0\overline{K}^0$ system, it is not possible to isolate one of the two eigenstates by means of the decay time distribution. The phenomenology of particle-antiparticle mixing in the different neutral meson systems will be discussed in more detail in Chapter 3.1

The first observation of $B^0-\overline{B}^0$ mixing was reported in 1987 by the Argus collaboration at the e^+e^- storage ring Doris II at DESY [73]. At Doris-II, positrons and electrons were collided at a centre-of-mass energy of 10.58 MeV, corresponding to the mass of the $\Upsilon(4S)$ resonance. As discussed in the previous section, the $\Upsilon(4S)$ is a bound $b\overline{b}$ state with a mass just above the $B\overline{B}$ production threshold. It decays to about 50% to $B^0\overline{B}^0$ and to about 50% to B^+B^- and therefore provides a clean source of $B^0\overline{B}^0$ and B^+B^- pairs. In an analysis of 88'000 recorded $\Upsilon(4S)$ decays, however, one event was found in which two B^0 meson candidates were reconstructed in flavour-specific semileptonic decay modes. A display of this event is shown in Figure 2.17. Employing the subscripts shown in the event display, one B^0 meson was reconstructed in the decay

$$B^0 \to D^{*-}\mu_1^+\nu_\mu \;\text{ with }\; D^{*-} \to D^0\pi_{1s}^- \;\text{ and }\; D^0 \to K_1^+\pi_1^-$$

while the other B^0 meson was reconstructed in the decay

$$B^0 \to D^{*-}\mu_2^+\nu_\mu \;\text{ with }\; D^{*-} \to D^-\pi^0 \;\text{ and }\; D^- \to K_2^+\pi_2^-\pi_2^- \;.$$

In both cases, the electric charges of the final-state particles uniquely identified the decaying particle as a B^0 meson. The observation of two B^0 meson decays in the same event implied that the initially produced $\overline{B}^0$ meson must have mixed into a B^0 meson at the time of its decay. A significant signal for $B^0-\overline{B}^0$ mixing was also observed through partially reconstructed events with two charged leptons (electrons or muons) in the final state. In analogy to the case of semileptonic kaon decays shown in Figure 2.9, b quarks decay to negative leptons and $\overline{b}$ quakrs decay to positive leptons. Therefore, only events with two oppositely charged leptons are expected to be observed in $\Upsilon(4S)$ decays if no $B^0-\overline{B}^0$ mixing occurs. The Argus collaboration found 50 same-sign dilepton events, out of which $25.2 \pm 5.0 \pm 3.8$ events were estimated to be due to various sources of background. The remaining $24.8 \pm 7.6 \pm 3.8$ events were attributed to a mixing signal. Finally, a mixing signal was also observed in a sample of events that contained one B^0 or $\overline{B}^0$ candidate that was fully reconstructed in a flavour-specific decay mode and a lepton of "wrong" charge from the decay of the opposite B meson. Combining the results, the time integrated mixing probability was calculated to be

$$\chi \;=\; \frac{\Gamma(B^0 \to \overline{B}^0)}{\Gamma(B^0 \to \overline{B}^0) + \Gamma(B^0 \to B^0} \;=\; 0.17 \pm 0.05.$$

As shown in Figure 2.16, the top quark can appear as a virtual particle in the internal loop of the box diagram and the mixing probability depends on its mass. From their measurement,

the Argus collaboration derived a lower bound of 50 GeV for the mass of the top quark. This was a relevant result at the time of the measurement, since the top quark was expected then to be lighter than we know it to be today. In fact, only a few years earlier the UA1 collaboration had claimed evidence for a top signal between 30 and 60 GeV [74].

The observation of $B^0-\overline{B}^0$ mixing was confirmed soon after by the CLEO collaboration at the e^+e^- collider CESR at Cornell [75].

2.11 Direct *CP* violation in the $K^0\overline{K}^0$ system (1999)

Following the discovery of the *CP* violating decay $K_L^0 \to \pi^+\pi^-$, a phenomenological analysis of the K^0-$\overline{K}^0$ system showed [76] that two mechanisms could contribute to the observed *CP* asymmetry: "indirect" *CP* violation in $K^0-\overline{K}^0$ mixing, caused by a relative phase between the transition amplitudes involving on-shell and off-shell intermediate states, and "direct" *CP* violation in the decay, caused by the interference of decay amplitudes with a relative complex phase.

In the CKM modell, both types of *CP* violation can occur in the neutral kaon system: *CP* violation in $K^0-\overline{K}^0$ mixing occurs because the transitions through on-shell and off-shell intermediate states are dominated by box diagrams with different internal quark lines and different CKM phases; *CP* violation in the decay can be caused by the interference of tree and penguin amplitudes, which have different CKM phases as depicted in Figure 2.18. A third mechanism, interference between mixing and decay, plays an important role in the $B^0-\overline{B}^0$ and $B_s^0-\overline{B}_s^0$ systems but is negligible in the $K^0-\overline{K}^0$ system. The three mechanisms will be discussed in more detail in Section 3.3.

However, as already mentioned in Section 2.5, the CKM model was only one of many possible theories that had been put forward to explain *CP* violation. An alternative group of models that retained great popularity until well into the 1990's were so-called superweak models first proposed by Wolfenstein in 1964 [77]. In these models, *CP* violation was caused by a new interaction that changed strangeness by two units and contributed only to $K^0-\overline{K}^0$ transitions. To explain the measured value of the *CP* asymmetry in $K_L^0 \to \pi^+\pi^-$, the coupling constant of this new interaction had to be of the order of $10^{-10}-10^{-11}$ times that of the weak interaction, hence the name superweak theory. As $K^0-\overline{K}^0$ mixing is by definition the only source of

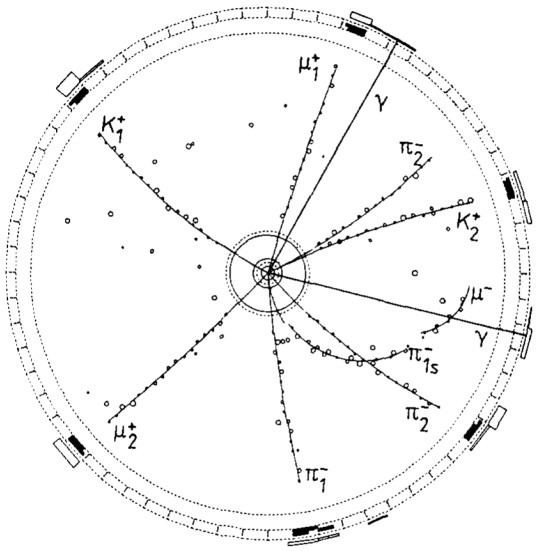

Figure 2.17: Fully reconstructed B^0B^0 event observed by Argus. The subscripts "1" and "2" indicate the decay products of the first and second B^0 meson, respectively. The decay chains are described in the text (from [73]).

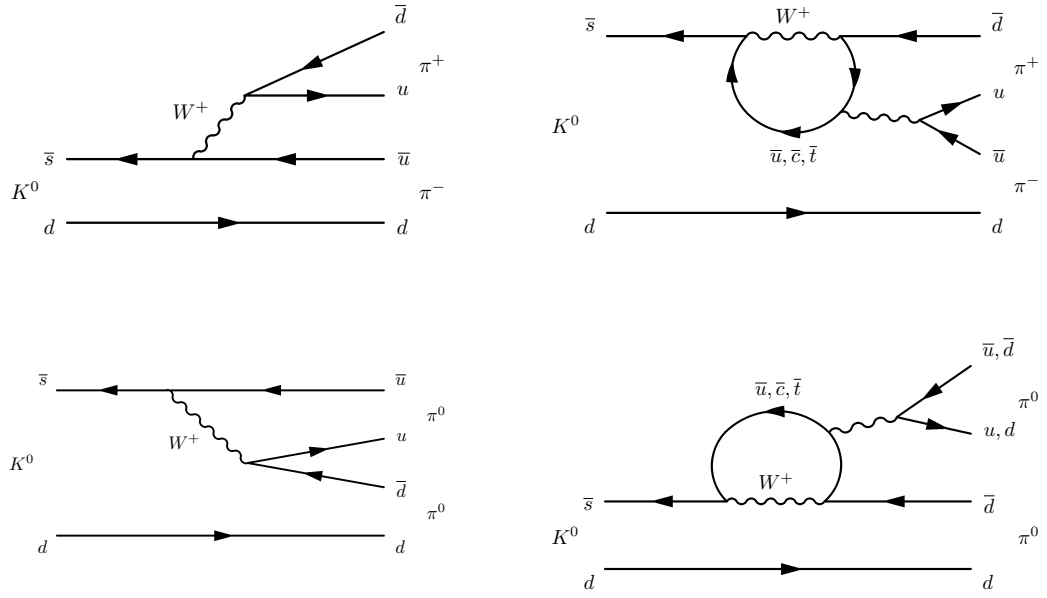

Figure 2.18: Feynman diagrams for (left) the tree amplitude and (right) the penguin amplitude contributing to the decays (top) $K^0 \to \pi^+\pi^-$ and (bottom) $K^0 \to \pi^0\pi^0$.

CP violation in the superweak models, these models would be ruled out by the observation of a direct *CP* violating asymmetry in the decay of neutral kaons[4].

Proof of *CP* violation in mixing had been provided in 1967 by the measurement of *CP* violating charge asymmetries in the semileptonic decays $K^0_L \to \pi e \nu_{\rm e}$ [39] and $K^0_L \to \pi\mu\nu_\mu$ [40]. Semileptonic decays proceed through a single decay amplitude and cannot receive any contribution from *CP* violation in decay.

A possible contribution from *CP* violation in decay can be probed by comparing the rates of *CP* violating K^0_L decays to two neutral pions and to two charged pions. Since *CP* violation in mixing is independent of the decay mode, it will yield the same effect in the $\pi^+\pi^-$ and $\pi^0\pi^0$ final states. The observation of different *CP* asymmetries in the two final states would therefore be proof of a contribution from *CP* violation in the decay, ruling out superweak theories.

In the usual notation, introduced e.g. in Ref. [78], *CP* violation in mixing is described by the complex-valued parameter ε, defined by

$$\begin{aligned} K^0_L &= \frac{1}{\sqrt{2(1+|\varepsilon|^2)}} \left\{ (K^0 - \overline{K}^0) \; + \; \varepsilon\,(K^0 + \overline{K}^0) \right\} \\ &= \frac{1}{\sqrt{2(1+|\varepsilon|^2)}} \left\{ (1 \; + \; \varepsilon)\, K^0 \; - \; (1 \; - \; \varepsilon)\, \overline{K}^0 \right\} \; , \end{aligned}$$

while *CP* violation in the decay is described by the complex-valued parameter ε'. A proper definition of the parameter ε' is for example given in Ref. [79]. In terms of these parameters, the decay amplitude ratios between the *CP* forbidden and *CP* allowed decays to two charged pions is

$$\eta_{+-} \; \equiv \; \frac{A(K^0_L \to \pi^+\pi^-)}{A(K^0_S \to \pi^+\pi^-)} \; = \; \varepsilon + \varepsilon'$$

and that for decays to two neutral pions is

$$\eta_{00} \; \equiv \; \frac{A(K^0_L \to \pi^0\pi^0)}{A(K^0_S \to \pi^0\pi^0)} \; = \; \varepsilon - 2\varepsilon' \; .$$

[4]In later years, Wolfenstein made an attempt to re-define the meaning of superweak theories such that they could also accommodate a small contribution from direct *CP* violation in the kaon system; the observation of *CP* violation in the B^0 meson system finally disproved super-weak theories also in this wider sense.

Superweak models predict $\varepsilon' = 0$ by definition, whereas in the Standard Model the real part of the ratio ε'/ε is predicted to be of the order of $10^{-3} - 10^{-2}$. The uncertainty of the Standard Model prediction is significant due to hadronic uncertainties from kaon form factors [80].

The first observations, in 1967, of the decay $K_L^0 \to \pi^0\pi^0$ resulted in estimates of $|\eta_{00}|$ that were significantly larger than the known value of $|\eta_{+-}|$ at the time, indicating the possibility of a large contribution from direct *CP* violation in decay. Subsequent measurements of $|\eta_{00}|$, however, yielded [81–88] inconsistent results, ranging from zero to 5×10^{-3} with claimed uncertainties between 0.3×10^{-3} and 0.5×10^{-3}.

Later experiments searching for direct *CP* violation measured the double ratio of *CP* violating and *CP* conserving decay rates

$$\frac{\Gamma(K_L^0 \to \pi^+\pi^-) \,/\, \Gamma(K_S^0 \to \pi^+\pi^-)}{\Gamma(K_L^0 \to \pi^0\pi^0) \;/\; \Gamma(K_S^0 \to \pi^0\pi^0)} \;\approx\; 1 \,+\, 6 \cdot \mathrm{Re}\left(\frac{\varepsilon'}{\varepsilon}\right),$$

in which many systematic uncertainties cancel to first order if the four decay modes are measured simultaneously in the same beam and the same detector: systematic effects related to kaon beam intensities cancel to first order in the ratios

$$\frac{\Gamma(K_L^0 \to \pi^+\pi^-)}{\Gamma(K_L^0 \to \pi^0\pi^0)} \quad \text{and} \quad \frac{\Gamma(K_S^0 \to \pi^+\pi^-)}{\Gamma(K_S^0 \to \pi^0\pi^0)} \;,$$

while those related to pion detection efficiencies cancel to first order in the ratios

$$\frac{\Gamma(K_L^0 \to \pi^+\pi^-)}{\Gamma(K_S^0 \to \pi^+\pi^-)} \quad \text{and} \quad \frac{\Gamma(K_L^0 \to \pi^0\pi^0)}{\Gamma(K_S^0 \to \pi^0\pi^0)} \;.$$

Between 1972 and 1988, a number of measurements of this double ratio were performed [89–93] and yielded results compatible with zero. In 1988, the NA31 collaboration at CERN reported first evidence [94] for direct *CP* violation. Their final result [95], published in 1993, was

$$\mathrm{Re}\,(\varepsilon'/\varepsilon) \;=\; (\,23.0 \,\pm\, 4.1\,(\mathrm{stat}) \,\pm\, 5.1\,(\mathrm{syst})\,) \,\times\, 10^{-4}\;,$$

corresponding to a deviation from zero with a significance of 3.3 Gaussian standard deviations. At the same time, however, the E731 collaboration at Fermilab reported [96]

$$\mathrm{Re}\,(\varepsilon'/\varepsilon) \;=\; (\,7.4 \,\pm\, 5.2\,(\mathrm{stat}) \,\pm\, 2.9\,(\mathrm{syst})\,) \,\times\, 10^{-4}\;,$$

compatible with absence of direct *CP* violation. To resolve this apparent discrepancy, two follow-up experiments — KTeV at Fermilab and NA48 at CERN — were initiated with the goal to measure $\mathrm{Re}\,(\varepsilon'/\varepsilon)$ to a precision of $(1-2) \times 10^{-4}$.

At this level of precision, second-order systematic effects in the measurement of the double ratio have to be considered with great care. Such second-order effects can emerge because different detectors, trigger and reconstruction algorithms have to be employed for the charged and neutral decay modes and two different beams have to be employed as sources of K_L^0 and K_S^0 decays. The production target for K_S^0 beam has to be close to this fiducial decay volume monitored by the detector, while the production target for the K_L^0 beam has to be far upstream to let the K_S^0 component decay away before the beam reaches the fiducial volume. Differences in the momentum spectra of the two beams will lead to differences in the distribution of opening angles of decay products and therefore to a different illumination of the detector and potentially different reconstruction efficiencies for K_L^0 and K_S^0 decays. The very different K_L^0 and K_S^0 lifetimes lead to different decay vertex distributions within the fiducial decay volume, again leading to different illumination of the detectors for K_L^0 and K_S^0 decays. These effects cancel in the double ratio as long as the two detectors for charged and neutral final states have identical detection and reconstruction efficiencies across the full acceptance. An artificial asymmetry will, however, be induced as soon as detection efficiencies for the charged and the

neutral final states vary differently across the acceptance[5]. Similarly, different variations in the K_S^0 and K_L^0 beam intensities will lead to different probabilities for random coincidences, which can result in artificial asymmetries if they affect trigger and reconstruction efficiencies for neutral and charged decays differently. It is also important to measure all four decay modes simultaneously, since relevant properties of the K_L^0 and K_S^0 beams and of the charged and neutral detectors can vary differently as a function of time.

In both experiments — in particular in the case of NA48 — great care was put into the design of the beams, detectors and analysis techniques in order to minimize possible sources of such secondary effects. In the following, only a brief and incomplete overview of some of the key aspects for each of the two experiments can be given. A comprehensive description of the NA48 measurement technique can be found in Ref. [97].

The generation of the beams for the KTeV experiment at Fermilab is illustrated in Figure 2.19. Two almost parallel K_L^0 beams were produced by colliding a beam of 800 GeV/c protons from the Tevatron into a single beryllium oxide target that was located 122 m upstream of the fiducial decay volume. To create a source of K_S^0 decays, a so-called regenerator consisting of 84 plates of 2 cm thick plastic scintillator was inserted into one of the two beams just upstream of the decay volume. As discussed in Section 2.5, different K^0 and $\overline{K}^0$ interaction cross sections in the material lead to the regeneration of a K_S^0 component in the initially pure K_L^0 beam. The total amount of material traversed by the beam was chosen such that the regenerated K_S^0 component made up 3% of the beam intensity downstream of the regenerator and therefore dominated the rate of decays to two pions in this beam. The scintillators were monitored by photomultiplier tubes to be able to veto inelastic interactions in the material of the regenerator. Moreover, the regenerator was swapped between the two beams every minute to even out possible asymmetries in detector acceptance. A sketch of the KTeV detector is shown in Figure 2.20. The detector for charged particles consisted of a forward magnetic spectrometer with two pairs of drift chambers upstream and downstream of a dipole magnet. A high-resolution CsI crystal calorimeter was employed to detect the photons from neutral final states. The detector was complemented by a scintillator hodoscope providing a fast trigger for charged particles and by a muon veto counter and photon veto counters to suppress backgrounds from the dominant semileptonic and three-pion K_L^0 decays. For both charged and neutral final states, the reconstructed position of the kaon decay vertex in the plane orthogonal to the beam direction was used to determine which of the two beams the event originated from and therefore whether it would be classified as a K_L^0 decay or a K_S^0 decay. Acceptance effects due to the very different K_S^0 and K_L^0 decay vertex distributions along the beam direction, shown in Figure 2.21, were corrected for using a Monte-Carlo simulation.

The beams and the detector of the NA48 experiment [99] are illustrated in Figures 2.22 and 2.23, respectively. Two distinct targets were employed to generate the K_L^0 and K_S^0 beams. The K_L^0 beam was generated by colliding 450 GeV/c protons from the CERN-SPS into a first target, located 126 m upstream of the fiducial decay volume. Protons that had not interacted in the K_L^0 target were then sent through a bent silicon crystal [100]. A small but fixed fraction of these protons was deflected by channeling in the lattice of this crystal and was then steered towards a second target, located just upstream of the fiducial volume, to generate the K_S^0 beam. This technique ensured that a fixed fraction of the initial proton beam impinged on the K_S^0 target and that the intensities of the K_L^0 and K_S^0 beams were affected equally by variations in the primary proton beam. The K_S^0 target was displaced laterally from the K_L^0 beam by 7.6 cm. To minimize acceptance effects due to this small displacement between the two beams, the K_S^0 beam was collimated such that it converged with

[5]To illustrate this, consider a simplified scenario in which all pions from K_S^0 decays go into region A of the detector, and all pions from K_L^0 decays go into region B. Assume further that $\pi^+\pi^-$ detection is to 99% efficient in region A but only 98% efficient in region B, while $\pi^0\pi^0$ detection is 99% efficient in region B and 98% efficient in region A. In the absence of any direct CP violation, the measured value of the double ratio will then be $(0.99/0.98)/(0.98/0.99) \approx 1.02$, corresponding to $\mathrm{Re}\,(\varepsilon'/\varepsilon) = 3.4 \times 10^{-3}$.

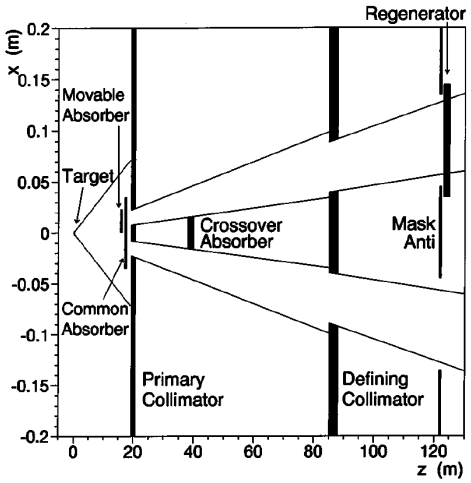

Figure 2.19: Layout of the KTeV beams. Note the different scales along the horizontal and vertical axes (from [98]).

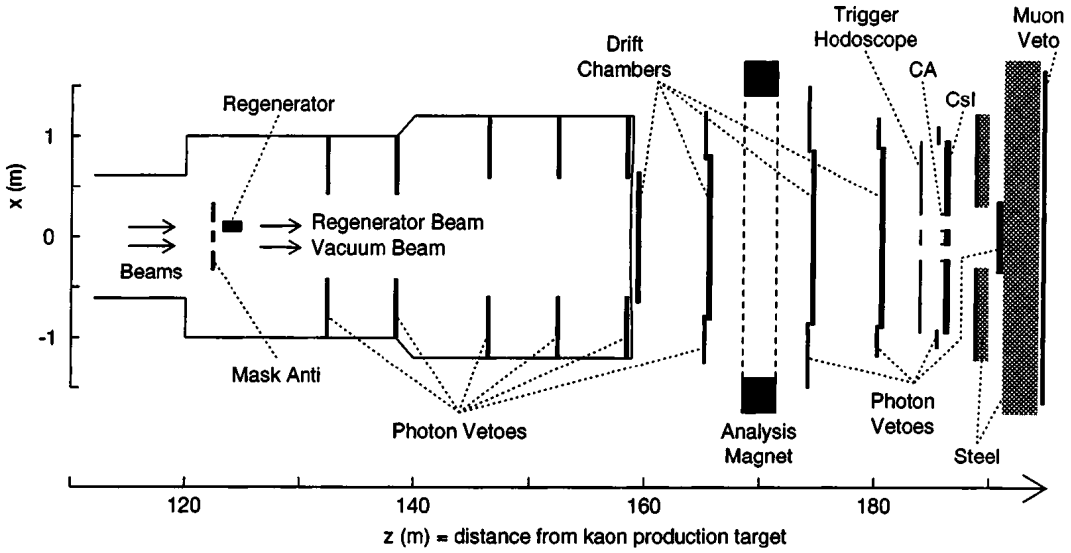

Figure 2.20: Layout of the KTeV experiment (from [98]).

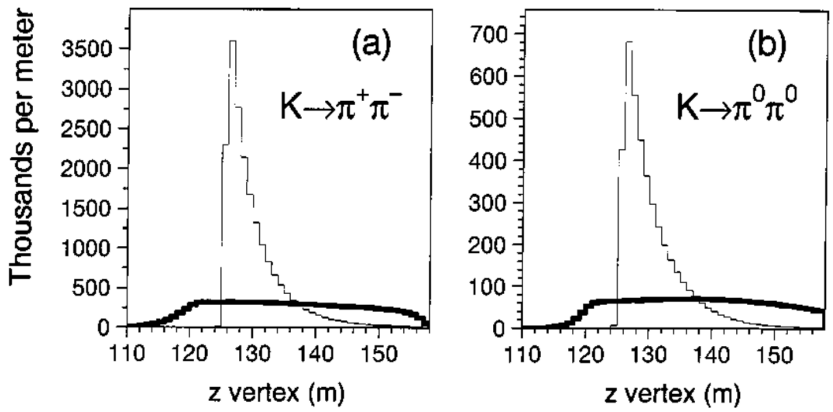

Figure 2.21: Measured longitudinal decay vertex distributions for kaon decays to (left) two charged pions and (right) two neutral pions. In both panels, thick lines show the distributions for the beam without regenerator and thin lines show the distributions for the beam in which the regenerator was inserted (from [98]).

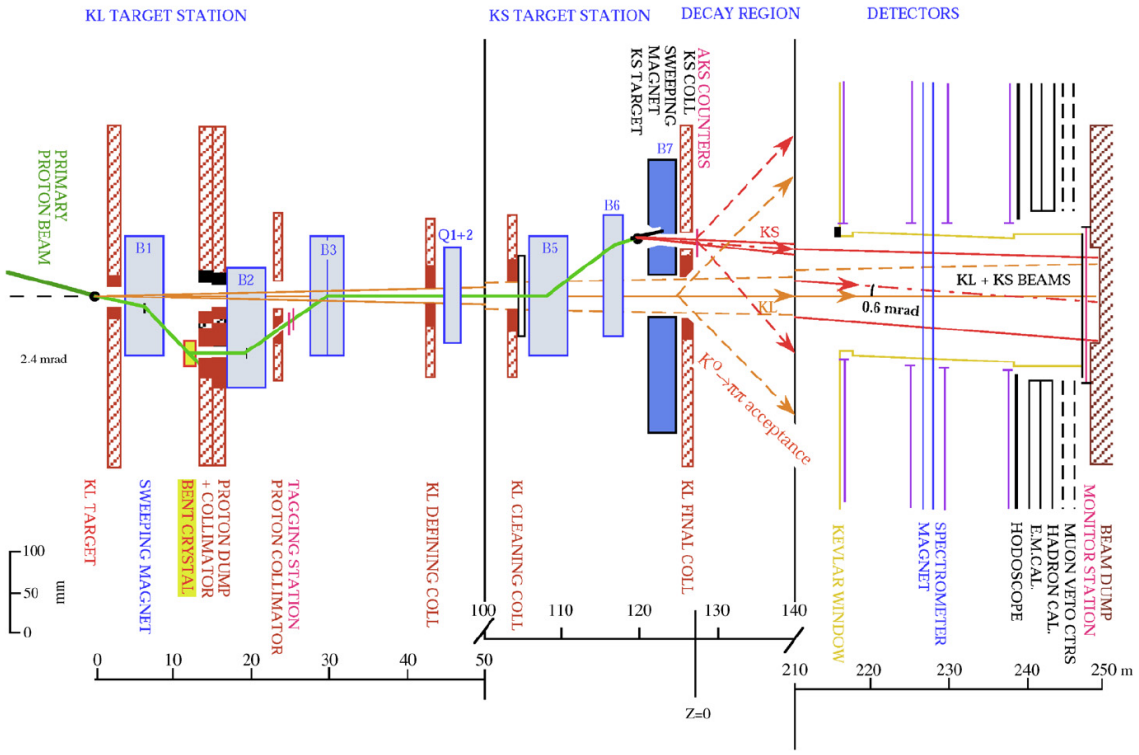

Figure 2.22: Layout of the NA48 beams. Note the different scales along the horizontal and vertical axes (from [99]).

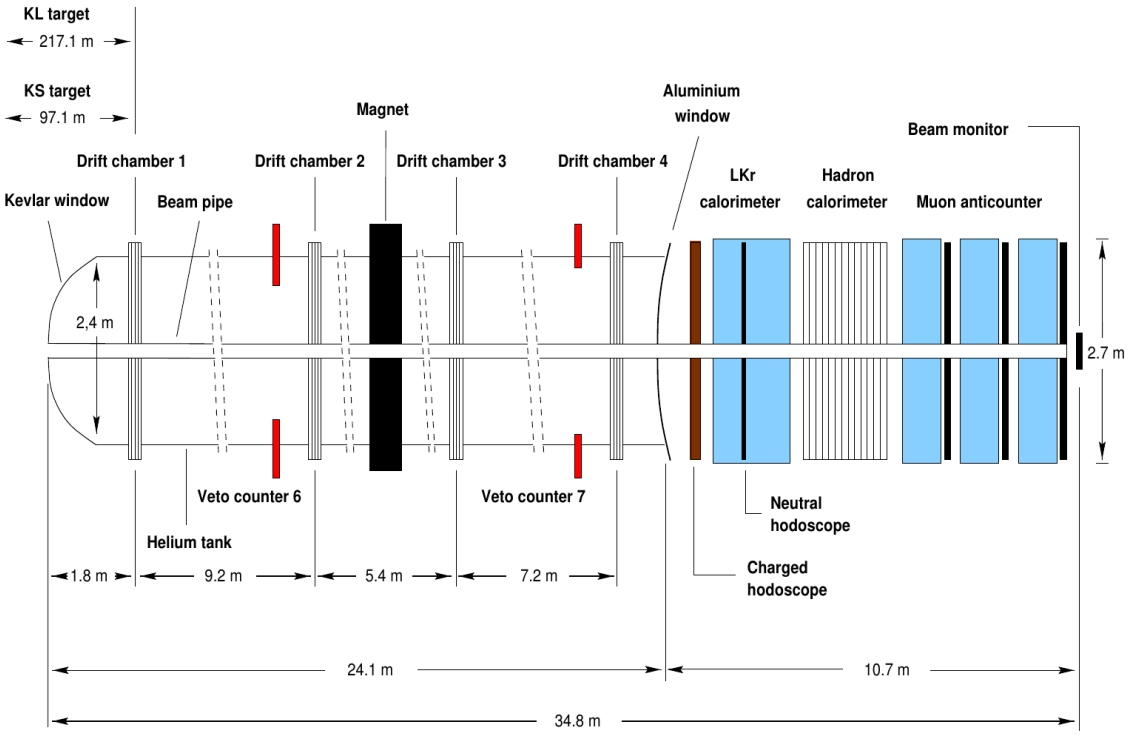

Figure 2.23: Layout of the NA48 detectors (from [97]).

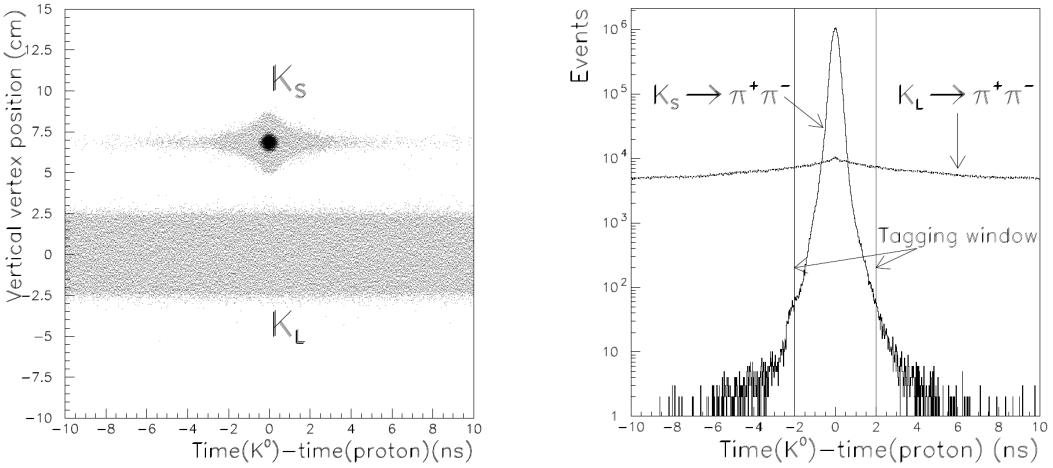

Figure 2.24: Performance of the K_S^0/K_L^0 tagging for decays to $\pi^+\pi^-$. The panel on the left shows the time difference between signals in the trigger hodoscope and the tagging detector versus the vertical position of the kaon decay vertex as reconstructed from the trajectories of the two charged pions. The vertex reconstruction allows a clear separation between decays from the K_S^0 and K_L^0 beams. As expected, events from the K_S^0 beam cluster around a time difference of zero, whereas the time difference for events from the K_L^0 beam is randomly distributed. The panel on the right shows the distribution of the time difference separately for $\pi^+\pi^-$ decays that were assigned to the K_L^0 beam and to the K_S^0 decays by means of their reconstructed decay vertex positions. The vertical lines indicate the ± 2 ns coincidence window that is employed to classify decays as K_S^0 or K_L^0 decays. True K_L^0 decays that accidentally fall within the coincidence window are wrongly classified as K_S^0 decays and true K_S^0 decays in the tail of the distribution outside the coincidence window are wrongly classified as K_L^0 decays. Note the logartihmic scale: both these fractions are small (from [97]).

the K_L^0 beam and overlapped with it in the centre of the detector. Moreover, the production angles at the K_L^0 target and at the K_S^0 target were chosen to produce similar momentum spectra for the K_L^0 and K_S^0 beams. Decays to $\pi^+\pi^-$ were reconstructed in a forward magnetic spectrometer consisting of two pairs of precision drift chambers upstream and downstream of a dipole magnet. A quasi-homogeneous LKr calorimeter was employed to detect the photons from decays to $\pi^0\pi^0$. The detector was complemented by a scintillator hodoscope providing a fast trigger for charged particles and by a hadron calorimeter, muon veto counters and photon "anti-counters" to suppress backgrounds from the dominant semileptonic and three-pion K_L^0 decays.

To classify events as K_L^0 or K_S^0 decays, a tagging counter was installed inside the proton beam line to the K_S^0 target. This counter consisted of an array of thin scintillator strips and recorded the passage of protons with a precision of around 0.1 ns. Event were classified as K_S^0 decays if a signal in the K_S^0 tagging counter was observed within a time window of ± 2 ns around the signal recorded in the trigger hodoscope for $\pi^+\pi^-$ decays or in the LKr calorimeter for $\pi^0\pi^0$ decays. If no signal in the K_S^0 tagging counter was observed within this time window, the corresponding event was classified as a K_L^0 decay. This method exploited the excellent time resolutions of 0.25 ns in the charged hodoscope and 0.3 ns in the LKr calorimeter and minimized a possible asymmetry in the event classification between the $\pi^+\pi^-$ and $\pi^0\pi^0$ decay modes. In the case of decays to $\pi^+\pi^-$, the decay vertex resolution in the plane transverse to the beam direction is sufficiencly precise to cleanly assign the decay vertex to the K_L^0 beam or the K_S^0 beam. This independent classification permits to estimate $K_L^0 \to K_S^0$ and $K_S^0 \to K_L^0$ misidentification probabilities due to random time coincidences or out-of-time signals. Figure 2.24 shows the measured time distributions separately for $\pi^+\pi^-$ decays that were assigned to the K_L^0 beam and to the K_S^0 decays by means of their reconstructed decay vertex positions, demonstrating that the misidentification probabilities are small.

An event weighting technique was applied to compensate for acceptance effects due to the

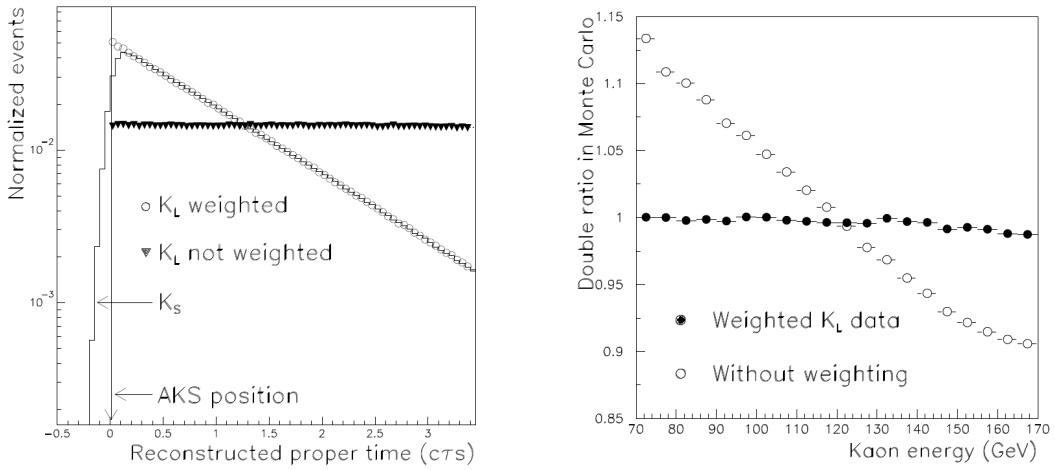

Figure 2.25: Effect of decay-time weighting. The panel on the left shows the reconstructed decay time distribution for K_S^0 events and for K_L^0 events before and after lifetime weighting. The AKS position defines the upstream end of the fiducial volume considerd in the analysis. The panel on the right shows the reconstructed value of the double ratio as a function of kaon energy in simulated events before and after lifetime weighting of the K_L^0 events. The significant bias that is visible before weighting is effectively removed by the weighting procedure (from [97]).

very different K_L^0 and K_S^0 lifetimes without having to resort to Monte-Carlo simulations. In the determination of the double ratio, each reconstructed K_L^0 event was counted with a weight

$$w \;=\; \exp\left\{-\frac{z_V}{\beta_K\gamma_K c}\cdot\left(\frac{1}{\tau_S}-\frac{1}{\tau_L}\right)\right\}\;,$$

where z_V is the reconstructed position of the kaon decay vertex along the K_L^0 beam axis, $\beta_K\gamma_K c$ is the Lorentz boost of the kaon in the laboratory frame and τ_L and τ_S are the known K_S^0 and K_L^0 lifetimes, respectively. The effect of this weighting is illustrated in Figure 2.25.

The KTeV and NA48 experiments collected data from 1996 till 1999 and from 1997 till 2001, respectively. In summer 1999, KTeV reported [101] the first observation of direct *CP* violation, based on a subset of the data collected in 1996-1997. Soon after, NA48 published [102] a first measurement based on the 1997 data set, which confirmed the observation. The final result of the NA8 experiment, based on a total of 5.3 million reconstructed $K_L^0\to\pi^0\pi^0$ decays and 22.5 million reconstructed $K_L^0\to\pi^+\pi^-$ decays, was published [103] in 2002 as

$$\mathrm{Re}\,(\varepsilon'/\varepsilon) \;=\; (\,14.7\,\pm\,1.4\,\pm\,0.9\,\pm\,1.5\,)\,\times\,10^{-4}\;,$$

where the first quoted uncertainty is statistical, the second includes systematic uncertainties related to the statistics of control samples and the third includes all remaining systematic uncertainties. The final result of the KTeV experiment, using their full data set of 6 million reconstructed $K_L^0\to\pi^0\pi^0$ decays and 25 million reconstructed $K_L^0\to\pi^+\pi^-$ decays, was published [104] in 2010 as

$$\mathrm{Re}\,(\varepsilon'/\varepsilon) \;=\; (\,19.2\,\pm\,1.1\,(\mathrm{stat})\,\pm\,1.8\,(\mathrm{syst})\,)\,\times\,10^{-4}\;.$$

These results finally established the existence of direct *CP* violation in the decay of neutral kaons and ruled out superweak models. They are compatible with the CKM picture of *CP* violation but cannot provide a quantitative test of the theory since predictions of $\mathrm{Re}\,(\varepsilon'/\varepsilon)$ suffer from large uncertainties related to non-perturbative kaon form factors.

2.12 *CP* violation in the $B^0\overline{B}^0$ system (2001)

The first observation of *CP* violation outside the neutral kaon system was reported in 2001 by the BaBar [105] and Belle [106] collaborations, who had measured the decay-time dependent rate asymmetry between the *CP*-conjugated decay modes $B^0 \to J/\psi K_S^0$ and $\overline{B}^0 \to J/\psi K_S^0$. With these measurements began the exploration of *CP* violating phenomena in the neutral, charged and strange B meson systems that will be the topic of Chapters 5 and 6.

In contrast to the neutral kaon system, a large number of decay modes in the B meson systems provides for a rich phenomenology that permits to perform quantitative tests of the CKM model of *CP* violation. Because of the relatively large mass of the b quark, Uncertainties due to form factors are in general smaller than in the kaon system. Moreover, it is possible to construct observables that are either intrinsically free from hadronic uncertainties or in which such uncertainties cancel to first order.

But before the measurement comes the experiment and in order to motivate the design of the experiments, it is helpful to introduce the basic phenomenology of the processes they attempt to analyze. This will be the goal of the next chapter.

Chapter 3

The Rules of the Game: A Short Phenomenology

In the following sections, the basic formalism of particle–antiparticle mixing in the neutral meson systems will be introduced, followed by classifications of heavy quark decays, and a short introduction of the three sources of *CP* violation in the CKM model of flavour-changing interactions in the quark sector. A basic understanding of these concepts will help in motivating the choices made in the design of the experimental facilities, discussed in Chapter 4.

3.1 Particle–antiparticle mixing in the neutral meson systems

The phenomenon of particle-antiparticle mixing in the neutral kaon system has been briefly introduced in Section 2.5. The same mechanisms that lead to $K^0 - \overline{K}^0$ transitions also cause particle-antiparticle mixing in the $D^0\overline{D}^0$, $B^0\overline{B}^0$ and $B_s^0\overline{B}_s^0$ systems. In all four systems, quark flavour is the only quantum number that distinguishes particle from antiparticle and since flavour is not conserved in weak interactions, second-order transitions such as the box diagrams shown in Figure 3.1 can cause transitions between particle and antiparticle. The basic formalism that is employed to describe these transitions is derived in the following. The neutral meson is denoted here as B^0 and the neutral antimeson as $\overline{B}^0$, but the formalism applies in exactly the same manner for $K^0\overline{K}^0$, $D^0\overline{D}^0$ and $B_s^0\overline{B}_s^0$. As shown at the end of this section, the resulting phenomenology is, however, rather different in each of the four systems, due to the fact that the relevant parameters assume different values.

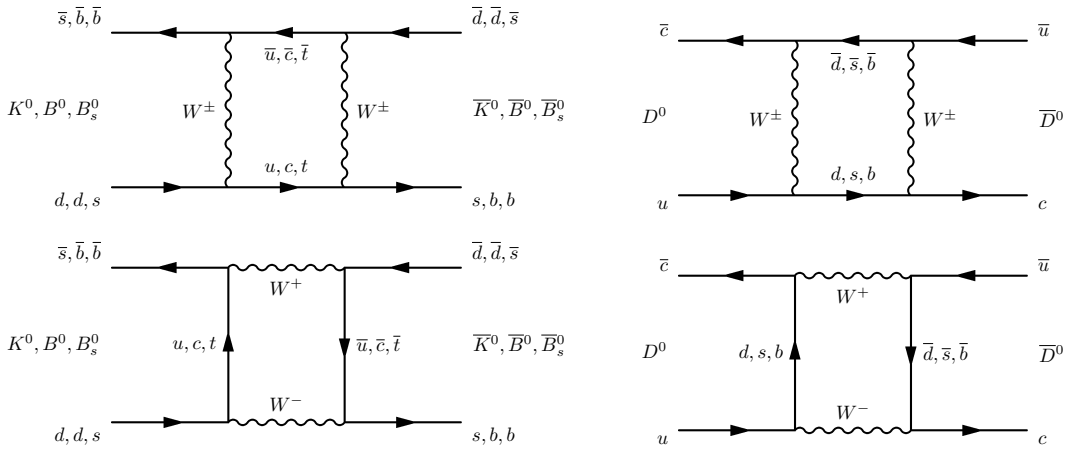

Figure 3.1: Example of box diagrams that cause particle-antiparticle mixing in (left) the $K^0\overline{K}^0$, $B^0\overline{B}^0$ and $B_s^0\overline{B}_s^0$ systems and (right) the $D^0\overline{D}^0$ system.

For the sake of simplicity, conservation of *CP* invariance will be assumed here. *CP* violation in mixing will be discussed in Section 3.3.

Due to the occurence of particle-antiparticle transitions, an initially pure B^0 or $\overline{B}^0$, produced in a strong interaction at a time $t = 0$, will evolve into a mixed state

$$|\,\Psi(t)\,\rangle \;=\; a(t)\,|\,B^0\,\rangle \;+\; b(t)\,|\,\overline{B}^0\,\rangle.$$

as a function of t. The time evolution of this mixed state can be described by a two-component Schröderinger equation

$$-i\,\frac{\partial}{\partial t}\left(\begin{array}{c} a(t) \\ b(t) \end{array}\right) \;=\; H\left(\begin{array}{c} a(t) \\ b(t) \end{array}\right),$$

with an effective Hamiltonian

$$H \;=\; \left(\begin{array}{cc} H_{11} & H_{12} \\ H_{21} & H_{22} \end{array}\right).$$

Since the B^0 and $\overline{B}^0$ have a finite lifetime and decay as well as mix into each other, probability is not conserved and the operator H is not Hermitian. However, following an approach first developed by Weisskopf and Wigner [107, 108], the operator H can be expressed by the sum of a hermitian operator

$$M \;\equiv\; \frac{1}{2}\left(H \,+\, H^{\dagger}\right),$$

that describes the propagation of the coupled system and an anti-hermitian operator

$$-i\,\frac{\Gamma}{2} \;\equiv\; \frac{1}{2}\left(H \,-\, H^{\dagger}\right),$$

that describes the decaying part of the amplitude. The diagonal elements of the 2×2 matrices M and Γ describe the B^0 and $\overline{B}^0$ mass and decay width, while their off-diagonal elements describe B^0-$\overline{B}^0$ mixing transitions via off-shell and on-shell intermediate states, respectively.

Hermeticity of the operators implies $M_{21} = M_{12}^*$ and $\Gamma_{21} = \Gamma_{12}^*$. Assuming *CPT* invariance, B^0 and $\overline{B}^0$ must have identical mass , $M \equiv M_{11} = M_{22}$, and decay width, $\Gamma \equiv \Gamma_{11} = \Gamma_{22}$, and the Hamiltonian H can be written as

$$H \;=\; \left(\begin{array}{cc} M - i\,\Gamma/2 & M_{12} - i\,\Gamma_{12}/2 \\ M_{12}^* - i\,\Gamma_{12}^*/2 & M - i\,\Gamma/2 \end{array}\right).$$

Diagonizing H then yields the eigenvalues

$$\omega_{H,L} \;=\; M \;-\; i\,\frac{\Gamma}{2} \;\pm\; \sqrt{\left(M_{12} - i\,\frac{\Gamma_{12}}{2}\right)\left(M_{12}^* - i\,\frac{\Gamma_{12}^*}{2}\right)}$$

and corresponding eigenstates

$$|\,B_{H,L}\,\rangle \;=\; p\,|\,B^0\,\rangle \,\mp\, q\,|\,\overline{B}^0\,\rangle\,,$$

where

$$\frac{q}{p} \;=\; -\sqrt{\frac{M_{12}^* - i\,\Gamma_{12}^*\,/\,2}{M_{12} - i\,\Gamma_{12}\,/\,2}}\,.$$

The "heavy" and "light" eigenstates, B_H and B_L, are states with well defined masses $m_{H,L}$ and decay widths $\Gamma_{H,L}$,

$$|\,B_H(t)\,\rangle \;=\; \left(p\,|\,B^0\,\rangle \,-\, q\,|\,\overline{B}^0\,\rangle\right)\; e^{-i\,m_H\,t}\; e^{-\Gamma_H\,t\,/\,2}$$

and

$$|\,B_L(t)\,\rangle \;=\; \Big(p\,|\,B^0\,\rangle \,+\, q\,|\,\overline{B}^0\,\rangle\Big)\; e^{-i\,m_L\,t}\; e^{-\Gamma_L\,t\,/\,2}\;,$$

where $m_{H,L}$ and $\Gamma_{H,L}$ are the real and imaginary parts of the eigenvalues, i.e.

$$\omega_{H,L} \;\equiv\; m_{H,L} \,-\, i\,\frac{\Gamma_{H,L}}{2}\;.$$

Furthermore, it is convenient to define the differences

$$\Delta m \;\equiv\; m_H \,-\, m_L$$

and

$$\Delta\Gamma \;\equiv\; \Gamma_H \,-\, \Gamma_L$$

of the masses and decay widths of the two mass eigenstates. The mass difference, Δm, is by definition positive, while the difference of decay widths, $\Delta\Gamma$, can be positive or negativem depending on whether the heavier mass eigenstate has shorter or longer lifetime than the lighter mass eigenstate.

Solving for $|\,B^0\,\rangle$ and $|\,\overline{B}^0\,\rangle$, the time evolution of initially pure flavour eigenstates $|\,B^0\,\rangle$ and $|\,\overline{B}^0\,\rangle$ produced at time $t = 0$ is obtained to be

$$|\,B^0\,\rangle(t) \;=\; g_+(t)\,\cdot\,|\,B^0\,\rangle \,+\, \frac{q}{p}\,\cdot\,g_-(t)\,\cdot\,|\,\overline{B}^0\,\rangle$$

and

$$|\,\overline{B}^0\,\rangle(t) \;=\; g_+(t)\,\cdot\,|\,\overline{B}^0\,\rangle \,+\, \frac{p}{q}\,\cdot\,g_-(t)\,\cdot\,|\,B^0\,\rangle,$$

with

$$\begin{aligned} g_\pm(t) \;&=\; \frac{1}{2}\,\Big(e^{-\omega_L t} \,\pm\, e^{\omega_H t}\Big) \\ &=\; \frac{1}{2}\,e^{i\,M\,t}\;e^{-\Gamma\,t\,/\,2}\;\Big(e^{i\,\Delta m\,t}\,e^{\Delta\Gamma\,t\,/\,4} \;\pm\; e^{-i\,\Delta m\,t}\,e^{-\Delta\Gamma\,t\,/\,4}\Big)\;. \end{aligned}$$

Finally, the time-dependent probabilities for a B^0 or a $\overline{B}^0$ produced at $t = 0$ to decay as a B^0 or a $\overline{B}^0$ at time $t > 0$ are

$$\begin{aligned} P_{B^0\to B^0}(t) \;&=\; |g_+(t)|^2 \;&=\; \frac{1}{2}\;e^{-\Gamma\,t}\,\left\{\cosh\left(\frac{\Delta\Gamma}{2}t\right) \,+\, \cos\left(\Delta m\,t\right)\right\} \\ P_{\overline{B}^0\to\overline{B}^0}(t) \;&=\; |g_+(t)|^2 \;&=\; \frac{1}{2}\;e^{-\Gamma\,t}\,\left\{\cosh\left(\frac{\Delta\Gamma}{2}t\right) \,+\, \cos\left(\Delta m\,t\right)\right\} \\ P_{B^0\to\overline{B}^0}(t) \;&=\; \left|\frac{q}{p}\right|^2\,|g_-(t)|^2 \;&=\; \frac{1}{2}\,\left|\frac{q}{p}\right|^2\,e^{-\Gamma\,t}\,\left\{\cosh\left(\frac{\Delta\Gamma}{2}t\right) \,-\, \cos\left(\Delta m\,t\right)\right\} \\ P_{\overline{B}^0\to B^0}(t) \;&=\; \left|\frac{p}{q}\right|^2\,|g_-(t)|^2 \;&=\; \frac{1}{2}\,\left|\frac{p}{q}\right|^2\,e^{-\Gamma\,t}\,\left\{\cosh\left(\frac{\Delta\Gamma}{2}t\right) \,-\, \cos\left(\Delta m\,t\right)\right\}\;. \end{aligned}$$

Violation of *CP* symmetry in $B^0 - \overline{B}^0$ mixing implies that

$$P_{B^0\to\overline{B}^0}(t) \;\neq\; P_{\overline{B}^0\to B^0}(t)\;,$$

i.e. that

$$\left|\frac{q}{p}\right|^2 \;\neq\; \left|\frac{p}{q}\right|^2 \;\Leftrightarrow\; \left|\frac{q}{p}\right| \;\neq\; 1\;.$$

and that the mass eigenstates

$$|\,B_{H,L}\,\rangle \;=\; p\,|\,B^0\,\rangle \,\mp\, q\,|\,\overline{B}^0\,\rangle,$$

are not aligned with the *CP* eigenstates

$$|\, B_{CP\pm}\,\rangle \;=\; \frac{1}{\sqrt{2}}\left(|\, B^0\,\rangle \,\pm\, |\,\overline{B}^0\,\rangle\right) .$$

Convenient experimental observables are the time-dependent mixing asymmetries

$$a_{\rm mix}(t) \;\equiv\; \frac{N_{\overline{B}^0\to B^0}(t) \,-\, N_{B^0\to\overline{B}^0}(t)}{N_{\overline{B}^0\to B^0}(t) \,+\, N_{B^0\to\overline{B}^0}(t)} \;=\; \frac{\cos\left(\Delta m\, t\right) \,+\, \delta\, \cosh\left(\frac{\Delta\Gamma}{2}\, t\right)}{\cosh\left(\frac{\Delta\Gamma}{2}\, t\right) \,+\, \delta\, \cos\left(\Delta m\, t\right)}$$

and

$$\overline{a}_{\rm mix}(t) \;\equiv\; \frac{N_{\overline{B}^0\to\overline{B}^0}(t) \,-\, N_{\overline{B}^0\to B^0}(t)}{N_{\overline{B}^0\to\overline{B}^0}(t) \,+\, N_{\overline{B}^0\to B^0}(t)} \;=\; \frac{\cos\left(\Delta m\, t\right) \,-\, \delta\, \cosh\left(\frac{\Delta\Gamma}{2}\, t\right)}{\cosh\left(\frac{\Delta\Gamma}{2}\, t\right) \,-\, \delta\, \cos\left(\Delta m\, t\right)}$$

with

$$\delta \;\equiv\; \frac{1-|q/p|^2}{1+|q/p|^2} .$$

Again, $|q/p| \neq 1$ implies $\delta \neq 0$ and $a_{\rm mix}(t) \neq \overline{a}_{\rm mix}(t)$, i.e. *CP* violation in mixing. This case will be discussed in Section 3.3. Assuming for now that *CP* symmetry is conserved in mixing, $\delta = 0$ and the expressions simplify to

$$a_{\rm mix}(t) \;=\; \overline{a}_{\rm mix}(t) \;=\; \frac{\cos\left(\Delta m\, t\right)}{\cosh\left(\frac{\Delta\Gamma}{2}\, t\right)} .$$

Introducing the average decay width

$$\overline{\Gamma} \;\equiv\; \frac{\Gamma_H \,+\, \Gamma_L}{2} ,$$

it is convenient to define the dimensionless parameters

$$x \;\equiv\; \frac{\Delta m}{\overline{\Gamma}}$$

and

$$y \;\equiv\; \frac{\Delta\Gamma}{2\overline{\Gamma}}$$

and express the mixing asymmetry as

$$a_{\rm mix}(t) \;=\; \overline{a}_{\rm mix}(t) \;=\; \frac{\cos\left(x\,\Gamma t\right)}{\cosh\left(y\,\Gamma t\right)} .$$

The mixing asymmetry shows a damped oscillatory behaviour as a function of time, with an oscillation frequency and a damping parameter that are determined by the mass difference and the lifetime difference between the two mass eigenstates in the meson-antimeson system, respectively. This behaviour applies to all four neutral meson-antimeson systems, $K^0\overline{K}^0$, $D^0\overline{D}^0$, $B^0\overline{B}^0$ and $B_s^0\overline{B}_s^0$. The phenomenologies differ due to the different mass differences, lifetimes and lifetime differences. The relevant parameters for each of the four systems are compiled in Table 3.1 and the resulting time-dependent mixing behaviour illustrated in Figures 3.2, 3.3, 3.4 and 3.5.

In the $K^0\overline{K}^0$ system, the decay width difference between the two mass eigenstates is large since all possible decay modes for the long-lived mass eigenstate are suppressed as discussed in Section 2.5. The two mass eigenstates are therefore labelled by their lifetimes rather than by their masses, i.e. K_S^0 for the shorter-lived, light mass eigenstate and K_L^0 for the longer-lived, heavy mass eigenstate. The decay width of the K_L^0 being negligibly small compared

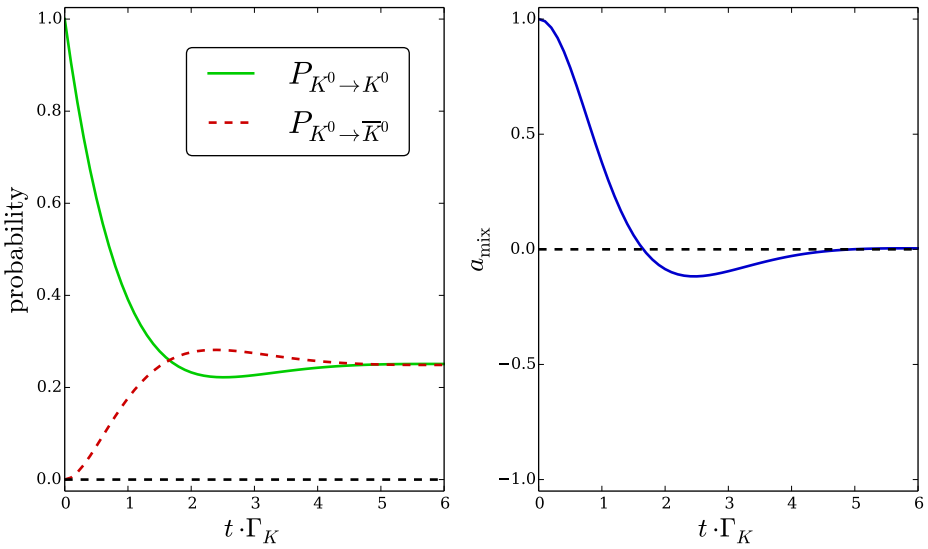

Figure 3.2: Illustration of $K^0\overline{K}^0$ mixing as a function of decay time expressed in units of the average K^0 lifetime. The effect of *CP* violation is neglected. Left: Probability for a K^0 produced at time $t = 0$ to decay as a K^0 or as a $\overline{K}^0$. Right: Mixing asymmetry.

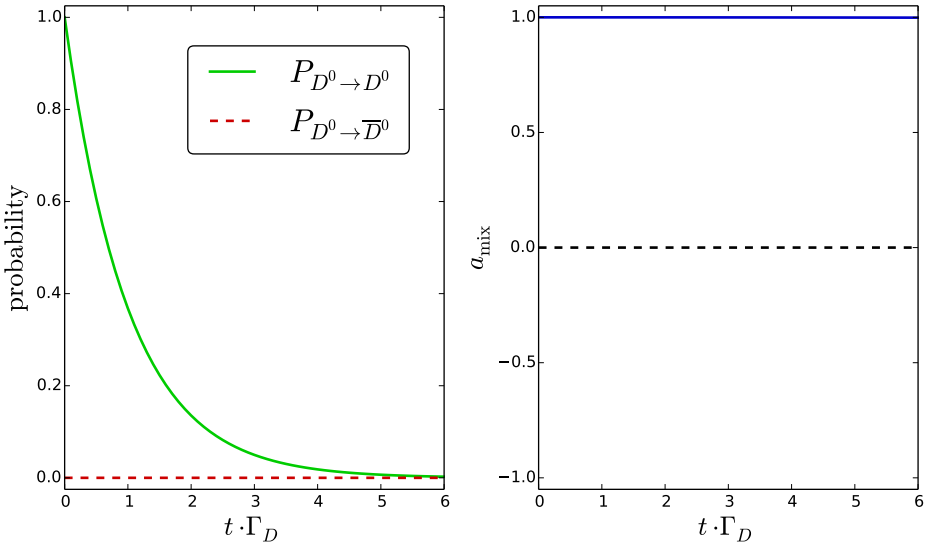

Figure 3.3: Illustration of $D^0\overline{D}^0$ mixing as a function of decay time expressed in units of the average D^0 lifetime. The effect of *CP* violation is neglected. Left: Probability for a D^0 produced at time $t = 0$ to decay as a D^0 or as a $\overline{D}^0$. Right: Mixing asymmetry.

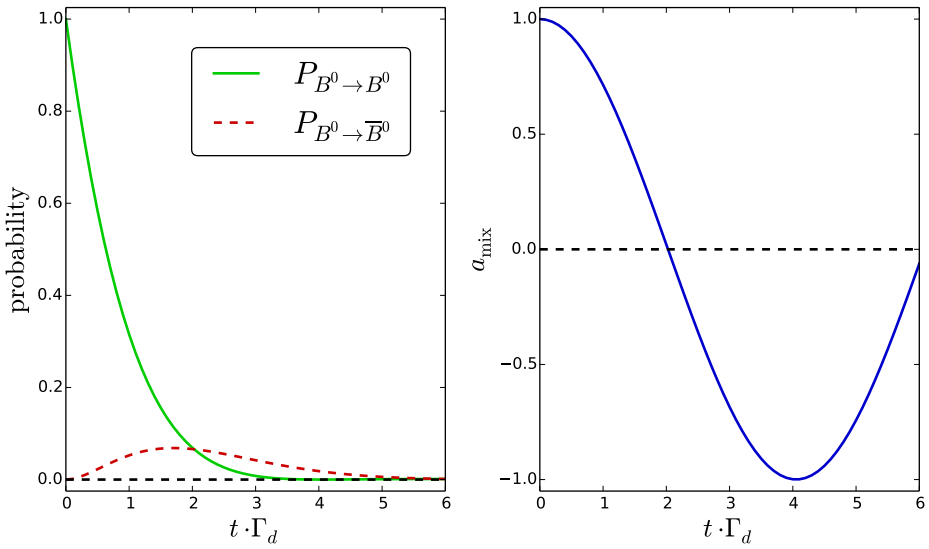

Figure 3.4: Illustration of $B^0\overline{B}^0$ mixing as a function of decay time expressed in units of the average B^0 lifetime. The effect of *CP* violation is neglected. Left: Probability for a B^0 produced at time $t = 0$ to decay as a B^0 or as a $\overline{B}^0$. Right: Mixing asymmetry.

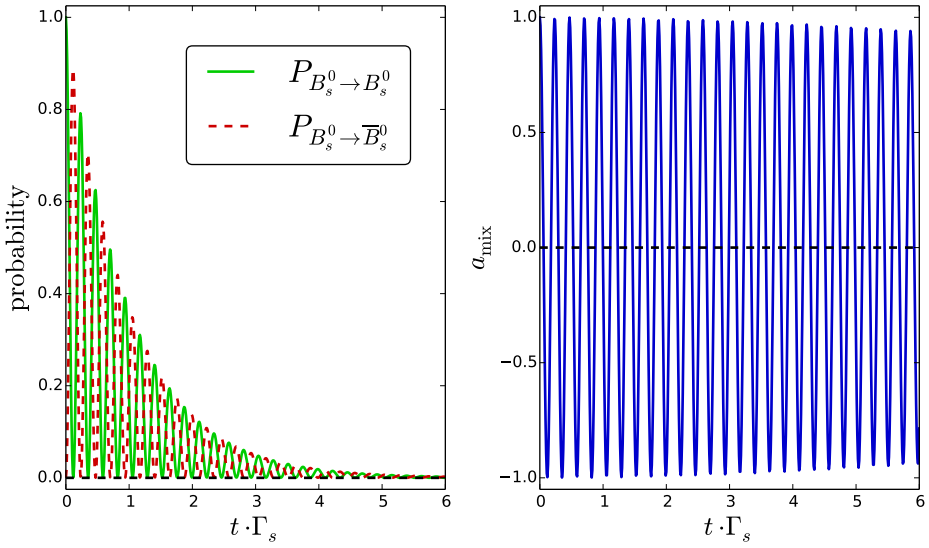

Figure 3.5: Illustration of $B_s^0\overline{B}_s^0$ mixing as a function of decay time expressed in units of the average B_s^0 lifetime. The effect of *CP* violation is neglected. Left: Probability for a B_s^0 produced at time $t = 0$ to decay as a B_s^0 or as a $\overline{B}_s^0$. Right: Mixing asymmetry.

Table 3.1: Compilation of the parameters relevant for mixing in the four neutral meson-antimeson systems. Values that are quoted with uncertainties are taken from the autumn-2014 compilation by the Heavy Flavour Averaging Group [2] resp. the 2014 edition of Review of Particle Physics [1]. Values quoted without uncertainties have been derived for the purpose of this table.

	$K^0\overline{K}^0$	$D^0\overline{D}^0$	$B^0\overline{B}^0$	$B_s^0\overline{B}_s^0$
$\tau = \frac{1}{\Gamma}$ [ps]	180	0.4101 ± 0.0015	1.519 ± 0.005	1.512 ± 0.007
Δm [ps^{-1}]	$(5.293 \pm 0.009) \times 10^{-3}$	$(0.95^{+0.41}_{-0.44}) \times 10^{-2}$	0.510 ± 0.003	17.757 ± 0.021
$\Delta\Gamma$ [ps^{-1}]	1.1×10^{-2}	3.5×10^{-2}	≈ 0	0.091 ± 0.008
$x = \Delta m \,/\, \overline{\Gamma}$	0.95	4.8×10^{-3}	0.775 ± 0.006	26.79 ± 0.08
$2y = \Delta\Gamma \,/\, \overline{\Gamma}$	2	$(1.29^{+0.14}_{-0.18}) \times 10^{-2}$	≈ 0	0.122 ± 0.009
$\chi = \frac{x^2+y^2}{2\,(1+x^2)}$	0.5	3.7×10^{-5}	0.1875 ± 0.017	0.499307 ± 0.000004

to that of the K_S^0, the decay width difference is essentially equal to the K_S^0 decay width. The oscillation parameter, x_K, and the damping parameter, y_K, being of similar magnitude, flavour oscillation in the $K^0\overline{K}^0$ system is strongly damped. The short-lived, light eigenstate has essentially decayed away after one oscillation period and only the long-lived, heavy mass eigenstate survives.

The situation is different in the other neutral meson-antimeson systems, where many decay modes exist and the lifetimes of the two mass eigenstates are therefore of similar magnitude. As discussed above, the decay width difference $\Delta\Gamma$ is given by the magnitude of the dispersive part of the mixing amplitude, while the mass difference Δm is determined by the magnitude of the absorptive part of the mixing amplitude. In the Standard Model, mixing is induced by the box diagrams shown in Figure 3.1. In the $B^0\overline{B}^0$ system, the contribution of the diagram with intermediate quark lines i and j ($i, j \in \{u, c, t\}$) can be written as

$$(V_{ib}V_{id}^*)(V_{jb}V_{jd}^*) \cdot \eta \cdot S_0(m_i^2/m^2, m_j^2/m_W^2) \ ,$$

where V_{ib}, V_{id}, V_{jb} and V_{jd} are the relevant CKM matrix elements, η describes short-distance QCD corrections, and the so-called Inami-Lim functions $S_0(x_i, x_j)$ [109] are polynomials of the squared masses of the intermediate quarks. Due to the large mass of the top quark, box diagrams with internal top-quark lines dominate over those with charm- or up-quark lines. The dispersive part of the mixing amplitude is therefore determined by the size of the box diagram with intermediate top quarks. Due to energy conservation, the absorptive part of the mixing amplitude, which proceeds through on-shell intermediate states, cannot receive contributions from internal top-quarks and is therefore dominated by diagrams with internal charm-quark lines. Both amplitudes are strongly suppressed by the smallness of the CKM matrix elements — both $|V_{tb}V_{td}^*|$ and $|V_{cb}V_{cd}^*|$ are of order λ^3 in terms of the Wolfenstein parameter $\lambda \approx 0.23$. While the mass difference between the two mass eigenstates is still sizeable due to the large value of the Inami-Lim factor, the decay width difference is negligibly small. This results in a weakly damped oscillation pattern. The time-integrated probability, χ_d, for a B^0 produced at $t = 0$ to decay as a $\overline{B}^0$ is sizeable.

Similar arguments hold in the $B_s^0\overline{B}_s^0$ system, except that the suppression of the mixing amplitudes due to the magnitude of the involved CKM matrix elements is less large — both $|V_{ts}V_{tb}^*|$ and $|V_{cs}V_{cb}^*|$ are both of order λ^2. The mass difference between the two mass eigenstates is therefore expected to be about a factor 25 larger than in the $B^0\overline{B}^0$ system and the decay width difference is not negligible here. Both expectations have been confirmed by measurements. The large value of Δm_s leads to rapid oscillations and the time-integrated mixing probability, χ_s, is 50%, i.e. a B_s^0 produced at $t = 0$ has equal probability to decay as a B_s^0 or a $\overline{B}_s^0$.

In the $D^0\overline{D}^0$ system, finally, the dispersive part of the mixing amplitude is dominated by the box diagram with internal b quark and the absorptive part of the mixing amplitude is

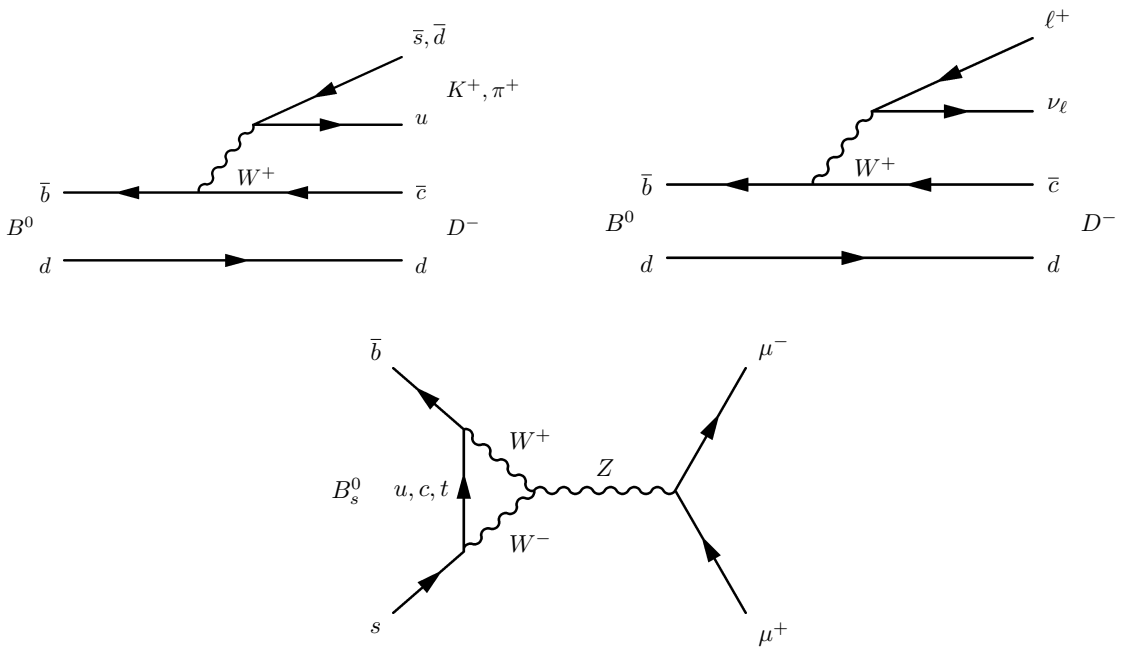

Figure 3.6: Examples of (top left) hadronic, (top right) semi-leptonic and (bottom) leptonic B-meson decays.

dominated by internal s quark lines. The Inami-Lim factors are therefore significantly smaller than the corresponding factors in the $B^0\overline{B}^0$ and $B_s^0\overline{B}_s^0$ systems. The absorptive part of the mixing amplitude is further suppressed by the magnitudes of the CKM matrix elements — $|V_{cb}V_{ub}| \propto \lambda^5$. Both the decay width difference and the mass difference between the two mass eigenstates are therefore very small, resulting in very little mixing. The time-integrated probability, χ_D, for a D^0 produced at $t = 0$ to decay as a $\overline{D}^0$ is negligibly small.

3.2 Classification of heavy quark decays

Ground-state hadrons that contain a heavy quark decay through the weak interaction. There are several criteria according to which such decays are classified: the type of final state particles created in the decay, the type of processes inlved in the decay, the colour flow between quarks in the initial and final state, and the magnitude of the involved CKM matrix elements.

Decays are called hadronic if they lead to a final state that contains only hadrons, they are called semi-leptonic if the final state contains a mix of hadrons and leptons, and they are called leptonic if the final state consists only of leptons. Examples of these three types of decays are illustrated in Figure 3.6. Note that decays leading to a purely leptonic final state are Flavour-Changing Neutral Current decays and, because of the GIM mechanism discussed in Section 2.6, can occur only via diagrams involving an internal loop.

Decays that involve a closed internal loop are called penguin diagrams, while diagrams that do not involve such loops are called tree diagrams. Examples of penguin and tree diagrams are shown in Figure 3.7. All else being equal, penguin diagrams are typically suppressed by a factor of about three compared to tree diagrams, because they involve a loop as well as an extra factor of α_{strong} at the scale of the b quark mass.

As depicted in Figure 3.7, hadronic decay diagrams can be further subdivided external diagrams, in which the created quark-antiquark pair ends up in the same meson and in internal dagrams in which the created quark and antiquark end up in two different mesons. In internal tree diagrams, the newly created quark-antiquark pair has to be produced with a matching combination of colour charge such that two colour-neutral mesons can be formed in combination

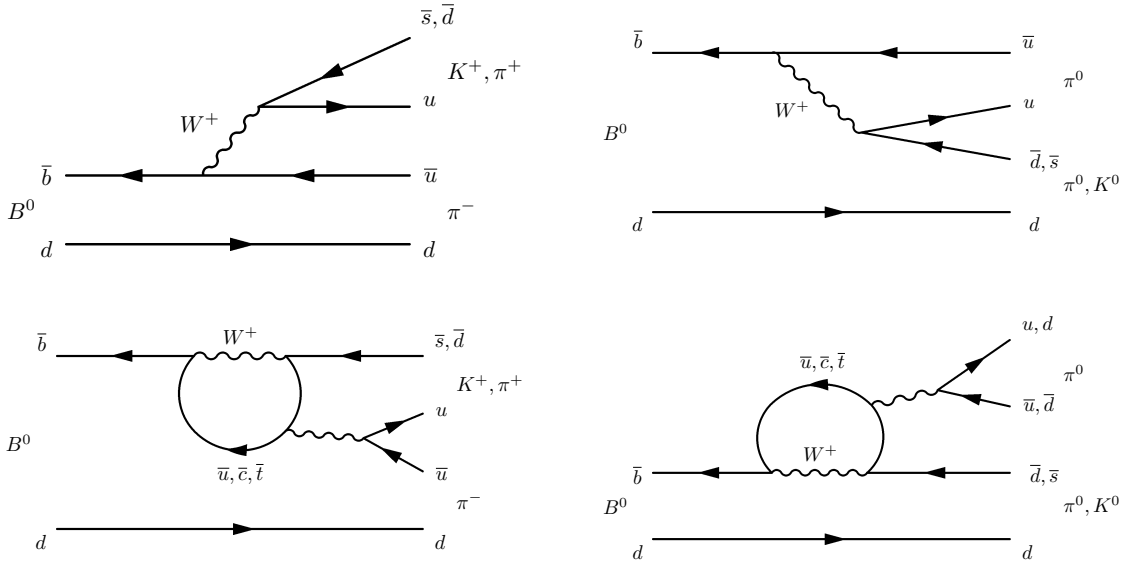

Figure 3.7: Examples for (top left) external and (top right) internal tree diagrams and for (bottom left) internal and (bottom right) external penguin diagrams.

with the incoming antiquark and quark. In external tree decays, no such restriction applies since the quark-antiquark pair is always created in a colour singlet state as required for forming a meson. The colour flow in the two types of diagrams is illustrated in Figs. 3.8. External tree diagrams have two independent colour loops for a total of 3×3 possible combinations of colour states, while internal tree diagrams have only one colour loop with three possible colour states. All else being equal, the decay amplitude for internal tree decays is therefore suppressed by a factor of three compared to that for the equivalent external tree diagrams. The two types of diagrams are also referred to as colour suppressed and colour allowed.

The situation for Penguin decays is more involved, as illustrated in Figure 3.9. Internal penguin diagrams have two colour loops and are therefore colour allowed. The naive external penguin diagram shown in Figure 3.9 has a single colour loop but is in fact forbidden, since gluons are colour octet objects and a single gluon cannot lead to a colour-singlet meson. Therefore, at least two gluons have to be exchanged in external penguin diagrams and, as shown in Figure 3.9, this again leads to two colour loops and no colour suppression. However, due to the exchange of a second gluon, these diagrams are suppressed by a factor α_{strong}. The suppression can be significant since the second gluon, which determines the relevant scale for α_{strong}, can be soft

The magnitude of the involved CKM matrix elements is usually expressed in terms of powers of the Wolfenstein parameter $\lambda = \sin\theta_C$, where $\theta_C \approx 0.23$ is the Cabibbo quark mixing angle. All b quark decay amplitudes are proportional to at least λ^2. These amplitudes are called Cabibbo allowed. Amplitudes that are proportional to λ^3 are called Cabibbo suppressed and amplitudes that are proportional to λ^4 are called doubly Cabibbo suppressed.

3.3 Sources of *CP* violation in the Standard Model

By definition, *CP* symmetry is violated if two charge-conjugated processes do not occur at the same rate. As will be shown below, this requires that at least two amplitudes with different weak phase contribute to the process. The weak phases change sign between the two charge-conjugated processes and interference effects can give rise to a *CP* violating rate difference. The complex phase in the CKM quark mixing matrix, introduced iN Section 1.3 is the only weak phase that appears in the Standard Model of particle physics and this phase is therefore

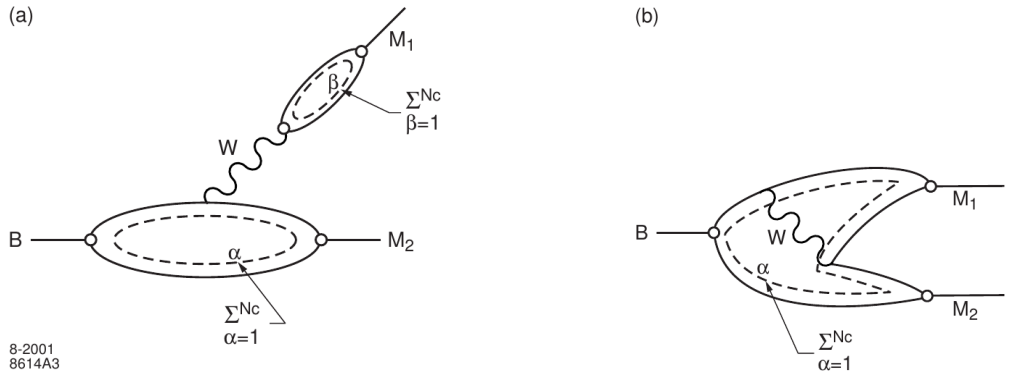

Figure 3.8: Illustration of the colour flow in (left) external and (right) internal tree diagrams (from [110]).

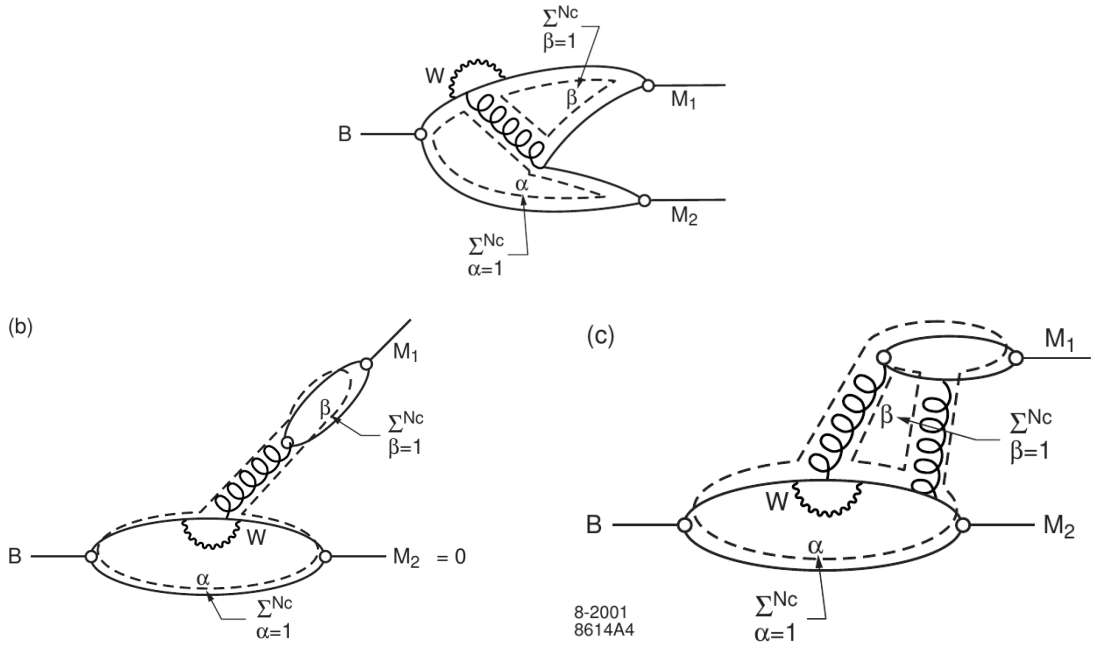

Figure 3.9: Illustration of the colour flow in (top) internal and (bottom) external penguin diagrams (from [110]). The naive penguin diagram shown in the bottom left diagram is forbidden since a single gluon is a colour octet object and cannot give rise to a meson, which has to be a colour singlet state

said to be the sole source of all *CP* violation in the Standard Model.

Three distinct mechanisms have been identified that can lead to *CP* violating asymmetries in the Standard Model:

- *CP* violation in mixing in the neutral meson-antimeson systems is caused by the interference of box diagrams with different internal quark lines. Mixing is the dominant source of *CP* violation in the $K^0\overline{K}^0$ system, while *CP* violation in mixing is predicted to be very small in the $B^0\overline{B}^0$ and $B_s^0\overline{B}_s^0$ systems.

- *CP* violation in decay is caused by the interference of decay diagrams with different weak phase and different strong phase leading to the same final state. This is the only possible source of *CP* violation for charged B mesons. In general, poorly known strong phases limit the precision with which the weak phase can be extracted from the measured asymmetry. There are, however, cases in which the weak phase can be cleanly determined

using a combination of several related decay modes and exploiting symmetries of the strong interaction between these modes.

- *CP* violation in the interference of mixing and decay can occur in the $B^0\overline{B}^0$ and $B_s^0\overline{B}_s^0$ systems if the B^0 or B_s^0 and the $\overline{B}^0$ or $\overline{B}_s^0$ can decay to the same final state. A prominent example is the final state $J/\psi K_S^0$, which allowed the B factories to establish *CP* violation in the $B^0\overline{B}^0$ system. A time-dependent *CP* violating is caused in such processes by the interference between the direct decay of the meson to the given final state and the amplitude for the process in which the meson first mixes to its antiparticle, which then decays to the same final state.

In the remainder of this section, the three mechanisms are discussed one by one

3.3.1 *CP* violation in mixing

Following the discussion in Section 3.1, and using again the $B^0\overline{B}^0$ system as a proxy for all four neutral meson-antimeson systems, *CP* symmetry is violated in mixing if the probability for an initial B^0 meson to decay after a time t as a $\overline{B}^0$ differs from the probability for an initial $\overline{B}^0$ meson to decay as a B^0 after the same time t. This is the case if

$$\left|\frac{q}{p}\right|^2 \;=\; \left|\frac{M_{12}^* - i\,\Gamma_{12}^*/2}{M_{12} - i\,\Gamma_{12}/2}\right| \;\neq\; 1\;,$$

i.e. if a non-vanishing complex phase appears between the dispersive part of the mixing amplitude, M_{12}, and its absorptive part, Γ_{12}.

As shown in Section 3.1, in the Standard Model the dispersive part of the $B^0-\overline{B}^0$ mixing amplitude is dominated by box diagrams with internal top-quark lines while its absorptive part is dominated by diagrams with internal charm-quark lines. The CKM phase between $(V_{tb}V_{td}^*)$ and $(V_{cb}V_{cd}^*)$ causes a relative phase between Γ_{12} and M_{12} as required for *CP* violation to occur in mixing. However, the generated *CP* asymmetry is expected to be small. Since diagrams with top-quark lines strongly dominate over diagrams with charm-quark lines, the dispersive part of the mixing amplitude dominates also dominates strongly over the absorptive part, i.e.

$$\Gamma_{12} \;\ll\; M_{12}\;,$$

which implies that

$$\frac{q}{p} \;\approx\; -\arg M_{12}$$

is almost a pure phase and

$$\left|\frac{q}{p}\right|^2 \;\approx\; 1\;.$$

Similar arguments hold in the $B_s^0\overline{B}_s^0$ system and the Standard Model therefore predicts *CP* violation in mixing to be very small in the $B^0\overline{B}^0$ and $B_s^0\overline{B}_s^0$ systems.

The situation is different in the $K^0\overline{K}^0$ system, where transitions with intermediate top quarks are significantly suppressed by the ratio of the magnitudes of the involved CKM matrix elements, $|V_{td}V_{ts}^*| \propto \lambda^5$ while $|V_{cd}V_{cs}^*| \propto \lambda$. As a consequence, the absorptive part of the mixing amplitude is less suppressed compared to the dispersive amplitude. Indeed, as discussed in Section 2.5, mixing is the dominant source of *CP* violation in the $K^0\overline{K}^0$ system.

CP violation in mixing is best probed in semileptonic decays, in which the flavour of the meson at its decay can be derived from the charge of the final-state lepton. At the quark level, conservation of electric charge implies that $\overline{b} \to \overline{c}\,\ell^+\nu_\ell$ and $\overline{b} \to \overline{c}\,\ell^+\nu_\ell$, and similar for the decay of s and $\overline{s}$ quarks. Consequently K^0, B^0 and B_s^0 mesons decay to positive leptons, while their antiparticles decay to negative leptons.

In the $K^0\overline{K}^0$ system, *CP* violation in mixing can be observed by a charge asymmetry in the semileptonic decays of the long-lived component,

$$|\,K_L^0\,\rangle \;=\; p\,|\,K^0\,\rangle \,+\, q\,|\,\overline{K}^0\,\rangle\,.$$

In the $B^0\overline{B}^0$ and $B_s^0\overline{B}_s^0$ systems, it is not possible to isolate one of the two mass eigenstates. Instead, one measures the asymmetry in the rate of wrong-sign decays

$$a_{\rm sl}^d \;\equiv\; \frac{\frac{d\Gamma}{dt}\left(\overline{B}^0 \to \ell^+ X\right) \,-\, \frac{d\Gamma}{dt}\left(B^0 \to \ell^- X\right)}{\frac{d\Gamma}{dt}\left(\overline{B}^0 \to \ell^+ X\right) \,+\, \frac{d\Gamma}{dt}\left(B^0 \to \ell^- X\right)} \;=\; \frac{1-|q/p|^4}{1+|q/p|^4}\;,$$

which is zero if *CP* symmetry is conserved in mixing. The semileptonic asymmetry $a_{\rm sl}^s$ in the $B_s^0\overline{B}_s^0$ system is defined in the same manner. Note that $a_{\rm sl}^d$ and $a_{\rm sl}^s$, although defined as an asymmetry of time-dependent decay rates, are in fact time-independent quantities. Regarding the initial flavour of the B meson at $t = 0$, one has to either rely on the assumption that equal numbers of B_q^0 and $\overline{B}_q^0$ mesons are produced in the beam-beam collisions, or the flavour at production has to be derived indirectly from other information in the event. The latter can be achieved by exploiting the fact that the creation of B mesons proceeds almost exclusively through the associated production of $b\bar{b}$ quark pairs. The flavour of the accompanying beauty hadron can be derived through the observation of flavour-specific signatures of its decay and it is then assumed that this flavour is opposite to the initial flavour of the B meson used in the measurement of the asymmetry. The approach is known as opposite side flavour tagging and will be discussed in Sections 4.1 and 4.2.

A related observable that probes *CP* violation in mixing is the so-called same-sign dilepton charge asymmetry

$$a_{sl} \;=\; \frac{N(\ell^+\ell^+X) - N(\ell^-\ell^-X)}{N(\ell^+\ell^+X) + N(\ell^-\ell^-X)}$$

in events in which both b hadrons decayed semileptonically. The observation of two negative leptons in such events implies that a B^0 or B_s^0 has mixed into a $\overline{B}^0$ or $\overline{B}_s^0$, while the observation of two positive leptons implies that a $\overline{B}^0$ or $\overline{B}_s^0$ has has mixed into a B^0 or B_s^0. If unequal numbers of events with two positive leptons and two negative leptons are observed, one of the two mixing processes must occur more frequently than the other and *CP* symmetry is violated in mixing. The D0 collaboration has published measurements of an unexpectedly large same-sign dilepton charge asymmetry, which are in tension with Standard Model predictions at the level of three standard deviations. However, these deviations have not been confirmed by complementary measurements at the B factories and at LHCb. These measurements will be discussed in Section 6.2.

3.3.2 *CP* violation in the decay

Taking again the $B^0\overline{B}^0$ system as a proxy for all four neutral meson-antimeson systems, *CP* symmetry is violated in the decay if the time-integrated decay rate of a neutral meson to a flavour-specific final state f differs from the decay rate of the $\overline{B}^0$ meson to the charge conjugated final state $\overline{f}$. The effect is often referred to as direct *CP* violation. In order for an observable *CP* asymmetry to be generated, it is necessary that at least two amplitudes with different weak and strong phases contribute to the decay. These are typically a tree amplitude and a penguin amplitude, as illustrated in Figure 3.10 for the example of the decay $B^0 \to K^+\pi^-$. In the case of two contributing amplitudes a_i $(i = 1, 2)$ with strong phases δ_i and weak phases ϕ_i, the total decay amplitude A_f for the decay $B \to f$ is given by

$$A_f \;=\; |a_1|\; e^{i(\delta_i\,+\,\phi_i)} \;+\; |a_2|\; e^{i(\delta_2\,+\,\phi_2)}$$

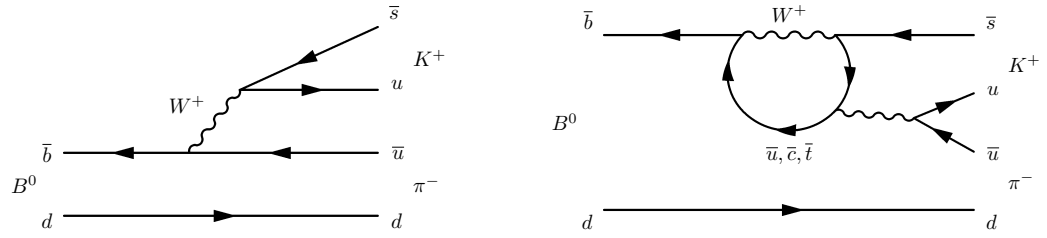

Figure 3.10: Feynman diagrams for (left) the tree amplitude and (right) the penguin amplitude contributing to the decay $B^0 \to K^+\pi^-$.

and the decay amplitude $\overline{A}_{\overline{f}}$ for the decay $\overline{B} \to \overline{f}$ is given by

$$\overline{A}_{\overline{f}} \;=\; |a_1|\; e^{i(\delta_i - \phi_i)} \;+\; |a_2|\; e^{i(\delta_2 - \phi_2)} \;.$$

Note, that the weak phases ϕ_i change sign between the two charge conjugated processes while the strong phases δ_i do not. The decay rates of the charge conjugated processes are therefore

$$\Gamma(B \to f) \;=\; |A_f|^2 \;=\; |a_1|^2 + |a_2|^2 + |a_1||a_2| \left(e^{-i(\delta_2 - \delta_1)}\, e^{-i(\phi_2 - \phi_1)} \;+\; e^{+i(\delta_2 - \delta_1)}\, e^{+i(\phi_2 - \phi_1)} \right)$$

and

$$\Gamma(\overline{B} \to \overline{f}) \;=\; |\overline{A}_{\overline{f}}|^2 \;=\; |a_1|^2 + |a_2|^2 + |a_1||a_2| \left(e^{-i(\delta_2 - \delta_1)}\, e^{+i(\phi_2 - \phi_1)} \;+\; e^{+i(\delta_2 - \delta_1)}\, e^{-i(\phi_2 - \phi_1)} \right)$$

and the time-integrated decay rate asymmetry is

$$a_f \;=\; \frac{\Gamma(B \to f) \;-\; \Gamma(\overline{B} \to \overline{f})}{\Gamma(B \to f) \;+\; \Gamma(\overline{B} \to \overline{f})} \;=\; \frac{2|a_1|\,|a_2|\,\sin(\delta_2 - \delta_1)\,\sin(\phi_2 - \phi_1)}{|a_1|^2 \;+\; |a_2|^2 \;+\; 2|a_1||a_2|\,\cos(\delta_2 - \delta_1)\,\cos(\phi_2 - \phi_1)} \;.$$

It can be seen from the right-hand side of this equation that both the weak phases and the strong phases of the contributing amplitudes have to differ in order to generate a *CP*-violating asymmetry in the decay rates. The interplay of strong and weak phases in generating such an asymmetry is illustrated in Figure 3.11.

The classic example of direct *CP* violation is that in the decay of neutral kaons to two pions, the measurement of which was discussed in Section 2.11. Also in this case, the *CP* asymmetry is generated by the interference of tree and penguin amplitudes, as illustrated in Figure 2.18. The two interfering decay amplitudes in the $K^0\overline{K}^0$ system are usually defined, however, in terms of the strong isospin of the two-pion final state (see Section 2.1 for a brief introduction of the concept of isospin). The isospin of the two final-state pions can combine to a total of $I = 0$ or $I = 2$, the state $I = 1$ being forbidden by Bose-Einstein statistics. The two decay amplitudes for the decay $K^0 \to \pi\pi$ are usually parametrized as

$$A(K^0 \to (2\pi)_{I=0,2}) \;=\; A_I\, e^{i\delta_I} \;,$$

where A_I is the complex, weak decay amplitude and δ_I is the strong phase. The corresponding amplitudes for the decay $\overline{K}^0 \to \pi\pi$ are then

$$A(\overline{K}^0 \to (2\pi)_{I=0,2}) \;=\; A_I^*\, e^{i\delta_I} \;.$$

The charged and neutral two-pion states contain different fractions of the two Isospin amplitudes,

$$|\,\pi^+\pi^-\,\rangle \;=\; \frac{1}{\sqrt{3}} \left(\sqrt{2}\,|\,\pi^+\pi^-, I = 0\,\rangle \;+\; |\,\pi^+\pi^-, I = 2\,\rangle \right)$$

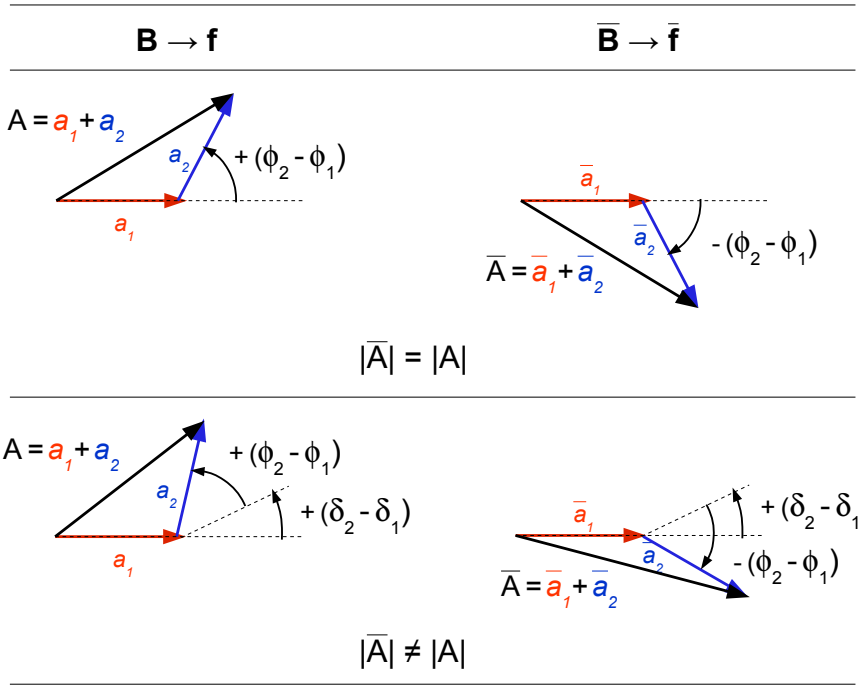

Figure 3.11: Illustration of the interplay between the strong phase difference $\delta_2 - \delta_1$ and the weak phase difference $\phi_2 - \phi_1$ of the two amplitudes a_1 and a_2 in generating a *CP* violating difference in the magnitude of the decay amplitudes $A = a_1 + a_2$ and $\overline{A} = \overline{a}_1 + \overline{a}_2$. Note that the magnitudes of a_1 as well as a_2 are the same in all four diagrams.

and

$$|\,\pi^0\pi^0\,\rangle \;=\; \frac{1}{\sqrt{3}}\left(|\,\pi^0\pi^0, I=0\,\rangle \;-\; \sqrt{2}\,|\,\pi^0\pi^0, I=2\,\rangle\right) \;,$$

leading to the parameter ε' that describes direct *CP* violation in the decay of neutral kaons,

$$\varepsilon' \;=\; \frac{i\,e^{i(\delta_2-\delta_0)}}{\sqrt{2}}\;\mathrm{Im}\left(\frac{A_2}{A_0}\right) \;.$$

Direct *CP* violating is small in the $K^0\overline{K}^0$ system due to the fact that the amplitude A_2 is strongly supressed compared to the amplitude A_0,

$$\frac{|A_2|}{|A_0|} \;\approx\; \frac{1}{22} \;,$$

and the interference is therefore small. The presence of the poorly known strong rescattering phases δ_2 and δ_0 introduces large uncertainties when trying to relate the measured value of ε' to the underlying weak CKM phases.

Direct *CP* violating asymmetries in the decay can be large in the $B^0\overline{B}^0$ and $B_s^0\overline{B}_s^0$ systems as well as in charged B mesons, where they are the only possible source of *CP* violation. The extraction of the interesting weak phases, however, is complicated also here by the poorly known values of the strong phases. In some cases, the weak CKM phases can be extracted cleanly by combining related decay modes and exploiting symmetries of the strong interaction to eliminate the strong phases. A prominent case is the determination of the CKM angle γ from measurements of direct *CP* asymmetries in the decay $B^\pm \to DK^\pm$, which will be discussed in Section 5.5.

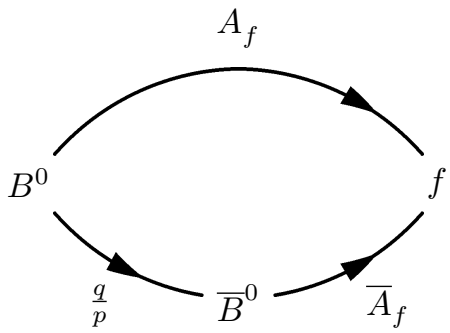

Figure 3.12: Illustration of the phases that lead to a *CP* violating asymmetry through the interference of mixing and decay in the $B^0\overline{B}^0$ and $B_s^0\overline{B}_s^0$ systems.

3.3.3 *CP* violation in the interference of mixing and decay

In the $B^0\overline{B}^0$ and $B_s^0\overline{B}_s^0$ systems, a *CP* violating asymmetry can also be induced by the interference of the mixing amplitude and the decay amplitude in decays to *CP* eigenstates f that are accessible to both the B^0 or B_s^0 and the $\overline{B}^0$ or $\overline{B}_s^0$ meson. The mechanism and its formulation are the same in the $B^0\overline{B}^0$ and $B_s^0\overline{B}_s^0$ systems and in the following the $B^0\overline{B}^0$ system will again be taken as a proxy for both. The two interfering amplitudes are on the one hand that for the direct decay of the B^0 to the final state f and on the other hand that for the process in which the B^0 first mixes into a $\overline{B}^0$ and the $\overline{B}^0$ then decays into the same final state. The involved phases are illustrated in Figure 3.12.

The relative phase between the two amplitudes for an initial B^0 meson is

$$\lambda_f \;=\; \left(\frac{q}{p}\right)\left(\frac{\overline{A}_f}{A_f}\right) \;,$$

while for an initial $\overline{B}^0$ meson it is

$$\left(\frac{p}{q}\right)\left(\frac{A_f}{\overline{A}_f}\right) \;=\; \frac{1}{\lambda_f} \;.$$

The interference of the two amplitudes leads to a time dependent decay rate asymmetry

$$\begin{aligned} a_f(t) \;&=\; \frac{\frac{d\Gamma}{dt}(\overline{B}^0_{(s)}(t)\to f) \;-\; \frac{d\Gamma}{dt}(B^0_{(s)}(t)\to f)}{\frac{d\Gamma}{dt}(\overline{B}^0_{(s)}(t)\to f) \;+\; \frac{d\Gamma}{dt}(B^0_{(s)}(t)\to f)} \\ &=\; \frac{-\,C_f\,\cos(\Delta m\,t) \;+\; S_f\,\sin(\Delta m\,t)}{\cosh(\Delta\Gamma\,t/2) \;+\; \Omega_f\,\sinh(\Delta\Gamma\,t/2)} \end{aligned}$$

with

$$C_f \;=\; \frac{1 \;-\; |\lambda_f|^2}{1 \;+\; |\lambda_f|^2} \quad ; \quad S_f \;=\; \frac{2\,\mathrm{Im}\,(\lambda_f)}{1 \;+\; |\lambda_f|^2} \quad ; \quad \Omega_f \;=\; 1 \;-\; C_f^2 \;-\; S_f^2$$

If a single amplitude dominates the decay, there can be no *CP* violating asymmetry in the decay and $|\overline{A}_f/A_f| = 1$. Assuming furthermore that *CP* violation in mixing is negligibly small — which is a valid approximation in the $B^0\overline{B}^0$ and $B_s^0\overline{B}_s^0$ systems — it follows that $|\lambda_f|^2 = 1$, $C_f = 0$ and $S_f = \mathrm{Im}\,(\lambda_f)$ such that the expression simplifies to

$$a_f(t) \;=\; \frac{\mathrm{Im}\,(\lambda_f)\,\sin(\Delta m\,t)}{\cosh(\Delta\Gamma\,t/2) \;+\; \left(1 - \mathrm{Im}(\lambda_f)^2\right) \times \sinh(\Delta\Gamma\,t/2)} \;.$$

Finally, in the $B^0\overline{B}^0$ system the decay width difference $\Delta\Gamma$ is negligibly small and the time-dependent *CP* asymmetry is then simply given by

$$a_f(t) \;=\; \mathrm{Im}(\lambda_f)\,\sin\left(\Delta m\, t\right)\;.$$

Since *CP* violating asymmetries can be large and no strong phases are involved in the extraction of the weak phase from the measured asymmetry, *CP* violation in the interference of mixing and decay in the $B^0\overline{B}^0$ and $B_s^0\overline{B}_s^0$ systems provides a powerful approach for measuring CKM phases. The most prominent example is the measurement of the CKM angle β from the measurement of the time-dependent *CP* asymmetry in so-called golden decay mode $B^0 \to J/\psi K_S^0$. This measurement will be discussed in Section 5.3.

Chapter 4

Introducing the Players: The Experimental Facilities

> The great advances in science usually result from new tools rather than from new doctrines.
>
> — Freeman J. Dyson, The American Mathematical Monthly 103 (1996) 800.

In this chapter, the main experimental facilities will be introduced that have shaped flavour physics over the last fifteen years. On the one hand, these are the two B factories, BaBar at SLAC and Belle at KEK, which employed high-luminosity e^+e^- colliders operating at the $\Upsilon(4S)$ resonance to produce large samples of $B^0\overline{B}^0$ and B^+B^- events. On the other hand, there are the two general purpose detectors, CDF and D0, at the Tevatron and more recently the dedicated heavy flavour experiment LHCb at the LHC, all of which exploit the large $b\bar{b}$ production cross section at high-energy hadron colliders to produce huge samples of all types of b hadrons. The following sections give a brief introduction to each of the experiments, discussing the experimental challenges and the specific advantages of each of the two approaches.

4.1 B factories: BaBar and Belle

B factories exploit the $\Upsilon(4S)$ resonance as a clean source of $B^0\overline{B}^0$ and B^+B^- pairs. The $\Upsilon(4S)$ is a $b\bar{b}$ state with quantum numbers $J^{PC} = 1^{--}$, allowing its exclusive production in e^-e^+ collisions, and with a mass just above the above the production thresholds for $B^0\overline{B}^0$ and B^+B^- pairs. The $\Upsilon(4S)$ decays with a probability of about 52 % to B^+B^- and with a probability of 48 % to $B^0\overline{B}^0$ [1].

A BaBar measurement of the $b\bar{b}$ excitation function in the region of the $\Upsilon(4S)$ resonance is shown in Figure 4.1. The absolute $e^-e^+ \to b\bar{b}$ production cross section at the $\Upsilon(4S)$ resonance is about 1 nb and the ratio of the $b\bar{b}$ production cross section to the total inelastic e^-e^+ cross section is about 25%. Taking into account the $\Upsilon(4S)$ branching fraction into $B^0\overline{B}^0$ of about 50 % and assuming a combined duty factor of accelerator and experiment of 30 %, the production of 10^7 $B^0\overline{B}^0$ pairs per year requires an instantaneous luminosity of

$$L = \frac{10^7}{(3.15 \times 10^7 \text{ s} \cdot 30\,\%) \cdot (10^{-33} \text{ cm}^2 \cdot 50\,\%)} \approx 2 \times 10^{33} \text{ cm}^{-2} \text{ s}^{-1}$$

The design luminosity of the PEP-II and KEKB colliders hosting the BaBar and Belle experiments was 3×10^{33} cm^{-2}s^{-1} and the record peak luminosity reached at KEKB was 2.1×10^{34} cm^{-2}s^{-1}. The BaBar experiment operated from 1999 until April 2008 and collected an integrated luminosity of 433 fb^{-1} at the $\Upsilon(4S)$ resonance, corresponding to 467×10^6 produced $B\overline{B}$ pairs (including $B^0\overline{B}^0$ and B^+B^-); the Belle experiment operated from 1999 until

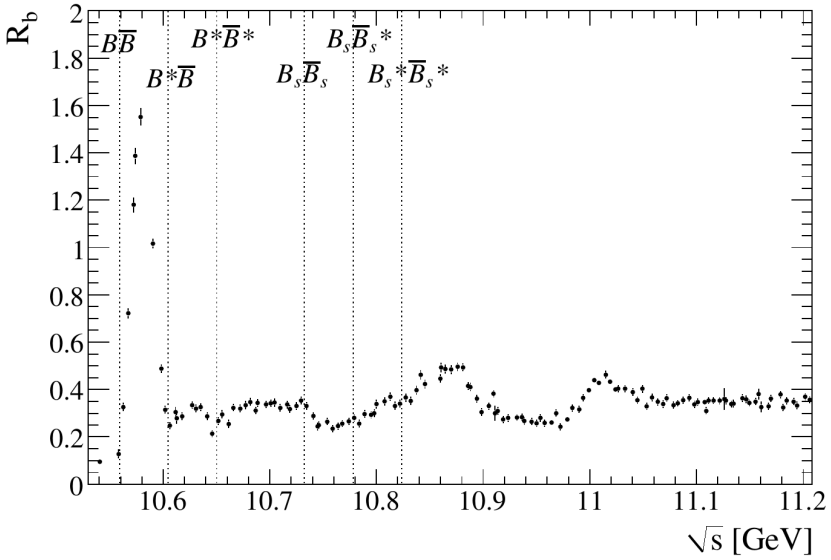

Figure 4.1: BaBar measurement of the $b\bar{b}$ production cross section, normalised to the cross section for $e^-e^+ \to \mu^-\mu^+$, as a function of the e^-e^+ center-of-mass energy. Vertical lines indicate the production thresholds for $B\overline{B}$ pairs (where $B\overline{B}$ stands for $B^0\overline{B}^0$ or B^+B^-), $B_s^0\overline{B}_s^0$ pairs and pairs involving radially excited $B^\star$ mesons. The $\Upsilon(4S)$ resonance is the narrow structure between the $B\overline{B}$ and $B^\star\overline{B}$ thresholds (from [111]).

November 2010 and collected an integrated luminosity of 711 fb^{-1} at the $\Upsilon(4S)$ resonance, corresponding to 772×10^6 produced $B\overline{B}$ pairs. Both BaBar and Belle collected smaller event samples also at other $\Upsilon(nS)$ resonances and at center-of-mass energies in between the resonances.

As discussed in Chapter 3, many interesting observables require to measure decay-time dependent rate asymmetries in the $B^0\overline{B}^0$ system. For two reasons, this would be impossible at a symmetric e^-e^+ collider in which the two beams have equal energies and the center-of-mass system of the collision is identical to the laboratory system. Firstly, the energy release in the decay is small. The momentum of the produced B^0 and $\overline{B}^0$ mesons in the centre-of-mass system of the collision is

$$p_B \;=\; \frac{1}{2}\,\sqrt{m^2_{\Upsilon(4s)} \,-\, (2\,m_{B^0})^2} \;=\; 327 \text{ MeV} \;,$$

corresponding to a Lorentz boost of $\beta\gamma = 0.064$. This results in a mean decay length of

$$\beta\gamma\, c\tau_{B^0} \;=\; 0.064 \cdot 3 \times 10^8 \text{ m/s} \cdot 1.5 \times 10^{-12} \text{ s} \;\approx\; 30 \times 10^{-6} \text{ m} \;=\; 30\ \mu\text{m} \;,$$

which is too short to be resolved within the measurement precision of modern vertexing detectors. Secondly, the decay of the $\Upsilon(4S)$ resonance produces the $B^0\overline{B}^0$ pair in a coherent state with the quantum numbers of the $\Upsilon(4S)$. Quantum entanglement implies that the two mesons oscillate in phase until the first of them decays. The flavour of the decaying B meson at the time of its decay determines the flavour of the surviving B meson at this time and only then does the surviving meson start to oscillate freely. Time-dependent observables therefore have to be measured as a function of the difference between the decay timess of the two mesons. In a symmetric e^-e^+ collider, the $B^0\overline{B}^0$ pair is produced back-to-back in the laboratory frame and only the sum of the two decay times can be measured. A measurement of the decay-time difference would require knowledge of the position of the e^-e^+ interaction in which the $\Upsilon(4S)$ was produced, but this position cannot be reconstructed since no other particles than the $B^0\overline{B}^0$ pair are produced in the collision. Both these problems were overcome at the asymmetric B factories, PEP-II and KEKB, by colliding electrons and positrons with unequal

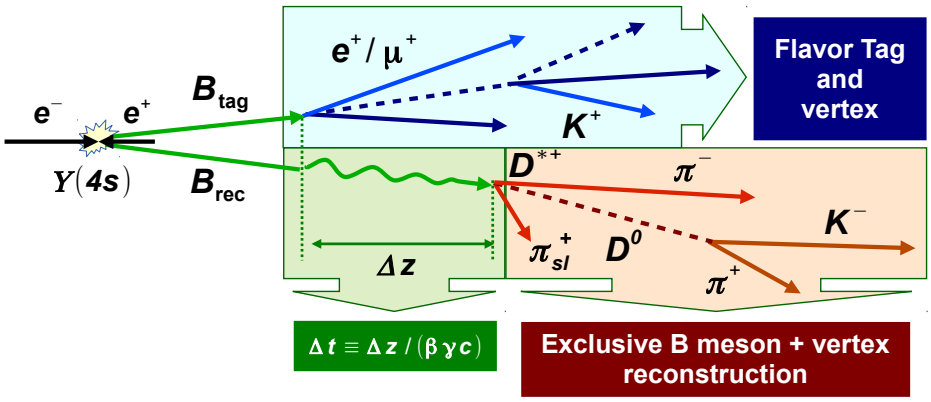

Figure 4.2: Illustration of the ingredients for the measurement of the $B^0-\overline{B}^0$ oscillation frequency at a B factory.

beam energies. The center-of-mass frame of the collision is then Lorentz boosted along the beam axis and this extra Lorentz boost gives the B^0 and $\overline{B}^0$ mesons a mean decay length in the laboratory system that is large enough to be measured with sufficient precision. Moreover, since the B^0 and the $\overline{B}^0$ meson are both boosted in the same direction along the beam axis, the distance between their decay vertices can be measured as illustrated in Figure 4.2. At the PEP-II accelerator, 9 GeV electrons were collided with 3.1 GeV positrons, resulting in a Lorentz boost of $\beta\gamma = 0.56$ and a mean decay length of the B mesons of $\beta\gamma\, c\tau_{B^0} \approx 255$ μm, while 8 GeV electrons were collided with 3.5 GeV positrons in KEKB, resulting in a Lorentz boost of $\beta\gamma = 0.425$ and a mean decay length of the B mesons of $\beta\gamma\, c\tau_{B^0} \approx 195$ μm.

The generic strategy for the measurement of a decay-time dependent rate asymmetry is illustrated in Figure 4.2 for the example of a measurement of the $B^0-\overline{B}^0$ oscillation frequency in the flavour-specific hadronic decay mode $B^0 \to D^{*+}\pi^-$ with $D^{*+} \to D^0\pi^+$ and $D^0 \to K^-\pi^+$. One of the two neutral B mesons from the decay of the $\Upsilon(4S)$ resonance, denoted as $B_{\rm rec}$ in the figure, is fully reconstructed in this decay mode. Its flavour at the time of its decay is revealed by the charges of the final-state particles. Since all final-state particles are reconstructed, the momentum of the $B_{\rm rec}$ candidate and the position of its decay vertex can be determined with good precision. The other two ingredients that are needed for a measurement of the decay-time dependent asymmetry have to be derived from the decay of the second B meson in the event, labelled $B_{\rm tag}$ in the figure. These are the position of the $B_{\rm tag}$ decay vertex, which defines the time of reference for the measurement of the decay-time difference, and the flavour of $B_{\rm tag}$ at the time of its decay, which per quantum entanglement defines the initial flavour of $B_{\rm rec}$. It is, however, not desirable to perform a full reconstruction of the $B_{\rm tag}$ candidate to derive the necessary information, since the large number of decay modes and the small branching fractions into any specific final state would lead to too large a loss in statistics. Instead, inclusive methods are employed to deriv exploting the fact that all measured tracks in the event that were not used in the reconstruction of the $B_{\rm rec}$ candidate must due to decay products of $B_{\rm tag}$. The position of the $B_{\rm tag}$ decay vertex can be estimated from an inclusive fit to these tracks, while the flavour of $B_{\rm tag}$ at the time of its decay is derived from so-called flavour tagging algorithms that search for flavour-specific signatures amongst them. Flavour-tagging algorithms will be discussed in more detail below. The signatures that they exploit include the charge of a lepton from semileptonic decays $b \to c\ell^-\overline{\nu}_\ell$ resp. $\overline{b} \to \overline{c}\ell^+\nu_\ell$ or the charge of a kaon from the decay chain $b \to c \to s$ resp. $\overline{b} \to \overline{c} \to \overline{s}$. The use of such inclusive methods in the determination of the flavour of the $B_{\rm tag}$ candidate and the position of its decay vertex leads to a loss in precision compared to a full reconstruction: flavour-tagging algorithms have a non negligible "mistag" probability for deriving the flavour wrongly and this causes a dilution of the measured asymmetry; a large fraction of B-meson decays involve long-lived charmed mesons

and the inclusion in the vertex fit of tracks from secondary decays of such charmed mesons can bias the reconstruction of the $B_{\rm rec}$ vertex position, leading to a deterioration in vertex resolution. The typical measurement uncertainty on the position of the $B_{\rm tag}$ decay vertex is quoted as $100 - 200$ μm in Ref. [112], compared to an average uncertainty of about 50 μm on the position of fully reconstructed $B_{\rm rec}$ decay vertices. However, these losses in precision are more than compensated for by the large increase in the numbers of reconstructed candidates that are available for the analyses.

The measurement of time-dependent *CP* asymmetries in the $B^0\overline{B}^0$ system proceeds along similar lines as that of the oscillation frequency described in the previous paragraph. The $B_{\rm rec}$ candidate is in this case reconstructed in a decay to a *CP* eigenstate, such as $J/\psi K^0_S$ for the measurement of the aangle β of the unitarity triangle or $\pi^+\pi^-$ for the measurement of the angle α. The flavour of the $B_{\rm rec}$ candidate at the time of its decay is not known in this case and is not needed for the measurement. The decay-time dependent rate asymmetry is measured between the number of $B_{\rm rec}$ candidates that were tagged as initial B^0 and those that were tagged as initial $\overline{B}^0$ mesons by the tagging algorithms. The relevant observable in this case is not the frequency but the amplitude of the measured asymmetry, which makes it necessary to precisely understand the dilution effects due to finite decay-vertex resolution and flavour-tagging performance.

Measurements of time-dependent rate asymmetries will be described in detail in the discussion of measurements of the $B^0 - \overline{B}^0$ oscillation frequency in Section 5.1 and measurements of the CKM angles β and α in Sections 5.3 and 5.4. The purpose of this brief overview of the analysis strategy was to highlight some of the key requirements for a successful B physics experiment at the $\Upsilon(4S)$ resonance:

- best possible angular coverage for both charged and neutral particles to capture all decay products from the decays of both B mesons;
- best possible vertex resolution to be able to determine the decay vertex difference Δz;
- best possible kaon/pion separation to be able to identify specific $B_{\rm rec}$ decay modes, and to be able to select tagging kaons amongst the remaining tracks.

This list of requirements lead to similar layouts for the BaBar and Belle detectors. Longitudinal cross sections through the two detectors are shown in Figures 4.3 and 4.4. Detailed technical descriptions of the two detectors can be found in Refs. [113] and [114], while a brief historic overview and a concise comparison of the two approaches is given in Ref. [112]. Both detectors followed the traditional barrel/endcap layout of collider experiments, but with a forward-backward asymmetric design reflecting the asymmetric beam energies. Both detectors comprised a silicon-microstrip vertex detector mounted closely around the beam pipe, surrounded by a drift chamber embedded in a solenoidal magnetic field to reconstruct the trajectories and momenta of charged particles, followed by detectors for kaon/pion identification, an electromagnetic calorimeter for electron/positron identification, photon and π^0 reconstruction, and finally a detector for the identification for muons and long-lived neutral hadrons such as K^0_L mesons. The main difference between the BaBar and Belle detectors was in the respective approaches towards kaon/pion identification. The BaBar experiment employed a special type of ring-imaging Cherenkov detector, dubbed DIRC, for this purpose while kaon/pion separation in Belle relied on a combination of threshold Cherenkov counters, a time-of-flight system and dE/dx measurements in the tracking drift chamber. The different detector components are described in the next paragraphs, followed by a short introduction to some of the relevant reconstruction techniques.

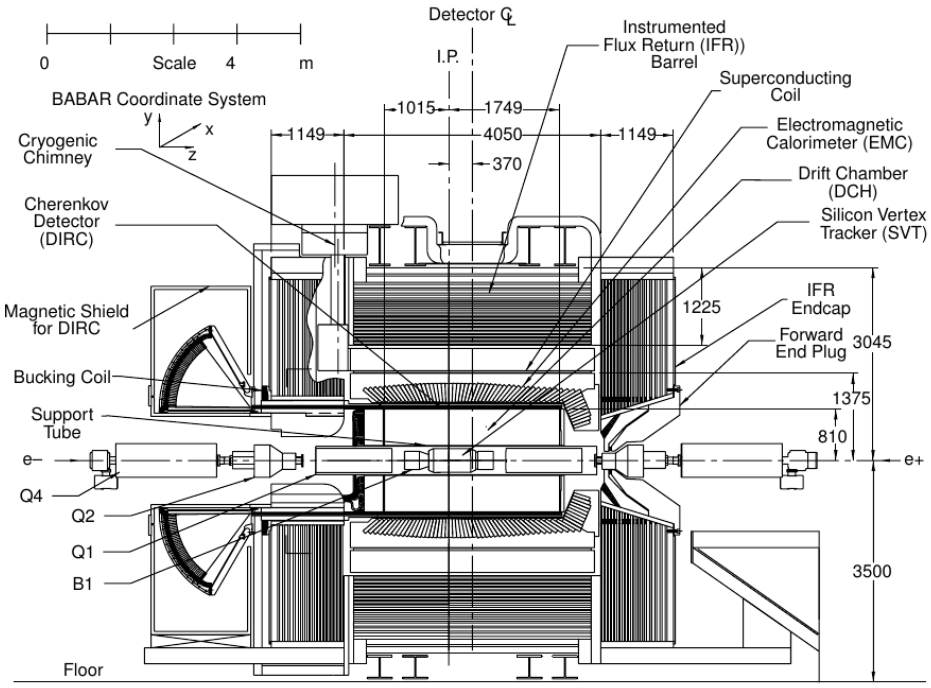

Figure 4.3: Longitudinal cross section of the BaBar detector. The main detector components are indicated: silicon vertex detector (SVT), drift chamber (DCH), ring-imaging Cherenkov counter (DIRC), electromagnetic calorimeter (EMC), and muon detector (Instrumented Flux Return, IFR). The e^-e^+ interaction region is in the centre of the SVT. The detector layout reflects the asymmetry of the collision: the higher-energy electron beam impinges from the left and the lower-energy positron beam from the right; the B mesons produced in the collision as well as their decay products are therefore Lorentz-boosted to the right (from [113]).

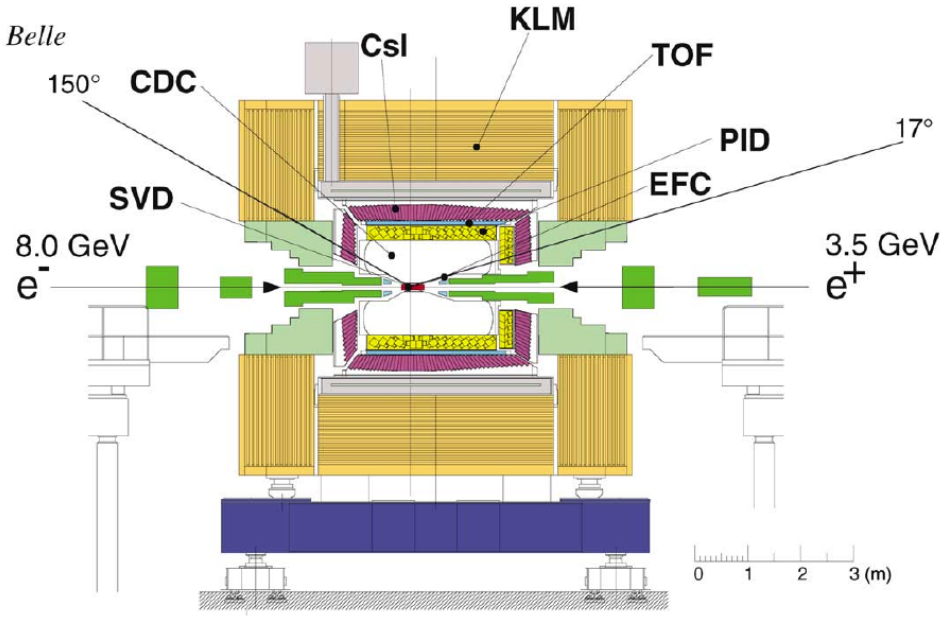

Figure 4.4: Longitudinal cross section of the Belle detector. The main detector components are indicated: silicon vertex detector (SVD), central drift chamber (CDC), threshold Cherenkov counters (PID) and time-of-flight counters (ToF), Cesium-Iodide calorimeter (CsI), muon and K_L^0 detector (KLM). The e^-e^+ interaction region is in the centre of the SVD; the higher-energy electron beam impinges from the left and the lower-energy positron beam from the right. The B mesons produced in the collision as well as their decay products are therefore Lorentz-boosted to the right and the detector layout reflects this asymmetry (from [114]).

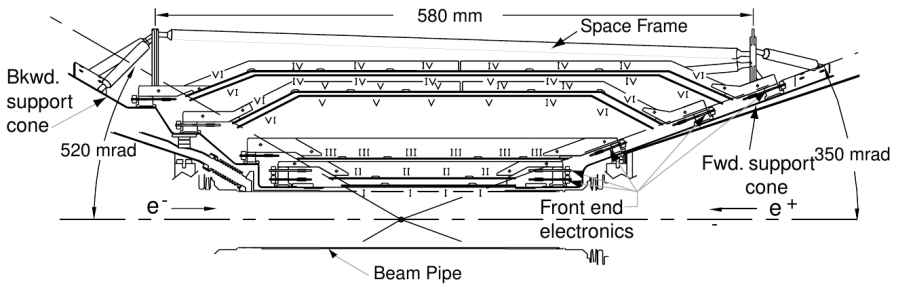

Figure 4.5: Longitudinal cross section of the BaBar vertex detector (from [113]).

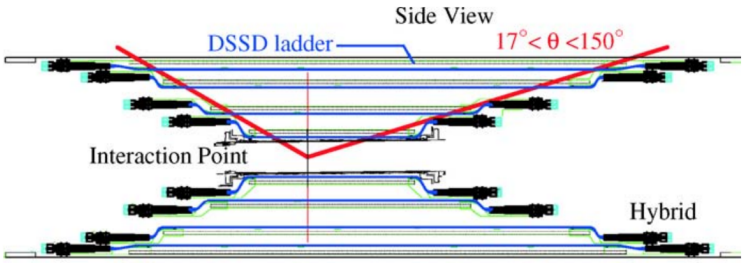

Figure 4.6: Longitudinal cross section of the Belle vertex detector (from [115]).

4.1.1 Detectors for vertex reconstruction

The precise reconstruction of the decay vertices of the two B mesons is particularly important in measurements of time-dependent CP asymmetries, where the finite vertex resolution leads to a dilution of the $B^0 - \overline{B}^0$ oscillation signal. To limit the impact of this dilution on the measurement, the distance between the two decay vertices of $B_{\rm rec}$ and $B_{\rm tag}$ should be reconstructed to better than about half the average B^0 decay length, i.e. to better than 130 μm in BaBar and to better than 100 μm in Belle. The parameters that limit the vertex resolution are on the one hand the spatial resolution of the detector itself and on the other hand the precision with which the measured track parameters can be extrapolated to the position of the vertices. To minimize the uncertainty due to the extrapolation, the spatial distance and the amount of material between the decay vertices and the first measurement point have to be kept as small as possible.

The BaBar and Belle vertex detectors consisted of cylindrical layers of 300 μm thick double-sided silicon strip detectors surrounding a thin beryllium beam pipe. The readout strips were oriented parallel to the beam axis on one side of the sensors and orthogonal to the beam axis on the other side of the sensors. Readout strip pitches in the inner layers of the detectors were 50 μm for the strips parallel the beam axis and 100 μm for those orthogonal to the beam axis.

The BaBar vertex detector (SVT) consisted of five concentrical detection layers as illustrated in Figure 4.5. The innermost layer was located at a radius of 32 mm from the beam axis. The amount of material crossed before the first measurement point corresponded to about 1-2% of a radiation length, depending on the polar angle of the particle. The total material budget of the five-layer SVT was of the order of $4 - 6\%$. The achieved vertex resolution for fully reconstructed decays of B mesons was about 55 μm in the direction along the beam axis and about 65 μm in the plane orthogonal to the beam axis.

The original Belle vertex detector (SVD) employed three detection layers, with the innermost layer placed at a radius of 30 mm from the beam axis. It was replaced in 2003 due to limited radiation tolerance of its readout electronics and silicon sensors. The new vertex detector (SVD2 [115]) consisted of four detection layers as illustrated in Figure 4.6. A new, smaller beam pipe was installed at the same time [116], allowing the innermost layer of the

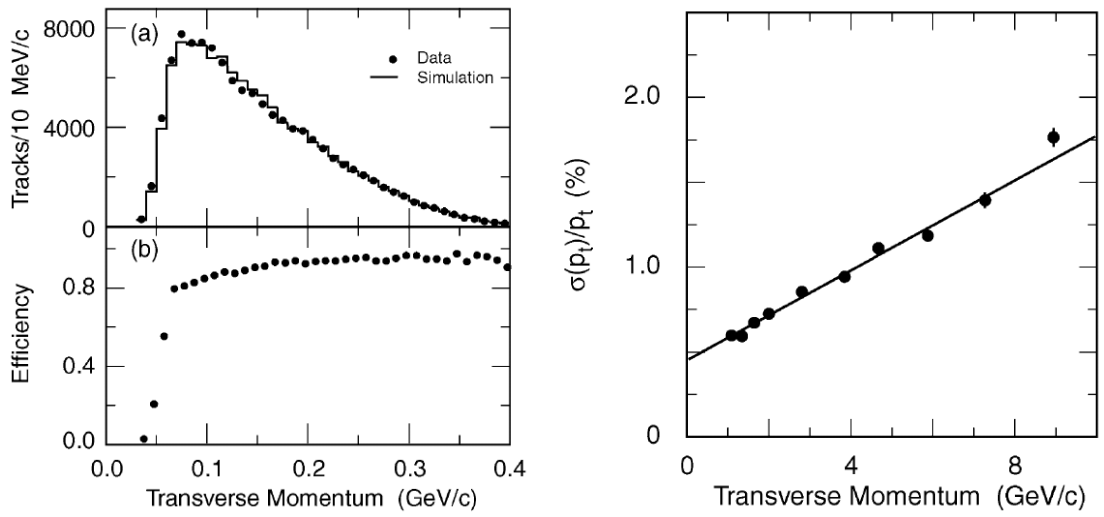

Figure 4.7: Performance of the track reconstruction as a function of transverse momentum p_{T} in BaBar: (top left) p_{T} distribution of charged particles, (bottom left) track reconstruction efficiency and (right) relative p_{T} resolution (from [113]).

SVD2 to be placed at a radius of only 20 mm from the beam axis. The new layout led to an improvement in the track impact parameter resolution for 1 GeV/c particles from about 60 μm to 42 μm.

4.1.2 Detectors for tracking of charged particles

The efficient reconstruction of the trajectories of charged particles and the precise determination of their momenta is an essential ingredient to almost all physics analyses. The trigger system relies to a large extent on information from the charged particle tracking system. Furthermore, both BaBar and Belle used dE/dx measurements in the tracking system as input for charged particle identification, in particular kaon/pion separation.

In both experiments, the tracking system consisted of the vertex detector and a cylindrical drift chamber, embedded in a solenoidal magnetic field with a field strength of 1.5 T. The majority of charged final-state particles at the B factories having momenta below 1 GeV/c, the momentum resolution is largely limited by multiple scattering in the material of the detectors. Low-Z drift gases were therefore chosen for the drift chambers to minimize their material budget.

The BaBar drift chamber (DCH) covered radii from 236 mm to 809 mm around the beam axis and consisted of 40 concentrical wire layers with wires arranged parallel to the beam axis or under small stereo angles. A gas mixture of 80% He and 20% C_4H_{10} was employed. Pulse-height measurements in the drift chamber provided a dE/dx resolution of about 7.5%, while the combined momentum resolution of the tracking system is quoted in Ref. [113] as $\sigma_{p_{\mathrm{T}}}/p_{\mathrm{T}} \approx 0.45\% + 0.13\% \cdot p_{\mathrm{T}}$.

The Belle drift chamber (CDC) covered radii from 83 mm to 863 mm around the beam axis and consisted of 50 concentrical wire layers and three cathode strip layers, the latter being used mainly for trigger purposes. Wires were arranged parallel to the beam axis or under small stereo angles. The drift gas was in this case a mixture of 50% He and 50% C_2H_6. The drift chamber provided a dE/dx resolution of about 6% and the combined momentum resolution of the tracking system is quoted in Ref. [114] as $\sigma_{p_{\mathrm{T}}}/p_{\mathrm{T}} \approx 0.3\% \cdot \sqrt{1 + p_{\mathrm{T}}^2}$.

4.1.3 Detectors for kaon/pion identification

The ability to efficiently identify charged kaons and separate them from the more prolifically produced charged pions is required at the B factories over a momentum range from well below 1 GeV/c up to above 4 GeV/c. Low-momentum kaons are employed in the flavour tagging algorithms discussed in Section 4.1.10 below, while kaon/pion separation at the higher end of the momentum range is required to separate the two-body decays $B^0 \to K^+\pi^-$ and $B^0 \to \pi^+\pi^-$. For momenta up to about 700 MeV/c, dE/dx measurements in the vertex detectors and drift chambers provided good separation power as illustrated in Figure 4.8. In BaBar, the SVT provided up to ten and the DCH up to 40 dE/dx measurements. To mitigate the effect of occasional large energy depositions in the long upper tail of the Landau distribution [117] that describes the dE/dx distribution for particles of a given not-too-low momentum, truncated means are formed using only the lowest 60% of the measurements in the SVT and the lowest 80% of the measurements in the DCH. In Belle analyses, only dE/dx measurements from the drift chamber are used and a truncated mean is formed using the lowest 80% of these measurements.

To provide charged kaon identification for higher-momentum particles, BaBar employed a novel type of ring-imaging Cherenkov counter, which they dubbed DIRC for "Detector of Internally Reflected Cherenkov light" [119]. The detector principle is based on the fact that the magnitude of the angle of incidence of photons is preserved upon reflection on flat surfaces. A schematic of the detector illustrating its principle of operation is shown in Figure 4.9. Thin, rectangular bars of synthetic silica with a mean refractive index of $n = 1.473$ are used as a Cherenkov radiator. Charged particles of mass m that traverse the radiator with momenta p above the Cherenkov threshold, $p > m/\sqrt{n^2-1}$, produce Cherenkov photons under an angle $\theta_C = \arccos(1/(n\beta))$ with respect to the particle direction, where $\beta = p/\sqrt{p^2+m^2}$. A refractive index of $n = 1.473$ corresponds to Cherenkov thresholds of about 130 MeV/c for charged pions and 450 MeV/c for charged kaons. For particles with $\beta \approx 1$, some of the produced Cherenkov photons will always lie within the limit for total internal reflection and will be transported to either end of the silica bar. The forward end of the bar is equipped with a plane mirror that reflects photons back towards its backward end. Photons reaching the backward end of the bar emerge into a 1.2 m long expansion volume and are finally detected in an array of densely packed photomultiplier tubes. The expansion volume is filled with purified water to minimize reflection losses at the material interfaces. Since angles are preserved during the internal reflections in the silica bar, the expected light pattern in the detection surface is essentially a conical section, where the opening angle of the cone is given by the Cherenkov angle, modified by the angle of refraction from the transistion from the silica into the water. An example of a recorded photon pattern is shown in Figure 4.9. An additional constraint for the reconstruction of the Cherenkov angles is obtained by recording the arrival time of the photomultiplier signals, which provides an independent measurement of the propagation of the photons. Two algorithms are used to reconstruct the DIRC data: one performs maximum-likelihood fits for the opening angle of the Cherenkov ring for each reconstructed track in the event, while the other performs a series of unbinned maximum likelihood fits for an entire event, iteratively taking into consideration all possible combinations of particle hypotheses for all reconstructed tracks in the event.

The DIRC detector concept is well matched to the layout of a collider experiment, especially considering the asymmetric beam energies at which PEP-II operates. The thin radiator bars take up little radial space in the barrel while the space consuming expansion volume and the heavy photomultiplier tubes can be located in the backward part of the detector, outside of the acceptance. A conventional RICH detector would have required significantly larger radial space, increasing the size and cost of the solenoid magnet and the electromagnetic calorimeter.

In Belle, a combination of threshold Cherenkov counters and time-of-flight counters was employed to provide pion and kaon identification at particle momenta above 700 MeV. The

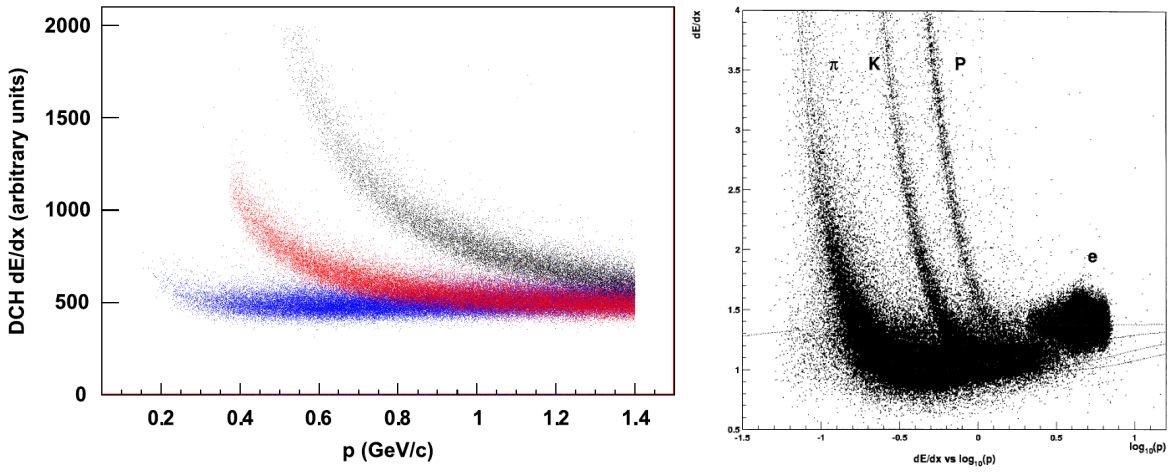

Figure 4.8: Measured dE/dx in the driftchambers as a function of the reconstructed track momentum in (left, from [118]) BaBar and (right, from [114]) Belle. In the panel on the left, blue dots are for a sample of pions, red dots for kaons and black dots for protons. Clean samples of pions and kaons were selected using the charge of the slow pion, $\pi^{\pm}_{\rm sl}$, from the decay $D^{*+} \to D^0\pi^+_{\rm sl}$ / $D^{*-} \to \overline{D}^0\pi^-_{\rm sl}$ to tag the kaon and pion in the subsequent decay $D^0 \to K^-\pi^+$ / $\overline{D}^0 \to K^+\pi^-$. A clean sample of protons was selected using the decay $\Lambda \to p\pi^-$. The two bands for pions and kaons are clearly separated at low momenta but start to overlap at momenta above 0.7 GeV/c.

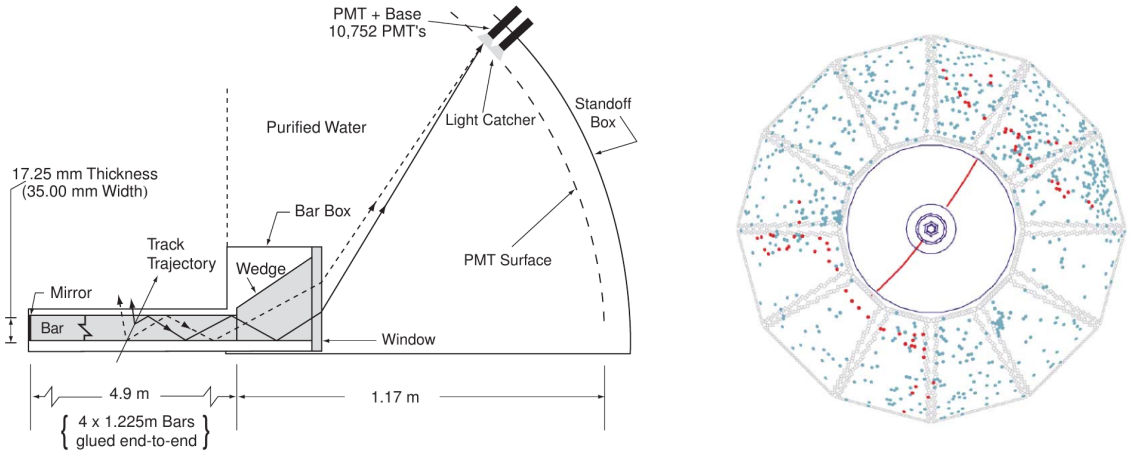

Figure 4.9: The DIRC detector as employed in BaBar. (Left) Schematic showing the main components and the measurement principle, (right) event display showing the pattern of Cherenkov photons measured for an $e^-e^+ \to \mu^-\mu^+$ event. The thicker, red dots indicate hits that remain if a time coincidence within 8 ns is required between the measured signals and the expected Cherenkov photon arrival times for the two muon tracks. The plots are taken from Refs. [113] and [119].

threshold Cherenkov counters consisted of an aerogel radiator that was read out by photomultiplier tubes. The refractive index of the aerogel was tuned to be between $n = 1.01$ and $n = 1.03$ for different polar angle regions, following the expected momentum distributions of the particles of interest. A refractive index of $n = 1.03$ corresponds to Cherenkov thresholds of about 550 MeV/c for pions and 2 GeV/c for kaons, while a refractive index of $n = 1.01$ corresponds to Cherenkov thresholds of about 950 MeV/c for pions and 3.5 GeV/c for kaons. The time-of-flight system consisted of an array of 128 fast scintillation counters that were read out with photomultiplier tubes. For a time resolution of 100 ps and a flight path of 1.2 m in length, the time-of-flight system could provide kaon/pion separation up to momenta of about 1.2 GeV/c. The photomultiplier tubes for the Cherenkov threshold counters as well as the time-of-flight counters had to be operated inside the 1.5 T magnetic field of the spectrometer magnet. The Lorentz force acting on the electrons drifting inside the tube leads to a significant gain reduction. To mitigate this effect, both detectors employed so-called fine-mesh photomultiplier tubes with 19 dynode stages and a large intrinsic gain of about 10^6. The gain loss due to the magnetic field was estimated to be up to a factor of 10^{-3} for phototubes that had to be placed parallel to the magnetic field lines.

4.1.4 Electromagnetic calorimetry

The electromagnetic calorimeters in BaBar and Belle serve two main purposes: the precise measurement of the energy and position of photons from B-meson decays and the identification of electrons by comparing the energy deposition of the particle with its momentum measured in the tracking system. Excellent energy resolution is required down to 20 MeV for photons from multi-body B-meson decays containing π^0 or η mesons, and up to above 4 GeV for photons from two-body decays such as $B^0 \to \pi^0\pi^0$ or $B^0 \to K^*\gamma$. Good spatial resolution on the measurement of the cluster positions is required for π^0 reconstruction at energies above 2 GeV, where the angular resolution starts to dominate the π^0 mass resolution. The reconstruction of π^0 decays at high momentum also requires a fine detector granularity to be able to resolve the two photons from the π^0 decay.

The layouts of the electromagnetic calorimeters of BaBar (EMC) and Belle (ECL) are shown in Figures 4.10 and 4.11, respectively. Both calorimeters employed finely segmented arrays of Thallium-doped Cesium-Iodide (CsI(Tl)) crystals that were read out by silicon photodiodes. The EMC in BaBar used a total of 6580 crystals in the barrel and endcaps while the ECL in Belle consisted of a total of 8736 crystals. The crystals had a tower-like, trapezoidal shape. Their lateral dimensions of the order of 50×50 mm^2 at the front face and 65×65 mm^2 at the rear face were matched to the Moliére radius [120, 121] of 38 mm in CsI(Tl). The depth of the crystals was of the order of 30 cm, corresponding to 16.2 radiation lengths.

In-situ monitoring and calibration of the calorimeters relied on electrons and positrons from elastic $e^-e^+ \to e^-e^+$ collisions (Bhabha scattering), for which the true energy can be calculated using the known relation between energy and polar angle. At BaBar and Belle, electrons and positrons from Bhabha scattering have energies in the range $3 - 9$ GeV. In BaBar, an independent calibration point at lower energies was provided by means of a source of 6.13 MeV photons that was generated by irradiating liquid Fluorinert with low-energy neutrons via the reaction $^{19}\mathrm{N}{+}n \to {}^{16}\mathrm{N}{+}\alpha$. The activated ^{16}N decays with a half-life of seven seconds to $^{16}\mathrm{N} \to {}^{16}\mathrm{O}^*{+}\beta$ followed by $^{16}\mathrm{O}^* \to {}^{16}\mathrm{O}{+}\gamma$. The activated fluid was pumped from the neutron generator to a manifold of thin-walled aluminium pipes that was mounted immediately in front of the crystals. The system was tuned to give a typical photon rate of 40 Hz per crystal, sufficiently large to obtain reasonably sized calibration samples, but low enough not to affect data taking and data quality. Employing the two calibration sources, the relative energy resolution of the BaBar calorimeter was found to vary from $\sigma_E/E \approx 5\%$ at $E = 6.13$ MeV to about 2% at 7.5 GeV, while the angular resolution improved from 12 mrad at the low energy to 3 mrad at high energy. This performance resulted in an average π^0 mass resolution of about

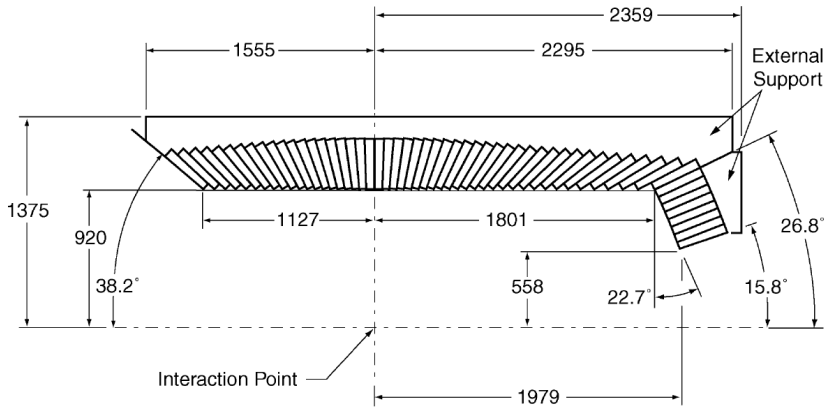

Figure 4.10: Layout of the BaBar electromagnetic calorimeter (from [113]).

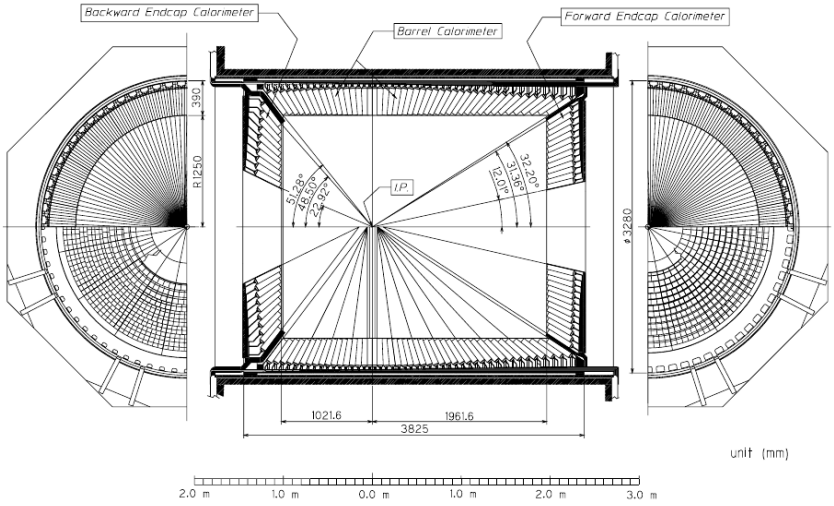

Figure 4.11: Layout of the Belle electromagnetic calorimeter (from [114]).

7 MeV/c^2. In Belle, $e^-e^+ \to \gamma\gamma$ events were employed in addition to Bhabha scattering in the calibration of the calorimeter. The relative energy resolution of the Belle calorimeter was found to improve from $\sigma_E/E \approx 4\%$ at $E = 100$ MeV to about 1.6% at 8 GeV. The performance in terms of the angular resolution was similar to that of the BaBar calorimeter and the average π^0 mass resolution was found to be 4.5 MeV/c^2 (all numbers quoted in this paragraph were taken from Ref. [112]).

4.1.5 Detectors for muons and long-lived neutral particles

The efficient and clear identification of muons is an important ingredient for flavour tagging algorithms, for the reconstruction of final states involving a J/ψ meson or other vector resonances, and for semileptonic and rare B , D and τ decays. The possibility to reconstruct K^0_L mesons allows complementary measurements of *CP* violating asymmetries, for example in decays to the *CP* eigenstate $B^0 \to J/\psi K^0_L$.

In both BaBar and Belle, the return yoke of the solenoid magnet was used as a muon filter and hadron absorber.

In BaBar, the detector was dubbed Instrumented Flux Return (IFR) and consisted of 19 detection layers in the barrel and 18 layers in the endcaps that were installed in gaps in the finely segmented steel of the return yoke. Resistive Plate Chambers (RPC) made from thin bakelite (phenolic polymer) sheets separated by a 2 mm gas-filled gap were initially

used as detector elements in both the barrel and the endcap regions. The detectors were operated in limited streamer mode, i.e. a high voltage was applied between the two plates such that a charged particle traversing the gap initiated a local discharge of the electrodes. This discharge was quickly quenched by the high resistivity of the bakelite plates. Already during the first year of operation, however, a large fraction of the RPC modules in the barrel and the forward endcap suffered aging problems and significant efficiency losses. The endcap detectors were subsequently replaced by second-generation RPCs of improved design and better performance [122], while the barrel detectors were eventually replaced by Limited Streamer Tubes [123].

The K_L^0 and muon detector (KLM) in Belle consisted of 15 detection layers in the barrel region and 14 layers in the endcaps, which were inserted in gaps in the return yoke and support structure of the solenoid magnet. Belle employed double-gap RPC detector modules with electrodes that were made of $2.0 - 2.4$ mm thick plates of glass with appropriately tuned resistivity. The detectors were operated in limited streamer mode and performed reliably until the end of the Belle operation. The total amount of iron in the KLM corresponded to 3.9 nuclear interaction lengths and K_L^0 candidates were identified by the hadronic shower they initiated in this material. This allowed to determine the direction of flight of the K_L^0 but not its energy. Discrimination between muons on the one hand and pions and kaons on the other hand was based on the range and the angle of deflection of the trajectory of the particle.

4.1.6 Triggering

The task of the trigger is to select events of interest with high, stable and well-understood efficiency and to reject background events to keep the total output rate at a level that is compatible with the processing and storage capacity of the offline computing system. Due to the clean event environment at the B factories, trigger efficiencies close to 100% for $B\overline{B}$ events could be achieved. In addition to $B\overline{B}$ events for physics analyses, samples of e^-e^+ (Bhabha) and $\gamma\gamma$ events were collected for calibration and luminosity determination. Backgrounds at the B factories were dominated by lost beam electrons and positrons interacting in the material of the beam pipe. In BaBar, at a luminosity $L = 3 \times 10^{33}$ cm^{-2} s^{-1} the rate of such background events with at least one reconstructed track with a transverse momentum $p_{\mathrm{T}} > 120$ MeV/c or an energy deposit $E > 100$ MeV was typically 20 kHz, to be compared to a $b\bar{b}$ production rate of 3.2 Hz at this luminosity.

In both Belle and BaBar, trigger algorithms were based primarily on simple particle signatures and topologies. This permitted to design the trigger to be robust and flexible with regard to changing beam background conditions and to provide for sufficient redundancy to allow the determination of trigger efficiencies. Both experiments used a first-level trigger (L1) that was implemented in hardware on custom-made electronics boards, followed by a second-level trigger that was implemented in software running on an online computing farm. For historical reasons, the second-level trigger was referred to as L3 in BaBar and as Level 4 in Belle.

The maximally allowed accept rate of the L1 trigger was determined by the bandwidth of the data acquisition systems and the capacity of the online computing farms. The limit was 3 kHz in BaBar and about 500 Hz in Belle. A simplified schematic of the BaBar L1 trigger scheme is shown in Figure 4.12. It was based on the reconstruction of track candidates in the drift chamber, showers in the electromagnetic calorimeter and track segments in the IFR. The drift-chamber trigger (DCT) consisted of three different types of electronics modules: track segment finder modules (TSF) combined information from four consecutive detection layers in a given segment of the drift chamber to identify combinations of hits that were compatible with belonging to a reasonably straight track originating from the origin; the binary link tracker (BLT) module linked these track segments together and classified track candidates according to the number of detection layers they were observed in; transverse-momentum discriminator modules (PTD) checked high-quality track candidates for their compatibility

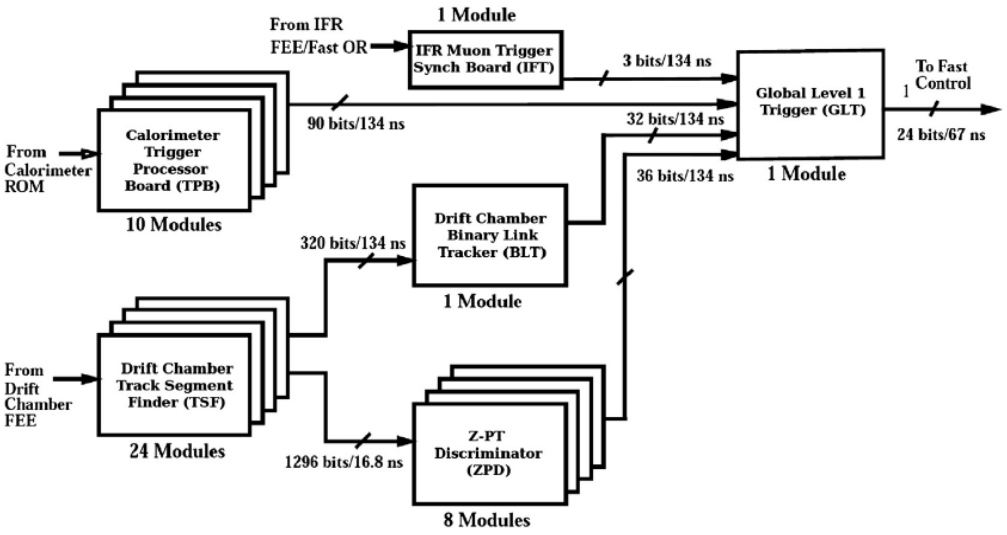

Figure 4.12: Simplified schematic of the BaBar L1 trigger (from [118]).

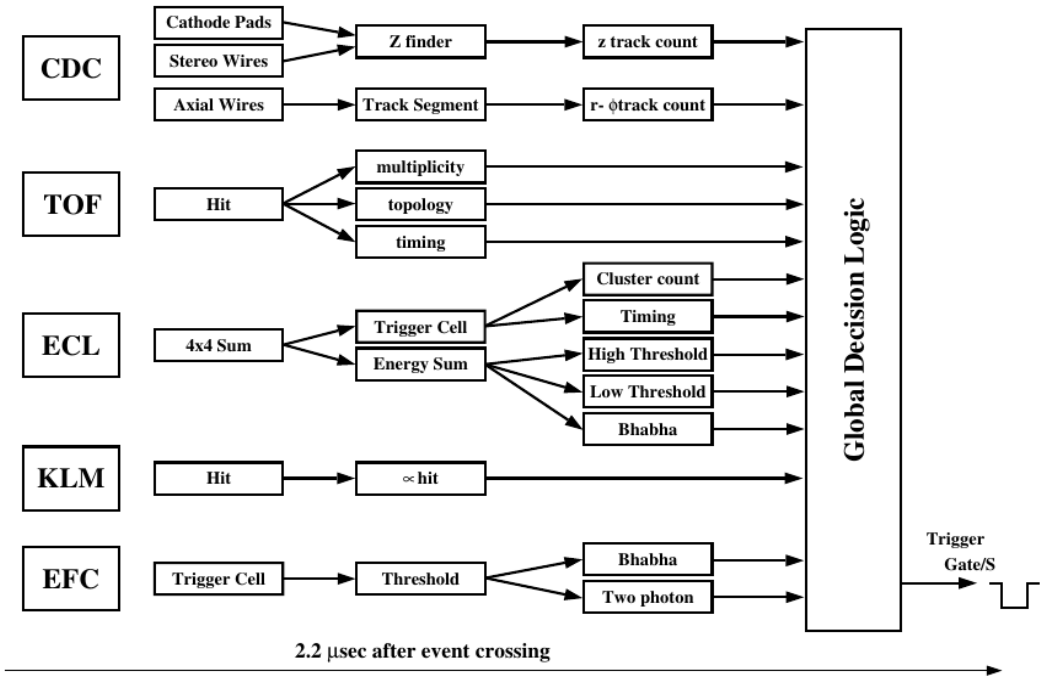

Figure 4.13: Simplified schematic of the Belle L1 trigger (from [124]).

with a configurable minimum transverse momentum. The original PTD modules only made use of information from detection layers that measured the coordinates in the bending plane of the solenoid magnet. To cope with the increasing instantaneous luminosities delivered by PEP-II, these modules were replaced in summer 2004 by so-called $z - p_{\mathrm{T}}$ discriminator modules (ZPD) that made use of information with finer granularity and from all detection layers. The calorimeter trigger (EMT) used the summed energy deposits in 280 pre-defined groups of crystals and compared these against thresholds to form trigger objects. The IFR trigger (IFT) formed for each the detection layer the logical OR of all readout strips in ten pre-defined sectors of the IFR, then formed coincidences between different detection layers within these sectors, and finally combining the information from different sectors to form topologies such as “one muon in endcap”, “two back-to-back muons in barrel” and five others.

The output information of the DCT, EMT and IFT were fed into a global L1 trigger module (GLT). As bunch crossings in BaBar occurred with a spacing of 4.2 ns, essentially continuous with respect to the 59.5 MHz clock of the BaBar electronics, the GLT module first needed to time-align the different trigger inputs. It then formed logical combinations of the trigger primitives and compared them with sets of configurable selection parameters to form a total of 24 specific trigger lines. The L1 algorithms were implemented in Field-Programmable Gate Arrays (FPGA) and the total latency of the L1 trigger was 11-12 μs. The Belle L1 trigger had a fixed latency of 2.2 μs, a maximum output rate of about 500 Hz and an efficiency of 99.5 % for $b\overline{B}$ events. As illustrated in Figure 4.13, it made use of information from the CDC, the TOF, the KLM and the electromagnetic calorimeters, ECL and EFC. The CDC trigger compared data from the drift chamber with pre-defined track patterns stored in memory lookup tables to determine the numbers, directions and transverse momenta of track candidates in the bending plane of the magnet ($r-\phi$) and the numbers and directions of track candidates in the projection along the beam axis (z). Other inputs to the trigger decision were the multiplicity and topology of hits measured in the TOF, the total energy and the number of clusters found in the ECL [125], time coincidences of hits in a subset of the detection layers in the KLM. Finally, information from the forward calorimeter (EFC) provided a trigger for Bhabha and two-photon events used for the determination of the luminosity. The information from these different trigger sources was fed into a global decision logic (GDL [124]), which performed the necessary time alignment and derived a variety of trigger streams based on track topologies, total energy, the number of isolated calorimeter clusters, muon candidates, and a dedicated Bhabha trigger. In addition, pre-scaled random triggers and triggers with very loose conditions were generated for monitoring purposes.

A large fraction of the background events passing the L1 triggers was still due to interactions of lost beam electrons and positrons in the material of the beam pipe or beam interactions with residual gas inside the beam pipe. To further reduce these backgrounds was the main purpose of the software triggers. The BaBar L3 trigger had access to the complete event data, including the output of the L1 trigger processors. It refined and augmented the selection methods employed in the L1 trigger, e.g. by using more refined algorithms for DCH track reconstruction and EMC clustering. The DCH based selection algorithm performed a fast pattern recognition, starting from the track segments identified by the TSF algorithm and using look-up tables derived from simulated samples of tracks. For identified track candidates, a simple fit of the track parameters was then performed, neglecting the effects of material interactions and magnetic field inhomogenities. This fit yielded moderate resolutions of 0.8 mm and 6.1 mm for the track impact parameters orthogonal and parallel to the beam axis, respectively, and of $\sigma(p_{\mathrm{T}})/p_{\mathrm{T}} \approx 1.9\% \cdot p_{\mathrm{T}}/$ GeV/c for the transverse momentum. The EMC based trigger algorithm identified energy clusters with a sensitivity sufficient for finding minimum ionizing particles. It selected clusters with a minimum energy and in time coincidence with the event and then employed look-up tables to determine the position, time and shower shape for these clusters. A variety of filters was then applied on the sets of reconstructed tracks and clusters to select and classify events for offline reconstruction. For example, drift chamber filters selected events with at least one track pointing back to the nominal e^-e^+ interaction point and with $p_{\mathrm{T}} > 600$ MeV/c or two such tracks with $p_{\mathrm{T}} > 250$ MeV/c. Calorimeter filters selected events with at least two clusters with $E > 350$ MeV or four clusters with $E > 100$ MeV. Bhabha events were rejected by putting constraints on the energy deposits, the track momenta and E/p and on the event topology, such as the colinearity of the two tracks in two-prong events. A small fraction of Bhabha events was retained for calibration purposes and for the determination of the luminosity. The output rate of the L3 trigger was initially 120 Hz but was allowed to go up to 800 Hz towards the end of data taking. The average L3 processing time for an event was 10 ms, dominated by the algorithms for the reconstruction of charged tracks. The Belle software trigger (Level 4) demanded a reconstructed track with $p_{\mathrm{T}} > 300$ MeV/c and compatible with originating from the nominal e^-e^+ interaction point, or an energy deposit

greater than 4 GeV in the ECL. The efficiency of the trigger was very close to 100% for events that passed the offline reconstruction requirements.

4.1.7 Particle identification

Particle identification criteria are applied in the offline reconstruction to assign particle hypotheses to the reconstructed tracks of charged particles.

Muon candidates are identified by the association of hits in the IFR (BaBar) respectively KLM (Belle) detectors with charged tracks reconstructed in the tracking detectors, taking into account the amount of material traversed by the particle along its trajectory. Muon identification efficiencies were determined using cosmic rays and samples of $\mu^+\mu^- e^- e^+$ and $\mu^+\mu^-\gamma$ final states, the probability of misidentifying pions for muons was measured using pions from the decay $K^0_S \to \pi^+\pi^-$ and from three-prong τ lepton decays. For momenta above 1.5 GeV/c, muon identification efficiencies above 90 % were achieved for fake rates of $6-8$ % in BaBar and below 5 % in Belle.

Electron candidates are identified as clusters in the electromagnetic calorimeters that can be associated to a charged track and for which the ratio of the cluster energy E to the track momentum p is close to one. The requirement on E/p is motivated by the fact that the electromagnetic showers initiated by electrons are expected to be well contained in the calorimeter, whereas hadronic showers due to pions, kaons or protons have significant energy leakage resulting in $E/p < 1$. In addition, requirements are applied on dE/dx measurements in the tracking detectors to be compatible with a minimum ionizing particle.

Kaon candidates are separated from pions and protons by combining particle identification information from the different detector components described in Section 4.1.3. In BaBar, these are the Cherenkov angle measured in the DIRC and the dE/dx measured in the DCH and in the SVT. Several methods have been employed to combine this information into a global probability for a given particle to be a kaon, pion or proton. In the first of these methods, individual likelihood functions were defined for each of the three subsystems and then multiplied to form a global likelihood. A particle is then identified as a kaon by cutting on the likelihood ratio

$$LR_K \;=\; \frac{L_K^{\mathrm{DIRC}} \times L_K^{\mathrm{DCH}} \times L_K^{\mathrm{SVT}}}{\sum_h \alpha_h \, (L_h^{\mathrm{DIRC}} \times L_h^{\mathrm{DCH}} \times L_h^{\mathrm{SVT}})} \quad \text{with} \;\; h \in \{\pi, K, p\} \;,$$

where α_h is a scaling factor that takes into account the expected multiplicities for the different particle types. Likelihood ratios for pions and protons are defined in the same manner. In addition to this global likelihood method, several multi-variate techniques have been employed, including algorithms based on an artifical neural network, on decision trees and on Error-Correcting Output Code (ECOC [126]). The ECOC technique uses as input the likelihood ratios defined above, along with the inputs used to calculate them, but also other variables such as the particle momentum, its polar and azimuthal angle, the number of measurements in the DIRC and in the DCH and input from the calorimeter. Multi-variate algorithms return for each particle hypothesis a classifier that can assume values between -1 for tracks that are very unlikely to be of the given particle type and $+1$ for tracks that are very likely to be of this particle type. The particle hypothesis for a given track is then decided by cutting on the value of this classifier. The specific cuts applied on the likelihood ratio or the multi-variate classifier can be adjusted to the needs of each specific analysis: tight cuts result in small misidentification probabilities and pure samples at the cost of low identification efficiencies, while loose cuts lead to higher identification efficiency but also larger misidentification probabilities and therefore less pure samples. The kaon identification performance of the likelihood ratio method and the ECOC algorithm is shown in Figure 4.14. As expected, it can be seen that the performance of the more sophisticated ECOC algorithm is generally superior to that of the simpler likelihood ratio method.

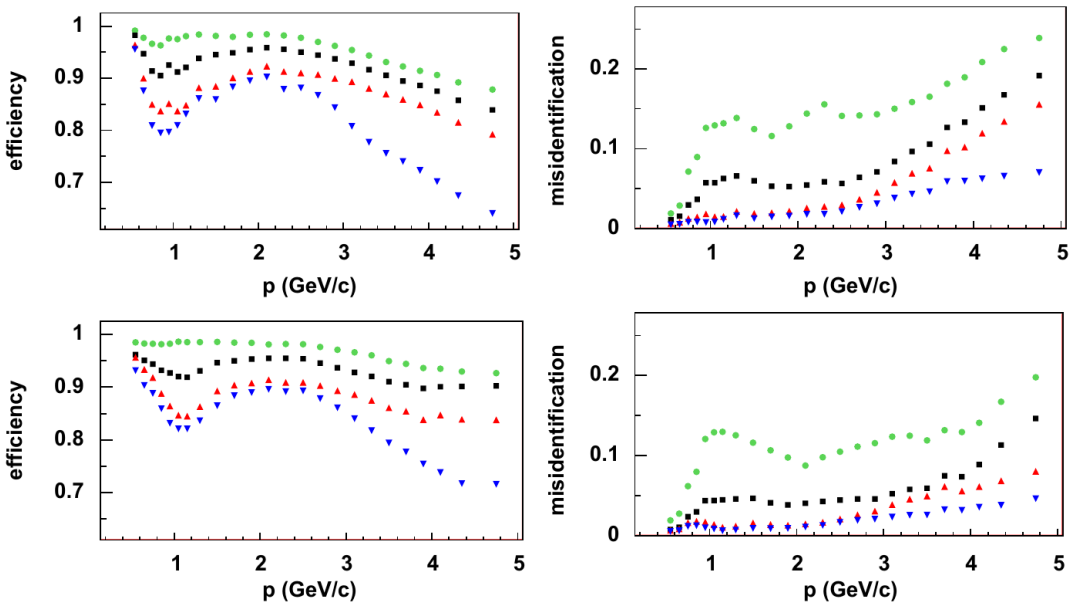

Figure 4.14: Kaon identification performance as a function of the particle momentum in BaBar using (top) likelihood ratios and (bottom) the ECOC algorithm mentioned in the text. The plots on the left show the efficiency for a true kaon to be correctly identified as a kaon while the plots on the right show the probability for a true pion to be misidentified as a kaon. Green circles are for "very loose" identification criteria (high efficiency at the cost of high misidentification probability), black squares are for "loose", red upward-pointing triangles for "tight" and blue downward-pointing triangles for "very tight" identification criteria. Clean samples of pions and kaons were selected using the charge of the slow pion, $\pi^{\pm}_{\rm sl}$, from the decays $D^{*+} \to D^0\pi^+_{\rm sl}$ and $D^{*-} \to \overline{D}^0\pi^-_{\rm sl}$ to tag the kaon and pion in the subsequent decay $D^0 \to K^-\pi^+$ respectively $\overline{D}^0 \to K^+\pi^-$ (from [118]).

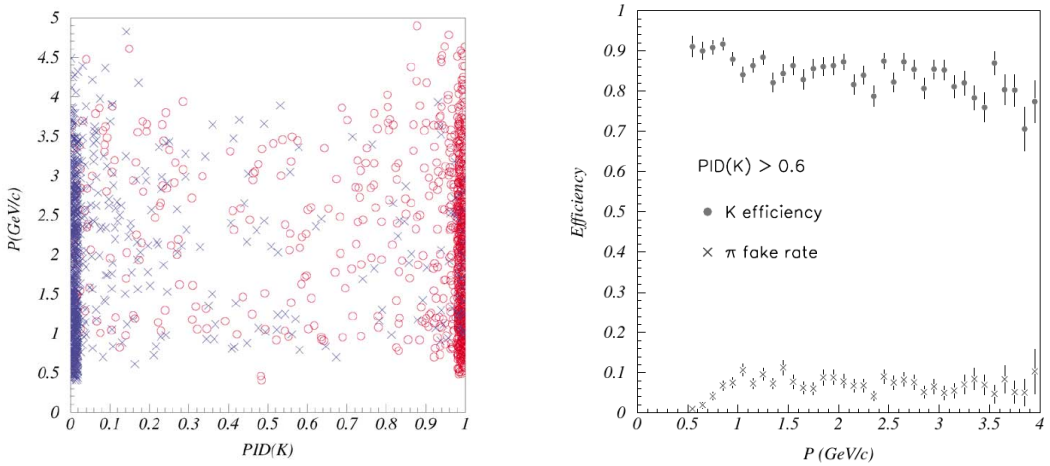

Figure 4.15: Illustration of the kaon identification performance as a function of the particle momentum in Belle: (left) distribution of the likelihood ratio PID(K) as a function of the particle momentum, P, where blue crosses indicate true pions while red circles indicate true kaons, and (right) efficiency for a true kaon to be correctly identified as a kaon and probability for a true pion to be misidentified as a kaon. Clean samples of pions and kaons were selected using the charge of the slow pion, $\pi^{\pm}_{\rm sl}$, from the decays $D^{*+} \to D^0\pi^+_{\rm sl}$ and $D^{*-} \to \overline{D}^0\pi^-_{\rm sl}$ to tag the kaon and pion in the subsequent decay $D^0 \to K^-\pi^+$ respectively $\overline{D}^0 \to K^+\pi^-$ (from [114]).

In Belle, kaon/pion/proton identification is based on dE/dx measurements in the CDC, time-of-flight measurements in the TOF, and the number of Cherenkov photons produced in the ACC. Individual likelihood functions were defined for each of the three subsystems and the product of these three likelihood functions gives the overall probabilities P_K for a particle to be a kaon and P_π for it to be a pion. A particle is then identified as a kaon or pion by cutting on the likelihood ratio

$$\mathrm{PID}(K) \;=\; \frac{P_K}{P_K \,+\, P_\pi} \;.$$

The performance of the overall kaon/pion identification in Belle is illustrated in Figure 4.15.

4.1.8 Reconstruction of neutral particles

Neutral pion candidates are formed in both experiments from pairs of neutral clusters in the electromagnetic calorimeter that give a combined invariant mass compatible with the π^0 mass if they are assumed to originate from the nominal e^-e^+ interaction point.

Candidates for $K^0_S \to \pi^+\pi^-$ decays in $B\overline{B}$ events are identified as pairs of tracks that point back to a common displaced vertex, for which the two-pion invariant mass is compatible with the K^0 mass, and for which the sum of their two momentum vectors is compatible with being parallel to the line of flight from the reconstructed decay vertex of the B meson to the two-pion vertex.

To reconstruct $K^0_S \to \pi^0\pi^0$ decay candidates in $B\overline{B}$ events, a first rough estimate of the K^0_S momentum vector is obtained by combining two π^0 candidates and assuming the K^0_S decay vertex to coincide with the nominal e^-e^+ collision point. In a second step, the K^0_S decay vertex is assumed to lie on a line that is defined by this estimated momentum vector and the reconstructed decay vertex of the B meson. The position of the K^0_S decay vertex along this line can then be determined by applying π^0 mass constraints on the pairs of photon clusters that form the two π^0 candidates. Finally, the K^0_S candidate is retained if the combined invariant mass of the two neutral pions, calculated assuming the estimated decay point, is compatible with the K^0 mass.

Finally, K^0_L candidates are identified as neutral clusters in the electromagnetic calorimeters that are not compatible with being due to a π^0, or as clusters in the IFR (BaBar) or KLM (Belle) detectors that are incompatible with being due to nuclear interactions of charged tracks. The K^0_L detection efficiency was measured using the reaction $e^-e^+ \to \phi\gamma$ with $\phi \to K^0_L K^0_S \gamma$ and was found to increase roughly linearly with the momentum of the K^0_L, from about 20 % at 1 GeV/c to 40 % at 4 GeV/c.

4.1.9 Reconstruction of B meson candidates

Events that passed the software trigger were stored on disk to be fully reconstructed offline. The offline event reconstruction builds upon information from the software triggers, but employs refined reconstruction algorithms to improve efficiencies and resolutions.

Additional track reconstruction algorithms are applied to find tracks that were missed by the software trigger. All track candidates are then fit using an algorithm based on a Kalman filter technique [127,128] that takes into account detailed descriptions of the material distribution in the detector and non-uniformities in the magnetic field. This fit yields a significantly improved momentum resolution compared to the simplified fit applied in the software triggers. The resolution on the transverse momentum attained in the offline reconstruction is quoted as

$$\frac{\sigma(p_\mathrm{T})}{p_\mathrm{T}} \;=\; 0.45\,\% + 0.13\,\% \cdot p_\mathrm{T}\,[\mathrm{GeV}/c]$$

for BaBar and as

$$\frac{\sigma(p_\mathrm{T})}{p_\mathrm{T}} \;=\; \sqrt{(0.34\,\%)^2 + (0.19\,\% \cdot p_\mathrm{T}\,[\mathrm{GeV}/c])^2}$$

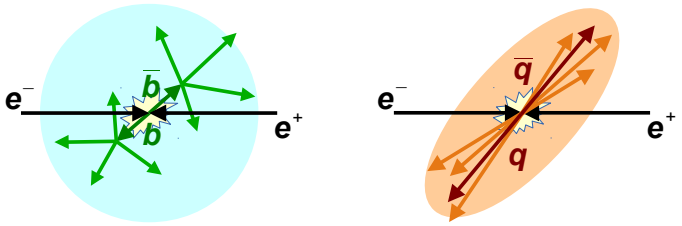

Figure 4.16: Naive illustration of the generic event topology for (left) $e^-e^+ \to \Upsilon(4S) \to B\overline{B}$ events and for (right) continuum background events of the type $e^-e^+ \to q\overline{q}$, where q denotes a d, u, s or c quark.

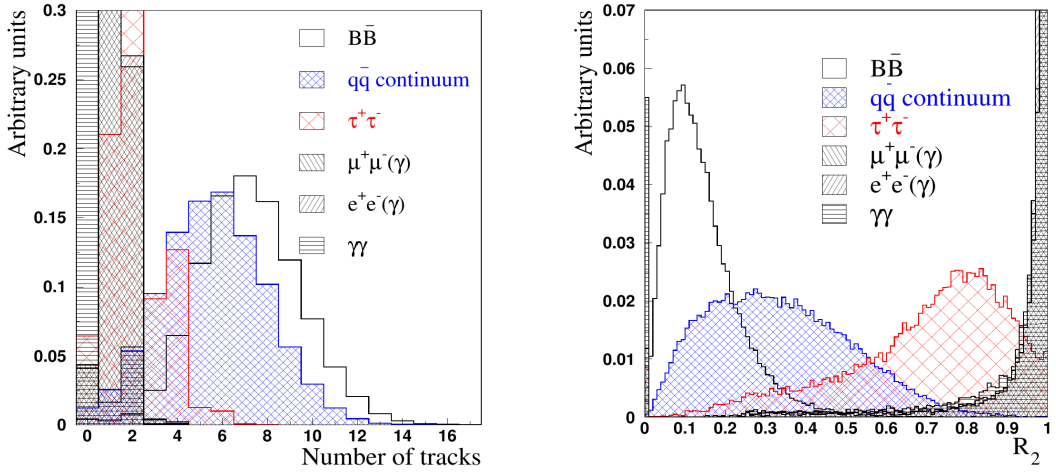

Figure 4.17: Distributions of (left) the number of reconstructed tracks and (right) the second Fox-Wolfram moment, R_2 for $e^-e^+ \to B\overline{B}$ events and for various categories of continuum backgrounds as indicated in the plot legends. (from [112]).

for Belle.

Refined algorithms are also applied to improve the reconstruction of clusters in the electromagnetic calorimeters. For example, local maxima in the energy distribution within the clusters are searched for to identify overlapping clusters caused by two or more nearby particles. The distance between the cluster centroid and the extrapolated impact points of charged tracks reconstructed in the tracking detectors is employed to associate clusters to charged particles. If no such association is found, the cluster is classified as being due to a neutral particle.

To further reduce backgrounds from non-$B\overline{B}$ events, an initial event selection is applied based on global event criteria, such as the number of reconstructed tracks or the sum of all energy deposits in the calorimeter. The distribution of the number of reconstructed tracks in $B\overline{B}$ events and in different categories of non-$B\overline{B}$ events is shown in Figure 4.17. Cuts on global event-shape variables in the centre-of-mass frame of the e^-e^+-collision are applied to suppress backgrounds from $e^-e^+ \to \overline{d}d$, $\overline{u}u$, $\overline{s}s$ or $\overline{c}c$ continuum events. Event-shape variables exploit the fact that the quark and the antiquark in such continuum events are produced with a significant momentum in the centre-of-mass frame, resulting in a jet-like event shape as illustrated in Figure 4.16, while the two B mesons in $e^-e^+ \to \Upsilon(4S) \to B\overline{B}$ events are produced almost at rest in the centre-of-mass frame and their decay products therefore tend to be distributed isotropically. One such event-shape variable that is used in both BaBar and Belle analyses is the so-called second Fox-Wolfram moment [129], $R_2 = H_2/H_0$, where

$$H_i \equiv \sum_{jk} \left\{ |\vec{p}_j|\,|\vec{p}_k| \times P_i(\cos(\vec{p}_j, \vec{p}_k)) \right\} ,$$

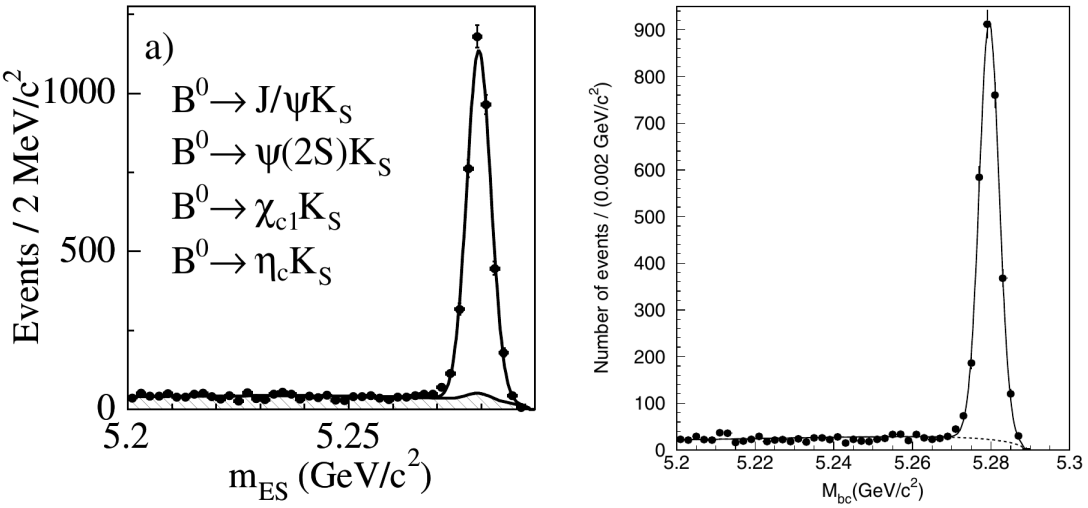

Figure 4.18: Distribution of the beam-energy substituted invariant mass, abbreviated as $m_{\rm ES}$ respectively $M_{\rm bc}$, for $B^0 \to J/\psi K^0_S$, $\psi(2s)K^0_S$, $\chi_{c1}K^0_S$ and $\eta_c K^0_S$ candidates in the ΔE signal region from (left) BaBar and (right) Belle measurements of the CKM angle β in these decay modes (from [131], [132]).

P_i is the Legendre polynomial of order i, and the sum runs over the momenta $\vec{p}_j$ and $\vec{p}_k$ for all pairs of reconstructed tracks in the event. The distribution of R_2 for $B\overline{B}$ events and for different categories of non-$B\overline{B}$ events is shown in Figure 4.17. Other variables use the thrust,

$$T \;\equiv\; \frac{\sum_j |\vec{T}\cdot\vec{p_j}|}{\sum_j |\vec{p_j}|}\;,$$

where the sum runs over the momenta $\vec{p_j}$ of the reconstructed tracks and the direction of the unit vector $\vec{T}$ is defined such that T is maximized for the given set of tracks. Another variable that provides discrimination power between $B\overline{B}$ events and continuum background is the response of the flavour-tagging algorithms described in the next section. Events with a high-quality flavour tag usually contain a high-momentum muon or electron, and these are rare amongst non-$B\overline{B}$ events. Finally, fake B candidates formed by random combinations of reconstructed final-state particles in non-$B\overline{B}$ events can be suppressed by means of the polar angle, θ_B, of the reconstructed momentum vector of the B candidate in the centre-of-mass frame of the e^-e^+ collision. Since B mesons are pseudoscalar particles with spin $J = 0$, their angular distribution follows a $\sin^2\theta_B$ dependence, while the two jets in non-$B\overline{B}$ events follow a $1 + \cos^2\theta_B$ distribution. Often, several of these discriminating variables are combined in a multi-variate discriminator, calculated as a Fisher discriminant [130] or derived via artificial neural network algorithms.

Most physics analyses require to reconstruct one of the two B mesons in the event, $B_{\rm rec}$, in an exclusive decay mode. Final state particles are selected based on their kinematic properties and on the particle identificaton criteria described in the previous two sections. A kinematic fit is then applied to these particles to reconstruct the decay vertex position, the energy and the invariant mass of the $B_{\rm rec}$ candidate. Constraints on the decay vertices and masses of intermediate resonances can help to significantly improve the measurement precision on the $B_{\rm rec}$ properties.

Two nearly uncorrelated kinematic variables exploiting energy conservation in the process $e^-e^+ \to \Upsilon(4S)B\overline{B}$ are then employed to statistically separate the signal from the remaining background. One of these is the energy imbalance

$$\Delta E \;\equiv\; E_B \,-\, E_{\rm beam}\,,$$

where E_B is the reconstructed energy of the $B_{\rm rec}$ candidate and $E_{\rm beam}$ the known beam energy, both evaluated in the centre-of-mass frame of the e^-e^+ collision. Energy conservation

implies that this energy imbalance should be zero for perfectly reconstructed signal candidates. The second variable is called "energy-substituted" invariant mass, $m_{\rm ES}$, in BaBar and "beam constrained" mass, $M_{\rm bc}$, in Belle. It is defined as

$$m_{\rm ES} \equiv M_{\rm bc} \equiv \sqrt{(E_{\rm beam})^2 - (p_B)^2}$$

and should be equal to the known mass of the B meson for perfectly reconstructed signal candidates. Here, p_B is the magnitude of the reconstructed momentum of the $B_{\rm rec}$ candidate in the centre-of-mass system of the e^-e^+ collision, while the reconstructed energy of the $B_{\rm rec}$ candidate has been replaced in the calculation by the more precisely known beam energy, $E_{\rm beam}$. Distributions of $m_{\rm ES}$ respectively $M_{\rm bc}$, for $B^0 \to (c\overline{c})K^0_S$ candidates in BaBar and Belle are shown in Figure 4.18.

4.1.10 Flavour tagging

As discussed in the introduction to this section and illustrated in Figure 4.2, one of the necessary ingredients for measurements of the $B^0-\overline{B}^0$ oscillation frequency and of time-dependent CP asymmetries in the $B^0\overline{B}^0$ system is the knowledge whether the second B meson in the event, $B_{\rm tag}$, decayed as a B^0 or as a $\overline{B}^0$. This knowledge can be derived in a large fraction of events, since the majority of B^0 and $\overline{B}^0$ decays leads to flavour-specific final states. A full reconstruction of $B_{\rm tag}$ candidates in specific flavour-specific decay modes would, however, lead to an unacceptably large loss in statistics due to the large number of possible decay modes and the corresponding small branching fractions. Therefore, so-called flavour tagging algorithms are employed that search for generic flavour-specific signatures amongst the reconstructed tracks that were not employed in the reconstruction of the $B_{\rm rec}$ candidate. These signatures are charged leptons from semileptonic decays $\overline{b} \to \overline{c}\ell^+\nu_\ell$, charged kaons or Λ baryons produced in the hadronization of strange quarks from the cascade decay $\overline{b} \to \overline{c} \to \overline{s}$, low-momentum charged pions from the decays $D^{*-} \to \overline{D}^0\pi$ of D^{*-} mesons produced in the hadronization of the charm quark from the decay $\overline{b} \to \overline{c}W^+$, charged high-momentum particles from the hadronization of the W^+ boson produced in this decay, or combinations of these signatures.

Two factors describe the performance of a flavour-tagging algorithm: the tagging efficiency, $\epsilon_{\rm tag}$, is defined as the fraction of all reconstructed $B_{\rm rec}$ decays for which a flavour tag can be assigned, and the mistag probability, $\omega_{\rm tag}$, is the fraction of the flavour-tagged $B_{\rm rec}$ decays for which the tagging decision is incorrect. Wrong tags dilute the observed charge asymmetry by a factor

$$D \equiv 1 - 2\,\omega_{\rm tag} \ .$$

while the statistical uncertainty on the measurement of the asymmetry generally scales with $1/\sqrt{Q_{\rm tag}}$, where

$$Q_{\rm tag} \equiv \epsilon_{\rm tag} \cdot D = \epsilon_{\rm tag} \cdot (1 - 2\,\omega_{\rm tag})$$

is usually referred to as the tagging power or effective tagging efficiency.

Relatively low mistag fractions and high effective tagging efficiencies can be achieved at the B factories, where all final-state particles are due to the decay of the $B_{\rm rec}$ or the $B_{\rm tag}$ meson. Moreover, since the two B mesons are emitted into opposite hemispheres in the centre-of-mass system, the respective decay products are relatively well separated from each other. The flavour tagging performance can therefore be assumed to good approximation to be independent of the specific $B_{\rm rec}$ decay mode and can be measured reliably using samples of fully reconstructed flavour-specific $B_{\rm rec}$ decays.

Lepton flavour-tagging algorithms rely mostly on the charge of high-momentum leptons from the semileptonic decays $\overline{b} \to \overline{c}\ell^+\nu_\ell$ and $b \to c\ell^-\overline{\nu}_\ell$: a positively charged lepton indicates a B^0 decay, a negatively charged lepton indicates a $\overline{B}^0$ decay. Leptons of opposite charge are produced via cascade decays $\overline{b} \to \overline{c} \to \overline{s}\ell^-\overline{\nu}_\ell$ and $b \to c \to s\ell^+\nu_\ell$. These "wrong-sign" leptons

can also be employed in the flavour-tagging algorithm since their lower momentum allows to distinguish them from the primary leptons produced in the semileptonic decay of b and $\overline{b}$ quarks. The clear tagging signature and the high purity of lepton identification allow to keep the mistag fraction low, while the tagging efficiency is limited by the relatively low branching fractions of semileptonic decays.

Higher tagging efficiency can be achieved in kaon tagging algorithms due to the large fraction of B^0 and $\overline{B}^0$ decays that involve charged kaons in the final state. The dominant source of charged kaons are cascade decays $\overline{b} \to \overline{c} \to \overline{s}$ and $b \to c \to s$, where a positive kaon indicates the decay of a B^0 meson, while a negative kaon indicates a $\overline{B}^0$ decay. The average multiplitiy of such "right-sign" kaons in B^0 and $\overline{B}^0$ decays has been measured to be $0.51 \pm 0.010.08$ [133]. Kaons of opposite charge can for example be produced in the hadronization of the $W^{\pm}$ meson from the decays $\overline{b} \to \overline{c}W^+$ and $b \to cW^-$. The average multiplicity of such "wrong-sign" kaons in B^0 and $\overline{B}^0$ decays is $0.13 \pm 0.010.05$ [133]. As their kinematic properties are similar to those of the right-sign kaons, they cannot be cleanly separated from these and constitute a source of wrong tags. Another source of wrong kaon tags are misidentified pions. Despite the larger mistag fraction, though, kaon tagging algorithms yield the highest tagging power at the B factories.

The strange quarks and antiquarks produced in cascade decays $\overline{b} \to \overline{c} \to \overline{s}$ and $b \to \overline{c} \to \overline{s}$ can also hadronize into $\overline{\Lambda}^0$ and Λ^0 baryons, where a $\overline{\Lambda}^0$ indicates a B^0 decay while a Λ^0 baryon indicates a $\overline{B}^0$ decay. Λ^0 and $\overline{\Lambda}^0$ candidates are formed from a track that has been identified as a proton or antiproton and a second track of opposite charge, which come from a common displaced decay vertex and yield an invariant mass compatible with the known Λ^0 mass. Λ^0 and $\overline{\Lambda}^0$ candidates provide clean tags but the tagging efficiency is low.

If the charmed quark or antiquark from the decay $\overline{b} \to \overline{c}W^+$ or $b \to cW^-$ hadronizes into a $D^{*\pm}$ meson, tagging information is provided by the charge of the low-momentum pion, $\pi^{\pm}_{\mathrm{sl}}$, from the subsequent decay $D^{*+} \to \overline{D}^0\pi^+_{\mathrm{sl}}$ or $D^{*-} \to D^0\pi^-_{\mathrm{sl}}$. The background from other low-momentum tracks is significant, but can be suppressed by exploiting correlations between the direction of flight of the $\pi^{\pm}_{\mathrm{sl}}$ candidate with the remaining particles from the decay of the B_{tag} candidate. Since the $\pi^{\pm}_{\mathrm{sl}}$ and the neutral D meson are produced nearly at rest in the rest frame of the decaying $D^{*\pm}$ meson, their momentum vectors will be aligned with each other in the B_{tag} rest frame and opposite that of the other B_{tag} decay products. The direction of flight of the $\pi^{\pm}_{\mathrm{sl}}$ candidate should therefore be aligned with the thrust axis of the particles on the B_{tag} side of the event. A π^-_{sl} indicates a B^0 decay while a π^+_{sl} indicates a $\overline{B}^0$ decay.

Finally, an inclusive tag can be derived from the charge of the track with the highest momentum in the center-of-mass frame of the $\Upsilon(4S)$ decay. Such high-momentum particles can be due to the hadronization of the $\overline{b}\tilde{\mathrm{q}}$uark, such as fast pions from the decays $B^0 \to D^{*-}\pi^+$ and $\overline{B}^0 \to D^{*+}\pi^-$ or they can be high-momentum leptons that failed the selection criteria for the lepton tag. High-momentum tracks of positive charge indicate a B^0 decay, those of negative charge indicate a $\overline{B}^0$ decay.

Both in BaBar and Belle, multivariate techniques are employed to select tagging candidates for the different tagging algorithms and to combine the results of these algorithms into a final flavour tag for the event. Artificial neural network algorithms trained on large samples of simulated $B^0\overline{B}^0$ events are employed in BaBar [131], while in Belle multi-dimensional lookup tables are used that were also derived from simulated $B^0\overline{B}^0$ events [134]. A simple schematic diagram of the tagging algorithm employed in Belle is shown in Figure 4.19. In both cases, input variables to these algorithms are the reconstructed momenta and decay angles of the tagging candidates and their associated particle-identification criteria, as well as information from the remaining event, such as the thrust axis of the B_{tag} candidate. The final output of the algorithms is a flavour tagging decision for the event as well as an estimate of the reliability of this decision. In Belle, the tagging decision was expressed as $q = +1$ for events in which the B_{tag} candidate was tagged as having decayed as a B^0 meson and $q = -1$ for events in which it

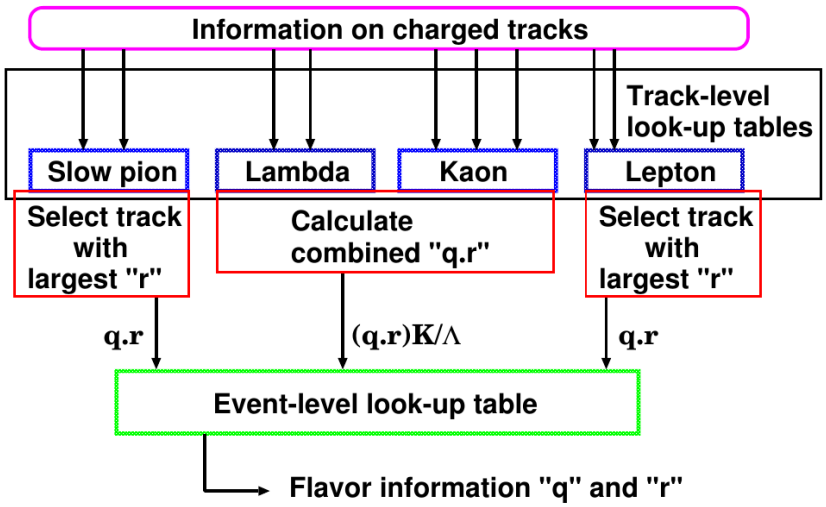

Figure 4.19: Schematic diagram of the flavour tagging algorithm employed in Belle, where $q = \pm 1$ indicates the tagging decision and $r \in [0, 1]$ indicates the estimated reliability of this decision (from [134]).

was tagged as having decayed as a $\overline{B}^0$ meson. The estimated reliability was expressed in terms of a continuous variable r that could assume values between $r = 0$ for no decision to $r = 1$ for unambiguous decisions. In BaBar, both informations were combined in one continuous variable $y \equiv q \cdot r$ that could assume values between -1 and $+1$.

The response of the algorithms was then calibrated on collision data using samples of events in which the $B_{\rm rec}$ candidate decayed into flavour-specific ("self-tagged") final states such as $B^0 \to D^{*-}\ell^+\nu_\ell$, $B^0 \to D^{*-}\pi^+$ and $B^0 \to D^-\pi^+$. The flavour-tagging algorithm was applied to these events and they were grouped into seven categories according to the value of r or $|y|$ returned by the algorithm. One of these seven categories contained events for which no tagging decision could be derived or for which r resp. $|y|$ was smaller than 0.1. Such events were not used in BaBar analyses, while in Belle analyses they were assigned a mistag probability $\omega = 0.5$, corresponding to a 50% probability for the decision to be correct or wrong. For the other six tagging categories, the average mistag fraction, ω, was determined from the calibration sample by comparing the decision of the flavour-tagging algorithm, q, with the true flavour of the $B_{\rm rec}$ candidate as derived from its decay products. In addition to the average mistag probability, also the difference $\Delta\omega$ between the mistag probabilities for true B^0 decays and true $\overline{B}^0$ decays was determined. The results of the final flavour-tagging calibrations performed at BaBar and Belle are shown in Tables 4.1 and 4.2, respectively. The overall, combined effective tagging efficiencies are quoted in Ref. [112] as $Q = (33.1 \pm 0.3)\,\%$ for BaBar and and $Q = (30.1 \pm 0.4)\,\%$ for Belle.

4.1.11 Reconstruction efficiencies and systematic uncertainties

Many measurements, e.g. measurements of absolute decay rates or cross sections, require the precise knowledge of reconstruction efficiencies. These were determined from large samples of simulated events. Various control channels were employed to study differences between simulation and collision data over a wide range of particle momenta and other kinematic properties of the events, detector occupancies and background levels. If differences were observed, systematic uncertainties were derived accordingly. If no significant deviation was found, the statistical uncertainty of the efficiency determination was assumed to cover possible systematic effects.

As an example, track reconstruction efficiencies in collision data and simulation were compared in BaBar employing large samples of $e^-e^+ \to \tau^-\tau^+$ events in which one τ lepton decayed

Table 4.1: Results of the final calibration of the BaBar flavour-tagging algorithm (from [112]). The tagging categories were given funny names but are essentially defined in terms of the estimated reliability $|y|$ returned by the algorithm. For a full definition of the tagging categories, see Ref. [112]. The average tagging efficiency $\epsilon_{\rm tag}$, mistag fraction ω and tagging power Q for each tagging category and for the full sample are quoted as well as the differences $\Delta\epsilon_{\rm tag}$, $\Delta\omega$ and ΔQ in these numbers between true B^0 and $\overline{B}^0$ candidates.

Category	$\varepsilon_{\rm tag}(\%)$	$\Delta\varepsilon_{\rm tag}(\%)$	$w(\%)$	$\Delta w(\%)$	$Q(\%)$	$\Delta Q(\%)$
`Lepton`	9.7 ± 0.1	0.2 ± 0.2	2.1 ± 0.2	0.2 ± 0.5	8.9 ± 0.1	0.1 ± 0.4
`Kaon I`	11.3 ± 0.1	-0.1 ± 0.2	4.1 ± 0.3	0.2 ± 0.6	9.6 ± 0.1	-0.1 ± 0.4
`Kaon II`	15.9 ± 0.1	-0.1 ± 0.2	13.0 ± 0.3	-0.2 ± 0.6	8.7 ± 0.2	0.0 ± 0.5
`Kaon-Pion`	13.2 ± 0.1	0.4 ± 0.2	23.0 ± 0.4	-1.3 ± 0.7	3.9 ± 0.1	0.5 ± 0.3
`Pion`	16.8 ± 0.1	-0.3 ± 0.3	33.3 ± 0.4	-2.7 ± 0.6	1.9 ± 0.1	0.6 ± 0.2
`Other`	10.6 ± 0.1	-0.5 ± 0.2	41.8 ± 0.5	5.9 ± 0.7	0.28 ± 0.03	-0.4 ± 0.1
Total	77.5 ± 0.1	-0.3 ± 0.5			33.1 ± 0.3	0.7 ± 0.8

Table 4.2: Results of the final calibrations of the Belle flavour-tagging algorithm (from [112]). The average tagging efficiency $\epsilon_{\rm tag}$ and mistag fraction ω for each tagging category are quoted as well as the difference $\Delta\omega$ between the mistag fractions for true B^0 and $\overline{B}^0$ candidates.

$r-$interval	$\varepsilon_{\rm tag}$	w	Δw
$0.000 - 0.100$	0.222 ± 0.004	0.5	0.0
$0.100 - 0.250$	0.145 ± 0.003	0.419 ± 0.004	-0.009 ± 0.004
$0.250 - 0.500$	0.177 ± 0.004	0.319 ± 0.003	$+0.010 \pm 0.004$
$0.500 - 0.625$	0.115 ± 0.003	0.223 ± 0.004	-0.011 ± 0.004
$0.625 - 0.750$	0.102 ± 0.003	0.163 ± 0.004	-0.019 ± 0.005
$0.750 - 0.875$	0.087 ± 0.003	0.104 ± 0.004	$+0.017 \pm 0.004$
$0.875 - 1.000$	0.153 ± 0.003	0.025 ± 0.003	-0.004 ± 0.002

leptonically as $\tau^{\pm} \to \mu^{\pm}\nu_{\mu}\nu_{\tau}$ while the other decayed semileptonically as $\tau^{\mp} \to \pi^{+}\pi^{-}\pi^{\mp}\nu_{\tau}$. Candidate events were selected by requiring an isolated muon candidate and either two or three charged tracks with associated particle-identification information compatible with the pion hypothesis. In events with two such tracks, the existence of a third particle was inferred from charge conservation and the track reconstruction efficiency was determined from the fraction of events for which a track for this third particle was found. No significant difference in this efficiency was found between collision data and simulation. The main limitation of this method was found to be the presence of multiple neutrinos in the final state, which did not allow to perform precise comparisons as a function of the direction and momentum of the inferred track. Other sources of systematic uncertainties associated to this method were related to potential backgrounds, for example from events involving K^0_S decays. The total systematic uncertainty of the method was estimated to be $(0.13-0.24)\,\%$. Track reconstruction efficiencies for low-momentum particles were compared using samples of low-momentum pions from decays $D^{*\pm} \to D^0\pi^{\pm}$. Here, the systematic uncertainty was found to be $1.5\,\%$ larger. Differences in the track reconstruction efficiency for positively charged and negatively charged particles can induce artificial asymmetries in mesurements of *CP* violating observables. This charge asymmetry was determined to be $(0.10 \pm 0.26)\,\%$, i.e. consistent with zero. Particle identification efficiencies in collision data and simulation were compared using control samples of B-meson decays involving a J/ψ meson, such as $B^{\pm} \to J/\psi\pi^{\pm}$, $B^{\pm} \to J/\psi K^{\pm}$ or $B^0 \to J/\psi K^{*0}$ with $K^{*0} \to K^{+}\pi^{-}$ and $\overline{B}^0 \to J/\psi\overline{K}^{*0}$ with $\overline{K}^{*0} \to K^{-}\pi^{+}$. Reconstructing the J/ψ meson in its decay to two charged leptons permitted to select clean event samples with an event environment similar to that in most physics analyses. Systematic uncertainties were studied by comparing the event yields in collision data and in simulation, with and without particle identification requirements applied.

Table 4.3: Operating parameters, approximate $b\bar{b}$ production cross sections and approximate number of $b\bar{b}$ pairs produced at high-energy hadron colliders, compared to the corresponding numbers for the B factories, BaBar and Belle. The quoted numbers of $b\bar{b}$ pairs do not take into account the effects of detector acceptance, trigger and reconstruction efficiencies.

	collisions	$\sqrt{s}$	$\sigma(b\bar{b})$	$\int L\,dt$	$b\bar{b}$ pairs
BaBar (1999-2008)	e^-e^+	10.58 GeV	1 nb	424 fb^{-1}	465×10^6
Belle (1999-2010)	e^-e^+	10.58 GeV	1 nb	711 fb^{-1}	771×10^6
CDF/D0 (2001-2011)	$p\overline{p}$	1.96 TeV	100 μb	10 fb^{-1}	$\approx 10 \times 10^{11}$
LHCb (2011)	pp	7 TeV	270 μb	1 fb^{-1}	$\approx 3 \times 10^{11}$
LHCb (2012)	pp	8 TeV	300 μb	2 fb^{-1}	$\approx 6 \times 10^{11}$
ATLAS/CMS (2011)	pp	7 TeV	270 μb	5 fb^{-1}	$\approx 14 \times 10^{11}$
ATLAS/CMS (2012)	pp	8 TeV	300 μb	20 fb^{-1}	$\approx 6 \times 10^{12}$
LHCb (2016-2018)	pp	13 TeV	500 μb	2 fb^{-1}/ year	1×10^{12}/ year
ATLAS/CMS (2016++)	pp	13 TeV	500 μb	45 fb^{-1}/ year	2×10^{13}/ year

4.2 Hadron colliders: advantages, disadvantages, differences

Asymmetric B factories operating at the $\Upsilon(4S)$ resonance provide a clean environment for the study of CP violating observables in the $B^0\overline{B}^0$ and B^+B^- systems. However, as the mass of the $\Upsilon(4S)$ resonance lies below the $B_s^0\overline{B}_s^0$ production threshold, B factories do not give access to the $B_s^0\overline{B}_s^0$ system. As described in Sections 5.1, 6.1 and 6.2, precise measurements of the $B_s^0-\overline{B}_s^0$ oscillation frequency and of CP violating observables in the $B_s^0\overline{B}_s^0$ system provide a powerful handle for testing the CKM picture of flavour-changing quark interactions and probing for possible effects from physics beyond the Standard Model. Towards the end of its operation, the Belle experiment collected some data at the $\Upsilon(5S)$ resonance, above the $B_s^0\overline{B}_s^0$ and $B_s^{0*}\overline{B}_s^{0*}$ production thresholds. However, the collected sample of $B_s^0\overline{B}_s^0$ pairs is small since the $b\bar{b}$ production cross section at the $\Upsilon(5S)$ is about three times lower than that at the $\Upsilon(4S)$ and the $\Upsilon(5S)$ has many possible decay modes in addition to that to $B_s^0\overline{B}_s^0$ pairs. In total, Belle collected about 7 million $B_s^{0(*)}\overline{B}_s^{0(*)}$ pairs in a data sample corresponding to an integrated luminosity of 121 fb^{-1}. This is to be compared to the sample of 772 million $B^0\overline{B}^0$ and B^+B^- pairs collected by the experiment.

Significantly larger samples of B_s^0 mesons and all other types of b hadrons can be collected by exploiting the large $b\bar{b}$ production cross section in hadron-hadron collisions at high energies. This approach has been pursued successfully by the CDF and D0 experiments at the Tevatron and more recently by the dedicated heavy-flavour experiment LHCb at the LHC. The Tevatron collided protons and antiprotons at a centre of mass energy of 1.96 TeV from 2002 till 2011, while the LHC collided protons on protons at centre-of-mass energies of 7 TeV in 2011 and 8 TeV in 2012, respectively. After a long shutdown for maintenance and consolidation of the accelerator in 2013/14, the LHC is expected to resume operation in 2015 at a centre-of-mass energy of 13 TeV. The Tevatron experiments and the LHCb experiment will be described in Sections 4.3 and 4.4, respectively.

The production of $b\bar{b}$ quark pairs in hadronic collisions can proceed through pair production ($q\overline{q}$ annihilation or gluon fusion), flavour excitation and gluon splitting processes, as illustrated in Figure 4.20. Figure 4.21 shows the calculated b quark production cross section as a function of the centre-of-mass energy in pp collisions, compared with other Standard-Model processes and split into the contributions from each of the three production processes. These calculations also apply to the 1.96 TeV $p\overline{p}$ collisions at the Tevatron, since the valence-quark dependent contribution to hard subprocesses is small at such high collision energies. The calculated total b quark production cross sections are in fact in good agreement with those measured at the Tevatron and the LHC. Approximate values are compiled in Table 4.3.

As illustrated in Figure 4.22 for the example of LHC operation conditions in 2012, the

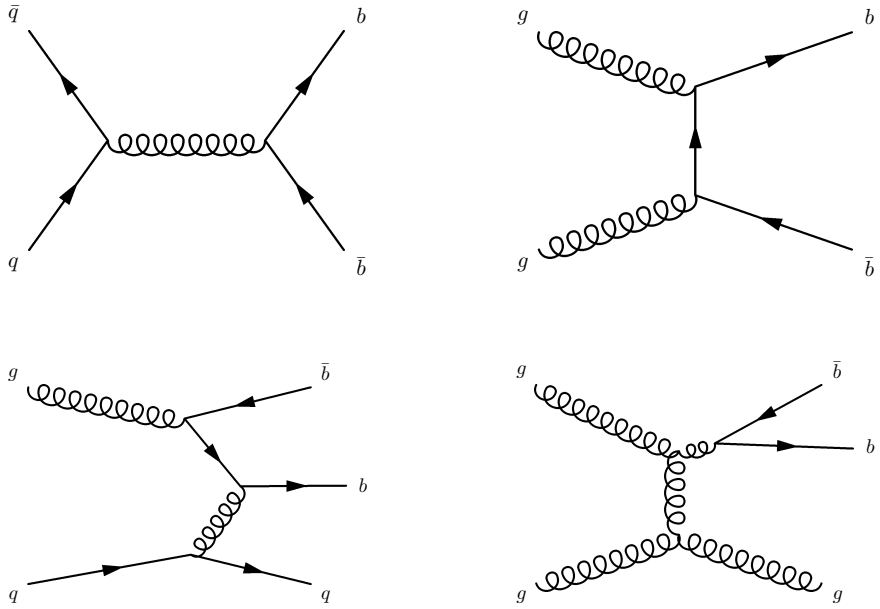

Figure 4.20: Feynman diagrams illustrating the main $b\bar{b}$ production mechanisms in hadron collisions: (top left) $q\bar{q}$ annihilation, (top right) gluon fusion, (bottom left) flavour excitation and (bottom right) gluon splitting.

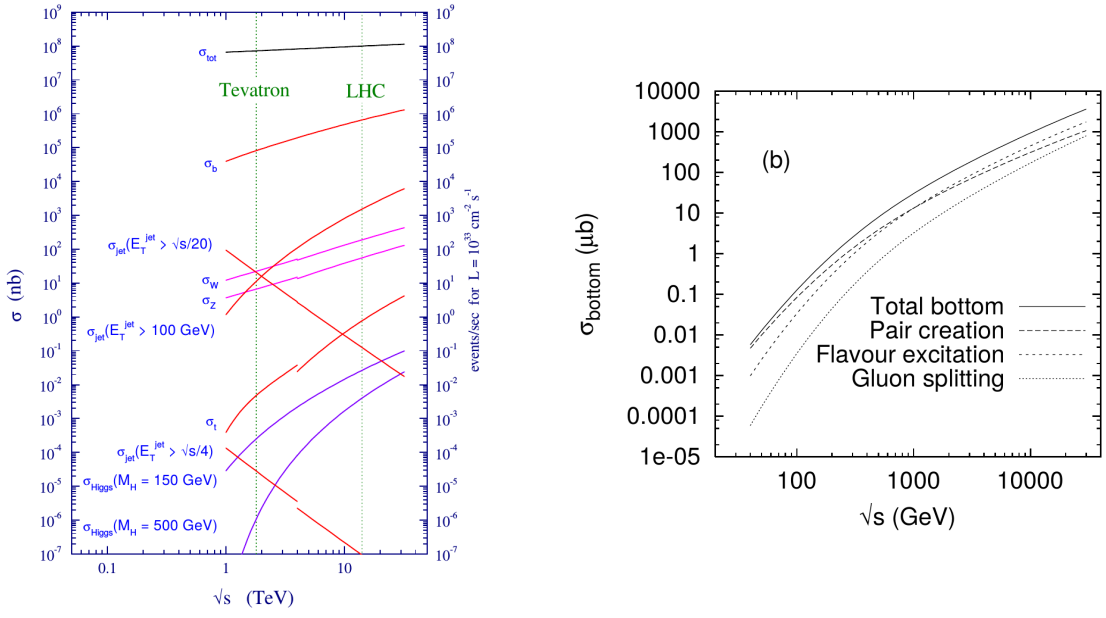

Figure 4.21: Calculated b quark production cross sections as a function of the centre-of-mass energy in pp collisions, (left, from [135]) compared to other Standard Model processes and (right, from [136]) split into the contributions from each of the three production processes.

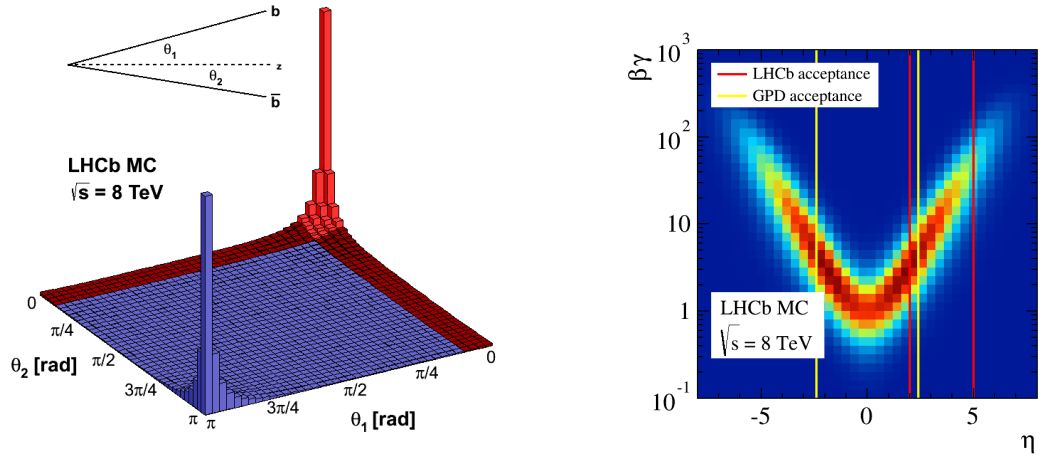

Figure 4.22: Results of PYTHIA [137] simulations of $b\bar{b}$ production in pp collisions at a centre-of-mass energy of 8 TeV, i.e. the LHC operation conditions in 2012: (left) distribution of b and $\bar{b}$ production angles, θ_1 and θ_2, with respect to the proton-proton beam axis and (right) distribution of the Lorentz boost $\beta\gamma$ versus the pseudo-rapidity $\eta = -\ln(\tan(\theta/2))$ of the produced b and $\bar{b}$ quarks. In the panel on the left, bins inside the acceptance of the LHCb experiment are marked in red. In the right panel, vertical lines indicate the acceptance boundaries of LHCb and of the two general purpose detectors (GPD), ATLAS and CMS, respectively (simulations and plots by Christian Elsasser).

production of $b\bar{b}$ pairs in high-energy hadron-hadron collisions is strongly peaked towards small angles with respect to the beam axis. This is because the mass of the b and $\bar{b}$ quark produced in the collision is small compared to the energy released in the collision. Each of the two partons (quarks or gluons) that interact to create the $b\bar{b}$ pair carries only a fraction of the momentum of its parent hadron and this fraction is in general not equal for the two interacting partons. Therefore, while the centre-of-mass frame of the hadron-hadron collision is at rest in the laboratory frame, the centre-of-mass frame of the underlying parton-parton interaction is usually Lorentz-boosted, in either direction, along the beam axis[1]. As a result, the b hadrons are produced with a large Lorentz boost in the laboratory frame, which increases significantly towards small angles with respect to the beam axis as illustrated in Figure 4.22. A larger Lorentz boost translates into a longer mean decay length of the b hadron in the laboratory frame and into higher momenta of its decay products. Particles with higher momenta suffer less from multiple scattering in the material of the detector and therefore permit a more precise reconstruction of the b hadron decay vertex. The longer decay length and the more precise determination of the decay vertex allow for a better resolution on the decay time of the b hadron. This is of particular importance for all measurements that require to resolve the rapid flavour oscillations in the $B_s^0\overline{B}_s^0$ system, such as measurements of the oscillation frequency (see Section 5.1) or time-dependent CP asymmetries in the $B_s^0\overline{B}_s^0$ system (see Section 6.1). The LHCb experiment is designed as a forward magnetic spectrometer in order to exploit these features of $b\bar{b}$ production at the LHC. The lifetime of the B^0 meson translates into a mean decay length of about 10 mm in LHCb, compared to 255 μm in BaBar and 195 μm in Belle.

In hadron-hadron collisions, the b quark and the $\bar{b}$ quark are not produced in an entangled state. They hadronize independently from each other into any type of b hadron, namely $B^{\pm}$, B^0, B_s^0, $B_c^{\pm}$ or Λ_b, or excited states of these. The hadronization fractions, i.e. the relative probabilities with which the different types of ground-state b hadrons are produced, are roughly

[1]The situation is different for the production of particles with large mass, such as the Higgs boson. Here, in order to produce such a particle, each of the two interacting partons must carry a large fraction of the momentum of its parent hadron. This forces the collision to be more symmetric and the Lorentz boost is therefore small.

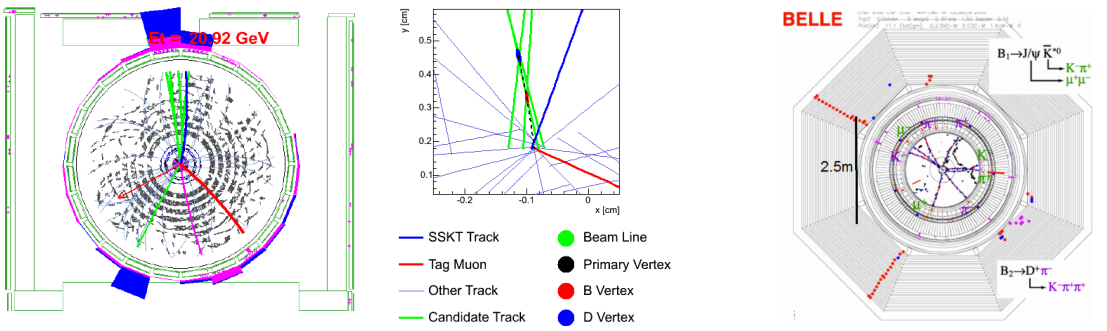

Figure 4.23: Event displays of (left) a $B_s^0 \to D_s\pi$ candidate with its underlying event in CDF and (right) a fully reconstructed $B^0\overline{B}^0$ event in Belle. In the left panel, thick green lines indicate the final-state particles from the B_s^0 decay, the thick blue and red lines indicate a charged kaon and a muon candidate that could be used for tagging the flavour of the B_s^0 meson at its production and the thin grey lines illustrate the tracks of particles from the underlying event. The close-up of the interaction region illustrates the displaced decay vertices of the B_s^0 and D meson (the latter produced in the decay of the D_s), which together with the large impact parameters of the decay products can be used as trigger signatures. In the panel on the right, note that there are hardly any detector signals that are not associated to one of the decay products of the two B mesons.

0.4 : 0.4 : 0.15 : 0.05 for $B^\pm : B^0 : B_s^0 : B_c^\pm : \Lambda_b$. Measurements by the LHCb collaboration [138] indicate that these fractions seem to depend on the kinematic properties of the initially produced b quark and therefore on the production process and energy.

High-energy hadron-hadron collisions as a source of b hadrons also pose significant experimental challenges compared to the clean environment of B factories. As Figure 4.21 shows, the inelastic cross-section is larger than the $b\bar{b}$ production cross section by about a factor of 800 at the Tevatron and by about a factor 160 at the LHC. Highly selective and efficient trigger algorithms are therefore required to extract the interesting signal events from the large background. These algorithms typically exploit generic features of b-hadron decays, such as displaced decay vertices or decay products with relatively high transverse momentum and large impact parameter with respect to primary collision vertices. Trigger efficiencies are typically of the order of 80% or more for decays involving muons in the final state but only 50% for decays to fully hadronic final states. By comparison, at the B factories trigger efficiencies close to 100 % were achieved for all types of B-meson decays.

A further challenge in hadron-hadron collisions is the large number of additional particles that are produced in the underlying hadronic interaction and cause additional signals in the detector. For illustration, Figure 4.23 shows event displays of a $B_s^0 \to D_s\pi$ candidate in CDF next to a fully reconstructed $B^0\overline{B}^0$ event in Belle. The mean number of reconstructed tracks in a typical event in CDF is 80, with tails extending up to above 300 tracks. More sophisticated reconstruction algorithms are required to extract the few particles of interest in a given event, leading to lower event reconstruction efficiencies compared to B factories, where essentially all particles in a $B\overline{B}$ event are due to the decays of the B meson and the $\overline{B}$ meson.

Measurements involving the reconstruction of neutral pions and, in particular, neutrinos are challenging in the hadronic environment. Neutrinos escape the detector unobserved but at the B factories their properties can be reconstructed indirectly by studying the energy and momentum imbalance of all reconstructed particles in the event. Such an approach is not feasible in hadronic interactions.

The general strategy for the measurement of time-dependent asymmetries at hadron colliders is illustrated in Figure 4.24, taking as an example a measurement of the $B_s^0 - \overline{B}_s^0$ oscillation frequency. Measurements of time-dependent CP asymmetries in the $B_s^0\overline{B}_s^0$ system or measurements in the $B^0\overline{B}^0$ system follow similar patterns. As the $b\bar{b}$ quark pair is not produced in a coherent state and the wave functions of the two produced b hadrons evolve independently

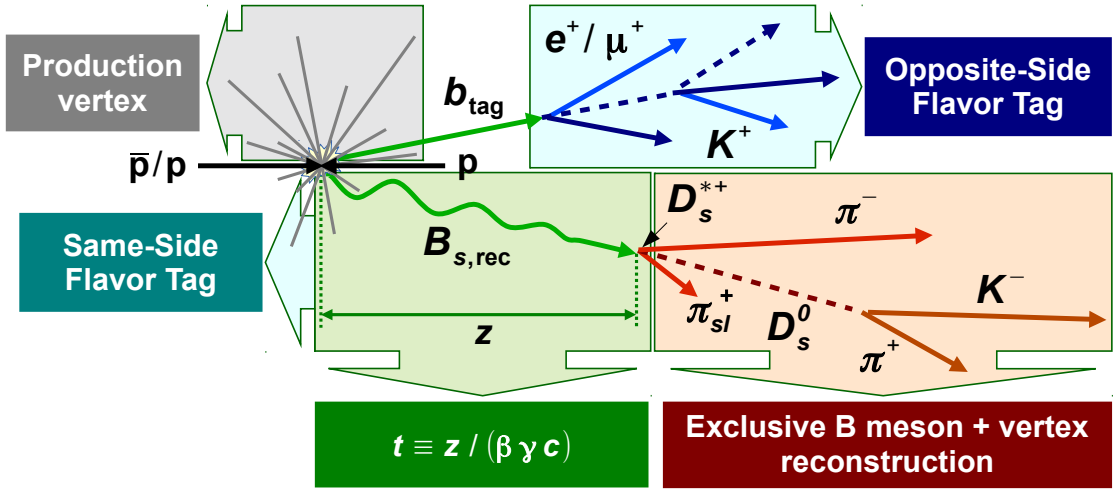

Figure 4.24: Illustration of the ingredients for the measurement of the B_s^0-$\overline{B}_s^0$ oscillation frequency at a hadron collider.

from each other, the point of reference for all time-dependent measurements is the primary collision vertex in which the $b\bar{b}$ quark pair was produced. This vertex can be reconstructed with good precision from the large number of tracks from the charged particles produced in the underlying hadronic interaction. Similar to the approach at B factories described in Section 4.1, a B_s^0 or $\overline{B}_s^0$ meson, denoted as $B_{\rm rec}$, is fully reconstructed in a flavour-specific final state, such as $B_s^0 \to D_s^{*+}\pi^-$ followed by $D_s^{*+} \to D_{\rm s}^0\pi_{\rm sl}^+$ and $D_{\rm s}^0 \to K^-\pi^+$. The charge of the final-state particles allows to determine the flavour of the $B_{\rm rec}$ candidate at the time of its decay, i.e. whether it decayed as a B_s^0 or $\overline{B}_s^0$ meson. The momentum of the $B_{\rm rec}$ candidate and the position of its decay vertex can be determined from a kinematic reconstruction of the decay chain. The final ingredient of the measurement is the initial flavour of the $B_{\rm rec}$ candidate, i.e. whether it was created as a B_s^0 meson or a $\overline{B}_s^0$ mesonin the hadronization of the $\bar{b}$ and b quark produced in the hadron-hadron collision. This information can be derived in a similar fashion as at the B factories by exploiting flavour-specific signatures from the decay of the second b hadron in the event, denoted as $b_{\rm tag}$ in the figure. Such opposite-side tagging algorithms exploit the charge signs of leptons or kaons or an appropriately weighted sum of the charges of all tracks assigned to a displaced secondary vertex or a jet of charged particles that could be caused by the hadronization and decay of the $b_{\rm tag}$ candidate. In addition to these opposite-side tagging algorithms, so-called same-side tagging algorithms can be employed to infer the initial flavour of the $B_{\rm rec}$ candidate. Same-side kaon tagging exploits the fact that the hadronisation process leading to a B_s^0 or $\overline{B}_s^0$ meson requires the creation of a $s\bar{s}$ quark pair in close vicinity to the initial $\bar{b}$ or b quark. The s quark will be absorbed in the creation of a B_s^0 meson, while the $\bar{s}$ quark can hadronize into a positive kaon. Likewise, the $\bar{s}$ quark will be absorbed in a $\overline{B}_s^0$ meson, leaving the s quark, which can hadronize into a negative kaon. Same-side tagging algorithms therefore search for charged kaons close in phase space to the $B_{\rm rec}$ candidate. In a similar fashion, same-side pion tagging algorithms can be employed to tag the initial flavour of B^0 or $\overline{B}^0$ mesons. At hadron colliders, a significant fraction of B^0 and $\overline{B}^0$ mesons is produced via decays of excited charged B mesons and the tagging pion can in this case be due to such a decay of an excited B meson as well as the hadronization process leading to the production of the B^0 or $\overline{B}^0$ meson.

Due to the large number of tracks from the underlying event, the identification of the correct tagging candidates is less clean than at the B factories, resulting in larger fraction of wrong tagging decisions. An additional source of wrong tagging decisions in opposite-side tagging algorithms is the fact that the $b_{\rm tag}$ hadron can be a neutral or strange B meson that had mixed at the time of its decay. As discussed in Section 4.1.10, a fraction $\omega_{\rm tag}$ of wrong

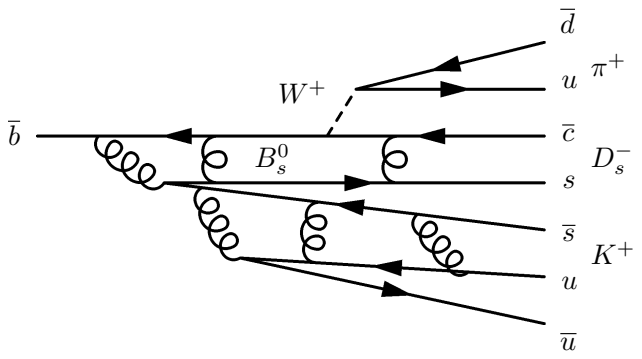

Figure 4.25: Illustration of the hadronization of a $\overline{b}$ quark to a B_s^0 meson, leading to the production of a charged kaon close in phase space to the B_s^0 meson.

tagging decisions leads to a dilution of the measured oscillation amplitude by a factor

$$D \equiv 1 - 2\omega_{\text{tag}} ,$$

while the statistical precision of asymmetry measurements scales with the so-called tagging power

$$Q_{\text{tag}} \equiv \epsilon_{\text{tag}} \cdot (1 - 2\omega_{\text{tag}}) ,$$

where the tagging efficiency ϵ_{tag} is given by the fraction of reconstructed B_{rec} candidates for which a tagging decision can be derived. Due to the larger mistag fractions, the tagging power that has been achieved at hadron colliders is almost an order of magnitude smaller than that obtained at the B factories.

The specific flavour tagging algorithms employed at the Tevatron experiments and at LHCb will be discussed in Sections 4.3.5 and 4.4.5, respectively.

4.3 The Tevatron: CDF II and D0

The first experiments to pursue a successful b-hadron physics programme at a hadron collider were the two general-purpose detectors, CDF II and D0, at the Tevatron. The primary goal of the Tevatron was to search for the top quark, the Higgs boson and as yet unknown heavy particles. During its first period of operation, between 1987 and 1996, protons and antiprotons were collided at a centre-of-mass energy of 1.8 TeV and an integrated luminosity of about 110 pb^{-1} was collected by each of the two experiments. This data taking period culminated in the first observation of the top quark by the CDF and D0 collaborations in 1995 [71, 72]. The accelerator then underwent a major upgrade to increase the collision energy and the instantaneous luminosity. The two experiments underwent comprehensive upgrades at the same time, to adjust to the new operating conditions and at the same time improve the performance of the detectors. During run II, which followed the upgrades and lasted from 2001 till 2011, the Tevatron operated at a center-of-mass energy of 1.96 TeV and at instantaneous luminosities exceeding 4×10^{32} cm^{-2}s^{-1}. An integrated luminosity of 12 fb^{-1} was delivered to the two experiments, out of which 9.6 fb^{-1} were collected. An important part of the detector upgrades in both CDF and D0 was the installation of new silicon micro-strip vertex detectors to allow an efficient and precise identification of large-impact parameter tracks and detached vertices from decays of b hadrons. The ability to efficiently and cleanly identify high-p_{T} jets containing a b quark (so-called "b tagging") was for example required for studies of top quark production through the decay $t \to Wb$ or in searches for (light) Higgs bosons via the decay $H \to b\overline{b}$. At the same time, the vertex detector upgrades enabled the experiments to perform dedicated studies in b-hadron physics.

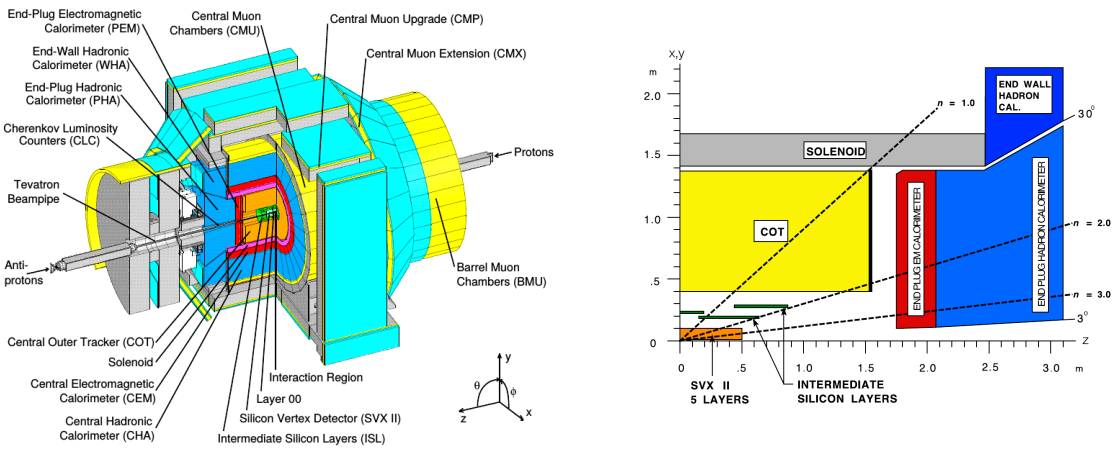

Figure 4.26: The CDF II detector for run II of the Tevatron: (left) isometric view and (right) schematic layout of its tracking system (from [139]).

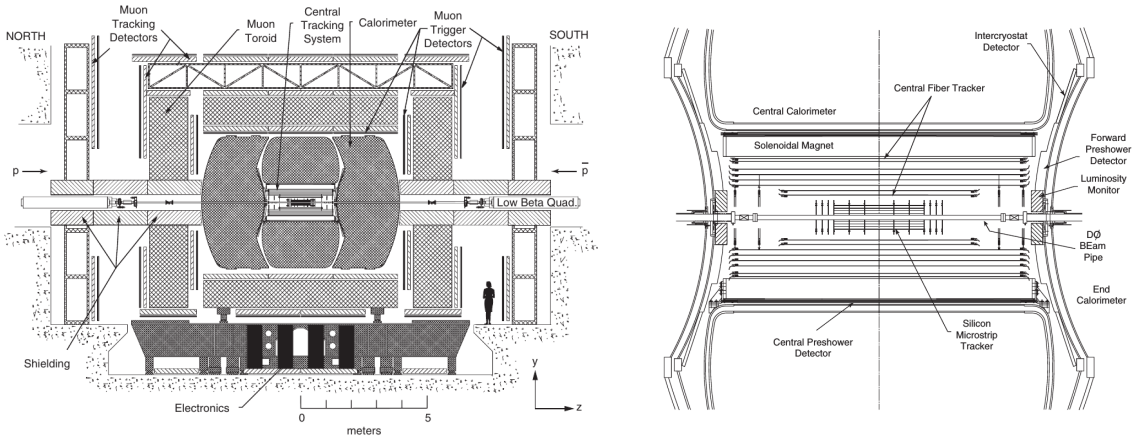

Figure 4.27: Cross sections through (left) the D0 detector for run II of the Tevatron and (right) its central tracking system (from [140]).

The potential of a b-hadron physics programme for run II of the Tevatron was explored in a series of workshops, the results of which are summarized in Ref. [141]. A dedicated experiment, dubbed BTeV, was proposed [142] in the year 2000. The BTeV collaboration grew to 175 physicists from 31 institutions in seven countries, but the plans for the experiment then fell prey to budgetary cuts during the dark ages of the Bush administration in 2005. The b-physics reach of the general purpose experiments, CDF II and D0, was more limited than that of a dedicated experiment could have been. Nevertheless, the two experiments pursued an active and successful measurement programme particularly in the $B_s^0\overline{B}_s^0$ system, to which the Tevatron provided unique access until the startup of the LHC in 2010. The main results of this effort are nicely summarized in Ref. [143]. Highlights were the first observation of $B_s^0\overline{B}_s^0$ oscillations, including a precise measurement of the $B_s^0\overline{B}_s^0$ oscillation frequency, and the first measurements of the CP violating phase in $B_s^0\overline{B}_s^0$ mixing, ϕ_s. These measurements are discussed in Sections 5.1 and 6.1, respectively. They have in the meantime been repeated with better precision at LHCb, but stand as important milestones in the recent history of flavour physics.

Views of the upgraded CDF II [144] and D0 [140] detectors are shown in Figs. 4.26 and 4.27, respectively. Both experiments follow the typical layout of general-purpose collider detectors, with silicon micro-strip vertex detectors surrounding the interaction region, followed by a tracking detector (an open-geometry wire chamber in CDF II, a scintillating fibre detector in D0)

embedded in the field of a solenoid magnet, electromagnetic and hadronic calorimeters and finally a muon system. The CDF II experiment made use of a displaced track trigger that allowed to select events containing tracks with large impact parameter with respect to the beam axis. This trigger was essential for the b-physics programme at CDF II. The b physics programme at D0 relied on efficient muon and dimuon triggers and concentrated on measurements of semileptonic $B \to \mu X$ decays and decays with a $J/\psi \to \mu^+\mu^-$ in the final state.

In the remainder of this section, the components of the two experiments most relevant for b-hadron physics, namely vertexing, tracking, triggering and charged particle identification, will be briefly described, followed by a short outline of the offline algorithms employed for flavour tagging. Throughout, the usual coordinates and variables employed in colliding beam experiments will be used: the z coordinate is measured along the beam direction while r and ϕ are the radial distance and azimuthal angle in the plane orthogonal to the beam direction, which is also the bending plane of the solenoid magnet. Particles are characterized by their transverse momentum, $p_{\rm T}$, which is the momentum component orthogonal to the magnetic field lines and therefore in the r–ϕ plane, and by their pseudo-rapidity, $\eta = -\ln(\tan\theta/2)$, where θ is the polar angle with respect to the beam axis. The transverse impact parameter of a track is defined as its distance from the $p\overline{p}$ interaction vertex in the point of closest approach in the r–ϕ plane. At the trigger levels, the $p\overline{p}$ interaction vertex could not be determined event–by–event and an average position was assumed for the calculation of the transverse impact parameter.

4.3.1 Detectors for vertex reconstruction

As explained in the previous paragraphs, the ability to precisely reconstruct the trajectories of charged particles close to the $p\overline{p}$ interaction region was a prerequisite for many measurements in CDF II and D0. In particular, the efficient and clean identification of tracks with large impact parameter was crucial for the selection of events containing a b decay and the suppression of the large background from generic inelastic $p\overline{p}$ interactions. The precise reconstruction of the B_s^0 decay vertex is required for measurements of decay-time dependent asymmetries in the $B_s^0\overline{B}_s^0$ system. The achievable precision in the reconstruction of impact parameters and vertex positions is limited by the measurement resolution of the detector, by the multiple scattering of the particles in the material of the detector and the beam pipe, and by the distance over which the track parameters have to be extrapolated from the first measurement point back to the interaction region. To obtain the best possible resolution, therefore, detectors have to be placed as close to the interaction region as possible and the amount of material, in particular the amount of dead material between the interaction region and the first measurement points, has to be kept as small as possible.

The layout of the CDF II silicon micro-strip detector system [139] is illustrated in Figure 4.28. It comprises three sub-systems, called Layer 00 (L00), SVX II and Intermediate Silicon Layer (ISL). The SVX-II was the central part of the vertex detector and played an important role in the displaced-track trigger described in Section 4.3.3 below. It consisted of five concentric, cylindrical detection layers at radii between 2.54 cm and 10.1 cm from the beam axis and used 300 μm thick double-sided silicon sensors. The readout strips on one side of the sensors had a readout pitch of 60 μm and were oriented parallel to the beam axis to precisely measure track coordinates in the r–ϕ plane. Position information in the z direction was provided by the readout strips on the other side of the sensors, oriented at 90° with respect to the beam axis in three of the layers and at a small stereo angle of 1.2° in the remaining two layers. The ISL [146] was located in between the SVX-II and the surrounding Central Outer Tracker (COT), which is described in the next section. Its main purpose was to improve the linking of track segments between the SVX-II and the COT and to increase the track reconstruction efficiency in the forward and backward regions of the detector, that were not covered by the COT. The ISL consisted of one cylindrical layer at a radius of 22 cm in the central

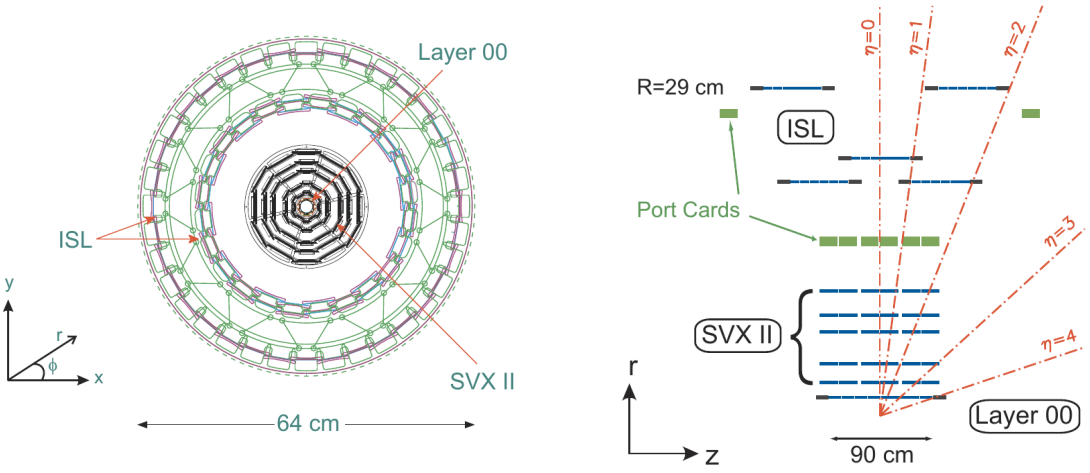

Figure 4.28: Cross sections through the CDF II silicon detector system, consisting of Layer 00, SVX II and ISL: (left) in the r–ϕ plane orthogonal to the beam axis and (right) in the r–z plane along the beam axis (from [139]).

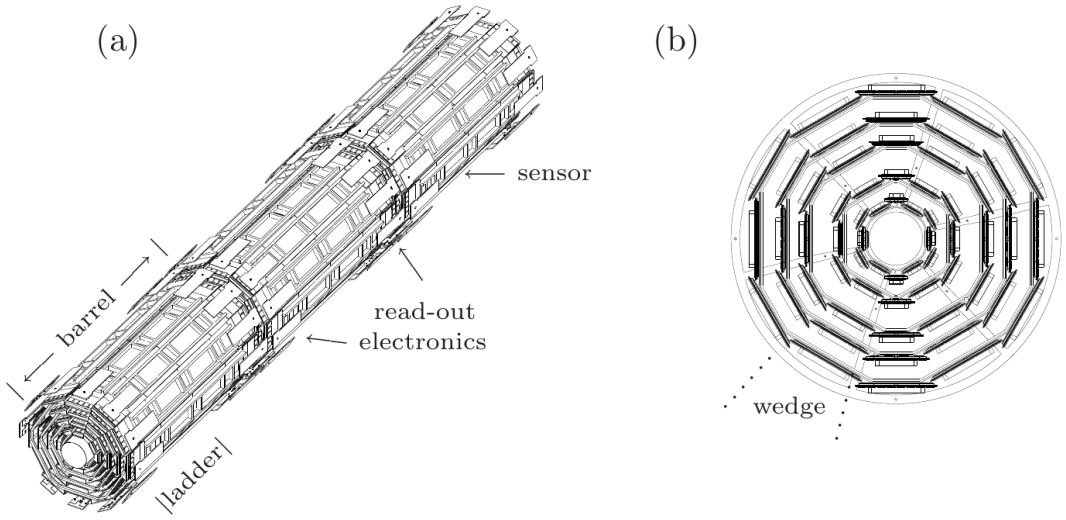

Figure 4.29: The SVX-II barrel detectors: (left) isometric view indicating the locations of readout electronics that introduce additional dead material; (right) cross section in the r–ϕ plane, indicating the 12-fold symmetry of the detector layout (from [145]).

region of the detector and two concentric layers at radii of 20 cm and 28 cm in the forward and backward regions. Similar to the SVX-II, it used 300 μm thick, double-sided sensors with readout strips that were oriented parallel to the beam axis on one side of the sensor and at a small stereo angle on the other side of the sensors. The readout strip pitch in the ISL was 112 μm. One disadvantage of the detector design was the relatively large amount of dead material from readout electronics, mechanical supports and cooling inside the acceptance of the experiment. On average, a particle at normal incidence traversed about 15% of a radiation length in the silicon detectors [147]. For this reason, the system was completed by an additional inner layer, the L00 [148,149], that was mounted directly on the beam pipe and had its silicon sensors located at distances of 1.35 cm and 1.62 cm from the beam axis. It used 300 μm thick single-sided sensors with a readout strip pitch of 50 μm and readout strips oriented parallel to the beam axis. Particular care was taken in the design of the L00 to minimize the dead material inside the acceptance of the tracking detector. The information from the L00 helped to significantly improve the resolution on the transverse track impact parameter by providing

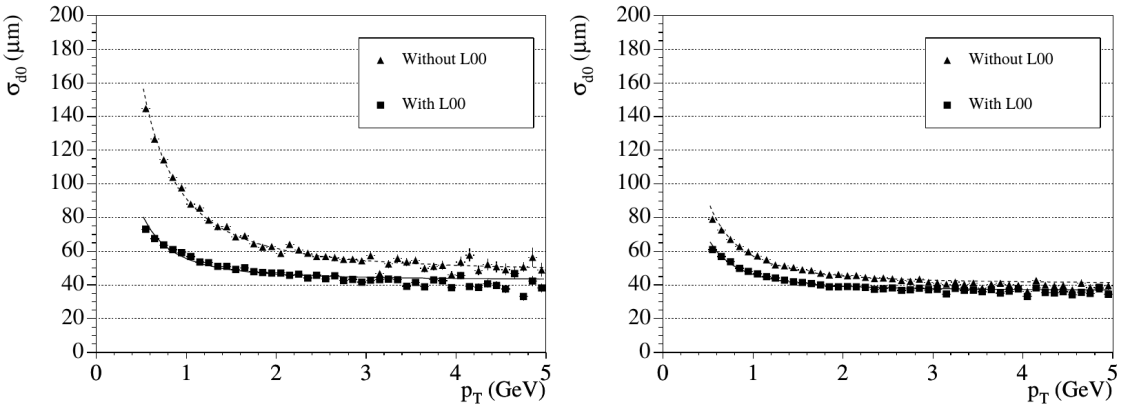

Figure 4.30: Comparison of the transverse impact parameter resolution as a function of the reconstructed transverse momentum of the candidate using or not using spatial information from the L00 detector for (left) particles that went through one of the readout hybrids in the SVX-II (see Figure 4.29) and therefore traversed a larger amount of dead material and (right) particles that did not cross any readout hybrid. The quoted resolutions include a constant contribution of 32 μm due to the finite beam size, which should be subtracted in quadrature (from [139]).

an additional position measurement close to the interaction point and mitigating the effects of multiple scattering in the material of the SVX-II. As illustrated in Figure 4.30, the improvement in the transverse impact parameter resolution was particularly large at the relatively low transverse momenta that are typical for particles from b hadron decays at the Tevatron.

The D0 Silicon Microstrip Tracker (SMT) had to provide vertexing and tracking capability over the full angular acceptance of the experiment. Its layout followed a different philosophy from the CDF II silicon system. As illustrated in Figure 4.31, the SMT consisted of a succession of barrels and disks arranged along the beam axis. Each barrel consisted of four concentric, cylindric detection layers at radii between 2.72 cm and 10.51 cm. The disks were planar detection layers oriented orthogonally to the beam axis. The so-called "F"-disks in the central part of the detector covered radii from 2.57 cm to 9.96 cm, while larger "H"-disks in the forward and backward regions extended from radii of 9.61 cm to 23.6 cm to provide similar coverage in η as those in the central part of the detector. The advantage of this complex layout was that the trajectories of particles produced at large angle with respect to the beam axis, could be measured precisely in the barrel detectors while the disks provided precise tracking information for particles produced at shallow angles with respect to the beam axis. The barrels used a combination of single-sided and double-sided silicon sensors. The single-sided sensors and one side of the double-sided sensors had readout strips with a pitch of 50 μm oriented parallel to the beam axis to provide precise coordinate measurements in the r–ϕ plane. The other side of the double-sided sensors had strips oriented either at 90% or at a small stereo angle of 2° to provide coordinate information along the beam axis. The disks were assembled from silicon sensors of trapezoidal shape with readout strips oriented at stereo angles of ±30° or ±15° with respect to the radial direction in the F-disks and H-disks, respectively.

In 2006, the SMT was complemented with an additional inner cylindrical detection layer, called "layer 0". It consisted of 300 μm thick single-sided silicon sensors that were located at radii of 1.61 mm and 1.76 mm from the beam axis. Readout strips were oriented parallel to the beam axis and had strip pitches of 71 μm and 81 μm in the inner and outer layer, respectively. Like for the L00 detector in CDF II, particular care was taken in the design of layer 0 to minimize its material budget. The beneficial impact of layer 0 on the transverse impact parameter resolution for low-p_T particles is illustrated in Figure 4.32.

Short digression: Another crucial aspect for operation at high energy, high luminosity hadron colliders is the harsh radiation environment to which the detectors

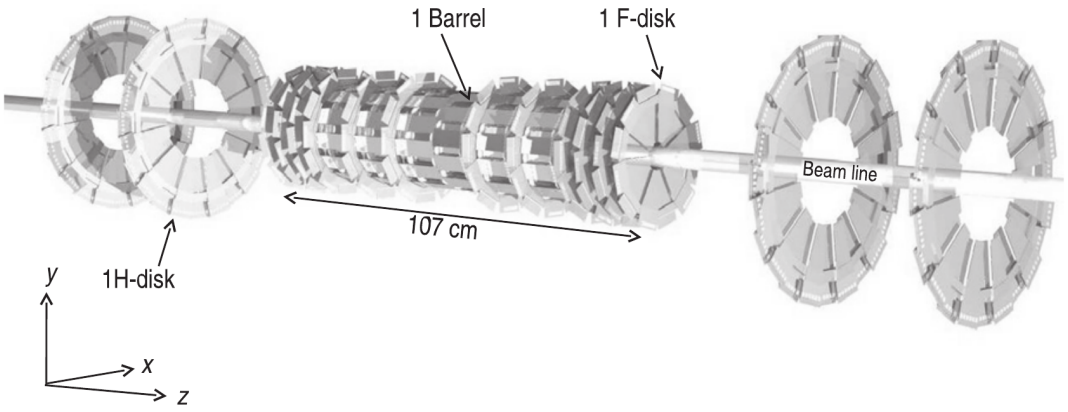

Figure 4.31: Isometric view of the D0 silicon microstrip tracker (SMT) consisting of six barrel detectors, twelve F disks, and four H disks (from [150]).

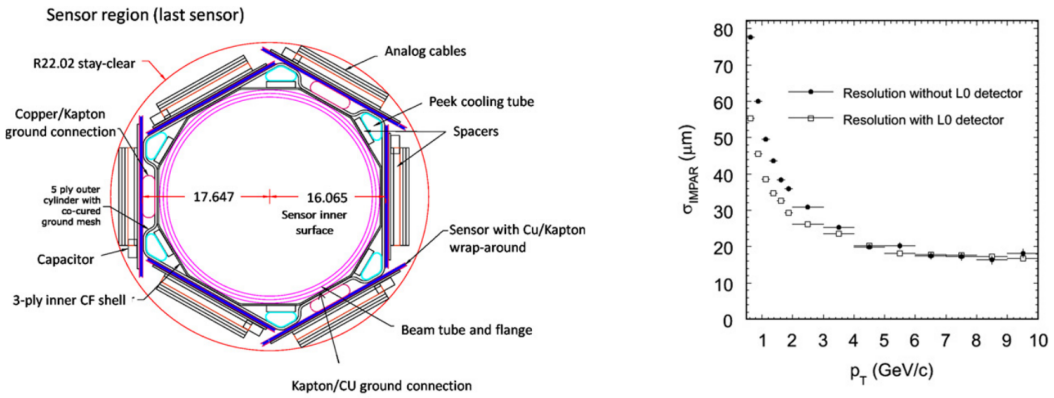

Figure 4.32: The D0 silicon layer 0: (left) cross section through the detector; (right) its effect on the transverse impact parameter resolution (both from [150]).

and their readout electronics are exposed. This is particularly relevant for the vertex detectors that have to operate close to the interaction points, where particle fluences are highest. A substantial effort has been invested over the last fifteen years to reach a detailed understanding of the mechanisms of radiation damage and to develop radiation tolerant detector technologies for the LHC. These technologies were, however, not yet available at the time when the CDF II and D0 vertex detectors were designed and the lifetime of the innermost detector modules in the SVX-II and the SMT was not expected to extend beyond an integrated delivered luminosity of at most 4-6 fb^{-1}, corresponding to a few years of operation. It was another purpose of the L00 and the layer 0 to compensate for the expected loss of efficiency in the inner modules of the SVX-II and the SMT. Single-sided silicon sensors were employed in the L00 and in layer 0, as these were expected to be more robust against the effects of radiation damage than double-sided sensors. Ref. [139] contains a detailed account of the very substantial effort that was undertaken by the SVX-II team to maintain the detector operational until the end of run II, well beyond its initial design lifetime, with only minor loss in physics performance.

4.3.2 Detectors for tracking of charged particles

The reconstruction of the trajectories and momenta of charged particles relied in CDF II on the silicon detectors described in the previous section and on the Central Outer Tracker (COT) that surrounded these detectors. The COT was an open-geometry drift chamber that spanned

a length of 310 cm along the beam axis and covered radii from 44 cm to 132 cm. The COT contained a total of 96 radial detection layers that were organized into eight super-layers of twelve layers each. Every second super-layer had axial wires, oriented parallel to the beam axis to provide precise position measurements in the r–ϕ plane, the remaining four super-layers had wires oriented at a small stereo angles of either $+3^\circ$ or -3° to provide position information along the z axis. A standard mixture of 50 % Argon and 50 % Ethane was used as drift gas. The resulting maximum drift time of 100 ns fitted well within the Tevatron bunch spacing of 396 ns. The signals collected on the anode wires were amplified, shaped, discriminated and fed into a TDC that recorded the leading and the trailing edge of the signals with a resolution of 1 ns. The time of the leading edge was employed to determine the drift time, resulting in a spatial resolution of about 175 μm for single hits. The time difference between leading and trailing edge provided a measure for the signal amplitude and therefore for the amount of energy deposited by the particle traversing the drift cell. These $\mathrm{d}E/\mathrm{d}x$ measurements provided input for the separation of kaons and pions at momenta above 2 GeV/c, as described in Section 4.3.4. Position measurements from the axial detection layers of the COT were used as input for the first-level trigger described in Section 4.3.3. The total material of the COT corresponded to 1.6 % of a radiation length at normal incidence. To allow the reconstruction of particle momenta, the COT and the silicon detectors were immersed in the field of a solenoid magnet that provided a homogenous magnetic field of 1.4 T with field lines parallel to the beam axis. In the central region of the detector, $|\eta| < 1$, a total of seven position measurements in the silicon sensors plus 96 measurements in the COT, distributed over a lever arm of about 130 cm, permitted to reconstruct the transverse momenta, p_T, of charged particles with relative precision $\sigma(p_\mathrm{T})/p_\mathrm{T} \approx 0.15\,\% \times p_\mathrm{T}\,[\mathrm{GeV}/c]$.

Charged particle tracking in D0 relied on the SMT described in the previous section and the Central Fibre Tracker (CFT). As illutrated in Figure 4.34, detection layers in the CFT were organized in eight concentric cylinders at radii from 20 cm to 52 cm, where each cylinder consisted of a pair of scintillating-fibre doublets. Fibres in the inner doublet of each pair were oriented parallel to the beam axis, those in the outer doublet were oriented at small stero

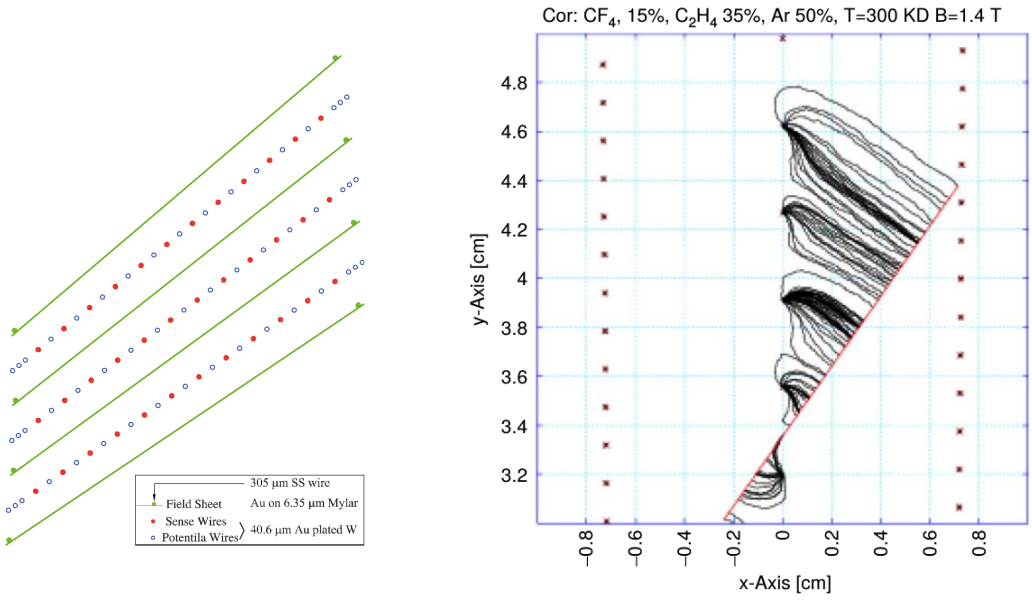

Figure 4.33: Central Outer Tracker in CDF II: (left) drift-cell geometry in one of the super-layers, where the twelve sense wires corresponding to the twelve detection layers are shown for three consecutive drift cells, as well as field forming wires and the thin cathode sheets that separate the drift cells; (right) simulation, performed using the Garfield/Magboltz [151] package, of electron drift lines for a high-p_T particle crossing the twelve detection layers in a super-layer (both from [152]).

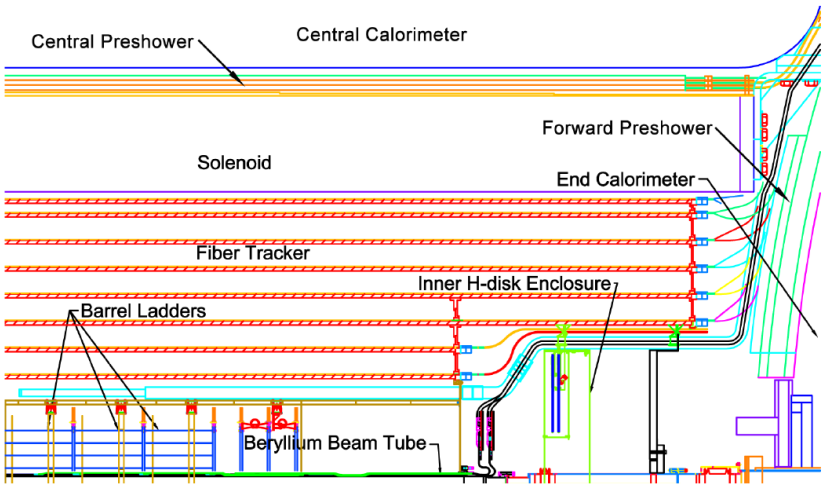

Figure 4.34: Longitudinal cross section of a quadrant of the D0 detector, illustrating the locations of the eight pairs of fibre doublets of the Central Fibre Tracker (from [153]).

angles of $\pm 3°$. The two fibre layers within a doublet were staggered by half a fibre diameter to provide full acceptance coverage. The fibres had a length of 166 cm in the innermost two cylinders and a length of 252 cm in the remaining cylinders. They were read out using Visible Light Photon Counters (VLPC), silicon-based photon detectors with high quantum efficiency in the visible range [154]. On average, ten photons could be detected for an ionizing particle crossing a fibre. The fibres had a diameter of 835 μm diameter, yielding a spatial resolution of about 100 μm per doublet. The SMT and the CFT were immersed in the 2 T field of a supra-conducting solenoid magnet.

4.3.3 Triggering

As discussed in Section 4.2, the large inelastic cross section in high-energy hadron collisions makes a selective and efficient trigger a crucial requirement for a successul b-physics programme at hadron colliders.

The CDF II trigger system consisted of three consecutive stages. The first level trigger received data at the Tevatron bunch crossing rate of 1.7×10^6 events per second, had a maximum latency of 5.5 μs and a maximum allowed output rate of 30 kHz. The second-level trigger had a typical execution time of $20 - 30$ μs and a maximum output rate of 1 kHz. The third-level trigger ran on a large CPU farm and performed a full event reconstruction using a speed-optimized version of the offline reconstruction code. The output rate of the third-level trigger was 100 Hz, at which events were saved for offline reconstruction.

A good overview of the level-1 and level-2 trigger algorithms that were of relevance for b-hadron physics is given in Ref. [155]. The cornerstone of the level-1 trigger decision was the "eXtremely Fast Tracker" (XFT) algorithm [156]. The XFT was implemented on programmable logic devices (PLD) and used hit information from the COT to reconstruct the two-dimensional trajectories in the r–ϕ plane of all particles with $p_{\mathrm{T}} > 1.5$ GeV/c. As described above, the detection layers in the COT were organized into eight so-called super-layers. Four of these super-layers had axial wires, oriented parallel to the beam axis, while the wires in the other four super-layers were oriented at a small stereo angle. The four super-layers with axial wires were used in the XFT. The first step of the algorithm was implemented in so-called "finder" chips. Each finder chip received the data from a fixed group of wires in one super-layer and compared the observed hit information with a stored set of valid patterns that could have been caused by a particle with $p_{\mathrm{T}} > 1.5$ GeV/c. The sets of valid patterns for each superlayer had been generated based on samples of simulated events. Each finder chip

forwarded a complete list of all matching patterns to one of 288 so-called "linker" chips. Each of these linker chips covered a 1.25° wide slice in the azimuthal angle ϕ. It compared the data it received from the finder chips from the four super-layers to sets of pre-defined patterns, selected the best matching pattern and returned the stored track coordinates corresponding to this pattern. The complete algorithm took no more than 1.9 μs and had an efficiency of 96% for finding tracks with $p_{\mathrm{T}} > 1.5$ GeV/c. The obtained resolution in p_{T} and ϕ was about a factor of ten worse than that of the full offline track reconstruction algorithm. The obtained track parameters were extrapolated to the electromagnetic calorimeter and the muon detectors and matched with measurements in these detectors to identify electron and muon candidates. The Level-1 trigger decision depended on the numbers of track candidates found above certain p_{T} thresholds and the associated particle types. Typical requirements were for example two track candidates with $p_{\mathrm{T}} > 2.5$ GeV/c or a single muon candidate with $p_{\mathrm{T}} > 4$ GeV/c.

The second-level Silicon Vertex Trigger (SVT) algorithm [157] was implemented on Associated Memory (AM) chips and Field-Programmable Gate Array (FPGA) chips. It used as input the list of track parameters returned by the XFT and the raw digitized data from the axial readout strips in the SVX-II. A cluster search was performed in the SVX-II data and for each found cluster its position in ϕ was calculated. This was followed by a pattern recognition to link the SVX-II clusters with the XFT track candidates, and finally a two-dimensional track fit to determine the relevant track parameters in the r–ϕ plane. The pattern recognition step was performed in parallel in twelve slices in ϕ, corresponding to the twelve-fold azimuthal symmetry of the SVX-II detector layout as shown in Figure 4.29. The XFT track parameters and the cluster positions in four selected layers in the SVX-II were compared to a set of pre-defined valid patterns to identify track candidates. The initial AM chips used for this pattern matching allowed to store 32'000 patterns each. The sets of patterns for each chip were defined based on samples of simulated events and provided a 95 % coverage for tracks with $p_{\mathrm{T}} > 2$ GeV/c. An impact-parameter resolution of 50 μm in the r–ϕ plane could be achieved, including a contribution of about 30 μm due to the finite size of the beam spot. As the instantaneous luminosity provided by the Tevatron gradually increased during run II, leading to busier and more complex events, a larger number of patterns was needed to provide finer granularity of the pattern matching, reduce the number of track candidates, and maintain the speed of the subsequent fitting algorithm. Therefore, the SVT was upgraded in 2007 with more powerful AM chips that allowed to store 512'000 patterns each. The track fit used six measurements, namely the four position measurements in the SVX-II and the position and curvature of the XFT track, to determine three track parameters at the point of closest approach to the $p\overline{p}$ interaction region — the p_{T} of the track, its azimuthal angle and its transverse impact parameter. The χ^2 of the fit was also calculated and was employed to remove poorly matched track candidates. The fitting algorithm was implemented on the FPGA chips and used linear approximations to calculate the constraints and estimate the track parameters. The overall execution time of the complete SVT algorithm was around 20 μs, depending on the complexity of the event, the algorithm had an efficiency of 90 % for tracks with hits in four layers of the SVX-II and gave a transverse impact parameter resolution close to that of the offline tracking algorithm if information from L00 was ignored. Data from L00 could not be used in the SVT.

Typical triggers used to collect samples of b-hadron decays were a "dimuon trigger" requiring two muon candidates with $p_{\mathrm{T}} > 1.5$ GeV/c to collect decays involving a J/ψ meson, a "displaced track + muon" trigger requiring one SVT track with significant transverse impact parameter and a muon candidate with $p_{\mathrm{T}} > 4$ GeV/c to collect samples of semi-leptonic decays, or a "two-track trigger" requiring two displaced tracks with $p_{\mathrm{T}} > 2$ GeV/c to collect samples of two-body charmless B-meson decays or samples of $B_s^0 \to D_s^- \pi^+$ decays for the measurement of the $B_s^0 - \overline{B}_s^0$ oscillation frequency. The importance of this trigger can be illustrated by a comparison of event yields: in run I, without SVT, no significant $B_s^0 \to D_s^- \pi^+$ signal could be found in a data set corresponding to an integrated luminosity of 0.1 fb^{-1}; in run II, using the SVT, a sample of 2000 $B_s^0 \to D_s^- \pi^+$ candidates was collected in an only ten times larger data

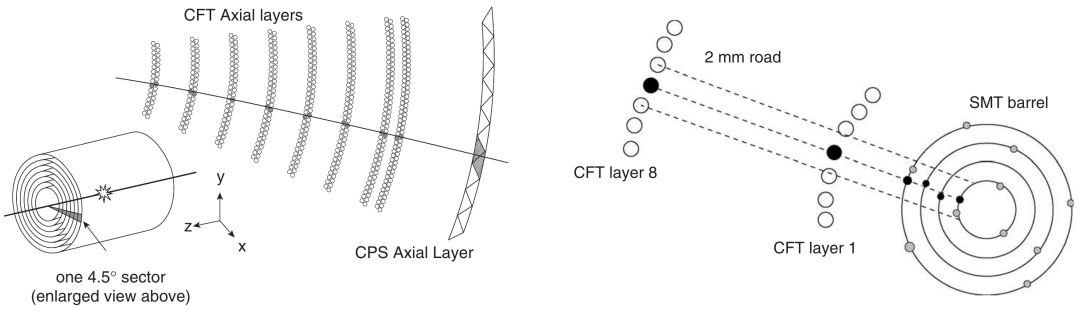

Figure 4.35: Pictorial illustrations of (left) the CTT and (right) the STT algorithm in D0 (from [140]).

set.

A brief overview of the D0 triggers and their use in the b-physics programme is given in Ref. [158]. The special strength of the D0 detector was its excellent muon identification system and this was reflected in the physics programme and the triggers it was based on. The D0 trigger system consisted of three consecutive stages. The first-level trigger was implemented in hardware, operated at the Tevatron bunch crossing rate of 1.7×10^6 per second, had a maximum latency of 3.5 μs and a maximum output rate of 2 kHz. It was based on energy measurements in the calorimeter and matching pre-coded patterns in the scintillating fibre tracker, pre-shower and muon detectors. The second-level trigger ran on custom-made pre-processor elements, had a typical processing time of 100 μs and a maximum output rate of 1 kHz. It refined the first level trigger decisions, for example by making use of the timing information of hits in the muon detectors. A Silicon Track Trigger algorithm using information from the silicon tracker to calculate transverse impact parameters was added to the second-level trigger in 2004. The third-level trigger ran on a farm of commercial processors and performed a simplified event reconstruction. The output rate of the third-level trigger was $50 - 100$ Hz, at which events were saved for offline reconstruction.

A main component of the first-level trigger was the Central Track Trigger (CTT). The primary goal of the CTT was to reconstruct the two-dimensional trajectories in the r–ϕ plane of particles with $p_{\rm T} > 1.5$ GeV/c and to return a list of the track candidates above a certain $p_{\rm T}$ threshold. It also allowed to link the track candidates to hits in the pre-shower detectors and to level-1 muon trigger objects to form high-$p_{\rm T}$ electron and muon candidates. The track reconstruction algorithm used hit information from the eight axial double layers of the CFT. The pattern recognition algorithm was implemented on FPGA chips and was executed in parallel in 80 sectors, each of which covered 4.5° in azimuthal angle ϕ. The data from a given ϕ sector were compared with a set of 20'000 pre-defined valid patterns. For each ϕ sector, a list of the up to six matched patterns with the highest associated values of $p_{\rm T}$ were returned. The algorithm was nearly 100% efficient for tracks with $p_{\rm T} > 1.5$ GeV/c that originated from within 1 mm of the nominal $p\overline{p}$ interaction point in the r–ϕ plane.

The Silicon Track Trigger (STT) was commissioned and added to the D0 second level trigger in 2004. The STT algorithm and its implementation are described in detail in Ref. [159]. The STT received all track candidates from the CTT and the raw data from the axial readout strips in the SMT barrel detectors. It performed a fast pattern recognition and a two-dimensional track fit in the r–ϕ plane to estimate transverse impact parameters. Data from different ϕ regions of the detector and from different events were processed in parallel in order to meet the time constraints of the second-level trigger. The pattern recognition step was executed on FPGA chips. A clustering algorithm was performed on the SMT raw data and the ϕ positions of the clusters were calculated. The track information received from the CTT was used to define a ±2 mm wide search road for each CTT candidate. All SMT clusters that fell into this road were associated to the track candidate, where the same cluster could be assigned

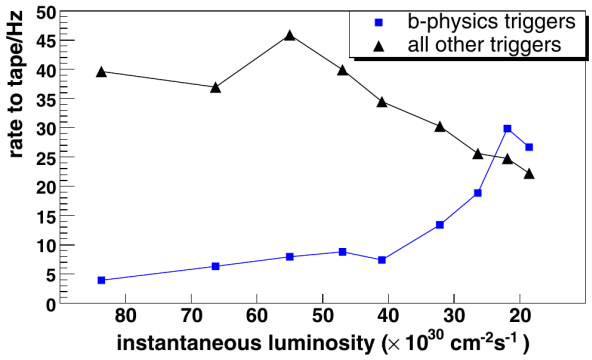

Figure 4.36: Rates of the events selected for offline analysis by b physics triggers and by non-b physics triggers as a function of the decaying instantaneous luminosity during a typical $p\overline{p}$ fill in the first years of run II (from [158]).

to several track candidates. The efficiency for assigning the correct cluster was found to be 98 % for particles with $p_{\mathrm{T}} > 1.5$ GeV/c and transverse impact parameter less than 2 mm. However, usually more one than one cluster per SMT layer was associated in this step to the same CTT track candidate. The remaining steps of the algorithm were executed on Digital Signal Processing (DSP) chips. First, a filtering was applied on the clusters assigned to a track candidate to select the best matching cluster in each SMT layer. Clusters outside a ± 1 mm road were discarded immediately; incompatible combinations of clusters were rejected by demanding that only clusters from the same SMT barrel detector or at most two adjacent barrels could be assigned to the same track candidate. Of the remaining clusters, that closest to the track candidate was selected. The positions of the selected clusters, together with the positions of the CTT track candidate at the innermost and outermost CFT layers were used to perform a χ^2 fit to a circular trajectory of the form $\phi(r) = d/r + kr + \phi_0$. The fit parameters were the transverse impact parameter d, the curvature k, and the azimuthal angle ϕ_0. As the fit function is linear in all three parameters, an analytical solution could be calculated using simple linear algebra. Approximate solutions were used to speed up the calculation and meet the limited computing resources of the FPGA chips. For example, a total of twelve million coefficient matrices for different possible hit configurations were stored in memory. The STT was successfully employed in the later part of run II to apply cuts on the transverse impact parameter of muon candidates. However, due to bandwidth limitations, it was not possible to use this trigger algorithm to form a pure displaced track trigger and collect samples of hadronic b decays.

All D0 triggers for b-hadron physics relied on muon signatures. Dimuon triggers, requiring two muon candidates above a certain p_{T} threshold, were usually based on information from the muon systems only, as these provided a significantly wider coverage in $|\eta|$ than the COT-based level-1 track trigger. Decay-time unbiased single muon triggers required a track-matched muon candidate, typically with $p_{\mathrm{T}} > 3 - 5$ GeV/c. Finally, decay-time biased single muon triggers demanded a track-matched muon candidate with significant transverse impact parameter with respect to the interaction region. As illustrated in Figure 4.36, the triggers for b-hadron physics were gradually activated during a Tevatron store, as the bandwidth required by high-p_{T} triggers decreased with decreasing beam currents and instantaneous luminosity.

4.3.4 Particle identification

As already discussed in the context of the B factories, the most challenging task in particle identification is to distinguish between charged kaons and pions. The challenge is even bigger in the environment of high-energy hadron collisions due to the large abundance of charged pions produced in the underlying event. As described in the next section, good kaon identifi-

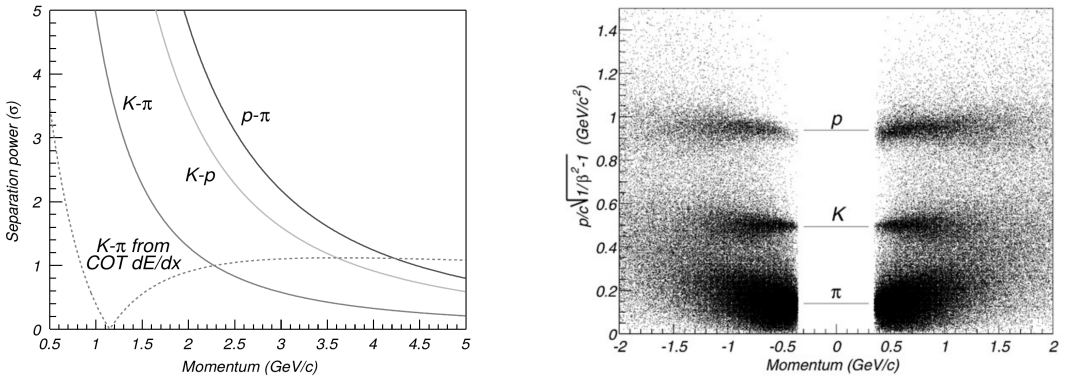

Figure 4.37: Illustration of the (left) expected and (right) measured performance of the time-of-flight detector in CDF II. The left panel shows the expected kaon/pion separation for a time-of-flight resolution of 100 ps, as a function of the particle momentum. The expected separation from $\mathrm{d}E/\mathrm{d}x$ measurements in the COT is shown for comparison. The right panel shows the distribution of the mass of the candidate as calculated from the measured time-of-flight versus the momentum measured from the curvature of its trajectory in the COT. The three horizontal lines correspond to the nominal masses of the proton and the charged kaon and pion (from [160]).

cation at the lower end of the momentum spectrum can contribute important input to flavour tagging algorithms. At higher momenta, good kaon/pion separation is for example important to separate the different final states in charmless two-body decays $B^0 \to \pi^+\pi^-$, $B^0 \to K^+\pi^-$, $B_s^0 \to K^-\pi^+$ and $B_s^0 \to K^+K^-$. Due to the relatively small mass difference between kaons and pions, it is not possible to distinguish between these decays using kinematic variables alone.

In CDF II, kaon identification relied on $\mathrm{d}E/\mathrm{d}x$ measurements in the COT drift chamber and on a time-of-flight (ToF) detector that was installed in between the outer wall of the COT and the cryostat of the supraconducting solenoid magnet, at a radial distance of about 138 cm from the beam axis. The ToF consisted of 216 scintillator bars of 4×4 cm^2 in cross section and 279 cm in length. Each bar was read out at both ends by photo-multiplier tubes operating in the 1.4 T field of the CDF II solenoid magnet. To correct for signal-height dependent time-walk in the readout electronics, not only the arrival time of the signal but also its signal height were recorded. An average time-of-flight resolution of 110 ps could be achieved, close to the initial design goal of 100 ps. The left panel in Figure 4.37 shows the expected kaon/pion separation for a time-of-flight resolution of 100 ps with Gaussian distributed uncertainties. With these assumptions, a two standard deviation separation between charged kaons and pions can be achieved for momenta up to 1.6 GeV/c. The momentum p, the path length L, and the time of flight, t, of a particle are related to its mass m as

$$m \;=\; \frac{p}{c} \cdot \sqrt{\left(\frac{c\,t}{L}\right)^2 - 1}\;\;.$$

A distribution of m calculated using measurements of t in the ToF and of p and L in the COT, is shown as a function of p in Figure 4.37. Three bands corresponding to signals from pions, kaons and protons are clearly visible at low momenta. As expected, the kaon and pion bands merge at momenta above 1.5 GeV/c. A limiting factor for the ToF was its relatively coarse granularity. As the instantaneous luminosities delivered by the Tevatron increased during the course of run II, the per-track efficiency decreased by up to 60% due to too high occupancies.

As described in the previous section, the COT provided up to 96 independent $\mathrm{d}E/\mathrm{d}x$ measurements for a particle traversing the full detector. The observed energy deposit, $\mathrm{d}E/\mathrm{d}x_{\mathrm{obs}}$, for a given track candidate was calculated as the 80% truncated mean of the associated $\mathrm{d}E/\mathrm{d}x$ measurements. The highest 20% of all measurements were discarded, as usual, to reduce the effect of large energy deposits from the upper tail of the Landau distribution. The most probable energy losses expected for the pion and kaon mass hypotheses, $\mathrm{d}E/\mathrm{d}x_{\pi}$ and

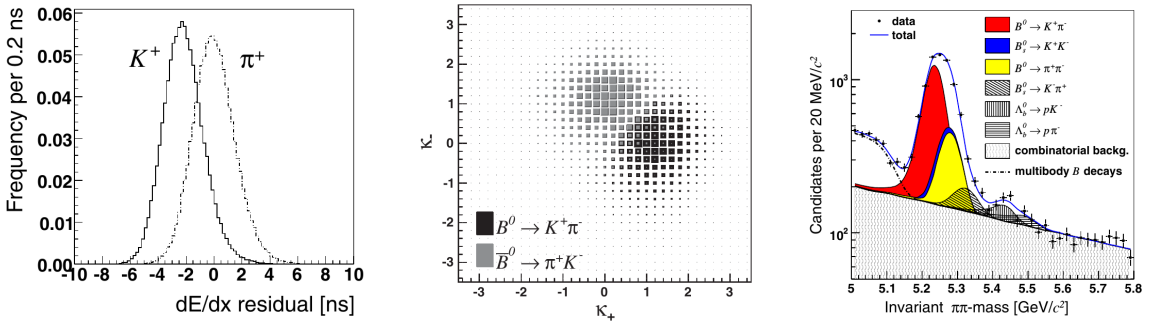

Figure 4.38: Illustration of kaon/pion separation in CDF II by means of $\mathrm{d}E/\mathrm{d}x$ measurements in the COT: (left, from [161]) distribution of the difference between the measured and the expected most probable value of $\mathrm{d}E/\mathrm{d}x$ for a pion with momentum corresponding to the measured curvature of the track; the $\mathrm{d}E/\mathrm{d}x$ is expressed here in units of time since the pulse height in a drift cell of the COT is measured by the length (time above threshold) of the signal pulse; (middle, from [162]) distribution of the measured kaonness κ as defined in the main text for the positive and the negative particle in samples of $B^0 \to K^+\pi^-$ and $\overline{B}^0 \to K^-\pi^+$ candidates; (right, from [162]) distribution of the invariant-mass, calculated assuming the pion mass for both final state particles, from a sample of charmless two-body b hadron decays. The individual contributions from the overlapping final states were estimated using kinematic variables as well as kaon/pion identification criteria and are indicated by different shadings as described in the legend of the plot.

$\mathrm{d}E/\mathrm{d}x_K$, were estimated using the momentum measured from the curvature of the track and a parametrization of the Bethe-Bloch equation, with parameters that were determined from control samples in collision data. The "kaonness" of the candidate was then defined as

$$\kappa \;\equiv\; \frac{\mathrm{d}E/\mathrm{d}x_{\mathrm{obs}} \;-\; \mathrm{d}E/\mathrm{d}x_{\pi}}{\mathrm{d}E/\mathrm{d}x_{K} \;-\; \mathrm{d}E/\mathrm{d}x_{\pi}} \;.$$

The performance of the particle identification based on the $\mathrm{d}E/\mathrm{d}x$ measurements was calibrated on collision data, using high-purity samples of kaons and pions from 1.5×10^6 decays $D^{*+} \to D^0\pi^+_{\mathrm{sl}}$ with $D^0 \to K^-\pi^+$ and $D^{*-} \to \overline{D}^0\pi^-_{\mathrm{sl}}$ with $\overline{D}^0 \to K^+\pi^-$. The charge of the low-momentum pion, $\pi^{\pm}_{\mathrm{sl}}$, provides a clear signature allowing to select high-purity samples of such decays and the sign of its charge unambiguously identifies the pion and the kaon from the subsequent D^0 and $\overline{D}^0$ decay.

Finally, the particle-identification information from time-of-flight and $\mathrm{d}E/\mathrm{d}x$ measurements was combined into a log-likelihood variable

$$\mathrm{CLL}(K) \;\equiv\; \log\left(\frac{P_{\mathrm{ToF}}(K)\cdot P_{\mathrm{d}E/\mathrm{d}x}(K)}{f_p\cdot P_{\mathrm{ToF}}(p)\cdot P_{\mathrm{d}E/\mathrm{d}x}(p) \;+\; f_\pi\cdot P_{\mathrm{ToF}}(\pi)\cdot P_{\mathrm{d}E/\mathrm{d}x}(\pi)}\right) \;,$$

where $P_{\mathrm{ToF}}(K,\pi,p)$ and $P_{\mathrm{d}E/\mathrm{d}x}(K,\pi,p)$ are the individual probability density distributions obtained from the respective time-of-flight and $\mathrm{d}E/\mathrm{d}x$ calibrations and the factors $f_p = 0.1$ and $f_\pi = 0.9$ are a-priori probabilities reflecting the average particle composition in events at CDF II. Using this combined log-likelihood, kaon/pion separation with a significance corresponding to 1.5 Gaussian standard deviations was obtained for momenta up to 5 GeV/c.

As mentioned before, the D0 detector provided no means of separating kaons and pions and the b physics programme in D0 concentrated on final states with muons. Flavour-tagging algorithms had to rely on lepton tags and jet charge tags as described in the following section.

4.3.5 Flavour tagging

As discussed in Section 4.2, two classes of algorithms can be employed at hadron colliders to infer the initial flavour of a reconstructed neutral or strange B meson candidate, B_{rec}:

opposite-side tagging algorithms seek to exploit flavour-specific signatures from the decay of the second b hadron in the event, $b_{\rm tag}$, while same-side tagging algorithms search for a charged kaon or pion that was produced in the hadronization process leading to the creation of $B_{\rm rec}$ and is therefore close to $B_{\rm rec}$ in phase-space.

Opposite-side tagging algorithms in CDF II and D0 search for a muon or electron from semi-leptonic decays of the $b_{\rm tag}$ hadron, or calculate the inclusive charge of a displaced vertex or a jet of particles from the hadronization and decay of $b_{\rm tag}$. A same-side kaon tagging algorithm was in addition employed in CDF II for studies in the $B_s^0\overline{B}_s^0$ system. The algorithms were refined over the years, for example by introducing multi-variate techniques, to improve their performance and achieve higher tagging power. In the following, the latest measurements of the $B_s^0-\overline{B}_s^0$ mixing phase ϕ_s in $B_s^0 \to J/\psi\phi$ decays by CDF II [163, 164] and D0 [165] will be used as examples to illustrate the approaches to flavour tagging in the two experiments. Measurements of ϕ_s will be discussed in Section 6.1.

The opposite-side lepton tagging algorithm in CDF II employed a multi-variate technique to select the best tagging candidate amongst all reconstructed tracks outside a cone around $B_{\rm rec}$. Input variables were muon or electron identification criteria and, if the lepton was found inside a jet of particles, its transverse momentum relative to the axis of this jet. In the case of electron candidates, their signed impact parameter, defined as the impact parameter of the reconstructed track with respect to the $p\overline{p}$ interaction point multiplied by the sign of the charge of the candidate, was used as an additional variable to discriminate against photon conversions in the material of the beam pipe or the vertex detector. Electrons and positrons from photon conversions are produced with zero opening angle with respect to the photon direction, leading to a signed impact parameter that is always positive, while electrons or positrons from B-meson decays can have positive or negative impact parameters with similar probability. Opposite-side jet charge algorithms exploit the observation of a correlation [166] between the flavour of a b or $\overline{b}$ quark and the charge signs of the particles that are produced close to it in phase space. This correlation is due to the charges of additional particles created in the hadronization process of the b or $\overline{b}$ quark as well as the decay products of the created b or $\overline{b}$ hadron. Cone-clustering algorithms[2] were employed to combine reconstructed tracks into jets. Jets were selected for the tagging algorithm if they contained a displaced vertex or at least one track with large impact parameter with respect to the reconstructed $p\overline{p}$ interaction point. If no such jet was found in a given event, the jet with the highest overall $p_{\rm T}$ in the event was selected. To derive a tagging decision, the weighted sum

$$Q \;\equiv\; \sum \left\{ Q_i \cdot p_{{\rm T}i} \cdot (1+P_i) \right\} \Big/ \sum \left\{ p_{{\rm T}i} \cdot (1+P_i) \right\}$$

was then formed over the charges $Q_i = \pm 1$ assigned to all tracks in the selected jet, where $p_{{\rm T}i}$ is the transverse momentum assigned to the track, and P_i is the estimated probability of the track to belong to the jet. An artificial neural network was employed to combine the results of the three opposite-side tagging algorithms and derive a tagging decision as well as an event-by-event estimate of the reliability of the decision. The reliability of the decision was exprssed in terms of a predicted dilution factor $D \equiv 1-2\omega$, where ω is the estimated probability for the tagging decision to be wrong. The neural network was trained using samples of simulated events. To correct for possible differences between simulation and collision data, the dilution factor predicted by the algorithm was re-calibrated on collision data using a large sample of $B^\pm \to J/\psi K^\pm$ decays. These decays have a similar signature as the signal decays of interest and the charge of the final-state kaon unambiguously defines the true charge and flavour of the $B^\pm$ meson at production. The opposite-side flavour-tagging algorithm was applied to the reconstructed events and the events were binned in terms of the predicted dilution factor. The actual average dilution factor for each of the bins was then measured by comparing the

[2]For a review of jet-clustering algorithms, see e.g. Ref [167].

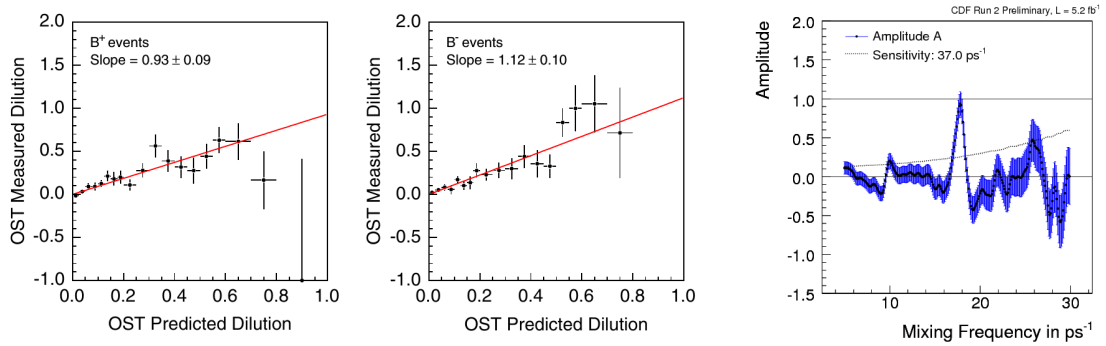

Figure 4.39: Illustration of the calibration of the flavour-tagging algorithms in CDF II: (left and middle) calibration of the predicted dilution factor of the opposite-side tagging algorithsm using self-tagging decays $B^{\pm} \to J/\psi K^{\pm}$; (right) calibration of the same-side kaon tagging algorithm fitting the amplitude of the $B_s^0 - \overline{B}_s^0$ oscillation in samples of $B_s^0 \to D_s^- \pi^+$ and $B_s^0 \to D_s^- \pi^+ \pi^+ \pi^-$ decays. For further explanations, see the main text (all three plots from [163]).

tagging decisions with the true charge of the reconstructed $B^{\pm}$ candidates. In the ideal case of a perfect initial calibration, the measured dilution factors should agree with those predicted, i.e. the relation between the two should be described by a straight line with slope one and offset zero. The actual results of the calibration are shown in Figure 4.39. The fit of a straight line yields slopes of 0.93 ± 0.09 for the sample of $B^+ \to J/\psi K^+$ decays and of 1.12 ± 0.10 for the sample of $B^- \to J/\psi K^-$ decays, both in good agreement with unity within their uncertainty. The central values of the fit results are employed in the physics analysis to scale the predicted dilution factors returned by the opposite-side tagging algorithm. Including this correction factor, an average dilution $D_{\mathrm{OST}} = 1 - 2\omega_{\mathrm{OST}} = (12.3 \pm 0.6)\,\%$ was measured. Combined with the tagging efficiency of $\epsilon_{\mathrm{OST}} = (92.8 \pm 0.1)\,\%$, the tagging power of the opposite-side tagging algorithm was found to be $\epsilon_{\mathrm{OST}} \cdot D_{\mathrm{OST}}^2 = (1.39 \pm 0.05)\,\%$.

The same-side kaon tagging algorithm was developed in CDF II using large samples of simulated $B_s^0 \to J/\psi\phi$ and $B_s^0 \to D_s^- \pi^+$ events. Time-of-flight and $\mathrm{d}E/\mathrm{d}x$ information was employed to identify kaon candidates within a cone around the B_{rec} candidate. Other parameters that were used to select the tagging candidate included a small impact parameter with respect to the $p\overline{p}$ interaction vertex and small transverse momentum relative to the B_{rec} flight direction. Ag ain, the tagging algorithm returns a tagging decision as well as an estimate of its reliablity. As the creation of the tagging kaon is related to the hadronization process leading to a B_s^0 or $\overline{B}_s^0$, the calibration of the algorithm on collision data had to be based on samples of B_s^0 and $\overline{B}_s^0$ decays. This was achieved by measuring the amplitude of the $B_s^0 - \overline{B}_s^0$ oscillation in samples of $B_s^0 \to D_s^- \pi^+$ and $B_s^0 \to D_s^- \pi^+ \pi^+ \pi^-$ decays. Measurements of the $B_s^0 - \overline{B}_s^0$ oscillation frequency in these decay modes are discussed in Section 5.1. Figure 4.39 shows the result of a fit for the amplitude A of the oscillation signal as a function of the assumed oscillation frequency. The fitted value of A should be compatible with zero everywhere except at the true value of the oscillation frequency, where it should be compatible with unity if dilution effects due to finite decay-time resolution and wrong flavour tags are correctly taken into account. The results of the fits show the expected behaviour, indicating a signal for $B_s^0 - \overline{B}_s^0$ oscillations. The fitted value of the amplitude in the maximum, $A = 0.94 \pm 0.15\,(\mathrm{stat}) \pm 0.13\,(\mathrm{syst})$, was in good agreement with unity within its uncertainty. The central value of this result was used in the physics analysis to scale the predicted dilution factors returned by the tagging algorithm by 1/0.94. Including this correction factor, the average dilution $D_{\mathrm{SSKT}} = (25.9 \pm 5.4)\,\%$ was measured. Combined with the measured tagging efficiency of $\epsilon_{\mathrm{SSKT}} = (52.2 \pm 0.7)\,\%$, this yielded a tagging power of $\epsilon_{\mathrm{SSKT}} \cdot D_{\mathrm{SSKT}}^2 = (3.5 \pm 1.4)\,\%$ for the same-side kaon tagging algorithm.

Flavour tagging in D0 relied on opposite-side lepton, vertex and event charge algorithms.

Opposite-side lepton tags searched for muon or electron candidates outside a cone around the reconstructed momentum vector of the $B_{\rm rec}$ candidate. Lepton candidates were selected applying the usual particle identification criteria. If a lepton candidate was found, the associated lepton jet charge

$$Q_\ell \equiv \frac{\sum (q_i \cdot p_{{\rm T}i})}{\sum p_{{\rm T}i}}$$

was calculated, summing over the lepton candidate itself and all tracks inside a cone around its reconstructed momentum vector, but excluding tracks that were used in the reconstruction of the $B_{\rm rec}$ candidate or fell inside a cone around the momentum direction of the $B_{\rm rec}$ candidate.

The secondary vertex charge algorithm searched for a displaced vertex amongst all tracks that were not used in the reconstruction of the $B_{\rm rec}$ candidate. The position of the vertex was required to be significantly displaced with respect to the reconstructed $p\overline{p}$ interaction vertex and at least two of the tracks assigned to the vertex had to have significant impact parameters in the r–ϕ plane. A momentum direction was then assigned to the vertex by calculating the vector sum of the measured momenta of all associated tracks. A minimum separation in azimuthal angle between this momentum direction and the direction of the momentum of the $B_{\rm rec}$ candidate was required. For vertices that fulfilled all these requirements, the secondary vertex charge was then calculated as

$$Q_{\rm SV} \equiv \frac{\sum (q_i \cdot p_{{\rm L}i})^{\,k}}{\sum (p_{{\rm L}i})^{\,k}}$$

where $p_{\rm L}$ are the longitudinal components of the track momenta with respect to the momentum direction of the vertex and the exponent $k = 0.6$ was determined empirically. Finally, the opposite-side event charge was defined as

$$Q_{\rm EV} \equiv \frac{\sum (q_i \cdot p_{{\rm T}i})}{\sum p_{{\rm T}i}} ,$$

summing over all reconstructed tracks with $0.5 < p_{\rm T} < 50$ GeV/c that were not used in the reconstruction of the $B_{\rm rec}$ candidate or fell within a cone around the reconstructed momentum vector of the $B_{\rm rec}$ candidate.

Distributions for each of the four tagging variables as measured in calibration samples of reconstructed $B^+ \to \overline{D}^0 \mu^+ \nu_\mu$ and $B^- \to D^0 \mu^- \overline{\nu}_\mu$ candidates are shown in Figure 4.40. These measurements were employed to define probability density functions $f_i(b \,|\, Q_i)$ for initial b quarks and $f_i(\overline{b} \,|\, Q_i)$ for initial $\overline{b}$ quarks. To construct a combined tagging response, the product of the likelihood-ratios

$$y \equiv \prod y_i \quad \text{with} \quad y_i \equiv \frac{f_i(\overline{b} \,|\, Q_i)}{f_i(b \,|\, Q_i)} \quad \text{and} \quad i \in (\mu, e, {\rm EV}, {\rm SV})$$

was calculated for the combination of Q_μ and $Q_{\rm SV}$ if a muon tag was found, for the combination of Q_e and $Q_{\rm SV}$ if an electron tag but no muon tag was found, and finally for the combination $Q_{\rm EV}$ and $Q_{\rm SV}$ if neither a muon nor an electron tag could be found in the event. Note that this method of combining the likelihood ratios implicitly assumes that the two combined tagging variables are uncorrelated. If no suitable secondary vertex was found, the corresponding likelihood ratio was set to $y_{\rm SV} = 1$, equivalent to equal probability for the b and $\overline{b}$ hypotheses. For mixing analyses it was found to be more convenient to express the tagging parameter as

$$d \equiv \frac{(1 - y)}{(1 + y)}$$

with $-1 < d < 1$. Values of $d > 0$ tag an initial b-quark and values of $d < 0$ tag an initial $\overline{b}$-quark. Larger values of $|d|$ indicate a higher reliability of the tagging decision. Considering only tags with $|d| > 0.3$ as valid, the tagging efficiency and power were found to be

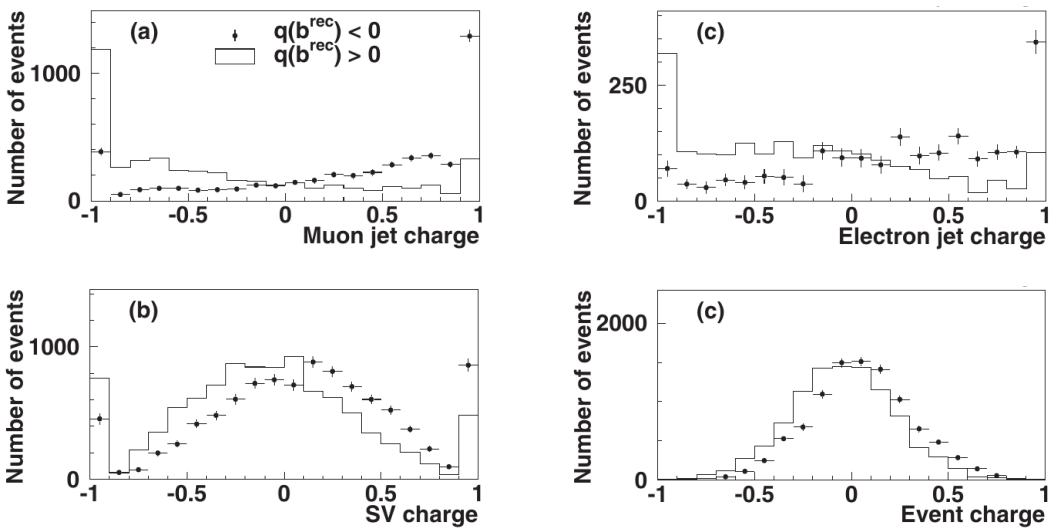

Figure 4.40: Distributions of the (top left) muon jet charge, (top right) electron jet charge, (bottom left) secondary vertex charge and (bottom right) opposite-side event charge as measured in D0 for calibration samples of $B^- \to D^0\mu^-\overline{\nu}_\mu$ candidates ("$q(b^{\rm rec}) < 0$") and $B^+ \to D^0\mu^+\nu_\mu$ candidates ("$q(b^{\rm rec}) > 0$") (all from [168]).

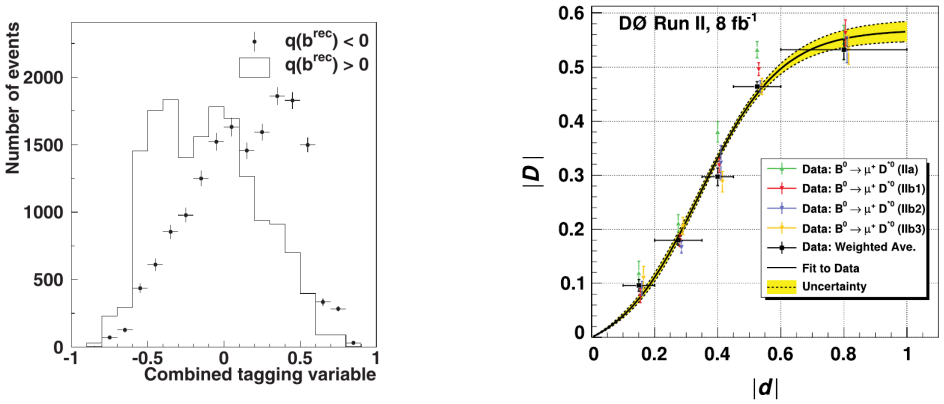

Figure 4.41: Combined flavour-tagging in D0: (left, from [168]) distributions of the combined tagging variable d as measured in calibration samples of $B^- \to D^0\mu^-\overline{\nu}_\mu$ candidates ("$q(b^{\rm rec}) < 0$") and $B^+ \to D^0\mu^+\nu_\mu$ candidates ("$q(b^{\rm rec}) > 0$"); (right, from [165]) average tagging dilution $|D|$ in bins of the tagging parameter $|d|$, as derived from the measurement of the $B^0-\overline{B}^0$ oscillation amplitude in semileptonic decays $B^0 \to D^{*\pm}\mu^\mp\nu_\mu$. In the panel on the right, different colours indicated measurements from different data-taking periods. The empirical fit function is described in the text.

$\epsilon = 19.95 \pm 0.21\%$ and $\epsilon D^2 = (2.48 \pm 0.21)\%$, respectively. A further calibration of the tagging parameter d on collision data was performed to derive an event-by-event tagging dilution $|D|$ for the measurement of the $B_s^0-\overline{B}_s^0$ mixing phase. This calibration was performed using a measurement of $B^0-\overline{B}^0$ oscillations in semileptonic decays $B^0 \to D^{*-}\mu^+\nu_\mu$ and $\overline{B}^0 \to D^{*+}\mu^-\overline{\nu}_\mu$. The amplitude of the oscillation signal and the corresponding average tagging dilution, $|D|$, were determined in five bins of the tagging parameter $|d|$ and the observed dependence of $|D|$ on $|d|$ was fit with an empirical function

$$|D| \;=\; \frac{p_0}{(1\,+\,\exp\left(p_1 - |d|\,/p_2\right))} \;-\; \frac{p_0}{(1\,+\,\exp\left(p_1 - p_1/p_2\right))}$$

This calibration was performed separately for four data taking periods corresponding to different detector configurations and instantaneous luminosities. The results, shown in Figure 4.41, are compatible with each other.

4.4 The LHC and LHCb

The possibility of installing a Large Hadron Collider, operating at beam energies of up to 10 TeV, inside the tunnel of the planned Large Electron-Positron collider (LEP) was first explored in a workshop organized by ECFA in Lausanne in 1984 [169], about one year before the excavation of the LEP tunnel actually started. One of the contributions to this workshop [170] already mentioned the possibility of exploiting the large $b\bar{b}$ production cross section at such a collider for precision measurements. It was also pointed out that a dedicated experiment would probably be needed to fully exploit this potential. At the second ECFA-LHC workshop, organized in Aachen in 1990, an entire working group was dedicated to the exploration of a possible B physics programme [171]. Three approaches were discussed: an external fixed-target experiment using an extracted proton beam, an internal fixed-target experiment using a gas jet target crossing one of the circulating proton beams, and a proton-proton collider experiment covering the forward acceptance. Each of these approaches had its specific advantages and disadvantages.

A major advantage of the collider approach is the much higher $b\bar{b}$ production cross section, both in absolute terms and relative to the total inelastic cross section. For a beam energy of 7 TeV, the centre-of-mass energy of the proton-proton interaction in a fixed target experiment is 118 GeV. The expected $b\bar{b}$ production cross section at this energy is 1 μb and only one in 40'000 inelastic collisions contains a $b\bar{b}$ quark pair. In collider mode, the centre of mass energy is 14 TeV, the expected $b\bar{b}$ cross section is 500 μb and a $b\bar{b}$ quark pair is produced in one of every 200 inelastic collisions.

A common advantage of fixed-target experiments is the large Lorentz boost of the collision frame, which results in average B meson flight distances of several centimeters, significantly longer than in a collider experiment. Longer decay lengths can present advantages for triggering, event reconstruction and measurements of decay-time dependent asymmetries. In an extracted beam experiment, it would be possible to place the vertex detector very close to the production target, making it conceivable to directly observe b decay vertices or the trajectories of charged B mesons inside the vertex detector. This could be particularly useful in studying decays such as $B^+ \to \tau\nu_\tau$. A technical challenge would have been the extraction of protons to generate an external beam without causing disturbance to the beams circulating in the LHC. It was proposed to achieve this by exploiting channeling in a bent crystal placed in the halo of the beams. A similar technique was later used successfully in the NA48 experiment to generate the secondary beam of protons directed to the K_S^0 target (see Section 2.11). However, there were concerns regarding the feasibility of such a scheme at the LHC. An advantage of an internal target would be the very small and well defined interaction region, providing precise a priori knowledge of the position of the $b\bar{b}$ production vertex. This could be exploited in efficient and robust trigger schemes making use of the impact parameter of charged particles from displaced B decay vertices. Internal gas jet targets had been employed at other accelerators and the possible disturbance of the LHC beams was expected to be negligible.

Three collaborations formed arond the three approaches and Letters of Intent were submitted to the CERN committees in 1993 for COBEX [172], a dedicated collider experiment for B physics at the LHC, Gajet [173], a fixed target experiment using an internal gas jet target, and LHB [174], a fixed target experiment at an extracted beam. Cross sections through the proposed detector layouts are shown in Figures 4.42, 4.43 and 4.44. All three detectors were forward spectrometers, equipped with a silicon micro-strip vertex detector very close to the interaction region, one or several large-aperture magnets with a tracking system, a RICH-based particle identification system providing $\pi/K/p$ separation over the full necessary momentum range, calorimeters and a muon system. The Letters of Intent were well received, but it was realized that the available resources would allow for only one experiment to be realized. The LHC experiments committee considered "that the collider mode experiment has the greater potential in view of the very high rate of b production, the much better signal/background ratio

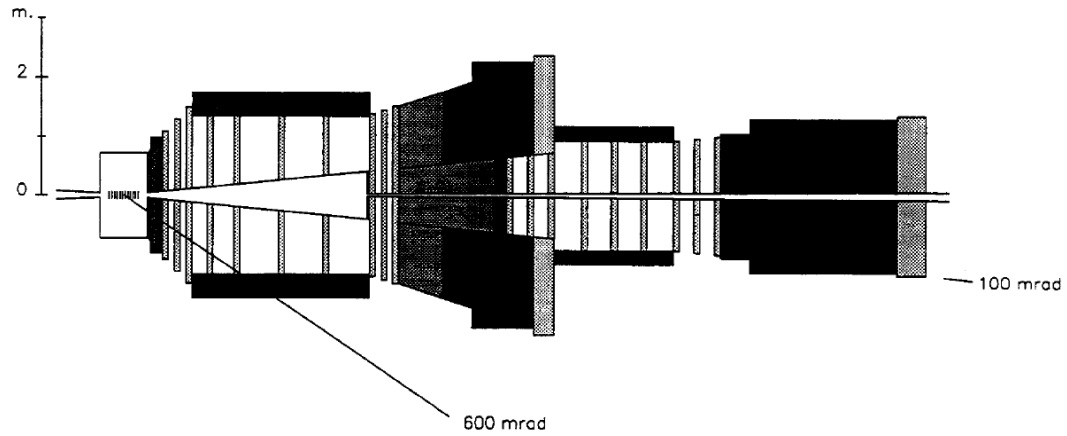

Figure 4.42: Longitudinal cross section of the proposed COBEX detector (from [172]).

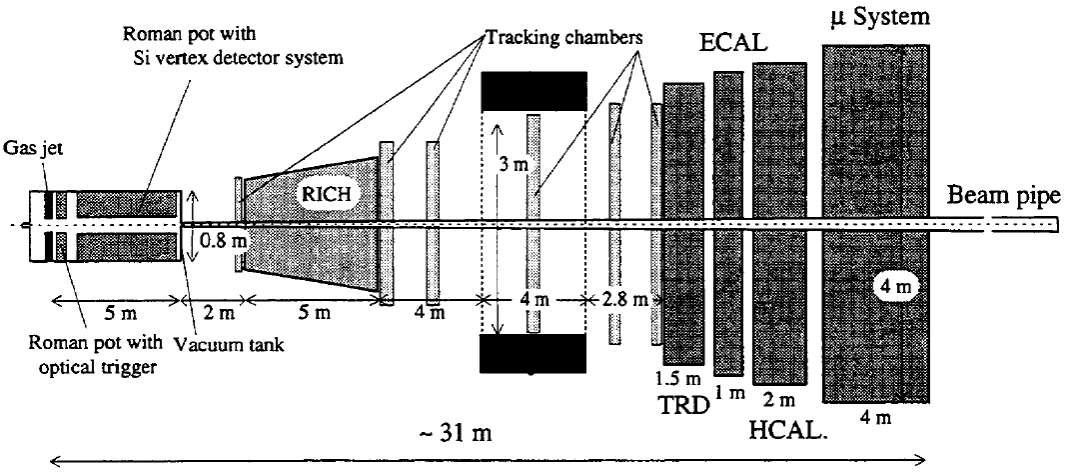

Figure 4.43: Longitudinal cross section of the proposed GAJET detector (from [173]).

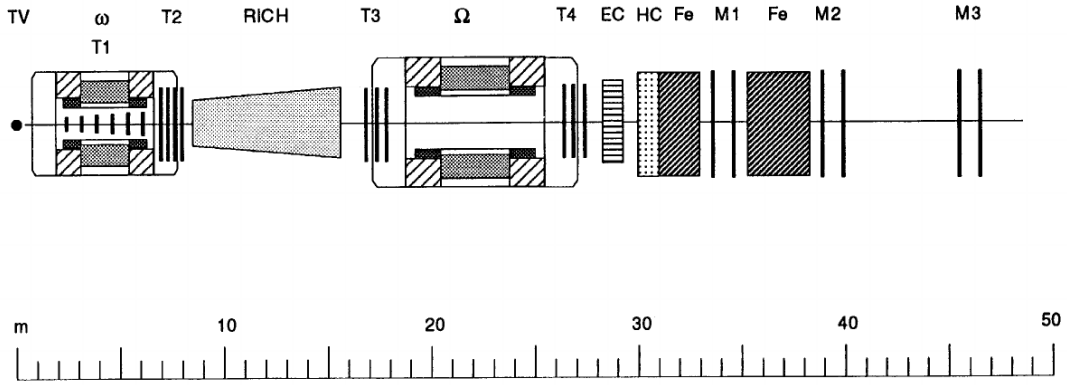

Figure 4.44: Longitudinal cross section of the proposed LHB detector (from [174]).

and the possibility of exploring other physics in the forward region at 14 TeV" and encouraged "all participants from the three proposals to join together to prepare a new letter of intent for a new collider mode b experiment" [175]. The Letter of Intent for the LHC-B experiment (spelled with a capital "B" at the time) was submitted and approved in 1995 [176], followed by a Technical Proposal [177] in 1998.

The layout of the proposed detector is shown in Figure 4.45. It consisted of a silicon-microstrip vertex detector (VELO), installed in a secondary vaccum inside the LHC vacuum vessel and consisting of 17 planar detector stations arranged along the beam axis; a superconducting dipole spectrometer magnet providing an integrated field of 4 Tm; eleven planar tracking stations using a hybrid GEM/MSGC technology in the region of high particle density close to the beam axis (Inner Tracker) and honeycomb drift chambers in the outer regions (Outer Tracker); two RICH detectors (RICH-1, RICH-2) with three radiators to provide efficient kaon/pion separation from $1 - 150$ GeV/c; a calorimeter system consisting of a Scintillating-Pad Detector (SPD), a pre-shower (PS), an electromagnetic calorimeter (ECAL) and a hadron calorimeter (HCAL); and a muon system (MUON 1-5). A four-level trigger was foreseen, making use of the generic features of b hadron decays, namely long lifetimes and high-p_{T} decay products. A so-called Level-0 trigger, operating at the LHC bunch crossing frequency of 40 MHz, was implemented in hardware and used partial information from the muon system and calorimeters to search for high-p_{T} muon, electron and hadron candidates. The maximum output rate of this Level-0 trigger was 1 MHz, at which the full detector was read out. A two-stage Level-1 trigger searched for displaced secondary vertices in a first stage and for high-p_{T} tracks confirming the Level-0 candidates in a second stage. A Level-2 trigger refined the vertex information from Level-1 by assigning momentum information to the tracks used in the reconstruction of the secondary vertices. Finally, a Level-3 trigger performed full and partial event reconstructions to select event samples for specific b hadron decay modes. The foreseen Level-3 accept rate was 200 Hz, at which data would be stored for offline analysis.

The experiment was designed to operate at an average instantaneous luminosity of 2×10^{32} cm^{-2}s^{-1} to maximize the number of LHC bunch crossings with a single proton-proton interaction. Events with multiple proton-proton interactions ("pile-up") were regarded as too difficult to reconstruct since the presence of several proton-proton interaction vertices could lead to ambiguities in the assignment of the b hadron decay vertex to the correct production vertex and therefore in the reconstruction of the b hadron decay length. Moreover, high particle multiplicities in the forward direction covered by the detector would make the reconstruction of events with multiple interactions time-consuming and inefficient. A fast vertex reconstruction algorithm based on information from two of the VELO stations was foreseen to actively suppress events with multiple proton-proton interactions already at the Level-0 trigger. Concurrent operation of LHCb with the two general-purpose experiments, ATLAS and CMS, running at much higher luminosities would be possible via appropriate tuning of the LHC beam parameters in the respective interaction points.

The detector layout and the trigger strategy underwent several revisions from the Technical Proposal to the experiment that was finally installed and operated successfully during run I of the LHC. For cost reasons and to avoid potential mechanical risks associated with the operation of superconducting coils, the spectrometer magnet was redesigned as a warm magnet providing the same field integral [180]. Following the observation of severe problems in the operation of MSGC/GEM detectors in the HERA-B experiment at DESY [181] and the decision by the CMS collaboration to abandon MSGC technology for the CMS tracking system [182], the design of the Inner Tracker was completely revised and a silicon micro-strip technology was adopted. The overall layout of the tracking system was significantly revised to reduce the material budget of the detector [183]. The tracking system described in the Technical Proposal had been designed for a Kalman-Filter based track reconstruction algorithm similar to that pioneered by the HERA-B experiment [184, 185]. The algorithm would start from track seeds in the four tracking stations downstream of the spectrometer magnet and identify track candidates

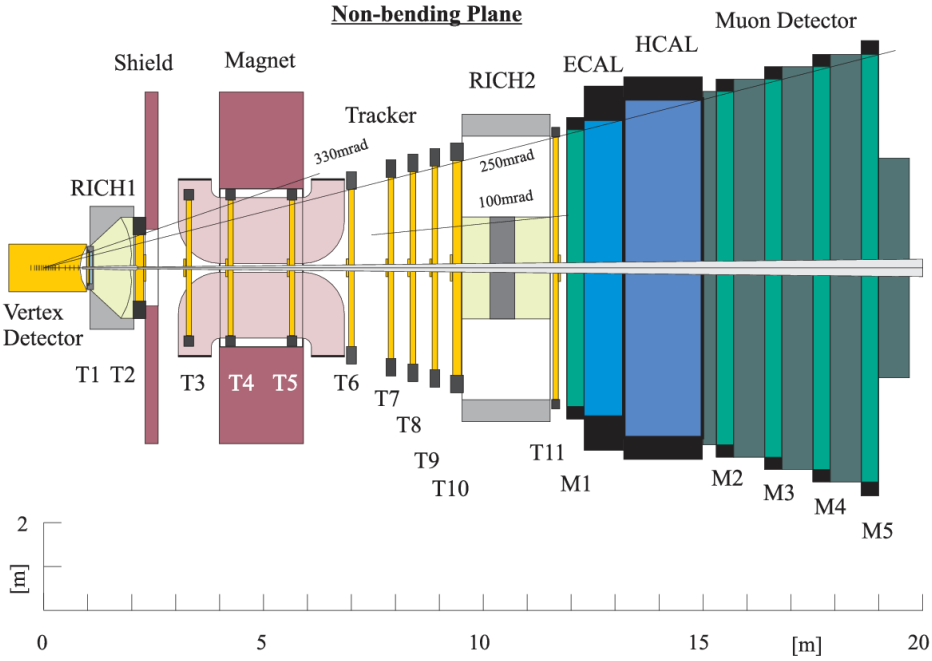

Figure 4.45: Longitudinal cross section of the LHC-B detector as foreseen in the Technical Proposal (from [177]).

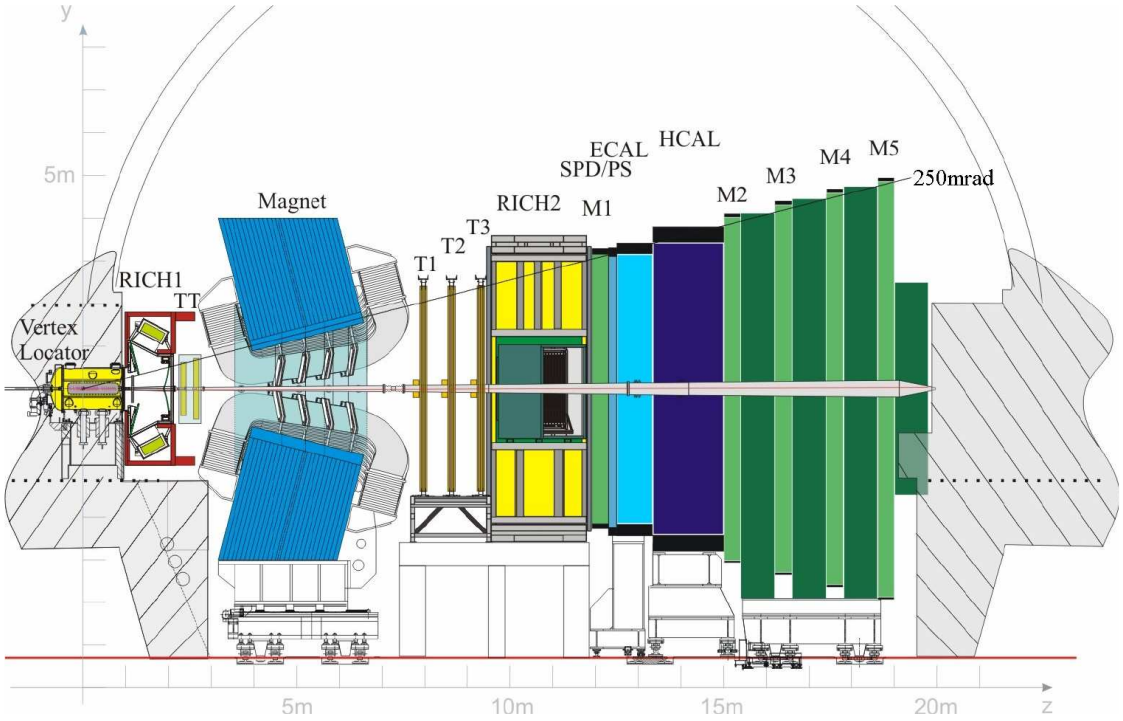

Figure 4.46: Cross section in the y–z plane of the LHCb detector. The envelop of the underground cavern at the LHC interaction point 8, in which the detector is installed, is indicated in light grey (from [178]).

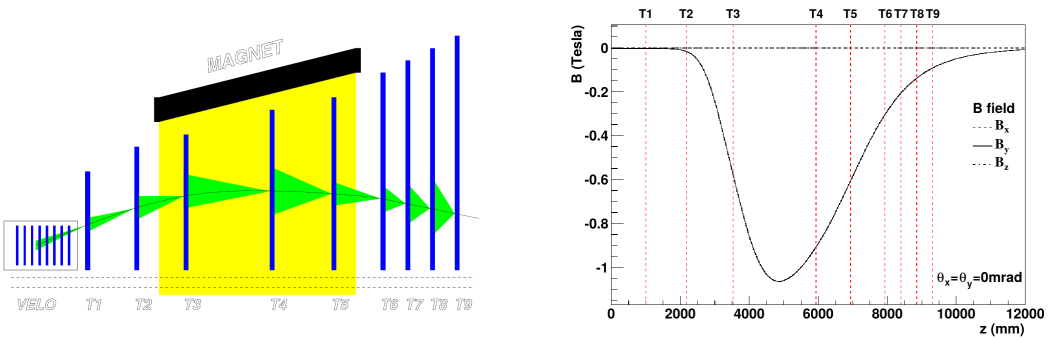

Figure 4.47: Motivation of the originally foreseen layout of the LHCb tracking system: (left) illustration of the iterative track finding algorithm on which the layout was based. Using hits in stations T9-T6, downstream of the spectrometer magnet and furthest from the *pp* interaction region, track parameters and their uncertainties are estimated assuming the track candidate to originate from the nominal *pp* interaction point. These track parameters are extrapolated to the nearest tracking station and a search window is defined based on the calculated impact point and its uncertainties. If a hit is found within this search window, it is added to the track candidate and the estimated track parameters and their uncertainties are updated accordingly. The updated track parameters are then used to define a search window in the next following tracking station and the procedure is repeated up till tracking station T1 closest to the interaction region. A Kalman-Filter approach was foreseen to be employed for the extrapolation and update steps, such that the final set of track parameters at station T1 corresponded to those obtained from a full track fit. (right) Strength of the magnetic field components seen by a particle travelling along the beam axis, together with the positions of the tracking stations. Tracking stations are densely spaced in the downstream region, where a track candidate consists of only a few hits, uncertainties on the track parameters are still large and extrapolation over long distances would lead to large search windows in the following station. They are less densely spaced in the region of highest magnetic field, where track parameters are estimated well enough to allow extrapolation over longer distances and where hit occupancies would be large due to low-momentum particles curling in the magnetic field and causing multiple hits in a single tracking station. Stations T1 and T2 sandwich RICH-1 and were envisaged to provide precise track parameter estimates for photon ring searches in the RICH detector (both from [179]).

by following them through the magnetic field towards the interaction region as illustrated in Figure 4.47. The number and positions of the tracking stations had been optimized to keep the search windows at each step of the algorithm reasonably small. The efficiency of this track finding algorithm for particles that originated from B-meson decays and traversed the full tracking system was well in excess of 90%. However, simulation studies demonstrated that a significant fraction of charged particles would be lost due to hadronic interactions in the material of the detector before they reached the tracking stations downstream of the magnet, as illustrated in Figure 4.48. The revised tracking system consisted of the VELO and only four tracking stations: one station (TT) in between RICH-1 and the dipole magnet and three stations (T1-T3) downstream of the magnet in front of RICH-2. The design of the VELO and RICH-1 were also improved to further reduce the material budget. After all modifications, the average amount of material traversed by a particle up to the entrance window of RICH-2 was estimated to correspond to 30% of a radiation length and 12% of a nuclear interaction length, about a factor of two smaller than the corresponding values estimated for the original design. Track reconstruction algorithms were developed that yielded efficiencies close to those estimated for the original layout. These algorithms will be briefly described in Section 4.4.2.

Another modification of the detector design was motivated by the realization that a Level-1 trigger algorithm based purely on the detection of displaced vertices in the VELO would not provide sufficient rejection power. The performance of the algorithm suffered due to a significant contamination from low-momentum particles that scatter in the material of the beam pipe and detector, leading to poorly reconstructed tracks with large impact parameters causing fake displaced vertices. It was shown that this limitation could be overcome by exploiting the

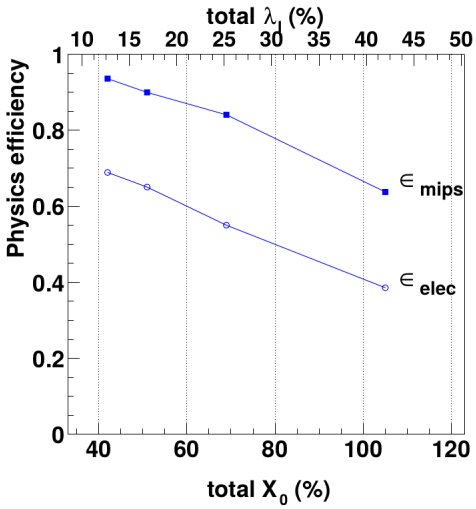

Figure 4.48: Estimated track reconstruction efficiencies including losses from interactions with the detector material for minimum ionizing particles (mips) and for electrons (elec) as a function of the assumed total amount of material of the LHCb spectrometer expressed in terms of radiation length, X_0, and nuclear interaction length, λ_I. The estimated material budget of the original LHCb tracking system corresponded to about 60% of a radiation length (from [179]).

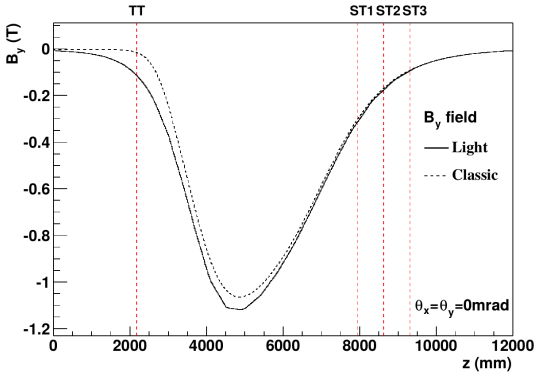

Figure 4.49: Magnitude of the vertical component of the magnetic field as seen by a particle travelling along the beam axis, together with the positions of the tracking stations in the revised layout of the LHCb tracking system. The two curves for the magnetic field strength correspond to the original layout of the RICH-1 magnetic shielding ("classic") and to the revised version ("light"), the latter leading to higher magnetic field in between the VELO and TT as needed for the Level-1 trigger algorithm described in the main text (from [179]).

stray field of the spectrometer magnet in between VELO and TT to assign a coarse momentum estimate to large-impact parameter tracks by using measurements from these two detectors alone [186]. The magnetic shielding of the RICH-1 photon detectors was re-designed to increase the strength of the stray field inside the active region between the VELO and the TT. The effect on the field strength is illustrated in Figure 4.49. In addition, to allow for a faster and more efficient track finding algorithm at the trigger level, the TT detector station was designed using silicon micro-strip detectors to cover the entire acceptance of the spectrometer. The trigger scheme itself underwent several revisions, also after the re-optimisation of the detector design. The trigger finally employed during LHC run I consisted of the Level-0 (L0) implemented in custom-made hardware and a two-stage "High-Level Trigger" (HLT) implemented in software and running on a large commercial CPU farm. The Level-1 algorithm for momentum measurements using VELO and TT, described in the previous paragraph, was in the end not implemented.

The final layout of the LHCb detector is illustrated in Figure 4.46, which also defines the LHCb coordinate system. LHCb uses a right-handed cartesian coordinate system with the z axis pointing along the beam axis from the nominal pp interaction point towards the detector and the y axis pointing vertically upwards, parallel to the field lines of the spectrometer magnet. Charged particles are therefore bent in the horizontal plane, i.e. the x–z plane. The polarity of the magnetic field is reversed every few weeks of operation in order to control and reduce possible systematic effects from left-right asymmetries in the detector performance. The LHCb detector is described in detail in Ref. [178]. In the following sections a brief description is given of those aspects of the experiment that distinguish it most from the general purpose detectors at the LHC: vertex and track reconstruction, triggering and kaon/pion identification.

4.4.1 Vertex reconstruction

As already discussed in the context of the B factories and the Tevatron experiments, excellent track impact parameter resolution is an important prerequisite for the efficient selection of b decay candidates. A precise reconstruction of the position of b decay vertices is required for all measurements of time-dependent asymmetries in the $B^0\overline{B}^0$ system and even more so in the rapidly oscillating $B_s^0\overline{B}_s^0$ system. Factors that limit the impact parameter and vertex resolution are the spatial resolution of the vertex detector, the extrapolation distance from the first measurement point to the interaction region and multiple scattering of particles in dead material between the production vertex and the first measurement point. In order to fully exploit the potential of the detector and obtain the best possible resolution, the vertex detector has to approach the interaction region as closely as possible with minimal amount of material in between the interaction region and the active detector elements.

These considerations led to a design of the VELO with silicon micro-strip detectors that are installed inside the LHC vacuum chamber, approach the beam axis to 8 mm with their active area and are separated from the pp interaction region only by a 300 μm thin corrugated aluminium foil. The VELO is organized in two halves that can be retracted horizontally from the beam axis to protect the sensors during beam injections. A photograph of one of these detector halves during its assembly is shown in Figure 4.50. Each half consists of 21 detector modules that are oriented perpendicular to the beam direction and arranged over a distance of about 100 cm along the beam axis as illustrated in Figure 4.51. The number of modules and their positions along the beam axis were chosen such that all particles produced within the approximately 5 cm long pp interaction region and under polar angles between 15 mrad and 300 mrad cross at least three modules. Each detector module consists of two half-disk shaped silicon sensors that are glued back to back onto a thin support frame. The sensors are 220 μm thin and have a small semi-circular cutout in the middle of the disk's diameter, which is where the beams pass through the detector. The geometry and strip layout of the sensors are illustrated in Figure 4.52. One of the two sensors on each module has concentric circular readout strips to measure the radial position, r, of particles, while the second sensor has almost radial readout strips to measure the azimuthal coordinate, ϕ. This geometry was chosen as it would allow for a fast two-dimensional vertex reconstruction in the $r-z$ plane, using information only from the r-measuring sensors. Such an algorithm was originally foreseen to be employed in the Level-1 trigger but was finally not implemented. The readout strip pitch varies across the surface of the sensors, decreasing from 100 μm at the outer rim of the sensors down to 40 μm for the innermost strips close to the beam axis. The performance of the VELO during physics data taking is described in Ref. [188]. As illustrated in Figure 4.53, the position resolution in the innermost region of the sensors has been measured to be as good as 4 μm. The figure also shows the track impact parameter resolution and vertex resolution measured in collision data.

Figure 4.50: Photograph of one half of the VELO detector during its assembly in the clean room [187].

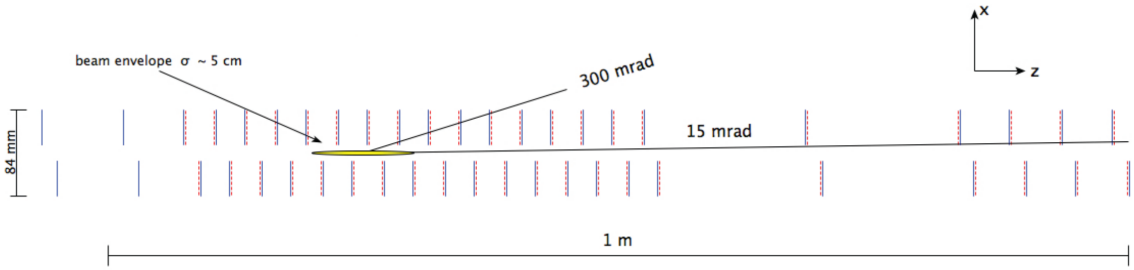

Figure 4.51: Arrangement of VELO modules along the beam axis. The pp interaction region and the polar angles defining the nominal acceptance of the LHCb spectrometer are indicated. Modules in the two halves of the detector are slightly offset along z to allow a small overlap in x when the detector is closed for data taking (from [188]).

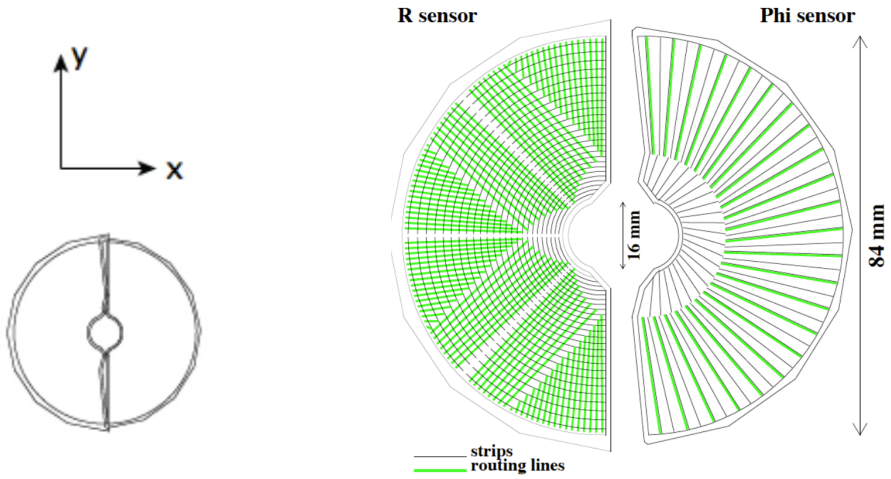

Figure 4.52: Layout of the silicon sensors of the VELO: (left) illustration of the overlap between the two halves in data taking position and (right) strip layout on the r- and ϕ-sensors, where black lines indicate the readout strips and Green lines indicate routing strips that are implemented in a second aluminium layer and serve to electrically connect the readout strips to the front-end electronics located close to the outer rim of the sensors (from [188]).

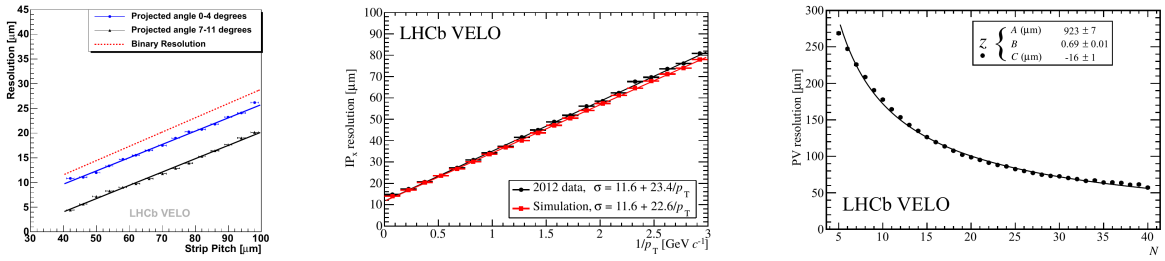

Figure 4.53: Illustration of the reconstruction precision achieved by the LHCb VELO: (left) spatial resolution as a function of readout strip pitch measured in collision data for different angles of incidence of the particles, (middle) impact parameter resolution in the x–z plane as a function of $1/p_{\mathrm{T}}$ in simulation and collision data and (right) vertex resolution in the z direction as a function of the number of tracks used in the determination of the vertex as measured in collision data. The impact parameter resolution is inversely proportional to the transverse momentum, due to the effects of multiple scattering in the material of the thin aluminium foil separating the detectors from the interaction region (all from [188]).

4.4.2 Tracking of charged particles

As mentioned in the introductory paragraphs to this section, the reconstruction of charged particle trajectories relies in LHCb on the VELO and the TT station in front of the spectrometer magnet and three tracking stations, T1–T3 downstream of the magnet. The TT is a large silicon micro-strip detector while two detector technologies are employed to cover the acceptance of the spectrometer in T1–T3: the region of highest particle density, close to the beam pipe, is covered here by a silicon micro-strip detector, the Inner Tracker (IT), while the remainder of each station is covered by a straw drift-tube detector, the Outer Tracker (OT).

The TT[3] consists of four planar detection layers with an active area covering about 140 cm in width and 130 cm in height. The layout is illustrated in Figure 4.54. Readout strips in the first and fourth detection layers are oriented parallel to the y axis to precisely measure track coordinates in the bending plane of the spectrometer magnet. The other two detection layers have readout strips rotated by stereo angles of $+5°$ and $-5°$, respectively, to provide information for pattern recognition along the y coordinate. For cost-saving reasons, the detector was designed to make use of silicon sensors that had been developed for the outer barrel of the CMS silicon tracker. The sensors have 10 cm long readout strips with a pitch of 183 μm, providing adequate position resolution of about 60 μm. As the density of charged particles falls rapidly with increasing polar angle in LHCb, several sensors were connected together in the outer regions of the detection planes to save on the number of readout channels. To minimize the amount of dead material, read-out electronics are located at the top and bottom ends of the detector modules, outside of the acceptance of the spectrometer. Up to 56 cm long interconnect cables made of straight copper lines on a thin Kapton substrate are employed to connect the readout electronics to the silicon sensors in the inner parts of the detector. After the Level-1 trigger was abolished, the main purpose of the TT is to improve the measurement of particle momenta by providing a precise position measurement at the entrance of the spectrometer magnet. For example, adding information from TT improves the invariant mass resolution for $J/\psi \to \mu^+\mu^-$ decays by about 20%. The TT also plays an important role in the reconstruction of K^0_S decays to two charged pions. A significant fraction of the K^0_S mesons decay outside of the acceptance of the VELO and the TT then provides the only measurements of the pion trajectories close to the K^0_S decay vertex and in front of the spectrometer magnet.

[3]The design of the TT was driven by its intended use in the Level-1 trigger [186]. For this reason, the detector was initially referred to as "Trigger Tracker", from which the abbreviation TT was derived. When the Level-1 trigger was abandoned and the TT no longer invoked in the trigger decision, the abbreviation was redefined to stand for "Tracker Turicensis" or "Zurich Tracker" for the fact that the detector had been designed and built at the Physik-Institut at Universität Zürich.

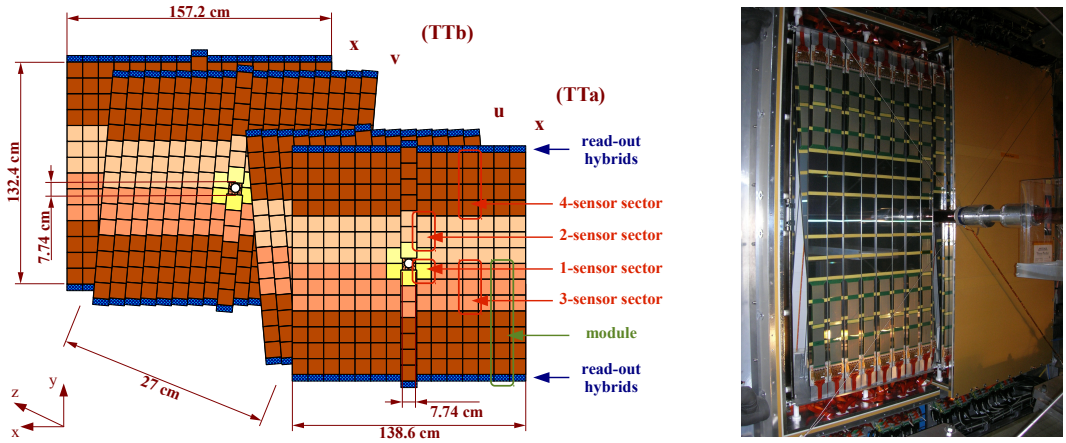

Figure 4.54: The TT detector in LHCb: (left) layout of the four detection layers and (right) photograph of the detector during its installation in LHCb. In the photograph, one half of the detector box is still open and the detector modules in one detection layer are visible. The LHC beam pipe can be seen passing through the center of the detector.

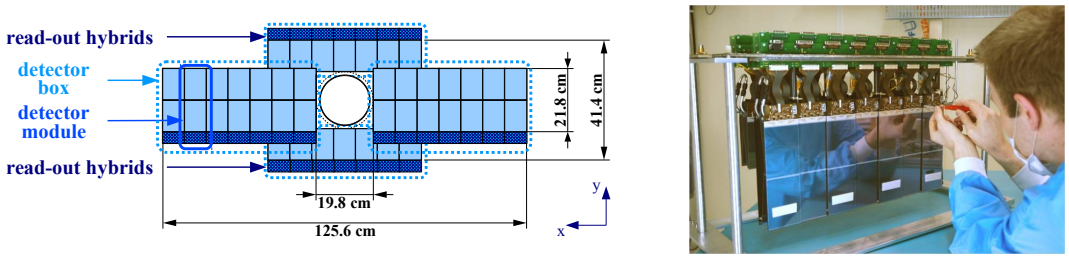

Figure 4.55: The IT detector in LHCb: (left) layout of one of the twelve detection layers and (right) photograph of one of the detector boxes during its assembly in the laboratory [189].

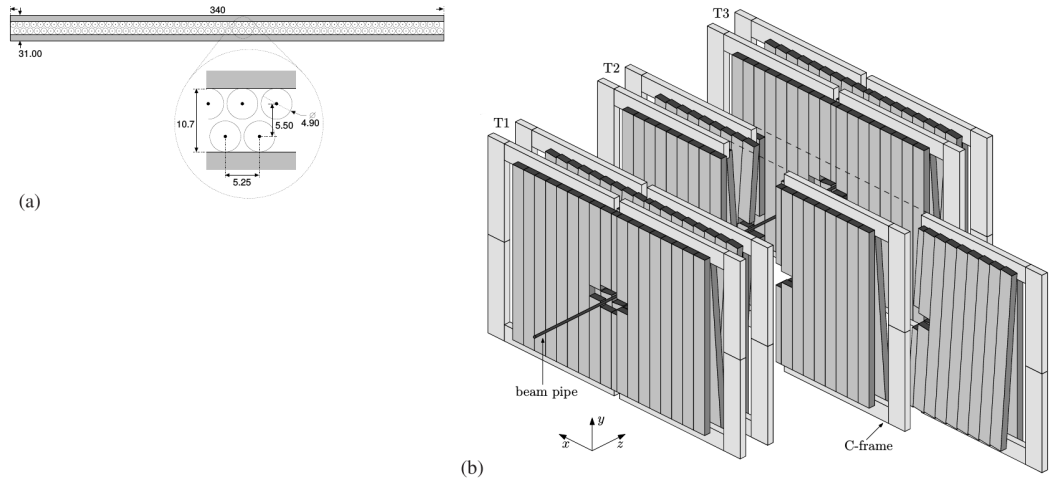

Figure 4.56: The OT detector in LHCb: (left) cross section of a detector module and (right) arrangement of the detection layers and stations, where two of the detection layers are shown in maintenance position, retracted from the beam pipe (from [190]).

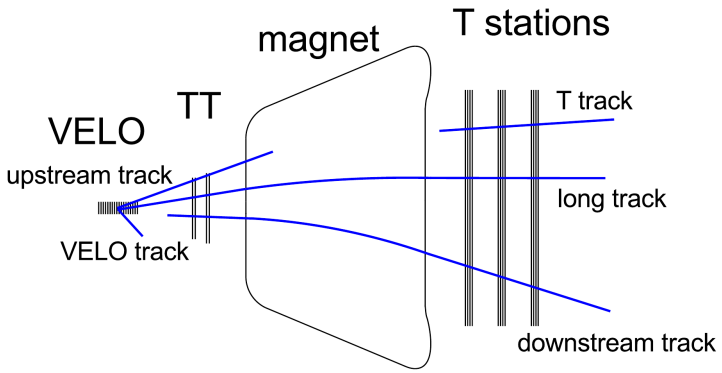

Figure 4.57: Illustration of track categories in LHCb(from [191]).

Each of the three IT and OT stations consists of four detection layers with the same arrangement of readout strips and wires, as in the TT: readout strips and wires are arranged parallel to the y axis in the first and last detection layers and at stereo angles of $\pm 5^\circ$ in the second and third layers. The IT is made of silicon micro-strip sensors with a readout strip pitch of 197 μm and a strip length of 11 cm and covers a cross-shaped area of about 40 cm in height and 120 cm in width. The Outer Tracker covers an area of about 5 m in height and 6 m in width, with a cross-shaped central hole that is covered by the IT. The OT detector modules consist of two staggered layers of straw drift tubes that have a diameter of 10 mm and are filled with an Ar/CO_2 gas mixture. The measured spatial hit resolution, including possible contributions from residual mis-alignment of detector modules, is about 60 μm in the IT and better than 200 μm in the OT.

An ensemble of pattern recognition algorithms has been developed that permits for efficient track reconstruction despite the small number of tracking stations. The relevant track categories are illustrated in Figure 4.57:

- "Long" tracks cross the entire spectrometer, creating hits in the VELO and T1–T3. These are the most useful tracks for the reconstruction of final-state particles for most decays of interest.

- Downstream tracks create hits only in TT and the T1–T3. These tracks can be due to the decays of K^0_S mesons or Λ baryons that decay outside the VELO. They are also used in searches for so far unknown long-lived exotic particles.

- Upstream tracks leave hits in the VELO and the TT, but are then bent out of the acceptance of the spectrometer in the field of the spectrometer magnet. Although only a coarse momentum measurement is possible for these tracks, they can be useful for flavour tagging purposes or to tag low-momentum pions from decays $D^{*\pm} \to D^0\pi^\pm$.

- VELO tracks are stubs reconstructed only in the VELO. They can be useful in the reconstruction of primary proton-proton interaction vertices. In particular, VELO tracks at large polar angles, outside the acceptance of the spectrometer, can help in the determination of the z position of these vertices.

- T tracks are track stubs reconstructed solely in the T1–T3. They are mostly due to secondary interactions in the material of the detectors or the LHC beampipe, but they can be useful for photon ring searches in the downstream RICH detector.

A description of the different track reconstruction algorithms is given in Ref. [192], which also provides further references. The reconstruction of long tracks begins with the searches for track segments in the VELO. Here, the fringe field of the spectrometer is negligibly small and

the trajectories of charged particles can be approximated by straight lines. Two algorithms are then employed in parallel to search for combinations of VELO track segments with hits in T1–T3. One of these algorithms starts by combining a given VELO track segment with a hit in one of the detection layers of T1–T3. The combination of a track segment and a hit on opposite sides of the spectrometer magnet allows to estimate the momentum of the potential track candidate and its trajectory. If hits are found close to this estimated trajectory in a sufficiently large number of the other detection layers of T1–T3, the VELO track segment is promoted to a long track candidate. The second algorithm first searches for stand-alone track segments in the T stations. The VELO track segments and the track segments from T1–T3 are then extrapolated to pre-defined z positions inside the magnet and at the end of the tracking system. If a pair of track segments is found for which the extrapolated positions and angles at these two z positions are in sufficiently good agreement, this pair is promoted to a long track candidate. Long-track candidates found by either algorithm are then interpolated to the z position of the TT station and matching hits in TT are assigned to the candidate. Finally, a so-called "clone killer" algorithm is applied to identify and remove duplicate track candidates found by both algorithms. The clone killing is based on the hits assigned to the track candidates. If two track candidates have a certain fraction of hits in common, the candidate with the smaller number of hits is discarded. A Kalman Filter based track fit, taking into account the expected multiple scattering and energy loss in the detector material [193], is then applied to the remaining long-track candidates to precisely determine the track parameters including the momentum. Track segments in the VELO and T1–T3 that were not used to form long tracks are extrapolated to the z position of the TT and algorithms similar to that employed in the forward tracking are employed to search for matching hits in the four detection layers of TT. If at least three matching hits are found, the track segment is promoted to an upstream or downstream track. All remaining track segments in the VELO and T1–T3 are categorized as VELO tracks and T tracks, respectively.

The track reconstruction efficiency for long tracks has been determined from collision data applying tag-and-probe methods to samples of $J/\psi \to \mu^+\mu^-$ decays. The concept of the method is illustrated in Figure 4.58: one of the two muons (the tag) is fully reconstructed as a long track, while the second muon (the probe) is reconstructed using information from parts of the detector that are not invoked in the track reconstruction algorithm. For example, the probe muon can be reconstructed using track segments from the muon system and hits in the TT, since hits in TT are not required in the reconstruction algorithms for long tracks. Thanks to the narrow mass of the J/ψ meson and the clean muon identification, a clear signal is obtained despite the less precise reconstruction of the tag muon. The efficiency of the track reconstruction algorithm can then be calculated as the fraction of reconstructed decays for which the probe muon can be matched to a reconstructed long track. The momentum spectrum of muons from $J/\psi \to \mu^+\mu^-$ decays covers the entire range interesting for most physics analyses and the large abundance of the decay allows to study the track reconstruction efficiency as a function of relevant variables, such as the particle momentum and its pseudo-rapidity or the track multiplicity of the event. The average track reconstruction efficiency was found to be larger than 95% in the interesting momentum region between 5 GeV/c and 200 GeV/c [191].

A downside of the small number of tracking stations is an increased risk of reconstructing fake tracks, formed by combinations of hits that were not caused by the same particle. Such fake tracks are mostly due to the matching of a correctly reconstructed VELO track segment with the wrong hits or the wrong track segment in the T stations. The fraction of fake tracks has been evaluated using samples of simulated events and was found to be about 6.5% on average and up to 20% for events with high particle multiplicities. However, most fake tracks have a low momentum assigned to them, since lower momenta correspond to larger deflections in the field of the spectrometer magnet and therefore more difficult matching. Since particles from b decays tend to have higher momenta, fake tracks do not pose a problem for most analyses. If required, however, their fraction can be further reduced, at the expense of a small

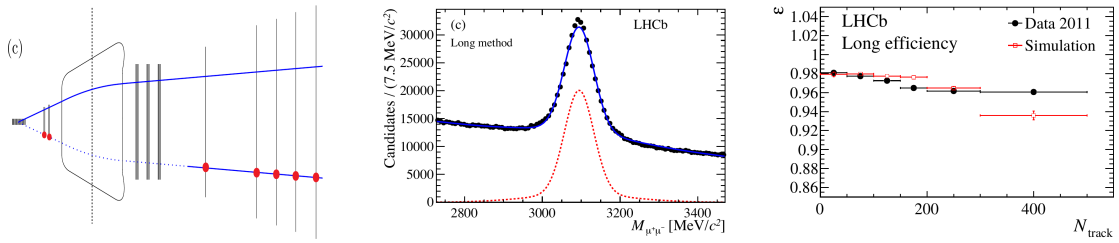

Figure 4.58: Illustration of one of the tag-and-probe methods employed to determine the reconstruction efficiency for long tracks: (left) sketch of the spectrometer with the VELO on the left and the muon stations on the right; the upper trajectory indicates the tag muon reconstucted as a long track, while the lower trajectory with the red dots indicates the probe muon and the hit information that is used for its reconstruction; (middle) invariant-mass distribution for $J/\psi \to \mu^+\mu^-$ candidates reconstructed from the combination of a tag muon and a probe muon; (right) reconstruction efficiency for long tracks as a function of the track multiplicity in the event, obtained by applying the tag-and-probe method to samples of simulated events and to collision data (all from [191]).

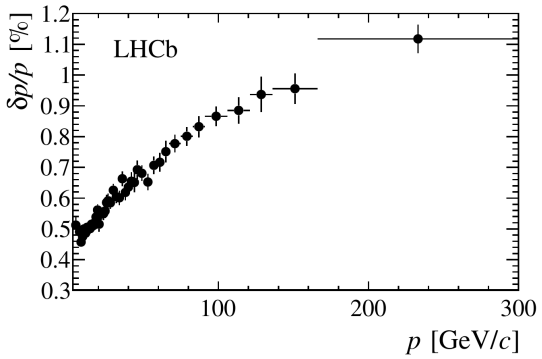

Figure 4.59: Relative momentum resolution as a function of momentum as extracted from the width of the $J/\psi \to \mu^+\mu^-$ signal in LHCb collision data (from [194]).

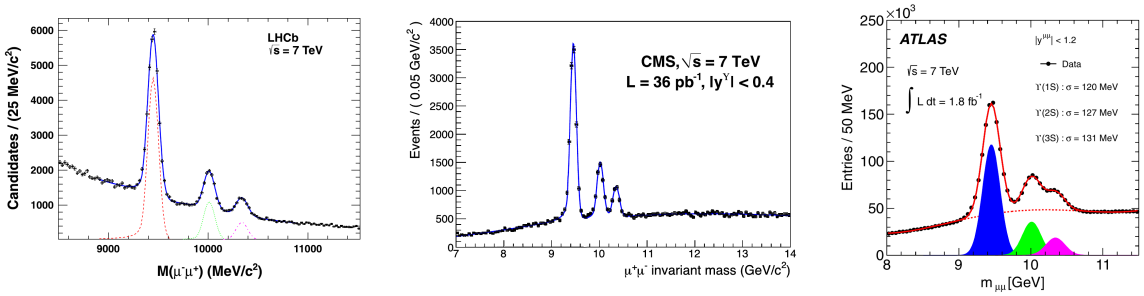

Figure 4.60: Dimuon invariant mass spectra in the region of the $\Upsilon(1S)$, $\Upsilon(2S)$ and $\Upsilon(3S)$ resonances as measured by the (left, from [195]) LHCb, (middle, from [196]) CMS and (right, from [197]) ATLAS experiments in pp collisions at a center of mass energy of 7 TeV. Better momentum resolution results in a better separation of the three resonances.

reduction in efficiency, by applying tighter requirements on the quality of the track fit or on the number of hits assigned to the track candidate.

On the other hand, the small number of detector stations results in a low material budget of the tracking system, reduced multiple scattering and therefore improved momentum resolution for correctly reconstructed tracks. The momentum resolution has been measured in collision data using samples of $J/\psi \to \mu^+\mu^-$ decays, as described in Ref. [194]. Due to the narrow intrinsic width of the J/ψ resonance and the large difference between the mass of the J/ψ meson and those of the final-state muons, the measured width of the J/ψ signal is completely dominated

by the precision of the momentum measurement for the two muons. The measured relative momentum resolution as a function of the momentum is shown in Figure 4.59 and ranges from 0.5% at 2 GeV/c to 0.8% at 100 GeV/c. Conversely, the excellent momentum resolution leads to an excellent invariant mass resolution, which is an important advantage in many physics analyses as it permits better background suppression and better separation of signals with similar decay kinematics. A comparison between LHCb and the two general purpose detectors at the LHC, ATLAS and CMS, is illustrated in Figure 4.60, using as an example the dimuon invariant mass spectra in the mass region of the three lightest $\Upsilon(nS)$ resonances as measured by the three experiments.

4.4.3 Triggering

As mentioned in the introduction to this section, the LHCb trigger concept underwent significant revisions from the initial ideas layed out in the Letter of Intent. The implementation and performance of the trigger that was in the end employed to collect data during run I of the LHC have been described in Refs. [198], [199] and [194]. The trigger consists of a hardware level (L0) that is implemented in custom-made electronics boards and a two-stage High Level Triggger (HLT1 and HLT2) that is implemented in software running on a large commercial CPU farm.

The L0 trigger operates at the 40 MHz bunch-crossing frequency of the LHC and has a fixed latency of less than 4 μs. Its maximum accept rate is limited to 1 MHz by the rate at which the LHCb detector can be read out. The trigger decision is based on input from the calorimeter and muon systems. In the L0 calorimeter trigger, the "transverse energies"

$$E_{\mathrm{T}} \equiv \sum_{i=1}^{4} E_i \sin\theta_i \ ,$$

are calculated for all groups of 2×2 calorimeter cells in the ECAL and the HCAL, where E_i is the energy deposit measured in cell i and θ_i is the polar angle between the z axis and the straight line from the nominal pp interaction point to the center of the cell. Three trigger signatures are derived from this information: the cluster with highest E_{T} in the ECAL with matching hits in both the Pre-Shower detector (PS) and the Scintillating Pad Detector (SPD) defines a L0 electron candidate; the cluster with the highest E_{T} in the ECAL with matching hits in the PS but not in the SPD defines a L0 photon candidate, and the cluster with the highest E_{T} found in the HCAL defines a L0 hadron candidate. A trigger is issued if a candidate above pre-defined thresholds is found in at least one of these three categories. In the L0 muon trigger, coincidences are formed of hits from the five muon stations that are compatible with the trajectory of a particle of transverse momentum $p_{\mathrm{T}} > 0.5$ GeV/c. A single-muon trigger is issued if at least one such candidate is found with a p_{T} above a pre-defined threshold, a dimuon trigger is issued if two candidates are found for which the scalar product of the two p_{T} values is larger than another pre-defined threshold. All threshold values employed in the L0 decisions have to be adjusted such that the total accept rate stays within the limit of 1 MHz.

Typical values of the trigger thresholds that were applied during run I of the LHC are shown in Table 4.4. These thresholds resulted in accept rates of about 400 kHz for muon triggers, 500 kHz for hadron triggers and 150 kHz for electron and photon triggers, including an overlap of approximately 10 % from events that were selected by more than one of the trigger signatures. The relatively low muon trigger thresholds reflect another advantage of the layout of the LHCb detector as a forward spectrometer: only muons with sufficiently large momentum are able to traverse a sufficient number of muon stations and create a valid trigger signature without being stopped in the absorber material. For muons produced under small angles with respect to the beam axis, this momentum requirement translates into a lower cutoff on transverse momentum than for muons that are produced under the larger polar angles that are typically covered by general purpose detectors.

Table 4.4: Typical L0 trigger thresholds applied in LHCb during data taking in run I of the LHC. Thresholds had to be increased for 2012 compared to 2011 to stay within the maximum allowed accept rate of 1 MHz despite higher instantaneous luminosity. A loose upper cut on the number of hits in the SPD counter was applied to veto events with very large event multiplicities that have poor reconstruction efficiency but would take up a large amount of computing time in the HLT and offline reconstruction (from [194]).

	p_{T} or E_{T}		SPD
	2011	2012	2011 and 2012
single muon	$1.48\,\mathrm{GeV}/c$	$1.76\,\mathrm{GeV}/c$	600
dimuon $p_{\mathrm{T}1} \times p_{\mathrm{T}2}$	$(1.30\,\mathrm{GeV}/c)^2$	$(1.60\,\mathrm{GeV}/c)^2$	900
hadron	$3.50\,\mathrm{GeV}$	$3.70\,\mathrm{GeV}$	600
electron	$2.50\,\mathrm{GeV}$	$3.00\,\mathrm{GeV}$	600
photon	$2.50\,\mathrm{GeV}$	$3.00\,\mathrm{GeV}$	600

The HLT algorithms have access to the full detector information. Several sequences of reconstruction and selection algorithms, called trigger lines, are executed on each event and an event is accepted and stored for offline reconstruction if it is selected by at least one of these trigger lines. Besides trigger lines for physics analyses, dedicated trigger lines have been designed for luminosity measurements and for calibration and monitoring purposes. In total, 38 HLT1 trigger lines and 131 HLT2 trigger lines were in use in 2011.

The starting point of the HLT1 algorithm was the reconstruction of track segments in the VELO. The offline VELO track reconstruction algorithm was applied for this purpose as it is sufficiently fast to be executed at the input rate of the HLT1. For events that had been selected by the L0 muon or dimuon hardware trigger, a search was then performed for matching combinations of good-quality VELO track segments and hits in the muon stations. To limit the execution time of the algorithm, search criteria were tuned to be sensitive to candidates with momenta above $6\,\mathrm{GeV}/c$. For events that had been selected by one of the other L0 trigger algorithms, a vertex-finding algorithm was performed to determine the positions of pp interaction vertices and track segments with significant impact parameter with respect to all reconstructed vertices were then searched for. Candidate pp interaction vertices were required to be formed by at least five track segments and have a position in the $x-y$ plane compatible with the position of the interaction region. As the position of the interaction region varies slightly from LHC fill to LHC fill, it was determined at the beginning of each fill from reconstructed VELO track segments. The position of the interaction region was then found to be stable within a few micrometers over the duration of a fill. The next step of the HLT1 algorithm consisted in applying the forward track reconstruction algorithm to those VELO track segments that had been selected by means of their impact parameter or matching hits in the muon system. To reduce the execution time of the algorithm, search criteria were tightened to be sensitive to track candidates with momenta above $3-6\,\mathrm{GeV}/c$. If such candidates are found, a simplified version of the Kalman filter fit is applied to determine a χ^2 for the track candidate as well as the track parameters and their covariance matrix at the point closest to the interaction region. The resolution obtained with this simplified fit is only a few percent worse than that achieved with the full algorithm applied in the offline reconstruction. Inclusive HLT1 trigger lines require either a single track or muon candidate with good χ^2 of the track fit, significant transverse momentum and impact parameter with respect to the reconstructed pp interaction vertices, or two muon candidates with either large invariant mass or significant impact parameters. Additional trigger lines are defined to select events with specific signatures such as high-p_{T} electron candidates, dispaced vertices or high-E_{T} jets. The combined accept rate of the HLT1 trigger lines was about 40 kHz in 2011 and 80 kHz in 2012.

At HLT2, the forward track reconstruction algorithm could then be performed on the full set of VELO track segments. Again, search criteria were tightened compared to those applied in the offline algorithm. The effective momentum requirements were $p > 5\ \mathrm{GeV}/c$

and $p_{\mathrm{T}} > 0.5$ GeV/c in 2011 and $p > 3$ GeV/c and $p_{\mathrm{T}} > 0.3$ GeV/c in 2012. Relaxing the search criteria and lowering the effective thresholds were made possible be upgrades of the HLT CPU farm and a more efficient use of its resources as described below. The offline muon-identification algorithm was then performed for all reconstructed long tracks to identify muon candidates and matching clusters in the ECAL were searched for to identify electron candidates. Photons and neutral pion candidates were reconstructed based on seeds found by the L0 calorimeter trigger algorithms. A combination of inclusive and exclusive trigger lines was then applied to select events for offline reconstruction. Inclusive single-muon trigger lines select events in which a muon candidate is found that has either a large transverse momentum or a significant impact parameter with respect to reconstructed pp interaction vertices and at least moderately high transverse momentum. Inclusive dimuon trigger lines require a pair of oppositely charged muon candidates that either form a displaced vertex or have an invariant mass that is loosely compatible with the mass of the J/ψ meson. In so-called topological inclusive trigger lines, a partial event reconstruction was performed and selection cuts were applied on quantities related to generic features of b hadron decays, such as displaced vertices or tracks with large impact parameters and large transverse momenta. Trigger objects were formed by combining two, three or four reconstructed tracks of good quality, significant impact parameter with respect to reconstructed pp interaction vertices and small mutual distances of closest approach. The trigger decision is based on a multi-variate classifier that uses as input the distances of closest approach of the tracks; the scalar sum of their transverse momenta, p_{T}, and the smallest of these p_{T}; the separation between the vertex formed by the trigger object and the closest reconstructed pp interaction vertex; the impact parameter of the trigger object with respect to this vertex; the invariant mass, m, of the trigger object and its so-called corrected invariant mass

$$m_{\mathrm{corr}} \equiv \sqrt{m^2 + |p_{\mathrm{T,miss}}|^2} + |p_{\mathrm{T,miss}}| \, .$$

Here, the quantity $p_{\mathrm{T,miss}}$ is the momentum imbalance of the trigger object with respect to its direction of flight, where the momentum of the trigger object is calculated by summing over the momenta of all assigned tracks and its direction of flight is estimated by the line pointing towards its decay vertex from the pp interaction vertex with respect to which it has the smallest impact parameter. For perfectly reconstructed decays the reconstructed momentum vector should be parallel to the direction of flight and $p_{\mathrm{T,miss}}$ should vanish. Including $p_{\mathrm{T,miss}}$ in the definition of the invariant mass corrects for the fact that the trigger object might not contain all final-state particles from the decay of the b hadron candidate.

Exclusive trigger lines are optimized to select dedicated event samples for specific decay modes that are not covered by the topological lines. A large fraction of the exclusive trigger lines are employed to select samples of so-called prompt charmed mesons that do not originate from b hadron decays but are directly produced in the pp interaction. Another typical example is an exclusive trigger line that selects samples of $B_s^0 \to K^+K^-$ decays without applying requirements on quantities related to the decay time of the B_s^0 candidate. Such a sample of events is required to perform an unbiased measurement of the effective B_s^0 lifetime in this decay mode. Exclusive trigger lines require the reconstruction of all final-state particles of the decay in question and tight cuts are applied on their invariant mass. Typically, a multi-variate classifier based on kinematical constraints is employed to further reduce the rate, before the rather time-consuming RICH particle identification algorithm is applied and its output is combined with kinematical information in a second multi-variate classifier.

The efficiency of the trigger algorithms relative to the offline reconstruction for a given physics analysis can be estimated from collision data, exploiting the fact that a given event can have been selected at the trigger level not only by the final-state particles of the signal decay under investigation, but also by decay products from the other b hadron in the event. Events for which the decay products of the signal b hadron alone would have been sufficient

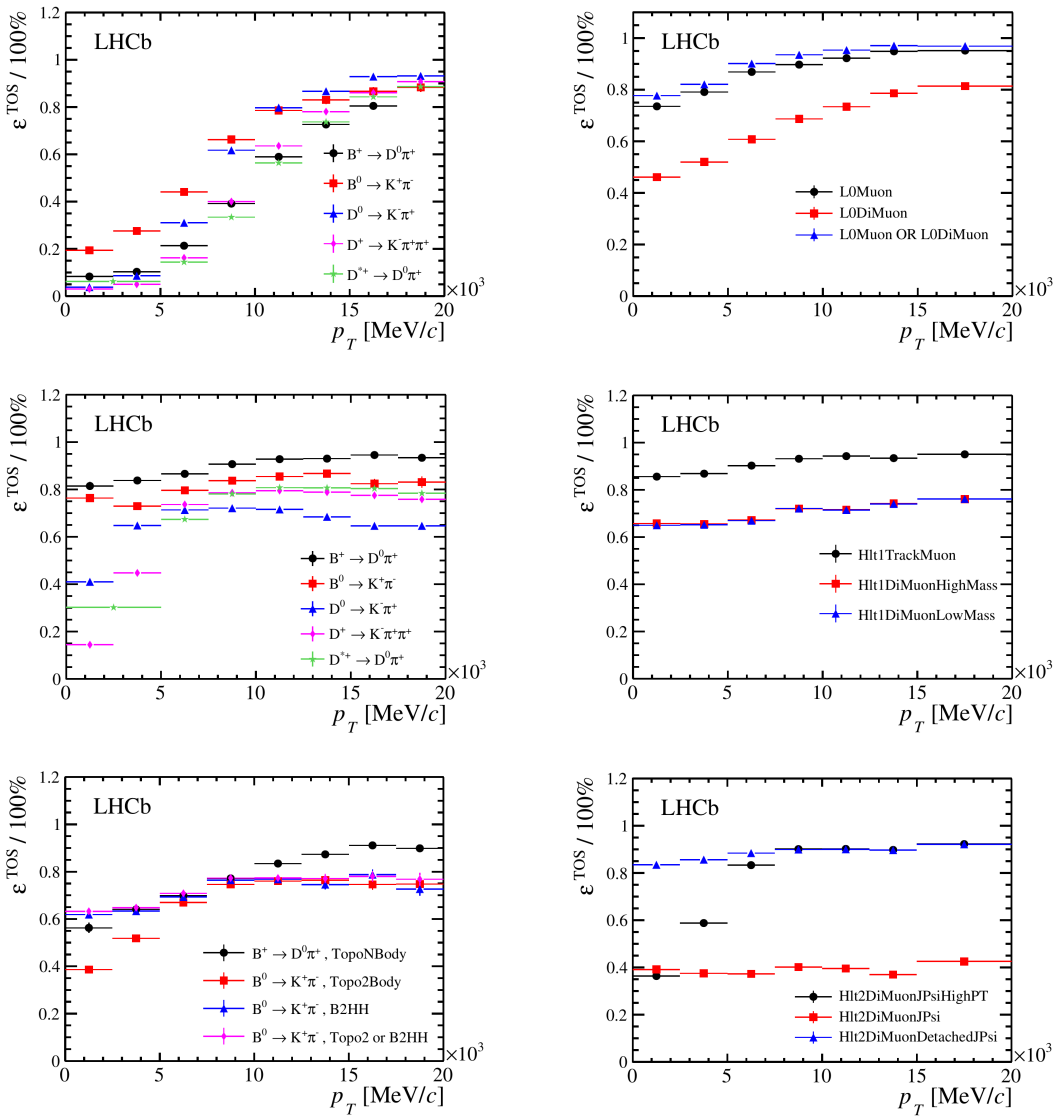

Figure 4.61: Measured TOS efficiencies as a function of the transverse momentum for offline-selected signal candidates at (top) Level-0, (middle) HLT-1 and (bottom) HLT-2 for (left) selected B-meson and D-meson decays to fully hadronic final states and (right) B-meson decays including a $J/\psi \to \mu^+\mu^-$ decay (from [194]).

to fire the trigger are classified as "Triggered on Signal" (TOS), while events for which the remainder of the event alone would have been sufficient to fire the trigger are classified as "Triggered Independent of Signal" (TIS). In LHCb, the same event can pass several trigger lines and can therefore be both TOS and TIS if the decay products of the signal b hadron fired one trigger line while particles from the remainder of the event fired another trigger line. Such events are classified as TIS&TOS. Denoting the numbers of these types of events contained in the final event sample as N^{TOS}, N^{TIS} and $N^{\text{TIS\&TOS}}$, respectively, TOS and TIS trigger efficiencies can be estimated from data as

$$\varepsilon^{\text{TOS}} \;=\; N^{\text{TIS\&TOS}}/N^{\text{TIS}} \quad \text{and} \quad N^{\text{TIS\&TOS}}/N^{\text{TOS}}$$

On the other hand, these efficiencies are defined as

$$\varepsilon^{\text{TOS}} \;\equiv\; N^{\text{TOS}}/N, \quad \text{and} \quad \varepsilon^{\text{TIS}} \;\equiv\; N^{\text{TIS}}/N,$$

where N is the true number of signal events in the analyzed data sample. Reversing the definition to express $N = N^{\text{TIS}}/\varepsilon^{\text{TIS}}$, total trigger efficiency can then be estimated from the

composition of the final event sample as

$$\varepsilon^{\text{trig}} \equiv N^{\text{trig}}/N = N^{\text{trig}} \cdot \varepsilon^{\text{TIS}}/N^{\text{TIS}}.$$

Due to phase-space correlations in the production of $b\bar{b}$ pairs, the TIS requirement can cause biases on the kinematic distribution of the signal events. To be able to correct for the effect of such biases, trigger efficiencies are estimated in bins of the relevant kinematic variables, such as p_{T} or the decay time of the signal b hadron.

4.4.4 Particle identification

The challenges of charged-hadron identification, i.e. the separation of charged kaons from pions and protons, and its importance for heavy flavour physics have already been stressed in Sections 4.1.7 and 4.3.4. In LHCb, two Ring-Imaging Cherenkov (RICH) detectors with a total of three radiators of different refractive indices provide efficient kaon-pion separation over a wide range of momenta from 2 GeV/c up to above 100 GeV/c. The upper end of this range is defined by the momentum spectrum of the kaons and pions from two-body charmless b decays $B^0 \to \pi^+\pi^-$, $B^0 \to K^+\pi^-$, $B_s^0 \to K^-\pi^+$ and $B_s^0 \to K^+K^-$. At the low end of the momentum spectrum, kaon identification is required in analyses of multi-body b decays and to select kaon candidates for flavour tagging algorithms, as described in the next section. Charged particles with momentum below 2 GeV/c tend to be bent outside the acceptance of the spectrometer in the field of the dipole magnet and are therefore of limited use for most physics analyses.

The layout of the RICH detector system exploits the correlation between the momenta and polar angles of final state particles in the forward region, as illustrated in Figure 4.62. Particle identification at low and intermediate momenta is provided by RICH-1, which is located right after the VELO and covers the full acceptance of the spectrometer, while particle identification at high momenta is provided by RICH-2, which is located downstream of the spectrometer magnet but covers only the forward region of the acceptance up to polar angles of about 120 mrad. This layout permitted cost savings by minimizing the surface of the sensitive areas that need to be covered by expensive photon detectors. Cross sections through the two detectors are shown in Figure 4.63. RICH-1 makes use of two radiators: Aerogel foam with a refractive index $n \approx 1.03$ and C_4F_{10} gas with $n \approx 1.0014$, while RICH-2 employs gaseous CF_4 with refractive index $n \approx 1.0005$ as radiator. In both cases, systems of tilted spherical and planar mirrors are employed to focus the Cherenkov photons produced in the radiators onto arrays of Hybrid Photo Diode (HPD) photon detectors that are located outside of the acceptance of the spectrometer. Cherenkov photons are produced under a fixed angle θ_C with respect to the flight direction of the particle and produce in the photon detection plane a ring with radius r_C centered around a position defined by the direction of flight of the particle.

A disadvantage of the chosen layout is that RICH-1 is located in front of the main tracking system and that multiple scattering of charged particles in its material affects the momentum resolution of the spectrometer. An important goal in the design of RICH-1 has therefore been to minimize the material of the gas enclosure and the mirror system located inside the spectrometer acceptance. The estimated material budget of RICH-1 corresponds to about 8% of a radiation length, roughly twice that of a tracking station. The effect of the multiple scattering of charged particles in the material of RICH-1 is mitigated by precise position measurements in TT and this is the main reason why adding TT hit information leads to a significant improvement of the momentum resolution for long tracks.

The particle identification performance has been studied and calibrated on collision data using large samples of protons, kaons and pions from $\Lambda^0 \to p\pi^-$ decays and from $D^{*+} \to D^0\pi^+$ decays followed by $D^0 \to K^-\pi^+$. In the Λ^0 decay, the proton and the pion are unambiguously identified by the kinematic reconstruction, while the charge of the low-momentum pion from the D^{*+} decay fixes the identities of the final-state particles in the subsequent D^0 decay. Particle trajectories measured in the tracking system were extrapolated to the mid-point along

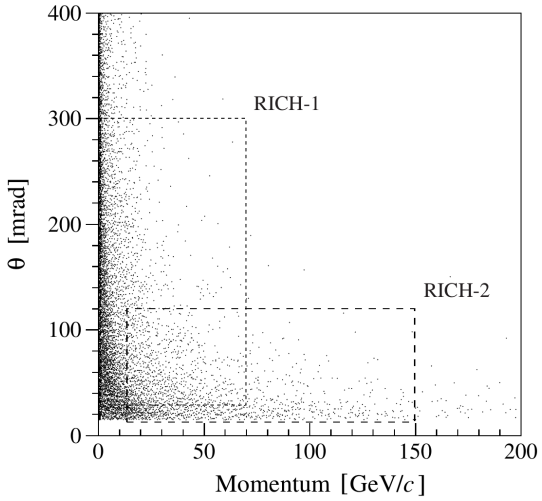

Figure 4.62: Distribution of polar angle versus momentum for all charged particles in a sample of simulated $B^0\pi^+\pi^-$ events. The regions covered by the two RICH detectors are indicated by the dashed rectangles (from [200]).

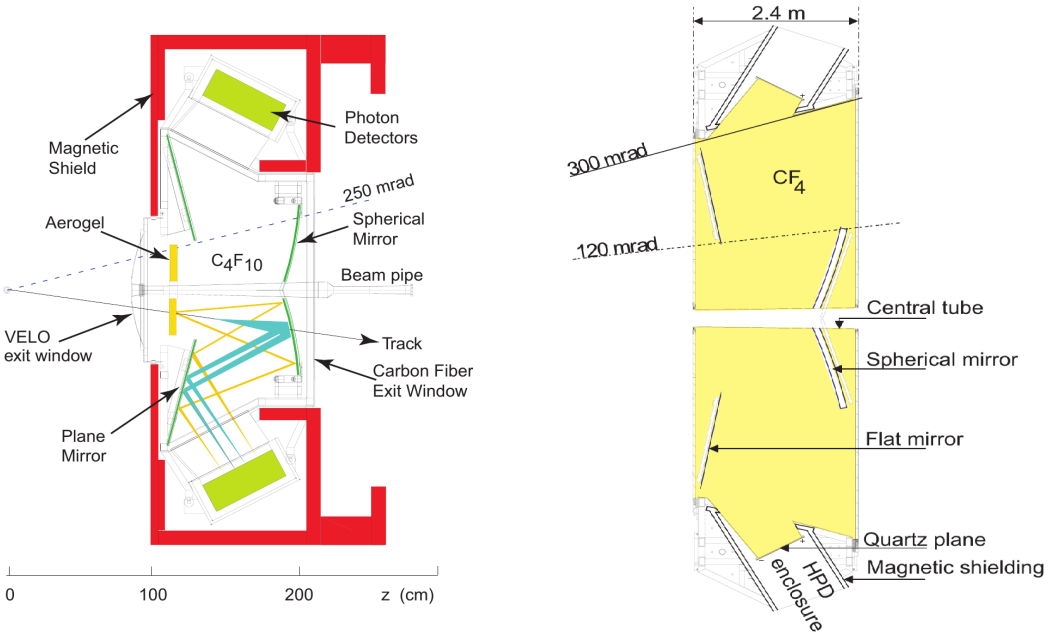

Figure 4.63: Cross sections through (left) RICH-1 and (right) RICH-2 showing the Cherenkov radiator volumes, the mirror system and the location of the photon detectors (both from [178]).

radiator volume and the angle of the track at this position is used to estimate the centre of the Cherenkov ring in the photo-detector plane. Photon candidates are assigned and the measured Cherenkov angle for each photon is compared to that expected for the known particle hypothesis. The differences between measured and expected angles in the C_4F_{10} radiator is shown in Figure 4.64 as well as the distribution of the number of detected Cherenkov photons for particles with momenta close to the saturation angle. On average, about 20 Cherenkov photons per ring are detected from the C_4F_{10} radiator, about 16 from the CF_4 radiator, but only about five from the Aerogel radiator. Due to this marginal performance, the Aerogel radiator has been removed after the end of LHC run I.

The average Cherenkov angle as determined from reconstructed rings of photons in the C_4F_{10} radiator for samples of well isolated tracks is shown in Figure 4.65 as a function of the

momentum of the corresponding track reconstructed in the tracking system. Separate bands for the different particle species are clearly visible. As expected, the bands merge at higher particle momenta, where particle identification is achievd by means of photons created in the CF_4 radiator.

In general, rings from different particles in the same event will overlap and it is not straightforward to unambiguously assign each measured photon to the correct track. Therefore, an iterative procedure using an overall event-likelihood is employed to derive the particle species for each track. Since pions are the by far most copiously produced particles, the algorithm starts by assuming the pion hypothesis for all tracks and an initial event log-likelihood is calculated for this hypothesis. For one track at a time, the particle hypothesis is then changed to electron, muon, pion, kaon or proton and the event log-likelihood is re-calculated for each of these hypotheses. This procedure is repeated for all reconstructed tracks to find the change that leads to the biggest increase in the log-likelihood. The particle hypothesis for the corresponding track is then fixed to its preferred value and the procedure is repeated for the remaining tracks. Some improvements to this basic recipee are implemented to speed up the convergence on the best solution. For example, if the change of the particle hypothesis for a given track results in a large improvement in the event log-likelihood, the hypothesis for this track can be fixed and the track removed from further optimization steps. Once the procedure has been completed and the particle hypotheses for all tracks have been assigned, particle identification classifiers for each track are determined by calculating the change $\Delta \log L$ in the overall event log-likelihood between the pion hypothesis for this track and each of the electron, muon, kaon and proton hypotheses. Cuts on these log-likelihood differences are applied in offline analyses to select particles of different species.

The performance of the kaon identification for a loose cut at $\Delta \log L(K-\pi) > 0$ and for a tight cut at $\Delta \log L(K-\pi) > 5$ is shown in Figure 4.66 as a function of the momentum of the associated track. Averaging over the full momentum range from 2 GeV/c to 100 GeV/c, the loose cut results in a 95% efficiency for correctly identifying a true kaon as a kaon and a 10% probability for misidentifying a true pion as a kaon. The tight cut results in a kaon identification efficiency of about 85% and a pion misidentification probability of about 3%. The kaon identification efficiency as a function of misidentification probability is also shown in Figure 4.66 for different ranges of track multiplicities. As expected, the performance deteriorates with increasing track multiplicity as the correct assigment of Cherenkov photons to tracks becomes increasingly difficult for busier events.

4.4.5 Flavour tagging

The approach to flavour tagging in LHCb is similar to that pursued at the Tevatron experiments as described in Section 4.3.4. Opposite-side tagging algorithms exploit the fact that b and $\bar{b}$ quarks are produced in particle-antiparticle pairs and look for flavour-specific signatures from the decay of the second b hadron in the event,$b_{\rm tag}$. The signatures employed in LHCb are the charge of a lepton from semileptonic decays of $b_{\rm tag}$, the charge of a kaon from the decay chain $b_{\rm tag} \to c \to s$ and the weighted sum of the charges of all tracks that are assigned to an inclusively reconstructed secondary vertex. In analyses of B_s^0 decays, same-side kaon tagging algorithms search for a charged kaon from the fragmentation chain leading to the signal B_s^0 meson. In a similar fashion, LHCb also uses a same-side pion tagging algorithm in analyses of B^0 decays.

The opposite-side tagging algorithms that have been employed in LHCb are described in Ref. [202]. Lepton and kaon tagging candidates are selected by requirements on the quality of the reconstructed track, such as the χ^2 returned by the track fit and the number of hits assigned to the track, and on its momentum and transverse momentum. To reject tracks from possible other pp interaction vertices in the same event, a large impact parameter with respect to any vertex other than that associated to the $B_{\rm rec}$ candidate is required. Tracks employed

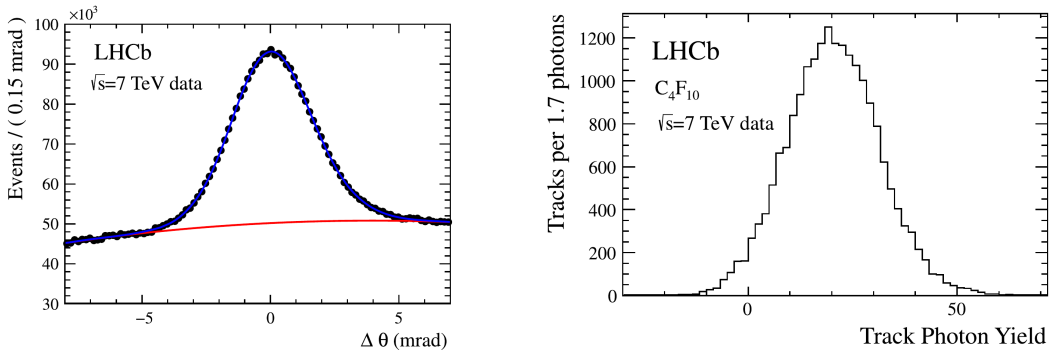

Figure 4.64: Measured distributions for Cherenkov photons from the C_4F_{10} radiator for a sample of kaons and pions from the decay $D^{*+} \to D^0\pi^+$ decays followed by $D^0 \to K^-\pi^+$: (left) difference between the expected and the measured emission angle and (right) number of observed photons for a sample of tracks with momentum close to that corresponding to the Cherenkov saturation angle (both from [201]).

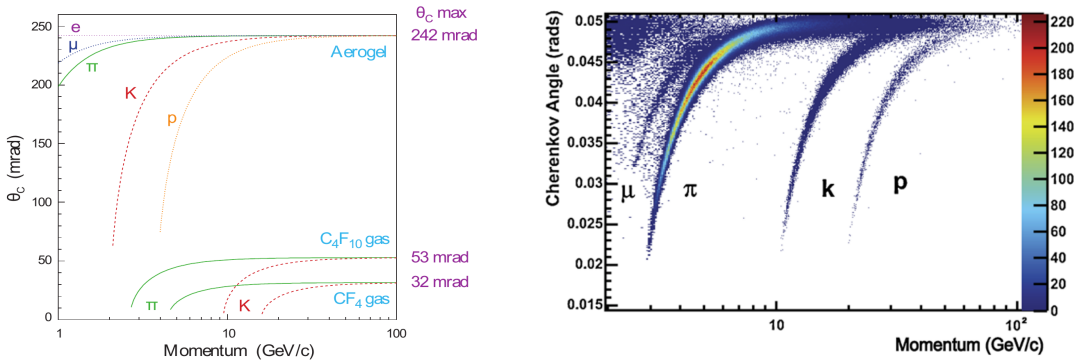

Figure 4.65: Cherenkov angle as a function of particle momentum for different particle species, (left, from [178]) calculated using the refractive indices of the different radiators and (right, from [201]) measured in the C_4F_{10} radiator.

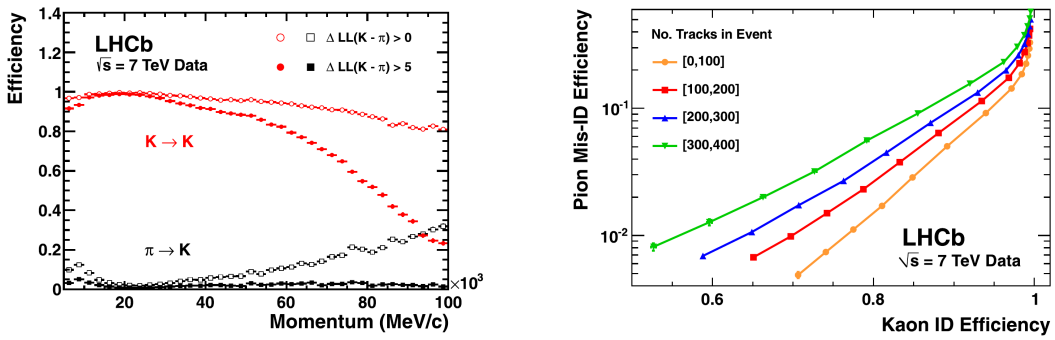

Figure 4.66: Performance of the kaon–pion separation as measured in a sample of $D^{*+} \to D^0\pi^+$ decays followed by $D^0 \to K^-\pi^+$: (left) kaon identification efficiency and pion misidentification probability as a function of particle momentum for a loose and a tight cut on the kaon identification classifier $\Delta L(K-\pi)$; (right) pion misidentification probability as a function of kaon identification efficiency for different ranges of the overall event track multiplicity (both from [201]).

in the reconstruction of the $B_{\rm rec}$ candidate are excluded as are any tracks that fall within a narrow cone around the direction of the reconstructed momentum vector of the $B_{\rm rec}$ candidate or any of its decay products. Finally, the usual selection criteria for b decay products are applied, including requirements on the transverse momentum and on the impact parameter with respect to the associated pp interaction vertex. Particle identification criteria based on information from the RICH detectors are applied. For muon candidates,associated hits in the muon system are required in addition, while cuts on the energy deposited in the ECAL and on the $\mathrm{d}E/\mathrm{d}x$ measured in the VELO are applied for electron candidates. The latter cut is applied to reject electrons from photon conversions in the material of the beam pipe or the VELO. If multiple candidates pass these requirements, that with the highest $p_{\rm T}$ is selected. For the vertex charge algorithm, an initial secondary vertex candidate is formed by combining two tracks that have a high transverse momentum and a significant impact parameter with respect to the pp interaction vertex and that form a good fit to a common vertex. Other tracks compatible with this vertex are added and cuts are applied on the scalar sum of the momenta of all assigned tracks, on the sum of their transverse momenta, on their combined invariant mass and on the sum of their impact paramters with respect to the primary vertex. For selected vertices, the vertex charge is calculated as

$$Q_{\rm vtx} \;\equiv\; \frac{\sum \{Q_i \, {p_{\rm T}}_i{}^{\kappa}\}}{\sum {p_{\rm T}}^{\kappa}},$$

where $p_{\rm T}$ is the transverse momentum of track i and the exponent $\kappa = 0.4$ was determined empirically to maximize the tagging power. A vertex charge tag is assigned if $|Q_{\rm vtx}| > 0.275$.

As at the B factories and the Tevatron experiments, tagging algorithms do not only return a tagging decision for a given event but also an estimate of the probability for this decision to be wrong. This event-by-event estimate of the mistag probability, η, is derived in LHCb by an artificial neural network algorithm that uses as input kinematic, topological and particle identification properties of the tagging candidate as well as general event properties. The neural network was trained on samples of simulated events and to correct for possible differences between simulation and collision data, the estimated mistag probability returned by the algorithm is re-calibrated on collision data using self-tagging control modes $B^+ \to J/\psi K^+$, $B^+ \to \overline{D}{}^0\pi^+$, $B^0 \to D^{*-}\mu^+\nu_\mu$ and $B^0 \to J/\psi K^{*0}$. In the decays of charged B mesons, the true charge of the B candidate is given by the charges of the final-state particles and the actual fraction of wrongly tagged events can be determined by comparing the tagging decision with this true charge. In the samples of B^0 decays, the actual mistag fraction can be extracted from a fit for the $B^0 - \overline{B}{}^0$ oscillation amplitude. Neglecting the dilution due to finite decay-time resolution, which is negligibly small for $B^0 - \overline{B}{}^0$ oscillations in LHCb, the decay-time dependent mixing asymmetry is given by

$$A(t) \;=\; (1 - 2\omega) \cdot \cos\left(\Delta m_d \, t\right) \,,$$

where ω is the true fraction of wrong tagging decisions. The calibration uses in all cases a simple linear relation

$$\omega(\eta) \;=\; p_0 \,+\, p_1 \cdot \left(\, \eta - \langle \eta \rangle \,\right) \,,$$

where $\langle \eta \rangle$ is the mean of the η distribution for the given flavour-tagging algorithm. The calibration parameters p_0 and p_1 can be determined from a fit to the actual mistag fraction in bins of η. The specific form of the linear parametrization was chosen as it minimizes the correlation between the two calibration parameters. If the initial estimates η are accurate, the fit should yield $p_0 = \langle \eta \rangle$ and $p_1 = 1$. The actual results of the calibration are close to these values, indicating that the training of the artificial neural network on simulated events leads to reasonable estimates.

Different calibration modes are employed since it can be important to calibrate the tagging performance on control samples that passed similar trigger and selection criteria as the sample

of signal decays for which the calibration is intended. The reason for this is that the trigger and selection criteria bias properties of the accompanying event in the selected sample and can therefore affect the performance of the tagging algorithm. For example, samples of decays to hadronic final states contain a significant fraction of events that were actually triggered by decay products of the accompanying b hadron. Since tracks that make a good tagging candidate also make a good trigger signature, selected event samples tend to be enriched in events with good tagging candidates. The calibration modes $B^+ \to J/\psi K^+$ and $B^0 \to J/\psi K^{*0}$ pass similar trigger and selection criteria as the decay modes $B_s^0 \to J/\psi\phi$, $B_s^0 \to J/\psi\pi^+\pi^-$, $B^0 \to J/\psi K_S^0$ and $B^0 \to J/\psi K^{*0}$, that are employed in measurements of CP phases in the $B_s^0\overline{B}_s^0$ and $B^0\overline{B}^0$ systems, while the decay $B^+ \to \overline{D}^0\pi^+$ passes a similar trigger selection as the decay $B_s^0 \to D^+\pi^-$, which is employed for the measurement of the $B_s^0 - \overline{B}_s^0$ oscillation frequency, Δm_s.

If several opposite-side tagging algorithms yield a decision for a given event, these are combined by calculating the probabilities

$$P(b) \equiv \frac{p(b)}{p(b)+p(\bar{b})} \quad \text{and} \quad P(\bar{b}) \equiv \frac{p(\bar{b})}{p(b)+p(\bar{b})}$$

with

$$p(b) \equiv \prod_i \left\{ \frac{1+q_i}{2} - q_i\,(1-\eta_i) \right\} \quad \text{and} \quad p(\bar{b}) \equiv \prod_i \left\{ \frac{1-q_i}{2} + q_i\,(1-\eta_i) \right\} ,$$

where q_i are the tagging decisions of the individual flavour-tagging algorithms and η_i are the estimated mistag probabilities. The combined tagging decision is then defined as the flavour assignment that yields the higher probability and the combined mistag probability is correspondingly set to either $\eta_{\rm OST} \equiv 1 - P(b)$ or $\eta_{\rm OST} \equiv 1 - P(\bar{b})$. This simple recipe for combining the different tagging algorithms does not take into account possible correlations, which can for example arise when a single-particle tagging candidate is included in the reconstruction of the inclusive vertex used in the vertex charge algorithm. To correct for possible biases from such correlations, another linear re-calibration, $\omega(\eta_{\rm OST}) = p_0 + p_1 \cdot (\eta_{\rm OST} - \langle\eta_{\rm OST}\rangle)$, is performed on collision data, following the same recipe as that employed in the calibration of the individual tagging algorithms.

The same-side kaon tagging algorithm employed in LHCb has been described first in Ref. [203]. To identify potential tagging candidates, similar selection requirements are appplied as in the opposite-side lepton and kaon tagging algorithm. These include requirements on the track reconstruction quality, on the momentum and transverse momentum of the candidate and its impact parameters with respect to other reconstructed pp interaction vertices. Tracks employed in the reconstruction of the $B_{\rm rec}$ candidate are excluded. Particle identification information from the RICH detectors is employed to select kaon candidates. To select particles produced close in phase space to the signal B_s^0 candidate, requirements are applied on the distance between the $B_{\rm rec}$ candidate and the tagging candidate in terms of pseudo-rapidity, $\Delta\eta$, and azimuthal angle, $\Delta\phi$, on the difference of the invariant masses $\delta Q \equiv m(B_{\rm rec}K) - m(B_{\rm rec})$, and on the impact parameter of the tagging candidate with respect to the production vertex of the $B_{\rm rec}$ candidate. If more than one candidate passes these selection criteria, that with the highest transverse momentum is selected. Again, the algorithm returns besides a tagging decision also an estimate of the mistag probability, which is derived from an artificial neural network algorithm. The neural network is calibrated on samples on simulated events and uses as input the transverse momenta of the $B_{\rm rec}$ candidate and the tagging candidate, $\Delta\eta$ and $\Delta\phi$, δQ, the number of reconstructed pp interaction vertices in the event and the number of tagging candidates that pass the selection. The estimated mistag probability returned by the neural network, $\eta_{\rm SSK}$, is re-calibrated on collision data by fitting for the amplitude of the decay-time

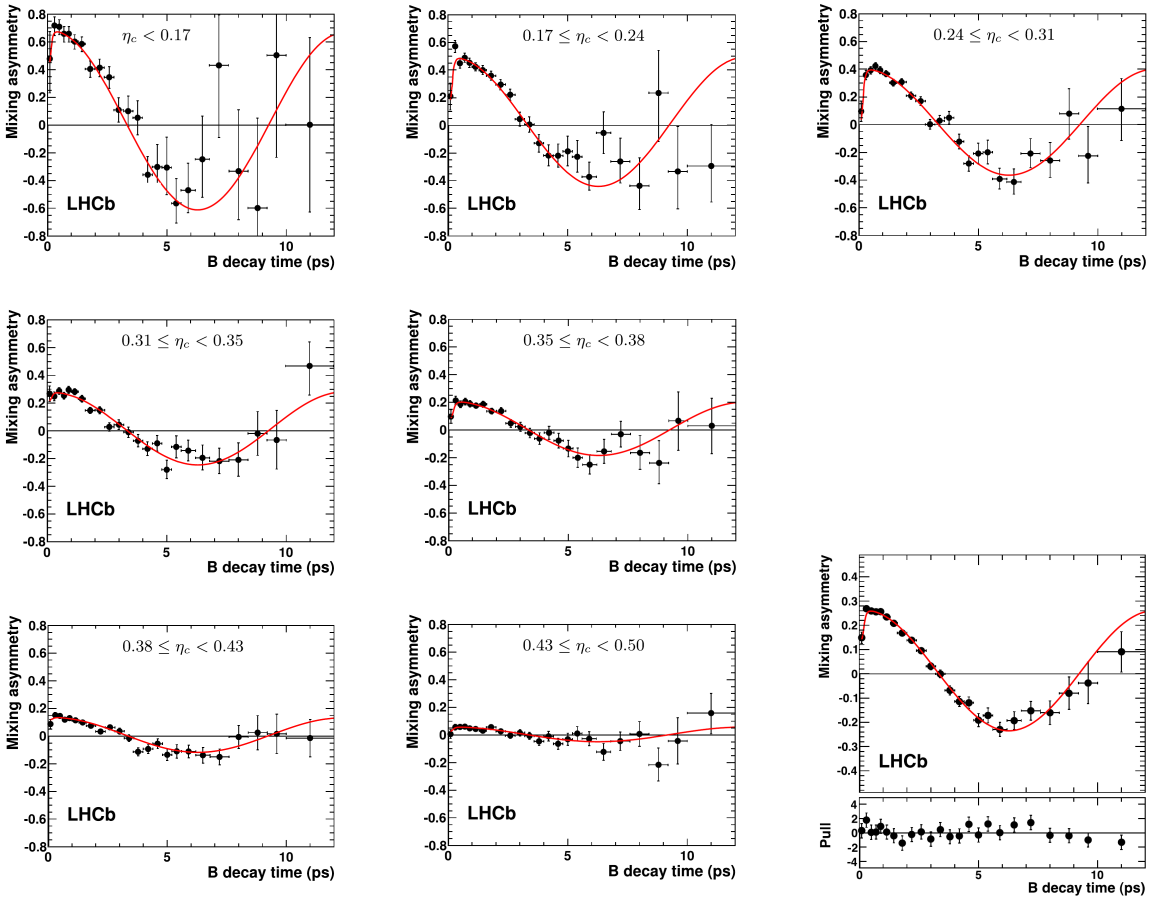

Figure 4.67: Illustration of the performance of the opposite-side tagging algorithm in LHCb: mixing asymmetry as a function of the reconstructed decay time as measured in samples of $B^0 \to D^{*-}\mu^+\nu_\mu$ candidates, for events in bins of increasing value of the estimated mistag probability, η_c, as indicated in the plot legends and (bottom right) for the combined sample (all from [202]).

dependent mixing asymmetry,

$$A(t) \;=\; (1 - 2\,\omega(\eta_{\rm SSK})) \cdot D_t \cdot \frac{\cos(\Delta m_s\, t)}{\cosh(\Delta\Gamma_s\, t\,/\,2)} \;,$$

in samples of $B_s^0 \to D_s^- \pi^+$ candidates. Here, the factor D_t describes the additional dilution of the observed amplitude due to the finite decay-time resolution, which cannot be neglected in the case of the rapid $B_s^0 - \overline{B}_s^0$ oscillations. Knowledge of D_t is therefore required in order to extract $\omega(\eta_{\rm SSK})$ and perform the calibration of the mistag probability.

An event-by-event estimate of the decay-time uncertainty is returned by the kinematic fit of the decay. However, the kinematic fit does not take into account all sources of uncertainties. A constant scale factor is therefore applied to thes estimate returned by the fit such that the average decay time resolution of the experiment is correctly reproduced. This scale factor is determined from collision data using samples of "fake" B_s^0 candidates that are formed by combining a prompt D^- meson produced in the pp collision vertex with a random pion produced in the same pp collision. The true decay time of these fake B_s^0 candidates is zero and the deviation of the measured decay-time from zero is a good measure for the true uncertainty on the decay-time measurement for the given candidate. The "pull" for each candidate is defined as the reconstructed decay time divided by the estimated decay-time uncertainty returned by the kinematic fit. If the estimates returned by the fit accurately reproduce the true reconstruction uncertainty, these pulls should be Gaussian distributed with mean zero and standard deviation one. The measured standard deviation of the pull distribution therefore gives the

desired scale factor that has to be applied to the fit estimates in order to correctly reproduce the true average decay-time resolution of the experiment.

The calibration of the estimated mistag probability, $\eta_{\rm SSK}$, uses the same linear relation, $\omega(\eta_{\rm SSK}) = p_0 + p_1 \cdot (\eta_{\rm SSK} - \langle\eta_{\rm SSK}\rangle)$, as is employed in the calibration of opposite-side tagging algorithms. The calibration parameters, p_0 and p_1 can be determined in a similar manner as in the calibration of the opposite-side tagging algorithms, namely by subdividing the sample of $B_s^0 \to D_s^- \pi^+$ candidates into bins of $\eta_{\rm SSK}$, fitting $A(t)$ to each of these subsamples and then fitting a straight line to the obtained values of ω as a function of $\eta_{\rm SSK}$. A more precise determination can be obtained by including p_0 and p_1 as parameters in the fit for $A(t)$, i.e. by fitting the function

$$A(t) \;\propto\; \{\, 1 \,-\, 2\,[\, p_0 \,+\, p_1 \cdot (\eta_{\rm SSK} - \langle\eta_{\rm SSK}\rangle)\,]\,\} \cdot D_t \cdot \frac{\cos\left(\Delta m_s t\right)}{\cosh\left(\Delta\Gamma_s/2\right)} \,.$$

The two methods give compatible results. The tagging power of the same-side kaon tagging algorithm is quoted as 1.5% in Ref. [203].

If for a given event both the opposite-side tagging algorithms and the same-side kaon tagging algorithm yield a tag, the two tagging decisions are combined and the combined mistag probability is calculated following the algorithm described above for the combination of the different opposite-side tagging algorithms.

The combined opposite-side tagging and same-side kaon tagging algorithms were first employed in the LHCb measurement of the *CP* violating phase ϕ_s from a combined analysis of $B_s^0 \to J/\psi\phi$ and $B_s^0 \to J/\psi\pi^+\pi^-$ using the 2011 data sample [204]. The tagging power was found to be $(2.3 \pm 0.06)\%$ for the opposite-side tagging algorithm, $(0.89 \pm 0.17)\%$ for the same-side kaon tagging algorithm and 3.13% for the combination.

Several improvements have been implemented since the publication of Ref. [204], such as the use of an artificial neural network algorithm to select the tagging candidates for the same-side kaon tagging algorithm. Recent measurements of ϕ_s using samples of $B_s^0 \to J/\psi\pi^+\pi^-$ decays [205] and $B_s^0 \to J/\psi K^+K^-$ decays [206] from the full run I data set found significantly improved values of the combined tagging power of $(3.89 \pm 0.25)\%$ and $(3.73 \pm 0.15)\%$, respectively. The measurements of ϕ_s will be described in Section 6.1.

As discussed above, a better performance of the opposite-side tagging algorithm is found in analyses that use hadronic B-meson decays, since a larger fraction of the selected events were triggered on decay products of the opposite-side b hadron, enriching the sample in good tagging candidates. Typical values for the combined tagging power found in analyses of hadronic B_s^0 decays are between 5.1% and 5.4% [207–209]

For analyses of time-dependent asymmetries in B^0 decays, a same-side pion tagging algorithm is being employed that follows a similar algorithm as the same-side kaon tagging algorithm described above, The tagging algorithm is slightly less performant since pions are significantly more abundant in the underlying event than are kaons and the selection of the correct tagging candidate is therefore less clean. In a measurement of the *CP* phase β from a sample of $B^0 \to J/\psi\pi^+\pi^-$ decays [210], a combined tagging power of $(3.26 \pm 0.17)\%$ was found using a combination of opposite-side tagging and same-side pion tagging algorithms.

Chapter 5

The Plot Unfolds: Mapping The Unitarity Triangle

> My husband and I, we both agreed the Unitary Triangle [...] is the prettiest plot of contemporary physics. Unfortunately, it turns out neither of us knows very much about the actual experiments that constrain the parameter space.
>
> — http://backreaction.blogspot.ch/2007/12/unitary-triangle.html

One of the main goals of experiments in b physics today is to probe the CKM picture of flavour-changing weak interactions. by searching for possible inconsistencies in overconstraint determinations of the sides and angles of the Unitarity Triangle introduced in Section 1.3. For three quark families, the CKM quark mixing matrix

$$V_{\rm CKM} = \begin{pmatrix} V_{ud} & V_{us} & V_{ub} \\ V_{cd} & V_{cs} & V_{cb} \\ V_{td} & V_{ts} & V_{tb} \end{pmatrix}$$

is fully described by three rotation angles and one complex phase. A standard parametrization of the CKM matrix is obtained by decomposing it into a product of three consecutive Euler rotations for each pair of families, and assigning the complex phase δ to the rotation between the first and the third family,

$$\begin{aligned} V_{\rm CKM} &= \begin{pmatrix} c_{12} & s_{12} & 0 \\ -s_{12} & c_{12} & 0 \\ 0 & 0 & 1 \end{pmatrix} \times \begin{pmatrix} c_{13} & 0 & s_{13}e^{-i\delta} \\ 0 & 1 & 0 \\ -s_{13}e^{-i\delta} & 0 & c_{13} \end{pmatrix} \times \begin{pmatrix} 1 & 0 & 0 \\ 0 & c_{23} & s_{23} \\ 0 & -s_{23} & c_{23} \end{pmatrix} \\ &= \begin{pmatrix} c_{13}c_{12} & c_{13}s_{12} & s_{13}e^{-i\delta} \\ -c_{23}s_{12} - s_{23}c_{12}s_{13}e^{-i\delta} & c_{23}c_{12} - s_{23}s_{12}s_{13}e^{-i\delta} & c_{13}s_{23} \\ s_{23}s_{12} - c_{23}c_{12}s_{13}e^{-i\delta} & -s_{23}c_{12} - c_{23}s_{12}s_{13}e^{-i\delta} & c_{13}c_{23} \end{pmatrix}, \end{aligned}$$

where $s_{ij} = \sin\theta_{ij}$, $c_{ij} = \cos\theta_{ij}$ and θ_{ij} is the rotation angle between the i^{th} and the j^{th} family.

The experimentally observed hierarchy in the magnitudes of the CKM matrix elements is reflected in the popular Wolfenstein parametrization,

$$V_{\rm CKM} = \begin{pmatrix} 1-\lambda^2/2 & \lambda & A\lambda^3(\rho - i\eta) \\ -\lambda & 1-\lambda^2/2 & A\lambda^2 \\ A\lambda^3(1-\rho-i\eta) & -A\lambda^2 & 1 \end{pmatrix} + O\left(\lambda^5\right),$$

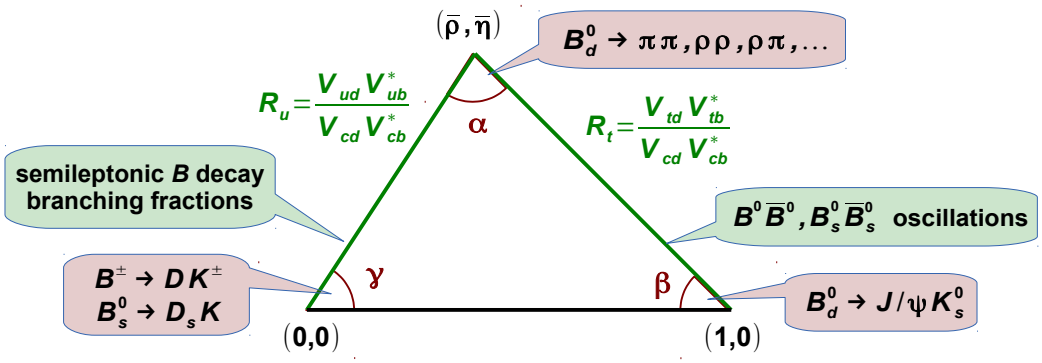

Figure 5.1: Sketch of the normalized Unitarity Triangle, indicating some of the processes that can be employed to measure the angles α, β and γ and the lengths of the sides, $|R_u|$ and $|R_t|$.

with

$$\begin{aligned} \lambda &\equiv s_{12} = |V_{us}| \,/\, \sqrt{|V_{ud}|^2 + |V_{us}|^2} \\ A\lambda^2 &\equiv s_{23} = \lambda\,|V_{cb}| \,/\, |V_{us}| \\ A\lambda^3\,(\rho - i\eta) &\equiv s_{13}e^{i\delta} = V_{ub}^* \,. \end{aligned}$$

Keeping terms up to the order of λ^5, the Wolfenstein parametrization becomes

$$V_{\rm CKM} = \begin{pmatrix} 1-\frac{\lambda^2}{2}-\frac{\lambda^4}{8} & \lambda & A\lambda^3(\rho - i\eta) \\ -\lambda + A^2\frac{\lambda^5}{2}(1-2(\rho+i\eta)) & 1-\frac{\lambda^2}{2}-\frac{\lambda^4}{8}\cdot(1+4A^2) & A\lambda^2 \\ A\lambda^3(1-(1-\frac{\lambda^2}{2})(\rho+i\eta)) & -A\lambda^2 + A^2\frac{\lambda^4}{2}(1-2(\rho+i\eta)) & 1-A^2\frac{\lambda^4}{2} \end{pmatrix} .$$

A sketch of the normalized Unitarity Triangle in the complex plane was shown in Figure 1.2 and is repeated here in Figure 5.1 for convenience. It reflects one of the unitarity conditions of the CKM matrix,

$$V_{ud}V_{ub}^* + V_{cd}V_{cb}^* + V_{td}V_{tb}^* = 0 \,,$$

after division by $V_{cd}V_{cb}^*$. In the Wolfenstein approximation up to order λ^3, the three terms of the sum are given by

$$\begin{aligned} V_{ud}V_{ub}^* &= (1-\lambda^2/2)\; A\,\lambda^3\; (\rho - i\eta) \;, \\ V_{cd}V_{cb}^* &= -\lambda\; (A\lambda^2) \;, \\ V_{td}V_{tb}^* &= A\lambda^3\; \left(1 - (1-\lambda^2/2)\; (\rho + i\eta)\right) \;. \end{aligned}$$

The base of the normalized triangle stretches by definition from $(0,0)$ to $(1,0)$ along the real axis. Its right side, opposite the origin of the complex plane, is given by

$$R_t = \frac{V_{td}V_{tb}^*}{V_{cd}V_{cb}^*} = 1 - \bar\rho + i\bar\eta$$

with

$$\begin{aligned} \bar\rho &\equiv (1-\lambda^2/2)\;\rho \\ \bar\eta &\equiv (1-\lambda^2/2)\;\eta \end{aligned}$$

and the length of this side

$$|R_t| = \frac{|V_{td}||V_{tb}|}{|V_{cd}||V_{cb}|} = \sqrt{(1-\bar\rho)^2 + \bar\eta^2}$$

can be determined from measurements of the $B^0-\overline{B}^0$ and $B_s^0-\overline{B}_s^0$ oscillation frequencies as discussed in Section 5.1 below. Measurements of the $B^0-\overline{B}^0$ oscillation frequency have been performed at the B factories, while the first measurement of the $B_s^0-\overline{B}_s^0$ oscillation frequency was one of the highlights of the b-physics programme at the Tevatron. Both measurements have been repeated with improved precison at LHCb, where they serve as an important benchmark to demonstrate the understanding of the detector performance. The precision in the determination of $|R_t|$ is limited by theoretical uncertainties.

The left side of the Unitarity Triangle is given by

$$R_u \;=\; \frac{V_{ud}V_{ub}^*}{V_{cd}V_{cb}^*} \;=\; \overline{\rho}+i\overline{\eta}$$

and the magnitudes of two of the CKM elements determining the length of this side,

$$|R_u| \;=\; \frac{|V_{ud}||V_{ub}|}{|V_{cd}||V_{cb}|} \;=\; \sqrt{\overline{\rho}^2+\overline{\eta}^2}\;,$$

are known with good precision: $|V_{ud}| = 1-\lambda^2/2$ and $|V_{cd}| = \lambda$, where $\lambda = \sin\theta_C$ and θ_C is the well-known Cabibbo angle. The magnitudes of the other two CKM elements can be determined from measurements of the branching fractions of exclusive semileptonic decays

$$\mathrm{BF}\,(B\to\pi\ell^+\nu_\ell) \;\propto\; |V_{ub}|^2$$

and

$$\mathrm{BF}\,(B\to D^{(*)}\ell^+\nu_\ell) \;\propto\; |V_{cb}|^2$$

or from measurements of inclusive semileptonic branching fractions

$$\mathrm{BF}\,(B\to X_u\ell^+\nu_\ell) \;\propto\; |V_{ub}|^2$$

and

$$\mathrm{BF}\,(B\to X_c\ell^+\nu_\ell) \;\propto\; |V_{cb}|^2\,,$$

where X_u and X_c indicate final states containing a u quark or a c quark, respectively. Finally, also the branching fraction of the leptonic decay $B^+\to\tau^+\nu_\tau$ is proportional to $|V_{ub}|$ in the Standard Model. The main interest in measuring this branching fraction, however, lies in the fact that it is sensitive to possible contributions from physics beyond the Standard Model, in particular in models with an extended Higgs sector. Measurements of all five branching fractions have been performed at the B factories, BaBar and Belle, and are described in Section 5.2. The extraction of the CKM matrix elements from the measured branching fractions requires the calculation of non-perturbative hadronic form factors, which introduces theory uncertainties. The current situation regarding the determination of $|R_u|$ is not entirely satisfactory since for both $|V_{cb}|$ and $|V_{ub}|$ a significant tension exists between the values extracted from exclusive measurements and those from inclusive measurements.

The angles of the Unitarity Triangle are related to the complex phase of the CKM matrix and can therefore be determined through measurements of CP violating observables. The angle

$$\beta \;=\; \arg\left(-\frac{V_{td}V_{tb}^*}{V_{cd}V_{cb}^*}\right)$$

can be determined with small theoretical uncertainty through the measurement of the time-dependent CP asymmetry in the golden decay channel $B^0\to J/\psi K_S^0$ and is currently the most precisely known parameter of the Unitarity Triangle. The measurement, which was the flagship analysis of the B factories, is described in Section 5.3.

The determination of the angle

$$\alpha \;=\; \arg\left(-\frac{V_{td}V_{tb}^*}{V_{ud}V_{ub}^*}\right)$$

from the time-dependent *CP* asymmetry in the decay $B^0 \to \pi^+\pi^-$ is complicated by a priori unknown contributions from Penguin diagrams with different complex phase from the dominant tree decay amplitude. An extraction of the angle α is possible by combining measurements of *CP* asymmetries in several decay modes of charged and neutral B mesons to two pions. These measurements have been performed at the B factories and are described in Section 5.4. As they require the reconstruction of decays to neutral pions, which is less efficient and clean than that for decays to charged final state particles, the angle α is less precisely known than the angle β. For the same reason, a precise measurement of α at hadron colliders does not seem feasible at the moment.

The third CKM angle,

$$\gamma \;=\; \arg\left(-\frac{V_{ud}V_{ub}^*}{V_{cd}V_{cb}^*}\right)$$

is currently the least well measured parameter of the Unitarity Triangle. Several methods have been conceived that allow a theoretically clean determination of γ from *CP* asymmetries in tree-level decays $B^\pm \to [f]_{\rm D} K^\pm$, where $[f]_{\rm D}$ denotes a final state that can be reached via an intermediate D^0 meson as well as an intermediate $\overline{D}^0$ meson. In practice, the precision of these measurements is limited by statistical uncertainties due to the small branching fractions of some of the involved decays, combined with a limited sensitivity of the experimental observables to the angle γ. Measurements of γ have been performed at the B factories, but the precision of the results is being surpassed now by measurements at LHCb. A theoretically clean determination of the angle γ can also be obtained from measurements of the time-dependent *CP* asymmetry in the decay $B_s^0 \to D_{\rm s} K$. This measurement is being pursued at LHCb. Measurements of the angle γ are discussed in Section 5.5.

Global CKM analyses combine perform fits to the measurements of various observables related to the sides and angles of the Unitarity Triangle to test the consistency of the CKM picture of flavour-changing quark interactions. Such analyses are performed by the CKMfitter [3] and UTfit [211] collaborations. The result from the latest of these fits, performed by the CKMfitter group and using measurements presented up to the CKM2014 conference in the beginning of September 2014, is illustrated in Figure 5.2. No significant discrepancies between the different observables or deviations from Standard Model expectations are observed. The precision of the measurements constrain subdominant contributions from physics to the Standard Model to a level of about 10-20 %. The impressive progress in experimental precision, mostly driven by measurements at the B factories and LHCb, is demonstrated by a comparison with Figure 5.3, which shows the constraints derived from measurements available twenty years ago, in 1995.

5.1 The length of the R_t side: $B^0-\overline{B}^0$ and $B_s^0-\overline{B}_s^0$ oscillation frequencies

As discussed in Section 3.1, $B^0-\overline{B}^0$ and $B_s^0-\overline{B}_s^0$ transitions are mediated via box diagrams as those shown in Figure 5.4. The magnitudes of the transition amplitudes of these box diagrams scale with the square of the masses of the intermediate quarks, transitions are therefore dominated by diagrams with two intermediate top quarks, the magnitude of the transition amplitude is proportional to $|V_{td}||V_{tb}|$ and therefore related to the length of the side R_t of the Unitarity Triangle,

$$|R_t| \;=\; \frac{|V_{td}|\,|V_{tb}|}{|V_{cd}|\,|V_{cb}|} \;=\; \sqrt{(1-\overline{\rho})^2+\overline{\eta}^2}\ .$$

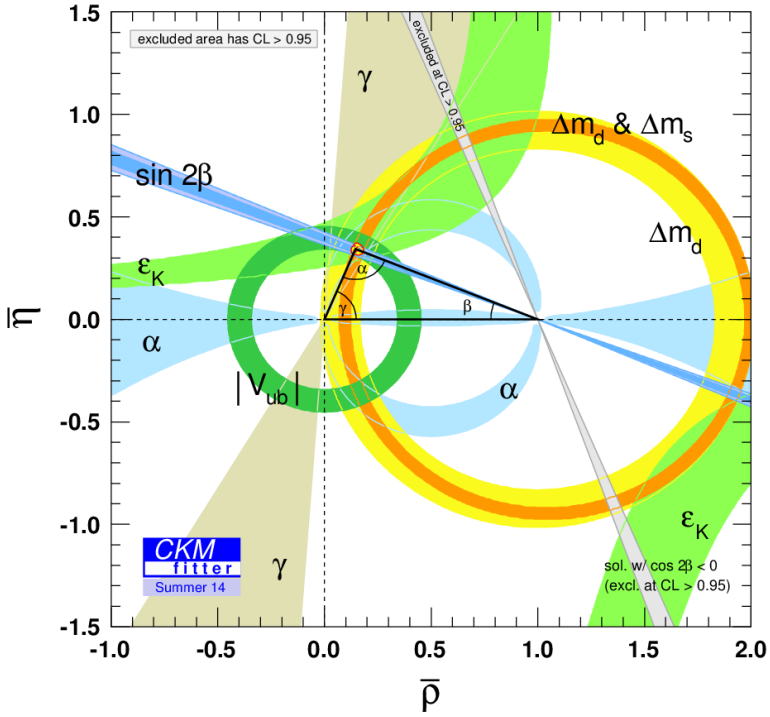

Figure 5.2: "The most beautiful plot of contemporary physics": constraints in the $(\overline{\rho}, \overline{\eta})$ plane from measurements of Unitarity Triangle parameters as compiled by the CKMfitter group [3] using measurements presented up to the beginning of September 2014. Shaded areas indicate 95 % confidence intervals fir the sides and angles of the Unitarity Triangle. The red dashed area indicates the 68 % confidence region for the position of the apex of the triangle.

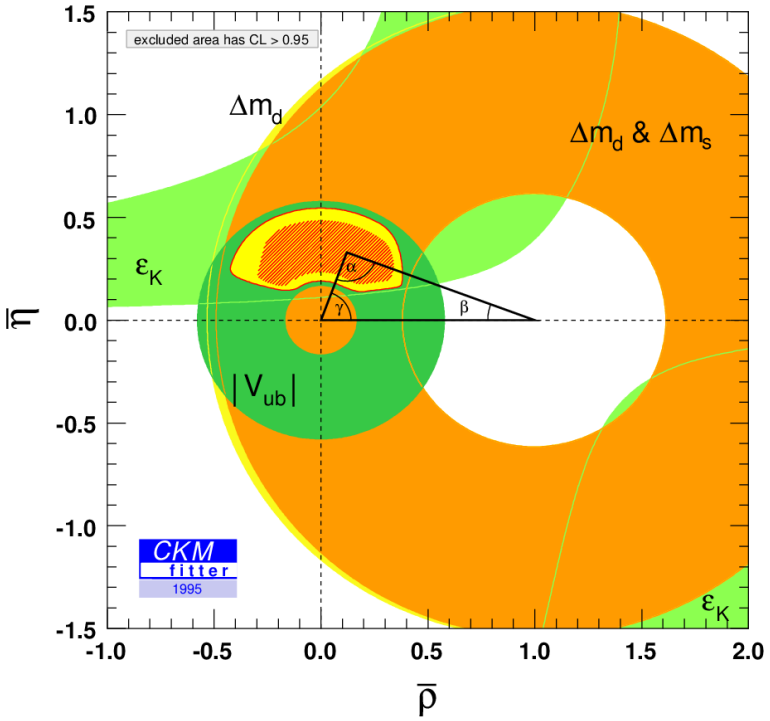

Figure 5.3: Constraints in the $(\overline{\rho}, \overline{\eta})$ plane from measurements of Unitarity Triangle parameters as compiled by the CKMfitter group [3] using measurements available in 1995.

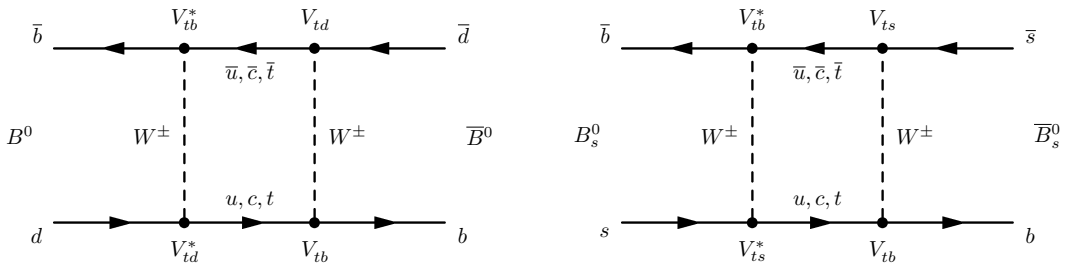

Figure 5.4: Examples of the box diagrams leading to (left) $B^0-\overline{B}^0$ and (right) $B_s^0-\overline{B}_s^0$ mixing. The CKM matrix elements for the dominating transition amplitudes with internal top quarks are indicated.

The second equality uses the Wolfenstein parameters $\overline{\rho} = (1 - \frac{\lambda^2}{2})\rho$ and $\overline{\eta} = (1 - \frac{\lambda^2}{2})\eta$ defined in the introduction to this chapter.

More specifically, the $B^0-\overline{B}^0$ oscillation frequency is given by

$$\Delta m_d \;=\; \frac{G_F}{6\pi^2}\, m_W^2\, \eta_b\, S_0(m_t^2/m_W^2)\, m_{B^0}\, f_{B_d}^2\, B_d\, |V_{td}|^2 |V_{tb}|^2 \;,$$

where G_F is the Fermi constant, m_W, m_t and m_{B^0} are the masses of the W boson, the top quark and the B^0 meson, respectively, the Inami-Lim function $S_0(m_t^2/m_W^2)$ describes the underlying electroweak contribution of the loop diagrams, η_b incorporates short-distance strong interaction effects that can be calculated in perturbative QCD, and the form factor f_{B_d} and bag parameter B_d describe long-distance QCD effects that cannot be treated perturbatively. The most precise determination of these non-perturbative parameters stems from Lattice-QCD calculations. It has an uncertainty of about 10% and limits the precision with which the magnitudes of the CKM matrix elements can be extracted from the measurement of the oscillation frequency.

Better precision in the determination of $|R_t|$ can be achieved by measuring the ratio of the $B^0-\overline{B}^0$ and $B_s^0-\overline{B}_s^0$ oscillation frequencies,

$$\frac{\Delta m_d}{\Delta m_s} \;=\; \frac{m_{B^0}}{m_{B_s^0}} \cdot \frac{f_{B_d}^2\, B_d}{f_{B_s}^2\, B_s} \cdot \frac{|V_{td}|^2}{|V_{ts}|^2} \;,$$

where $f_{B_s}^2$ and B_s are the QCD form factor and bag parameter for the B_s^0 meson and

$$\frac{|V_{td}|^2}{|V_{ts}|^2} \;=\; \frac{|A\lambda^3(1-\rho-i\eta)|^2}{|A\lambda^2|^2} \;=\; \lambda^2\left((1-\rho)^2+\eta^2\right) \;\propto\; |R_t|^2$$

in the Wolfenstein approximation. Uncertainties from Lattice QCD calcuations on the ratio

$$\xi \;\equiv\; \frac{f_{B_d}^2\, B_d}{f_{B_s}^2\, B_s}$$

are of the order of 3%.

Experimental determinations of Δm_d and Δm_s proceed via measurements of the time-dependent mixing asymmetries

$$a_{\rm mix}(t) \;\equiv\; \frac{N_{\rm unmixed}(t) \,-\, N_{\rm mixed}(t)}{N_{\rm unmixed}(t) \,+\, N_{\rm mixed}(t)} \;\propto\; \frac{\cos\left(\Delta m_{(d,s)}\, t\right)}{\cosh\left(\Delta\Gamma_{(d,s)}\, t\right)} \;,$$

where $N_{\rm unmixed}(t)$ denotes the number of events in which the flavour of the B^0 or B_s^0 meson at the time t of its decay was the same as at $t = 0$ and $N_{\rm mixed}(t)$ denotes the number of events in which the B^0 or B_s^0 meson decayed with flavour opposite to that at $t = 0$. The decay width

difference $\Delta\Gamma_d$ between the two mass eigenstates in the $B^0\overline{B}^0$ system is negligibly small, while $\Delta\Gamma_s \approx 10\%$ in the $B_s^0 B_s^0$ system. Furthermore, Δm_d and the average decay constant, $\overline{\Gamma}_d$, of the two mass eigenstates in the $B^0\overline{B}^0$ system are of similar size such that Δm_d can also be extracted from the time-integrated mixing asymmetry,

$$\chi_d \equiv \int_0^\infty a_{\rm mix}(t)\,dt = \frac{\Delta m_d{}^2}{2\,\overline{\Gamma}_d{}^2 + \Delta m_d{}^2}.$$

In the case of the $B_s^0\overline{B}_s^0$ system, the oscillation frequency Δm_s is much larger than the mean decay constant, $\overline{\Gamma}_s$, implying that B_s^0 and $\overline{B}_s^0$ mesons typically change flavour several times before they decay. The time-integrated mixing probability, χ_s, is close to 50% and has essentially no sensitivity to the value of Δm_s.

The first observation of $B^0-\overline{B}^0$ mixing by the Argus collaboration in 1987 has been described in Section 2.10. Later measurements of the time-integrated mixing probability were performed at Argus [212] and CLEO [213]. Both Argus and CLEO were experiments at symmetric e^-e^+ colliders operating at the $\Upsilon(4S)$ resonance and, as explained in Section 4.1, this precluded measurements of decay-time dependent mixing asymmetries due to the inability to measure the decay lengths of the two B mesons. First measurements of the decay-time dependent $B^0-\overline{B}^0$ mixing asymmetry were performed using B^0 and $\overline{B}^0$ mesons from Z boson decays at the four LEP experiments [214–220] and at the SLD experiment at the Stanford Linear Collider [221, 222], as well as B^0 and $\overline{B}^0$ mesons produced in high-energy $p\overline{p}$ collisions at CDF during run I of the Tevatron [223–226]. These experiments also performed searches for $B_s^0\overline{B}_s^0$ oscillations [227–235] but were not able to resolve a signal and could therefore only set lower limits on Δm_s.

Significantly more precise measurements of Δm_d were performed at BaBar [236–239] and Belle [240–242] and more recently at LHCb [243, 244]. The first observation of $B_s^0-\overline{B}_s^0$ oscillations and the determination of Δm_s at CDF II [245, 246] was one of the highlights of the b-physics programme at run II of the Tevatron. The precision of the CDF II result has now been surpassed by measurements at LHCb [244, 247, 248]. The measurements of Δm_d at BaBar, Belle and LHCb and those of Δm_s at CDF II and LHCb will be described in the remainder of this section.

5.1.1 Measurements of the $B^0\overline{B}^0$oscillation frequency Δm_d

The basic strategy for measurements of time-dependent asymmetries at the asymmetric B factories has been described in Section 4.1. Such measurements rely on the fact that pairs of B^0 and $\overline{B}^0$ mesons from $\Upsilon(4S)$ decays are produced in a quantum-entangled state and oscillate in phase until the first of them decays. The information that needs to be extracted from each selected event in order to perform a measurement of the $B^0-\overline{B}^0$ oscillation frequency is the flavour of each of the two neutral B mesons at the time of its decay and the proper-time difference between their two decays.

Pure samples of events can be selected and a clean reconstruction of the selected events performed if one of the two B mesons, $B_{\rm rec}$, is fully reconstructed in a flavour-specific hadronic final state such as the decay $B^0 \to D^{*+}\pi^-$ followed by $D^{*+} \to D^0\pi^+$ and $D^0 \to K^-\pi^+$ that was used as an illustration in Figure 4.2. Reconstructing all particles from the decay of the $B_{\rm rec}$ candidate allows for a precise determination of its momentum and of the position of its decay vertex. The flavour of the $B_{\rm rec}$ candidate at the moment of its decay is revealed by the charges of the final-state particles. As the $B_{\rm rec}$ candidate is fully reconstructed, all remaining tracks in the event must be due to the decay of the second B meson in the event, $B_{\rm tag}$. The decay vertex of the $B_{\rm tag}$ candidate can be reconstructed from an inclusive fit to these remaining tracks. Its flavour at the time of its decay can be inferred by applying flavour-tagging algorithms to these remaining tracks as discussed in Section 4.1.10. The measured distance

between the two decay vertices can be translated into the decay-time difference in the rest frame of the $B_{\rm rec}$ candidate using the measured momentum of the $B_{\rm rec}$ candidate. Measurements using fully reconstructed hadronic decays have been performed at both BaBar and Belle. The disadvantage of this approach is the relatively small size of the event samples that can be attained. Branching fractions for B^0 and $\overline{B}^0$ decays into specific hadronic final states are small and the need to reconstruct a relatively large number of final-state particles reduces the selection and reconstruction efficiency. Larger event yields can be obtained in semileptonic decay modes, which have larger branching fraction. The clean signature of a muon or electron of high momentum allows to collect relatively clean samples of events. However, semileptonic decays involve a final-state neutrino that escapes undetected and the momentum and invariant mass of the $B_{\rm rec}$ candidate cannot be measured precisely. The decay-time difference Δt has to be approximated in this case from the distance between the two decay vertices along the beam axis and the Lorentz boost of the $\Upsilon(4S)$ rest frame in the laboratory system. The loss in precision due to this approximation is in fact small compared to the uncertainty on the decay length itself, since the momenta of the two B mesons in the $\Upsilon(4S)$ rest frame are small. A third approach that has been pursued at both BaBar and Belle is to search for events with two charged high-momentum leptons, without reconstructing the remainider of the event. Assuming that each of the two leptons was created in the semileptonic decay of one of the two neutral B mesons in the event, their charges tag the flavours of the two B mesons at the time of their decay. The positions of the two decay vertices were estimated by the positions of closest approach of the reconstructed lepton trajectories to the e^-e^+ beam axis. Event samples are significantly less pure and the decay length resolution worse than for the other two methods, but a high reconstruction efficiency allows to collect large samples of events. Finally, the BaBar collaboration published an analysis, in which $B_{\rm rec}$ candidates were partially reconstructed in a semileptonic decay and the flavour of the $B_{\rm tag}$ candidate and the position of its decay vertex of were implied by a second charged lepton in the same event.

Measurements at the B factories using fully reconstructed hadronic decays

Both the BaBar and the Belle collaboration published measurements of Δm_d in fully reconstructed hadronic final states [236, 242] that were based on early event samples corresponding to about 30 million $B\overline{B}$ pairs produced at the $\Upsilon(4S)$ resonance[1]. The early Belle result was superseded by a later measurement [132] that employed a combination of decays to hadronic final states as well as semileptonic decays and was based on a larger data sample corresponding to about 152 million produced $B\overline{B}$ pairs. In all these analyses, $B_{\rm rec}$ candidates were reconstructed in the flavour-specific decay modes $B^0 \to D^-\pi^+$ followed by $D^- \to K^+\pi^-\pi^-$ as well as $B^0 \to D^{*-}\pi^+$ and $B^0 \to D^{*-}\rho^+$ followed by $D^{*-} \to \overline{D}^0\pi^-$ and $\overline{D}^0 \to K^+\pi^-$, $K^+\pi^-\pi^0$ or $K^+\pi^-\pi^+\pi^-$. In the BaBar measurement, the decay modes $B^0 \to D^{(*)-}a_1^+$ with $a_1^+ \to \pi^+\pi^-\pi^+$ were considered in addition, as well as D meson decays to a K^0_S meson and one or two pions. The BaBar analysis and the second Belle analysis also included the decay mode $B^0 \to J/\psi K^{*0}$ with $K^{*0} \to K^+\pi^-$ and $J/\psi \to \mu^+\mu^-$ or e^+e^-.

In all analyses, cuts on event-shape variables as discussed in Section 4.1.9 were applied to reduce background from non-$B\overline{B}$ events. The extraction of the signal component from the selected sample of $B_{\rm rec}$ candidates was based on the energy imbalance, ΔE, and the beam-energy substituted invariant mass, $m_{\rm ES}$, introduced in Section 4.1.9. Measured distributions of $m_{\rm ES}$ are shown in Figure 5.5 and demonstrate the low levels of background in the event samples.

[1] In BaBar and Belle publications, the integrated luminosity collected at the $\Upsilon(4S)$ resonance is often expressed in terms of the number of produced $B\overline{B}$ pairs, where this number includes both B^+B^- and $B^0\overline{B}^0$ pairs. The methods that were employed to extract these numbers from the collected data are described in Ref. [112]. The total integrated luminosity collected at the $\Upsilon(4S)$ resonance by the Belle experiment is quoted as 711 fb^{-1} or 772×10^6 produced $B\overline{B}$ pairs [112], while that collected at the BaBar experiment is quoted as 424 fb^{-1} or 465×10^6 produced $B\overline{B}$ pairs in Ref. [249] and as 424 fb^{-1} or 471×10^6 produced $B\overline{B}$ pairs in Ref. [112].

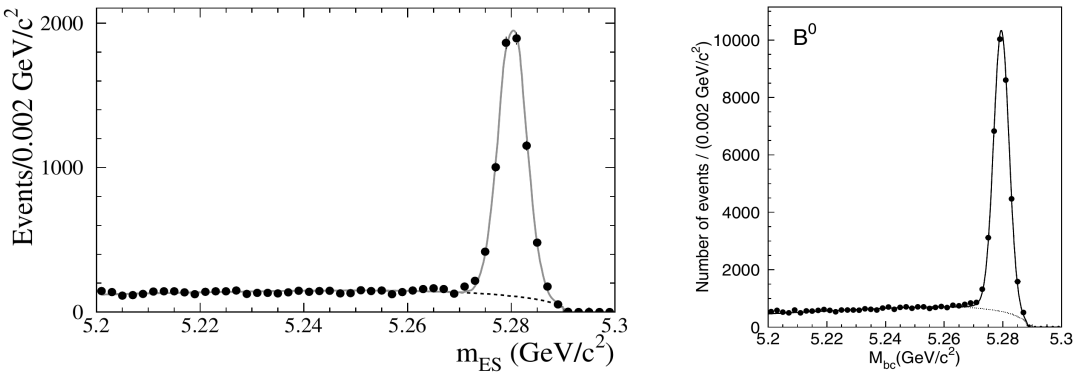

Figure 5.5: Distribution of the beam-energy substituted invariant mass for B^0 and $\overline{B}^0$ candidates reconstructed in hadronic final states from the measurements of Δm_d in (left, from [236]) BaBar using fully reconstructed decays to hadronic final states and (right, from [132]) Belle employing a combination of fully reconstructed decays to hadronic final states and semileptonic decays.

In a signal region defined by $5.27 < m_{\rm ES} < 5.29$ GeV/c^2, a total of about 35'500 candidates in fully reconstructed hadronic final states were found in the combined Belle analysis [132], with purities of about 90 % in the decays to $D^-\pi^+$ and $D^{*-}\pi^+$ and 95 % in the decay to $J/\psi K^{*0}$. For comparison, the sample of semileptonic decays obtained in the same analysis contained about 85'000 candidates with a purity of about 78 %.

The $B_{\rm tag}$ decay vertex was reconstructed from tracks that were not used in the reconstruction of the $B_{\rm rec}$ candidate. To reduce possible biases on the reconstructed position of the vertex, tracks were excluded in the BaBar analysis if they passed kaon identification criteria, since it was found that kaons mostly originate from secondary decay vertices of D mesons. For the same reason, tracks were excluded in the Belle analysis if they were compatible with originating from the decay of a K^0_S meson. In the Belle analysis, the vertex fit included a constraint on the e^-e^+ interaction region. The technique is described in Ref. [250] and was employed in many of the later Belle analyses. It allowed to estimate the position of the $B_{\rm tag}$ decay vertex even in the case that only one track was found in the event that could be assigned to its decay. This was found to be the case in about 22 % of the events selected for the analysis discussed here. The mean position and the profile of the interaction region was determined in regular intervals during data taking using reconstructed tracks from hadronic e^-e^+ interactions.

Flavour tagging was in both analyses based on the signatures discussed in Section 4.1.10: high-momentum leptons from $\overline{b}\to\overline{c}\ell^+\nu_\ell$ transitions, lower-momentum leptons from subsequent $\overline{c}\to\overline{s}\ell^-\overline{\nu}_\ell$ transitions, charged kaons and Λ baryons from $\overline{b}\to\overline{c}c\overline{s}$ transitions, low-momentum pions from $D^{*-}\to D^0\pi^-$ decays from the $B_{\rm tag}$ decay chain and high-momentum pions from decays of the type $B^0\to D^{(*)-}\pi^+$. As described in Section 4.1.10, each event was assigned to one of seven tagging categories according to the response of the tagging algorithm.

Decay-time distributions for events tagged as mixed and unmixed and the resulting time-dependent mixing asymmetry from the BaBar analysis are shown in Figure 5.6, the mixing asymmetry measured in the combined Belle analysis is shown in Figure 5.7. The value of Δm_d was extracted from unbinned maximum likelihood fits to the data. The signal component in the fit function was parametrized as

$$P_{\rm mix}(\Delta t) \;=\; \frac{1}{4\,\tau_{B^0}}\,\Big\{\,e^{-|\Delta t|/\tau_{B^0}}\;(\,1\,\pm\,\Delta\omega_k\,+\,q\,(1-2\,\omega_k)\,\cos\,(\Delta m_d\,\Delta t)\,)\,\Big\}\;\otimes\;R(\Delta t)\;,$$

where $q=+1$ for events tagged as unmixed and $q=-1$ for events tagged as mixed, ω_k is the average mistag fraction for tagging category k and $\pm\Delta\omega_k$ describes the difference in mistag fractions for B^0 and $\overline{B}^0$ candidates. Finally, the convolution with the empirical function $R(\Delta t)$ takes into account the dilution of the oscillation amplitude due to the finite decay-time resolution. The decay-time resolution was parametrized in the BaBar analysis by a sum

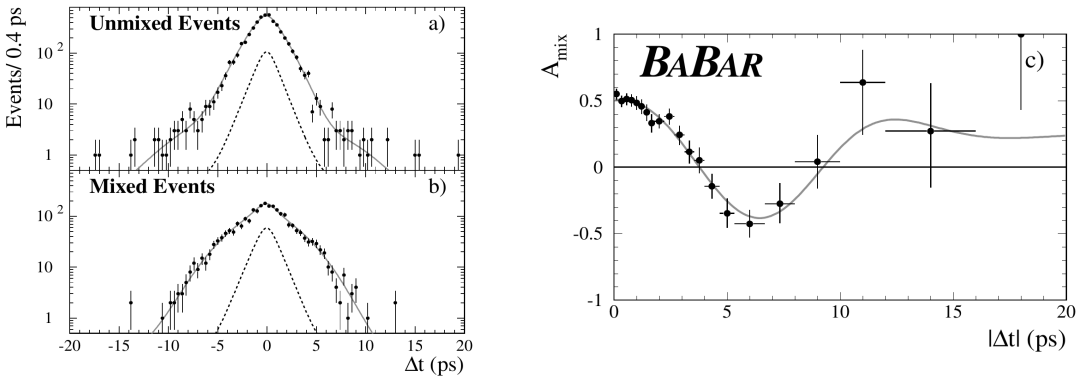

Figure 5.6: Distributions of (left) Δt for event candidates tagged as unmixed and mixed and (right) the resulting mixing asymmetry as a function of $|\Delta t|$ from the BaBar measurement of Δm_d using fully reconstructed decays to hadronic final states. Solid lines indicate the projections of the maximum likelihood fits to the data, while dashed lines indicate the component assigned to background contributions (from [236]).

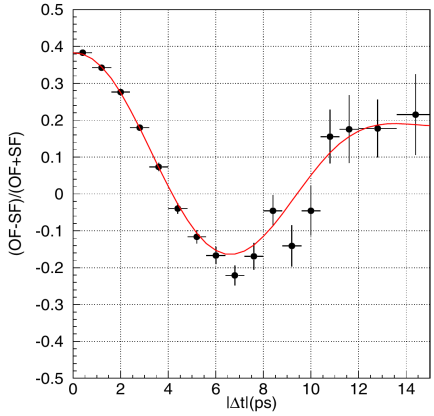

Figure 5.7: Mixing asymmetry as a function of $|\Delta t|$ as observed in the Belle measurement of Δm_d using a combination of semileptonic decays and fully reconstructed decays to hadronic final states. The solid line indicates the projection of the maximum likelihood fit to the data (from [132]).

of three Gaussian functions with different means and widths, while the resolution function employed in the Belle measurement is described in Ref. [250]. In total, the fit functions employed in the BaBar and Belle analyses contained 44 and 32 fit parameters, respectively. Besides Δm_d, these included the values of ω_k and $\Delta\omega_k$, the parameters describing the decay-time resolution function, $R(\Delta t)$, and a number of parameters describing the fractions and decay-time distributions of background components in the selected sample.

The results of the measurements in terms of Δm_d are shown in Figure 5.13 under the labels "*BABAR* B^0_d*(full)/L,K,NN*" and "*BELLE* B^0_d*(full)+D$\ell\nu$/comb*", respectively. In the case of the BaBar analysis, the precision of the result was limited by its statistical uncertainty, while in the case of the Belle analysis, which was based on a larger data sample and included semileptonic decays in addition to the decays to hadronic final states, the statistical and systematic uncertainty were similar in size. Systematic uncertainties were found to be dominated in the BaBar analysis by the uncertainty on the B^0 meson lifetime, which was fixed in the fit to its world-average value, and by the understanding and modeling of the Δt resolution for signal candidates. In the Belle analysis, systematic uncertainties were found to be dominated by the understanding of background contributions in the semileptonic sample, and from effects related to the vertex reconstruction. The latter included the understanding of possible biases from the constraint on the interaction-region discussed above, from track selection criteria,

from the range in Δt over which the fit is performed and from possible misalignment of the vertex detector.

Measurements at the B factories using semileptonic decays

The BaBar collaboration published a measurement of Δm_d using semileptonic decays [238] that was based on an early data sample corresponding to 23 million produced $B\overline{B}$ pairs. The Belle collaboration published an early measurement using only semileptonic decays [241] that was based on a data sample corresponding to about 31 million produced $B\overline{B}$ pairs. The result of this first Belle analysis was superseded by their combined analysis [132] of semileptonic and hadronic decays that was already discussed in the previous paragraphs. All analyses employed the semileptonic decay mode $B^0 \to D^{*-}\ell^+\nu_\ell$, where ℓ could be an electron or a muon and D^* candidates were reconstructed in the same decay modes that were employed in the hadronic analysis described in the previous paragraphs, namely $D^{*-} \to \overline{D}^0\pi^-$ followed by $\overline{D}^0 \to K^-\pi^+$, $K^- \to \pi^+\pi^0$ or $K^- \to K^+\pi^-\pi^+\pi^-$. Again, the BaBar analysis also considered final states with a K^0_S meson and one or two pions.

The selection of signal candidates exploited the presence of a high-momentum charged lepton and the distinct signature of the decay $D^{*-} \to \overline{D}^0\pi^-$. Initial selection cuts were placed on global event-shape variables and on the magnitudes of the momenta of the final-state particles and the D^* candidate. The opening angle between the momentum vector of the D^{*-} candidate and that of the charged lepton was required to be larger than 90° in the rest frame of the e^-e^+ collision. Two discriminating variables were then employed to extract the signal component from the selected samples of candidates. One of these was the difference between the reconstructed invariant masses of the D^{*-} candidate and the $\overline{D}^0$ candidate, which can be reconstructed with excellent resolution due to the low momentum of the pion that is emitted in the decay $D^{*-} \to \overline{D}^0\pi^-$. The second discriminating variable exploited energy and momentum conservation in the decay $B \to D^*\ell\nu_\ell$, which yields for the squared invariant mass of the neutrino

$$\begin{aligned} m_\nu^2 &= (E_B - E_{D^*\ell})^2 - (\vec{p}_B + \vec{p}_{D^*\ell})^2 \\ &= m_B^2 + m_{D^*\ell}^2 - 2\,E_B E_{D^*\ell} + 2\,|\vec{p}_B|\,|\vec{p}_{D^*\ell}|\,\cos\theta_{B,D^*\ell}\ , \end{aligned}$$

where m_B, E_B and $\vec{p}_B$ are the invariant mass, energy and momentum of the decaying B meson and $m_{D^*\ell}$, $E_{D^*\ell}$ and $\vec{p}_{D^*\ell}$ are the same quantities for the $D^*\ell$ system produced in the decay. Setting $m_\nu^2 = 0$, the cosine of the opening angle between the momenta of the B meson and the emitted $D^*\ell$ system is given by

$$\cos\theta_{B,D^*\ell} = \frac{2E_B E_{D^*\ell} - m_B^2 - m_{D^*\ell}^2}{2|\vec{p}_B|\,|\vec{p}_{D^*\ell}|}\ .$$

The value of $\cos\theta_{B,D^*\ell}$ in the rest frame of the e^-e^+ collision was calculated setting m_B to the nominal mass of the B^0 meson, taking E_B as half the known centre-of-mass energy of the e^-e^+ collision and setting $|\vec{p}_B| = \sqrt{E_B^2 - m_B^2}$. The invariant mass, energy and momentum of the $D^*\ell$ system were determined from the reconstruction of the events. For signal candidates, $\cos\theta_{B,D^*\ell}$ has a physical meaning and, baring resolution effects, has to assume values between -1 and $+1$. For background, no such constraints apply and a broad distribution is observed that extends far beyond the physically meaningful boundaries. Measured distributions of the two discriminating variables are shown in Figure 5.8 together with the estimated signal and background components in the sample of selected candidates. Considered background components included non-$B\overline{B}$ continuum events, wrongly reconstructed D^* candidates, true D^* candidates combind with a wrong or misidentified lepton, and partially reconstructed decays of the type $B \to D^*\pi\ell\nu_\ell$, where B can be a neutral or charged B meson and the extra pion

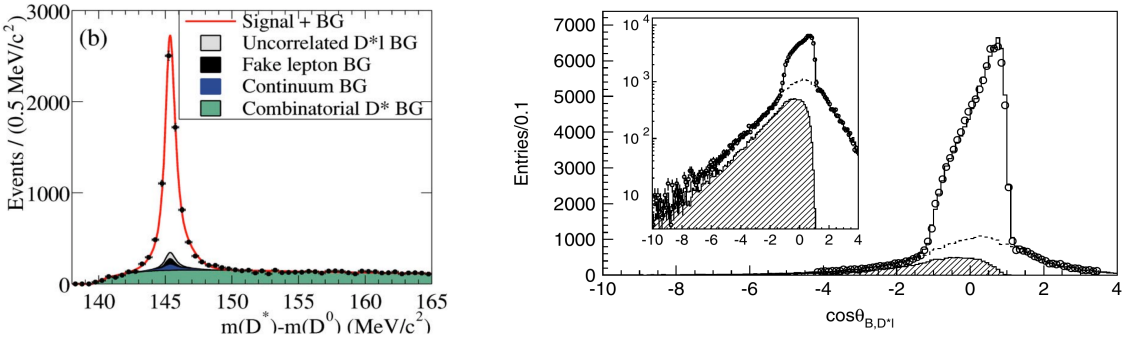

Figure 5.8: Distributions of the discriminating variables employed in measurements of Δm_d in semileptonic decays: (left, from [238]) the difference between the reconstructed D^{*+} and D^0 invariant masses for selected $D^{*+}\mu^+$ candidates in the BaBar analysis and (right, from [132]) the variable $\cos\theta_{B,D^*\ell}$ from the combined Belle analysis using semileptonic and hadronic decays. In the left panel, the solid red line indicates the result of the fit to the data and shaded areas indicate the different background components as described in the plot legend. In the right panel, the shaded area indicates the component attributed to partially reconstructed background from $B \to D^*\pi\ell\nu_\ell$ decays, while the dashed line indicates the total background component.

failed to be reconstructed. Backgrounds from non-$B\overline{B}$ continuum events were estimated from data collected below $\Upsilon(4S)$ resonance. Wrongly reconstructed D^* candidates from sidebands in the distribution of $m_{D^*} - m_{D^0}$ distribution or from combinations of D candidates with a low-momentum pion of the wrong charge. Combinations of a true D^* candidate with the wrong lepton were estimated from a control sample in which the D^{*0} candidate and the charged lepton were emitted into the same hemisphere in the $\Upsilon(4S)$ rest frame and for which the reconstructed momentum vector of the lepton candidate was artificially reversed. Finally, backgrounds from partially reconstructed decays were estimated from the measured $\cos\theta_{B,D^*\ell}$ distribution, where the expected shapes of this distribution for signal events and partially reconstructed events were estimated from samples of simulated events. As already mentioned, a total of 85'000 semileptonic candidates were found in the combined Belle analysis [132], out of which the fit assigned about 78 % to the signal component. For comparison, the fully reconstructed hadronic sample contained about 35'500 candidates with purities between (90 − 95) %.

The position of the $B_{\rm rec}$ decay vertex was determined from a fit to the trajectory of the charged lepton and the reconstructed momentum vector of the $\overline{D}^0$ candidate, while the position of the $B_{\rm tag}$ decay vertex was reconstructed from a fit the remaining tracks in the event in the same manner as in the hadronic analysis discussed in the previous paragraphs. Flavour tagging also relied on the same algorithms as in the hadronic analyses described above.

The result of the combined Belle measurement has already been discussed. The decay-time distributions and the decay-time dependent mixing asymmetry as measured in the BaBar analysis are shown in Figure 5.9. The value of Δm_d was extracted from an unbinned maximum likelihood fit to the data, where the decay-time distribution of the signal component was described by the same function form as in the hadronic analysis discussed above. The decay-time resolution function was described in this case by the sum of two Gaussian functions and a third Gaussian convolved with an exponential function. This exponential term was included in the resolution function to take into account possible biases in the fitted position of the $B_{\rm tag}$ decay vertex due to the inclusion of tracks from secondary D decays.

The fit function employed in this BaBar analysis contained a total of 72 free parameters, out of which 21 described the decay-time model, decay-time resolution function and tagging performance for the signal component and the remaining 51 described the fractions of the different background components and the modelling of their decay-time distributions. The result of the analysis in terms of Δm_d is listed in Figure 5.13 under the label "*BABAR* $D^*\ell\nu$/*LK,NN*".

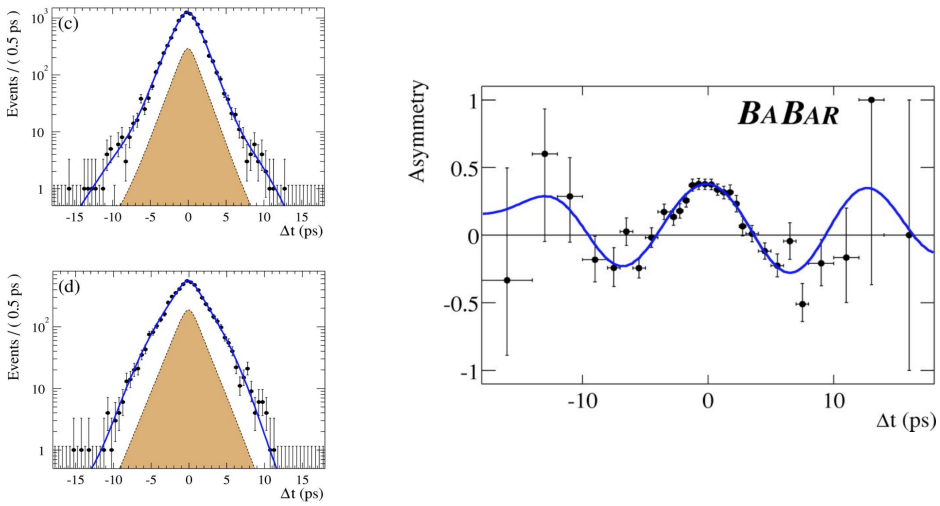

Figure 5.9: Results of the BaBar measurement of Δm_d using semileptonic decays: (left) distributions of Δt for event candidates tagged as unmixed and mixed and (right) the resulting mixing asymmetries as a function of Δt. The solid lines show the projections of the the maximum likelihood fits to the data. The shaded areas in the Δt distributions indicate the component assigned to background contributions (from [238]).

The precision of the measurement was limited by the statistical uncertainty. The systematic uncertainty was dominated by the limited size of the samples of simulated events that were employed to investigate possible biases of the fit procedure, in particular of effects from the modeling of background contributions. Other sources of systematic uncertainties were the internal alignment of the vertex detector and the overall length-scale of the detector.

Measurements at the B factories using inclusive dilepton pairs

Measurements of Δm_d using inclusive dilepton pairs at BaBar [237] and Belle [240] were based on data samples corresponding to 23 and 32 million produced $B\overline{B}$ pairs, respectively.

To suppress non-$B\overline{B}$ backgrounds, candidate events in both analyses were required to contain five or more than five reconstructed tracks pointing back to the e^-e^+ interaction region and fulfill requirements on event shape variables as well as on the squared invariant mass of all reconstructed particles, or the total reconstructed energy and the sum momentum of the reconstructed momenta.

Selected events were then required to contain at least two charged leptons with well reconstructed tracks pointing back to the interaction region, neither of which was compatible with being due to a J/ψ decay or, in the case of an electron, with a photon conversion if combined with another reconstructed particle fulfilling loose lepton identification criteria. If more than two charged leptons were reconstructed in a given event, the two candidates with the highest momenta in the $\Upsilon(4S)$ rest frame were retained. The opening angle between the two lepton candidates was used as a discriminating variable to suppress events in which both leptons originated from a cascade decay of the same B meson. About 99'000 dilepton candidates passed the selection requirements in the BaBar analysis, while about 50'000 same-sign and 23'000 opposite-sign lepton pairs were retained in the Belle analysis.

Different procedures were applied in the two analyses to estimate the z positions of the decay vertices of the two B mesons along the beam axis. In the BaBar analysis, the position of the primary e^-e^+ interaction in the r–ϕ plane orthogonal to the beam axis was estimated on an event-by-event basis by performing a vertex fit using the two lepton tracks and a constraint on the beam spot. The points of closest approach of the two lepton tracks to this vertex position in the r–ϕ plane were then determined and the corresponding z positions were used as estimates for the positions of the B meson decay vertices. In the Belle analysis, samples

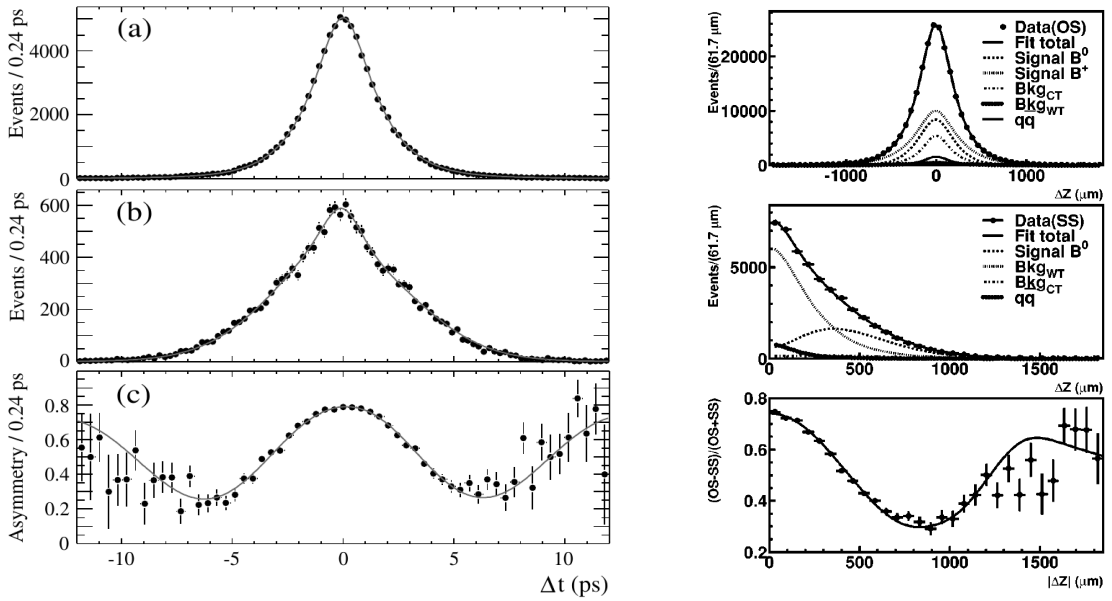

Figure 5.10: Distributions of Δt, Δz or $|\Delta z|$, for (top) opposite-sign and (middle) same-sign dilepton pairs and (bottom) the resulting mixing asymmetries from (left, from [237]) the BaBar and (right, from [240]) the Belle measurements of Δm_d using inclusive dilepton pairs. The solid lines show the projections of the maximum likelihood fits to the data. In the Δz distributions from Belle, different background components are indicated as well, where "$\mathrm{Bkg_{CT}}$" refers to the sum of all "correct-tag" background components due to opposite-sign lepton pairs from B^+B^- events and unmixed $B^0\overline{B}^0$ events and same-sign lepton pairs from mixed $B^0\overline{B}^0$ events, while "$\mathrm{Bkg_{WT}}$" refers to the sum of all "wrong-tag" background components, due to opposite-sign lepton pairs from mixed $B^0\overline{B}^0$ events and same-sign lepton pairs from B^+B^- events.

of e^-e^+ interactions to charged particles were employed to estimate on a run-by-run basis the position and profile of the e^-e^+ interaction region in the r–ϕ plane and the intersections of the two lepton tracks with this interaction region was employed to estimate the z positions of the two B meson decay vertices.

The measured distributions for opposite-sign and same-sign lepton pairs and the corresponding time-dependent asymmetries are shown in Figure 5.10 together with the results of binned maximum likelihood fits to extract the value of Δm_d. The fit was performed in terms of Δz in the Belle analysis and in terms of the decay-time difference, Δt, in the BaBar analysis. In both cases, the known Lorentz boost of the $\Upsilon(4S)$ frame in the laboratory system was used to translate between the two quantities. In both analyses a signed difference was calculated, where in the BaBar analysis, the z position corresponding to the lower-momentum lepton was subtracted from that corresponding tp the higher-momentum lepton, while in the Belle analysis the z position corresponding to the negative lepton was subtracted from that corresponding to the positive lepton.

The fit functions contained terms for the signal component and various sources of backgrounds. The signal component was in both cases described by a term proportional to $\cos(\Delta m_d \Delta t)$, convolved with an empirical function to model the decay time resolution. In the BaBar analysis, this resolution function was modelled by the sum of three Gaussian functions with different width, where the fractions and widths of the three Gaussians were free parameters in the fit to the data. Samples of J/ψ candidates were employed to verify that this parametrization provides a good description of the resolution. For J/ψ decays, the true Δz between the two leptons is zero and the measured Δz distribution therefore reflects resolution effects. In the Belle analysis, the histogrammed Δz distribution as measured in a control sample of J/ψ decays was employed as a lookup table to describe the resolution function.

Sources of backgrounds are B^+B^- events in which both the B^+ and the B^- decayed

semileptonically, opposite-side $B^0\overline{B}^0$ and B^+B^- cascade events in which only one B meson decayed semileptonically and the second lepton was created in a $b \to c \to \ell$ cascade of the other B meson, same-side cascade events in which both leptons were created in the decay chain of the same B meson and, finally, leptons from non-$B\overline{B}$ events. The background component from non-$B\overline{B}$ events was estimated in both analyses from data collected at a e^-e^+ collision energy below the $\Upsilon(4S)$ resonance. In the BaBar analysis, the components from semileptonic B^+B^- events and from same-side cascade events were each described in the fit by the convolution of an exponential function and the same resolution function that was used for the signal component. The component from opposite-side $B^0\overline{B}^0$ cascade events was described by a $\cos(\Delta m_d\,\Delta t)$ term convolved with a modified resolution function to take into account the finite lifetime of intermediate charm mesons. The component from opposite-side B^+B^- cascade events was described by the convolution of an exponential function with the same modified resolution function. In the Belle analysis, the different sources of backgrounds were grouped together according to their topology into same-sign and opposite-sign dilepton pairs from decays of charged B meson pairs and mixed and unmixed neutral B meson pairs. The decay-time distributions for each of these categories was derived from samples of simulated events, where an additional Gaussian smearing was applied to the reconstructed values of Δz to correct for a small difference in resolution that was found in the J/ψ control samples in simulated data and collision data.

The results of these two analyses are listed in Figure 5.13 under the labels "*BABAR* ℓ/ℓ" and "*BELLE* ℓ/ℓ", respectively. Due to the larger analysed data sample, the statistical uncertainty on the Belle measurement is slightly smaller than that on the BaBar measurement. Systematic uncertainties are of similar size and were found to be dominated by the knowledge of the lifetimes of charged and neutral B mesons, which were in both analyses fixed to their world average values at the time of the measurement, and by effects related to the understanding of the resolution functions.

BaBar **measurement using partially reconstructed semileptonic decays**

The BaBar collaboration also published an analysis [239] that was based on a data sample corresponding to 88 million produced $B\overline{B}$ pairs and searched for combinations of a high-momentum charged lepton and a low-momentum pion of opposite charge to tag semileptonic decays $B^0 \to D^{*-}\ell^+\nu_\ell$ with $D^{*-} \to \overline{D}^0\pi^-$. The D^0 candidate was not reconstructed, allowing large selection and reconstruction efficiencies. The decay vertex of the $B_{\rm rec}$ candidate was reconstructed from a fit to the tracks of the lepton and pion candidates, with a constraint on the beam spot position in the plane transverse to the beam axis. The position of the beam spot was determined on a run-by-run basis using samples of e^-e^+ interactions in which two charged particles were created. The χ^2 probability of this vertex fit was combined with the reconstructed momenta of the two particles in a likelihood variable to discriminate between signal and background. As a further discriminating variable, the squared invariant mass of the undetected neutrino was then estimated as

$$m_\nu^2 \;\equiv\; (E_{B^0} - E_{D^{*+}} - E_\ell)^2 \;-\; (\vec{p}_{D^{*+}} - \vec{p}_\ell)^2 \;\;,$$

where the energy E_{B^0} of the decaying B meson was substituted by half the e^-e^+ collision energy, the direction of flight of the D^{*-} meson was approximated by that of the pion and the absolute momentum, $|\vec{p}_{D^{*+}}|$, and energy, $E_{D^{*+}}$, of the D^{*-} meson were estimated from the measured momentum of the pion using a calibration derived from simulated samples of events. Within the precision of the approximations, m_ν^2 should yield values close to zero for signal decays, while a wide distribution extending to negative values is expected for random combinations of charged leptons and pions.

The composition of the sample of selected candidates was determined from a fit to the measured distribution of m_ν^2 as shown in Figure 5.11. The contribution from combinatorial

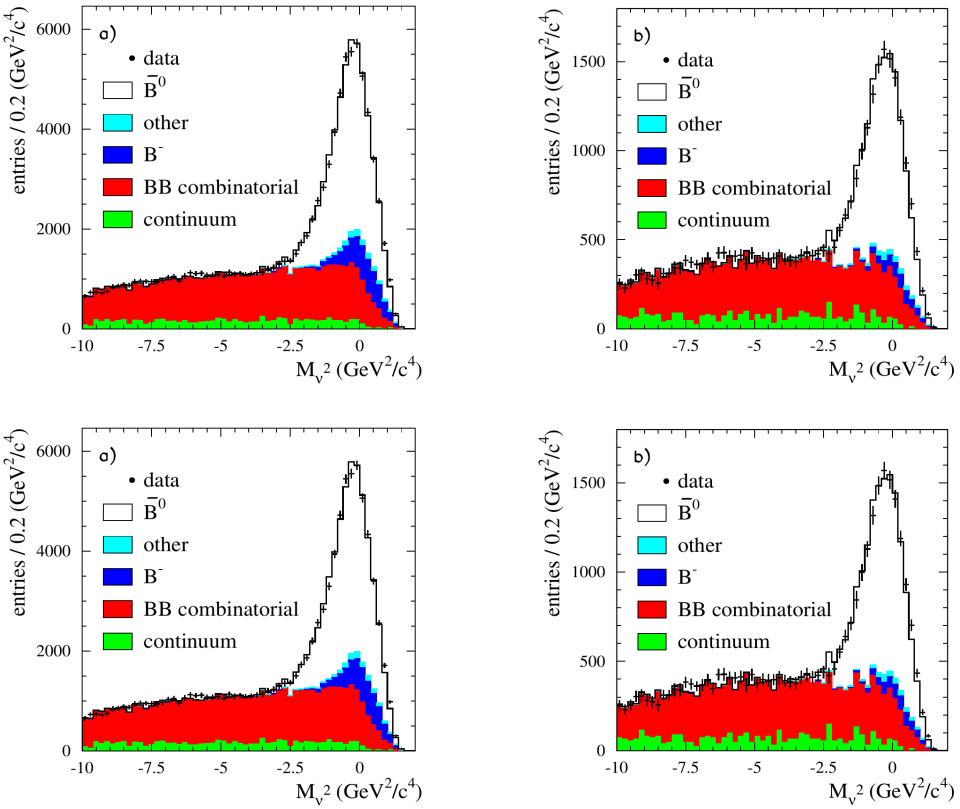

Figure 5.11: Distributions of (top) the missing invariant mass and (bottom) the cosine of the angle between the slow pion candidate and the tagging lepton candidate for events tagged as (left) unmixed and (right) mixed in the BaBar Δm_d analysis using partially reconstructed semileptonic decays. Different background contributions are indicated by the shaded areas according to the legends shown in the plots (from [239]).

background from non-$B\overline{B}$ events was determined from collision data collected at e^-e^+ collision energies below the $\Upsilon(4S)$ resonance. The shape of the distribution for combinatorial background from $B\overline{B}$ events was determined from simulated samples of events and cross-checked on collision data using combinations of high-momentum leptons and low-momentum pions of equal charge sign. The shapes of the signal component and of background contributions peaking in m_ν^2 were determined from simulated samples of events. Besides the decay mode $B^0D^{*-}\ell^+\nu_\ell$, the signal component included contributions from the decay mode $B^0D^{*-}\pi^0\ell^+\nu_\ell$, from hadronic decays $B^0 \to D^{*-}h^-$ with the hadron h^- being misidentified as a lepton, and from decay modes $B^0 \to D^{*-}\tau^+\nu_\tau$, $B^0 \to D^{*-}D_s^+$ and $B^0 \to D^{*-}DX$ with the τ^+, D_s^+ or D meson decaying into a final state including a charged lepton. Background contributions peaking in the m_ν^2 distribution were dominated by the decay mode $B^+ \to D^{*-}\pi^+\ell^+\nu_\ell$ and decays of the type $B^+ \to D^{*-}\pi^+X$ in which the pion was misidentified as a charged lepton. The partial reconstruction of the candidates does not allow to distinguish between $B^0D^{*-}\pi^0\ell^+\nu_\ell$ and $B^+ \to D^{*-}\pi^+\ell^+\nu_\ell$. The relative ratio between these two contributions was therefore constrained to 1 : 2 assuming isospin conservation. Out of a total of 77'000 reconstructed and flavour-tagged candidates with $m_\nu^2 > -2.5$, the fit assigned about 20'000 candidates to the various background components.

Flavour tagging relied on the charge of a second high-momentum lepton in the remainder of the event, no other flavour tagging algorithms were invoked. The position of the B_{tag} decay vertex along the beam axis was approximated by the point of closest approach of the tagging lepton to the position of the beam spot in the r–ϕ plane. The decay time difference, Δt, was estimated from the distance of the two decay vertex positions along the beam axis and

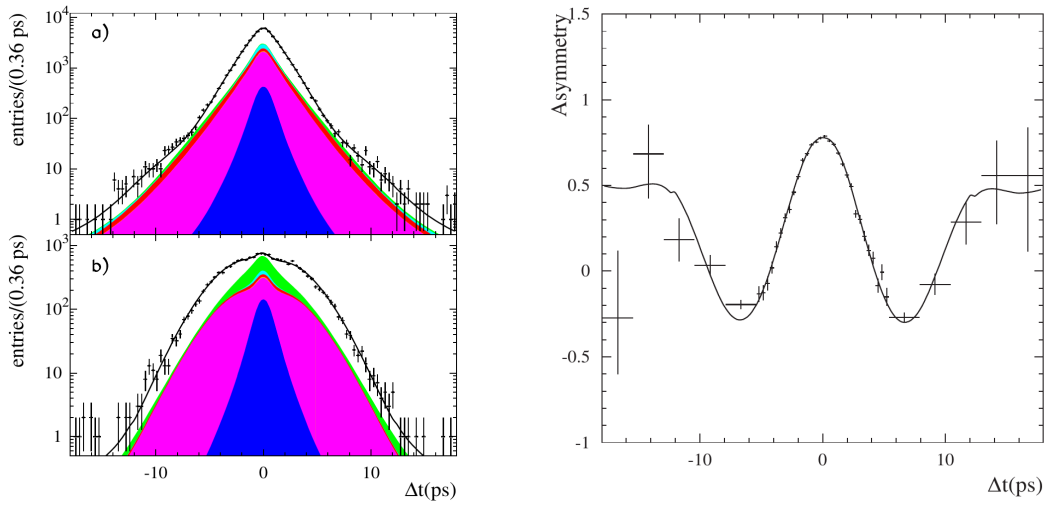

Figure 5.12: Distributions of (left) Δt for events tagged as (top) unmixed and (bottom) mixed and (right) the resulting mixing asymmetries from the BaBar Δm_d measurement using partially reconstructed semileptonic decays. The solid lines show the projection of the maximum likelihood fit to the data. In the Δt distributions, different background components are indicated by shaded areas, where the legend is the same as in the lower plots in Figure 5.11 above (from [239]).

the boost of the $\Upsilon(4S)$ rest frame in the laboratory system. In addition, an estimate of the decay-time uncertainty, $\sigma_{\Delta t}$, was derived from the estimated uncertainties on the positions of the two vertices.

The value of Δm_d was extracted from the data by a maximum-likelihood fit in bins of Δt and $\sigma_{\Delta t}$. The signal component was described in the fit by a term proportional $\cos(\Delta m\,\Delta t)$, convolved with the sum of three Gaussian distributions to model the decay-time resolution. A second term was included in the fit function to describe combinations of $\ell\pi$ signal candidates with a wrongly identified tagging lepton from the decay chain of the $B_{\rm tag}$ meson. Such leptons are mostly due to cascade decays $b\to c\to\ell$ and tend to have the opposite charge to the lepton from the semileptonic decay of the b quark. This contribution was therefore described in the fit by a term proportional to $-\cos(\Delta m\,\Delta t)$, convolved with a sum of three Gaussian functions. The widths and fractions of these Gaussians were fixed to be the same as for the signal component but their offsets were allowed to float independently to take into account the finite lifetime of the intermediate charm meson. A third term was included to take into account combinations of $\ell\pi$ signal candidates with wrongly identified tagging leptons from the decay chain of the D^* signal candidate. Such leptons tend to be emitted at a small angle with respect to the flight direction of the D^* meson and their fraction in the sample of selected candidates was estimated from a fit to the measured distribution of $\cos\theta_{\pi\ell}$ as shown in Figure 5.11, where $\theta_{\pi\ell}$ is the opening angle between the low-momentum pion and the tagging lepton candidates. In the fit to the decay-time distribution, this component was described by an exponential function convolved with a sum of three Gaussian functions. The component of the peaking background was similarly split into three terms according to the source of the tagging lepton. All three terms were described by exponential functions convolved with sum of three Gaussian functions, where the parameters of these Gaussian functions were fixed to be the same as those of the corresponding components describing the signal contribution. Combinatorial background contributions from B^+B^- and $B^0\overline{B}^0$ events were taken into account by another set of terms of the same functional form as those for the peaking background, but with independent fit parameters. Finally, background from non-$B\overline{B}$ events was parametrized by anothr exponential function convolved with a sum of three Gaussian functions.

The measured Δt distributions for mixed and unmixed events and the mixing asymmetry as a function of Δt are shown in Figure 5.12 together with the results of the fit. The result of

this analysis in terms of Δm_d is listed in Figure 5.13 under the label "*BABAR* $D^*\ell\nu$*(part)*/ℓ". Systematic and statistic uncertainties were found to contribute equally to the uncertainty on the measurement. Systematic uncertainties were found to be dominated by the understanding of the length scale and alignment of the detector, the statistical uncertainty on the determination of possible fit biases from simulated samples of events, observed variations in the result of the fit when varying the fit ranges in Δt and $\sigma_{\Delta t}$, the description of outliers in the decay-time resolution, and the description of the contamination due to wrong tagging leptons from cascade decays of B_{tag}.

Measurements at LHCb

In the meantime, the most precise measurement of Δm_d stems from an LHCb analysis based on the 2011 data sample, corresponding to an integrated luminosiy of 1 fb^{-1} collected in proton-proton collisions at a centre-of-mass energy of 7 TeV. The analysis strategy was similar to that of Δm_s measurements in LHCb, which will be described in the next section. B_{rec} candidates were reconstructed in the flavour-specific hadronic decay modes $B^0 \to D^-\pi^+$ with $D^- \to K^+\pi^-\pi^-$ and $B^0 \to J/\psi K^{*0}$ with $J/\psi \to \mu^+\mu^-$ and $K^{*0} \to K^+\pi^-$. To suppress backgrounds from misidentified decays $B_s^0 \to J/\psi\phi$, $K^+\pi^-$ candidates were rejected if their invariant mass was compatible with the nominal ϕ mass when the kaon mass hypothesis was applied to the pion candidate. The selection of $D^-\pi^+$ candidates was based on the response of a multi-variate classifier that combined discriminating variables related to the quality of the B^0 and D^- vertex reconstructions, the displacement of the B^0 decay vertex from the primary pp interaction vertex and the consistency between the directions of the reconstructed B^0 and D^- momentum vectors and the B^0 and D^- flight directions as determined from the lines connecting their respective production and decay vertices. This multivariate classifier was trained on collision data using a sample of $B_s^0 \to D_s^-\pi^+$ candidates with $D_s^- \to K^-K^+\pi^-$. Potential backgrounds from misidentified $D_s^- \to K^-K^+\pi^-$ decays in the $B^0 \to D^-\pi^+$ signal sample were suppressed by vetoing all reconstructed candidates for which one of the final-state pions passed loose kaon identification requirements and which yielded an invariant mass compatible with the nominal D_s^- mass when the kaon mass hypothesis was applied for this pion. Finally, the reconstructed decay time of the B_{rec} candidate was required to be larger than 0.3 ps. This cut significantly reduces backgrounds from random combinations of particles from the primary proton-proton interaction at only a small loss in sensitivity. Events at short decay times carry little information on the flavour oscillation since the mixing asymmetry, proportional to the cosine of the decay time, changes only slowly at small decay times.

The initial flavour of the B_{rec} candidate was derived from a combination of opposite-side flavour tagging algorithms and a same-side pion tagging algorithm as described in Section 4.4.5.

The value of Δm_d was extracted from a simultaneous maximum-likelihood fit to the invariant mass distribution and the measured mixing asymmetry as a function of the reconstructed decay time of the B_{rec} candidates. The fit procedure was similar to that employed in the Δm_s anlyses described below. The fit yielded about 88'000 signal candidates in the $B^0 \to D^-\pi^+$ decay mode and 40'000 signal candidates in the $B^0 \to J/\psi K^{*0}$ decay mode. The values of Δm_d obtained in the $D^-\pi^+$ and $J/\psi K^{*0}$ samples were found to be compatible within their statistical uncertainties. The assigned systematic uncertainties were dominated by the modeling of the fit function and by the knowledge of the length scale of the detector. Systematic effects related to the decay time resolution were small due to the resolution of 0.05 ps which to the $B^0-\overline{B}^0$ oscillation period of 12 ps. The combined result of the measurement is quoted in Figure 5.13 as "*LHCb* B_d^0*(full)/OST,SST*".

As shown in Figure 5.13, the results from different experiments and from different final states are in good agreement with each other. The Heavy Flavour Averaging Group determine a world average of

$$\Delta m_d \;=\; 0.510 \,\pm\, 0.003 \text{ ps}^{-1} \;,$$

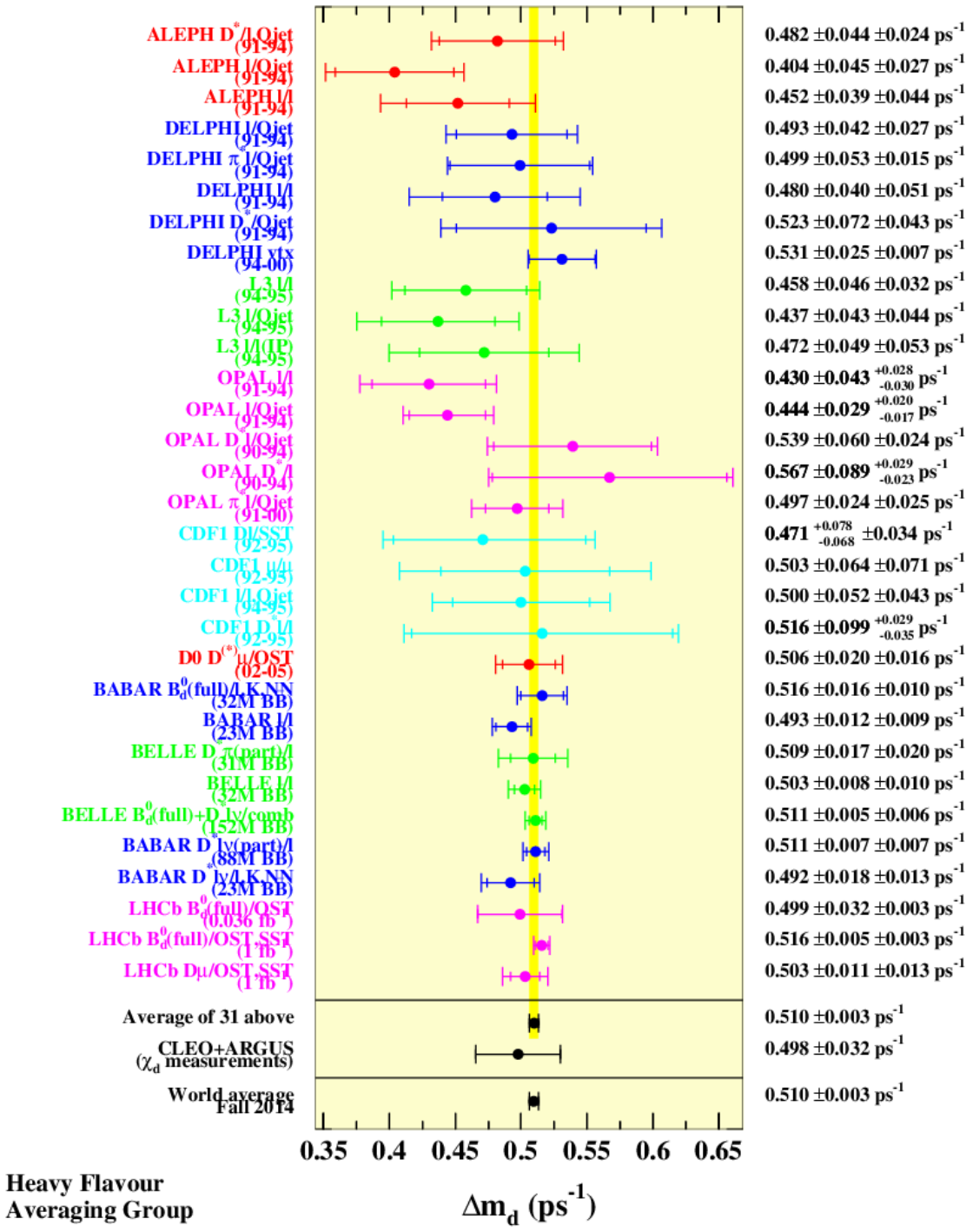

Figure 5.13: List of Δm_d measurements and their average as compiled by the Heavy Flavour Averaging Group [2] in autumn 2014.

which has a relative uncertainty of less than 0.65%.

5.1.2 Measurements of Δm_s

The basic approach for measurements of time-dependent asymmetries at hadron colliders has been described in Section 4.2. In hadron-hadron interactions, $b\bar{b}$ quark pairs are not produced in an entangled state. They evolve independently from each other and hadronize into any combination of a b hadron and a $\bar{b}$ hadron. Measurements of the $B_s^0 - \overline{B}_s^0$ oscillation frequency

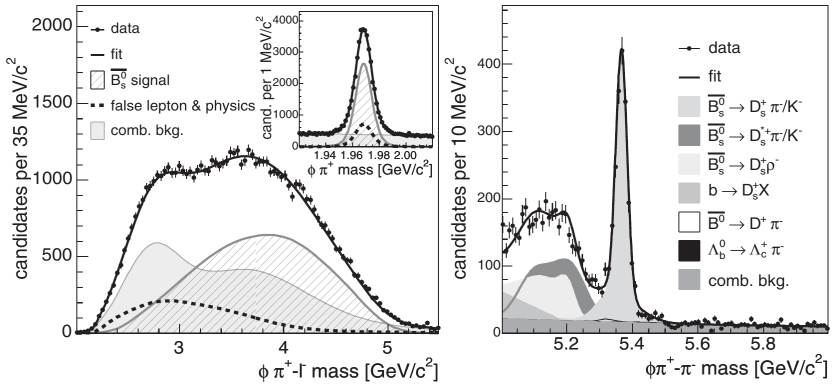

Figure 5.14: Invariant mass distributions for $B_{\rm rec}$ candidates from the measurement of Δm_s in CDF II, reconstructed in (left) semileptonic and (right) hadronic final states with $D_s^- \to \phi\pi^-$. The different signal and background contributions are described in the plot legends (from [245]).

are performed in samples of events in which a $\overline{B}_s^0$ or B_s^0 meson was created, which could then be reconstructed in a decay to a flavour-specific final state. The reconstructed B_s^0 or $\overline{B}_s^0$ meson will again be referred to as $B_{\rm rec}$ in the following.

The mixing asymmetry is measured as a function of the reconstructed decay time of the $B_{\rm rec}$ candidate with respect to its production in the hadron-hadron collision. This requires the reconstruction of the momentum of the $B_{\rm rec}$ candidate, of the position of its decay vertex and of the position of the hadron-hadron interaction vertex in which it was produced. The position of the production vertex can be reconstructed with good precision using the tracks of other charged particles produced in the same hadronic interaction as the $B_{\rm rec}$ candidate. To achieve the excellent decay time resolution that is required to resolve the rapid $B_s^0 - \overline{B}_s^0$ oscillations, $B_{\rm rec}$ candidates are best reconstructed in exclusive hadronic final states in which all decay products are measured, permitting a precise determination of the $B_{\rm rec}$ momentum.

The flavour-tagging algorithms that are employed to infer the initial flavour of the $B_{\rm rec}$ candidate, i.e. its quark content at the time of its production in the hadron-hadron collision, have been discussed in Sections 4.3.5 and 4.4.5. Opposite-side tagging algorithms rely on flavour-specific signatures from the decay of the opposite-side b hadron, $b_{\rm tag}$, while same-side kaon tagging algorithms search for a charged kaon produced in the hadronization process leading to the reconstructed B_s^0 or $\overline{B}_s^0$ candidate.

The first two-sided bound on the value of Δm_s was obtained by the D0 collaboration [251] at run II of the Tevatron. The first observation of a significant oscillation signal and the first measurement of Δm_s were reported by the CDF II collaboration soon after. Measurements of Δm_s at CDF II and at LHCb will be described in the remainder of this section.

Measurements at CDF II

The analyses that lead to the first observation of $B_s^0 - \overline{B}_s^0$ oscillations and the first measurement of Δm_s at the CDF II experiment [245, 246] were based on a data set corresponding to an integrated luminosity of 1 fb^{-1}, collected in $p\overline{p}$ collisions at a centre-of-mass energy of 1.96 TeV. They employed a combination of fully reconstructed hadronic decay modes $B_s^0 \to D_s^-\pi^+$ and $B_s^0 \to D_s^-\pi^+\pi^-\pi^+$ and semileptonic decay modes $B_s^0 \to D_s^-\ell^+\nu_\ell$, in each case followed by $D_s^- \to \phi\pi^-$, $D_s^- \to K^{*0}K^-$ and $D_s^- \to \pi^-\pi^+\pi^-$, with $\phi \to K^+K^-$ and $K^{*0} \to K^+\pi^-$. In the second of the two analyses, described in Ref. [245], also partially reconstructed hadronic decays $B_s^0 \to D_s^{*-}\pi^+$ and $B_s^0 \to D_s^-\rho^+$ were considered, where the neutral pion or photon from the subsequent decays $D_s^{*-} \to D_s^-\pi^0$, $D_s^{*-} \to D_s^-\gamma$ or $\rho^+ \to \pi^+\pi^0$ was not reconstructed. In all these decay modes, the charges of the final-state particles identify the flavour of the $B_{\rm rec}$ candidate at the time of its decay.

At the L1 trigger level, candidates were selected by the requirement of two oppositely charged tracks with transverse momenta above a certain threshold and the scalar sum of their transverse momenta above a second threshold. The L2 trigger decision relied on the SVT described in Section 4.3.3 and required two tracks that had a relative opening angle between 2° and 90°, significant impact parameter with respect to the beam axis and formed a vertex in the r–ϕ plane that was significantly displaced from the beam axis. At the L3 trigger level, the decisions from the L1 and L2 levels were confirmed from a complete event reconstruction. The offline selection of $B_{\rm rec}$ candidates was then based on the invariant masses of the D_s^-, ϕ and K^{*0} candidates, the reconstructed transverse momenta of the $B_{\rm rec}$ candidate and its decay products, the quality of the reconstructed $B_{\rm rec}$ and D_s^- decay vertices and their displacement from the reconstructed position of the $p\overline{p}$ interaction vertex. In the second of the two analyses, also kaon identification information was employed, which allowed to relax kinematic selection requirements and significantly increase the selection efficiencies. In the case of the hadronic decay modes, the selection criteria were combined in a multivariate classifier, which was trained on samples of simulated signal events and background from the upper sidebands in the distribution of the reconstructed invariant mass of $B_{\rm rec}$ candidates.

As an example, the measured invariant-mass distributions for $B_{\rm rec}$ candidates reconstructed in the decay mode $D_s^- \to \phi\pi^-$ are shown in Figure 5.14. The effect of the not reconstructed missing final-state particles is clearly visible in the invariant mass distributions for the semileptonic and partially reconstructed hadronic decays modes and is significantly more pronounced in the former sample than in the latter. The decay time of the $B_{\rm rec}$ candidates was calculated from its measured decay length and momentum. In the case of partially reconstructed hadronic and semileptonic decay modes, the decay time calculated in this manner is biased since the momentum of the $B_{\rm rec}$ candidate is not fully measured. As this bias cannot be corrected on an event-by-event basis, the calculated decay time was convolved in the fit for the oscillation signal with the distribution of a correction factor derived from simulated samples of events.

The search for a $B_s^0 - \overline{B}_s^0$ oscillation signal and the measurement of Δm_s made use of simultaneous unbinned maximum-likelihood fits to the reconstructed invariant mass and the decay time of the selected $B_{\rm rec}$ candidates. Combining all D_s^- decay modes, the fit assigned to the signal component 5'600 fully reconstructed and 3'100 partially reconstructed hadronic decays and 61'500 candidates in the semileptonic decays. The decay-time distribution of the signal component was parametrized in this fit as

$$P_{\rm sig}(t) \;=\; \epsilon(t) \;\times\; \left\{ \frac{\overline{\Gamma}_s}{2}\, e^{-\overline{\Gamma}_s t} \left[1 \;+\; A \cdot q_{\rm tag}\,(1 - 2\omega_{\rm tag}) \cdot \cos\left(\Delta m_s t\right) \right] \right\} \;\otimes\; G(t\,|\,0, \sigma_t)$$

where $q_{\rm tag} = +1$ for events tagged as unmixed and $q_{\rm tag} = -1$ for events tagged as mixed, A is the fitted amplitude of the oscillation, $\epsilon(t)$ describes the decay-time dependence of the reconstruction efficiency, $\omega_{\rm tag}$ is an event-by-event estimate of the mistag probability, σ_t is an event-by-event estimate of the decay-time resolution, and $G(t\,|\,0, \sigma_t)$ denotes a Gaussian probability density function with mean 0 and event-dependent standard deviation σ_t.

The decay-time dependence of the reconstruction efficiency was determined from simulated samples of events. The initial flavour of the $B_{\rm rec}$ candidate at the time of its production was derived from a combination of opposite-side flavour tagging algorithms and a same-side kaon tagging algorithm as described in Section 4.3. The estimated mistag probability returned by the opposite-side tagging algorithms was calibrated using samples of $B^\pm$ decays and flavour-specific decays of B^0 and $\overline{B}^0$ mesons, assuming that the performance of the tagging algorithms is independent on the hadronization and decay of $B_{\rm rec}$. This assumption could not be made for the same-side kaon tagging algorithm and the estimated mistag probability returned by this algorithm was therefore derived from simulated samples of events.

An event-by-event estimate of the uncertainty on the decay time measurement was derived from the parameters returned by the track fit. A constant correction factor was applied to

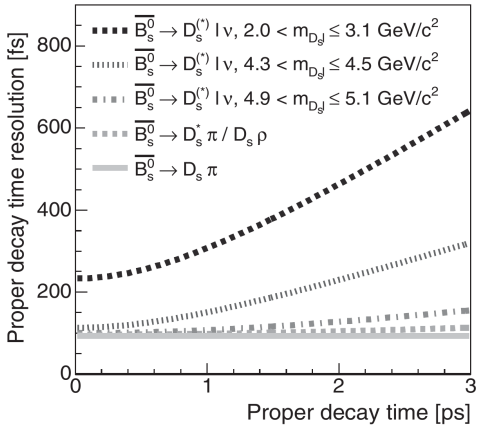

Figure 5.15: Estimated decay-time resolution as a function of the value of the decay time for $B_{\rm rec}$ candidates in fully reconstructed hadronic decay modes $B_s^0 \to D_s^- \pi^+$, in partially reconstructed decay modes $B_s^0 \to D_s^{*-} \pi^+ / D_s^- \rho^+$ and in semileptonic decay modes $B_s^0 \to D_s^- \ell^+ \nu_\ell$. The latter sample is further subdivided into different ranges of the reconstructed invariant mass, $m_{D_s \ell}$, of the $D^- \ell^+$ system. A small value of $m_{D_s \ell}$ indicates that the unreconstructed particles carried away a large fraction of the $B_{\rm rec}$ momentum, while a value of $m_{D_s \ell}$ close to the mass of the B_s^0 meson implies that only small fraction of the $B_{\rm rec}$ momentum could have been carried away by the unreconstructed particles (from [245]).

this estimate to compensate for the fact that the track fit cannot perfectly model effects from the interactions of particles with the material of the detector or from possible residual misalignments. This correction factor was derived from collision data using a large sample of fake signal candidates that were formed by combining one or three charged tracks and a prompt D^- candidate from the primary $p\overline{p}$ interaction vertex. The true decay time for these fake signal candidates is zero and the distribution of the measured decay times gives a good estimate for the true decay-time resolution. Including the correction factor, the average decay-time resolution for fully reconstructed hadronic decays was estimated to be 87 ps. The decay-time resolution for partially reconstructed hadronic and semileptonic decays was worse and deteriorated with increasing value of the decay time due to the spread in the missing momentum from not reconstructed particles. The estimated decay-time resolution as a function of the decay time is shown in Figure 5.15.

The search for an oscillation pattern followed an approach that had initially been developed for flavour-oscillation searches at LEP [252] and consisted in a modified Fourier analysis of the decay-time spectrum. The value of the oscillation amplitude, A, was determined from a series of maximum likelihood fits to the measured decay time distribution as a function of the assumed value of Δm_s. Provided that dilution effects due to the finite decay time resolution and non zero mistag fraction are correctly calibrated, the fit should yield a value consistent with $A = 1$ at the true value of the oscillation frequency and values close to $A = 0$ otherwise. The result of the measurement at CDF II is shown in Figure 5.16. A clear signal was observed at a value of $\Delta m_s = 17.77$ ps^{-1}, where the fitted value of the amplitude, $A = 1.21 \pm 0.20\,(\text{stat})$, is compatible with $A = 1$ and deviates from $A = 0$ with $A/\sigma_A = 1.21/0.20 = 6.05$ standard deviations. Systematic uncertainties on A and σ_A were dominated by effects related the understanding of the decay-time resolution and the mistag fraction. They cancel to first order in the ratio A/σ_A and therefore have negligible impact on the significance of the signal. The lower right panel in Figure 5.16 shows the logarithm of the ratio of the likelihoods calculated for fixed values of $A = 0$ and of $A = 1$ for the full event sample and separately for the samples of hadronic final states and semileptonic final states. It demonstrates that the significance of the signal at $\Delta m_s = 17.77$ ps^{-1} is essentially entirely due to the hadronic final states. The statistical uncertainty on the measured value of Δm_s was determined by fixing the value of the amplitude to $A \equiv 1$ and repeating the fit with Δm_s as free fit parameter.

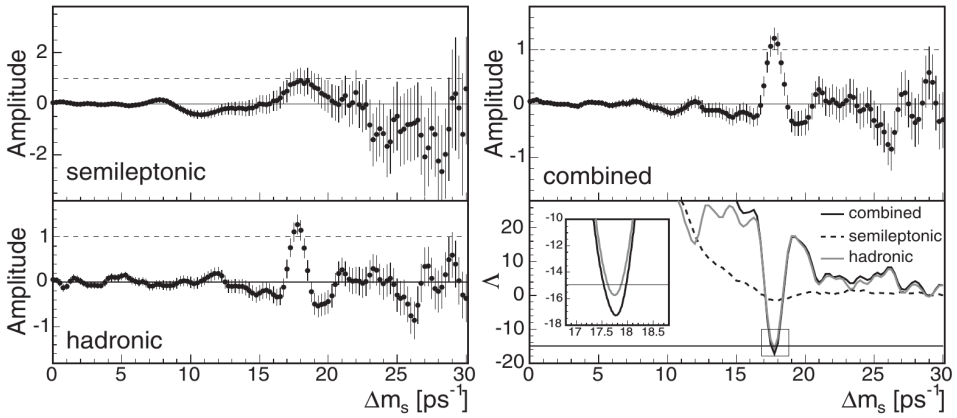

Figure 5.16: Results of the amplitude fit employed in the CDF II measurement of Δm_s. The panels on the left and the top right show the fitted value of the oscillation amplitude and its uncertainty as a function of the assumed value of Δm_s in the hadronic, semileptonic and combined event samples, respectively. Error bars indicate the statistical uncertainty σ_A returned by the fit. The lower right panel shows the logarithm, Λ, of the ratio of the likelihoods for $A = 0$ and for $A = 1$ as a function of the assumed value of Δm_s, for the full data sample and for the hadronic and semileptonic samples separately. The dashed horizontal line at $\Lambda = -15$ corresponds to a probability of 5.7×10^{-7} or five Gaussian standard deviations of observing a signal of this amplitude or larger in a sample of randomly tagged candidates (from [245]).

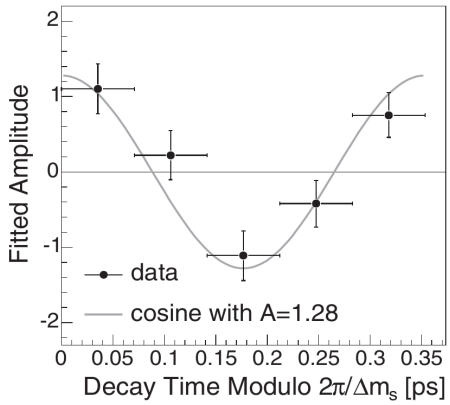

Figure 5.17: Values of the mixing amplitude obtained from fits to the fully reconstructed hadronic sample in five bins of the reconstructed decay time modulo the measured oscillation period from the CDF II analysis of Δm_s. The superposed cosine curve uses parameters from the full Δm_s fit to the fully hadronic sample (from [245]).

Systematic uncertainties on Δm_s due to the knowledge of the absolute scale of the decay time measurement were investigated, including possible biases on the reconstruction of the primary $p\overline{p}$ interaction vertex due to the possible inclusion in the vertex fit of decay products from the opposite-side b hadron, uncertainties in the alignment of the silicon vertex detector, and biases in track fitting. The final result of the measurement was quoted as

$$\Delta m_s \;=\; 17.77 \,\pm\, 0.10\,(\text{stat}) \,\pm\, 0.07\,(\text{syst})\ \text{ps}^{-1}\ .$$

The central value of this result corresponds to an oscillation period of 363 fs, about four times the average decay time uncertainty for fully reconstructed hadronic decays.

Measurements at LHCb

The first measurement of the $B_s^0 - \overline{B}_s^0$ oscillation frequency published by the LHCb collaboration [247] was based on the data set collected in the year 2010, corresponding to an inte-

grated luminosity of only 0.036 fb^{-1}. A total of 1380 fully reconstructed $B_s^0 \to D_s^- \pi^+$ and $B_s^0 \to D_s^- \pi^+ \pi^- \pi^+$ candidates was extracted and, despite the small analyzed data set, the precision of the Δm_s measurement was already superior to that of the CDF II result. The comparison serves to underline the importance of the decay-time resolution for measurements of time-dependent asymmetries in the $B_s^0 \overline{B}_s^0$ system. In the LHCb analysis, the average decay time resolution for fully reconstructed $B_s^0 \to D_s^- \pi^+$ decays was found to be 44 fs, a factor of two better than that achieved in the analysis at CDF II. The superior decay time resolution is partially due to the larger Lorentz boost with which the B_s^0 mesons are produced in LHCb (see Figure 4.22) and partially due to the excellent vertex resolution resulting from the layout and design of the LHCb vertex detector described in Section 4.4.

A second measurement of Δm_s using fully reconstructed hadronic decays [248] was performed using the 2011 data set, corresponding to an integrated luminosity of 1 fb^{-1} collected at a pp collision energy of 7 TeV. The analysis was based on the decay modes $B_s^0 \to D_s^- \pi^+$ followed by $D_s^- \to \phi\pi^-$, $D_s^- \to K^{*0}\pi^-$, $D_s^- \to K^-K^+\pi^-$, $D_s^- \to K^-\pi^+\pi^-$ and $D_s^- \to \pi^-\pi^+\pi^-$, with $\phi \to K^+K^-$ and $K^{*0} \to K^+\pi^-$. Candidates were selected at the software trigger level by requiring a good-quality secondary vertex that was significantly displaced from the reconstructed pp interaction vertex and was formed by two, three or four reconstructed tracks which fulfilled requirements on their transverse momenta. The selection of signal candidates in the offline reconstruction made use of a multivariate classifier that combined information on the significance of the impact parameters of the final-state particles with respect to the reconstructed pp interaction vertex, the displacement of the decay vertices of the $B_{\rm rec}$ and D_s^- candidates in the plane transverse to the beam axis, and the angle between the reconstructed momentum vector of the $B_{\rm rec}$ candidate and the line connecting the pp interaction vertex with the reconstructed decay vertex of the $B_{\rm rec}$ candidate. Additional requirements were placed on the reconstruction quality of tracks and vertices, on particle identification criteria, on the sum of the transverse momenta of the final state particles and on the reconstructed invariant masses of intermediate particles. The measured invariant-mass distributions of $B_{\rm rec}$ candidates in each of the five decay modes are shown in Figure 5.18. A total of about 34'000 candidates was selected in the five decay modes. The background contamination in the signal region was found to be small and to consist of combinatorial background from random combinations of particles and of B^0 and Λ_b decays with a misidentified final-state particle. The combinatorial background was estimated by extrapolation from the upper sidebands in the invariant-mass distribution of the $B_{\rm rec}$ candidates, while the contributions from misidentified B^0 and Λ_b decays were estimated from samples of simulated events.

The value of Δm_s was extracted from a simultaneous fit to the measured invariant-mass and decay-time distributions of $B_{\rm rec}$ candidates in the five considered decay modes. The decay-time distribution of the signal component was described in the fit as

$$P_{\rm sig}(t) \;=\; \left\{ \frac{\overline{\Gamma}_s}{4}\, e^{-\overline{\Gamma}_s t} \left[\cosh\left(\frac{\Delta\Gamma_s}{2} t\right) \,+\, q_{\rm tag}(1-2\omega_{\rm tag}) \cdot \cos\left(\Delta m_s t\right) \right] \right\} \,\otimes\, G(t\,|\,0,\sigma_t) \,\times\, \epsilon(t)\ ,$$

where $\Delta\Gamma_s$ is the decay-width difference between the two mass eigenstates in the $B_s^0 \overline{B}_s^0$ system, $q_{\rm tag} = +1$ for events tagged as unmixed and $q_{\rm tag} = -1$ for events tagged as mixed, $\omega_{\rm tag}$ is the calibrated estimate of the mistag probability, σ_t is the calibrated estimate of the decay-time resolution and $G(t\,|\,0,\sigma_t)$ describes a Gaussian probability density function with mean zero and standard deviation σ_t. Finally, $\epsilon(t)$ describes the decay-time dependence of the reconstruction efficiency.

The value of $\Delta\Gamma_s$ was fixed in the fit to that found in an LHCb measurement of CP violating asymmetries in the $B_s^0 \overline{B}_s^0$ system, which will be described in Section 6.1. Flavour tagging relied on a combination of opposite-side tagging algorithms and a same-side kaon tagging algorithm as described in Section 4.4. The event-by-event estimate of the mistag probability, $\eta_{\rm tag}$, returned

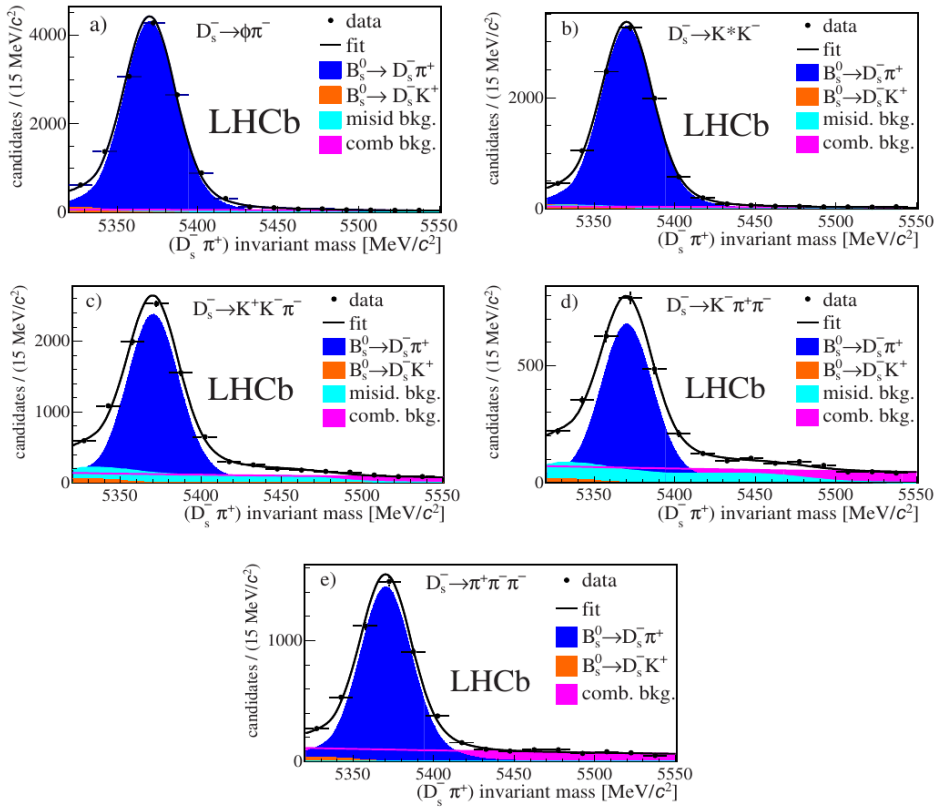

Figure 5.18: Distributions of the $D_s^-\pi^+$ invariant mass for selected candidates in the five D_s^- decay modes utilized in the LHCb measurement of the $B_s^0-\overline{B}_s^0$ oscillation frequency, Δm_s, in the decay $B_s^0\to D_s^-\pi^+$. The respective D_s^- decay modes are listed in each of the five panels. Different shadings indicate the signal component and different background components as described in the plot legends, where "misid. bkg." refers to background from B^0 and Λ_b decays with a misidentified final-state particle and "comb. bkg." refers to combinatorial background from random combinations of final-state particles (from [248]).

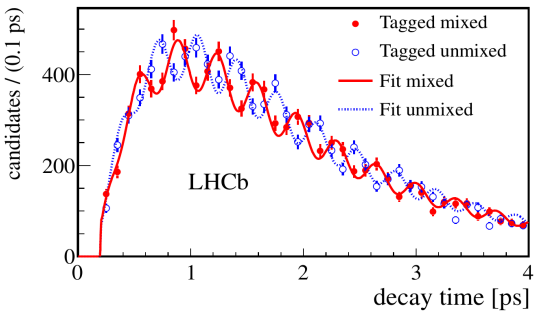

Figure 5.19: Decay-time distributions for signal candidates tagged as mixed and signal candidates tagged as unmixed, from the LHCb messurement of the $B_s^0-\overline{B}_s^0$ oscillation frequency, Δm_s in the decay $B_s^0\to D_s^-\pi^+$. The expected oscillation pattern is clearly visible over several oscillation periods. The plotted lines show the projection of the fit result (from [248]).

by each of the two algorithms was calibrated by parametrizing it in the fit for Δm_s as

$$\omega_{\rm tag} \equiv p_0 + p_1(\eta_{\rm tag} - \langle\eta_{\rm tag}\rangle) ,$$

where p_0 and p_1 were free fit parameters. Finally, the event-by-event estimate of the decay-time resolution, σ_t, was derived from the output of the track and vertex fitting algorithms and was calibrated on collision data in a similar manner as in the measurement at CDF II described in the previous paragraphs: fake $B_{\rm rec}$ candidates were formed by combining a prompt D_s^- candidate with a random track from the same pp interaction vertex and the measured decay times for these candidates were used as an estimate for the true decay-time resolution. Including this calibration, the average decay time resolution was found to be 44 fs, as in the first LHCb measurement. The decay-time acceptance, $\epsilon(t)$, was described by a functional form derived from samples of simulated events.

The result of the fit for Δm_s is shown in Figure 5.19. A clear oscillation signal is visible over a total of ten oscillation periods. Systematic uncertainties on Δm_s were found to be dominated by the knowledge of the absolute length scale of the vertex detector and the momentum scale of the spectrometer. The first contribution was estimated from comparisons of survey data with the results of a track-based alignment and by studies of track distributions in the vertex detector, the second was estimated from a dedicated study that compared the reconstructed invariant-mass spectra for various narrow resonances with well established known masses to calibrate the momentum scale of the LHCb spectrometer. A smaller contribution to the systematic uncertainty was found to be possible biases on the reconstructed decay time due to selection criteria and reconstruction algorithms. Other possible sources of systematic uncertainties were investigated but were found to be negligible. The result of the measurement,

$$\Delta m_s = 17.768 \pm 0.023\,({\rm stat}) \pm 0.006\,({\rm syst})\ {\rm ps}^{-1} .$$

dominates the current knowledge on the value of Δm_s.

As another proof of the detector performance, the LHCb collaboration also published a measurement of Δm_s based on a sample of semileptonic decays $B_s^0 \to D_s^- \mu^+ X$ that was extracted from the data collected in 2011 [244]. The analysis searched for $D_s^-\mu^+$ candidates originating from a common decay vertex, where D_s^- candidates were reconstructed in the decay $D_s^- \to K^-K^+\pi^-$. Selection criteria were applied on the quality of the track and vertex reconstruction, on particle-identification information and on the momenta of the reconstructed particles, on invariant masses, and on the displacements of the reconstructed decay vertices. The distribution of the reconstructed $K^+K^-\pi^+$ invariant-mass for selected $K^-K^+\pi^-\mu^+$ candidates is shown in Figure 5.20. Clean signals are observd at the known D^- and D_s^- masses, over a flat combinatorial background formed by random $K^-K^+\pi^-$ combinations. The sample was split into two by placing a cut at an invariant mass in between the D^- and D_s^- signals. Candidates in the upper part of the invariant-mass spectrum were used to search for the $B_s^0 - \overline{B}_s^0$ oscillation signal and measure its frequency, while candidates in the lower part of the spectrum were employed for a simultaneous measurement of the $B^0 - \overline{B}^0$ oscillation frequency, Δm_d. Figure 5.20 also shows the distribution of the normalized $K^-K^+\pi^-\mu^+$ invariant-mass, defined as

$$n \equiv \frac{m(K^-K^+\pi^-\mu^+) - m_D - m_\mu}{m_B - m_D - m_\mu}$$

where m_B, m_D and m_μ are the nominal masses of the $B_{(s)}^0$ and $D_{(s)}^-$ meson and the muon, respectively. Fully reconstructed candidates should be distributed around $n = 1$, while in fact a broad distribution is observed as not all final-state particles are reconstructed. A correction factor was applied to the reconstructed $B_{\rm rec}$ candidate momentum to reduce the effect of the missing particles on the decay-time resolution. This correction factor was parametrized as a function of the observed $K^-K^+\pi^-\mu^+$ invariant mass and was determined from samples

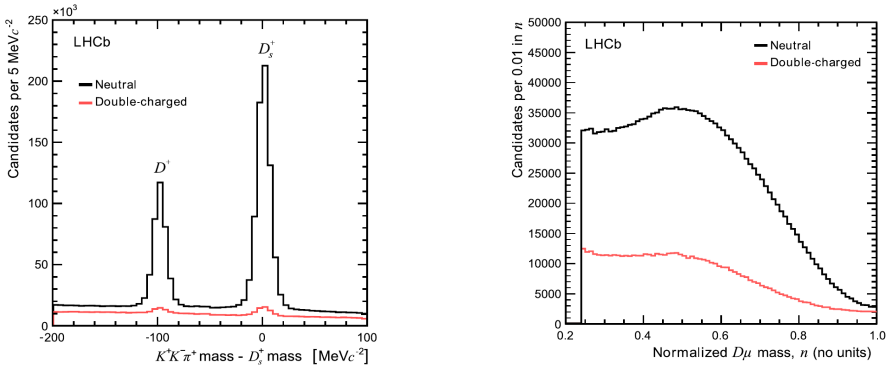

Figure 5.20: Distributions of (left) the $K^-K^+\pi^-$ invariant mass and (right) the normalized $K^-K^+\pi^-\mu^\pm$ invariant mass defined in the text, for $K^-K^+\pi^-\mu^\pm$ candidates from the LHCb analysis using semileptonic decays. "Neutral" refers to signal candidates in which the $K^-K^+\pi^-$ combination and the muon have opposite charge, "double-charged" refers to a background sample of candidates formed by a $K^-K^+\pi^-$ combination and a muon with same charge (from [244]).

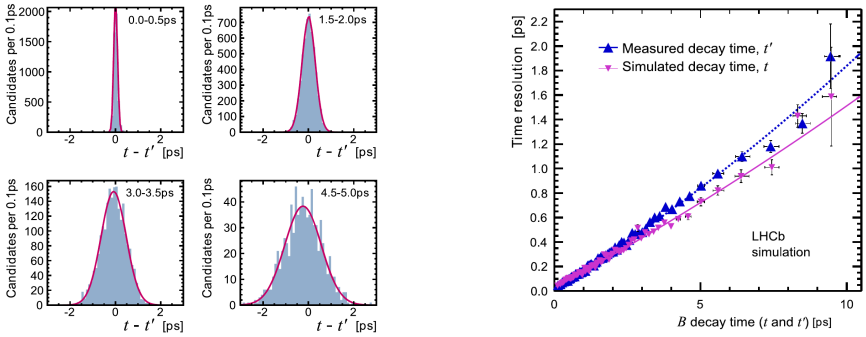

Figure 5.21: Decay time resolution as a function of the decay time for simulated samples of semileptonic decays of B mesons in LHCb. The decay time resolution is estimated from Gaussian fits to the distribution of the reconstructed decay times in bins of either the generated ("simulated") or the reconstructed ("measured") decay time. The small difference in the results is taken into account as a source of systematic uncertainty in the Δm_s measurement (from [244]).

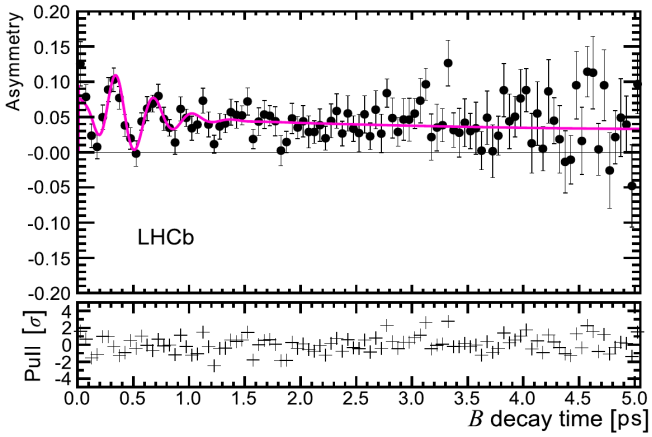

Figure 5.22: Decay-time dependent mixing asymmetry for $K^-K^+\pi^-\mu^+$ signal candidates measured in LHCb. The upper panel shows the measured asymmetry in bins of the calibrated decay time together with the projection of the fit function. The lower panel shows the difference between the value of the fitted function and the observed asymmetry in each bin, divided by the uncertainty on the observed asymmetry. For a good fit, these values should be spread around zero according to a Gaussian distribution with standard deviation one (from [244]).

of simulated events. The resulting decay-time resolution as estimated from samples of simulated events is shown as a function of the decay time in Figure 5.21. Flavour tagging relied on the usual combination of opposite side tagging algorithms and the same-side kaon tagging algorithm. A multi-dimensional binned maximum likelihood fit to the messured $K^+K^-\pi^+$ invariant mass, the normalized $K^-K^+\pi^-\mu^+$ invariant mass, n, the measured decay time, and the response of the flavour tagging algorithms was performed to extract the oscillation signal and measure Δm_s. The fit took into account a signal component and three categories of background, characterized by their reconstructed decay time and $K^-K^+\pi^-$ invariant mass: prompt D_s^- background with a $K^-K^+\pi^-$ invariant mass compatible with the D_s^- mass but small decay time compatible with D_s^- and muons from the primary pp interaction, prompt combinatorial background with small decay time and $K^-K^+\pi^-$ invariant mass outside a D_s^- signal region, and long-lived cominatorial background with $K^-K^+\pi^-$ invariant mass outside a D_s^- signal region but long decay time. The fitted decay time asymmetry for the signal component, characterized by long decay time and $K^-K^+\pi^-$ invariant mass compatible with the D_s^- mass is shown in Figure 5.22. A clear oscillation signal is visible, which is gradually washed out by the deteriorating decay-time resolution at increasing decay time. The statistical significance of the signal was found to correspond to 5.8 Gaussian standard deviations. Systematic uncertainties were found to be dominated by a small bias in the fitted value observed in samples of simulated events, by the parametrization of the decay-time resolution as a function of the decay time, and by possible biases on the decay-time correction factor due to differences between simulation and collision data. While the precision of the final result,

$$\Delta m_s \;=\; 17.93 \,\pm\, 0.22\,(\text{stat}) \,\pm\, 0.15\,(\text{syst})\ \text{ps}^{-1}\ ,$$

cannot compete with the more precise measurements using fully reconstructed hadronic decays, the measurement demonstrated the ability of the LHCb detector to resolve the rapid $B_s^0 - \overline{B}_s^0$ oscillations also in semileptonic decay modes.

5.2 The length of the R_u side: branching fractions of semileptonic b decays

The length of the side R_u, connecting the origin of the complex plane to the apex of the normalized Unitarity Triangle, is given by

$$|R_u| \;=\; \left|\frac{V_{ud}V_{ub}^*}{V_{cd}V_{cb}^*}\right| \;=\; \sqrt{\overline{\rho}^2+\overline{\eta}^2}\ ,$$

where the second equality uses the Wolfenstein parameters $\overline{\rho} = (1-\frac{\lambda^2}{2})\rho$ and $\overline{\eta} = (1-\frac{\lambda^2}{2})\eta$ defined in the introduction to this chapter.

The CKM elements $V_{cd} = \sin\theta_C$ and $V_{ud} = \sqrt{1-\sin^2\theta_C}$ are related to the well Cabibbo angle, θ_C, and their magnitudes are therefore known to good precision. The magnitudes of the other two CKM matrix elements can be determined by measuring the branching fractions of semileptonic b decays to charmed final states, $\text{BF}\,(b\to c\,\ell^+\nu_\ell) \propto |V_{cb}|^2$, and to charmless final states, $\text{BF}\,(b\to u\,\ell^+\nu_\ell) \propto |V_{ub}|^2$, respectively. The precision with which the magnitudes of the CKM matrix elements can be extracted from the measurements of the branching fractions is limited by theoretical uncertainties due to low-energy QCD effects that cannot be treated perturbatively.

From the point of view of experiments, the preferred approach is to measure branching fractions of exclusive decays, such as $B^+\to D^{(*)0}\ell^+\nu_\ell$ or $B^0\to D^{(*)-}\ell^+\nu_\ell$ and $B^+\to\pi^0\ell^+\nu_\ell$ or $B^0\to\pi^-\ell^+\nu_\ell$. The tree-level Feynman diagrams for these decays are shown in Figure 5.23. Precise measurements of the exclusive branching fractions can be performed at the B factories, where the integrated luminosity is well known and the kinematic properties of the undetected

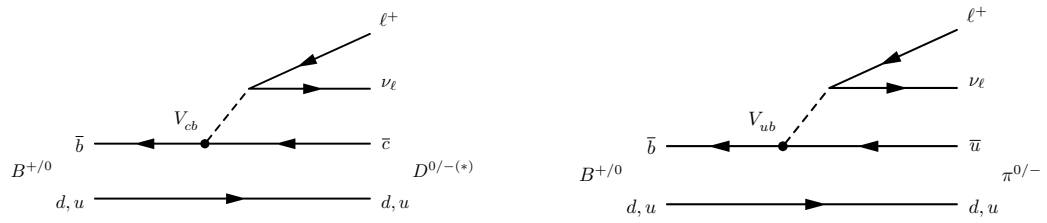

Figure 5.23: Feynman diagrams illustrating exclusive semileptonic B^0 and B^+ decays sensitive to (left) the CKM matrix element V_{cb} and (right) the CKM matrix element V_{ub}.

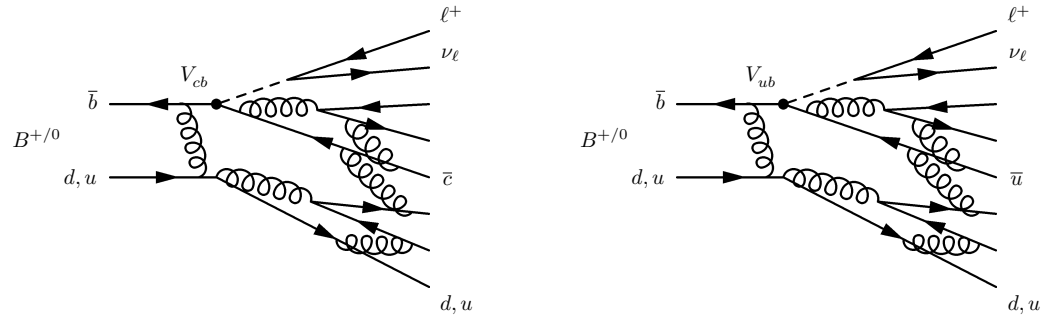

Figure 5.24: Feynman diagrams illustrating inclusive semileptonic b decays sensitive to (left) the CKM matrix element V_{cb} and (right) the CKM matrix element V_{ub}.

neutrino can be derived from the topology and kinematics of the remainder of the event. However, theoretical calculations of exclusive branching fractions suffer from significant uncertainties due to QCD effects related to the hadronization process in which the final-state hadrons are created.

Theoretical uncertainties are smaller in the calculation of the inclusive branching fractions $B \to X_c\, \ell^+ \nu_\ell$ and $B \to X_u\, \ell^+ \nu_\ell$, where B denotes a charged or neutral B meson and X_c and X_u denote a charmed or charmless hadronic final state, respectively. Generic Feynman diagrams illustrating such inclusive decays are shown in Figure 5.24. However, measurements of inclusive branching fractions are experimentally more challenging than those of the exclusive branching fractions. The most challenging measurement is that of $\mathrm{BF}\,(B \to X_u\, \ell^+ \nu_\ell)$, due to large backgrounds from the more abundant process $b \to X_c\, \ell^+ \nu_\ell$. Using the Wolfenstein parametrization, $|V_{ub}| = A\lambda^3$, $|V_{ub}| = A\lambda^2$ and

$$\frac{\mathrm{BF}\,(b \to u \ell^+ \nu_\ell)}{\mathrm{BF}\,(b \to c \ell^+ \nu_\ell)} \;\approx\; \frac{|V_{ub}|^2}{|V_{cb}|^2} \;=\; \lambda^2 \;\approx\; 0.05\,.$$

Cuts on the kinematics and topology of the final state particles allow to isolate clean samples of $B \to X_u \ell^+ \nu_\ell$ decays in regions of phase space that are not accessible to $B \to X_c \ell^+ \nu_\ell$ due to the larger mass of the c quark. However, the extrapolation of the measured partial branching fraction from these small regions in phase space to the full inclusive branching fraction then has to rely on theoretical assumptions that introduce new uncertainties. Larger fractions of the full phase space can be explored in so-called "tagged" analyses, in which the opposite-side B meson in the event, B_{tag}, is reconstructed in exclusive final states. Additional kinematical constraints on the properties of the event can then be derived, which permit a more efficient suppression of backgrounds from decays $B \to X_c \ell^+ \nu_\ell$. This gain comes, however, at the expense of significantly reduced statistics due to the small branching fractions to specific B_{tag} final states.

Finally, as illustrated in Figure 5.25, the Standard Model amplitude for leptonic decays of charged B mesons is proportional to $|V_{ub}|$. The amplitudes are helicity suppressed due to

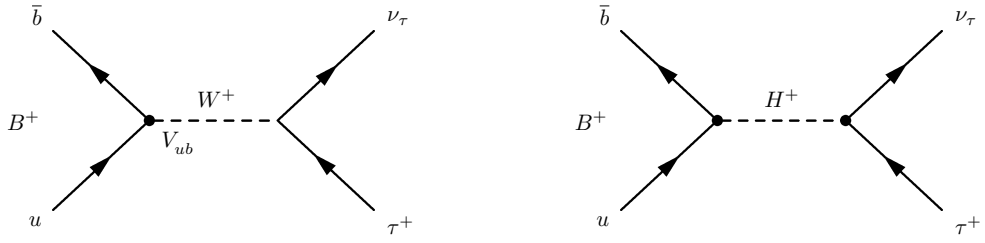

Figure 5.25: Feynman diagrams for the decay $B^+ \to \tau^+ \nu_\tau$ in (left) the Standard Model and (right) possible extentions to the Standard Model with charged Higgs bosons.

the $V - A$ character of the weak interaction. The decays $B^+ \to e^+ \nu_e$ and $B^+ \to \mu^+ \nu_\mu$ have not yet been observed with the most stringent upper limits on their branching fractions being at the level of 1×10^{-6} at 90 % confidence level [253, 254]. Because of the larger mass of the τ lepton, the helicity suppression is less strong in the decay $B^+ \to \tau^+ \nu_\tau$ and measurements of the branching fraction for this decay have been employed to measure $|V_{ub}|^2$. The main interest in this measurement is in the sensitivity of the branching fraction to possible contributions from physics beyond the Standard Model. In particular, the branching fraction can be significantly enhanced in models with charged scalar particles such as possible charged Higgs bosons as illustrated in Figure 5.25. Early measurements of BF $(B^+ \to \tau^+ \nu_\tau)$ seemed to indicate a possible deviation from the value of $|V_{ub}|$ extracted from semileptonic decays, but the tension has been significantly reduced by recent results published by the Belle collaboration are in goo.

In the remainder of this section, the five types of analyses are described in turn, beginning with measurements of $|V_{cb}|$ and $|V_{ub}|$ in exclusive decay modes, followed by measurements using inclusive decays, and finally the measurement of BF $(B^+ \to \tau^+ \nu_\tau)$. The section concludes with a brief comparison of the results obtained from the different approaches. Both for $|V_{cb}|$ and for $|V_{ub}|$, the results from exclusive and inclusive measurements are not in good agreement with each other.

5.2.1 Determination of $|V_{cb}|$ from exclusive semileptonic decays

Measurements of $|V_{cb}|$ have been performed in exclusive semileptonic decays of neutral and charged B mesons to $D^* \ell^\pm \nu_\ell$ and $D \ell^\pm \nu_\ell$, where ℓ can be an electron or muon and charged or neutral D^* or D mesons are fully reconstructed in a variety of hadronic decay modes. In all cases, analyses rely on the measurement of the differential branching fraction as a function of the velocity transfer to the D^* or D meson,

$$\omega \equiv \frac{P_B \cdot P_{D^{(*)}}}{m_B \, m_{D^{(*)}}} = \frac{m_B^2 + m_{D^{(*)}}^2 - q^2}{2 \, m_B m_{D^{(*)}}} ,$$

where m_B and $m_{D^{(*)}}$ are the known masses of the decaying B meson and the D or D^* meson, $P_B \cdot P_{D^{(*)}}$ is the scalar product of their measured four-momenta and q^2 is the squared momentum transfer to the $\ell^+ \nu_\ell$ pair. In the rest frame of the decaying B meson, ω corresponds to the Lorentz boost of the D^* or D meson. The relationship between ω and q^2 is illustrated in Figure 5.26: the minimum velocity transfer to the D^* or D meson, $\omega_{\rm min} = 1$, corresponds to the maximal momentum transfer to the leptonic system, $q^2_{\rm max} \approx 10.69$ GeV^2, while the minimum momentum transfer to the leptonic system, $q_{\rm min} = 0$, corresponds to the maximum velocity transfer to the D or D^* meson, $\omega_{\rm max} \approx 1.5$.

Following the nomenclature of the Review of Particle Physics [1], the differential branching fractions as a function of ω can be parametrized as

$$\frac{d\Gamma}{d\omega} (B \to D^* \ell \nu_\ell) = \frac{G_F^2}{48\pi^2} |V_{cb}|^2 \, m_B^5 \, (\omega^2 - 1)^{1/2} \, P(\omega) \, \eta_{\rm ew}^2 \, F^2(\omega)$$

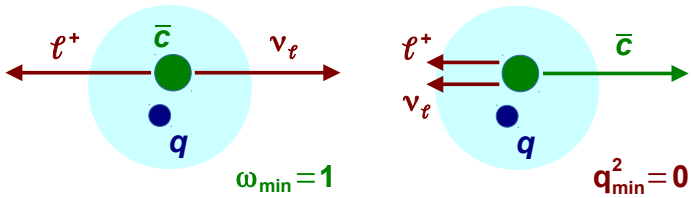

Figure 5.26: Illustration of the relationship between the velocity transfer to the $D^{(*)}$ meson, ω, and the squared momentum transfer to the lepton pair, q^2, in the the rest frame of the B meson decaying to $D\ell\nu_\ell$ or $D^*\ell\nu_\ell$. In the case of (left) minimum ω and maximum q^2, the D orD^* meson is created at rest in the B rest frame, while the ℓ and the ν_ℓ are produced back-to-back with respect to each other; in the case of (right) maximum ω and minimum q^2, the $D^{(*)}$ meson and the $\ell\nu_\ell$ pair are produced back-to-back with respect to each other.

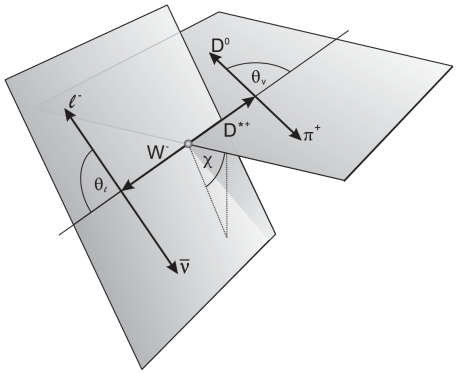

Figure 5.27: Definition of the helicity angles employed in the measurement of $F(1)|V_{cb}|$ from the differential cross section of exclusive decays $B \to D^{(*)}\ell^+\nu_\ell$ (from [255]).

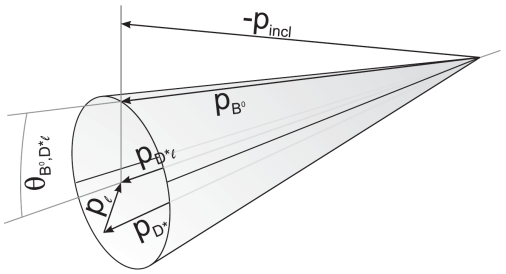

Figure 5.28: Illustration of the angle $\cos\theta_{B,D^{(*)}\ell}$ employed analyses of the semileptonic decays $B \to D^{(*)}\ell^+\nu_\ell$ (from [255]).

and

$$\frac{d\Gamma}{d\omega}(B \to D\ell\nu_\ell) \;=\; \frac{G_F^2}{48\pi^2}\,|V_{cb}|^2\,(m_B + m_D)^2\,m_D^3\,(\omega^2-1)^{3/2}\,\eta_{\rm ew}^2\,G^2(\omega)$$

respectively, where G_F denotes the Fermi constant, $P(\omega)$ is a phase-space factor, $\eta_{\rm ew}$ is an electroweak correction factor and $F(\omega)$ respectively $G(\omega)$ are the hadronic form factors that dominate the theory uncertainty.

A discussion of the theoretical treatment of these form factors can be found in the dedicated review in the Review of Particle Physics [1] and the references therein. In the limit of infinite quark masses, $F(1) = 1$ and $G(1) = 1$. Corrections to these approximations can be estimated from Heavy-Quark Effective Theory (HQET) or calculated in Lattice QCD approaches. The current precision of Lattice-QCD calculations is quoted as $\approx 2\%$ on the value of $F^2(1)$ and as $\approx 5\%$ on the value of $G^2(1)$. The D^* meson being a vector particle, $F(\omega)$ receives contributions from two axial form factors and one vector form factor, which in HQET are related to each other by Heavy Quark Symmetry (HQS). Models based on HQET are employed to parametrize the form factors as a function of ω in the case of the $G(\omega)$ and as functions of ω and the helicity angles of the final-state particles, defined in Figure 5.27, in the case of $F(\omega)$. The parametrization of $G(\omega)$ depends on one free parameter, which is usually taken as the slope, ρ_D^2, of $G(\omega)$ as a function of ω at $\omega = 1$. The parametrization of $F(\omega)$ depends on three unknown parameters, which are taken as the values at $\omega = 1$ of the slope, $\rho_{D^*}^2$, of $F(\omega)$ and the ratios, R_1 and R_2, of the two axial form factors with respect to the vector form factor.

Early measurements of $|V_{cb}|$ in exclusive decay modes were performed at Argus [256], at the LEP experiments [257–262] and at CLEO [263, 264], but the most precise results stem

from measurements at the B factories. Analyses using the decay modes $B^0 \to D^{*-}\ell^+\nu_\ell$ were published by the BaBar [265, 266] and Belle [255, 267] collaborations. The BaBar collaboration published in addition an analysis [268] in decays of $B^+ \to \overline{D}^{*0}e^+\nu_{\rm e}$. Measurements in $B^0 \to D^-\ell^+\nu_\ell$ were again published by the Belle [269] and BaBar [270] collaborations. Finally, the BaBar collaboration published [271] a global analysis of semileptonic decays fo neutral and charged B mesons to final states involving a D^* or D meson. The latest of these analyses will be described in the next paragraphs.

Measurements in decay modes $B \to D^*\ell^+\nu_\ell$

The BaBar collaboration published [266] a combined measurement of $F(1)|V_{cb}|$, $\rho^2_{D^*}$, $R_1(1)$ and $R_2(1)$ in the decay $B^0 \to D^{*-}\ell^+\nu_\ell$ that was based on 52'800 reconstructed signal candidates extracted from a data sample corresponding to 79 fb^{-1} collected at the $\Upsilon(4S)$ resonance. The Belle collaboration published an analysis [255] that made use of a sample of 120'000 reconstructed signal candidates extracted from their full data sample collected at the $\Upsilon(4S)$ resonance.

In both analyses, D^{*-} candidates were identified by their decay to a $\overline{D}^0$ meson and a low-momentum charged pion, where the $\overline{D}^0$ meson was reconstructed in its decay to $K^+\pi^-$. In the BaBar analysis, the decay modes $\overline{D}^0 \to K^+\pi^-\pi^+\pi^-$ and $\overline{D}^0 \to K^+\pi^-\pi^0$ were considered in addition. Selection criteria were applied on the invariant mass of the $\overline{D}^0$ candidate, on the quality of the $\overline{D}^0$ and D^{*-} vertex fits and on the momenta of theD^* candidate and the charged lepton.

Two discriminating variables were employed in both analyses to determine the signal component in the selected sample of candidates: the distribution of the difference between invariant masses of the D^* candidate and the D candidate, $\Delta m = m_{D^*} - m_D$, and the distribution of the variable $\cos\theta_{B,D^*\ell}$ that was already introduced in Section 5.1.1 in the context of measurements of the $B^0-\overline{B}^0$ oscillation frequency in semileptonic decays. Momentum and energy conservation in the decay $B^0 \to D^{*-}\ell^+\nu_\ell$ imply that

$$\cos\theta_{B,D^*\ell} \;=\; \frac{2E_BE_{D^*\ell} - m_B^2 - m_{D^*\ell}^2}{2\,|\vec{p}_B|\;|\vec{p}_{D^*\ell}|}\;,$$

where $\theta_{B,D^*\ell}$ is the angle between the momentum vectors of the decaying B^0 meson and the $D^*\ell$ system. Setting m_B to the nominal mass of the B^0 meson, E_B to half the known centre-of-mass energy of the e^-e^+ collision and $|\vec{p}_B| \equiv \sqrt{E_B^2 - m_B^2}$, the calculated value of $\cos\theta_{B,D^*\ell}$ must lie for signal events in the range $[-1,+1]$ within the precision of the reconstruction. For background events, no such restriction applies and the distribution of $\cos\theta_{B,D^*\ell}$ extends far beyond the range of physically meaningful values. In the Belle analysis, the measured transverse momentum of the charged lepton was employed as a third discriminating variable besides Δm and $\cos\theta_{B,D^*\ell}$.

Examples of the distributions of Δm and $\cos\theta_{B,D^*\ell}$ as obtained in the BaBar and Belle analyses are shown in Figures 5.29 and 5.30 together with the estimated composition of the samples of candidates. Six sources of background were considered in the analyses: combinatorial background from a charged lepton and random combinations of kaons and pions; continuum background from charged leptons and correctly reconstructed D^* candidates produced in $e^-e^+ \to c\bar{c}$ processes; fake lepton background from combinations of a correctly reconstructed D^* candidate with a misidentified charged hadron; uncorrelated $D^*\ell$ background, in which a correctly reconstructed D^* candidate was combined with a correctly identified charged lepton from the decay of the other B meson in the event; and correlated $D^*X\ell\nu_\ell$ background from decays $B \to D^*\pi\ell\nu_\ell$, $B^0 \to D^{*-}\tau\nu_\tau$ with $\tau \to \ell^+\nu_\ell$, or $B^0 \to D^*X_c$ followed by a semileptonic decay of the charmed hadron, X_c. In the BaBar analysis, the fraction of combinatorial background was estimated from the measured distribution of Δm. The fraction of continuum

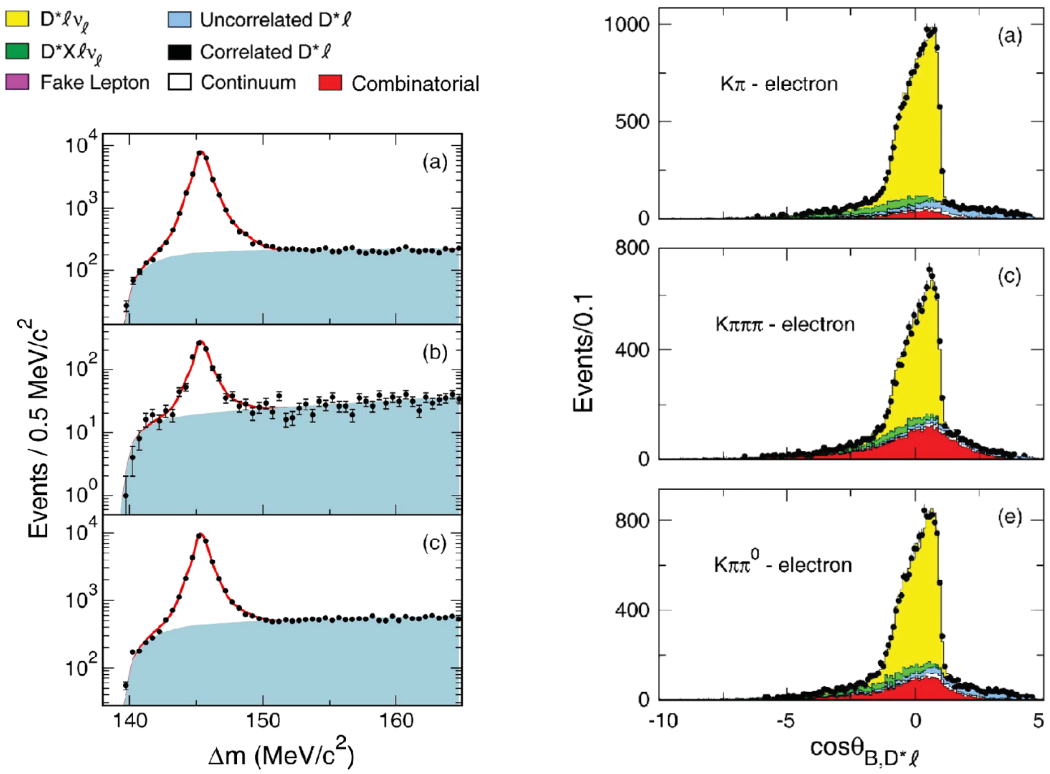

Figure 5.29: Distributions of the discriminating variables (left) Δm and (right) $\cos\theta_{B,D^*\ell}$ as obtained in the BaBar measurement of $F(1)|V_{cb}|$ in the decay $B^0 \to D^{*-}\ell^+\nu_\ell$. The distributions of Δm are shown for (top) $D^*\ell$ candidates collected at the $\Upsilon(4S)$ resonance, (middle) candidates collected at a e^-e^+ collision energy below the $\Upsilon(4S)$ resonance and (bottom) combinations of a D^* candidate and a hadron in events in which no particle passed lepton identification criteria. The distributions for $\cos\theta_{B,D^*\ell}$ are shown for D^*e candidates reconstructed in the D^* final states indicated in the plots. Different colours indicate signal and background components as explained in the legend and the main text (from [266]).

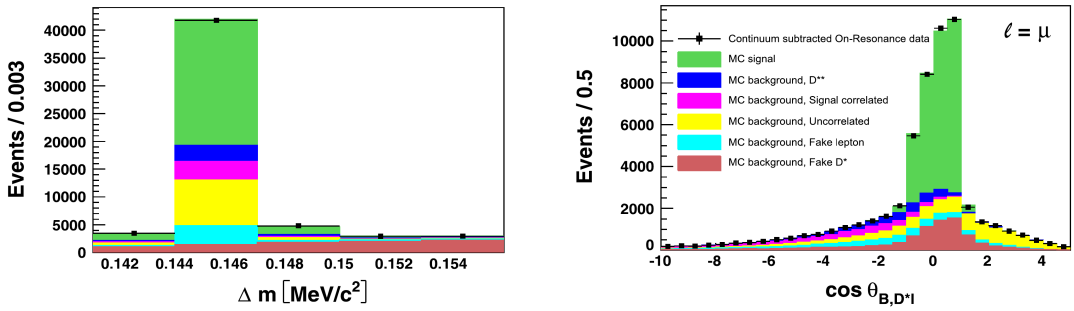

Figure 5.30: Distributions of the discriminating variables (left) Δm and (right) $\cos\theta_{B,D^*\ell}$ as obtained in the Belle measurement of $F(1)|V_{cb}|$ in the decay $B^0 \to D^{*-}\ell^+\nu_\ell$. Different colours indicate signal and background contributions as explained in the legend and the main text (from [255]).

background was estimated from the signal component in the Δm distribution for data collected at e^-e^+ collision energies below the $\Upsilon(4S)$ resonance. The fraction of fake-lepton background was estimated from the signal component in the Δm distribution for events in which no particle fulfilled lepton identification criteria. The fraction of uncorrelated and correlated backgrounds were determined from a χ^2 fit to the $\cos\theta_{B,D^*\ell}$ distribution, where the shapes of the signal component and the different background components were determined from samples of simulated events. In the Belle analysis, the component from continuum background was estimated

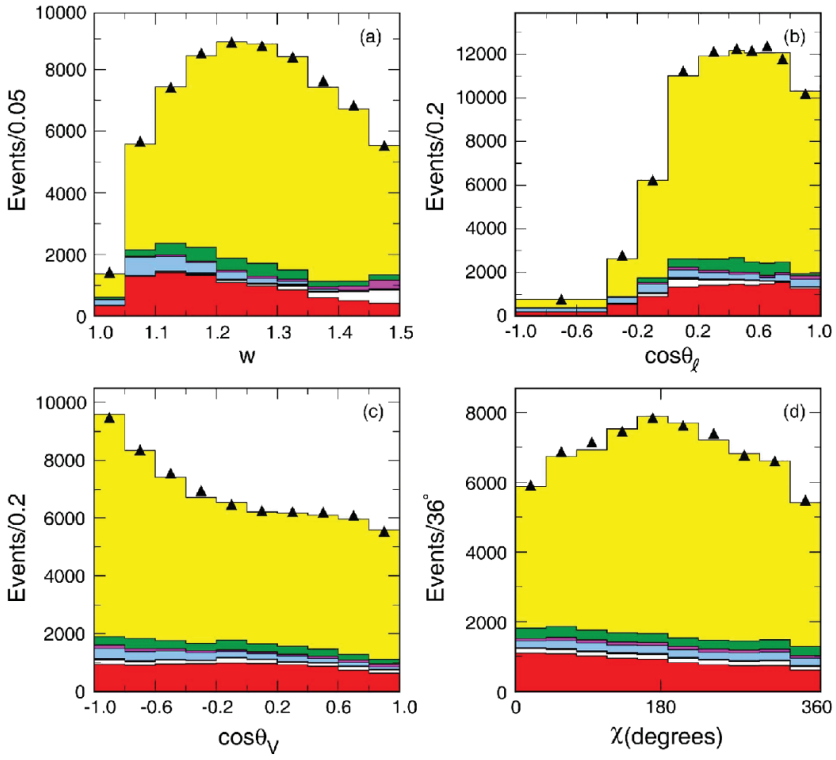

Figure 5.31: Distributions of ω and the three angular variables $\cos\theta_\ell$, $\cos\theta_V$ and χ as obtained in the BaBar measurement of $F(1)|V_{cb}|$ in the decay $B \to D^*\ell\nu_\ell$. The results of the fit to the data are superimposed, where different colours indicate signal and background components as defined in Figure 5.29 above (from [266]).

from data collected at beam energies below the $\Upsilon(4S)$ resonance and the remaining background components were estimated from a simultaneous three-dimensional fit to the distributions in the discriminating variables. The shapes of the signal and background components in these variables were modelled from samples of simulated events.

The value of $F(1)|V_{cb}|$ was then extracted simultaneously with those of $\rho^2_{D^*}$, $R_1(1)$ and $R_2(1)$ from one-dimensional fits to the measured distributions in ω and the three helicity angles defined in Figure 5.27.

The calculation of ω requires knowledge of the momentum of the decaying B meson. However, the reconstruction of the signal candidate only allows to constrain its direction of flight onto the cone defined by $\cos\theta_{B,D^*\ell}$. In the BaBar analysis, four possible values of ω, corresponding to four values of the azimuthal angle around this cone, were calculated and their arithmetic average was employed in the further analysis. In the Belle analysis, the direction of flight of the decaying B meson was estimated as illustrated in Figure 5.28: the momentum vector $\vec{p}_{\rm incl}$ of the second B meson in the event was estimated by summing over all tracks and neutral clusters that were not employed in the reconstruction of the signal candidate. Exploiting the fact that the two B mesons are produced back-to-back in the centre-of-mass system of the e^-e^+ collision, the vector defined by $-\vec{p}_{\rm incl}$ was then projected onto the cone defined by $\cos\theta_{B,D^*\ell}$.

The measured distributions of ω and the three helicity angles are shown together with the results of the fits in Figures 5.31 and 5.32. The fit result in terms of $F(\omega)|V_{cb}|$ is shown in Figure 5.33. The measurement of $F(1)|V_{cb}|$ was found in both analyses to be limited by systematic uncertainties, dominated by the knowledge of particle identification and track reconstruction efficiencies and, in the case of the BaBar analysis, by the knowledge of D^0 branching fractions.

The BaBar collaboration also published a similar analysis in the decay $B^+ \to \overline{D}^{*0}e^+\nu_{\rm e}$ [268]. The values of $F(1)|V_{cb}|$ and $\rho^2_{D^*}$ were determined from a fit to the measured distributions in

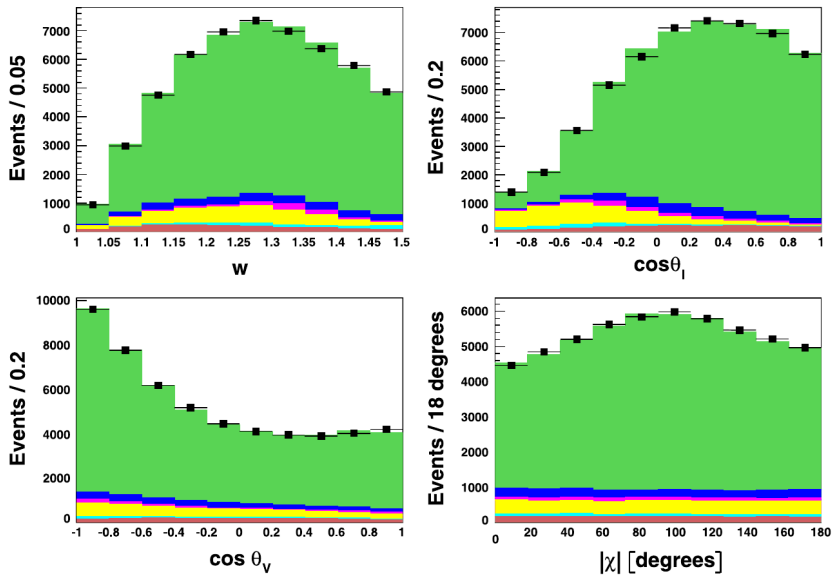

Figure 5.32: Distributions of ω and the three angular variables $\cos\theta_\ell$, $\cos\theta_V$ and χ as obtained in the Belle measurement of $F(1)|V_{cb}|$ in the decay $B \to D^*\ell\nu_\ell$. The results of the fit to the data are superimposed, where different colours indicate signal and background contributions as defined in the legends shown in Figure 5.30 above (from [255]).

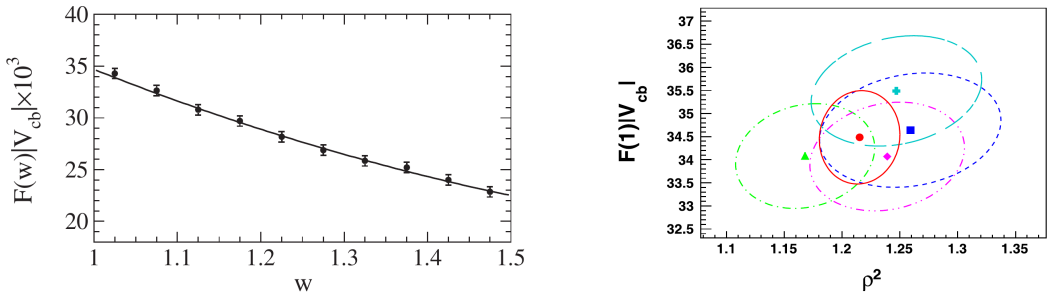

Figure 5.33: Illustration of the results of the BaBar and Belle measurements of $F(1)|V_{cb}|$ in the decay $B^0 \to D^{*-}\ell^+\nu_\ell$: (left, from [266]) projection of the fit result for $F(\omega)|V_{cb}|$ as a function of ω as obtained in the BaBar analysis; (right, from [255]) one-standard-deviation confidence contours in the $F(1)|V_{cb}|-\rho^2_{D^*}$ plane as obtained in the Belle analysis. Here, dashed lines indicate the results for different subsamples of the data, while the red marker and the full red line indicates the combined result for the full data sample.

ω and the decay angles, while the values of R_1 and R_2 were fixed to those obtained in the analysis described in the previous paragraphs.

Measurements in decay modes $B \to D\ell^+\nu_\ell$

The D meson being a pseudo-scalar particle, the measurement of $G(1)|V_{cb}|$ in decays $B \to D\ell\nu_\ell$ does not require an angular analysis. However, the precision of the measurement suffers from the suppression of the decay rate near $\omega = 1$, by substantial backgrounds from partially reconstructed decays $B \to D^*\ell\nu_\ell$, and by a larger contamination from combinatorial backgrounds due to the lack of the clear signature of a slow pion from the decay $D^* \to D\pi$.

The Belle collaboration published a measurement of $G(1)|V_{cb}|$ in the decay mode $B^0 \to D^-\ell^+\nu_\ell$ with $D^- \to K^+\pi^-\pi^-$ [269] based on an early data set corresponding to 10.8 million produced $B\overline{B}$ pairs. An inclusive reconstruction of all remaining tracks and all neutral clusters in the event was performed to estimate the missing energy and momentum due to the undetected

neutrino as

$$E_{\rm miss} \equiv 2\,E_{\rm beam} - \sum E_i$$

and

$$\vec{p}_{\rm miss} \equiv -\sum \vec{p}_i \ ,$$

where the sums run over all reconstructed tracks and neutral energy clusters in the event and mass hypotheses for charged particles were assigned based on particle identification criteria. The invariant mass

$$m^2_{\rm miss} \equiv E^2_{\rm miss} - |\vec{p}_{\rm miss}|^2$$

was required to be close to zero. Events were rejected if they contained an additional lepton candidate since this would imply the presence of an additional undetected neutrino. To suppress events with other undetected particles, selection criteria were applied on the sum of the charges of all reconstructed particles and on the angle between the missing momentum of the event with respect to the beam axis.

The same sources of backgrounds were considered as in the analyses of $B^0 \to D^*\ell\nu$ discussed in the previous paragraphs: combinatorial background from random combinations of final-state particles, continuum background from non-$B\overline{B}$ events, fake-lepton background from misidentified hadrons, uncorrelated background from combinations of a D meson from the decay of one B meson and a charged lepton from the decay of the second B meson in the event, and correlated background from $B \to DX\ell\nu_\ell$ in which the particle of particles X were missed in the reconstruction. The following discriminating variables were employed to determine the composition of the sample of selected candidates and to extract the signal component: the invariant mass of the $K\pi\pi$ system, the variable

$$\cos\theta_{B,D\ell} \equiv = \frac{2E_B E_{D\ell} - m^2_B - m^2_{D\ell}}{2\,|\vec{p}_B|\ |\vec{p}_{D\ell}|}$$

defined in the same manner as $\cos\theta_{B,D^*\ell}$ discussed previously, the energy imbalance

$$\Delta E \equiv (E_D + E_\ell + |\vec{p}_{\rm miss}|) - E_{\rm beam} \ ,$$

where the energy of the neutrino was estimated by $|\vec{p}_{\rm miss}|$ since the missing momentum of the event could be reconstructed with better precision than the missing energy, and the beam-energy substituted invariant mass

$$m_{bc} \equiv \sqrt{E^2_{\rm beam} - |\vec{p}_D + \vec{p}_\ell + \alpha\,\vec{p}_{\rm miss}|^2} \ ,$$

where the momentum of the neutrino was estimated by the missing momentum of the event and the factor $\alpha \equiv 1 + \Delta E/|\vec{p}_{\rm miss}|$ was introduced to effectively set $\Delta E = 0$ for the calculation of m_{bc}.

The measured ω distribution before background subtraction is shown in Figure 5.34 as well as the result of a fit to the binned ω distribution to extract the values of $G(1)|V_{cb}|$ and ρ^2_D. The uncertainty on $G(1)\cdot|V_{cb}|$ was found to be dominated by the systematic uncertainty on the reconstruction of the neutrino properties.

Based on their full data set collected at the $\Upsilon(4S)$ resonance, the BaBar collaboration performed a combined "tagged" analysis of the decay modes $B^0 \to D^-\ell^+\nu_\ell$ and $B^+ \to D^0\ell^+\nu_\ell$ [270], in which the opposite-side B meson in the event was fully reconstructed in hadronic decay modes $B_{\rm tag} \to DX^\pm_{\rm tag}$, where $X^\pm_{\rm tag}$ denotes a combination with total charge ±1 of up to five charged pions or kaons, up to two K^0_S candidates and up to two neutral pions and D denotes a D^0 candidate reconstructed in decays to $K^-\pi^+$, $K^-\pi^+\pi^0$, $K^0_S\pi^+\pi^-$, $K^0_S\pi^+\pi^-\pi^0$, $K^0_S\pi^0$, K^+K^-, $\pi^+\pi^-$ or $K^0_SK^0_S$, a D^+ candidate reconstructed in decays to $K^-\pi^+\pi^+$, $K^-\pi^+\pi^+\pi^0$, $K^0_S\pi^+$, $K^0_S\pi^+\pi^0$, $K^+K^-\pi^+$, $K^0_SK^+$ or $K^0_S\pi^+\pi^+\pi^-$, a D^{*+} candidate reconstructed in decays to $D^0\pi^+$ or $D^+\pi^0$, or a D^{*0} candidate reconstructed in decays to $D^0\pi^0$ or $D^0\gamma$. In total, about

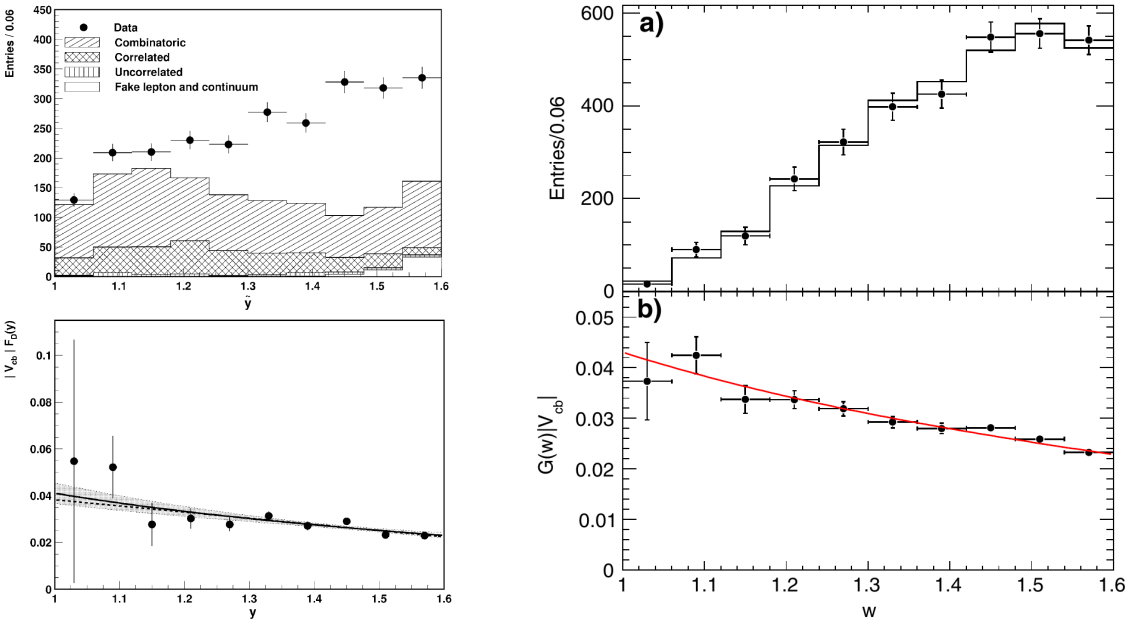

Figure 5.34: Distribution of ω (called $\tilde{y}$ in the Belle analysis) and the results of binned fit for $G(1)|V_{cb}|$ and ρ_D^2 as obtained in the (left, from [269]) the Belle analysis and (right, from [270]) the tagged BaBar analysis using the decay $B \to D\ell\nu_\ell$. The ω distribution from the Belle analysis is shown before, that from the BaBar analysis after background subtraction.

1000 exclusive final states were considered in the reconstruction of B_{tag} candidates. The selection of these candidates relied on the reconstructed beam-energy substituted invariant mass. The same combination of final states was employed in various other hadronic tagged analyses in BaBar, some of which will be discussed later in this section.

Having performed a full reconstruction of the opposite-side B meson, the missing invariant mass of the event as well as the value of ω could then be determined with good precision. An extended maximum likelihood fit to the distribution of the squared missing mass of the events was performed to determine the $B \to D\ell^+\nu_\ell$ signal yields in ten bins of ω, considering background contributions from combinatorial and continuum background, from misidentified leptons and from other semileptonic decays of B mesons. The extracted signal yields and the result of the fit for $G(\omega)|V_{cb}|$ are shown in Figure 5.34.

Combined BaBar analysis of $B \to D^*\ell^+\nu_\ell$ and $B \to D\ell^+\nu_\ell$

Finally, the BaBar collaboration published a combined analysis of $B \to \overline{D}^*\ell^+\nu_\ell$ and $B \to \overline{D}\ell^+\nu_\ell$ decays [271] based on a data set corresponding to 230 million produced $B\overline{B}$ pairs. The analysis made use of inclusive samples of $\overline{D}^0\ell^+$ and $D^-\ell^+$ candidates, where $\overline{D}^0$ and D^- candidates were reconstructed in the final states $K^+\pi^-$ and $K^+\pi^-\pi^-$, respectively. Combinatorial background from random combinations of kaons and pions was estimated and subtracted from sidebands in the invariant-mass distribution of D meson candidates, and continuum background from non-$B\overline{B}$ events was determined from data collected at e^-e^+ collision energies below the $\Upsilon(4S)$ resonance and The remaining sample of candidates then contains contributions from $B \to \overline{D}\ell^+\nu_\ell$ and $B \to \overline{D}^*\ell^+\nu_\ell$ signal decays and backgrounds from fake leptons and from correlated and uncorrelated $\overline{D}\ell$ combinations as defined in the previous paragraphs.

Three discriminating variables were employed to separate these components: the variable $\cos\theta_{B,D\ell}$, and the momenta of the $\overline{D}$ candidate and the ℓ^+ candidate in the centre-of-mass frame of the e^-e^+ collision. The shapes of the distributions in these variables for the different decay modes were modelled from samples of simulated events. As an example, expected and observed distributions in the two momenta are shown in Figure 5.35. The values of R_1 and R_2

were fixed to those obtained in Ref. [266]. The results of the fit, including the full covariance matrix for the fit parameters, were then employed to calculate $F(1)|V_{cb}|$ and $G(1)|V_{cb}|$. The measurement uncertainty was found to be dominated by systematic uncertainties related to the track reconstruction, the knowledge of the branching fractions for the various B and$D$ decays employed in generating samples of simulated events, radiative corrections, and lepton particle-identification efficiencies.

Summary of results

The different BaBar and Belle results are in good agreement with each other and with earlier measurements from the LEP experiments and CLEO. A compilation of the results, prepared by the Heavy Flavour Averaging Group, is shown in Figure 5.36. The BaBar and Belle analyses extract values for $|V_{cb}|$ ranging between 37.5×10^{-3} and 39.9×10^{-3}, quoting statistical and experimental systematic uncertainties of a couple of percent and uncertainties of about $(2.5 - 3.5)\%$ due to hadronic form factors. Using recent Lattice-QCD calculations of $F(1)$ and $G(1)$, the Heavy Flavour Averaging Group [2] quote averages of

$$|V_{cb}| \;=\; (\,38.94 \,\pm\, 0.49\,(\text{exp}) \,\pm\, 0.58\,(\text{theo})\,) \times 10^{-3}$$

for the determination from decays $B \to \overline{D}^{*} \ell^{+} \nu_{\ell}$ and

$$|V_{cb}| \;=\; (\,39.45 \,\pm\, 1.42\,(\text{exp}) \,\pm\, 0.88\,(\text{theo})\,) \times 10^{-3}$$

for the determination from decays $B \to \overline{D} \ell^{+} \nu_{\ell}$. The 2014 edition of the Review of Particle Physics [1] quotes a world average of

$$|V_{cb}| \;=\; (\,39.5 \,\pm\, 0.8\,) \times 10^{-3}$$

from measurements of exclusive decays.

5.2.2 Determination of $|V_{ub}|$ from exclusive semileptonic decays

Determinations of $|V_{ub}|$ from the exclusive decays $B^0 \to \pi^{-} \ell^{+} \nu_{\ell}$ or $B^{+} \to \pi^0 \ell^{+} \nu_{\ell}$ rely on the measurement of their differential cross section as a function of the squared momentum transfer to the lepton system,

$$q^2 \;\equiv\; (P_B \,-\, P_\pi)^2 \;=\; (P_\ell \,+\, P_\nu)^2 \;,$$

where P_B, P_π, P_ℓ and P_ν are the four-vectors of the decaying B meson and the three final-state particles, respectively. Following the notation of the Review of Particle Physics [1], the differential cross section as a function of q^2 can be parametrized as

$$\frac{d\Gamma\,(B \to \pi \ell \nu_\ell)}{dq^2} \;=\; \frac{G_F^2}{24\pi^2}\,|V_{ub}|\,|p_\pi|^3\,|f_{+}(q^2)|^2 \;,$$

if the mass of the charged lepton is neglected. Here, $|p_\pi|$ is the momentum of the pion in the rest frame of the decaying B meson and $f_{+}(q^2)$ is the relevant hadronic form factor incorporating non-perturbative QCD effects. A discussion of the theoretical treatment of this form factor can be found in the dedicated review in Ref. [1] and the references therein. Calculations of $f_{+}(q^2)$ rely on lattice QCD [272, 273] and light-cone sum rules [274]. Light-cone sum rules provide information near $q^2 = 0$, while lattice-QCD calculations are restricted to large values of q^2. Low values of q^2 correspond to a large momentum and a small wavelength of the pion. Calculations on the lattice would require a fine lattice spacing that is currently still out of reach. The interpolation between the two regimes is possible using analyticity and unitarity bounds, in particular making use of the heavy-quark limit. Such interpolations yield a smooth transition

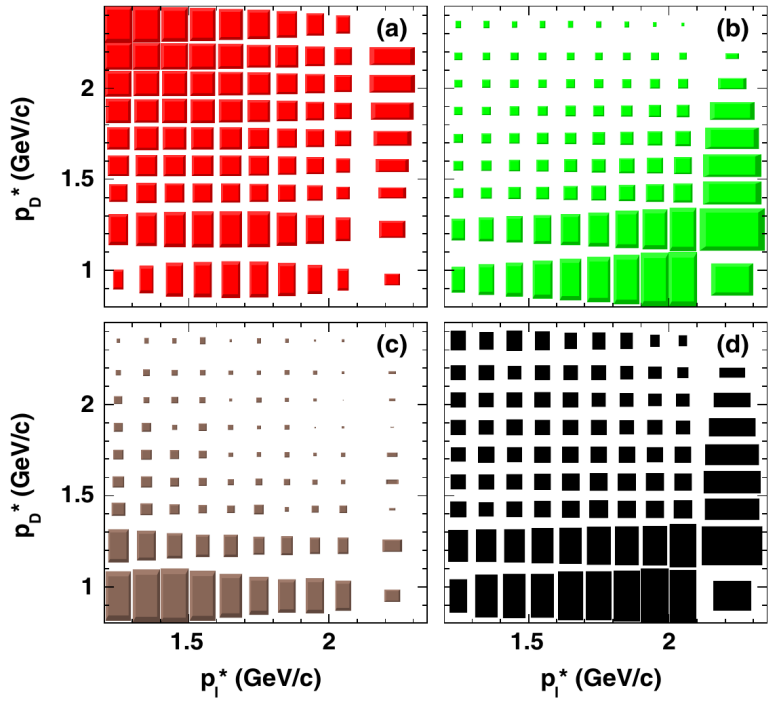

Figure 5.35: Distribution of the momenta of D and electron candidates for selected De^+ pairs in samples of (top left) simulated $B \to De^+\nu_e$ decays, (top right) simulated $B \to D^*e^+\nu_e$ decays, (bottom left) correlated and uncorrelated background in samples of simulated events and (bottom right) collision data after subtraction of combinatorial and continuum backgrounds, as obtained in the BaBar measurement of $F(1)|V_{cb}|$ and $G(1)|V_{cb}|$ using inclusive $D^{(*)}\ell$ pairs (from [271]).

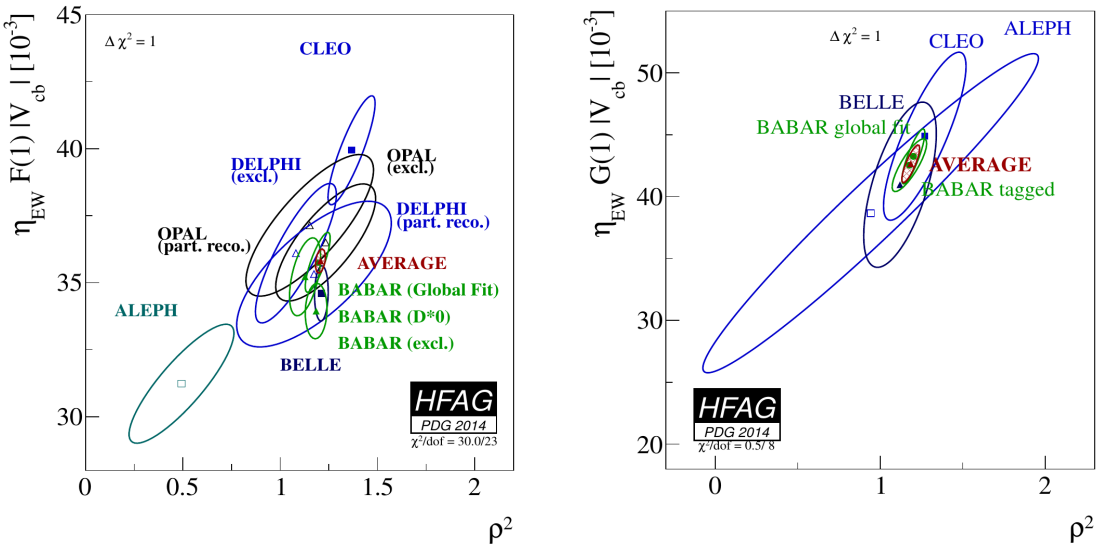

Figure 5.36: Compilation of results for (left) $\eta_{\rm EW}F(1)|V_{cb}|$ vs $\rho^2_{D^*}$ and (right) $\eta_{\rm EW}G(1)|V_{cb}|$ vs ρ^2_D, as prepared by the Heavy Flavour Averaging Group [2] for the 2014 edition of the Review of Particle Physics.

between the two regimes, giving some confidence in the approach. Current uncertainties on calculations from lattice-QCD and light-cone sum rules are quoted as about 10%.

Recent measurements of the differential cross section have been performed at CLEO [275–277], BaBar [278–284] and Belle [285–287]. Three approaches have been pursued: untagged analyses [275–278, 280, 282–284, 286], in which the kinematic properties of the undetected neutrino are inferred from an inclusive reconstruction of the remainder of the event; hadronic tagged analyses [279, 287], in which the second B meson in the event, $B_{\rm tag}$, is fully reconstructed in a number of hadronic decay modes; and semileptonic tagged analyses [279, 281, 285], in which $B_{\rm tag}$ candidates are reconstructed in semileptonic decay modes. Untagged measurements give the highest event yields but suffer from worse resolution and larger backgrounds than tagged measurements. In tagged measurements, the flight direction of the signal B meson can be constrained by the reconstruction of the $B_{\rm tag}$ candidate, resulting in a more precise reconstruction of the neutrino properties and better suppression of backgrounds. However, this comes at the expense of significantly reduced event yields due to the small branching fractions to specific $B_{\rm tag}$ final states and the finite efficiencies in reconstructing of $B_{\rm tag}$ candidates. In the following, the three types of measurements at the B factories will be briefly described.

Untagged analyses

The BaBar collaboration published an untagged analysis [284] that was based on the full data set corresponding to 462 million produced $B\overline{B}$ pairs. The latest untagged analysis published by the Belle collaboration was based on a data set corresponding to 657 million produced $B\overline{B}$ pairs. The two analyses followed similar patterns, except that the BaBar measurement included the decays $B^0 \to \pi^- \ell^+ \nu_\ell$ as well as $B^+ \to \pi^0 \ell^+ \nu_\ell$, while the Belle analysis considerd only decays of neutral B mesons. Candidates were formed by combining a high-momentum muon or electron candidate with a pion candidate of opposite charge or, in the case of the decay $B^+ \to \pi^0 \ell^+ \nu_\ell$, with a π^0 candidate formed from two photon clusters. Muon candidates were rejected if they formed an invariant mass compatible with the mass of the J/ψ meson when combined with another track. Further selection criteria were applied on event-shape variables, on kinematic properties of the lepton and pion candidates and on the helicity angle of the charged lepton, the latter being defined as the angle between the momentum of the lepton and the direction opposite to the momentum of the decaying B meson in the rest frame of the $\ell\nu_\ell$ system. The energy imbalance, $E_{\rm miss} \equiv 2E_{\rm beam} - \sum E_i$, and momentum imbalance, $\vec{p}_{\rm miss} \equiv -\sum \vec{p}_i$, of the event were calculated by summing over all reconstructed tracks and neutral clusters and the squared missing mass of the event,

$$m^2_{\rm miss} \;\equiv\; E^2_{\rm miss} - |\vec{p}_{\rm miss}|^2 \;,$$

was required to be compatible with zero within the precision of the measurement. Furthermore, the variable

$$\cos\theta_{B,\pi\ell} \;\equiv\; \frac{2\,E_B E_{\pi\ell} - m_B^2 - m_{\pi\ell}^2}{2\;|\vec{p}_B|\;|\vec{p}_{\pi\ell}|}$$

was defined in analogy to the variables $\cos\theta_{B,D^*\ell}$ and $\cos\theta_{B,D\ell}$ employed in measurements of $|V_{cb}|$ from exclusive semileptonic decays and its value was required to assume a value within the physically meaningful range.

The extraction of the signal component from the sample of selected candidates relied on the energy imbalance, ΔE, and beam-energy substituted invariant mass, $m_{\rm ES}$, of the B candidate as defined in Section 4.1. The momentum and energy of the undetected final-state neutrino were estimated in the calculation of ΔE and $m_{\rm ES}$ by the missing momentum, $\vec{p}_{\rm miss}$, of the event and its magnitude, respectively.

To avoid the rather large uncertainty due to this estimation of the neutrino momentum and energy, the the squared momentum transfer to the $\ell\nu_\ell$ system was calculated from the four-vectors of the decaying B meson and the final-state pion as $q^2 = (P_B - P_\pi)^2$. The reconstruction

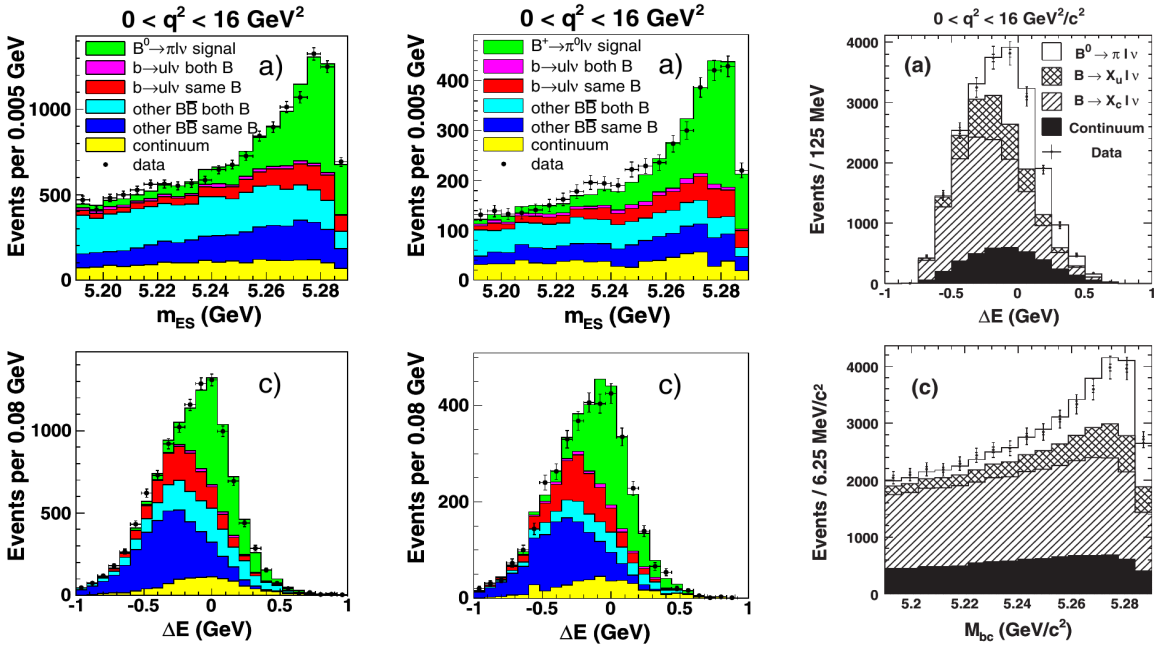

Figure 5.37: Measured distributions of the beam-energy substituted invariant mass, $m_{\rm ES}$ or $M_{\rm bc}$, and the energy imbalance, ΔE, of (left, from [284]) $B^0 \to \pi^- \ell^+ \nu_\ell$ and (middle, from [284]) $B^+ \to \pi^0 \ell^+ \nu_\ell$ candidates from the BaBar analysis and (right, from [286]) $B^0 \to \pi^+ \ell^+ \nu_\ell$ candidates from the Belle analysis of $|V_{ub}|$ in these decay modes. In all cases, distributions are shown summed over all q^2 bins from 0 to 16 GeV$^2/c^2$. The results of the fit to the data are superimposed, where different shadings indicate the signal and background components as defined by the respective plot legends.

of the signal candidate only allows to constrain the momentum of the decaying B meson to lie on the cone defined by $\cos\theta_{B,\pi\ell}$. Therefore, four possible values of q^2, corresponding to four equidistant values of the azimuthal angle around this cone, were calculated and their average was used for the further analysis. In forming the average, each of the four value was weighted with $\sin^2\theta_B$, where θ_B is the angle between the beam direction and the assumed flight direction of the B candidate in the rest frame of the e^-e^+ collision. This weighting was motivated by the fact that B mesons are pseudoscalar particles and their differential production cross section follows a $\sin^2\theta_B$ distribution.

Signal yields in bins of q^2 were determined from two-dimensional maximum-likelihood fits to the measured distributions in ΔE and $m_{\rm ES}$. Thirteen q^2 bins were employed in the BaBar analysis and twelve in the Belle analysis. Examples for the measured distributions are shown in Figure 5.37 together with projections of the fit results. Besides the signal component, the fit functions included components for backgrounds from $B \to X_u \ell^+ \nu_\ell$ decays other than $B \to \pi \ell^+ \nu_\ell$, from other $B\overline{B}$ decays and from non-$B\overline{B}$ continuum events. In the BaBar analysis, the background components from $B \to X_u \ell^+ \nu_\ell$ and other $B\overline{B}$ decays were further subdivided into a component from events in which the charged lepton and the pion were produced in the decay of the same B meson and a component in which one of them was produced in the decay of one B meson and the other in the decay of the second B meson in the event. In both analyses, the background from other $B\overline{B}$ decays was found to be dominated by semileptonic decays $B \to X_c \ell^+ \nu_\ell$. The expected shapes of the ΔE and $m_{\rm ES}$ distributions for the signal and background components were obtained from samples of simulated events. Unfolding procedures based on samples of simulated events were applied to correct the binned q^2 distribution for bin-to-bin migrations due to detector and reconstruction effects. Simulated samples of events were also employed to determine selection and reconstruction efficiencies.

Systematic uncertainties on the measurements of the differential branching fractions were found to be dominated on the one hand by the understanding of detector and reconstruction

effects and on the other hand by the understanding of backgrounds from non-$B\overline{B}$ continuum events in the case of the Belle analysis and backgrounds from other $\overline{b} \to \overline{u}\ell^+\nu_\ell$ decays in the case of the BaBar analysis.

Hadronic tagged measurements

The BaBar collaboration published a hadronic tagged analysis [279] based on a data set corresponding 232 million produced $B\overline{B}$ pairs, the Belle collaboration published such an analysis [287] based on their full data set, corresponding to 772 million produced $B\overline{B}$ pairs. In the BaBar analysis, the opposite-side B meson, $B_{\rm tag}$, was fully reconstructed in the same combination of about 1000 exclusive final states that was employed in in their measurements of $|V_{cb}|$ from hadronic tagged samples of $B \to D^{(*)}\ell^+\nu_\ell$ decays described in Section 5.2.1 above. In the Belle analysis, a multivariate algorithm based on an artificial neural network was employed to select $B_{\rm tag}$ candidates in about 1100 fully reconstructed hadronic decay modes. The performance of this algorithm was evaluated on collision data employing samples of $B \to X_c\ell^+\nu_\ell$ candidates as a proxy for the signal decays.

Both analyses considered the signal decay modes $B^+ \to \pi^0\ell^+\nu_\ell$ and $B^0 \to \pi^-\ell^+\nu_\ell$. In addition to the particles employed in the reconstruction of the $B_{\rm tag}$ candidate, events were required to contain a charged lepton candidate and a π^0 candidate or an oppositely charged track that did not fulfill lepton or a kaon identification criteria. Events were rejected if they contained additional tracks or significant residual energy deposits in calorimeter. Muon candidates were rejected if they formed an invariant mass compatible with the known J/ψ mass when combined with the second charged track. Electron candidates were vetoed if they were compatible with being due to a photon conversion.

For correctly reconstructed events, the only missing particle should be the neutrino from the semileptonic decay of the signal candidate. The squared momentum transfer to the $\ell\nu_\ell$ system could be determined to good precision as $q^2 = (P_\ell + P_{\rm miss})^2$, where $P_{\rm miss} = P_{\Upsilon(4s)} - P_{B_{\rm tag}} - P_\pi - P_\ell$ is the missing four-momentum of the event. Moreover, the missing mass of the event, $m^2_{\rm miss} \equiv |P_{\rm miss}|^2$, should be close to zero.

Signal yields in bins of q^2 were determined from fits to the measured $m_{\rm ES}$ distribution of the $B_{\rm tag}$ candidates to extract the fraction of correctly tagged events and fits to the $m^2_{\rm miss}$ distribution to extract the fraction of signal candidates. The binning in q^2 was determined by the signal yields. Only three bins were employed in the BaBar analysis, while seven and thirteen bins were employed in the Belle analysis of the decays $B^+ \to \pi^0\ell^+\nu_\ell$ and $B^0 \to \pi^+\ell^+\nu_\ell$, respectively. Measured distributions of $m^2_{\rm miss}$ from the BaBar and Belle analyses, summed over all bins in q^2, are shown together with the results of the fits in Figure 5.38.

The precision on the measurement of the differential branching fractions was in both analyses limited by statistical uncertainties. The largest contributions to the systematic uncertainty were found to be due to the knowledge of reconstruction efficiencies and the understanding of background contributions from other $B \to X_u\ell^+\nu_\ell$ decays in the case of the BaBar analysis and by the understanding of the $B_{\rm tag}$ reconstruction efficiency in the case of the Belle analysis.

Semileptonic tagged measurements

The latest semileptonic tagged analysis published by the BaBar collaboration [281] was based on a data set corresponding to 383 million produced $B\overline{B}$ pairs. The Belle collaboration published a semileptonic tagged analysis [285] that was based on a data set corresponding to about 275 million produced $B\overline{B}$ pairs. In both analyses, $B_{\rm tag}$ candidates were reconstructed in the decays of charged and neutral B mesons to $D^*\ell^+\nu_\ell$ and $D\ell^+\nu_\ell$, where D^* candidates were reconstructed in their decays $D^{*+} \to D^0\pi^+$, $D^{*+} \to D^+\pi^0$, $D^{*0} \to D^0\pi^0$ and, in the case of the BaBar analysis, $D^{*0} \to D^0\gamma$. Charged D candidates where reconstructed in their decays to $K^+\pi^-\pi^+$ and $K^0_S\pi^+$ in the BaBar analysis and in a total of seven fully reconstructed hadronic

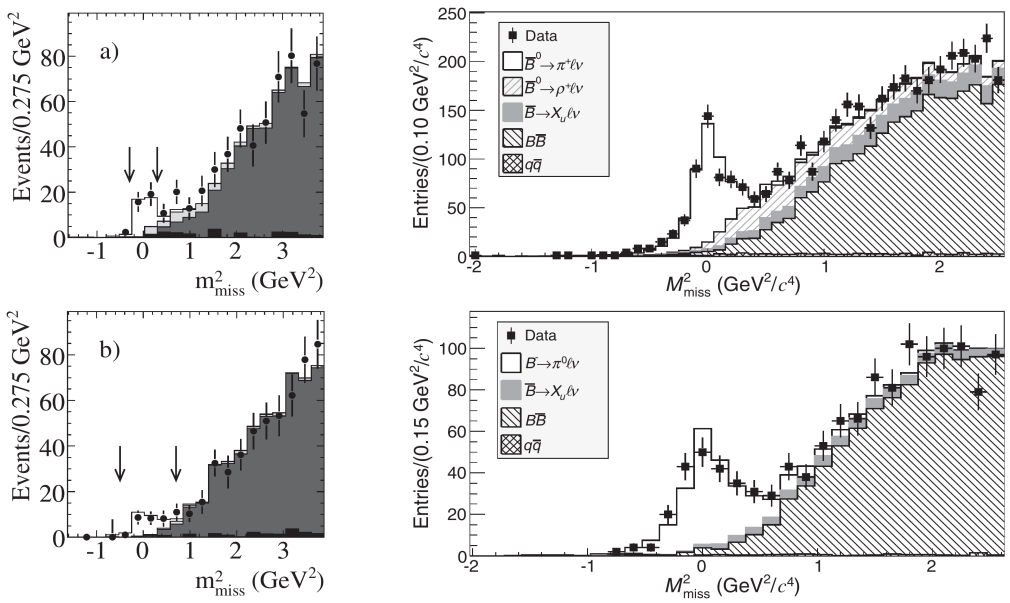

Figure 5.38: Distribution of the squared missing invariant mass as observed in (top) $B^0 \to \pi^0 \ell^+ \nu_\ell$ and (bottom) $B^+ \to \pi^0 \ell^+ \nu_\ell$ candidates in the hadronic tagged (left, from [279]) BaBar and (right, from [287]) Belle measurements of $|V_{ub}|$ in these decay modes. The results of fits to the data are superimposed, where in the panels on the left white histograms indicate the signal component, light grey histograms indicate the background component from other $B \to X_u \ell^+ \nu_\ell$ decays, dark grey histograms indicate backgrounds from $B \to X_c \ell^+ \nu_\ell$ decays and black histograms indicate backgrounds from other sources. Vertical arrows indicate the boundaries of the signal regions. The meaning of the different shadings in the panels on the right are explained in the legends of the plots.

decay modes to combinations of charged and neutral kaons in the Belle analysis. Neutral D candidates were fully reconstructed in four hadronic decay modes in the BaBar analysis and in ten decay modes in the Belle analysis.

In both analysis, the reconstructed D^* or D candidate was paired with a charged lepton candidate and the angle $\cos\theta_{B,D^{(*)}\ell}$ between the $D^{(*)}\ell$ system and the $B_{\rm tag}$ candidate was calculated as defined in the discussion of exclusive measurements of $|V_{cb}|$ in Section 5.2.1. A loose requirement was applied on the value of $\cos\theta_{B,D^{(*)}\ell}$ to suppress backgrounds.

Exactly one additional charged lepton candidate was required in the remainder of the event. Pairs of leptons compatible with being due to a J/ψ decay were rejected as well as electron candidates that were compatible with being due to a photon conversion. In the Belle analysis, the charged leptons on the tag side and the signal side were required to have opposite charge. In the case of $B^0\overline{B}^0$ events, this requirement leads to a signal loss due to $B^0 - \overline{B}^0$ mixing. This loss was estimated from samples of simulated events.

The charged lepton candidate was then combined with a π^0 candidate or a track of opposite charge from the remainder of the event to form $B \to \pi\ell^+\nu_\ell$ candidates. The angle $\cos\theta_{B,\pi\ell}$ between the $\pi\ell$ system and the direction of flight of the decaying B meson was calculated as defined in the previous paragraphs and a loose requirement was applied on its value to suppress backgrounds. As the two B mesons are produced back-to-back in the centre-of-mass frame of the e^-e^+ collision, their directions of flight must lie on the intersection of the two cones defined by $\cos\theta_{B,D^{(*)}\ell}$ and $\cos\theta_{B,\pi\ell}$ as illustrated in Figure 5.28. This leads to the requirement

$$\cos^2\phi_B \;=\; \frac{\cos^2\theta_{B,D^{(*)}\ell} \,+\, \cos^2\theta_{B,\pi\ell} \,+\, 2\cos\theta_{B,D^{(*)}\ell}\cos\theta_{B,\pi\ell}\cos\gamma}{\sin^2\gamma}\;,$$

where γ is the angle between the reconstructed momenta of the $D^{(*)}\ell$ system and the $\pi\ell$ system and ϕ_B is the angle between the direction of flight of the B meson and the plane defined by the

momenta of the $D^{(*)}\ell$ and the $\pi\ell$ systems. For signal events, $\cos^2\phi_B \leq 1$, while for background this variable has no physical meaning and follows a broad distribution.

The kinematic reconstruction does not permit to determine the sign of ϕ_B and the flight direction of the signal B candidate is known only up to a two-fold ambiguity. The value of q^2 was therefore approximated, neglecting the momentum of the B meson in the laboratory system, as

$$q^2 \approx (m_B - E_\pi)^2 - |\vec{p}_\pi|^2,$$

where E_π and $\vec{p}_\pi$ are the reconstructed energy and momentum of the pion candidate. The analysis was performed in three bins in q^2. The signal yield in each bin was obtained from fits to the measured $\cos^2\phi_B$ distributions, where the expected shapes of the distributions for signal and background components were determined from samples of simulated events. Measured distributions of $\cos^2\phi_B$ from the BaBar and Belle analyses, summed over all bins in q^2, are shown together with the results of the fits in Figure 5.38.

The reconstruction efficiency for $B_{\rm tag}$ candidates was determined from collision data, applying the analysis to event samples in which both B mesons were reconstructed in semileptonic decays to $B \to D^{(*)}\ell^+\nu_\ell$. The reconstruction efficiency for the signal B meson were determined from samples of simulated events. In both analyses, the precision on the measurement of the differential branching fractions was limited by its statistical uncertainty. Systematic uncertainties were found to be dominated by the understanding of detector and reconstruction effects, by the modelling of signal and background distributions from simulated events and by the calibration of the $B_{\rm tag}$ reconstruction efficiency, which in turn was limited by statistical uncertainties due to the size of the available control sample.

Summary of results

In all analyses described above, values of $|V_{cb}|$ are extracted from the measured differential branching fractions. The obtained results range from 3×10^{-3} to 4×10^{-3}, with quoted statistical uncertainties of 3% to 6% for untagged analyses and of 10% to 12% for tagged analyses. Systematic uncertainties from experiment are quoted as 2% to 5% and uncertainties due to form-factor normalizations as 10% to 15%.

The Heavy Flavour Averaging Group [2] has calculated averages of the measured partial branching fractions and used these averages along with form factor normalizations based on two lattice QCD calculations [272,273] and two calculations based on light-cone sum rules [274,288] to determine combined values of $|V_{ub}|$. The results of the four calculations are consistent with each other. No attempt was made to form an average of these results or select a best value. The Heavy Flavour Averaging Group also performed simultaneous fits of form factor parameterizations to the four most precise BaBar and Belle measurements [282,284,286,287], together with either four points in the high-q^2 region obtained from lattice QCD calculations [273] or a point at $q^2 = 0$ obtained from light-cone sum rules [289]. The results of these two fits are shown in Figure 5.41. The fits give χ^2 probabilities of 5.3% and 2.9% and yield values of $|V_{ub}| = (3.28 \pm 0.29) \times 10^{-3}$ and $|V_{ub}| = (3.53 \pm 0.29) \times 10^{-3}$, respectively. The 2014 edition of the Review of Particle Physics [1] quotes the first of the two results

$$|V_{ub}| \;=\; (3.28 \pm 0.29) \times 10^{-3}.$$

as the value of $|V_{ub}|$ from exclusive measurements.

5.2.3 Determination of $|V_{cb}|$ from inclusive semileptonic decays

At the parton level, the decay rate for the inclusive process $b \to c\ell\nu_\ell$ is determined by the value of $|V_{cb}|$ and by the masses, m_b and m_c, of the beauty and charm quark. Perturbative and non-perturbative effects due to the strong interaction can be calculated [290–292] employing Heavy

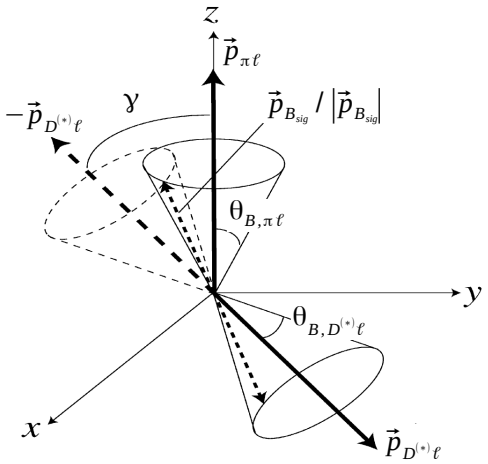

Figure 5.39: Illustration of the decay topology in semileptonic tagged events: the z axis is defined by the momentum vector of the $\pi\ell$ system, the y axis is defined such that the momentum vector of the $D^{(*)}\ell$ system lies in the $y-z$ plane. The momentum vectors of the decaying B mesons must lie on the intersections of the two cones defined by $\cos\theta_{B,\pi\ell}$ and $\cos\theta_{B,D^{(*)}\ell}$. The short-dashed arrow indicates one of the two solutions. The angle ϕ_B is not shown, it is the angle between the direction of flight of the signal B meson and the $y-z$ plane (adapted from [285])

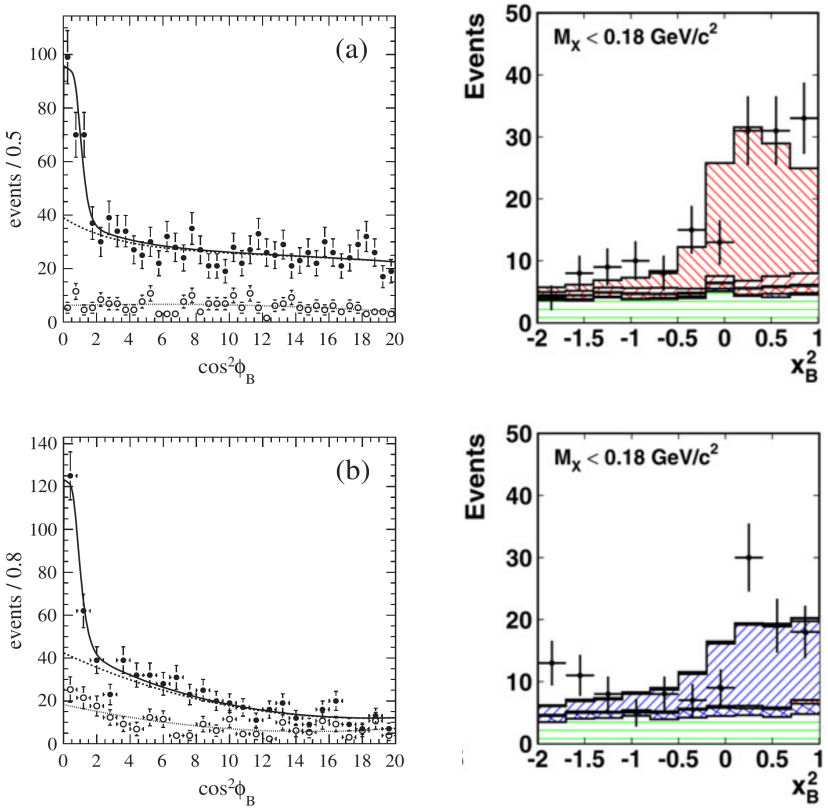

Figure 5.40: Measured distributions of $\cos^2\phi_B$, respectively $x_B^2 \equiv 1-\cos^2\phi_B$, for selected (top) $B^0\to\pi^-\ell^+\nu_\ell$ candidates and (bottom) $B^+\to\pi^0\ell^+\nu_\ell$ candidates from the semileptonic tagged measurements of $|V_{ub}|$ in (left, from [281]) BaBar and (right, from [285]) Belle. The results of fits to the data are superimposed. In the panels on the left, dotted lines indicate the component from combinatorial background and dashed lines indicate the contribution from other background components. In the panels on the right, the red falling hatching indicates the $B^0\to\pi^-\ell^+\nu_\ell$ signal component, blue rising hatching indicates the $B^+\to\pi^0\ell^+\nu_\ell$ component, red rising and red and blue crossed hatchings indicate background components from other $B\to X_u\ell^+\nu_\ell$ decays, and green horizontal hatching indicate other $B\overline{B}$ background components.

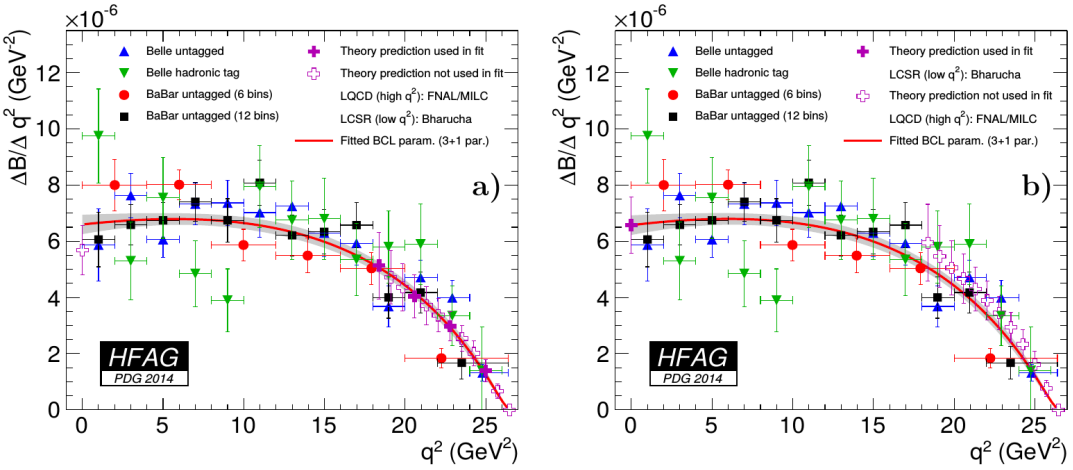

Figure 5.41: Simultaneous fits to BaBar and Belle measurements of the differential $B \to \pi \ell^+ \nu_\ell$ branching fraction as a function of q^2 combined with (left) four points at high values of q^2 obtained from Lattice-QCD calculations and (right) a point at $q^2 = 0$ from light-cone sum rules, as prepared by the Heavy Flavour Averaging Group for the 2014 edition of the Review of Particle Physics (from [2]).

Quark Expansion (HQE) theory based on local Operator Product Expansion (OPE) [293]. Expansions in $1/m_b$ and the strong coupling constant, α_s, to order $1/m_b^3$ yield four non-perturbative parameters, that are usually denoted as $\mu_\pi^2(\mu)$, $\mu_G^2(\mu)$, $\rho_D^3(\mu)$ and $\rho_{LS}^3(\mu)$ and are functions of the renormalization scale, μ, that is employed to separate long-distance and short-distance QCD dynamics. The four parameters can be related to the shapes of the energy distributions of the charged lepton and of distribution of the squared invariant mass of the hadronic system, m_X^2, in inclusive decays $B \to X_c \ell^+ \nu_\ell$. This allows to extract the value of $|V_{cb}|$ together with the values of the non-perturbative parameters from fits to the measured decay rates and the moments of order n,

$$M_\ell^{(n)}(E_{\rm min}) \equiv \frac{\int_{E_\ell=E_{\rm min}}^{\infty} E_\ell^n \, (d\Gamma/dE_\ell) \, dE_\ell}{\int_{E_\ell=E_{\rm min}}^{\infty} (d\Gamma/dE_\ell) \, dE_\ell}$$

or

$$M_X^{(n)}(p_{\rm min}) = \frac{\int_{p_\ell=p_{\rm min}}^{\infty} (m_X^2)^n \, (d\Gamma/dp_\ell) \, dp_\ell}{\int_{p_\ell=p_{\rm min}}^{\infty} (d\Gamma/dp_\ell) \, dp_\ell} \, ,$$

of these distributions as functions of a lower cut on the energy, $E_{\rm min}$, or the momentum, $p_{\rm min}$, of the charged lepton.

The effective masses, $m_b(\mu)$ and $m_c(\mu)$, of the b and the c quark have to be evaluated at the same value of the renormalization scale as the non-perturbative parameters and this requires the choice of a suitable renormalisation scheme. Two schemes have been applied and yield comparable results and uncertainties. The kinetic scheme [294, 295] makes use of the masses that enter non-relativistic expressions for the kinetic energy of the heavy quarks and can be calculated using heavy-quark sum rules. In the 1S scheme [296] the b quark mass is related to perturbative expressions for the measured mass of the $\Upsilon(1S)$ resonance.

Additional experimental input that allows to constrain the value of m_b can be employed to reduce the theory uncertainty on the determination of $|V_{cb}|$. Since the moments measured in semileptonic decays are sensitive to the difference between the masses of the beauty and charm quarks, such additional constraints can also be obtained from direct measurements of the mass of the charm quark. Alternatively, additional input can be obtained from measurements of the moments of the photon-energy spectrum in inclusive radiative decays $B \to X_s \gamma$, where X_s denotes a hadronic system containing a strange quark.

Moments of the m_X^2 distribution in inclusive semileptonic decays have been measured at CLEO [297], CDF [298], DELPHI [299], BaBar [300, 301] and Belle [302], while moments of

the E_ℓ^2 spectrum and have been measurred at CLEO [303], DELPHI [299], BaBar [301, 304] and Belle [305]. Measurements of the photon-energy spectrum and its moments in inclusive radiative decays $B \to X_s\gamma$ have been performed at CLEO [306], BaBar [307,308] and Belle [309, 310]. The most recent measurements of these observables at BaBar and Belle will be described in the following.

Moments of the squared hadronic invariant-mass distribution

Moments of the m_X^2 distribution as a function of the minimum momentum, $p_{\rm min}$, of the charged lepton have been measured in hadronic tagged analyses, where the opposite-side B meson, $B_{\rm tag}$, was fully reconstructed in a variety of hadronic decay modes. A charged lepton with momentum above $p_{\rm min}$ was required in the remainder of the event. All remaining tracks and neutral energy deposits were assigned to the X_c system and their invariant mass was calculated. A cut on the missing energy of the event was applied to suppress backgrounds.

The BaBar collaboration published a measurement [301] based on a data set corresponding to 232 million produced $B\overline{B}$ pairs, in which the 1st to 6th moments of the m_X^2 spectrum were determined for values of $p_{\rm min}$ between 0.8 GeV/c and 1.9 GeV/c. Opposite-side $B_{\rm tag}$ candidates were reconstructed in the same combination of about 1100 hadronic decay modes that was employed in hadronic tagged measurements of exclusive semileptonic decay rates discussed in the previous paragraphs. The total selection efficiency for $B_{\rm tag}$ candidates was quoted as 0.4%. In the calculation of m_X^2, particle identification criteria were employed to assign a mass hypothesis to each track. To improve the resolution on m_X^2, a kinematic fit was performed imposing constraints on energy and momentum conservation between the initial and final states, on the masses of the two B meson candidates in the event to be equal and on the invariant mass of the unreconstructed neutrino to be zero. In the extraction of the signal component from the selected event sample, continuum background from non-$B\overline{B}$ events, combinatorial background in which the $B_{\rm tag}$ candidate was wrongly reconstructed, and residual backgrounds from misidentified signal decays were considered. Continuum and combinatorial backgrounds were estimated from a fit to the measured $m_{\rm ES}$ distribution of $B_{\rm tag}$ candidates while residual backgrounds were estimated from samples of imulated events. An event-by-event correction factor based on calibration curves determined from samples of simulated events were applied to correct for biases due to the detector acceptance, finite reconstruction efficiency and resolution, and final-state radiation of the charged lepton. Examples of the corrected moments as functions of the value of $p_{\rm min}$ are shown in Figure 5.42. Systematic uncertainties were found to be dominated by the understanding of background and signal modelling, possible differences in the reconstruction efficiency between simulated data and collision data, particle identification performance, and the mentioned bias correction.

The Belle collaboration published a measurement [302] based on a data set corresponding to 152 million produced $B\overline{B}$ pairs, in which the 1st, 2nd central and 2nd non-central moments of the m_X^2 distribution were determined for values of $p_{\rm min}$ between 0.7 GeV and 1.9 GeV. In this analysis, decays of $B_{\rm tag}$ candidates to $D^{(*)}\pi^+$, $D^{(*)}\rho^+$, and $D^{(*)}a_1^+$ were considered, where a_1^+ candidates were reconstructed by combining a ρ^0 candidate with a charged pion and $\rho^+$and ρ^0 candidates were reconstructed in their decays to two pions. An initial estimate for the four-momentum of the X_c system was formed by summing over the four-momenta of all remaining charged tracks and unmatched energy calorimeter deposits in the event. An estimate of the four-momentum, P_ν, of the neutrino was calculated from the momentum imbalance of the event and the four-momentum of the X_c system was re-calculated as

$$P_X \;\equiv\; P_{\Upsilon(4s)} - P_{B_{\rm tag}} - P_\ell - P_\nu \;.$$

This iterative procedure was found to improve the resolution on m_X^2 by almost a factor two compared to the initial estimate. Backgrounds from non-$B\overline{B}$ continuum events were estimated

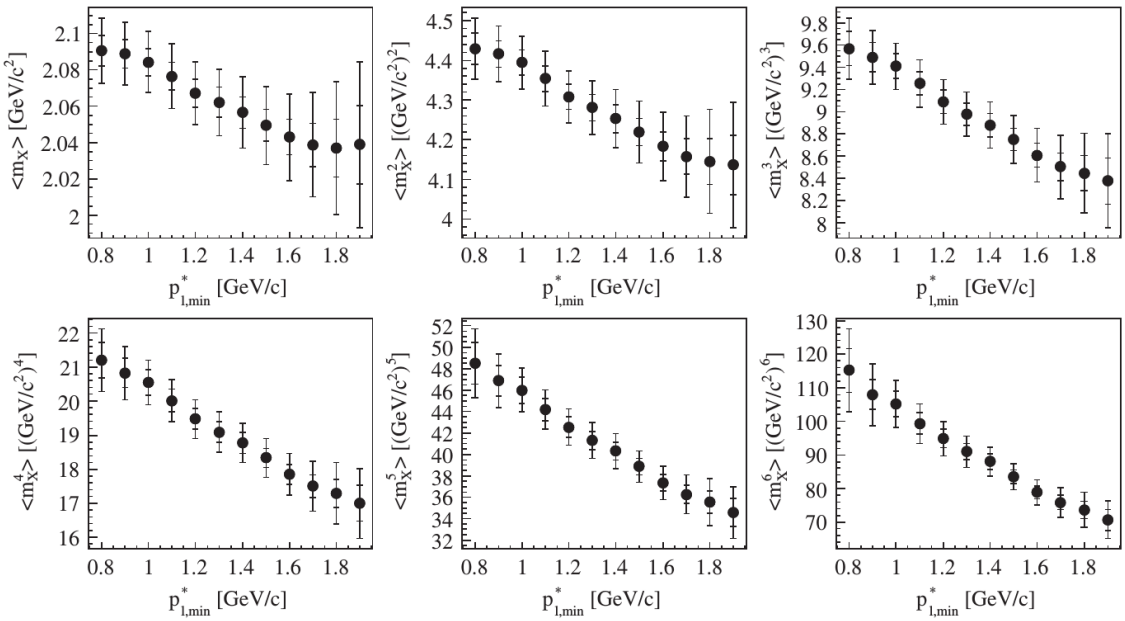

Figure 5.42: First to sixth moments of the hadron energy spectrum as a function of the minimum momentum of the charged lepton, denoted here as $p^*_{\ell,\mathrm{min}}$, as measured in the BaBar analysis of inclusive decays $B \to X_c \ell^+ \nu_\ell$. The inner error bars show statistical uncertainties, the outer error bars show statistical and systematic uncertainties added in quadrature (from [301]).

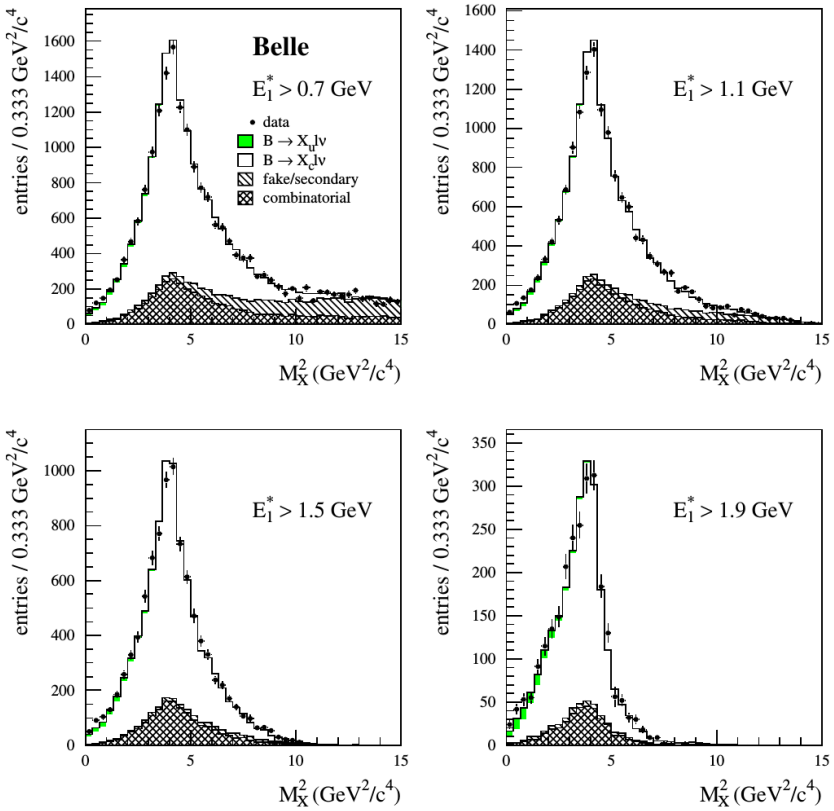

Figure 5.43: Distribution of the squared invariant-mass, denoted here as M_X^2, for different cuts on the minimum energy of the lepton candidate, as measured in a Belle measurement of inclusive decays $B \to X_c \ell^+ \nu_\ell$. The shaded areas indicate different background contributions as listed in the plot legend (from [302]),

from collision data collected at a e^-e^+ collision energy below the $\Upsilon(4S)$-resonance, combinatorial backgrounds and backgrounds from secondary or misidentified leptons were estimated from samples of simulated events. The measured m_X^2 distributions for different cuts on the minimum energy of the lepton candidate are shown in Figure 5.43. An unfolding technique using samples of simulated events was applied to correct the binned m_X^2 spectrum for bin-to-bin migrations due to detector effects and the finite measurement resolution. Systematic uncertainties were found to be dominated by the understanding of possible remaining backgrounds, by the knowledge of branching fractions and form factors assumed in the generation of simulated event samples, by the binning and unfolding technique, and by the estimation of reconstruction efficiencies.

Moments of the electron energy distribution

The Belle collaboration published an analysis of the E_e distribution [305], which was based on the same data set corresponding to 152 million produced $B\overline{B}$ pairs, and in which the first four moments of the distribution were determined for values of $E_{\rm min}$ from 0.4 to 2.0 GeV.

In this analysis, $B_{\rm tag}$ candidates were again fully reconstructed in a variety of hadronic decay modes. A high-momentum electron candidate was then required amongst the remaining tracks. If several such candidates were found in the same event, that that with the highest momentum was selected. Continuum background from non-$B\overline{B}$ events was estimated from data collected at collision energies below the $\Upsilon(4S)$ resonance, while combinatorial background was estimated from samples of simulated events. Secondary electrons from the decay chain $b \to c \to q\ell\nu_\ell$ were suppressed in events where the $B_{\rm tag}$ candidate was a charged B meson by requiring that the electron candidate had the opposite charge of the $B_{\rm tag}$ candidate. A similar requirement was not applied for events in which the $B_{\rm tag}$ candidate was a neutral B meson in order not to reject events in which one of the two B mesons in the event had mixed at the time of its decay. Therefore, the background contamination due to secondary electrons is significantly larger in the sample of neutral B candidates than it is in the sample of charged B candidates. This background, as well as contributions from charmless semileptonic decays $B \to X_u\ell\nu_\ell$, electrons from decays of J/ψ or $\psi(2s)$ mesons, $\pi^0 \to e^+e^-\gamma$ or photon conversions and misidentified electrons were estimated from a fit to the measured electron momentum spectrum, where the expected shapes for these backgrounds as well as for the signal mode were obtained from samples of simulated events. Samples of simulated events were also employed to unfold the measured spectrum for distortions due to final-state radiation of the electron as well as biases from detector effects and selection criteria. The measured electron momentum and energy distributions as well as the moments of the electron energy distribution are shown in Figures 5.44 and 5.45. Systematic uncertainties of this measurement were found to be dominated by the understanding of the effects of the event selection, electron track reconstruction and electron identification efficiencies, the estimation of backgrounds, and the modelling of signals and backgrounds in the generation of the samples of simulated events.

The BaBar collaboration performed a measurement [304] of the 1st, 2nd and 3rd central moments of the electron energy spectrum for energy thresholds between 0.6 and 1.5 GeV that was based on a data set corresponding to 51 million produced $B\overline{B}$ pairs. The analysis was "reevaluated" in Ref. [301] using updated measurements of the branching fractions for background decay modes as well as performing an improved evaluation of systematic uncertainties. In this analysis, opposite-side $B_{\rm tag}$ candidates were not fully reconstructed. Events were required to contain a minimum of five reconstructed tracks or four tracks and two photon clusters were required to select collisions in which a hadronic interaction took place. An electron candidate with momentum between 1.4 and 2.3 GeV/c was then required to tag the event as a $B\overline{B}$ event. A second electron candidate with a momentum above 0.5 GeV/c was required to measure the energy spectrum and its moments. The sample of selected events was split into unlike-sign events, in which the two electron candidates were of opposite charge and and like-sign events, in

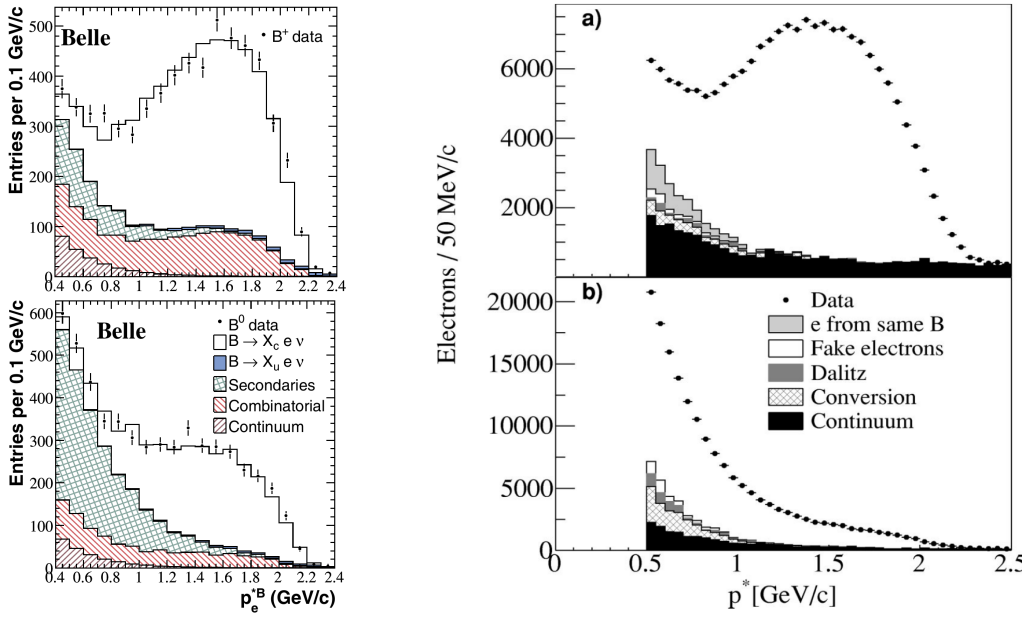

Figure 5.44: Distributions of (left, from [305]) the electron momentum in the rest frame of the B candidate for selected electron candidates in events tagged as decays of (top) charged and (bottom) neutral B mesons as obtained in the Belle analysis of inclusive decays $B \to X_c \ell^+ \nu_\ell$, and of (right, from [304]) the electron momentum in the rest frame of the $e^- e^+$ collision for (top) unlike sign and (bottom) like-sign dielectron candidates from the BaBar analysis of such decays. In all panels, shaded histograms indicate background contributions as explained in the plot legends and the main text.

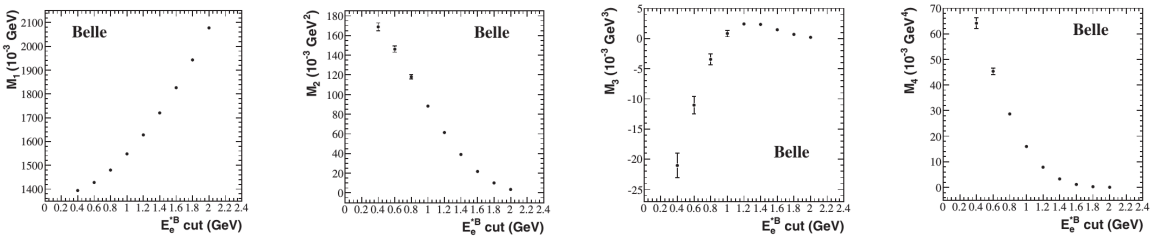

Figure 5.45: First to fourth moments of the electron energy spectrum as a function of the electron threshold energy, denoted here as E_e^{*B}, as obtained in the Belle analysis of inclusive decays $B \to X_c \ell^+ \nu_\ell$ (from [305]).

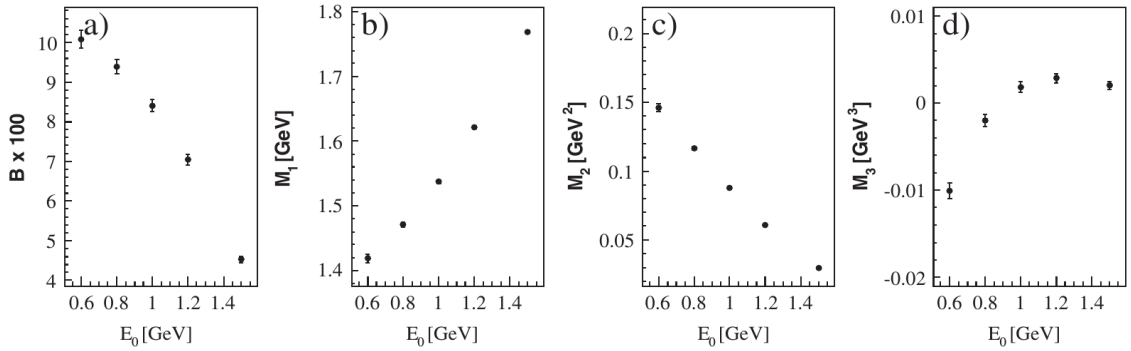

Figure 5.46: Inclusive branching fraction and first to third moments of the electron energy spectrum as a function of the electron threshold energy, denoted here as E_0, as obtained in the BaBar analysis of inclusive decays $B \to X_c \ell^+ \nu_\ell$ (from [301]).

which the two electron candidates were of same charge. Signal events in which each of the two selected electron candidates originated from the primary semileptonic decay of one of the two B mesons in the event will belong to the unlike-sign sample, except in $B^0\overline{B}^0$ events in which one of the two neutral B mesons had mixed into its antiparticle at the moment of its decay. In addition to the signal component, the unlike-sign sample contains backgrounds from J/ψ decays and from secondary electrons due to the decay chain $b \to c \to q\ell\nu_\ell$. Such backgrounds were suppressed by cuts on the invariant mass of the electron pair and on the opening angle between the two electron candidates. Continuum backgrounds from non-$B\overline{B}$ events in both the unlike-sign and like-sign samples were estimated from collision data collected below the $\Upsilon(4S)$ resonance, backgrounds from photon conversions, decays $\pi^0 \to e^+e^-\gamma$ and misidentified hadrons were estimated from control samples in collision data. Backgrounds due to electrons from τ decays, secondary electrons from the decay chain $b \to c\bar{c}s$, and from J/ψ and $\psi(2s)$ decays in which one electron was missed, were estimated from samples of simulated events. The number of signal candidates in a given bin i in electron energy was calculated as

$$N^i \;=\; \frac{1-f_0\chi_0}{1-2f_0\chi_0}\,\frac{N^i_{e^+e^-}}{\epsilon^i} \;-\; \frac{f_0\chi_0}{1-2f_0\chi_0}\,N^i_{e^\pm e^\pm}\;,$$

where $N^i_{e^+e^-}$ and $N^i_{e^\pm e^\pm}$ are the background-subtracted numbers of unlike-sign and like-sign events, f_0 is the branching fraction for the $\Upsilon(4S)$ decays to a pair of neutral B mesons and χ_0 is the time-integrated $B^0-\overline{B}^0$ mixing probability. The binned electron spectrum obtained in this manner was corrected for effects of electron bremsstrahlung using simulated samples of events. The small background contamination from charmless semileptonic decays $B \to X_u\ell\nu_\ell$ was also estimated from simulation. The result of the measurement in terms of the inclusive branching fraction and the moments of the energy distribution as a function of the minimum electron energy are shown in Figure 5.46. The quoted systematic uncertainties on these measurements are dominated by the understanding of the electron identification efficiency, by bremsstrahlung correction and by the understanding of the background from cascade decays $\bar{b} \to \bar{c}\ell^+$.

Moments of the photon-energy spectrum in inclusive radiative decays

Moments of the photon energy spectrum in radiative decays $B \to X_s\gamma$ provide input on the mass of the b quark, m_b, and can be employed to reduce the theory uncertainty on the determination of $|V_{cb}|$ from inclusive semileptonic decays. In the rest frame of the b quark, the emitted photon is monochromatic with energy $E_\gamma \approx m_b/2$. The observed photon energy is smeared by the motion of the b quark inside the B meson and the energy distribution is therefore sensitive to m_b. The BaBar collaboration published three analyses of the photon spectrum between 1.9 GeV and 2.6 GeV. In the first of these analyses [307], the X_s system was reconstructed employing a total of 38 final states containing a charged kaon or a K^0_S candidate together with up to four pions, or an η meson and a pion, or three kaon candidates and a pion. The energy of the photon was estimated as

$$E_\gamma \;\equiv\; \frac{m_B^2 - m_X^2}{2m_B}\,,$$

where m_B is the known mass of the B meson and m_X is the measured invariant mass of the X_s system. In this manner, the photon energy could be estimated to a precision of about (1–5) GeV, compared to a resolution of 50 MeV on the measurement of energy deposits in the electromagnetic calorimeter. The X_s system was combined with a photon candidate to form B meson candidates. Photon candidates were rejected if they gave an invariant mass consistent with a π^0 or η meson if combined with a second photon in the event. Cuts on event shape variables as well as on the energy imbalance, ΔE, and the beam-energy substituted invariant mass, $m_{\rm ES}$, of the $X_s\gamma$ system were employed to reject continuum backgrounds. Distributions of $m_{\rm ES}$ for simulated signal and background samples are shown in Figure 5.47. Backgrounds from

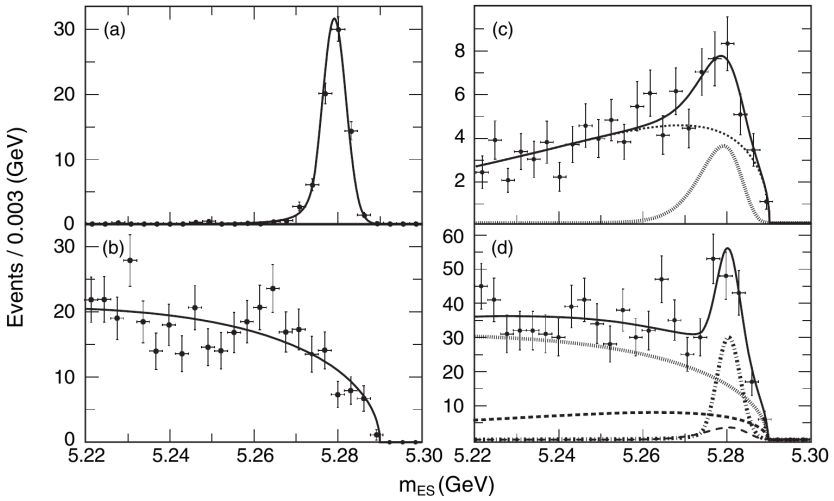

Figure 5.47: Fits to the $m_{\rm ES}$ distribution for reconstructed samples of (top left) simulated signal events, (bottom left) simulated continuum background, (top right) simulated $B\overline{B}$ backgrounds, and (bottom right) on-peak data from the first BaBar analysis of the photon energy spectrum in radiative decays $B \to X_s\gamma$. In the upper right panel, the dashed line indicates contributions from combinatorial background and the dotted line indicates contributions from peaking backgrounds. In the lower right panel, the dotted-dashed line indicates the fitted signal contribution, the dotted line indicates continuum background, the long-dashed line peaking $B\overline{B}$ background and the dashed line combinatorial $B\overline{B}$ background (from [307]).

misidentified B-meson decays were estimated from samples of simulated events. Reconstruction and selection efficiencies were also determined from simulation. Systematic uncertainties on the measurement of the moments were found to be dominated by the fit employed to extract the signal component, the modelling of peaking backgrounds, and the estimation of the fraction of the missing X_s states that were not included in the analysis.

In the second BaBar analysis [308], a high-momentum lepton from the decay of the opposite-side B meson, $B_{\rm tag}$, was employed to tag $B\overline{B}$ events. No attempt was made to reconstruct the X_s system and the photon energy was determined from the measured energy deposit in the calorimeter. Remaining continuum background from non-$B\overline{B}$ events was further reduced by a cut on the angle between the tagging lepton and the photon candidate and by requiring a significant missing energy of the event due to the undetected neutrino of the semileptonic $B_{\rm tag}$ decay. Backgrounds from $B\overline{B}$ events with photons from π^0 or η decays, hard bremsstrahlung photons, or wrongly reconstructed photon candidates from misidentifed electrons or anti-neutron annihilations in the calorimeter were estimated from simulated samples of events. Systematic uncertainties in this analysis were found to be dominated by the estimation of these backgrounds.

The third BaBar analysis [311] employed fully reconstructed hadronic decays of $B_{\rm tag}$ candidates to select $B\overline{B}$ events, similar to the hadronic tagged analyses of semileptonic decays described above. The photon energy was again estimated from the measured energy deposit in the calorimeter. Requiring a fully reconstructed $B_{\rm tag}$ candidate led to smaller event yields in this analysis and the sample of selected candidates was subdivided into 100 MeV wide bins in the photon energy. The signal yield in each bin was determined from a fit to the $m_{\rm ES}$ distribution of the $B_{\rm tag}$ candidates. Selection efficiencies and bin-to-bin migrations in the photon energy spectrum were estimated from samples of simulated events. The systematic uncertainty in this measurement was found to be dominated by the understanding of the background subtraction.

The Belle collaboration performed a fully inclusive analysis of the photon energy spectrum between 1.8 and 2.8 GeV [309, 312]. Cuts on event-shape variables were employed to suppress

continuum background from non-$B\overline{B}$ events. The remaining continuum background was estimated from collision data collected at energies below the $\Upsilon(4S)$ resonance. Backgrounds from $B\overline{B}$ events, including real photons from π^0, η, ω, η', and J/ψ decays or from bremsstrahlung and wrongly reconstructed photon candidates from mididentified electrons or energy deposits from K_L^0 mesons or antineutrons, were estimated from simulated samples of events. Simulated samples of events were also employed to estimate selection and reconstruction efficiencies as well as biases on the energy spectrum due to the response of the calorimeter and due to the unmeasured momentum of the decaying B meson in the $\Upsilon(4S)$ rest frame. Statistical and systematic uncertainties on the measured moments were found to be of similar magnitude, where the quoted systematic uncertainties were dominated by the understanding of bias corrections on the energy spectrum.

A later Belle analysis [310] extended the measured range of photon energies down to 1.7 GeV and combined a fully inclusive reconstruction as in the previous analysis with a smaller event sample in which a charged lepton candidate from the decay of the opposite-side B meson was required to further suppress non-$B\overline{B}$ background. The remainder of the analysis was similar to that of the earlier measurements, except that an unfolding procedure similar to that described in Ref. [302] was performed to correct for distortions of the energy spectrum due to the response of the calorimeter. This approach avoided the need for the bias correction that was the largest source of systematic uncertainties in the earlier analysis. The precision of the measurement of the moments was found to be limited by systematic uncertainties, with the largest contribution being due to the understanding of the background subtraction.

Summary of results

Various fits to the data based on Heavy Quark Expansion were performed by both the BaBar [301, 313] and Belle [309] collaborations, resulting in measurements of $|V_{cb}|$ between 41.4×10^{-3} and 42.0×10^{-3}, with quoted uncertainties of about 1% from experiment and $(1-2)\%$ from theory. Global fits using input from different experiments have been performed in Refs. [2,295,314,315]. Recent fits performed by the Heavy Flavour Averaging Group are shown in Figure 5.48. The results from different approaches, using the kinetic or the 1S renormalization schemes, are in good agreement with each other. In the 2014 edition of the Review of Particle Physics [1] an arithmetic average of these results is formed and a value of

$$|V_{cb}| \;=\; (42.2 \pm 0.7) \times 10^{-3}$$

is quoted as the world average from inclusive semileptonic decays.

5.2.4 $|V_{ub}|$ from inclusive semileptonic decays

The total inclusive branching fraction for charmless semileptonic decays $B \to X_u \ell^+ \nu_\ell$ can be calculated to a precision of about 5% employing Heavy Quark Expansion theory in a similar manner as in the cslculation of the branching fraction for the decays $B \to X_c \ell^+ \nu_\ell$. Measurements of the total inclusive branching fraction are, however, challenging due to the large backgrounds from $B \to X_c \ell^+ \nu_\ell$ decays.

Good signal-to-background ratios can be achieved in restricted regions of phase space, in which decays to charmed mesons are suppressed to due to the larger mass of the c quark. The extrapolation of the measured partial cross section to the full phase space then relies on structure functions or shape functions that describe the momentum distribution of the b quark inside the B meson. These shape functions cannot be calculated from first principles, but they can be assumed to leading order to be independent of the specific b decay mode under consideration. Under this assumption, parametrizations of the leading shape functions can be derived in terms of HQE parameters and the values of these parameters can be determined from measurements of moments of the photon enegy spectrum in radiative decays $B \to X_s \gamma$

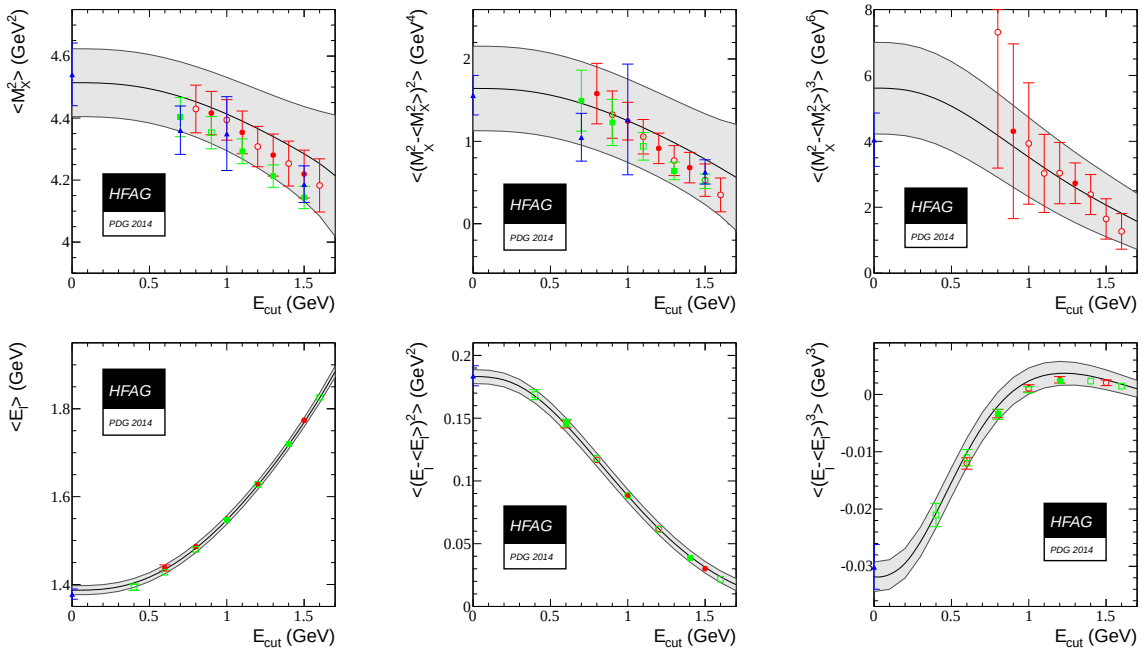

Figure 5.48: Fits to combined measurements of the moments of the (top) invariant mass of the hadron system and (bottom) electron energy spectrum as performed by the Heavy Flavour Averaging Group for the 2014 edition of the Review of Particle Physics. In all panels, measurements from the BaBar collaboration are shown by red circles, those by the Belle collaboration by green squares and those from Delphi, CDF and CLEO by blue triangles. Filled symbols indicate that the measurement was employed in the fit, while open symbols indicate measurements that were not included in the fit (from [2]).

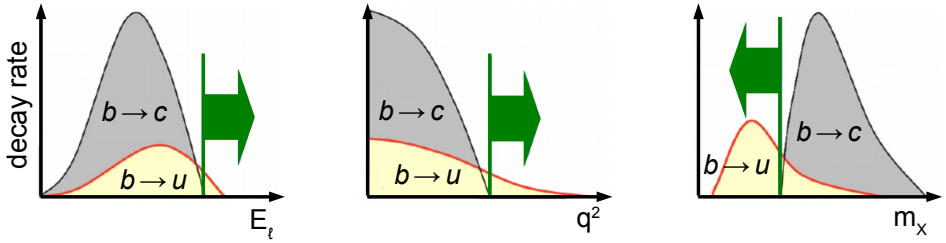

Figure 5.49: Illustration of variables that can be employed to select regions of phase space accessible to charmless semileptonic decays $B \to X_u \ell^+ \nu_\ell$ but not to decays $B \to X_c \ell^+ \nu_\ell$. In decays $B \to X_c \ell^+ \nu_\ell$, the larger mass of the c quark limits the possible energy, E_ℓ, of the charged lepton emitted in the decay and the squared momentum transfer, q^2, to the $\ell\nu_\ell$ pair, while the invariant mass, m_X of the hadronic system has to be at least as large as the mass of a D meson.

and of the lepton energy and X_c invariant mass spectra in semileptonic decays $B \to X_c \ell^+ \nu_\ell$ discussed in the previous section.

Early measurements of partial cross sections were performed at the LEP experiments [316–319], more precise measurements at CLEO [320], BaBar [321–325] and Belle [326–329]. Selected measurements from BaBar and Belle will be discussed in the remainder of this section. Untagged measurements [321,322,326,327] employed cuts on the momentum of the electron, on the squared momentum transfer to the lepton system, q^2, or on the invariant mass of the hadronic system, m_X, to select regions of phase space in which $B \to X_c \ell^+ \nu_\ell$ decays are suppressed due to kinematic constraints as illustrated in Figure 5.49. These untagged measurements yield large statistics but suffer from theoretical uncertainties due to the extrapolation from the small measured phase-space region. In tagged analyses [323–325, 328, 329], the opposite-side B meson, $B_{\rm tag}$, was fully reconstructed in a number of hadronic decay modes. Event yields are significantly reduced due to the small branching fractions for specific $B_{\rm tag}$ decay modes, but

the additional constraints from the reconstruction of $B_{\rm tag}$ allow a more precise determination to the kinematic properties of the signal decay and allow to explore larger regions of phase space, resulting in reduced theory uncertainties.

Untagged analyses

The BaBar [321] and Belle [327] collaborations published untagged analyses based on early data sets, corresponding to 88 million and 29 million produced $B\overline{B}$ pairs, respectively, in which the electron momentum spectrum was investigated close to its kinematic endpoint. By energy and momentum conservation in the decay, the maximum momentum of the electron in rest frame of the decaying B meson is about 2.6 GeV/c in decays $B \to X_u e^+ \nu_{\rm e}$ but only 2.3 GeV/c in decays $B \to X_c e^+ \nu_{\rm e}$. The fact that the momentum of the decaying B meson cannot be measured in untagged inclusive measurements leads to a smearing of the electron momentum spectrum by about 200 MeV/c in the rest frame of the e^+e^- collision. Expected distributions of the electron momenta in various $B \to X_c \ell^+ \nu_\ell$ and $B \to X_u \ell^+ \nu_\ell$ decays as obtained from simulated samples of events in BaBar are shown in Figure 5.50.

The BaBar measurement explored the electron momentum range from 2.0 to 2.6 GeV/c, the Belle measurement that from 1.9 to 2.6 GeV/c. In both analyses, electron candidates were rejected if they gave an invariant mass compatible with the known mass of the J/ψ meson when combined with a second electron candidate of opposite charge in the event. At least four resp. five reconstructed tracks were required and cuts on event-shape variables were applied to suppress continuum background from non-$B\overline{B}$ events. The sum of the four-vectors of all reconstructed tracks and neutral energy deposits was computed and a significant missing momentum of the event was required to tag the undetected neutrino from the semileptonic decay. The BaBar analysis required in addition a large opening angle between the momentum vector of the electron candidate and the missing momentum vector. The Belle analysis required a large opening angle between the momentum vector of the electron candidate and the thrust axis of the event, where this thrust axis was calculated including the missing momentum. The remaining background from non-$B\overline{B}$ events was estimated in both analyses from data collected at a collision energy below the $\Upsilon(4S)$resonance. Backgrounds from $B\overline{B}$ events were estimated by fitting the measured electron momentum spectrum with templates derived from samples of simulated background and signal events as illustrated in Figure 5.51. The simulations relied on model assumptions for the branching fractions and shape functions for the different decay modes and these assumptions limited the precision of the branching fraction measurement, together with systematic uncertainties related to the understanding of event reconstruction efficiencies.

The Belle collaboration published a second untagged measurement [326], based on a data set corresponding to 85 million produced $B\overline{B}$ pairs, in which both electrons and muons were considered and the signal region was defined by $q^2 > 8.0$ GeV$^2/c^2$ and $m_X < 1.7$ GeV/c^2. An inclusive reconstruction of the full event was performed and the energy and momentum of the undetected neutrino were estimated by the missing momentum and the missing energy of the event. The missing invariant mass, $m^2_{\rm miss} \equiv E^2_{\rm miss} - |\vec{p}_{\rm miss}|^2$ of the event was required to be small to suppress events with additional unreconstructed particles. The most likely combination of particles belonging to the X_u system was determined in an iterative procedure. The method made use of six discriminating variables, namely the the missing mass of the event and the momentum, the energy, the polar angle, the charge multiplicity and the charge sign of the opposite-side B candidate. Samples of simulated events were employed to derive for each of these variables a likelihood function, $L_{\rm corr}$, for correctly reconstructed events and a likelihood function, $L_{\rm rand}$, for events in which tracks were randomly assigned to the decays of the signal B meson, $B_{\rm sig}$, and the opposite-side B meson, $B_{\rm tag}$. For events selected in collision data, an initial value of the likelihood ratio $W \equiv L_{\rm rand}/(L_{\rm rand} + L_{\rm corr})$ was calculated, assigning the charged lepton, the neutrino and about one third of the remaining tracks, chosen

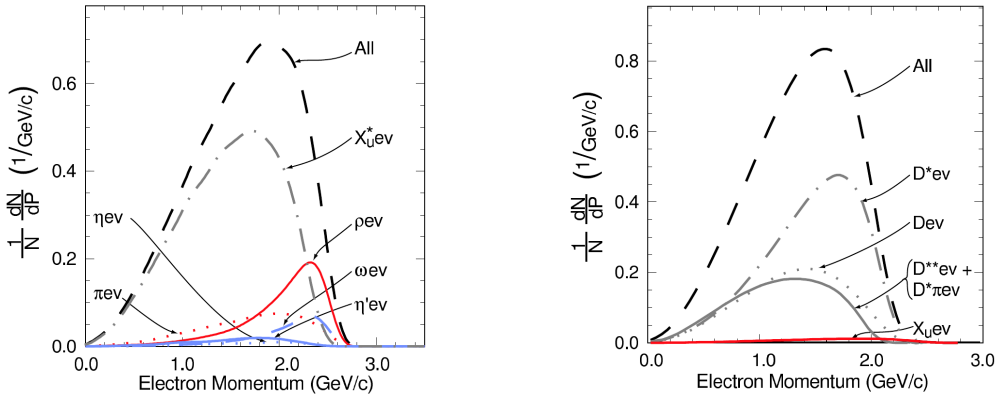

Figure 5.50: Electron momentum spectra from simulated (left) $B \to X_u e^+ \nu_e$ and (right) $B \to X_c e^+ \nu_e$ decays in BaBar (from [321]).

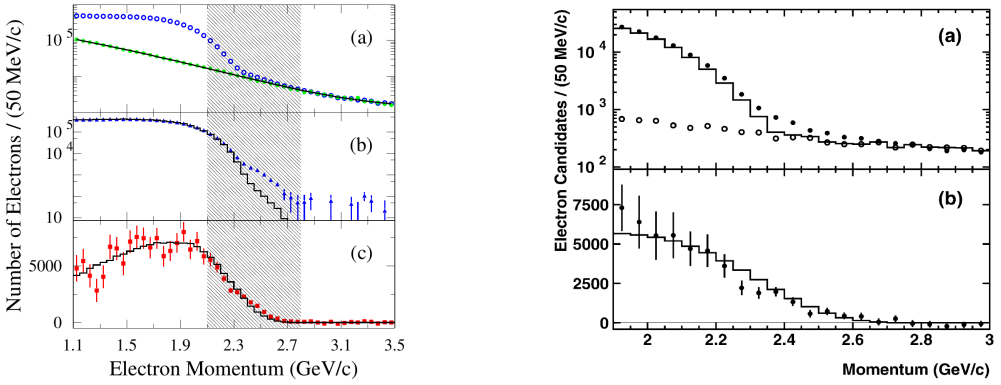

Figure 5.51: Electron momentum spectra as measured in the untagged (left, from [321]) BaBar and (right, from [327]) Belle measurements of inclusive semileptonic decays $B \to X_u e^+ \nu_e$. The upper left panel shows in blue open circles the measured spectrum for data collected on the $\Upsilon(4S)$ resonance and in green filled circles the spectrum for data collected at a $e^- e^+$ collision energy below the $\Upsilon(4S)$ resonance, the middle left panel shows in blue triangles on-resonance data after subtraction of the estimated non-$B\overline{B}$ background and as a histogram the estimated $B\overline{B}$ background as obtained from simulated samples of events, and the lower left panel shows in red squares on-resonance data after subtraction of all backgrounds and as a histogram the expected spectrum from simulated samples of events that were generated using a shape function derived from BaBar measurements of moments in $B \to X_c \ell^+ \nu_\ell$ and $B \to X_s \gamma$ decays. The upper right panel shows in filled circles data collected on the $\Upsilon(4S)$ resonance, in open circles the appropriately scaled distribution for non-$B\overline{B}$ data collected at a collision energy below the $\Upsilon(4S)$ resonance and as a histogram the sum of the estimated non-$B\overline{B}$and $B\overline{B}$ backgrounds. The lower right panel shows in filled circles the distribution for data collected on the $\Upsilon(4S)$ resonance after background subtraction and as a histogram the expected distribution for $B \to X_u e^+ \nu_e$ decays including final state radiation.

at random, to the $B_{\rm sig}$ candidate candidate and all remaining tracks to the $B_{\rm tag}$ candidate. Tracks were then swapped in an iterative procedure between the $B_{\rm sig}$ and the $B_{\rm tag}$ candidate to identify the combination of assignments that resulted in the lowest value of W. Events were accepted that resulted in a value of $W < 0.1$ and that fulfilled additional requirements on the individual discriminating variables. To suppress continuum background from non-$B\overline{B}$ events, a minimum value of the opening angle was required between the flight direction of the lepton candidate and the thrust axis of the $B_{\rm tag}$ candidate. The method was cross-checked on collision data using control samples of $B \to D^* \ell \nu_\ell$ and $B \to J/\psi X$ events. The remaining non-$B\overline{B}$ background was estimated from data collected at a $e^- e^+$ collision energy below the $\Upsilon(4S)$ resonance, backgrounds from $B \to X_c \ell \nu_\ell$ and other $B\overline{B}$ backgrounds were estimated

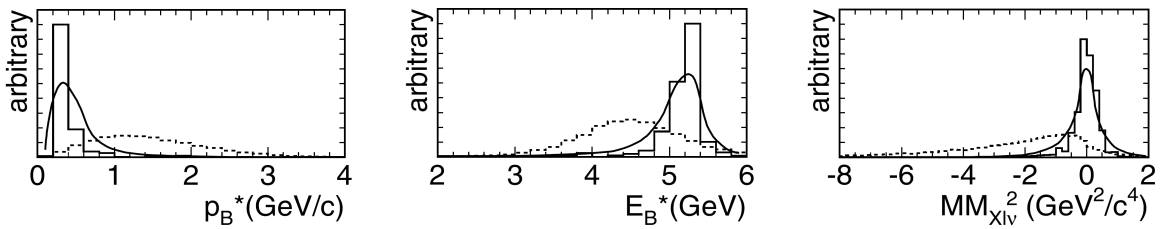

Figure 5.52: Distributions of the (left) momentum and (middle) energy assigned to the opposite-side B candidate, and of the (right) squared missing mass of the event, from the untagged Belle analysis of inclusive decays $B \to X_u \ell^+ \nu_\ell$. Solid curves shows these distributions for correctly reconstructed samples of simulated events, while dashed and solid histrograms show the distributions for collision data before and after the minimization of the likelihood ratio W, respectively (from [326]).

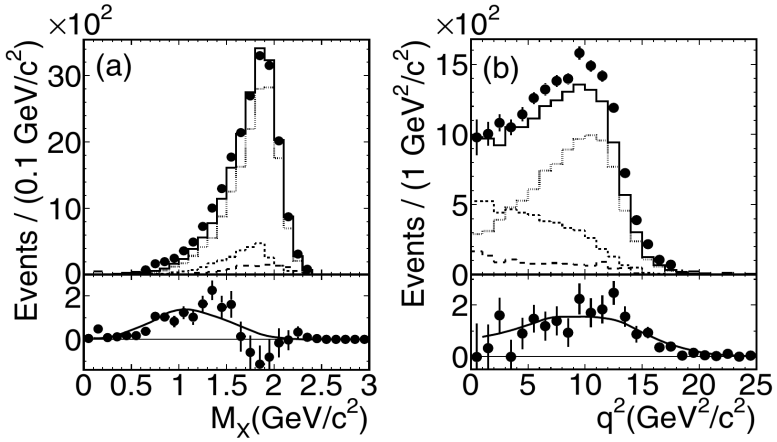

Figure 5.53: Distribution of (left) the reconstructed invariant mass of the X_u system and (right) the squared momentum transfer to the $\ell^+\nu_\ell$ system from the untagged Belle analysis of inclusive decays $B \to X_u \ell^+ \nu_\ell$. The results of the fit to the data are superimposed. In the upper panels, points show the distribution measured in collision data, dotted lines indicate the background component from $B \to D^* \ell^+ \nu_\ell$ decays, short dashed line indicate the background component from $B \to D \ell^+ \nu_\ell$ decays. long dashed lines indicate other background components and the solid line shows the sum of all background components. In the lower panels, points show the data after background subtraction and solid lines show the distributuons predicted from simulated samples of events (from [326])

by extrapolation from the region $m_X > 1.8$ GeV/c^2, using templates derived from samples of simulated events. Selection and reconstruction efficiencies were estimated from samples of simulated events. The precision of the branching fraction measurement was found to be limited by systematic uncertainties, where the largest quoted contributions were due to the understanding of reconstruction efficiencies and the estimation of $B\overline{B}$ backgrounds.

The BaBar collaboration published an analysis [322] based on a data set corresponding to 88 million produced $B\overline{B}$ pairsm in which the signal region was defined by cuts on the squared momentum transfer, q^2, and the energy, E_e, of the electron. An inclusive reconstruction of the event was performed and the missing momentum and missing energy were calculated. The missing invariant mass of the event was required to be small and the opening angle between the momentum vector of the selected electron candidate and the thrust vector of the remainder of the event was required to be large. The momentum vector, $\vec{p}_\nu$, of the undetected neutrino was estimated from the missing momentum of the event, applying a momentum-dependent correction factor derived from samples of simulated events in order to compensate for biases from other particles in the event that escaped detection. The four-momentum of the neutrino was then defined as $P_\nu \equiv (|\vec{p}_\nu|, \vec{p}_\nu)$ to calculate $q^2 = (P_e^2 + P_\nu^2)$. For given values of q^2 and E_e, energy and momentum conservation in the decay $B \to X \ell^+ \nu_\ell$ imply that the squared invariant

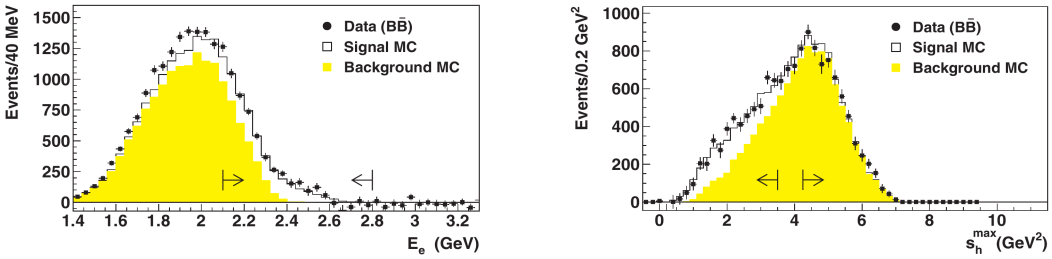

Figure 5.54: Distributions of the (left) energy of the electron candidate and (right) the maximum kinematically possible value, $s_h^{\max}$, of the squared invariant mass of the hadronic system, from the untagged BaBar analysis of inclusive decays $B \to X_u \ell^+ \nu_\ell$. The expected distribution for signal and background events are shown as well as indicated by the plot legends (from [322]).

mass, s_h, of the hadronic system X cannot exceed the value

$$s_h^{\max} = \begin{cases} m_B^2 + q^2 - 2\,m_B\,(\eta_- \times E_e + \eta_+ \times q^2/(4E_e)) & \text{for } \pm 2\,E_e > \pm\eta_\pm \times \sqrt{q^2} \\ m_B^2 + q^2 - 2\,m_B\,\sqrt{q^2} & \text{otherwise} \end{cases}$$

where $\eta_\pm \equiv \sqrt{(1 \pm \beta)/(1 \mp \beta)}$ and β is the velocity of the decaying B meson in the $\Upsilon(4S)$ rest frame. To suppress backgrounds from decays $B \to X_c \ell^+ \nu_\ell$, the value of $s_h^{\max}$ defined in this manner was required to be smaller than the square of the known D^0 mass. Continuum backgrounds from non-$B\overline{B}$ events were estimated and subtracted using collision data collected below the $\Upsilon(4S)$ resonance, while $B\overline{B}$ backgrounds and reconstruction efficiencies were estimated from simulation, tuned on collision data using a $B \to DXe^+\nu_e$ control sample as well as a control sample selected by requiring $s_h^{\max} > 4.25$ GeV^2. The uncertainty on the branching fraction measurement received similar contributions from statistical and systematic uncertainties, where the quoted systematic uncertainty was dominated by the understanding of reconstruction efficiencies and the modelling of signal and $B \to X_c \ell^+ \nu_\ell$ background components.

Tagged analyses

The BaBar and Belle collaborations published several tagged analyses in which the opposite-side B meson, $B_{\rm tag}$, was fully reconstructed in a variety of hadronic decay modes. The latest of the BaBar analyses [325] was based on the full BaBar data set, corresponding to 472 million produced $B\overline{B}$ pairs. Decays of neutral or charged $B_{\rm tag}$ candidates to a D or D^* meson and up to five charged pions or kaons and up to two K_S^0 or π^0 candidates were considered in this analysis, where D^* candidates were reconstructed in their decays to $D\pi$ or $D\gamma$ and D candidates were reconstructed in ten decay modes to different combinations of charged and neutral kaons and pions. Out of the total of 1113 considered $B_{\rm tag}$ decay modes, only those 342 modes were retained for the measurement for which a signal purity in excess of 20% was found in the analysis of samples of simulated events. The latest Belle analysis [329] was based on a data set corresponding to 657 million produced $B\overline{B}$ pairs and employed decays of charged and neutral $B_{\rm tag}$ candidates to $D^{(*)}\pi^+$, $D^{(*)}\rho^+$, $D^{(*)}a_1^+$ and $D^{(*)}D_s^{(*)+}$, where again D^* candidates were reconstructed via their decays to $D\pi$ and $D\gamma$ and D candidates were reconstructed in a total of 13 decay modes to different combinations of charged and neutral kaons and pions. In both analyses, the selection of $B_{\rm tag}$ candidates was based on their energy imbalance, ΔE, and beam-energy substituted invariant mass, $m_{\rm ES}$. Combinatorial background from wrongly reconstructed $B_{\rm tag}$ candidates was estimated from the measured distribution in $m_{\rm ES}$. In the Belle analysis, continuum background from non-$B\overline{B}$ events was estimated from data collected at collision energy below the $\Upsilon(4S)$ resonance.

In both analyses, an electron or muon candidate with momentum above 1 GeV/c and a trajectory compatible with originating from the e^-e^+ interaction region was required in the

remainder of the event. The charge of this lepton had to be opposite that of the $B_{\rm tag}$ candidate if the $B_{\rm tag}$ candidate was a charged B meson. No requirement on the sign of the lepton charge was made in case the $B_{\rm tag}$ candidate was a neutral B meson. To reject leptons from J/ψ or π^0 decays or photon conversions, appropriate vetoes were applied on the invariant mass of the lepton candidate in combination with another track or lepton in the remainder in the event. The four-momentum $(E_X, \vec{p}_X)$ of the X_u system was estimated by summing over all remaining tracks and neutral energy deposits in the remainder of the event.

In the Belle analysis, a multi-variate classifier was then employed to suppress backgrounds from $B \to X_c \ell^+ \nu_\ell$ decays. This classifier was based on input from 17 discriminating variables, including quantities related to the quality of the event reconstruction, such as $m_{\rm ES}$, kinematic variables such as the missing mass of the event, q^2, the invariant mass, m_X, of the X_u system and the difference between its reconstructed energy and momentum, and finally topological information such as the presence of a low-momentum pion from $D^* \to D\pi$ decays, the number of charged and neutral kaons or the total charge of the event, calculated by summing over the charges of all reconstructed tracks. Kaons can be produced via the $b \to c \to s$ decay chain but are rare in charmless $B \to X_u \ell^+ \nu_\ell$ decays. The total charge of the event can deviate from zero if not all tracks are reconstructed. The probability for this to occur is correlated with the event multiplicity, which tends to be higher in $B \to X_c \ell^+ \nu_\ell$ decays than in charmless $B \to X_u \ell^+ \nu_\ell$ decays. Similar discriminating variables were employed in the BaBar analysis, but individual cuts on each of the variables were applied instead of combining them in a single multivariate classifier. Distributions of some of these variables from the BaBar analysis are shown in Figure 5.55. The combination of many discriminating variables permitted in both analyses to extend the measurement of the partial branching fractions to about 90% of the $B \to X_u \ell^+ \nu_\ell$ phase space, leading to a significant reduction in the theory uncertainty related to the extrapolation to the full phase space.

In the Belle analysis, remaining continuum backgrounds from non-$B\overline{B}$ events were estimated using collision data collected below the $\Upsilon(4S)$ resonance, combinatorial backgrounds from wrongly reconstructed $B_{\rm tag}$ candidates were estimated from the measured distribution in $m_{\rm ES}$, using templates derived from samples of simulated events. Samples of simulated events were also employed to estimate remaining backgrounds from $B \to X_c \ell^+ \nu_\ell$ decays and other misidentified B-meson decays. In the BaBar analysis, continuum background and combinatorial background were subtracted from fits to the measured $m_{\rm ES}$ distribution.

To reduce uncertainties related to the understanding of reconstruction efficiencies, the $B \to X_u \ell^+ \nu_\ell$ decay rate was measured in the BaBar analysis relative to the total semileptonic decay rate and the known value of the total semileptonic branching fraction was employed to convert the decay rate into a measurement of the branching fraction.

Samples of simulated events were employed to determine selection and reconstruction efficiencies in the case of the Belle analysis, or the ratios of reconstruction efficiencies in the case of the BaBar analysis. The quoted statistical and systematic uncertainties on the branching fraction measurements were in both cases similar in size. Systematic uncertainties included contributions from effects related to the understanding of reconstruction efficiencies, signal and background simulation and background subtraction.

Summary of results

In each of the analyses described in the previous paragraphs, values of $|V_{ub}|$ were extracted employing various theory approaches. In the untagged analyses, values of $|V_{ub}|$ between 3.95×10^{-3} and 5.08×10^{-3} were found, with quoted uncertainties between 5.5% and 13% from experiment and between 6.5% and 13% from theory. Results from the tagged analyses were more consistent with each other, the latest two analyses quoting results of 4.33×10^{-3} and 4.41×10^{-3} with uncertainties of about 5.5% from experiment and about $(3.5 - 9)$% from theory.

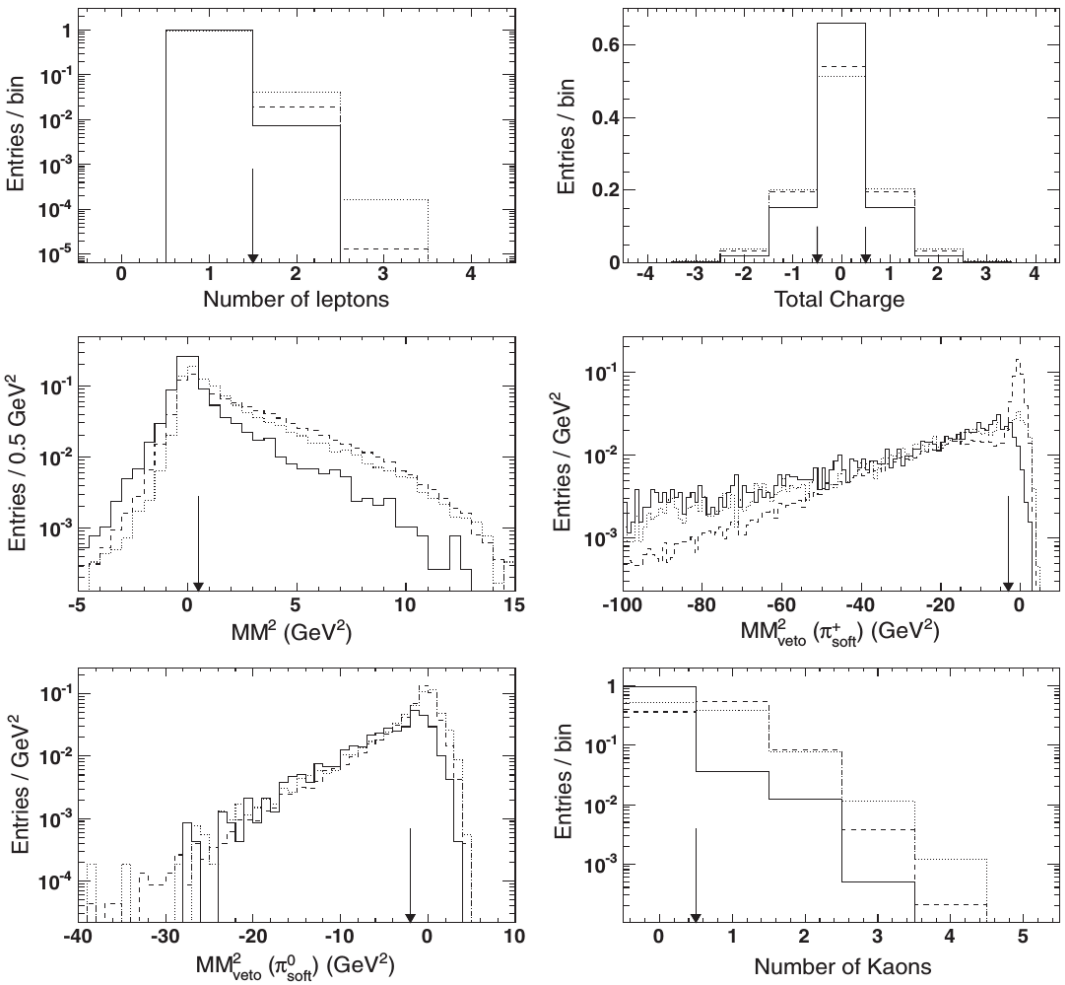

Figure 5.55: Distributions of discriminating variables employed in the latest tagged BaBar measurements of the inclusive $B \to X_u e \nu_e$ branching fraction. Solid lines indicate the distributions for simulated signal events while dashed lines indicate the distributions for background events. Arrows indicate the cut values employed to select signal candidates (from [325]).

The Heavy Flavour Averaging Group [330] combined twelve measurements and calculated averages of $|V_{ub}|$ employing four different theoretical approaches [331–337], as shown in Figure 5.56. No attempt was made to average the results obtained from the different theoretical models or to select a best value. The 2014 edition of the Review of Particle Physics [1] concludes that theoretical uncertainties are difficult to quanitify, but derives some confidence in the results from the observation that different calculations yield similar values and uncertainty estimates for $|V_{ub}|$ and that the calculated partial decay widths for different regions of phase space are in good agreement with the ratios of measured branching fractions. The arithmetic average of the four results obtained by the Heavy Flavour Averaging Group,

$$|V_{ub}| \;=\; (4.14 \,\pm\, 0.15\,(\mathrm{exp})\,^{+0.15}_{-0.17}\,(\mathrm{theo})) \times 10^{-3}\;,$$

is quoted as the world average of $|V_{ub}|$ from inclusive semileptonic decays.

5.2.5 The leptonic decay $B^+ \to \tau^+ \nu_\tau$

In the Standard Model, the branching fraction for the decay $B^+ \to \ell^+ \nu_\ell$ is given by

$$\mathrm{BF}\,(B^+ \to \ell^+ \nu_\ell) \;=\; \frac{G_F^2\, m_B\, m_\ell^2}{8\pi} \left(1 - \frac{m_\ell^2}{m_B^2}\right)^2 f_B^2\, |V_{ub}|^2\, \tau_B\,,$$

Figure 5.56: Compilations of the values of $|V_{ub}|$ extracted from twelve different measurements at CLEO, BaBar and Belle as prepared by the Heavy Flavour Averaging Group for the 2014 edition of the Review of Particle Physics. The four panels show the results obtained using a different theoretical approaches as listed in the legend of each panel (from [330]).

where G_F is the Fermi constant, m_B is the mass of the decaying B meson and m_ℓ the mass of the charged final-state lepton, f_B is the B-meson decay constant and τ_B is the lifetime of the B meson. The proportionality to m_ℓ^2 reflects the helicity suppression due to the $V-A$ character of the weak interaction. As a consequence, decays to muons and electrons are strongly suppressed compared to the decay to τ leptons. The decay constant, f_B, incorporates perturbative and non-perturbative effects of the strong interaction. It can be calculated in Lattice QCD and different calculations [338–342] yield consistent results. The CKMfitter group [3] formed an average of these results and quotes an uncertainty of about 2.5% on the value of f_B. A global CKM fit excluding direct measurements of the $B^+ \to \tau^+ \nu_\tau$ branching fraction, performed by the CKMfitter group [3] at the end of 2014, yielded

$$\mathrm{BF}\,(B^+ \to \tau^+ \nu_\tau) \;=\; (0.758\,^{+\,0.080}_{-\,0.059}) \times 10^{-4}\ .$$

However, the decay amplitude is sensitive to contributions from possible New Physics, in particular in models with extended Higgs sectors. The interference between Standard Model processes and New Physics processes can lead to a siginificant deviation of the branching fraction from the Standard-Model prediction.

Experimental searches for the decay $B^+ \to \tau^+\nu_\tau$ have been performed using leptonic τ^+ decays to $\mu^+\nu_\mu\overline{\nu}_\tau$ and $e^+\nu_e\overline{\nu}_\tau$, as well as hadronic decays to $\pi^+\overline{\nu}_\tau$, $\pi^+\pi^0\overline{\nu}_\tau$, and $a_1^+\overline{\nu}_\tau$ with $a_1^+ \to \pi^+\pi^-\pi^+$. Measurements are challenging since in most final states the only detectable signature is a single charged track.

Measurements have been performed at BaBar and Belle, using the reconstruction of the opposite-side B meson, $B_{\rm tag}$, in hadronic or semileptonic decay modes to derive kinematical constraints that allowed to discriminate between backgrounds and signal candidates. The technique is similar to the tagging methods employed in analyses of semileptonic decays of B mesons described in the previous sections. First evidence for the decay with a statistical significance corresponding to more than three Gaussian standard deviations was obtained by a Belle analysis using hadronic tagging [343]. Subsequent measurements at BaBar [344–347] and Belle [348], employing hadronic [344, 347] or semileptonic [345, 346, 348] tagging, yielded results for the branching fractions that were consistent with each other and with the first Belle measurement, but exceeded the Standard-Model prediction. The most recent measurements at Belle [349, 350], however, resulted in values for the branching fraction that are compatible with the Standard Model prediction. These analyses will be described in the following.

Hadronic tagged analyses

In hadronic tagged analyses, charged $B_{\rm tag}$ candidates were fully reconstructed in decays to D^0 or D^{*0} candidates and a π^-, ρ^-, a_1^- or $D_s^{(*)-}$, or combinations of charged or neutral pions and kaons, where D^{*0} candidates were reconstructed in their decay to $D^0\pi^0$ or $D^0\gamma$ and D^0 candidates were reconstructed in a variety of decays to charged or neutral kaons and pions. The energy imbalance, ΔE, and the beam-energy substituted invariant mass, $m_{\rm ES}$, were employed to select $B_{\rm tag}$ candidates and estimate background contributions in the sample of selected candidates. In addition to the particles employed in the reconstruction of the $B_{\rm tag}$ candidate, events were required to contain exactly one reconstructed track, that fulfilled muon, electron or pion identification criteria and had an electric charge opposite to that of the $B_{\rm tag}$ candidate, or one charged and one neutral pion. No further tracks pointing back to the interaction region or energy depositions in the calorimeter compatible with a π^0 or K_L^0 decay were allowed in the event. A significant missing momentum was required to enhance the fraction of events with undetected neutrinos in the final state. Further discrimination between signal and background was based on the total "extra" energy deposited in calorimeter clusters that were not assigned to decay products of the τ^+ or $B_{\rm tag}$ candidate. This extra energy, denoted as $E_{\rm extra}$ in BaBar and as $E_{\rm ECL}$ in Belle, should be small for correctly reconstructed signal events, which contain no interacting particles in addition to the decay products of the τ and the $B_{\rm tag}$. For background events, $E_{\rm extra}$ can be large due to additional particles that escaped reconstruction. The background contamination in the signal region close to $E_{\rm extra} = 0$ was estimated by fits to the measured $E_{\rm extra}$ distribution. These fits usually were based on templates derived from samples of simulated events. Samples of simulated events were also employed to estimate selection and reconstruction efficiencies. The simulation was validated or calibrated on collision data using control channels. In particular, systematic uncertainties associated to possible differences between simulation and collision data were estimated employing samples of so-called double tagged events, in which signal candidates were reconstructed in a semileptonic decay mode such as $B^+ \to D^{(*)0}\ell^+\nu_\ell$. Clean samples of such double-tagged events can be extracted from collision data and the final-state neutrino provides a signature similar to that in $B^+ \to \tau^+\nu_\tau$ events.

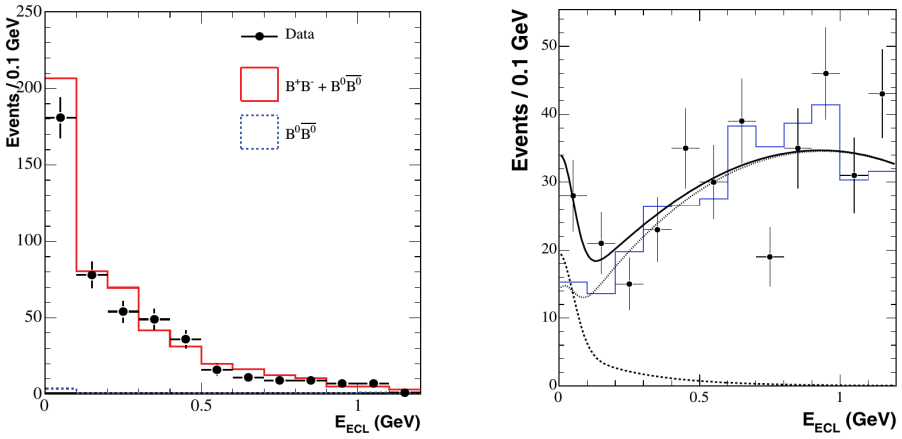

Figure 5.57: Distributions of the extra energy as defined in the main text, for (left) the double-tagged control sample and (right) $B^+ \to \tau^+ \nu_\tau$ candidates from the hadronic tagged Belle analysis in which the first evidence for this decay was found. In the panel on the left, points with error bars indicate the distribution for collision data and histograms indicate the distributions for samples of simulated events. In the panel on the right, points with error bars indicate the distribution for collision data, the histogram indicates the distribution for simulated samples of background events and the full line indicates the result of the fit to the collision data. The dashed line indicates the signal component and the dotted line the background component as assigned by the fit (from [343]).

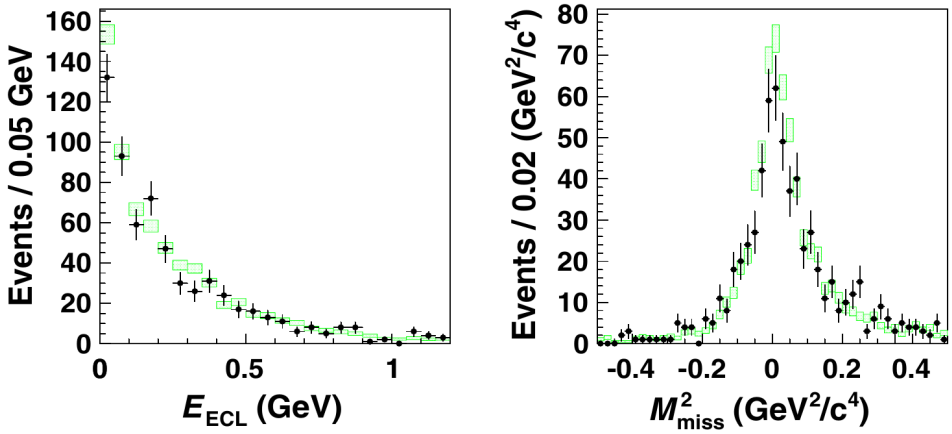

Figure 5.58: Distributions of (left) the extra energy and (right) the squared missing mass of the event for the double-tagged control sample as obtained in the latest hadronic tagged Belle analysis of the decay $B^+ \to \tau^+ \nu_\tau$. In both panels, points with error bars show the distribution for collision data and green rectangles show the distribution for reconstructed samples of simulated events (from [349]).

The first evidence for the decay $B^+ \to \tau^+ \nu_\tau$ with a significance exceeding three Gaussian standard deviations was obtained in a hadronic tagged analysis published by the Belle collaboration [343] and based on a data set corresponding to 449 million produced $B\overline{B}$ pairs. Figure 5.57 shows the reconstructed E_{extra} distributions for the double-tagged control samples as obtained from collision data and from simulation. Good agreement between collision data and simulation is found. Also shown in Figure 5.57 is the observed E_{extra} distribution for $B^+ \to \tau^+ \overline{\nu}_\tau$ candidates in collision data, together with the results of a fit in which the background distribution was described by a template derived from reconstructed samples of simulated events, while the shape of the signal distribution was parametrized as the sum of a Gaussian function with mean $E_{\text{extra}} = 0$ and a decaying exponential function. An excess of candidates in the signal region close to $E_{\text{extra}} = 0$ was observed and the background-only hypothesis was excluded with a statistical significance corresponding to 3.5 Gaussian standard

deviations. Systematic uncertainties related to the modelling of the signal and background shapes in this fit as well as the systematic uncertainty on the determination of the reconstruction efficiency for $B_{\rm tag}$ candidates were estimated using samples of double tagged events. The measured branching fraction was quoted as

$$\mathrm{BF}\,(B^+ \to \tau^+ \nu_\tau) \;=\; (\,1.79\,^{+\,+0.56}_{-\,-0.49}\,(\mathrm{stat})\,^{+\,+0.46}_{-\,-0.51}\,(\mathrm{syst})\,) \times 10^{-4}\;.$$

The latest hadronic tagged Belle analysis [349] was based on their full data set, corresponding to 772 million produced $B\overline{B}$ pairs. Charged $B_{\rm tag}$ candidates were reconstructed using a hierarchical artificial neural network algorithm [351] that considered a total of 615 exclusive hadronic decay modes. This approach yielded a 2.2 times higher reconstruction efficiency compared to the earlier Belle analysis described above. The $B^+ \to \tau^+ \nu_\tau$ signal yield was extracted from a two-dimensional extended maximum likelihood fit to the measured distributions of $E_{\rm extra}$ and the squared missing mass of the event, $M^2_{\rm miss}$. Signal and background templates for the fit were derived from samples of simulated events. Samples of double-tagged events were again employed to validate the simulated $E_{\rm extra}$ and $M^2_{\rm miss}$ distributions for the signal component on collision data. Good agreement was found, as demonstrated in Figure 5.58. The background templates were validated on collision data using events in the $M^2_{\rm miss}$ and $E_{\rm extra}$ sidebands, events in which the $B_{\rm tag}$ meson was reconstructed in a B^0 decay mode, and events in which the τ candidate had the same charge as the $B_{\rm tag}$ candidate. the systematic uncertainty associated to the reconstruction efficiency for $B_{\rm tag}$ candidates was estimated using double-tagged events in the same manner as in the earlier Belle analysis. The measured branching fraction is quoted as

$$\mathrm{BF}\,(B^+ \to \tau^+ \nu_\tau) \;=\; (\,0.72\,^{+\,+0.27}_{-\,-0.25}\,(\mathrm{stat}) \,\pm\, 0.11\,(\mathrm{syst})\,) \times 10^{-4}\;,$$

which is significantly lower than the results obtained in earlier hadronic tagged analyses by Belle and BaBar. To probe possible sources of the discrepancy between the two Belle analyses, the new analysis strategy was also applied to the partial data sample on which the earlier Belle measurement had been based and only to the additional data sample that had not been included in the earlier analysis. These cross checks led the authors to the conclusion that the difference between the old and new results can be explained by a statistical fluctuation.

Semileptonic tagged analyses

In semileptonic tagged analyses, $B_{\rm tag}$ candidates were partially reconstructed in decay modes $B^- \to D^{(*)0} \ell^- \overline{\nu}_\ell$, where D^{*0} candidates were reconstructed in their decay to $D^0\pi^0$ or $D^0\gamma$ and D^0 candidates were reconstructed in a variety of hadronic decay modes to a charged or neutral kaon and one or several pions. Higher event yields than in hadronic tagged analyses can be obtained due to the larger branching fraction to semileptonic decays, but due to the undetected neutrino the reconstruction of the final state is less clean. The variable $\cos\theta_{B,D^{(*)}\ell}$, that was also employed in the analyses of exclusive semileptonic decays of B mesons discussed in Sections 5.2.1 and 5.2.2, was employed to discriminate between $B_{\rm tag}$ signal and background candidates. As a reminder, for true semileptonic decays of B mesons, $\cos\theta_{B,D^{(*)}\ell}$ is the cosine of the opening angle between the momentum vectors of the $D^{(*)}\ell$ system and the decaying B meson and should therefore assume values in the physically meaningful range $-1 \leq \cos\theta_{B,D^{(*)}\ell} \leq 1$. For background, $\cos\theta_{B,D^{(*)}\ell}$, has no meaning and can assume values outside this range. The remainder of the analyses followed a similar approach to that employed in the hadronic anlyses described in the previous paragraph. Exactly one reconstructed track compatible with muon, electron or pion identification criteria, or one charged and one neutral pion forming an invariant mass compatible with the nominal mass of the ρ^+ meson were required in the remainder of the event. Candidates that were also compatible with kaon identification criteria were rejected. Electron candidates were rejected if they were compatible

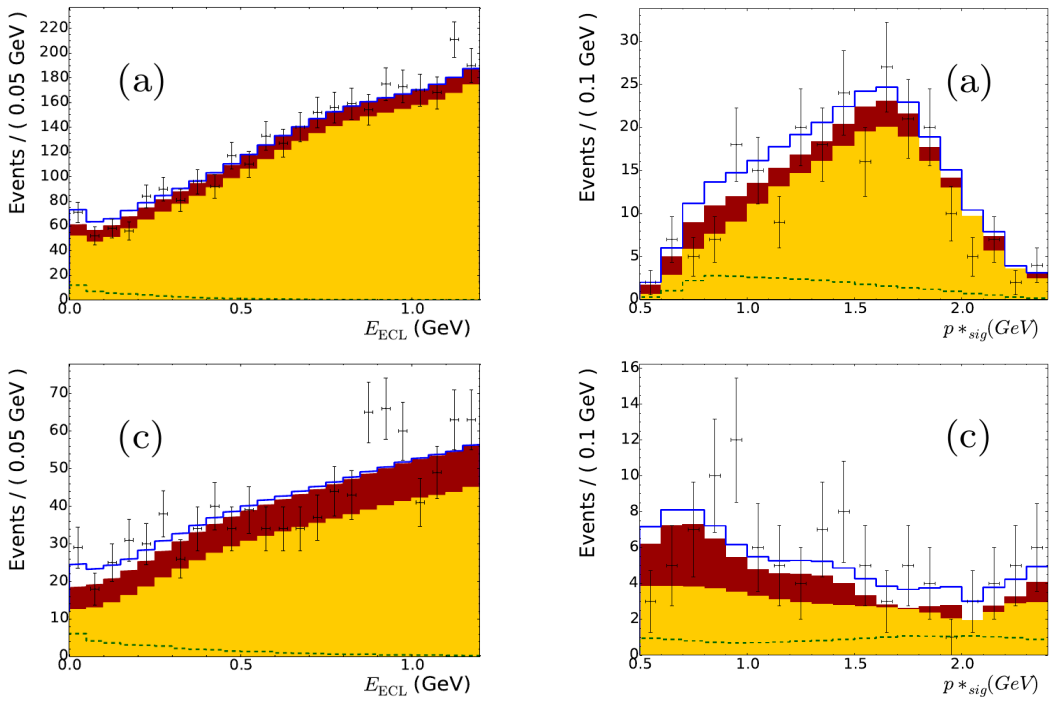

Figure 5.59: Distributions of (left) the extra energy of the event and (right) the momentum of the τ decay candidate for (top) $\tau^+ \to \mu^+ \nu_\mu \overline{\nu}_\tau$ candidates and (bottom) $\tau^+ \to \pi^+ \overline{\nu}_\tau$ candidates from the latest semileptonic tagged Belle analysis of the decay $B^+ \to \tau^+ \nu_\tau$. In all panels, points with error bars indicate the distribution measured in collision data and the solid line shows the result of the fit to the data. The dashed line indicates the signal component, the orange area the $B\overline{B}$ background component and the red area the non-$B\overline{B}$ background component as assigned by the fit (from [350]).

with originating from a photon conversion when combined with any of the other tracks in the event. No other reconstructed tracks pointing back to the interaction region or energy deposits compatible with π^0 or K^0_L candidates were allowed in the event. An upper cut was applied on the momentum of the candidate to suppress backgrounds from two-body decays of B mesons, in which one of the two final-state particles escaped detection. Further background suppression was achieved by analysing event shape variables, the missing momentum and the missing invariant mass of the event. Remaining backgrounds were again estimated from fits to the distribution of the extra energy, $E_{\rm extra}$. Samples of simulated events were employed to derive templates for these fits as well as to estimate selection and reconstruction efficiencies. The simulation was validated on collision data using various control channels, including samples of double tagged events in which signal candidates were reconstructed in semileptonic decay modes such as $B^\pm \to D^{(*)0} \ell^\pm \nu_\ell$.

The latest semileptonic tagged Belle analysis [350] was based on their full data sample, corresponding to 772 million produced $B\overline{B}$ pairs. A multivariate classifier combining information on the momenta, flight directions and invariant masses of final-state particles and decaying particles was employed to select $B_{\rm tag}$ candidates. A second multi-variate classifier using event-shape variables and kinematic properties of the $B_{\rm tag}$ candidate was employed to further suppress backgrounds. The number of $B^+ \to \tau^+ \nu_\tau$ signal candidates was estimated from a two-dimensional fit to the distributions of $E_{\rm extra}$ and of the momentum, $p^*_{\rm sig}$, of the τ decay candidate in the $\Upsilon(4S)$ rest frame. The measured distributions are shown in Figure 5.59 together with the results of the fit. The fit was based on templates derived from samples of simulated events. Again, control samples of double-tagged events were employed to compare the $E_{\rm extra}$ and $p^*_{\rm sig}$ distributions in simulation and collision data and no significant discrepancies were found. The systematic uncertainty associated with the selection and

Table 5.1: Average values of $|V_{cb}|$ and $|V_{ub}|$ as determined from measurements in inclusive and exclusive decays, and the combined averages, as quoted in the 2014 edition of the Review of Particle Physics [1]. In both cases, the Particle Data Group review warns that the agreement between inclusive and exclusive values is marginal and that their "combination should be treated with caution". The last line shows the result of an indirect determination from a global Standard Model fit of CKM parameters by the CKMfitter group [3] as performed at the end of 2014. The fit included results presented up to the CKM2014 conference in the beginning of September 2014, but excluded all direct measurements of $|V_{cb}|$ and $|V_{ub}|$.

	$\lvert V_{cb}\rvert$	$\lvert V_{ub}\rvert$
exclusive	$(39.5 \pm 0.8) \times 10^{-3}$	$(3.28 \pm 0.29) \times 10^{-3}$
inclusive	$(42.2 \pm 0.7) \times 10^{-3}$	$(4.14 \pm 0.15\,^{+0.15}_{-0.17}) \times 10^{-3}$
combination	$(41.1 \pm 1.3) \times 10^{-3}$	$(4.13 \pm 0.49) \times 10^{-3}$
CKM fit	$(41.2\,^{+2.6}_{-1.3}) \times 10^{-3}$	$(3.455\,^{+0.227}_{-0.095}) \times 10^{-3}$

reconstruction efficiency for $B_{\rm tag}$ candidates was evaluated by using double-tagged events to measure the branching fractions for the decays $B^+ \to D^{*0}\ell^+\nu_\ell$ and $B^+ \to D^0\pi^+$. Comparing the obtained results with the world averages at the time of the measurement, the simulation was found to slightly overestimate the reconstruction efficiencies and an appropriate correction factor was applied in the determination of the measurement of the $B^+ \to \tau^+\nu_\tau$ branching fraction. A signal corresponding to a statistical significance of 3.8 Gaussian standard deviations was observed in the $B^+ \to \tau^+\nu_\tau$ analysis and the branching fraction was measured as

$$\mathrm{BF}\,(B^+ \to \tau^+\nu_\tau) \;=\; (\,1.25 \,\pm\, 0.28\,(\mathrm{stat}) \,\pm\, 0.27\,(\mathrm{syst})\,) \times 10^{-4}\ ,$$

which does not deviate significantly from the Standard Model expectation.

5.2.6 Summary and comparison of $|V_{ub}|$ results

The averages for $|V_{cb}|$ and $|V_{ub}|$ from inclusive and exclusive measurements as quoted in the 2014 edition of the Review of Particle Physics [1] are summarized in Table 5.1, together with results from global CKM fits of Unitarity Triangle parameters excluding the direct measurements of $|V_{ub}|$ and $|V_{cb}|$. Both for $|V_{cb}|$ and for $|V_{ub}|$, the results from inclusive and exclusive measurements are only marginally consistent with each other, indicating that the experimental and/or theoretical tools employed in these measurements might be less well understood than claimed by the authors of the respective publications. Global CKM fits yield results that are roughly consistent with those obtained in direct measurements, as illustrated in Figure 5.60. From the point of view of experiments, the B factories seem to have exploited their potential. At LHCb, exclusive measurements are challenging[2] while inclusive measurements seem hardly feasible due to the lack of external kinematic constraints.

A comparison between the values of $\sin(2\beta)$ (see Section 5.3) and the branching fraction of the leptonic decay $B^+ \to \tau^+\nu_\tau$, prepared by the CKMfitter group, is shown in Figure 5.61. The earlier tension between the results of the two measurements and the global CKM fit has reduced significantly with the recent measurements of the branching fraction by the Belle collaboration.

The measurements of the $B^+ \to \tau^+\nu_\tau$ branching fraction seem to exemplify a general observation regarding branching fractions that are derived from early measurements of signals with low significance: such branching fractions tend to be biased towards high values since the

[2] At the 2015 Moriond conference in La Thuile, the LHCb collaboration presented a measurement of $|V_{ub}|$ in the exclusive decay $\overline{\Lambda}_b^0 \to \overline{p}\mu^+\nu_\mu$. The result, $|V_{ub}| = (\,3.27 \,\pm\, 0.23\,) \times 10^{-3}$ [352], is in good agreement with those obtained in exclusive semileptonic decays of B mesons at the B factories and has similar precision as these.

fact that an evidence for the signal was found is more likely to be due to an upwards statistical fluctuation rather than a downwards fluctuation.

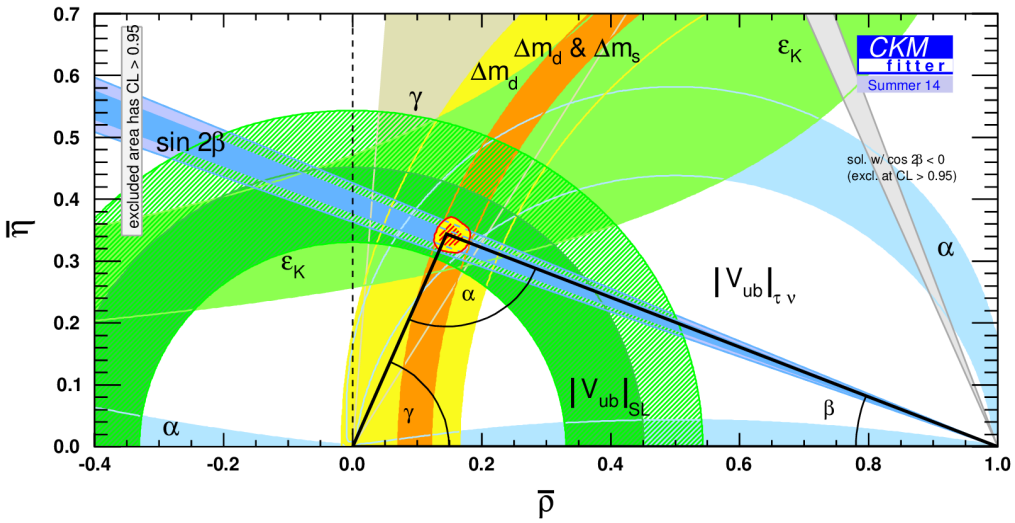

Figure 5.60: Result of a global CKM fit in the $(\overline{\rho}, \overline{\eta})$ plane prepared by the CKMfitter group [3], including results presented up to the CKM2014 conference in the beginning of September 2014. The plain dark green band indicates the constraint on the length of the R_u side from inclusive and exclusive semileptonic decays of B mesons and the hashed green band indicates the constraint from measurements of the $B^+ \to \tau^+ \nu_\tau$ branching fraction.

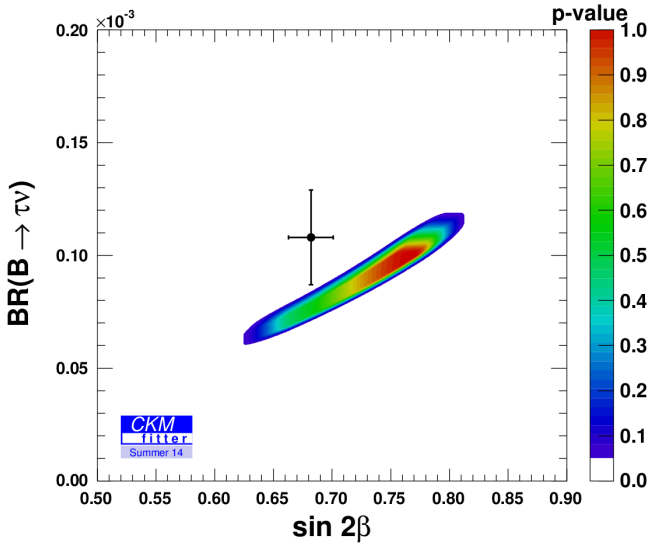

Figure 5.61: Comparison of results for the parameter $\sin(2\beta)$ and for the $B^+ \to \tau^+ \nu_\tau$ branching fraction as prepared by the CKMfitter group [3], including results presented up to the CKM2014 conference in the beginning of September 2014. The point with error bars indicates the averages of direct measurements of the two quantities, while the colourful areas indicate confidence regions obtained from a global CKM fit.

5.3 The angle β: mixing-induced CP violation in $\overline{b} \to \overline{c}c\overline{s}$ and $\overline{b} \to \overline{s}s\overline{s}$ transitions

The angle β between the base of the Unitarity Triangle and the side R_t opposite the origin of the complex plane is defined by

$$\beta \equiv \phi_1 \equiv \arg\left(-\frac{V_{cd}V_{cb}^*}{V_{td}V_{tb}^*}\right)$$

and is the currently most precisely measured parameter of the Unitarity Triangle. Including direct measurements presented until the beginning of September 2014, the CKM fitter group [3] quotes a world average of $\sin(2\beta) = 0.682 \pm 0.019$, while the latest world average quoted by the UTfit group [211] is $\sin(2\beta) = 0.680 \pm 0.024$.

The most precise determination of the angle β stems from measurements of the time-dependent CP-violating asymmetry in the "golden" decay mode $B^0 \to J/\psi K_S^0$. This decay mode provides the textbook example of a time-dependent CP asymmetry that is caused by the interference of mixing and decay as described in Section 3.3. The final state $J/\psi K_S^0$ can be reached through decays of both B^0 mesons and $\overline{B}^0$ mesons, it is a CP eigenstate and the decay amplitude is dominated to good approximation by a single weak phase. The decay presents attractive features also from the point of view of experiment. Reconstructing the decay in the final states $J/\psi \to \ell^+\ell^-$ and $K_S^0 \to \pi^+\pi^-$, the two charged leptons from the decay of the J/ψ provide for high trigger efficiencies and the displaced J/ψ and K_S^0 decay vertices provide a clear signature that permits efficient discrimination between signal and backgrounds. Moreover, the visible branching fraction,

$$\mathrm{BF}(B^0 \to J/\psi K^0) \times \mathrm{BF}(J/\psi \to \ell^+\ell^-) \times \mathrm{BF}(K^0 \to K_S^0 \to \pi^+\pi^-) \approx 1.8 \times 10^{-5} ,$$

is not too small.

The decay $B^0 \to J/\psi K_S^0$ is a decay of a pseudoscalar particle with spin $J = 0$ to a vector particle with spin $J = 1$ and a pseudoscalar with spin $J = 0$. The conservation of angular momentum in the decay forces the $J/\psi K_S^0$ pair to be produced with relative angular momentum $L = 1$ and therefore in a CP eigenstate. The CP phase is convention dependent and is usually defined such that the final state is CP odd.

The decay amplitude is dominated by the tree processes shown in Figure 5.62. The leading penguin decay amplitudes shown in Figure 5.63 are expected to contribute at a level of 10%, but are dominated by the same weak phase as the tree amplitude. This can be demonstrated by formally decomposing the decay amplitude as

$$A_{J/\psi K^0} = P_t \cdot (V_{tb}^* V_{ts}) + (T + P_c) \cdot (V_{cb}^* V_{cs}) + P_u \cdot (V_{ub}^* V_{us}) ,$$

where T, P_t, P_c, and P_u denote the amplitudes of the tree process and the penguin processes with intermediate top, charm and up quarks, after the respective weak phases have been factored out. Exploiting one of the unitarity conditions of the CKM matrix to substitute

$$V_{tb}^* V_{ts} = -V_{cb}^* V_{cs} - V_{ub}^* V_{us} ,$$

the decay amplitude can be rewritten

$$A_{J/\psi K^0} = (T + P_c - P_t) \cdot (V_{cb}^* V_{cs}) + (P_u - P_t) \cdot (V_{ub}^* V_{us}) .$$

The second term on the right-hand side of the equation is suppressed by the ratio of the magnitudes of the CKM elements,

$$\frac{|V_{ub}^* V_{us}|}{|V_{cb}^* V_{cs}|} \propto \frac{\lambda^4}{\lambda^2} = \lambda^2 ,$$

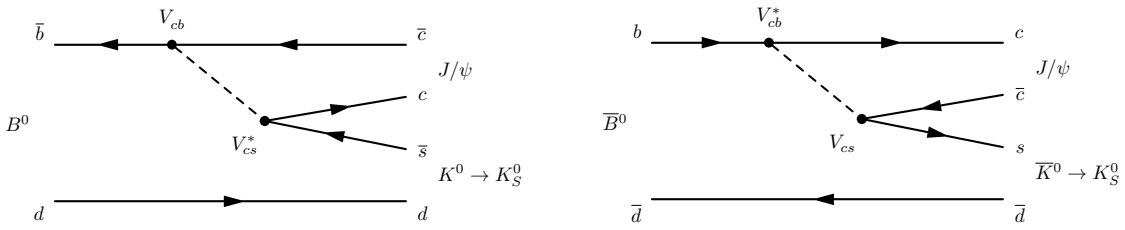

Figure 5.62: Tree diagrams for the decays (left) $B^0 \to J/\psi K_S^0$ and (right) $\overline{B}^0 \to J/\psi K_S^0$.

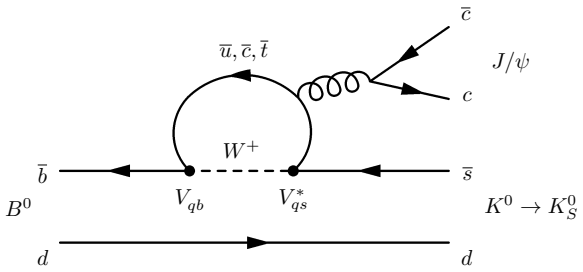

Figure 5.63: Leading penguin diagrams for the decay $B^0 \to J/\psi K_S^0$. The index q stands for u, c or t, depending on the type of the virtual quark appearing in the inner loop.

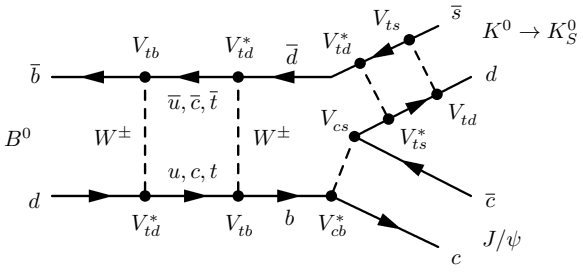

Figure 5.64: Feynman diagram illustrating the process $B^0 \to \overline{B}^0 \to J/\psi K_S^0$, including the $K^0 - \overline{K}^0$ mixing that leads to the decay of the K^0 meson as a K_S^0.

with the Wolfenstein parameter $\lambda = \sin\theta_C \approx 0.23$. Taking into account the factor of ten suppression of the penguin amplitudes compared to the tree amplitude, the decay amplitude is therefore expected to be dominated by the phase of $(V_{cb}^* V_{cs})$ to more than 99%.

Including the weak phase of the subsequent $K^0\overline{K}^0$ mixing that leads to the decay of the produced neutral kaon as a K_S^0 meson, the relative weak phase between the direct decay $B^0 \to J/\psi K_S^0$ and the decay after mixing, $B^0 \to \overline{B}^0 \to J/\psi K_S^0$, is given by

$$\begin{aligned}
\lambda_{J/\psi K_s^0} &= -\left(\frac{q}{p}\right)_{B^0} \cdot \left(\frac{\overline{A}_{J/\psi K_s^0}}{A_{J/\psi K_s^0}}\right) \cdot \left(\frac{q}{p}\right)_{K^0} \\
&= -\left(\frac{V_{td}V_{tb}^*}{V_{td}^*V_{tb}}\right) \cdot \left(\frac{V_{cs}^*V_{cb}}{V_{cs}V_{cb}^*}\right) \cdot \left(\frac{V_{cd}^*V_{cs}}{V_{cd}V_{cs}^*}\right) \\
&= -\left(\frac{V_{cd}^*V_{cb}}{V_{td}^*V_{tb}}\right) \cdot \left(\frac{V_{td}V_{tb}^*}{V_{cd}V_{cb}^*}\right) \\
&= -2 \cdot \arg\left(\frac{V_{td}V_{tb}^*}{V_{cd}V_{cb}^*}\right) \qquad = \quad -2\,\beta\ .
\end{aligned}$$

Following the argumentation in Section 3.3, the time-dependent *CP* asymmetry in decays to

the final state $f = J/\psi K^0_S$ is then given by

$$a_{J/\psi K^0_s}(t) \;=\; \mathrm{Im}\,\lambda_{J/\psi K^0_s}\,\sin(\Delta m_d\, t) \;=\; \sin(2\beta)\,\sin(\Delta m_d\, t)\,.$$

Taking into consideration the possibility of direct *CP* violation due to an interference of the dominant tree amplitude with the small contamination of penguin amplitudes of different phase, a cosine-term is added to the time-dependent asymmetry, which then takes the form

$$a_{J/\psi K^0_s}(t) \;=\; S\,\sin(\Delta m_d\, t) \;-\; C\,\cos(\Delta m_d\, t)$$

with

$$S \;=\; \frac{2\cdot\sin(2\beta)}{1+|\lambda_{J/\psi K^0_s}|^2} \quad \text{and} \quad C \;=\; \frac{1-|\lambda_{J/\psi K^0_s}|^2}{1+|\lambda_{J/\psi K^0_s}|^2}\,.$$

Most analyses include the cosine term in their fit to the measured asymmetry and find results for C compatible with zero.

The above derivation holds as well for other B^0 decay modes via $\overline{b}\to\overline{c}c\overline{s}$ transitions, such as decays to the *CP*-odd final states $\psi(2s)K^0_S$, $\eta_c K^0_S$ or $\chi_{c1}K^0_S$, or to the *CP*-even final state $J/\psi K^0_L$, in which the sign of the oscillation signal is simply reversed. These decay modes have lower branching fractions or reconstruction efficiencies than the "golden" decay mode $B^0\to J/\psi K^0_S$, but are included in measurements of $\sin(2\beta)$ at the B factories in order to further increase event yields. Measurements of $\sin(2\beta)$ in these decay modes at BaBar and Belle and at LHCb are described in the next part of this section.

Due to the symmetry of the sine function, the measurement of $\sin(2\beta)$ alone determines the angle β only up to a four-fold ambiguity, corresponding to the transformations $\beta\to\pi/2-\beta$ and $\beta\to\pi+\beta$. The first of these ambiguities has been resolved by the measurement of the sign of $\cos(2\beta)$ in a time-dependent angular analysis of the decay $B^0\to J/\psi K\pi$ with invariant masses of the $K\pi$ pair in the vicinity of the mass of the K^{*0} meson. The K^{*0} meson is a vector particle with spin $J=1$ and $K\pi$ pairs from the decay of a K^{*0} meson are therefore produced in a P-wave with relative angular momentum $L_{K\pi}=1$. The relative angular momentum between the $K\pi$-pair and the J/ψ can then be $L_{J/\psi(K\pi)}=0,1$ or 2 and the final state is a mixture of *CP* even and *CP* odd. In addition, there is a non-resonant S-wave component of $K\pi$ pairs that were not produced via an intermediate K^{*0} meson and have relative angular momentum $L_{K\pi}=0$. For this non-resonant component, the relative angular momentum between the $K\pi$ pair and the J/ψ meson has to be $L_{J/\psi(K\pi)}=1$ and the final state $J/\psi K\pi$ is *CP* odd. A total of four amplitudes with different strong phases and different sign of the weak phase are therefore involved in the decay. The magnitudes and strong phases of these amplitudes can be determined together with the weak phase through a time-dependent angular analysis of the final-state particles. An analysis of the evolution of the strong phases as a function of the invariant $K\pi$ mass in the vicinity of the resonance allows to resolve the ambiguity in the sign of the weak phase. This analysis was performed by the BaBar collaboration and is described in the third part of this section.

The *CP*-violating phase in $\overline{b}\to\overline{s}s\overline{s}$ transitions such as the decay $B^0\to\phi K^0_S$ shown in Figure 5.65 is referred to as $2\beta_{\mathrm{eff}}$ and is almost equal to 2β in the Standard Model. The decay can only proceed through penguin diagrams and is therefore sensitive to possible contributions from physics beyond the Standard Model. In analogy to the case of the decay $B^0\to J/\psi K^0_S$ discussed above, the decay amplitude can formally be written as

$$A_{\phi K^0} \;=\; (P_c - P_t)\cdot(V^*_{cb}V_{cs}) \;+\; (P_u - P_t)\cdot(V^*_{ub}V_{us})\,.$$

The second term on the right-hand side of the equation is suppressed by the ratio of the magnitudes of the CKM elements, $\lambda^2\approx 0.05$, and the contamination from the "wrong" CKM phase is still small, though about a factor ten larger than in the case of the decay $B^0\to J/\psi K^0_S$.

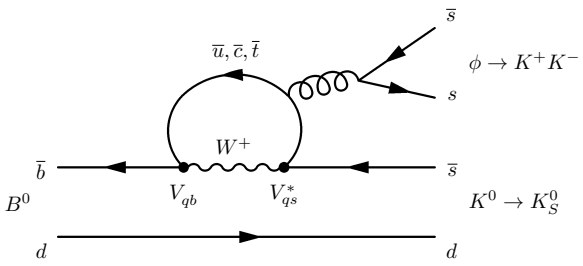

Figure 5.65: Feynman diagram for the decay $B^0 \to \phi K_S^0$. The index q stands for u, c or t, depending on the type of the virtual quark that appears in the inner loop.

Recent Standard Model calculations yield estimates for the difference $\sin(2\beta_{\rm eff}) - \sin(2\beta)$ between -0.01 and $+0.04$ [353–355]. Measurements of $\sin(2\beta_{\rm eff})$ have been performed by BaBar and Belle and will be briefly described in the fourth and final part of this section. Early measurements seemed to indicate a possible deviation from the value of $\sin(2\beta)$ measured in $\overline{b} \to \overline{c}c\overline{s}$ transitions, stirring some interest in the community. More recent results are, however, in good agreement with $\sin(2\beta)$.

5.3.1 Measurements of $\sin(2\beta)$ in $B^0 \to J/\psi K_S^0$ and other $\overline{b} \to \overline{c}c\overline{s}$ transitions

Early studies of $B^0 \to J/\psi K_S^0$ decays were performed by the Aleph [356] and Opal [357] collaborations at LEP and by the CDF collaboration [358] at run I of the Tevatron. However, none of these measurements lead to the observation of a significant *CP*-violating asymmetry. The BaBar and Belle collaborations published their first measurements [359,360] in early 2001 and reported the first observations of a non-zero value of $\sin(2\beta)$ later that year [105, 106]. Both collaborations published several updates of these measurements using increasingly large data samples and more refined reconstruction algorithms [132, 361–366]. The latest BaBar and Belle analyses [367, 368], using the full data sets collected at the $\Upsilon(4S)$ resonance, are described below. The BaBar collaboration also published an analysis using hadronic decays of the J/ψ from $B^0 \to J/\psi K_S^0$ [369], but the precision of this measurement is limited by lower trigger and reconstruction efficiencies. The LHCb collaboration has published a first measurement of $\sin(2\beta)$ in $B^0 \to J/\psi K_S^0$ decays using the 2011 data sample [370], but the precision of this result cannot yet compete with that of the final measurements from the B factories. The latest BaBar and Belle measurements and the LHCb measurement are described in the following.

Measurements at the B factories

Measurements of time-dependent *CP* asymmetries at the B factories follow a similar pattern as the measurements of the $B^0 - \overline{B}^0$ oscillation frequency described in Section 5.1.1. The decay of a $\Upsilon(4S)$ produces $B^0\overline{B}^0$ pairs in a quantum-entangled state. One of the two neutral B mesons, $B_{\rm rec}$, is fully reconstructed in the decay mode of interest, while flavour-specific signatures from the decay of the second B meson, $B_{\rm tag}$, are employed to infer the initial flavour content of $B_{\rm rec}$ at the time of the decay of $B_{\rm tag}$. The decay time difference $\Delta t = (z_{\rm rec} - z_{\rm tag})/(\beta\gamma c)$ is calculated from the reconstructed positions, $z_{\rm rec}$ and $z_{\rm tag}$, of the $B_{\rm rec}$ and $B_{\rm tag}$ decay vertices. However, in order to extract the *CP* violating weak phase, it is the oscillation amplitude rather than the oscillation frequency that needs to be measured with good precision. This requires an excellent understanding of the dilution of the observed oscillation amplitude due to reconstruction effects such as imperfect flavour tagging and finite decay-time resolution. Taking these effects into account, the measured asymmetry is given by

$$a_{\rm meas}(\Delta t) \;=\; (1 - 2\,\omega_{\rm tag}) \cdot \sin(2\beta) \cdot \int \sin(\Delta m_d\,\Delta t') \cdot R(\Delta t - \Delta t')\,d\Delta t'\,,$$

where Δt and $\Delta t'$ indicate the measured and the true decay time, respectively, the function $R(\Delta t - \Delta t')$ describes the decay-time resolution and $\omega_{\rm tag}$ is the mistag fraction of the flavour-tagging algorithm.

Both the BaBar [367] and Belle [368] collaborations published measurements of $\sin(2\beta)$ based on their full data sets, corresponding to 465 million and 772 million produced $B\overline{B}$ pairs, respectively. In both analyses, decays to the *CP*-odd eigenstates $J/\psi K^0_S$, $\psi(2s)K^0_S$ and $\chi_{\rm c1}K^0_S$ were considered as well as decays to the *CP* even eigenstate $J/\psi K^0_L$. The BaBar analysis considered in addition decays to the *CP* odd final state $\eta_{\rm c}K^0_S$ and to the *CP* mixed final state $J/\psi K^{*0}$. As described in the introductory paragraphs of this section, the *CP* even and *CP* odd contributions in the final state $J/\psi K^{*0}$ can in principle be separated by a time-dependent angular analysis, but no such attempt was made here and this final state therefore contributed only little to the precision of the measurement.

In both analyses, the different $c\overline{c}$ resonances were reconstructed in their decays $J/\psi \to \ell^+\ell^-$, $\psi(2s) \to \ell^+\ell^-$ and $\psi(2s) \to J/\psi\pi^+\pi^-$, $\chi_{\rm c1} \to J/\psi\gamma$ and $\eta_{\rm c} \to K^0_S K^+ K^-$, while K^0_S candidates were reconstructed in their decay two charged pions. In the BaBar analysis, decays of K^0_S candidates to two neutral pions were in addition considered in the decay mode $B^0 \to J/\psi K^0_S$. The BaBar analysis also made use of a large samples of $B_{\rm rec}$ decays to flavour-specific final states $D^{(*)-}\pi^+$, $D^{(*)-}\rho^+$ and $D^{(*)-}a_1^+$ in order to estimate effects due to imperfect flavour tagging and finite decay time resolution. Here, D^- candidates were reconstructed in $D^- \to K^+\pi^-\pi^-$ and $D^- \to K^0_S\pi^-$ while D^{*-} candidates were reconstructed in their decay $D^{*-} \to D^0\pi^-$ with $D^0 \to K^+\pi^-$, $D^0 \to K^+\pi^-\pi^0$, $D^0 \to K^+\pi^-\pi^+\pi^-$ and $D^0 \to K^0_S\pi^+\pi^-$.

The event selection was based on the energy imbalance, ΔE, and the beam-energy substituted invariant mass, $m_{\rm ES}$, introduced in Section 4.1 for all decay modes except $B_{\rm rec} \to J/\psi K^0_L$, for which it was based on ΔE alone in the case of the BaBar analysis and on the momentum p^*_B of the $B_{\rm rec}$ candidate as measured in the $\Upsilon(4S)$ rest frame in the case of the Belle analysis. Measured distributions of the discriminating variables for the selected candidates are shown in Figure 5.66. Combinatorial background from non-$B\overline{B}$ events was estimated from a fit to the $m_{\rm ES}$ sideband region. Backgrounds from $B\overline{B}$ events including a correctly reconstructed J/ψ meson were estimated from simulation and other backgrounds were estimated from sidebands in the $\ell^+\ell^-$ invariant mass distribution.

The standard flavour-tagging algorithms discussed in Section 4.1.10 were applied to derive a tagging decision, q, for each selected event and to assign it to one of seven mutually exclusive tagging categories. In the fit for the *CP* violating observables, the values of the average mistag probability, ω_k, and average difference, $\Delta\omega_k$, between the mistag probabilities for B^0 and $\overline{B}^0$ candidates corresponding to this tagging category were then assigned to the event.

The decay time difference was calculated as $\Delta t = (z_{\rm rec} - z_{\rm tag})/(\beta\gamma c)$, where $z_{\rm rec}$ and $z_{\rm tag}$ are the reconstructed positions along the beam axis of the $B_{\rm rec}$ and $B_{\rm tag}$ decay vertices, respectively, and $(\beta\gamma c)$ is the known Lorentz boost of the $\Upsilon(4S)$ rest frame in the laboratory system. The position of the $B_{\rm rec}$ decay vertex was determined from a fit to the tracks assigned to the decay of the $B_{\rm rec}$ candidate, while the position of the $B_{\rm tag}$ decay vertex was determined from a fit to the tracks that were not employed in the reconstruction of the $B_{\rm rec}$ candidate. To improve the vertex resolution, the vertex reconstruction algorithm employed in the Belle analysis included a constraint on the beam-spot position. In the case of the BaBar analysis, the fit for the $B_{\rm tag}$ vertex position included a constraint derived from the beam-spot position and the reconstructed momentum vector of the $B_{\rm rec}$ candidate. The average beam-spot position was determined in both BaBar and Belle on a run-by-run basis. In the BaBar analysis, tracks that resulted in a large contribution to the χ^2 returned by the $B_{\rm tag}$ vertex fit were iteratively removed from the fit in order to reduce the bias on the reconstructed position of the $B_{\rm tag}$ decay vertex due to final-state particles from secondary decay vertices in events in which the $B_{\rm tag}$ decay involved long-lived charmed mesons. Moreover, the measured momentum of the fully reconstructed $B_{\rm rec}$ candidate was employed in the BaBar analysis to correct the calculated value of Δt for the small momentum of the $B_{\rm rec}$ candidate in the $\Upsilon(4S)$ rest frame.

This correction led to an average improvement of about 5 % in the decay-time resolution and reduced the correlation between the decay time resolution and the decay time. The decay-time resolution was modelled in the BaBar analysis by a sum of three Gaussian distributions with separate means and standard deviations. In the case of the Belle analysis, it was described by an empirical function that has been described in Ref. [250] and takes into account effects of detector resolution, potential biases on the reconstructed value of $z_{\rm tag}$ due to the possible inclusion of tracks from secondary decay vertices of long-lived charmed particles or K^0_S mesons, and the small effect caused by neglecting the Lorentz boost of the $B_{\rm rec}$ candidate in the $\Upsilon(4S)$ rest frame.

In the Belle analysis, the parameters describing the flavour-tagging performance were determined from collision data using flavour-specific semileptonic and hadronic $b\to c$ decays, while the parameters describing the vertex resolution were determined from collision data employing control samples of $B\to J/\psi X$ and $B\to D^{(*)}X$ decays. In the BaBar analysis, these parameters were extracted together with the values of S and C by performing a simultaneous fit to the selected samples of candidates in decays to *CP* eigenstates and flavour-specific final states. The decay-time distribution for the signal component in decays to *CP* eigenstates was modelled in both analyses as

$$g_q(\Delta t) \;=\; \frac{e^{-|\Delta t|/\tau_{B^0}}}{4\tau_{B^0}}\cdot\{(1-q\,\Delta\omega_k)\,+\,q\,(1-2\omega_k)\,\times\,[S\,\sin(\Delta m_d\,\Delta t)\,-\,C\,\cos(\Delta m_d\,\Delta t)]\}\;\;,$$

convolved with the respective decay-time resolution functions, where $q=+1$ for events in which $B_{\rm rec}$ is tagged as a $\overline{B}^0$ candidate and $q=-1$ for events in which it is tagged as a B^0 candidate. The decay-time distributions for B^0 and $\overline{B}^0$ decays to flavour-specific final states were modelled in the BaBar analysis as

$$g_{B^0}(\Delta t) \;=\; \frac{e^{-|\Delta t|/\tau_{B^0}}}{4\tau_{B^0}}\cdot\{(1-\Delta\omega_k)\,+\,q\,(1-2\omega_k)\,\times\,\cos(\Delta m_d\,\Delta t)\}$$

and

$$g_{\overline{B}^0}(\Delta t) \;=\; \frac{e^{-|\Delta t|/\tau_{B^0}}}{4\tau_{B^0}}\cdot\{(1+\Delta\omega_k)\,+\,q\,(1-2\omega_k)\,\times\,\cos(\Delta m_d\,\Delta t)\}\;\;,$$

respectively, convolved with the same decay-time resolution function. In this case, $q=+1$ for candidates tagged as unmixed and $q=-1$ for candidates tagged as mixed by the flavour tagging algorithm. In both analyses, the background component peaking in $m_{\rm ES}$, attributed to $B\overline{B}$ events, was modelled by the same decay-time dependence and resolution as the signal component, but with the values of the *CP* violation parameters, S and C, set to zero. The decay-time distribution for combinatorial background was modelled by the sum of a prompt component and an exponential function, convolved with a double Gaussian function to model the decay-time resolution. The parameters describing the decay-time distribution of the combinatorial background component were free fit parameters in the BaBar analysis. In the Belle analysis, they were fixed from a fit to events in sidebands of the $m_{\rm ES}$ distribution for all decay modes except for $B_{\rm rec}\to J/\psi K^0_L$, where they were determined from simulated events and from events in sidebands of the $\ell^+\ell^-$ invariant-mass distribution.

In the case of the Belle analysis, the only free parameters in the final fit to the data were the *CP* violation parameters, S and C. The fit function employed in the BaBar analysis contained 69 free parameters in addition to S and C. For the signal component, these included seven parameters to describe the decay-time resolution function, twelve parameters to describe the average mistag fractions and possible differences in mistag fractions between B^0 and $\overline{B}^0$ candidates, another six parameters to describe a possible difference in tagging efficiency between B^0 and $\overline{B}^0$ candidates, and one parameter to account for a possible difference in reconstruction efficiency between B^0 and $\overline{B}^0$ candidates. The remaining 43 fit parameters described

the tagging performance, decay-time dependence and decay-time resolution, and possible *CP*-violating asymmetries in background components. The values of the B^0 lifetime, τ_{B^0}, and the $B^0-\overline{B}^0$ oscillation frequency, Δm_d, were fixed in both analyses to their world averages at the time of the measurement. The measured decay-time distributions and decay-time dependent mixing asymmetries for the *CP* odd and *CP* even samples are shown in Figure 5.67 together with the projections of the fit results.

The final results of the measurements in terms of $\sin(2\beta)$ are listed in Figure 5.69. The *CP* violating parameter C was measured to

$$C \;=\; 0.024 \,\pm\, 0.020\,(\text{stat}) \,\pm\, 0.016\,(\text{syst})$$

in the BaBar analysis and

$$C \;=\; -0.006 \,\pm\, 0.016\,(\text{stat}) \,\pm\, 0.012\,(\text{syst})$$

in the Belle analysis. Both results are compatible with vanishing direct *CP* violation.

The quoted systematic uncertainties on the determination of $\sin(2\beta)$ were dominated in the BaBar analysis by possible differences in the decay-time resolution and tagging performance between decays to flavour-specific final states and decays to *CP* eigenstates, and by the understanding of the fractions and *CP* content of background components. In the case of the Belle analysis, they were dominated by effects related to the vertex reconstruction and the modelling of the decay-time resolution, followed by the understanding of the tagging performance and of potential biases due to the fitting procedure.

Measurement at LHCb

The LHCb collaboration published [370] a first measurement of the time-dependent *CP* asymmetry in the decay $B^0 \to J/\psi K^0_S$, based on the 2011 data set corresponding to an integrated luminosity of 1 fb^{-1} collected at a *pp* collision energy of 7 TeV. In this analysis, J/ψ and K^0_S candidates were reconstructed in their decays $J/\psi \to \mu^+\mu^-$ and $K^0_S \to \pi^+\pi^-$, respectively. Two categories of K^0_S candidates were distinguished: *long* candidates, for which both final-state pions left hits in the vertex detector, and *downstream* candidates, for which the trajectories of the two final-state pions had to be reconstructed using information from the main tracking system alone. *Downstream* candidates are typically due to K^0_S mesons that decay outside the acceptance of the vertex locator and are less precisely reconstructed than *long* K^0_S candidates. The selection of event candidates exploited the clear topology of the decay $B^0 \to J/\psi K^0_S$. The reconstructed tracks of the two charged pions assigned to the K^0_S decay were required to be clearly separated from all reconstructed *pp* collision vertices in the event and the reconstructed K^0_S decay vertex had to be significantly displaced from these *pp* collision vertices. Candidate B_{rec} decays were formed by combining a J/ψ candidate and a K^0_S candidate that were compatible with originating from a common vertex and had a combined invariant mass within a 100 MeV/c^2 wide window around the known mass of the B^0 meson. The decay vertex of the K^0_S candidate was then required to be significantly displaced from the reconstructed decay vertex of the B_{rec} candidate. The decay time, t, of the B_{rec} candidate was reconstructed from a kinematic fit constraining the momentum of the B^0 candidate to point back to the position of its associated *pp* collision vertex. The uncertainty on the reconstructed decay time was estimated for each event using the results of this fit. Candidates with a reconstructed decay time $t < 0.3$ ps were removed to suppress the large component of combinatorial background at small measured decay times. Candidates with an estimated decay-time uncertainty $\sigma_t > 0.2$ ps were removed to suppress poorly reconstructed events. A small drop in reconstruction efficiency was observed at large decay times and was corrected for using samples of simulated events. The invariant mass distribution of the 8200 reconstructed and flavour-tagged candidates is shown in Figure 5.68. The initial flavour of the B_{rec} candidate was inferred from a combination

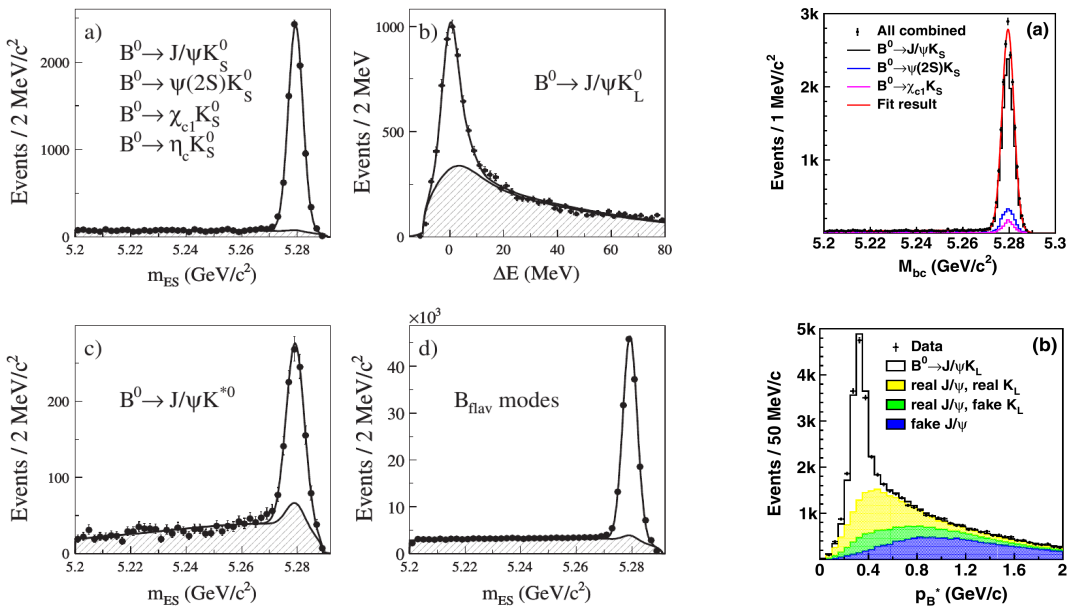

Figure 5.66: Distributions of the beam-energy substituted invariant mass, $m_{\rm ES}$ resp. $M_{\rm bc}$, for $B_{\rm rec} \to (c\bar{c})K^0_S$ candidates and distribution of ΔE resp. p^*_B for $B_{\rm rec} \to J/\psi K^0_L$ candidates in (left and middle) BaBar and (right) Belle. In the panels on the left, $m_{\rm ES}$ distributions are also shown for the *CP* mixed final state $J/\psi K^{*+}$ and for the flavour-specific final states used in the analysis. Background contributions are indicated by the shaded areas (from [367, 368]).

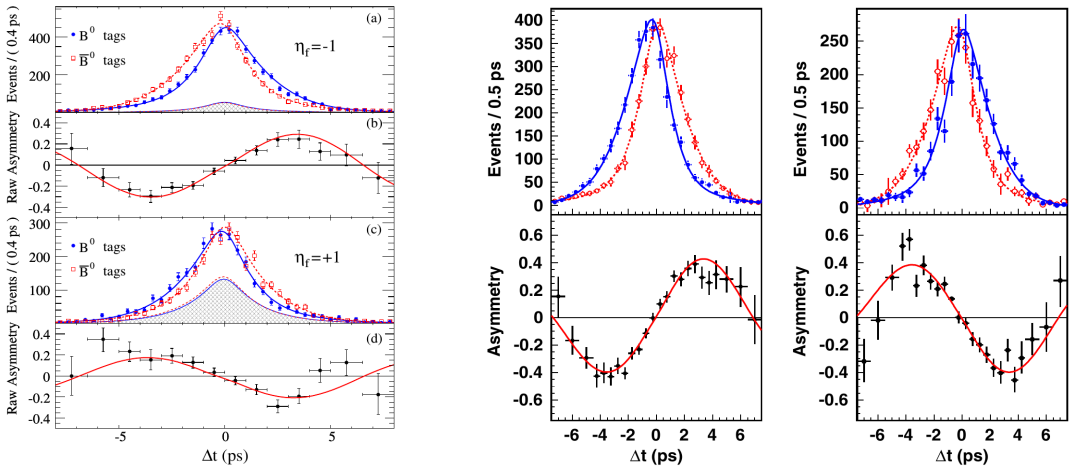

Figure 5.67: Decay-time distributions for events tagged as B^0 decays and events tagged as $\overline{B}^0$ decays and the resulting decay-time dependent mixing asymmetry in (left) BaBar and (middle and right) Belle. The upper left panels and the middle panels show distributions for decays to *CP*-odd final states $(c\bar{c})K^0_S$, while the lower left panels and the rightmost panels show distributions for decays to the *CP*-even final state $J/\psi K^0_L$. Projections of the fit functions are shown as solid lines (from [367, 368]).

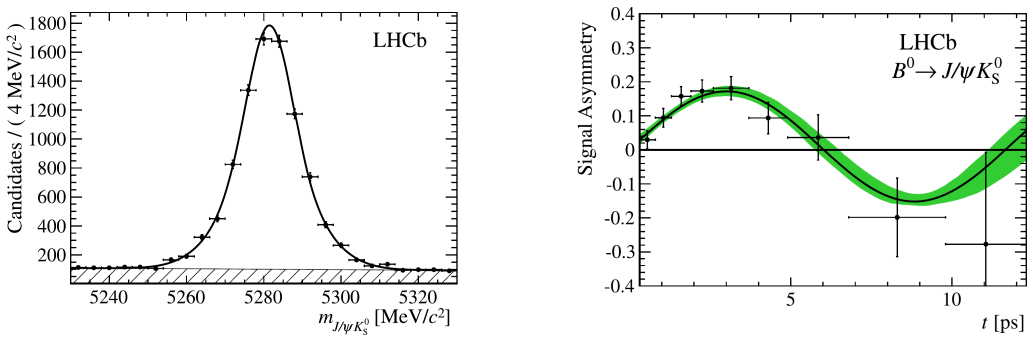

Figure 5.68: (left) Distribution of the invariant mass for $B^0 \to J/\psi K^0_S$ candidates from the LHCb analysis of *CP*-violating parameters in this decay. The solid line indicates the projection of the fit result and the grey area indicates the background component; (right) The *CP*-violating asymmetry in bins of the decay time. Here, the solid line indicates the projection of the signal component of fit result and the shaded band indicates the statistical uncertainty corresponding to one standard deviation (from [370]).

of opposite-side flavour tagging algorithms [202] as described in Section 4.4. The estimated mistag probability $\eta_{\rm tag}$ returned by the tagging algorithm was calibrated on collision data, comparing it to the observed fraction of wrongly tagged candidates in samples of self-tagging decays $B^\pm \to J/\psi K^\pm$. In this calibration, the fraction of wrong tags was determined separately for B^+ decays and B^- decays and the observed difference was used in the analysis to estimate the difference in the mistag fraction for B^0 candidates and $\overline{B}^0$ candidates. A possible small difference in tagging efficiency between B^0 candidates and $\overline{B}^0$ candidates was neglected in the analysis and taken into account as a source of systematic uncertainty. The event-by-event estimate of the decay-time uncertainty was calibrated on collision data employing samples of prompt J/ψ candidates produced in the pp collisions. The true decay time for these J/ψ candidates is zero by definition and the reconstructed decay time gives a good measure of the true decay-time uncertainty for the given candidate. After calibration, the average decay-time resolution for $B_{\rm rec} \to J/\psi K^0_S$ candidates was found to be about 55 fs for *long* candidates, in which information from the vertex detector was available to reconstruct the K^0_S decay vertex, and about 65 fs for *downstream* candidates in which the K^0_S decay vertex was reconstructed using information from the main tracking system alone. A simultaneous maximum likelihood fit to the reconstructed invariant mass of the $J/\psi K^0_S$ candidates, their reconstructed decay time and the estimated decay-time resolution, the flavour-tagging decision and the estimated mistag probability was performed to extract the *CP*-violating parameters S and C. The fit function contained a term to describe the signal component and a term to describe backgrounds. The invariant-mass distribution for the signal component was described by the sum of two Gaussian functions with common mean, while the invariant mass distribution for the background component was described by a falling exponential function. The decay-time distribution for the background component was modelled by the sum of two exponential functions, convolved with the decay-time resolution function. The decay-time distribution for the signal component was parametrized as

$$
\begin{aligned}
P_{\rm sig}(t) \;\propto\; & e^{-t/\tau_B} \times \{ \\
& 1 - q_{\rm tag}\,\Delta\omega_{\rm tag} \;-\; A_P\, q_{\rm tag} \left(1 - 2\omega_{\rm tag}(\eta_{\rm tag})\right) \\
& - \left[q_{\rm tag} \left(1 - 2\omega_{\rm tag}(\eta_{\rm tag})\right) \;-\; A_P \left(1 - q_{\rm tag}\Delta\omega_{\rm tag}\right) \right] \cdot S \,\sin\left(\Delta m_d\, t\right) \\
& + \left[q_{\rm tag} \left(1 - 2\omega_{\rm tag}(\eta_{\rm tag})\right) \;-\; A_P \left(1 - q_{\rm tag}\Delta\omega_{\rm tag}\right) \right] \cdot C \,\cos\left(\Delta m_d\, t\right) \\
& \} \;,
\end{aligned}
$$

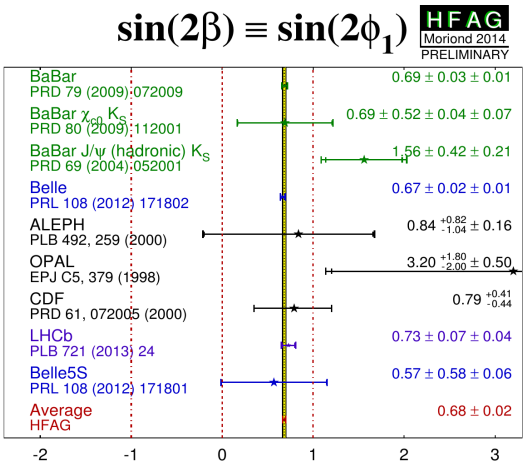

Figure 5.69: Compilation of measurements of the CKM parameter $\sin(2\beta)$ and their average, as performed by the Heavy Flavour Averaging Group, including results presented by September 2014 (from [2]).

convolved with the same decay-time resolution function, where $q_{\rm tag} = +1$ for candidates tagged as B^0 and $q_{\rm tag} = -1$ for candidates tagged as $\overline{B}^0$, while $\omega_{\rm tag}(\eta_{\rm tag})$ is the calibrated mistag probability and $\Delta\omega_{\rm tag}$ the estimated difference in the mistag fractions between B^0 tags and $\overline{B}^0$ tags. The parameter A_P describes the small asymmetry in production rates of $\overline{B}^0$ and B^0 mesons in pp collisions. This asymmetry had been measured in earlier LHCb analyses [371, 372] to be $A_P = -0.015 \pm 0.013$. All parameters related to the description of the decay time resolution and decay-time acceptance were fixed in the fit while the parameters describing the flavour tagging performance and the production asymmetry were constrained within their statistical uncertainties using Gaussian probability density functions. The B^0 lifetime, τ_B, and the $B^0 - \overline{B}^0$ oscillation frequency were free parameters in the fit together with the CP-violating parameters, S and C. The fit results of $\tau_B = 1.496 \pm 0.018$ ps and $\Delta m_d = 0.53 \pm 0.05$ ps^{-1} were both in good agreement with the known world average values of these quantities. The measured decay-time dependent CP-violating asymmetry is shown in Figure 5.68 and exhibits the expected osillatory behaviour. Systematic uncertainties on the determination of S and C were found to be dominated by effects related to the understanding of the tagging calibration and the modelling of the distributions for the background component. Systematic effects related to the decay-time resolution are small since the measurement uncertainty is much smaller than the $B^0 - \overline{B}^0$ oscillation period. The result of the measurement in terms of $\sin(2\beta)$ is shown in Figure 5.69 and the CP violating parameter C was measured to

$$C \;=\; 0.03 \;\pm\; 0.09\,(\text{stat}) \;\pm\; 0.01\,(\text{syst})\;.$$

Both results are in good agreement with those from the B factories. While this measurement cannot yet compete in precision with the results obtained at the B factories, it constituted the first significant observation of a non-vanishing CP asymmetry in the decay $B^0 \to J/\psi K^0_S$ at a hadron collider[3].

5.3.2 Resolution of the phase ambiguity in $B^0 \to J/\psi K^{*0}$

As both the J/ψ meson and the K^{*0} meson are vector particles with internal spin $J = 1$, the $J/\psi K^{*0}$ pair in the decay $B^0 \to J/\psi K^{*0}$ can be produced with relative angular momentum

[3] A new LHCb measurement [373] of $\sin(2\beta)$ in the decay $B^0 \to J/\psi K^0_S$ based on the full run I data set, corresponding to an integrated luminosity of 3 fb^{-1} collected at pp collision energies of 7 TeV and 8 TeV, was presented at the 2015 Moriond conference in La Thuile. The quoted results, $\sin(2\beta) = 0.731 \pm 0.035\,(\text{stat}) \pm 0.020\,(\text{syst})$ and $C = -0.038 \pm 0.032\,(\text{stat}) \pm 0.005\,(\text{syst})$, are compatible with the earlier LHCb measurement and with those from the B factories.

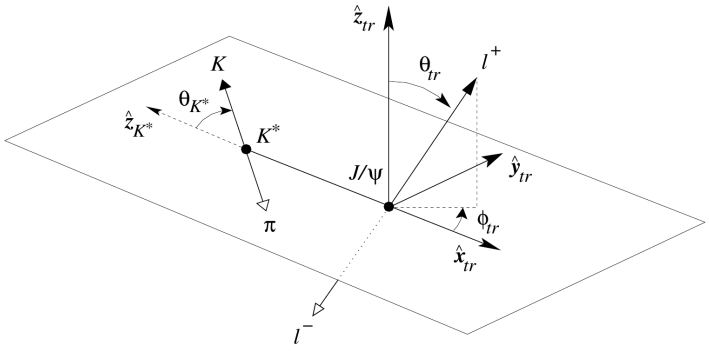

Figure 5.70: Definition of transversity angles $(\theta_{K^*}, \theta_{tr}, \phi_{tr})$ as employed in the BaBar time-dependent angular analysis of $B^0 \to J/\psi K^{*0}$: the K^{*0} helicity angle θ_{K^*} is the angle between the negative flight direction of the B meson and the flight direction of the kaon in the K^{*0} rest frame, θ_{tr} and ϕ_{tr} are the polar and azimuthal angle of the positive lepton defined in the J/ψ rest frame (from [374]).

$L = 0, 1$ or 2. The states with $L = 0$ and $L = 2$ are *CP* even while the state with $L = 1$ is *CP* odd. Reconstructing $J/\psi \to \ell^+\ell^-$ and $K^{*0} \to K^+\pi^-$, the decay is fully characterized by the $K^+\pi^-$ invariant mass and three angles between the directions of flight of the four final-state particles. An angular analysis of the final state particles allows to statistically separate the even and odd *CP* components. It is convenient to perform this angular analysis in the so-called transversity basis, in which the decay amplitude is decomposed according to the polarizations of the two vector mesons with respect to their direction of motion, i.e. with respect to the $B^0 \to J/\psi K^{*0}$ decay axis in the rest frame of the B^0 meson. In this decomposition, the amplitude A_0 describes the state in which the two vector mesons are polarized longitudinally along the decay axis, while the amplitudes $A_\parallel$ and $A_\perp$ describe the states in which the polarization vectors of the two vector mesons are parallel and orthogonal with respect to each other in the plane perpendicular to the decay axis. Each of the three amplitudes has a well-defined *CP* symmetry: the amplitudes A_0 and $A_\parallel$ are *CP* even and the amplitude $A_\perp$ is *CP* odd. The decay angles corresponding to the transversity basis, $\omega \equiv (\theta_{K^*}, \theta_{tr}, \phi_{tr})$, are defined in Figure 5.70. Expressions for the differential decay rates and the time-dependent decay rate asymmetry are derived in Refs. [374] and [375]. Summing over B^0 and $\overline{B}^0$ decays, the time-integrated differential decay rate as a function of the transversity angles is found to be

$$\begin{aligned} g(\omega) &\equiv \frac{1}{\Gamma}\,\frac{d^3\Gamma\,(B \to J/\psi K^*)}{d\omega} \\ &\propto f_1(\omega)\,|A_0|^2 \;+\; f_2(\omega)\,|A_\parallel|^2 \;+\; f_3(\omega)\,|A_\perp|^2 \\ &\quad + f_4(\omega)\,|A_\parallel||A_\perp|\,\sin(\delta_\perp - \delta_\parallel) \\ &\quad + f_5(\omega)\,|A_0||A_\parallel|\,\cos(\delta_\parallel - \delta_0) \\ &\quad + f_6(\omega)\,|A_0||A_\perp|\,\sin(\delta_\perp - \delta_0)\;, \end{aligned}$$

where $\delta_0, \delta_\parallel$ and $\delta_\perp$ are the strong phases of the transversity amplitudes and the dependence on the decay-angles is given by

$$\begin{aligned} f_1(\omega) &= 2\cos^2\theta_{K^*}\,(1 - \sin^2\theta_{tr}\,\cos^2\phi_{tr}) \\ f_2(\omega) &= \sin^2\theta_{K^*}\,(1 - \sin^2\theta_{tr}\,\cos^2\phi_{tr}) \\ f_3(\omega) &= \sin^2\theta_{K^*}\,\sin^2\theta_{tr} \\ f_4(\omega) &= \sin^2\theta_{K^*}\,\sin(2\theta_{tr})\,\sin\phi_{tr} \\ f_5(\omega) &= \tfrac{1}{2}\sqrt{2}\,\sin(2\theta_{K^*})\,\sin^2\theta_{tr}\sin(2\phi_{tr}) \\ f_6(\omega) &= \tfrac{1}{2}\sqrt{2}\,\sin(2\theta_{K^*})\,\sin(2\theta_{tr})\cos\phi_{tr}\;. \end{aligned}$$

Assuming that no direct *CP* violation occurs in the decay, the time-dependent differential decay-rates are

$$\begin{aligned} g_q(\omega) &\equiv \frac{1}{\Gamma}\frac{d^4\Gamma\,(B\to J/\psi K^*)}{d\omega\,dt} \\ &\propto \frac{\Gamma_d}{2}\,e^{-\Gamma_d t}\;\times\;A(\omega)\;\times\;\Bigg\{ \\ &\quad 1\;+\;q\cdot\left[\frac{P(\omega)}{A(\omega)}\cos\left(\Delta m_d\,t\right)\;+\;\left(\frac{S(\omega)}{A(\omega)}\sin\left(2\beta\right)\;+\;\frac{C(\omega)}{A(\omega)}\cos\left(2\beta\right)\right)\sin\left(\Delta m_d\,t\right)\right]\Bigg\}\;, \end{aligned}$$

where $q=+1$ for an initial B^0 meson and $q=-1$ for an initial $\overline{B}^0$ meson, β is the angle of the Unitarity Triangle, and the dependence on the decay angles is given by

$$\begin{aligned} A(\omega) &= f_1(\omega)\,|A_0|^2\;+\;f_2(\omega)\,|A_\parallel|^2\;+\;f_3(\omega)\,|A_\perp|^2\;+\;f_5(\omega)\,|A_0||A_\parallel|\,\cos\left(\delta_\parallel-\delta_0\right) \\ P(\omega) &= f_4(\omega)\,|A_\parallel||A_\perp|\,\sin\left(\delta_\perp-\delta_\parallel\right)\;+\;f_6(\omega)\,|A_0||A_\perp|\,\sin\left(\delta_\perp-\delta_0\right) \\ S(\omega) &= f_1(\omega)\,|A_0|^2\;+\;f_2(\omega)\,|A_\parallel|^2\;-\;f_3(\omega)\,|A_\perp|^2\;+\;f_5(\omega)\,|A_0||A_\parallel|\,\cos\left(\delta_\parallel-\delta_0\right) \\ C(\omega) &= -f_4(\omega)\,|A_\parallel||A_\perp|\,\cos\left(\delta_\perp-\delta_\parallel\right)\;-\;f_6(\omega)\,|A_0||A_\perp|\,\cos\left(\delta_\perp-\delta_0\right)\;. \end{aligned}$$

Finally, the decay-time dependent decay rate asymmetry is

$$\begin{aligned} a(\omega,t) &\equiv \frac{g_+(\omega,t)\;-\;g_-(\omega,t)}{g_+(\omega,t)\;+\;g_-(\omega,t)} \\ &= \frac{P(\omega)}{A(\omega)}\cos\left(\Delta m_d\,t\right)\;+\;\left\{\frac{S(\omega)}{A(\omega)}\sin\left(2\beta\right)\;+\;\frac{C(\omega)}{A(\omega)}\cos\left(2\beta\right)\right\}\sin\left(\Delta m_d\,t\right). \end{aligned}$$

A vanishing value of the *CP* odd amplitude, $|A_\perp|=0$, implies $P(\omega)=C(\omega)=0$ as well as $S(\omega)=A(\omega)$ and the equation reduces to the usual expression for decays to *CP* eigenstates. Similarly, vanishing values of the *CP* even amplitudes, $|A_0|=|A_\parallel|=0$, imply $P(\omega)=C(\omega)=0$ and $S(\omega)=-A(\omega)$.

Due to the symmetries of the sine and cosine functions, the differential decay rates and the decay-rate asymmetry are invariant under the simultaneous phase-transformation

$$\Big(\left(\delta_\parallel-\delta_0\right),\,\left(\delta_\perp-\delta_0\right),\,\cos\left(2\beta\right)S\;wav\Big)\;\leftrightarrow\;\Big(-\left(\delta_\parallel-\delta_0\right),\,\pi-\left(\delta_\perp-\delta_0\right),\,-\cos\left(2\beta\right)\Big)$$

and the value of $\cos(2\beta)$ can a priori be measured only up to a sign-ambiguity, since the values of the strong phases are not known. This ambiguity can, however, be resolved by taking into account that the $K^+\pi^-$ pair can also be produced in an S-wave state with relative angular momentum $L=0$, without going through an intermediate K^{*0} resonance. An early BaBar measurement of decay amplitudes in the decay $B\to J/\psi K^*$ had indicated that this S-wave contribution is not negligible for $K\pi$ invariant masses in the region of the K^* resonance. Including an S-wave amplitude, $A_S\equiv|A_S|e^{i\delta_S}$, four more terms have to be added to the time-integrated differential decay rate, which becomes

$$\begin{aligned} g_{S+P}(\omega) \;\propto\; & g(\omega)\;+\;f_7(\omega)\,|A_S|^2 \\ & +\;f_8(\omega)\,|A_S||A_\parallel|\,\cos\left(\delta_\parallel-\delta_S\right) \\ & +\;f_9(\omega)\,|A_S||A_\perp|\,\sin\left(\delta_\perp-\delta_S\right) \\ & +\;f_{10}(\omega)\,|A_S||A_0|\,\cos\left(\delta_S-\delta_0\right)\;\}\;, \end{aligned}$$

with the additional angular terms

$$\begin{aligned} f_7(\omega) &= \tfrac{2}{3}\left(1\;-\;\sin^2\theta_{tr}\,\cos^2\phi_{tr}\right) \\ f_8(\omega) &= -\tfrac{1}{3}\sqrt{6}\,\sin\theta_{K^*}\,\sin^2\theta_{tr}\,\sin\left(2\phi_{tr}\right) \\ f_9(\omega) &= \tfrac{1}{3}\sqrt{6}\,\sin\theta_{K^*}\,\sin\left(2\theta_{tr}\right)\,\cos\phi_{tr} \\ f_{10}(\omega) &= \tfrac{4}{3}\sqrt{3}\,\cos\theta_{K^*}\left(1\;-\;\sin^2\theta_{tr}\,\cos^2\phi_{tr}\right). \end{aligned}$$

The phase ambiguity still remains when looking at the angular distributions for a fixed value of the $K\pi$ invariant mass, but it can be resolved by investigating the evolution of the phase difference between the S-wave amplitude and the P-wave amplitudes as a function of the $K\pi$ invariant mass. The P-wave amplitudes are expected to undergo a large positive phase shift as they go through a resonance at the mass of the K^* meson, while the phase of the non-resonant S-wave amplitude is expected to change only slowly as a function of the $K\pi$ invariant mass in this region.

An analysis of this behaviour was performed by the BaBar collaboration [374], based on a data set corresponding to about 88 million produced $B\overline{B}$ pairs. As the available event sample was not sufficiently large to fix all parameters in a simultaneous fit to the measured time-dependent angular distribution, the analysis was carried out in three distinct steps. In the first step, parameters of the three P-wave amplitudes, neglecting the S-wave amplitude, were determined from an analysis of the time-integrated angular distribution in a ± 100 MeV/c^2 wide mass window around the nominal mass of the K^* resonance. In a second step, the S-wave amplitude was included in the analysis and the phase ambiguity was resolved by an analysis of the time-integrated angular distribution in eleven bins of the $K\pi$ invariant mass between 0.8 GeV/c^2 and 1.5 GeV/c^2. These two steps made use of decays $B^+ \to J/\psi K^0_S \pi^+$ and $B^+ \to J/\psi K^+ \pi^0$ as well as $B^0 \to J/\psi K^+ \pi^-$, assuming identical behaviour of the P-wave amplitudes in these isospin-related decay modes. In a third step, a measurement of $\cos(2\beta)$ was performed in a time-dependent angular analysis of a statistically independent sample of $B^0 \to J/\psi K^0_S \pi^0$ candidates with an invariant mass of the $K^0_S\pi^0$ pair within a ± 100 MeV/c^2 wide window around the nominal mass of the K^* resonance. In this step, the parameters of the P-wave amplitudes were fixed to the values determined in the first step and the contribution from the S-wave amplitude was again neglected. The selection of event candidates for all decay modes was based on the usual kinematical variables, namely the energy imbalance, ΔE, of the $B_{\rm rec}$ candidate and its beam energy-substituted invariant mass, $m_{\rm ES}$. Distributions of $m_{\rm ES}$ for selected candidates in the four final states are shown in Figure 5.71. Combinatorial background in the signal region was estimated by extrapolation from the $m_{\rm ES}$ sidebands and its contribution was subtracted from the measured angular distributions assuming that it followed the same angular shape as the signal. Another source of background in the individual final states is cross-feeds, in which a genuine $J/\psi K^*$ event is reconstructed in the wrong K^* mode, for example if the kaon from a $K^{*+} \to K^+\pi^0$ decay is combined with a charged pion to form a $K^{*0} \to K^+\pi^-$ candidate. Since the different final states are assumed to follow the same angular distribution, these cross-feeds were treated as part of the signal. A good understanding of the detector acceptance and the reconstruction efficiency as a function of the decay angles is required for the angular analysis. They were estimated from samples of simulated events, taking into account contributions from the cross-feeds mentioned before. The result of the time-integrated angular analyses is illustrated in Figure 5.72. The contribution from the S-wave amplitude is found to increase slowly as a function of the $K\pi$ invariant mass, while the P-wave amplitudes show the expected behaviour of a resonance around the mass of the K^* meson. A clear phase shift between the S-wave amplitude and the P-wave amplitudes is observed at the K^* mass. The solution

$$\Big((\delta_\parallel - \delta_0)\,,\, (\delta_\perp - \delta_0)\,,\, \cos(2\beta) \Big)$$

shows the expected behaviour of decreasing phase difference $(\delta_S - \delta_0)$. As can be seen in Figure 5.71, the decay mode $B_{\rm rec} \to J/\psi K^{*0}$ with $K^{*0} \to K^0_S\pi^0$, that was used for the time-dependent angular analysis, suffered from larger backgrounds than the decay modes used in the time-integrated angular analysis. Therefore, its angular distribution was modelled separately in the fit for $\cos(2\beta)$ using a parametrization derived from samples of simulated events. The analysis itself followed the usual pattern. Flavour tagging was based on the standard algorithm discussed in Section 4.1.10. The decay time difference Δt was calculated in the usual manner from the reconstructed positions of the $B_{\rm rec}$ and $B_{\rm tag}$ decay vertices and the Lorentz boost of

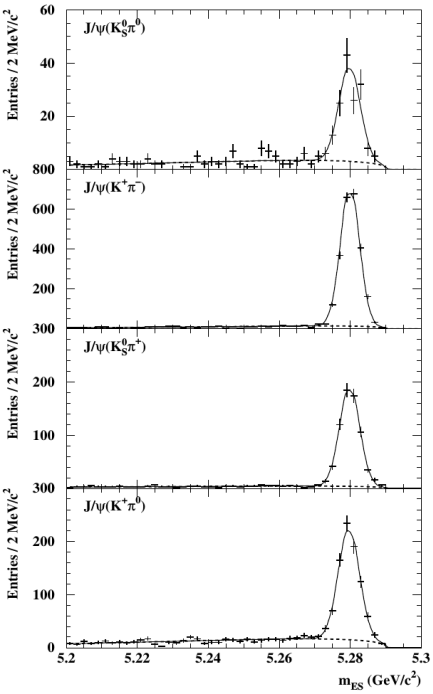

Figure 5.71: Distributions of the beam-energy substituted invariant mass $m_{\rm ES}$ for the different $B_{\rm rec} \to J/\psi K^*$ decay modes employed in the BaBar analysis to measure the sign of $\cos(2\beta)$ (from [374]).

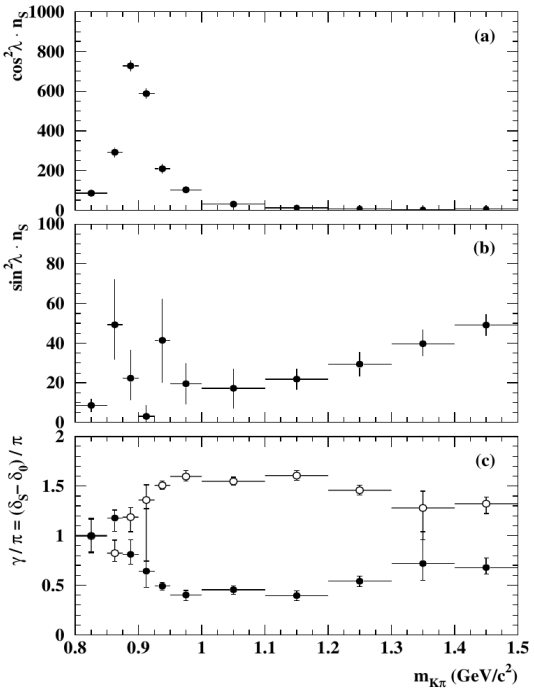

Figure 5.72: Relative strengths of the (top) P-wave and (middle) S-wave amplitudes in bins of the $K\pi$ invariant mass in the region around the K^* resonance and (bottom) the relative phase $\delta_S - \delta_0$ between the S-wave amplitude and one of the P-wave amplitudes. The evolution of the phase difference as a function of $K\pi$ invariant mass is shown for the two ambiguous solutions. The solution showing the expected negative trend is selected as the "physical solution" (from [374]).

the $\Upsilon(4S)$ rest frame in the laboratory system. The decay-time resolution was described by the sum of three Gaussian distributions with separate means and widths. The effects of imperfect tagging performance and finite decay-time resolution were estimated in the fit for $\cos(2\beta)$ by simultaneously fitting large samples of flavour-specific decays $B_{\rm rec} \to D^{(*)\pm}\pi^{\mp}$, $B_{\rm rec} \to D^{(*)\pm}\rho^{\mp}$, $B_{\rm rec} \to D^{(*)\pm}a_1^{\mp}$ and $B_{\rm rec} \to J/\psi K^{*0}$ with $K^{*0} \to K^+\pi^-$.

The results of the time-dependent angular analysis are illustrated in Figure 5.73. A fit for $\cos(2\beta)$, fixing the value of $\sin(2\beta)$ to its world-average value at the time of the measurement, resulted in

$$\cos(2\beta) \;=\; +2.72\,^{+\,0.50}_{-\,0.79}\,(\text{stat}) \,\pm\, 0.27\,(\text{syst})$$

and the value of $\cos(2\beta)$ was determined to be positive at 86% confidence level.

5.3.3 Measurements of $\sin(2\beta_{\rm eff})$ in $\overline{b} \to \overline{s}s\overline{s}$ transitions

Initial measurements of $\sin(2\beta_{\rm eff})$ by the BaBar and Belle collaborations investigated the resonant decays $B^0 \to \phi K^0_S$ with $\phi \to K^+K^-$ and $B^0 \to \eta K^0_S$ with $\eta \to K^+K^-$. In both cases, the final state is a CP eigenstate. The decaying B^0 meson and the K^0_S meson are pseudoscalar particles with spin $J = 0$, while the ϕ meson is a vector particle with spin $J = 1$ and the η meson is a pseudoscalar particle with spin $J = 0$. Angular momentum conservation in the decay requires the ϕK^0_S pair to be produced with relative angular momentum $L = 1$, and therefore in a CP-odd eigenstate, while the ηK^0_S must be produced with $L = 0$ and therefore in a CP-even eigenstate. In later measurements, time-dependent Dalitz-plot analyses were performed to

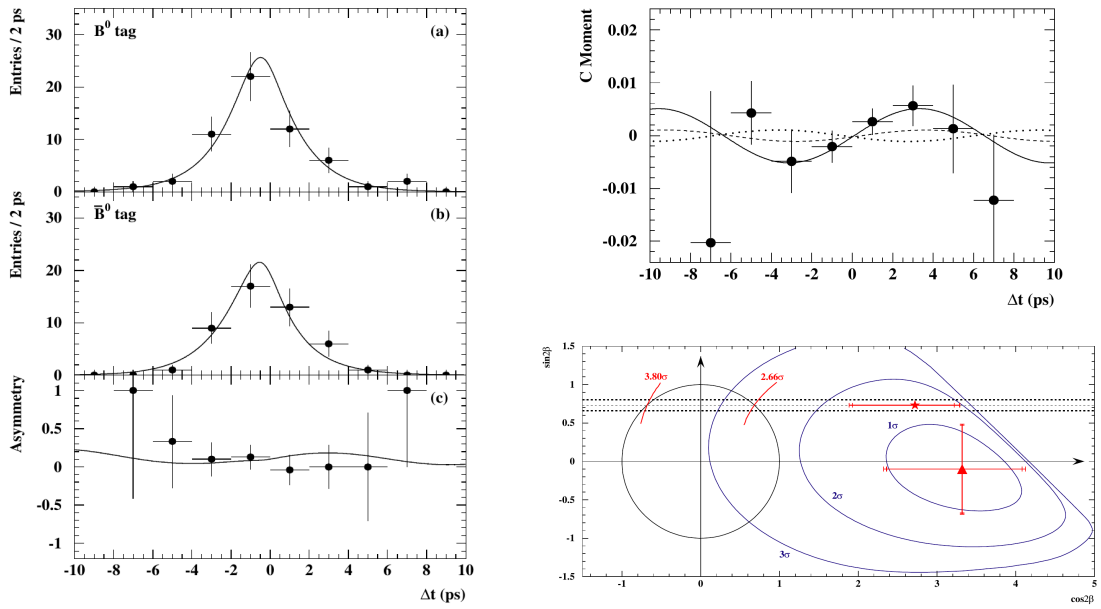

Figure 5.73: (left) Decay-time distribution of $B_{\rm rec} \to J/\psi K^{*0}$ candidates tagged as (top) B^0 and (middle) $\overline{B}^0$ decays and (bottom) their time-dependent asymmetry; (top right) evolution of the $\cos(2\beta)$ term as a function of the reconstructed decay time and (bottom right) results of the fit for $\sin(2\beta)$ and $\cos(2\beta)$. In the bottom right panel, error bars indicate the fit results when floating both $\sin(2\beta)$ and $\cos(2\beta)$ and when constraining the value of $\sin(2\beta)$ to its world average value at the time of the measurement, indicated by the horizontal bands. Blue curves indicate contours of constant change in log-likelihood corresponding to 1,2 and 3 Gaussian standard deviations, the black circle indicates physical values with $\sin^2(2\beta) + \cos^2(2\beta) = 1$. (from [374]).

exploit the interference between these resonant components and the non-resonant component $B^0 \to K^+K^-K^0_S$ in order to determine not only $\sin(2\beta_{\rm eff})$ but also the direct CP phase $C \equiv -A_{K^+K^-K^0_S}$. Earlier measurements had shown that non-resonant K^+K^- pairs are mostly produced in an S-wave state, i.e. with relative angular momentum $L = 0$. The non-resonant final state $K^+K^-K^0_S$ is therefore mostly CP even.

The concept of Dalitz plot analyses was introduced by Richard Henry Dalitz in 1953 [376, 377] to study the spin nature of the kaon through its decay to three pions and has since then been widely applied to analyse resonant structures in three-body decays. Decays are characterized by the squared invariant masses of two pairs of the three final-state particles. For phase-space distributed decays of a spin-0 particle, events are evenly distributed within the kinematically allowed region in the two-dimensional space defined by these two variables. Decay dynamics, such as intermediate resonances, can cause structures in the distribution of the events across the Dalitz plot and the study of such structures allows to draw conclusions on the dynamics involved in the decay. In terms of the decay $B^0 \to K^+K^-K^0_S$, the two Dalitz variables can be defined as

$$\begin{aligned} s_+ &\equiv m^2(K^+, K^0_S) \\ s_- &\equiv m^2(K^-, K^0_S)\ . \end{aligned}$$

An example of a Dalitz plot derived from a sample of simulated decays including resonant as well as non-resonant components is shown in Figure 5.74.

Neglecting effects from acceptance, trigger and reconstruction efficiencies, the time-dependent

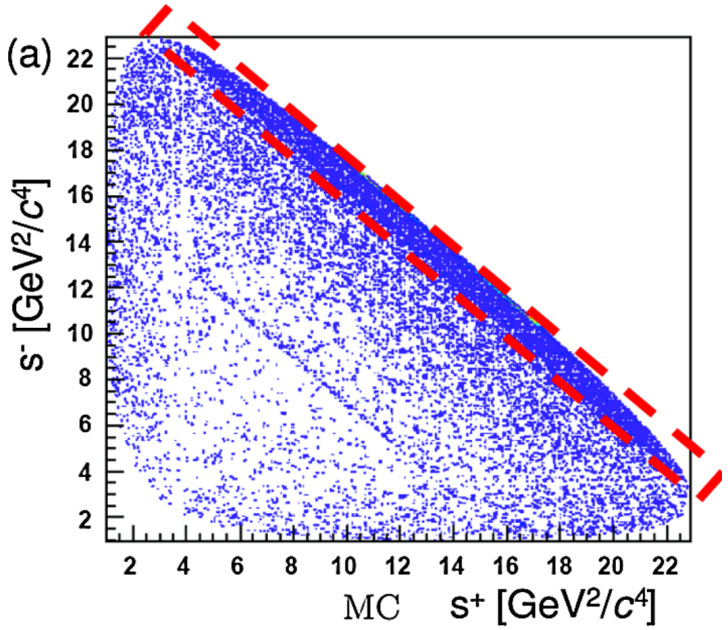

Figure 5.74: Dalitz plot of simulated $B^0 \to K^+K^-K^0_S$ events in terms of the variables $s^+ \equiv m^2(K^+, K^0_S)$ and $s^- \equiv m^2(K^-, K^0_S)$. Resonant structures in the K^+K^- invariant mass spectrum are visible as falling diagonal lines. In particular, the rectangle along the upper right edge marks the region of the $\phi \to K^+K^-$ resonance (from [378]).

decay rate as a function of these Dalitz variables can be expressed as

$$\begin{aligned}\frac{d\Gamma}{ds_+\, ds_-\, d\Delta t} \;\propto\; & \frac{e^{-|\Delta t|/\tau_B}}{4\tau_B} \times \{ \\ & (1 - q_{\rm tag}\,\Delta\omega_{\rm tag}) \cdot (|A|^2 + |\overline{A}|^2) \\ & - q_{\rm tag}\,(1 - 2\omega_{\rm tag}) \cdot (|A|^2 - |\overline{A}|^2)\,\cos(\Delta m_d\,\Delta t) \\ & + q_{\rm tag}(1 - 2\omega_{\rm tag}) \cdot 2\,{\rm Im}\,(e^{-i2\beta}\,\overline{A}A^*)\,\sin(\Delta m_d\,\Delta t)\ \}\end{aligned}$$

convolved with a function describing the decay-time resolution. As usual, Δt denotes the decay-time difference between the $B_{\rm rec}$ candidate and the $B_{\rm tag}$ candidate, $q_{\rm tag} = +1$ for events tagged as B^0 decays and $q_{\rm tag} = -1$ for events tagged as $\overline{B}^0$ decays, $\omega_{\rm tag}$ describes the mistag fraction and $\Delta\omega_{\rm tag}$ a possible difference in the mistag fractions for B^0 and $\overline{B}^0$ candidates; m_B and τ_B are the known mass and lifetime of the B^0 meson and Δm_d is the known $B^0 - \overline{B}^0$ oscillation frequency. The dependence on the Dalitz variables is contained in the complex amplitudes A and $\overline{A}$ for B^0 decays and $\overline{B}^0$ decays, respectively. In the presence of several contributing amplitudes, these can be parametrized as

$$\begin{aligned} A &\equiv \sum a_i \cdot F_i(s_+, s_-) \\ \overline{A} &\equiv \sum \overline{a}_i \cdot \overline{F}_i(s_+, s_-)\ , \end{aligned}$$

where a_i contains the weak phase of the decay amplitude i and $F_i(s_+, s_-)$ describes its dynamics due to the strong interaction. For B^0 and $\overline{B}^0$ decays,

$$\overline{F}_i(s_+, s_-) \;=\; (-1)^L\, F_i(s_+, s_-)\ ,$$

where L is the relative angular momentum between the K^+ and the K^-. The mixing-induced CP violating phase for the amplitude i is

$$\beta_{\rm eff} \;=\; \frac{1}{2}\arg\left(e^{2i\beta} a_i \overline{a}_i^*\right)\ ,$$

while the direct *CP*-violating asymmetry in the decay is given by

$$A_{K^+K^-K^0_S} \;=\; \frac{|\overline{a}_i|^2 - |a_i|^2}{|\overline{a}_i|^2 + |a_i|^2} \; .$$

Both the BaBar collaboration and the Belle collaboration published measurements of $\sin(2\beta_{\rm eff})$ and $A_{K^+K^-K^0_S}$. The Belle measurement [378] was based on a data set corresponding to 657 million produced $B\overline{B}$ pairs and employed K^0_S candidates reconstructed in their decays to two charged pions. The BaBar analysis [379] was based on their full data set, corresponding to 472 million produced $B\overline{B}$ pairs, and made use of K^0_S candidates reconstructed in their decays to $\pi^+\pi^-$ as well as $\pi^0\pi^0$. The event selection was in both analyses based on the usual discriminating variables: the energy imbalance, ΔE, the beam energy-substituted invariant mass, $m_{\rm ES}$, and event-shape variables. Backgrounds from decays $B^0 \to D^- K^+$ and $B^0 \to \overline{D}^0 K^0_S$ with $\overline{D}^0 \to K^+K^-$ and from decays $B^0 \to J/\psi K^0_S$ with $J/\psi \to K^+K^-$ were suppressed in the Belle analysis by rejecting candidates with a reconstructedd $K^-K^0_S$ or K^+K^- invariant mass compatible with the nominal masses of the D^-, D^0 or J/ψ mesons. In the BaBar analysis, the background components from such decays were estimated from samples of simulated events.

The decay-time difference, Δt, was calculated in both analyses in the usual manner from the $B_{\rm rec}$ and $B_{\rm tag}$ decay vertex positions and the known boost of the $\Upsilon(4S)$ rest frame in the laboratory system. The same decay-time resolution functions and the same flavour tagging algorithm were employed as in the latest measurements of $\sin(2\beta)$ in the decay $B^0 \to J/\psi K^0_S$ described in Section 5.3.1 above. The parameters describing the decay-time resolution functions and the tagging performances were fixed to their values found in the $\sin(2\beta)$ measurements.

Simultaneous maximum-likelihood fits to ΔE, $m_{\rm ES}$, the Dalitz variables, the measured decay-time differences and the tagging response were performed to analyse the composition of the samples of selected candidates and to estimate the values of $\sin(2\beta_{\rm eff})$ and the direct *CP*-violating asymmetry $A_{K^+K^-K^0_S}$. The measured ΔE and $m_{\rm ES}$ distributions are shown together with projections of the fit results in Figures 5.75 for the Belle analysis and in Figure 5.76 for the BaBar analysis. In addition to the signal component, the fit functions contained terms for $B^0\overline{B}^0$ and B^+B^- backgrounds and for combinatorial background from non-$B\overline{B}$ events.

The distribution of events in the Dalitz plot was modelled in both analyses by isobar models including amplitudes for the $\phi(1020)$ and $f_0(980)$ resonances as well as a non-resonant component. The isobar model employed in the Belle analysis contained in addition components for the $f_X(1500)$ and χ_{c0} resonances, while the BaBar model included components for the $f_0(1500)$, $f_0(1710)$, $f'_0(1525)$, and χ_{c0} resonances.

The line shape of the $f_0(980)$ component was modelled by a Flatté function [380], while the $\phi(1020)$ and the other resonant components were modelled as relativistic Breit-Wigner functions. The parameters describing these distributions were fixed to the known values for the respective resonances at the time of the measurement. The shapes of the Dalitz-plot distributions for the non-resonant $K^+K^-K^0_S$ component and for non-$B\overline{B}$ backgrounds were parametrized in the Belle analysis as two-dimensional histograms derived from samples of simulated events and from sideband regions in the ΔE and $m_{\rm ES}$ distribution, respectively. In the BaBar analysis, the non-resonant component was modelled by an empirical polynomial function of the Dalitz variables, with parameters determined from the fit to the data. The fit was performed in the BaBar analysis simultaneously to the $K^0_S \to \pi^+\pi^-$ and $K^0_S \to \pi^0\pi^0$ samples, where the parameters describing the Daliz-plot distributions were constrained to be the same for the two samples, while other parameters were allowed to fluctuate separately. The BaBar fit contained a total of 90 parameters, including event yields for the signal and background categories, parameters describing the complex amplitudes in the isobar model and parameters describing the signal and background shapes in the three discriminating variables, ΔE, $m_{\rm ES}$ and the multivariate classifier derived from event-shape variables.

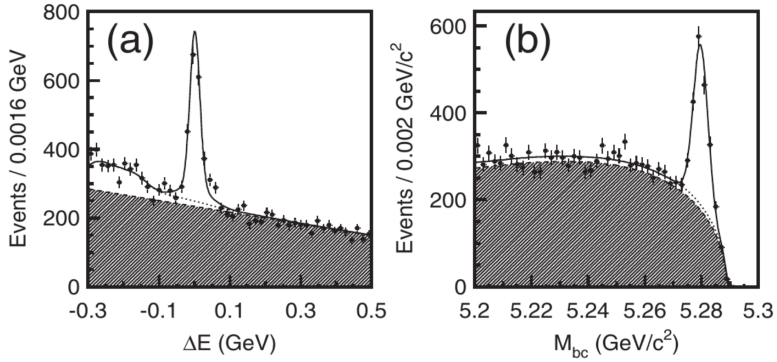

Figure 5.75: Distribution of (left) the energy imbalance and (right) the beam-energy substituted invariant mass for $K^+K^-K^0_S$ candidates employed in the Belle Dalitz-plot analysis of the decay $B^0 \to K^+K^-K^0_S$. The shaded areas indicate the estimated combinatorial background contribution and the dotted lines show the total background estimates (from [378]).

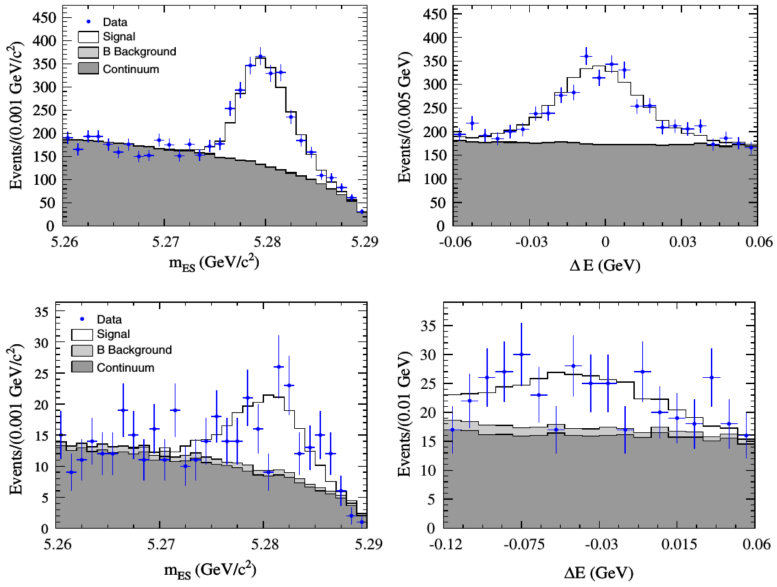

Figure 5.76: Distributions of (left) the beam-energy substituted invariant mass and (right) the energy imbalance for $K^+K^-K^0_S$ candidates employed in the BaBar Dalitz-plot analysis of the decay $B^0 \to K^+K^-K^0_S$. The upper panels show the distributions for candidates with $K^0_S \to \pi^+\pi^-$, the lower panels those for candidates with $K^0_S \to \pi^0\pi^0$. Shaded areas indicate the estimated background contributions as explained in the plot legends (from [379]).

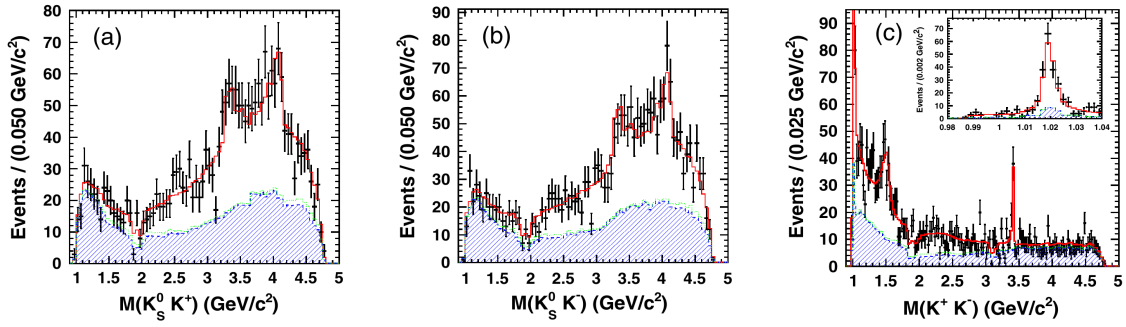

Figure 5.77: Invariant-mass distributions for (left) $K^0_S K^+$ pairs, (middle) $K^0_S K^-$ pairs, and (right) K^+K^- pairs from the Belle Dalitz-plot analysis of the decay $B^0 \to K^+K^-K^0_S$. The insert in the panel on the right shows a close-up of the region around the mass of the $\phi(1020)$ meson (from [378]).

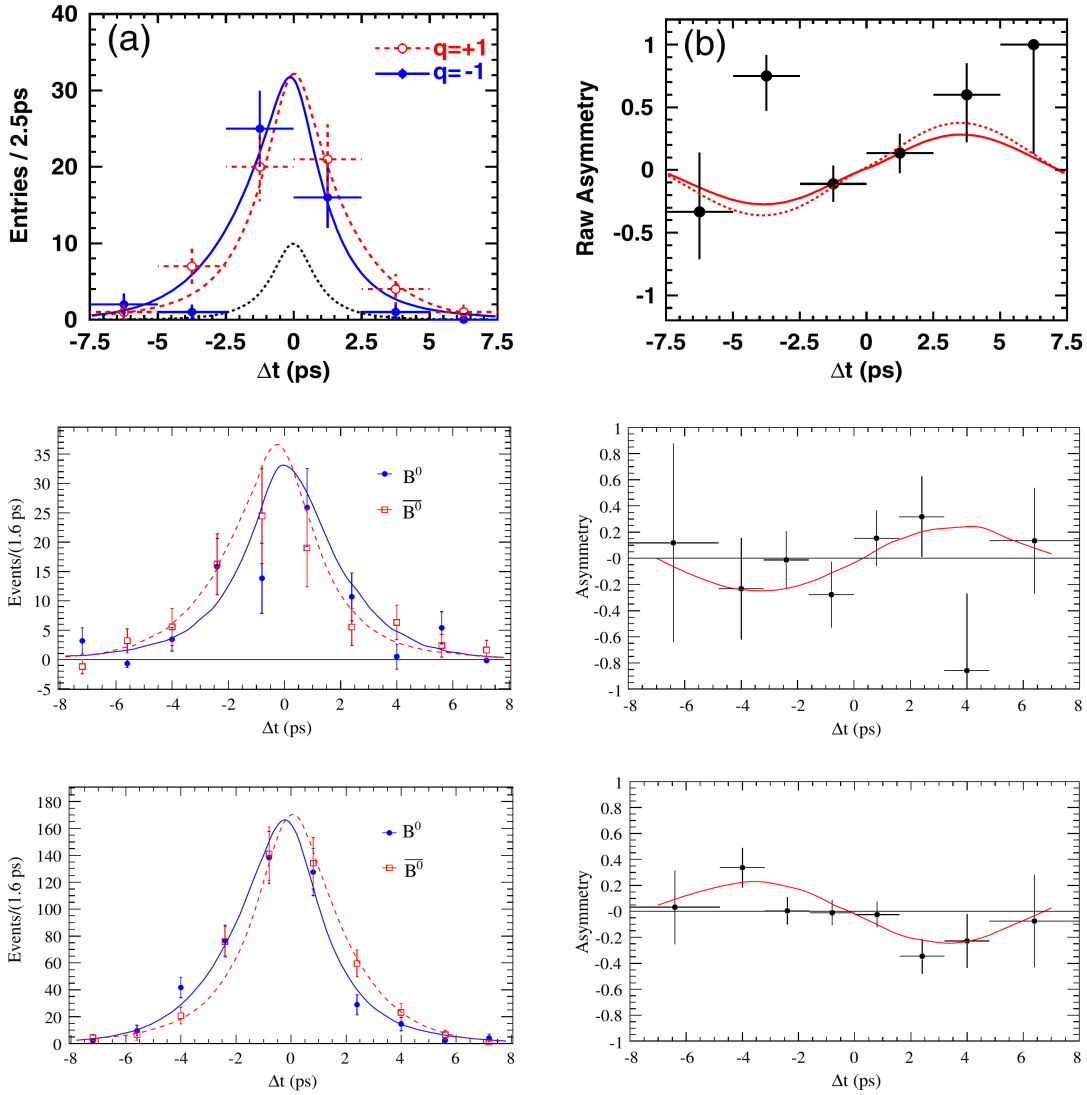

Figure 5.78: (left) Distribution of the decay-time differences for selected candidates tagged as B^0 or $\overline{B}^0$ and (right) decay-time dependent CP asymmetry for $B^0 \to K^+K^-K^0_S$ candidates in the region of the $\phi(1020)$ resonance from the (top row) Belle, and (middle row) BaBar analyses and (bottom row) for $B^0 \to K^+K^-K^0_S$ candidates outside the $\phi(1020)$ region from the BaBar analysis. As expected, the oscillation patterns inside and outside the $\phi(1020)$ region show opposite polarities due to the different relative angular momentum of the K^+K^- system. Full lines indicate the projections of the best fit solutions. In the upper right panel, the dotted line illustrates the expected oscillation pattern using the value of $\sin(2\beta)$ as measured in $B^0 \to (c\bar{c})K^0_S$ analyses (from [378, 379]).

The Belle and BaBar fits gave four and five ambiguous solutions, respectively, corresponding to different contributions from the considered decay amplitudes, but with values for $\sin(2\beta_{\rm eff})$ that were consistent within the uncertainties returned by the fits. Measured invariant-mass distributions from the Belle analysis are shown together with projections of the fit function for the best fit solution in Figure 5.77. Decay-time distributions for selected candidates tagged as B^0 and $\overline{B}^0$ decays and the corresponding decay-time dependent asymmetries from both analyses are shown in Figure 5.78 together with the results of the fits. Results from the Belle analysis are shown for candidates in the region of the $\phi(1020)$-resonance, results from the BaBar analysis are shown both for candidates in the region of the $\phi(1020)$-resonance and for candidates outside this region. The decay-time dependent asymmetries show the expected oscillation patterns, with opposite signs for candidates from the P-wave dominated region around the mass of the $\phi(1020)$ meson and for candidates from the S-wave dominated

remainder of the Dalitz-plot.

Systematic uncertainties on $\sin(2\beta_{\rm eff})$ were found to be dominated in both analyses by uncertainties related to the Dalitz models. Other sources of systematic uncertainties were possible fit biases due to the low statistics in the event samples, the parametrization of the decay-time resolution function and effects related to the reconstruction of the decay vertices. The results for the best fit solutions for candidates in the Dalitz-plot region corresponding to the $\phi(1020)$ resonance were quoted as

$$\beta_{\rm eff}(\phi K^0_S) \;=\; (\,32.2 \,\pm\, 9.0\,({\rm stat}) \,\pm\, 2.6\,({\rm syst}) \,\pm\, 1.4\,({\rm Dalitz\ model})\,)^\circ$$

in the Belle analysis and as

$$\beta_{\rm eff}(\phi K^0_S) \;=\; (\,21 \,\pm\, 6\,({\rm stat}) \,\pm\, 2\,({\rm syst})\,)^\circ$$

in the BaBar analysis. Results compatible with these were in both cases found for candidates in the region of the $f_0(980)$ resonance and for candidates outside the resonant $\phi(1020)$ and $f_0(980)$ regions. Within the relatively large uncertainties, results are compatible with the value of $\sin(2\beta)$ obtained in $\overline{b}\to\overline{c}c\overline{s}$ processes. The fit results for $A_{K^+K^-K^0_S}$ had similarly large uncertainties and were compatible with vanishing direct *CP* asymmetry.

Exploiting the interference between S-wave amplitudes and P-wave amplitudes in the non-resonant region, the mirror solution $(\pi-\beta_{\rm eff})$ could be excluded in the BaBar analysis with a significance corresponding to 4.8 Gaussian standard deviations.

5.4 The angle α: mixing-induced *CP* violation in $\overline{b}\to\overline{u}u\overline{d}$ transitions

The angle α at the apex of the Unitarity Triangle is defined by

$$\alpha \;\equiv\; \arg\left(-\frac{V_{td}V^*_{tb}}{V_{ud}V^*_{ub}}\right)$$

and can in principle be measured from the amplitude of the time-dependent *CP* asymmetry in decays of neutral B mesons to pairs of charged pions. The final state is a *CP* eigenstate that is accessible to B^0 as well as $\overline{B}^0$ decays and the *CP* violating asymmetry is caused by the interference between mixing and decay. The decay amplitudes are dominated by the tree processes shown in Figure 5.79, for which the *CP* violating phase is

$$\lambda_{\pi\pi} \;\equiv\; \left(\frac{q}{p}\right)_{B^0}\cdot\left(\frac{\overline{A}_{\pi\pi}}{A_{\pi\pi}}\right) \;=\; \left(\frac{V^*_{tb}V_{td}}{V_{tb}V^*_{td}}\right)\cdot\left(\frac{V^*_{ub}V_{ud}}{V_{ub}V^*_{ud}}\right) \;=\; 2\,\arg\left(\frac{V_{td}V^*_{tb}}{V^*_{ud}V_{ub}}\right) \;=\; 2\alpha\ .$$

However, the decay can also proceed through the penguin processes shown in Figure 5.80 and the contribution from the penguin amplitudes with different weak phase from the tree amplitude is not negligible. This can be shown by formally expressing the decay amplitude as

$$A_{\pi\pi} \;=\; (T+P_u)\cdot(V_{ud}V^*_{ub}) \,+\, P_c\cdot(V_{cd}V^*_{cb}) \,+\, P_t\cdot(V_{td}V^*_{tb})\ ,$$

where T, P_u, P_c, and P_t denote the amplitudes of the tree process and the penguin processes with intermediate up, charm and top quarks, after the respective weak phases have been factored out. Exploiting the unitarity of the CKM matrix to substitute

$$V^*_{cb}V_{cd} \;=\; -V^*_{ub}V_{ud} \,-\, V^*_{tb}V_{td}\ ,$$

the decay amplitude can be rewritten

$$A_{\pi\pi} \;=\; (T+P_u-P_c)\cdot(V_{ud}V^*_{ub}) \,+\, (P_t-P_c)\cdot(V_{td}V^*_{tb})\ .$$

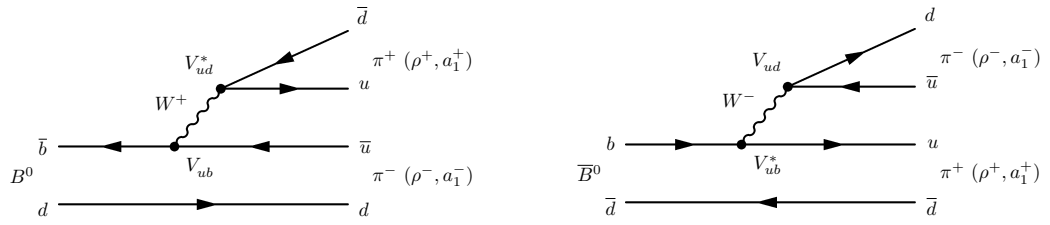

Figure 5.79: Tree diagrams for the decays (left) $B^0 \to \pi^+\pi^-$ and (right) $\overline{B}^0 \to \pi^-\pi^+$. The same diagrams also apply for the decays to $\rho^+\rho^-$, $\rho^\pm\pi^\mp$ and $a_1^\pm\pi^\mp$ discussed in this section.

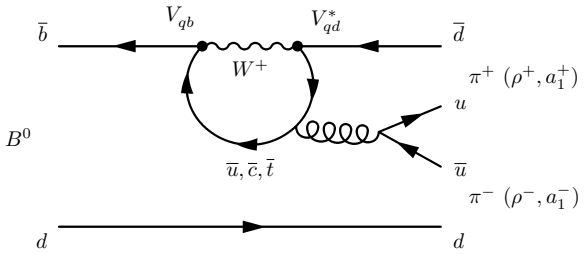

Figure 5.80: Leading penguin diagrams for the decay $B^0 \to \pi^+\pi^-$. The index q stands for u, c or t, depending on the type of the virtual quark that appears in the inner loop. The same diagram also applies for the decays to $\rho^+\rho^-$, $\rho^\pm\pi^\mp$ and $a_1^\pm\pi^\mp$ discussed in this section.

Both $V_{ud}V_{ub}^*$ and $V_{td}V_{tb}^*$ are proportional to the third power of the Wolfenstein parameter λ and the second term on the right-hand side of the equation is therefore not CKM suppressed with respect to the first term. The measured branching fractions for the decays $B^0 \to K\pi$ and $B^0 \to \pi\pi$ in fact indicate that penguin contributions should be significant. For the case of pure tree amplitudes one would expect

$$\frac{\mathrm{BF}\,(B^0 \to K^+\pi^-)}{\mathrm{BF}\,(B^0 \to \pi^+\pi^-)} \;\approx\; \left|\frac{V_{us}}{V_{ud}}\right|^2 \;=\; \lambda^2 \;\approx\; 0.05\;,$$

whereas the ratio of the measured branching fractions [1] is

$$\frac{\mathrm{BF}\,(B^0 \to K^+\pi^-)}{\mathrm{BF}\,(B^0 \to \pi^+\pi^-)} \;=\; \frac{(19.6 \pm 0.5) \times 10^{-6}}{(5.12 \pm 0.19) \times 10^{-6}} \;\approx\; 4\;.$$

A rough quantitative estimate of the ratio P/T of the penguin amplitudes, P, over the tree amplitude, T, in the decay $B^0 \to \pi^+\pi^-$ can be derived by assuming that this decay is dominated by the tree process and that the decay amplitude $A(B^0 \to K^+\pi^-)$ is dominated by the penguin process. Under these assumptions,

$$\frac{A(B^0 \to K^+\pi^-)}{T} \;\approx\; \sqrt{\frac{\mathrm{BF}\,(B^0 \to K^+\pi^-)}{\mathrm{BF}\,(B^0 \to \pi^+\pi^-)}} \;\approx\; 2$$

and

$$\frac{P}{A(B^0 \to K^+\pi^-)} \;\approx\; \left|\frac{V_{td}}{V_{ts}}\right| \;\approx\; 0.2\;,$$

such that

$$\frac{P}{T} \;=\; \frac{A(B^0 \to K^+\pi^-)}{T} \cdot \frac{P}{A(B^0 \to K^+\pi^-)} \;\approx\; 0.4\;.$$

Following the argumentation in Section 3.3, the time-dependent CP asymmetry in neutral B-meson decays to the final state $f = \pi^+\pi^-$ is given by

$$a_{\pi^+\pi^-}(t) \;=\; S_{\pi^+\pi^-}\,\sin(\Delta m_d\, t) \;-\; C_{\pi^+\pi^-}\,\cos(\Delta m_d\, t)$$

where $C_{\pi^+\pi^-}$ is a measure for the direct *CP* violating asymmetry caused by the interference of decay amplitudes with different weak and strong phases and

$$S_{\pi^+\pi^-} \;=\; \sqrt{1 - C^2_{\pi^+\pi^-}} \cdot \sin\left(2\alpha - 2\Delta\alpha\right)$$

describes the *CP* violating asymmetry due to the interference of mixing and decay. The expected significant contributions from penguin processes to the decay amplitude can cause a non-zero value of C_f as well as a shift, $\Delta\alpha$, of the weak phase with respect to the angle α of the Unitary Triangle.

Following an approach first described in Ref. [381] and in Refs [382, 383], the phase shift $\Delta\alpha$ can be extracted from an isospin analysis of the complex decay amplitudes

$$\begin{array}{rcl} A_{+-} & \equiv & A\left(B^0 \to \pi^+\pi^-\right) \\ A_{00} & \equiv & A\left(B^0 \to \pi^0\pi^0\right) \\ A_{+0} & \equiv & A\left(B^+ \to \pi^+\pi^0\right) \end{array}$$

and

$$\begin{array}{rcl} \overline{A}_{+-} & \equiv & A\left(\overline{B}^0 \to \pi^+\pi^-\right) \\ \overline{A}_{00} & \equiv & A\left(\overline{B}^0 \to \pi^0\pi^0\right) \\ \overline{A}_{-0} & \equiv & A\left(B^- \to \pi^-\pi^0\right) \,. \end{array}$$

In all these cases, Bose-Einstein statistics imply that the $\pi\pi$ final state must have even isospin, i.e. $I = 0$ or $I = 2$. In the final state $\pi^+\pi^0$, moreover, the third component of the isospin is $I_3 = 1$ and this final state can therefore assume only $I = 2$, but not $I = 0$. Tree diagrams can lead to both $I = 0$ and $I = 2$ final states, but penguin diagrams cannot lead to final states with $I = 2$ since the exchanged gluon is an isospin singlet state with $I = 0$. Therefore, tree diagrams as well as penguin diagrams can contribute to the decays $B^0 \to \pi^+\pi^-$ and $B^0 \to \pi^0\pi^0$ and their charge conjugates, whereas the decays $B^\pm \to \pi^\pm\pi^0$ can only proceed via tree diagrams. Expanding the decay amplitudes in terms of the isospin amplitudes, A_0 and A_2, for a B meson to decay into a $\pi\pi$ final state with defined isospin $I = 0$ or $I = 2$,

$$\begin{array}{rcl} \left(1/\sqrt{2}\right) A_{+-} & = & A_2 - A_0 \\ A_{00} & = & 2A_2 + A_0 \\ A_{+0} & = & 3A_2 \end{array}$$

and similary for the charge-conjugated processes, yields two relations between the decay amplitudes, namely

$$\left(1/\sqrt{2}\right) A_{+-} \;+\; A_{00} \;=\; A_{+0}$$

and

$$\left(1/\sqrt{2}\right) \overline{A}_{+-} \;+\; \overline{A}_{00} \;=\; \overline{A}_{-0} \,,$$

which can be represented as two triangles in the complex plane. As derived above, the amplitude A_2 receives contributions only from the tree diagram and can therefore be parametrized as

$$A_2 \;\equiv\; |A_2|\, e^{i\delta_2}\, e^{i\phi_T} \,,$$

where δ_2 is the strong phase of the $I = 2$ final-state interaction and ϕ_T is the weak phase of the tree decay. The amplitude for the charge-conjugated process is

$$\overline{A}_2 \;\equiv\; |A_2|\, e^{i\delta_2}\, e^{-i\phi_T} \,,$$

implying

$$|A_2| \;=\; |\overline{A}_2|$$

and therefore

$$|A_{+0}| \;=\; |\overline{A}_{-0}| \,.$$

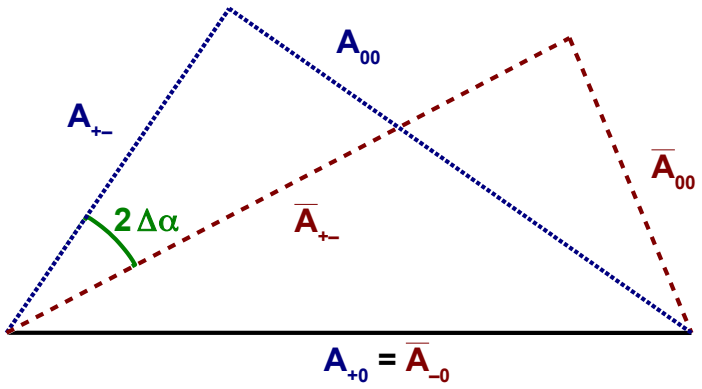

Figure 5.81: Illustration of the two isospin triangles employed to extract the phase shift $\Delta\alpha$ due to penguin contributions in the $B \to \pi^+\pi^-$ decay amplitude.

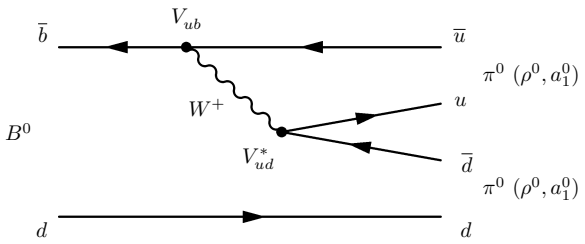

Figure 5.82: Tree-decay diagram for the decay $B^0 \to \pi^0\pi^0$. The same diagram also applies for the decays to $\rho^+\rho^-$, $\rho^\pm\pi^\mp$ and $a_1^\pm\pi^\mp$ discussed in this section.

Adopting a phase convention such that $\phi_T = 0$, the two triangles have one side in common and, as illustrated in Figure 5.81, the phase shift $2\Delta\alpha$ is given by the angle between the two sides corresponding to the amplitudes A_{+-} and $\overline{A}_{+-}$. The construction of the two triangles and the determination of the CKM angle α requires measurements of the three branching fractions BF $(B^0 \to \pi^+\pi^-)$, BF $(B^0 \to \pi^0\pi^0)$ and BF $(B^\pm \to \pi^\pm\pi^0)$ as well as the *CP* violation parameters $S_{\pi^+\pi^-}$, $C_{\pi^+\pi^-}$ and the time-integrated direct *CP* asymmetry $C_{\pi^0\pi^0}$. Measurements of time-dependent *CP* asymmetries in the decay mode $B^0 \to \pi^0\pi^0$ are currently not feasible due to large uncertainties in the reconstruction of the decay vertex position of the decaying B meson. The isospin analysis allows to determine the angle α up to an eight-fold ambiguity. A two-fold ambiguity stems from the symmetry of the sine function describing the time-dependent *CP* asymmetry, while different relative orientations of the isospin triangles, flipping one triangle horizontally or vertically with respect to the other, lead to a four-fold ambiguity in the determination of $\Delta\alpha$. The experimentally most challenging measurement is that of the $\pi^0\pi^0$ final state due to the lower branching fraction for this decay as well as the lower reconstruction efficiency for neutral pions compared to charged pions. As illustrated in Figure 5.82, the tree amplitude for the decay $B^0 \to \pi^0\pi^0$ is colour suppressed and this decay can therefore be expected to be dominated by the penguin amplitude.

Measurements of the CKM angle α can also be performed in analyses of time-dependent *CP* asymmetries in other $\overline{b} \to \overline{u}u\overline{d}$ transitions. Decays to $\rho^+\rho^-$, $\rho^0\rho^0$ and $\rho^\pm\rho^0$, with each of the two ρ mesons decaying to a pair of pions, can be treated in a similar manner as the decays to the $\pi\pi$ final states discussed above. The ρ meson being a spin-1 vector particle, the $\rho\rho$ pair can be produced with relative angular momenta $L = 0, 1$ or 2 and the final state is in principle not a *CP* eigenstate. Angular analyses by BaBar [384] and Belle [385] have, however, shown that the $\rho\rho$ pairs are in fact produced to almost 100% in the longitudinally polarized state, which is *CP* even. The small *CP* odd contribution from *CP* odd polarization states is neglected in current analyses of the *CP* asymmetry and a systematic uncertainty is assigned

to account for this approximation. The branching fraction for the penguin-dominated decay $B^0 \to \rho^0\rho^0$ is found to be small compared to that for the decay $B^0 \to \rho^+\rho^-$, indicating that the contribution from penguin amplitudes in $B^0 \to \rho^+\rho^-$ decays and the resulting phase shift $\Delta\alpha$ can be expected to be small.

As proposed in Ref. [386], an unambiguous and theoretically clean determination of the CKM angle α can be obtained through a time-dependent Dalitz-plot analysis in decays of neutral B mesons to $\rho^+\pi^-$, $\rho^-\pi^+$ and $\rho^0\pi^0$. With the ρ meson decaying to a pair of pions, six interfering amplitudes lead to the final state $\pi^+\pi^-\pi^0$, namely

$$\begin{array}{rcrcl} A_+ & \equiv & A\,(B^0 \to \rho^+\pi^-) & \equiv & e^{-i\alpha}\,T_+ \,+\, P_+ \\ A_- & \equiv & A\,(B^0 \to \rho^-\pi^+) & \equiv & e^{-i\alpha}\,T_- \,+\, P_- \\ A_0 & \equiv & A\,(B^0 \to \rho^0\pi^0) & \equiv & e^{-i\alpha}\,T_0 \,+\, P_0 \end{array}$$

and

$$\begin{array}{rcrcl} \overline{A}_+ & \equiv & \frac{q}{p}\,A\,(B^0 \to \rho^+\pi^-) & \equiv & e^{+i\alpha}\,T_+ \,+\, P_+ \\ \overline{A}_- & \equiv & \frac{q}{p}\,A\,(B^0 \to \rho^-\pi^+) & \equiv & e^{+i\alpha}\,T_- \,+\, P_- \\ \overline{A}_0 & \equiv & \frac{q}{p}\,A\,(\overline{B}^0 \to \rho^0\pi^0) & \equiv & e^{+i\alpha}\,T_0 \,+\, P_0 \quad , \end{array}$$

where T and P indicate the contribution from tree and penguin amplitudes and q/p is the CP phase of the $B^0 - \overline{B}^0$ mixing amplitude. Isospin relations in this decay show that

$$P_0 \;=\; -\frac{1}{2}\,(P_+ + P_-)$$

and the angle α can be extracted from the ratio of decay amplitudes

$$\frac{\overline{A}_+ \,+\, \overline{A}_- \,+\, 2\overline{A}_0}{A_+ \,+\, A_- \,+\, A_0} \;=\; e^{2i\alpha}\,.$$

The extraction of the magnitudes and relative phases between these amplitudes relies on a decay-time dependent measurement of interference patterns in the $\pi^+\pi^-\pi^0$ Dalitz-plot. Such interference patterns can occur in regions of phase space in which contributions from different $B^0 \to \rho\pi$ decay modes overlap. That such overlap regions do exist is illustrated in the decay-time integrated Dalitz plot shown in Figure 5.83, obtained from simulated samples of events.

Finally, measurements of neutral B-meson decays to $a_1^\pm\pi^\mp$, with the $a_1^\pm$ meson decaying to $\rho\pi$ followed by $\rho \to \pi\pi$, permit to extract an effective weak phase $\alpha_{\rm eff} = \alpha + \Delta\alpha$. Upper limits on the possible value of $\Delta\alpha$ can be derived assuming SU(3) flavour symmetry and relating decay rates measured in $B^0 \to a_1^\pm\pi^\mp$ to CP averaged decay rates measured in the SU(3)-related processes $B^+ \to a_1^+K^0$ and $B^+ \to K_1^0(1270, 1400)\pi^+$ or $B^0 \to a_1^-K^+$ and $B^0 \to K_1^+(1270, 1400)\pi^-$.

The extraction of the angle α from combined measurements of branching fractions and CP violating observables in $B \to \pi\pi$, $B \to \rho\rho$, $B \to \rho\pi$ and $B \to a_1\pi$ decays is the prerogative of the asymmetric B factories and measurements in all these decay modes have been performed at both BaBar and Belle. Precise measurements at hadron colliders do not seem feasible due to the difficulty in reconstructing clean event samples in the decay modes to final states including neutral pions that are required in all approaches. The LHCb collaboration has published a measurement of the CP violating observables in the decay $B^0 \to \pi^+\pi^-$. The interest, here, is the combination with similar measurements in the decay mode $B_s^0 \to K^+K^-$, which should allow to derive constraints on the CKM angle γ assuming SU(3) flavour symmetry.

Constraints on the CKM phase α have been derived in individual BaBar and Belle analyses and in a combined analysis, which the joint BaBar and Belle collaborations have published recently. Constraints combining all available measurements have also been derived by the CKMfitter group and the UTFit group. In the remainder of this section, measurements performed in the decay modes $B^0 \to \pi^+\pi^-$, $B \to \rho\pi$ and $B \to \rho\rho$ will be described in turn and then the resulting constraints on the CKM phase α will be discussed.

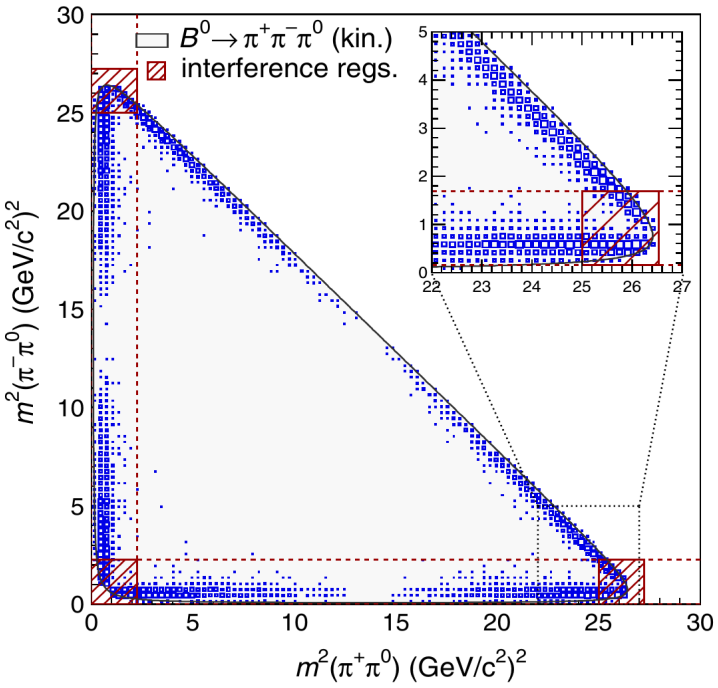

Figure 5.83: Dalitz plot for a sample of simulated $B^0 \to \pi^+\pi^-\pi^0$ events. Decays via the $\rho^+\pi^-$, $\rho^-\pi^+$ and $\rho^0\pi^0$ intermediate states populate the regions close to the left edge, the lower edge and the upper right edge of the kinematically allowed region, respectively. The insert shows a close-up of one of the corners of the Dalitz plot, where two amplitudes interfere. The simulation did not include detection and reconstruction effects and the amplitudes were set to $A_+ = A_- = A_0 = 1$ (from [387,388]).

5.4.1 Measurements in $B \to \pi\pi$ decays

Several measurements of branching fractions and *CP* violating observables in $B^0 \to \pi^+\pi^-$, $B^0 \to \pi^0\pi^0$ and $B^\pm \to \pi^\pm\pi^0$ decays have been performed by the BaBar [389–395] and Belle [396–400] collaborations. The LHCb collaboration published a measurement [401] of *CP* asymmetries in the decay $B^0 \to \pi^+\pi^-$.

Measurements in the decay mode $B^0 \to \pi^+\pi^-$

The final BaBar [395] and Belle [400] measurements in the decay mode $B^0 \to \pi^+\pi^-$ were based on their full data samples, corresponding to 467 and 772 million produced $B\overline{B}$ pairs, respectively. Both analyses followed a similar pattern to that employed in the measurements of $\sin(2\beta)$ in decays $B \to J/\psi K^0_S$ described in Section 5.3. One B meson, $B_{\rm rec}$, was fully reconstructed in the signal decay. The remaining reconstructed particles in the event were used to reconstruct the decay vertex of the opposite-side B meson, $B_{\rm tag}$, and to infer its flavour of the time of its decay and thereby tag the initial flavour of the $B_{\rm rec}$ candidate as a B^0 or $\overline{B}^0$. The decay time difference, Δt, was estimated from the distance between the reconstructed $B_{\rm rec}$ and $B_{\rm tag}$ decay vertices along the beam axis and the known boost of the $\Upsilon(4S)$ rest frame in the laboratory system. In both analyses, $B^0 \to \pi^+\pi^-$ signal candidates were formed by combining two well-reconstructed tracks fulfilling loose requirements on their impact parameters with respect to the nominal e^-e^+ interaction region. An initial event selection was based on the beam-energy substituted invariant mass, $m_{\rm ES}$, and the energy imbalance, ΔE, of the signal candidate as defined in Section 4.1, and on different combinations of event shape variables. The *CP* violation parameters, $S_{\pi^+\pi^-}$ and $C_{\pi^+\pi^-}$, were then determined from a multi-dimensional maximum likelihood fit to $m_{\rm ES}$, ΔE, a combined event-shape variable, particle identification information, tagging information and the measured decay-time difference of the selected candidates. Particle identification algorithms as described in Section 4.1.7 were

employed to distinguish between $B_{\rm rec} \to \pi^+\pi^-$, $K^+\pi^-$ and K^+K^- candidates and to suppress backgrounds from $p\pi^-$ and pK^- combinations. The decay $B^0 \to K^+\pi^-$ was treated as a source of background in the Belle analysis, while a measurement of the direct *CP* violating asymmetry in this decay mode was included in the BaBar analysis.

The same flavour-tagging algorithms, discussed in Section 4.1.10, as in the latest measurements of $\sin(2\beta)$ were applied to derive a tagging decision, q, for each selected event and to assign the event to one of seven mutually exclusive tagging categories, k, and the corresponding average mistag probability, ω_k, and difference between the mistag probabilities for B^0 and $\overline{B}^0$ candidates, $\Delta\omega_k$, were assigned to the event in the further analysis. The average values of ω_k and $\Delta\omega_k$ for each tagging category were determined from samples of self-tagging flavour-specific decays of B mesons.

The decay-time resolution for signal candidates was modelled using the same functional forms as in the latest measurements of $\sin(2\beta)$, i.e. the sum of three Gaussian functions in the case of the BaBar analysis and the function described in Ref. [250] in the case of the Belle analysis.

The decay-time distribution for the signal component was modelled in both analyses as

$$\begin{aligned} g_q(\Delta t) \;=\; & \frac{e^{-|\Delta t|/\tau_B}}{4\tau_B} \times \{\, (1 - q\,\Delta\omega_k) \,+ \\ & q\,(1-2\omega_k) \times \left[\, S_{\pi^+\pi^-} \sin(\Delta m_d\,\Delta t) \,-\, C_{\pi^+\pi^-} \cos(\Delta m_d\,\Delta t) \,\right] \} \;, \end{aligned}$$

convolved with the respective decay-time resolution function, where $q = +1$ for events tagged as $\overline{B}^0$ candidates and $q = -1$ for events tagged as B^0 candidates. The values of the B^0 lifetime, τ_B, and of the $B^0 - \overline{B}^0$ oscillation frequency, Δm_d, were fixed to their world-averages at the time of the measurements.

In addition to the signal component, the fit function employed in the Belle analysis contained terms for six sources of background, namely peaking backgrounds from neutral B-meson decays to $K^+\pi^-$, K^+K^-, $K^-\pi^+$ and K^+K^-, backgrounds from other charmless decays of neutral and charged B mesons, and continuum background from non-$B\overline{B}$ events. The fit function employed in the BaBar analysis included a total of 28 contributions, distinguishing between different combinations of final state particles and the available particle identification information for each of the two tracks.

Measured distributions for some of the discriminating variables as obtained in the Belle analysis are shown in Figure 5.84 together with projections of the fit results. The measured Δt distributions and the resulting decay-time dependent *CP* asymmetries for the $B^0 \to \pi^+\pi^-$ signal component from both analyses are shown in Figure 5.85. The results of the two analyses,

$$\begin{aligned} S_{\pi^+\pi^-} &= -0.64 \,\pm\, 0.08\,(\text{stat}) \,\pm\, 0.03\,(\text{syst}) \\ C_{\pi^+\pi^-} &= -0.33 \,\pm\, 0.06\,(\text{stat}) \,\pm\, 0.03\,(\text{syst}) \end{aligned}$$

from Belle and

$$\begin{aligned} S_{\pi^+\pi^-} &= -0.68 \,\pm\, 0.10\,(\text{stat}) \,\pm\, 0.03\,(\text{syst}) \\ C_{\pi^+\pi^-} &= -0.25 \,\pm\, 0.08\,(\text{stat}) \,\pm\, 0.02\,(\text{syst}) \end{aligned}$$

from BaBar, are in good agreement with each other. The precision of the measurements is in both cases limited by the statistical uncertainty. The quoted systematic uncertainties on $S_{\pi^+\pi^-}$ were dominated by effects related to the parametrization of the decay-time resolution, the reconstruction of the $B_{\rm rec}$ and $B_{\rm tag}$ decay vertices, and the understanding of the flavour tagging performance. The quoted systematic uncertainty on $C_{\pi^+\pi^-}$ was dominated by possible *CP* violating effects in $B_{\rm tag}$ decays.

The published LHCb analysis was based on the 2011 data set, corresponding to an integrated luminosity of 1.0 fb^{-1} collected at a pp collision energy of 7 TeV. The selection of

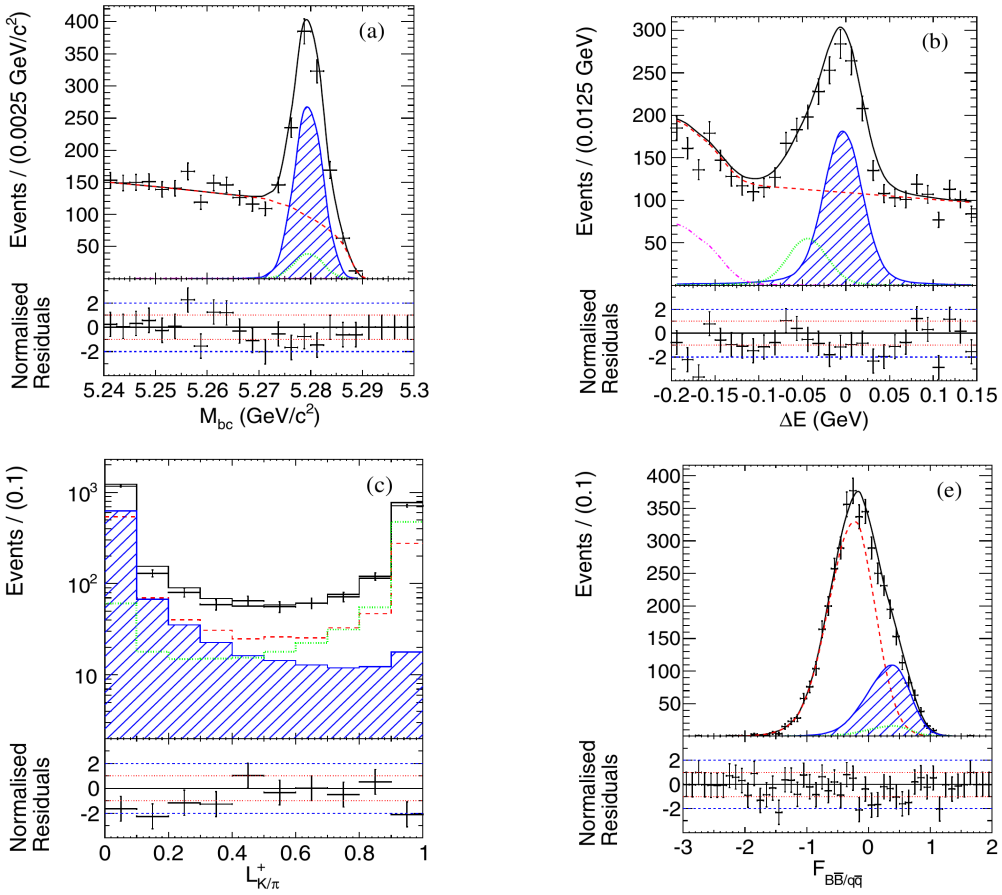

Figure 5.84: Distributions of (top left) the beam-energy substituted invariant mass, (top right) the energy imbalance, (bottom left) the combined kaon-pion identification variable and (bottom right) the combined event-shape variable for selected candidates from the Belle analysis of *CP* violating asymmetries in the decay $B^0 \to \pi^+\pi^-$. The results of the maximum likelihood fit to the data are superimposed, where blue hatched areas indicate the $B^0 \to \pi^+\pi^-$ signal component, green dotted curves indicate the $B \to K^+\pi^-$ component, purple dash-dotted curves indicate the component attributed to other $B\overline{B}$ backgrounds and dashed red curves indicate the sum of all background components (from [400]).

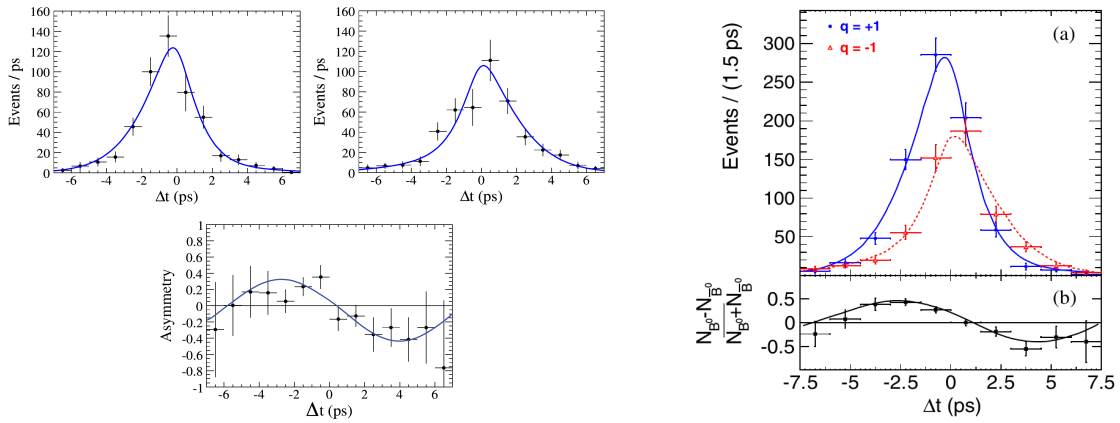

Figure 5.85: Decay time distributions for signal candidates tagged as B^0 and $\overline{B}^0$ decays, and the resulting decay-time dependent *CP* asymmetry from the latest (left, from [367]) BaBar and (right, from [368]) Belle analyses of *CP* violating observables in the decay $B^0 \to \pi^+\pi^-$.

signal candidates was based on the transverse momenta of the two final state particles and their invariant mass, the quality of the track reconstruction, the impact parameter of the two tracks with respect to the reconstructed *pp* collision vertex and their distance of closest approach to each other as well as on the invariant mass of the B candidate, its decay time, its transverse momentum and its impact parameter with respect to the *pp* collision vertex. Particle identification information was then applied to split the sample of selected candidates into mutually exclusive categories corresponding to $B^0 \to \pi^+\pi^-$, $B^0 \to K^+\pi^-$, and $B_s^0 \to K^+K^-$. Sources of backgrounds considered in the $B^0 \to \pi^+\pi^-$ sample were other two-body b hadron decays with a final-state particle that was misidentified as a pion, random combinations of two oppositely charged tracks that accidentally fulfill the selection criteria, and pairs of oppositely charged tracks from partially reconstructed 3-body B-meson decays. The same combination of opposite-side flavour tagging algorithms [202], described in Section 4.4, as in the first LHCb measurement of $\sin(2\beta)$ in $B^0 \to J/\psi K_S^0$ decays was employed to infer the initial flavour of the $B_{\rm rec}$ candidate. The algorithm returned a tagging decision and an estimate, $\eta_{\rm tag}$, of the mistag probability. Events were split into five mutually exclusive intervals of $\eta_{\rm tag}$. For each of these intervals, the average mistag fractions for B^0 candidates, ω_k, and for $\overline{B}^0$ candidates, $\overline{\omega}_k$, were determined from samples of flavour-specific decays $B^0 \to K^+\pi^-$ and $B_s^0 \to K^-\pi^+$. The same control samples were employed to estimate the expected $B\overline{B}$ production asymmetry in *pp* collisions. The *CP* violating parameters, $C_{\pi^+\pi^-}$ and $S_{\pi^+\pi^-}$, were determined from a maximum likelihood fit to the measured invariant-mass and decay-time distributions of the selected candidates. In this fit, the decay-time resolution was modelled by a single Gaussian function with a width of 50 fs, as derived from large samples of charmonium decays to $\mu^+\mu^-$ pairs. The acceptance as a function of the decay-time was modelled by an empirical function derived from samples of simulated signal events. The B^0 lifetime was a free parameter in the fit, whereas the value of Δm_d was fixed to its world average at the time of the measurement. The parameters describing the tagging performance and the $B\overline{B}$ production asymmetry were constrained in the fit to the values obtained from the calibration sample. The measured invariant-mass distribution, the decay-time distribution and the resulting time-dependent raw *CP* asymmetry are shown in Figure 5.86 together with the results of the fit.

The results of the analysis,

$$\begin{aligned} S_{\pi^+\pi^-} &= -0.71 \pm 0.13\,(\text{stat}) \pm 0.02\,(\text{syst}) \\ C_{\pi^+\pi^-} &= -0.38 \pm 0.15\,(\text{stat}) \pm 0.02\,(\text{syst}) \ , \end{aligned}$$

are compatible with the corresponding measurements from BaBar and Belle. While the precision of the LHCb measurement is not yet competitive in terms of its statistical uncertainty, the systematic uncertainties are of comparable size to those quoted in the BaBar and Belle analyses. The quoted systematic uncertainties on both $S_{\pi^+\pi^-}$ and $C_{\pi^+\pi^-}$ are dominated by effects related to the determination of the flavour tagging performance, to the modelling of the decay-time dependence for combinatorial background and to the uncertainty on the world-average value of Δm_d. Effects related to the decay-time resolution are small, since the uncertainty on the measurement of decay-times is small in LHCb compared to the $B^0 - \overline{B}^0$ oscillation period.

A comparison of the three results in the $(S_{\pi^+\pi^-}, C_{\pi^+\pi^-})$ plane is shown in Figure 5.87.

Measurements in the decay modes $B^0 \to \pi^0\pi^0$ and $B^+ \to \pi^+\pi^0$

As discussed in the introduction to this section, measurements of $S_{\pi^+\pi^-}$ and $C_{\pi^+\pi^-}$ need to be complemented by measurements of the branching fractions for the decays $B^0 \to \pi^0\pi^0$ and $B^+ \to \pi^+\pi^0$ and of the time-integrated direct *CP* asymmetry, $C_{\pi^0\pi^0}$, in the decay $B^0 \to \pi^0\pi^0$ in order to extract constraints on the CKM angle α. Measurements of the branching fraction for the decay $B^0 \to \pi^+\pi^-$ have been performed both at BaBar [392] and at Belle [399]. A BaBar measurement of the $B^0 \to \pi^0\pi^0$ branching fraction and of $C_{\pi^0\pi^0}$, based on their full

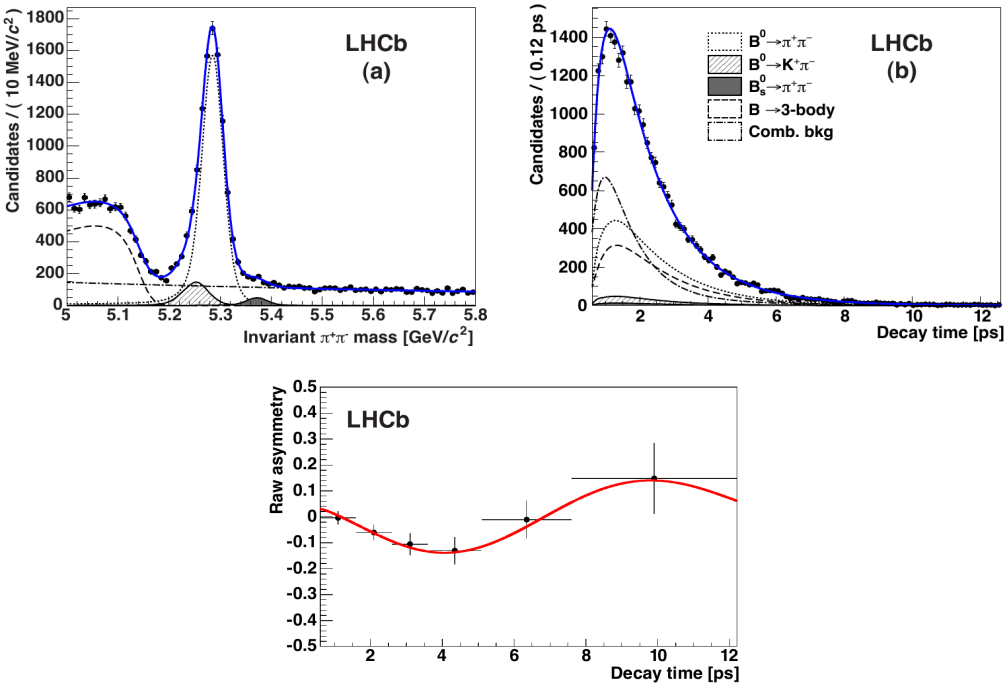

Figure 5.86: Distributions of the (top left) $\pi^+\pi^-$ invariant mass and (top right) decay time for selected candidates and (bottom) the resulting decay-time dependent *CP* asymmetry from the first LHCb analysis of *CP* violating observables in the decay $B^0\to\pi^+\pi^-$. The results of the maximum-likelihood fit to the data are superimposed, indicating in the upper panels different signal and background components as described in the plot legend (from [401])

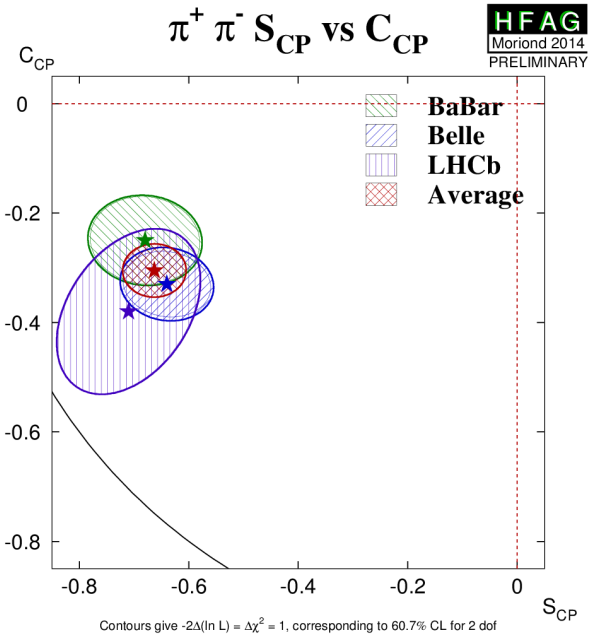

Figure 5.87: Comparison of the BaBar, Belle and LHCb measurements of the *CP* violating parameters $S_{\pi^+\pi^-}$ and $C_{\pi^+\pi^-}$ in the decay $B^0\to\pi^+\pi^-$, and their average as prepared by the Heavy Flavour Averaging Group taking into account measurements available through summer 2014 (from [2]).

data set, was published in conjunction with their measurement of $S_{\pi^+\pi^-}$ and $C_{\pi^+\pi^-}$ described above [395]. The Belle collaboration published a measurement [396] based on a data set corresponding to 275 million produced $B\overline{B}$ pairs. Both analyses used π^0 candidates formed by two isolated photon candidates, defined as clusters in the electromagnetic calorimeter that fufilled requirements on the deposited energy and the shower shape and that were isolated from any reconstructed tracks. A minimum opening angle between the momentum vectors of the photon candidates in the π^0 rest frame and the momentum vector of the π^0 candidate in the laboratory system was required to suppress random combinations of photon candidates. In the BaBar analysis, one of the two π^0 candidates was also allowed to be reconstructed as a single, merged cluster compatible with overlapping energy depositions from two photons, or as a e^+e^- pair compatible with originating from a photon conversion in the material of the detector. The selection of $B^0 \to \pi^0\pi^0$ candidates relied on the beam-energy substituted invariant mass, $m_{\rm ES}$, and the energy imbalance, ΔE, of the $B_{\rm rec}$ candidate and on combinations of event-shape variables. The signal component in the selected event sample was extracted in the Belle analysis by a two-dimensional maximum likelihood fit to the measured distributions in $m_{\rm ES}$ and ΔE and in the BaBar analysis by a three-dimensional maximum likelihood fit to the distributions of $m_{\rm ES}$, ΔE and a combined event-shape variable. The results of the fits in terms of the $m_{\rm ES}$ and ΔE distributions are shown in Figure 5.88 for the BaBar analysis and in Figure 5.89 for the Belle analysis. The likelihood function contained contributions for the $B^0 \to \pi^0\pi^0$ signal component, for backgrounds from partially reconstructed decays $B^+ \to \rho^+\pi^0$ with $\rho^+ \to \pi^+\pi^0$ and $B^0 \to K^0_S\pi^0$ with $K^0_S \to \pi^0\pi^0$, and for continuum background from non-$B\overline{B}$ events. The standard BaBar and Belle flavour tagging algorithms were applied to derive the initial flavour of the signal B meson candidate and to sort event candidates into categories according to the tagging quality. The time-integrated direct *CP* asymmetry $C_{\pi^0\pi^0}$ was extracted from a fit to the event yields in each of the tagging categories as

$$n_k \;=\; \frac{1}{2}\, f_k\, N_{\pi^0\pi^0}\, \left[1 - q\,(1-2\chi)(1-2\omega_k)\, C_{\pi^0\pi^0}\right] \;,$$

where f_k is the fraction of candidates in tagging category k, $N_{\pi^0\pi^0}$ is the total number of signal candidates and χ is the time-integrated $B^0-\overline{B}^0$ mixing probability, which was fixed in the fit to its world-average value at the time of the measurement. The precision of the measurements of $C_{\pi^0\pi^0}$ is limited by the statistical uncertainty. The leading systematic uncertainies were found in the BaBar measurement to be due to the understanding of the flavour tagging performance and to effects of peaking backgrounds in the selected signal sample.

The constraints on the CKM angle α that were derived from isospin analyses based on these measurements will be discussed in the final part of this section.

5.4.2 Measurements in $B \to \rho\rho$ decays

Both the BaBar [384,402–406] and Belle [385,407–409] collaborations performed measurements of branching fractions, polarization fractions and *CP* asymmetries in decays $B^0 \to \rho^+\rho^-$ [384, 385, 402, 403, 407], $B^0 \to \rho^0\rho^0$ [404, 405, 408] and $B^\pm \to \rho^\pm\rho^0$ [406, 409] and combined these measurements in isospin analyses to derive constraints on the angle α.

The latest BaBar [384] and Belle [407] measurements of the *CP* violating observables in the decay $B^0 \to \rho^+\rho^-$ were based on data sets corresponding to 384 and 535 million produced $B\overline{B}$ pairs, respectively. The BaBar analysis included a measurement of the branching fraction and the fraction of longitudinal polarization in this decay, while the Belle collaboration had measured these in an earlier analysis [385] to be

$$\mathrm{BF}\,(B^0 \to \rho^+\rho^-) \;=\; \Big(22.8 \,\pm\, 3.8\,(\mathrm{stat})\, {}^{+\,2.3}_{-\,2.6}\,(\mathrm{syst})\Big) \times 10^{-6}$$

and

$$f_L \;=\; 0.941\, {}^{+\,0.034}_{-\,0.040}\,(\mathrm{stat}) \,\pm\, 0.030\,(\mathrm{syst}) \;,$$

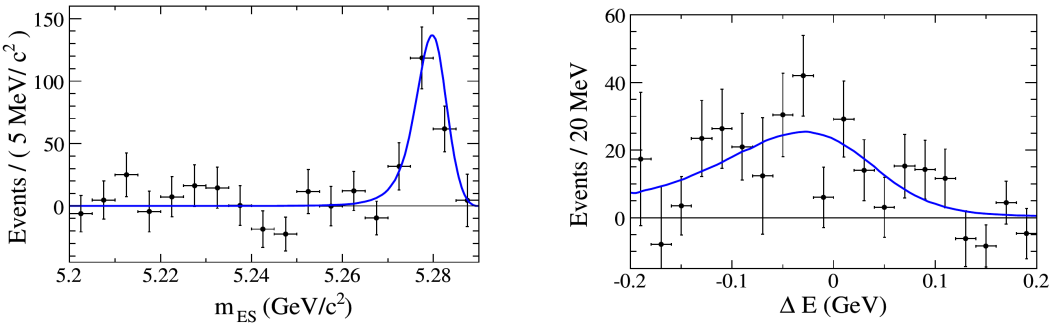

Figure 5.88: Distributions of (left) the beam-energy substituted invariant mass, $m_{\rm ES}$, and (right) the energy imbalance, ΔE, for selected $B^0 \to \pi^0\pi^0$ candidates from the BaBar measurement of the branching fraction and time-integrated CP violating asymmetry in this decay mode (from [395]).

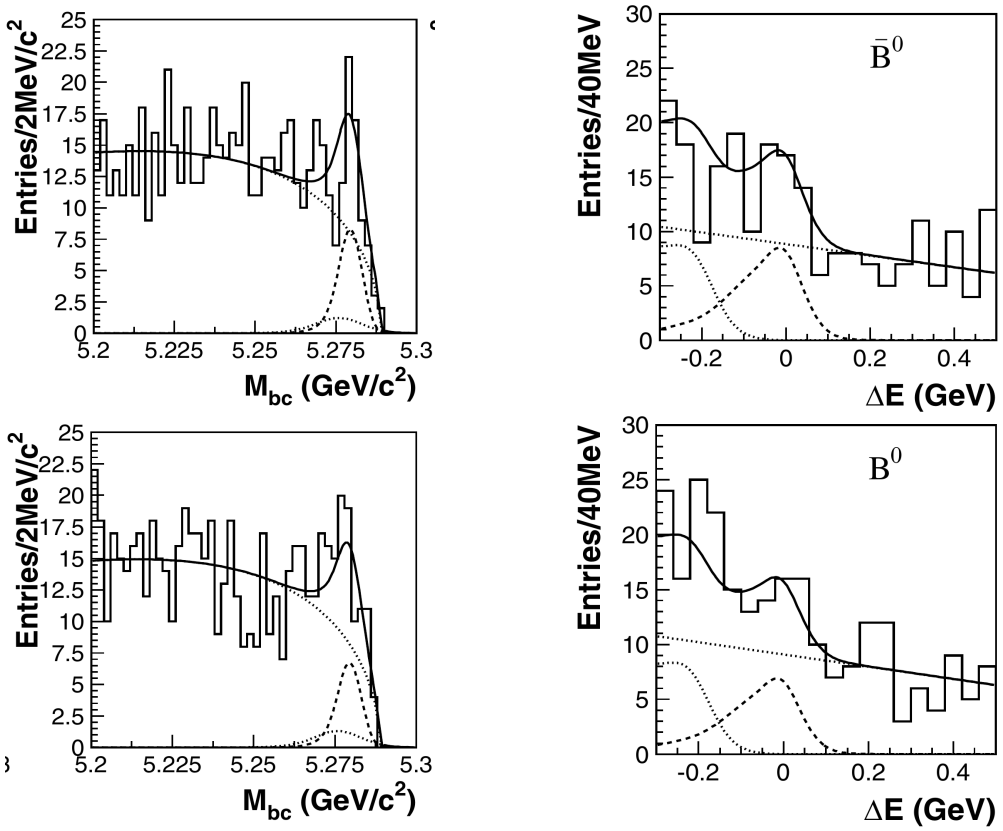

Figure 5.89: Distributions of (left) the beam-energy substituted invariant mass, denoted as $M_{\rm bc}$, and (right) the energy imbalance, ΔE, for selected candidates tagged as (top) initial $\overline{B}^0 \to \pi^0\pi^0$ and (bottom) $B^0 \to \pi^0\pi^0$, from the Belle measurement of the branching fraction and time-integrated CP violating asymmetry in this decay mode. The solid line shows the result of the maximum-likelihood fit to the data, the dashed line indicates the signal component, the dotted line the component assigned to continuum background and the dash-dotted line the $B^+ \to \rho^+\pi^0$ background component (from [396]).

respectively.

Candidate $\rho^\pm$ mesons were reconstructed in their decays to $\pi^\pm\pi^0$ with $\pi^0 \to \gamma\gamma$. Two oppositely charged ρ candidates were combined to form $B_{\rm rec}$ candidates. The selection of signal candidates was based on the $\pi^\pm\pi^0$ invariant masses and the cosine of the helicity angles of the two ρ candidates as well as the beam-energy substituted invariant mass, $m_{\rm ES}$, the energy imbalance, ΔE, and combinations of event shape variables, The helicity angles θ, defined in Figure 5.90, provide discrimination against spurious combinations of low-momentum π^0 candidates, which yield values of $\cos\theta$ close to ± 1. The decay vertex of the $B_{\rm rec}$ candidate

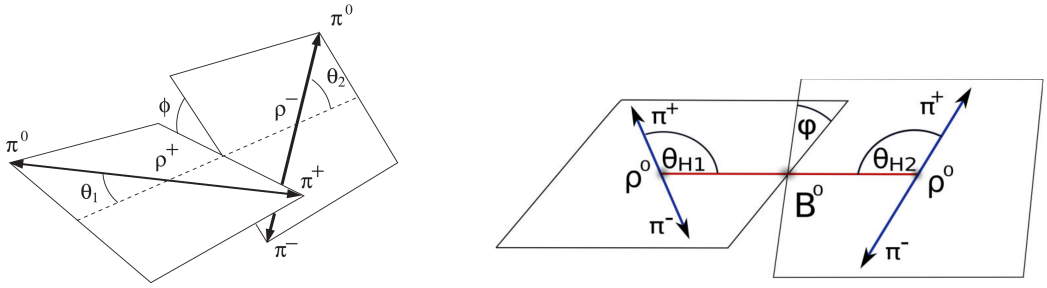

Figure 5.90: Definition of the helicity angles, θ, of the ρ mesons in the decays (left) $B^0 \to \rho^+\rho^- \to \pi^+\pi^0\pi^-\pi^0$ and (right) $B^0 \to \rho^0\rho^0 \to \pi^+\pi^-\pi^+\pi^-$ (from [384, 408]).

was reconstructed from the tracks of the two charged final-state pions and the decay vertex of the opposite-side B meson, $B_{\rm tag}$, was reconstructed from a fit to the remaining tracks in the event. The decay-time difference, Δt, was calculated in the usual manner from the distance between the two decay vertices along the beam axis and the known boost of the $\Upsilon(4S)$ rest frame in the laboratory system. The decay-time resolution was parametrized as usual by a triple-Gaussian function in the BaBar analysis and by the function described in Ref. [250] in the Belle analysis. The BaBar publication quotes a root mean square resolution of 1.1 ps on Δt. The standard BaBar and Belle flavour tagging algorithms were applied to derive the initial flavour of the $B_{\rm rec}$ candidate and to sort candidates into categories according to the tagging quality.

In the BaBar analysis, the longitudinal polarization fraction, f_L, and the *CP* violating parameters for the longitudinally polarized decay amplitude, S_L and C_L, were extracted from a maximum likelihood fit to the measured distributions of Δt and the set of discriminating variables listed above. The corresponding distributions are shown in Figure 5.91 together with projections of the fit results. Possible correlations between the variables were neglected in the fit and a systematic uncertainty was assigned for this approximation. The time-dependence of the longitudinally polarized signal component was described by

$$\begin{aligned} g_q(\Delta t) \;=\; & \frac{e^{-|\Delta t|\tau_{B^0}}}{4\tau_{B^0}} \times \{(1 - q\,\Delta\omega_k) \; + \\ & q\,(1-2\omega_k) \times [S_L \sin(\Delta m_d\,\Delta t) \; - \; C_L \cos(\Delta m_d\,\Delta t)]\} \;\; , \end{aligned}$$

convolved with the decay-time resolution function. The likelihood function included a term of the same functional form for the small transverse polarized signal component, but the corresponding *CP* violating parameters, S_T and C_T were set to zero in the fit, effectively reducing the time dependence for the transverse polarized amplitudes to a simple exponential function. A systematic uncertainty was assigned for this approximation.

In the Belle analysis, the fit was performed in two steps. In a first step, signal and background yields were estimated from a maximum likelihood fit to $m_{\rm ES}$, ΔE and a combined event-shape variable. The corresponding distributions with the results of this fit are shown in Figure 5.92. In a second step, the *CP* violation parameters were extracted from a one-dimensional fit to the measured Δt distribution, with signal and background fractions fixed to the values obtained in the first step. The transverse polarized amplitude was ignored in the Belle analysis and a systematic uncertainty was assigned for this approximation.

Simulation studies showed that about half the selected signal candidates in the BaBar analysis and about one third of the selected signal candidates in the Belle analysis were in fact reconstructed with at least one wrongly assigned pion, i.e. one of the four pions from the signal decay was replaced in the reconstruction by a random pion from the remainder of the event. This does not lead to a bias on the measurement as long as the two charged pions are correctly reconstructed, but if one or both charged pions are wrongly chosen, the position of

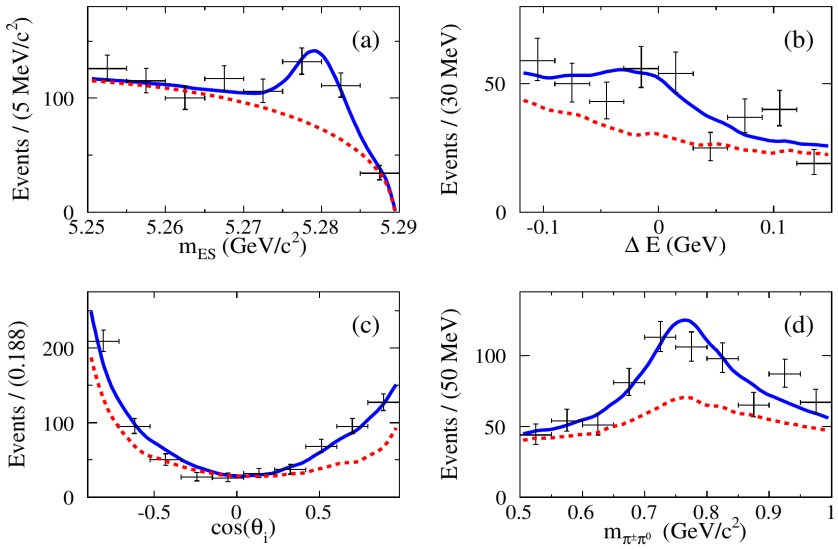

Figure 5.91: Distributions of the (top left) beam-energy substituted invariant mass, (top right) energy imbalance, (bottom left) ρ helicity angle and (bottom right) $\pi^+\pi^-$ invariant mass for selected $B^0 \to \rho^+\rho^-$ candidates in the best flavour-tagging category from the BaBar analysis of *CP* violating observables in this decay. The results of the maximum likelihood fit are superimposed, where the red dashed line indicates the background component (from [384]).

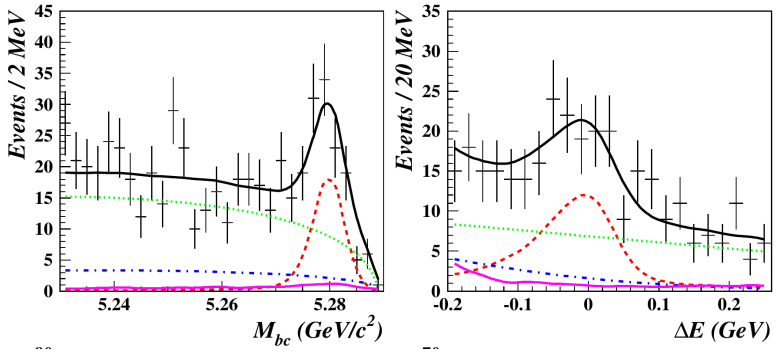

Figure 5.92: Distributions of the beam-energy substituted invariant mass, denoted here as $M_{\rm bc}$, and the energy imbalance, ΔE, for selected $B^0 \to \rho^+\rho^-$ candidates in the best flavour-tagging category from the Belle analysis of *CP* violating observables in this decay. The results of the maximum likelihood fit are superimposed, where the red dashed line indicates the combined $\rho^+\rho^-$ and $\rho\pi^+\pi^-$ component, the green dotted line indicates the component assigned to continuum background, and the blue dot-dashed and magenta full lines indicate backgrounds from B-meson decays to charmed and charmless background, respectively (from [407]).

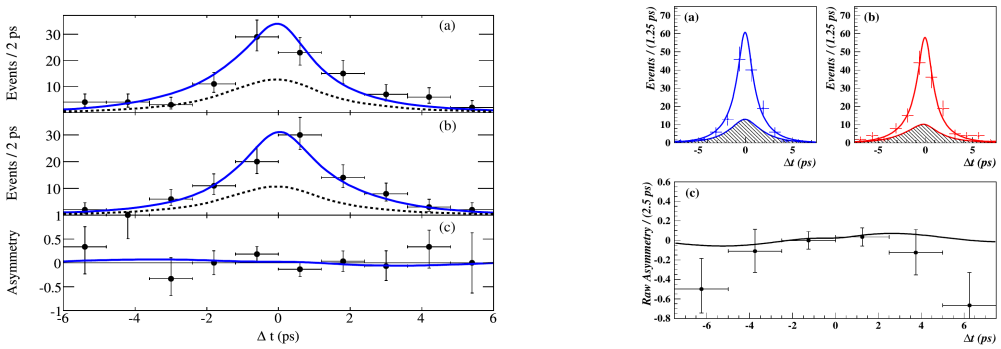

Figure 5.93: Distribution of the decay time differences for selected candidates tagged as B^0 respectively as $\overline{B}^0$ and the resulting decay-time dependent *CP* asymmetry from (left) the BaBar analysis and (right) the Belle analysis of *CP* violating observables in the decay $B^0 \to \rho^+\rho^-$ (from [384, 407]).

the $B_{\rm rec}$ decay vertex and therefore the decay time difference Δt will be wrongly reconstructed. This class of events was dubbed self-cross-feed. Its time dependence was described in the Belle analysis by a simple exponential function with an effective lifetime determined from samples of simulated events. In the BaBar analysis, it was described by a similar functional form as the signal component, but with separate parameters for the *CP* violating parameters S and C.

In addition to the terms for correctly reconstructed signal and for self-cross-feed, the likelihood functions contained separate terms for B^0 and $B^\pm$ decays to charmed final states, for B^0 and $B^\pm$ decays to charmless final states and for non-$B\overline{B}$ background. The Belle analysis also included a separate term for decays to $\rho\pi\pi$, where one of the two pairs of pions was not produced via a ρ resonance.

The BaBar analysis yielded a branching fraction

$$\mathrm{BF}\,(B^0 \to \rho^+\rho^-) \;=\; \Big(25.5 \,\pm\, 2.1\,(\mathrm{stat})\,{}^{+\,3.6}_{-\,3.9}\,(\mathrm{syst})\Big) \times 10^{-6}$$

compatible with the earlier Belle result and a polarization fraction

$$f_L \;=\; 0.992 \,\pm\, 0.024\,(\mathrm{stat})\,{}^{+\,0.026}_{-\,0.013}\,(\mathrm{syst})\;,$$

confirming the assumption that the $\rho^+\rho^-$ final state is close to 100% longitudinally polarized.

The results of the fits for the decay-time dependent *CP* aymmetry are shown in Figure 5.93. The extracted values for the *CP* violating parameters,

$$\begin{aligned} S_{\rho^+\rho^-} &= 0.19 \,\pm\, 0.30\,(\mathrm{stat}) \,\pm\, 0.08\,(\mathrm{syst}) \\ C_{\rho^+\rho^-} &= -0.16 \,\pm\, 0.21\,(\mathrm{stat}) \,\pm\, 0.08\,(\mathrm{syst}) \end{aligned}$$

from the Belle analysis and

$$\begin{aligned} S_{\rho^+\rho^-,\mathrm{long}} &= -0.17 \,\pm\, 0.20\,(\mathrm{stat})\,{}^{+\,0.05}_{-\,0.06}\,(\mathrm{syst}) \\ C_{\rho^+\rho^-,\mathrm{long}} &= 0.01 \,\pm\, 0.15\,(\mathrm{stat}) \,\pm\, 0.06\,(\mathrm{syst}) \end{aligned}$$

from the BaBar measurement, are compatible within their uncertainties. The precision on all measurements was limited by the statistical uncertainty. In the BaBar analysis, the systematic uncertainty on $S_{\rho^+\rho^-,\mathrm{long}}$ was found to be dominated by effects related to the parametrization of the likelihood function, by the knowledge of branching fractions for background decays of B mesons, and by possible fit biases caused by neglecting correlations between input variables. The systematic uncertainty on $C_{\rho^+\rho^-,\mathrm{long}}$ was found to be dominated by effects related to the parametrization of the likelihood function and by possible *CP* violating effects in the decay of the opposite-side B meson. In the Belle analysis, the systematic uncertainty on $S_{\rho^+\rho^-}$ was found to be dominated by a possible *CP* asymmetry in decays $B \to \rho\pi\pi$, by the possible bias caused by neglecting the amplitude for transverse polarization, and by the knowledge of signal and background fractions. The systematic uncertainty on $C_{\rho^+\rho^-}$ was found to be dominated by these same effects and by possible *CP* violating effects in the decay of the opposite-side B meson.

The BaBar collaboration published a measurement [405] of the branching fraction, the fraction of longitudinal polarization and *CP* violating parameters in the longitudinally polarized component in $B^0 \to \rho^0\rho^0$ decays, based on their full data set corresponding to 465 million produced $B\overline{B}$ pairs. The Belle collaboration performed a measurement [408] of the branching fraction and the fraction of longitudinal polarization based on their final data set, corresponding to 772 million produced $B\overline{B}$ pairs, but did not measure *CP* parameters in this decay mode.

In both analyses, ρ^0 candidates were reconstructed in their decays to two charged pions. The selection of signal candidates was again based on the beam-energy substituted invariant mass, $m_{\rm ES}$, the energy imbalance, ΔE, and combinations of event-shape variables. In the

Belle analysis, appropriate cuts on the invariant masses of various two-pion and three-pion combinations were applied to suppress backgrounds from B-meson decays to charmed final states and to final states containing a K^0_S meson. The branching fraction and the fraction of longitudinal polarization was extracted in the Belle analysis from a maximum likelihood fit to ΔE, a combined event-shape variable, the invariant masses of the two $\pi^+\pi^-$ pairs and the helicity angles of the two ρ^0 candidates, defined in Figure 5.90. The standard Belle flavour tagging algorithm was applied and the fit was performed separately in each of the seven tagging categories, as this was found to improve the suppression of continuum background. The results of the fit are shown in Figure 5.94. In the BaBar analysis, the decay vertex of the $B_{\rm rec}$ candidate was reconstructed from a fit to the four charged final-state pions, the decay vertex of the opposite-side B meson was estimated from a fit to the remaining tracks in the event, and the decay-time difference Δt was estimated in the usual manner from the separation of the two decay vertices along the beam axis and the known boost of the $\Upsilon(4S)$ rest frame in the laboratory system. The standard BaBar flavour tagging algorithm was applied to derive the initial flavour of the $B_{\rm rec}$ candidate and to sort event candidates into tagging categories according to the estimated mistag probability. The branching fraction, the fraction of longitudinal polarization and the *CP* violating parameters were then extracted from a fit to $m_{\rm ES}$, ΔE, a combined event-shape variable, the invariant masses of the two $\pi^+\pi^-$ pairs, the helicity angles of the two ρ^0 candidates, the decay-time difference Δt, and its estimated uncertainty $\sigma_{\Delta t}$. The results of the fit are shown in Figure 5.95 and the resulting time-dependent *CP* asymmetry is shown in Figure 5.96.

The BaBar and Belle analyses found

$$\mathrm{BF}\,(B^0 \to \rho^0\rho^0) \;=\; (0.92 \,\pm\, 0.32\,(\mathrm{stat}) \,\pm\, 0.14\,(\mathrm{syst})) \times 10^{-6}$$

and

$$\mathrm{BF}\,(B^0 \to \rho^0\rho^0) \;=\; (1.02 \,\pm\, 0.30\,(\mathrm{stat}) \,\pm\, 0.15\,(\mathrm{syst})) \times 10^{-6}$$

respectively, which is significantly smaller than the measured branching fraction for the decay $B^0 \to \rho^+\rho^-$. As the decay $B^0 \to \rho^0\rho^0$ is dominated by penguin decay amplitudes, this observation can be employed using isospin symmetry to imply that the contribution from penguin amplitudes should be small also in the decay $B^0 \to \rho^+\rho^-$. The bias on the weak phase α can therefore be expected to be smaller in $B^0 \to \rho^+\rho^-$ than in $B^0 \to \pi^+\pi^-$.

Some tension exists between the measured polarization fractions. The BaBar measurement resulted in

$$f_L(\rho^0\rho^0) \;=\; 0.75\,^{+\,0.11}_{-\,0.14}\,(\mathrm{stat}) \,\pm\, 0.05\,(\mathrm{syst})$$

while the Belle measurement yielded

$$f_L(\rho^0\rho^0) \;=\; 0.21\,^{+\,0.18}_{-\,0.22}\,(\mathrm{stat}) \,\pm\, 0.15\,(\mathrm{syst})\;.$$

The BaBar measurement of the *CP* violating parameters resulted in

$$\begin{aligned} S_{\rho^0\rho^0,\mathrm{long}} &= 0.19 \,\pm\, 0.30\,(\mathrm{stat}) \,\pm\, 0.08\,(\mathrm{syst}) \\ C_{\rho^0\rho^0,\mathrm{long}} &= -0.16 \,\pm\, 0.21\,(\mathrm{stat}) \,\pm\, 0.08\,(\mathrm{syst})\;. \end{aligned}$$

The final ingredients for an isospin analysis in $B^0 \to \rho\rho$ decays are the branching fraction and the fraction of longitudinal polarization in charged B-meson decays $B^\pm \to \rho^\pm\rho^0$. These have been measured by Belle [409] and by BaBar [406] using data samples corresponding to about 85 million and 232 million produced $B\overline{B}$ pairs, respectively.

Constraints on the CKM angle α that have been derived from isospin analyses combining these measurements will be discussed in the final part of this section.

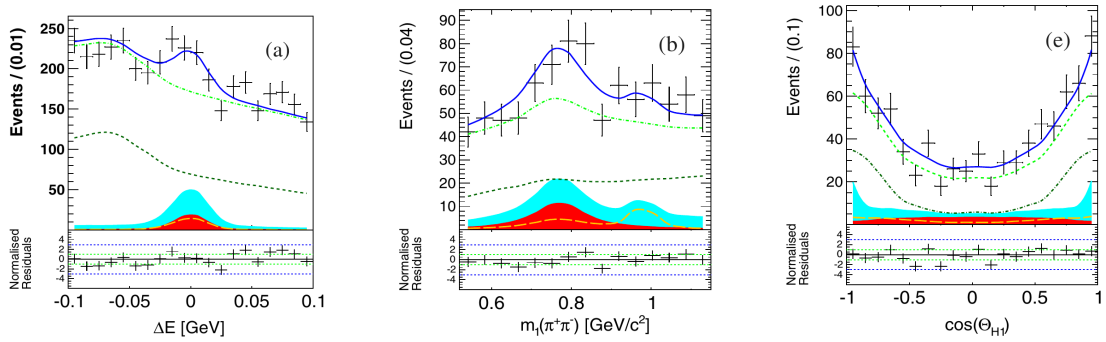

Figure 5.94: Distributions of (left) the energy imbalance, (middle) the two-pion invariant mass and (right) the ρ helicity angle for the selected candidates from the Belle analysis of *CP* violating observables in the decay $B^0 \to \rho^0\rho^0$. The results of the maximum-likelihood fit to the data are superimposed, where the red shaded areas indicate the signal component, the orange long-dashed curve indicates the $B^0 \to f_0\rho^0$ component, the cyan shaded areas indicate the sum of all $B \to \pi^+\pi^-\pi^+\pi^-$ components, the dark green dashed curve shows the non-peaking $B\overline{B}$ background component and the bright green dash-dotted curve shows the sum of all non-peaking background components (from [408]).

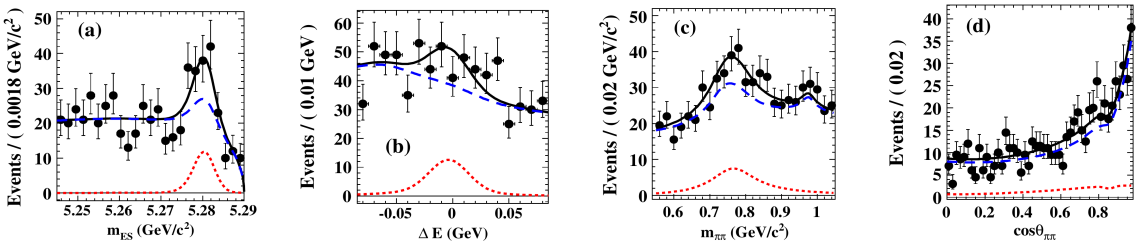

Figure 5.95: Distributions of the (from left to right) beam-energy substituted invariant mass, the energy imbalance, the two-pion invariant mass, and the cosine of ρ helicity angle for the sample of selected candidates from the BaBar analysis of *CP* violating observables in the decay $B^0 \to \rho^0\rho^0$. The results of the maximum-likelihood fit to the data are superimposed, where red dotted curves indicate the signal component and blue dashed curves indicate the sum of all background components (from [405]).

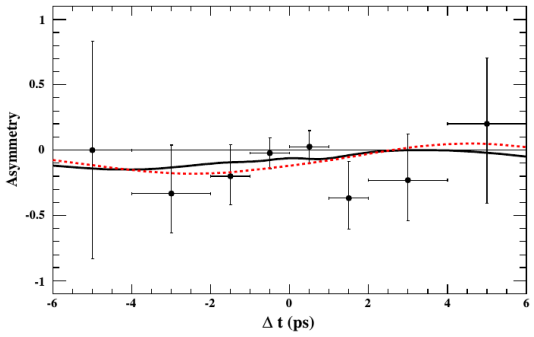

Figure 5.96: Decay-time dependent *CP* asymmetry measured in the BaBar analysis of *CP* violating asymmetries in the decay $B^0 \to \rho^0\rho^0$ (from [405])

5.4.3 Measurements in $B^0 \to (\rho\pi)^0$ decays

Ignoring reconstruction effects, the decay-time dependent decay rate for the decay of neutral B mesons via intermediate states $\rho^\pm\pi^\mp$ and $\rho^0\pi^0$ to the final state $\pi^+\pi^-\pi^0$ is given by

$$f_q(\Delta t) \;=\; \frac{e^{-|\Delta t|\tau_{B^0}}}{4\tau_{B^0}} \times \Big\{ |A|^2 + |\overline{A}|^2$$

$$- q \left(|A|^2 - |\overline{A}|^2 \right) \cos\left(\Delta m_d \Delta t\right) + q\, 2\,\mathrm{Im}\left(\frac{q}{p}\, \overline{A} A^* \right) \sin\left(\Delta m_d \Delta t\right) \Big\}$$

where $q = +1$ for an initial B^0 meson and $q = -1$ for an initial $\overline{B}^0$ meson. The decay amplitudes A and $\overline{A}$ can be parametrized as

$$\begin{aligned} A &= f_+ A_+ + f_- A_- + f_0 A_0 \\ \overline{A} &= f_+ \overline{A}_+ + f_- \overline{A}_- + f_0 \overline{A}_0 \end{aligned}$$

where A_+, A_- and A_0 contain the information on the strong and weak phases of the decays via an intermediate ρ^+, ρ^- or ρ^0 meson and f_+, f_- and f_0 incorporate the corresponding kinematic and dynamic properties of these decays and therefore describe the distribution of the events in the Dalitz plot.

Time-dependent Dalitz-plot analyses of $B^0 \to \pi^+\pi^-\pi^0$ decays were performed both in BaBar [387, 388] and in Belle [410, 411]. The BaBar collaboration published a measurement [388] based on their final data set, corresponding to 471 million produced $B\overline{B}$ pairs, while the latest published Belle measurement [411] was based on a data set corresponding 449 million produced $B\overline{B}$ pairs.

In both analyses, signal candidates were formed by combining two oppositely charged pion candidates with a $\pi^0 \to \gamma\gamma$ candidate. As usual, the selection of signal candidates was based on their beam-energy substituted invariant mass, m_{ES}, and energy imbalance, ΔE, as well as a combination of event-shape variables. In the BaBar analysis, the reconstructed value of ΔE was recalibrated, using a parametrization derived from an analysis of samples of simulated events, to correct for an observed correlation of the ΔE resolution with the $\pi^+\pi^-$ invariant mass. The decay vertex of the signal B candidate was reconstructed from the two charged pions and the decay vertex of the opposite-side B meson was estimated from a fit to the remaining tracks in the event. The decay-time difference Δt was calculated in the usual manner from the distance between the two decay vertices along the beam axis and the known boost of the $\Upsilon(4S)$ rest frame in the laboratory system. The decay-time resolution was parametrized in the usual manner by a triple Gaussian function in the BaBar analysis and by the function described in Ref. [250] in the Belle analysis. The standard BaBar and Belle flavour tagging algorithms were applied to derive the initial flavour of the signal B candidate and sort event candidates into categories according to the quality of the tagging information.

A maximum likelihood fit was then performed to m_{ES} and ΔE, a combined event-shape variable, two Dalitz-plot variables and the decay-time difference, Δt, for the selected signal candidates. The ρ resonances were modelled in the fit as modified relativistic Breit-Wigner resonances. The BaBar fit included additional terms to describe contributions from the radial excitation, $\rho(1450)$. In addition to the signal components, the likelihood functions contained terms for self-cross feed, for backgrounds from decays of neutral and charged B mesons and for continuum background from non-$B\overline{B}$ events. Measured distributions for m_{ES}, ΔE, the two-pion invariant masses and the ρ helicity angles as obtained in the Belle analysis are shown in Figures 5.97 and 5.98 together with the projections of the fit results.

The fit was performed in terms of 27 real parameters

$$\begin{aligned} U_\kappa^{\pm} &\equiv |A_\kappa|^2 + q\,|\overline{A}_\kappa|^2 \\ U_{\kappa\sigma}^{\pm,\mathrm{Re}} &\equiv \mathrm{Re}\left(A_\kappa A_\sigma^* + \overline{A}_\kappa \overline{A}_\sigma^* \right) \\ U_{\kappa\sigma}^{\pm,\mathrm{Im}} &\equiv \mathrm{Im}\left(A_\kappa A_\sigma^* + \overline{A}_\kappa \overline{A}_\sigma^* \right) \\ I_\kappa &\equiv \mathrm{Im}\left(\overline{A}_\kappa A_\kappa^* \right) \\ I_{\kappa\sigma}^{\mathrm{Re}} &\equiv \mathrm{Re}\left(\overline{A}_\kappa A_\sigma^* - \overline{A}_\sigma A_\kappa^* \right) \\ I_{\kappa\sigma}^{\mathrm{Im}} &\equiv \mathrm{Im}\left(\overline{A}_\kappa A_\sigma^* - \overline{A}_\sigma A_\kappa^* \right) \end{aligned}$$

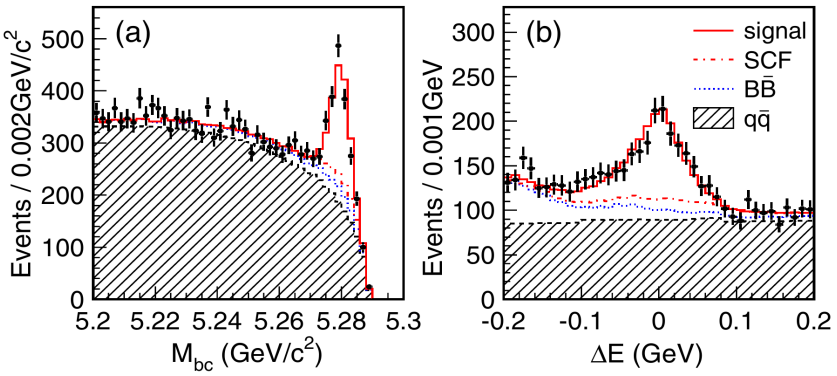

Figure 5.97: Distributions of the (left) beam-energy substituted invariant mass and (right) energy imbalance for the sample of selected candidates from the Belle analysis of *CP* violating asymmetries in the decay $B^0 \to (\rho\pi)^0$. The results of the maximum likelihood fit to the data is superimposed as explained in the plot legend (from [411])

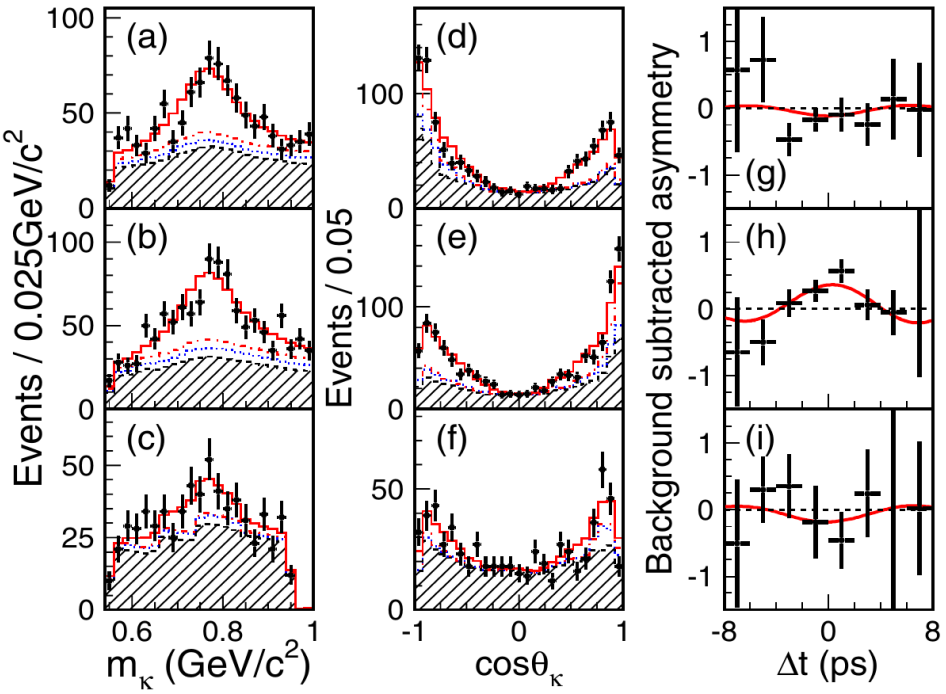

Figure 5.98: Distributions of the (left) $\pi\pi$ invariant mass, (middle) cosines of the ρ candidates, and (right) the decay-time dependent *CP* asymmetries for (top) $\rho^+\pi^-$, (middle) $\rho^-\pi^+$ and (bottom) $\rho^0\pi^0$ candidates as measured in the Belle analysis of *CP* violating asymmetries in the decay $B^0 \to (\rho\pi)^0$. The results of the maximum likelihood fit to the data are superimposed as explained in the legend in Figure 5.97 above (from [411])

where $\kappa, \sigma \in (+, -, 0)$ for the decay via an intermediate ρ^+, ρ^- or ρ^0 meson. In these parameters,

$$|A|^2 \pm |\overline{A}|^2 \;=\; \sum_{\kappa} |f_\kappa|^2 \, U_\kappa^{\pm} \;+\; \sum_{\kappa<\sigma} 2\left(\mathrm{Re}\,(f_\kappa f_\sigma^*)\, U_{\kappa\sigma}^{\pm,\mathrm{Re}} \;-\; \mathrm{Im}\,(f_\kappa f_\sigma^*)\, U_{\kappa\sigma}^{\pm,\mathrm{Im}}\right)$$

and

$$\mathrm{Im}\left(\frac{q}{p}\,\overline{A}A^*\right) \;=\; \sum_{\kappa} |f_\kappa|^2 \, I_\kappa \;+\; \sum_{\kappa<\sigma} \left(\mathrm{Re}\,(f_\kappa f_\sigma^*)\, I_{\kappa\sigma}^{\mathrm{Im}} \;+\; \mathrm{Im}\,(f_\kappa f_\sigma^*)\, I_{\kappa\sigma}^{\mathrm{Re}}\right) .$$

The time-integrated direct *CP* violation is

$$A_{CP} \;=\; \frac{U_+^+ \,-\, U_-^+}{U_+^+ \,+\, U_-^+}$$

while the time-dependent *CP* violation parameters are

$$S_{\rho^\pm\pi^\mp} \;=\; \frac{I_+}{U_+^+} \,+\, \frac{I_-^-}{U_-^+}$$

and

$$C_{\rho^\pm\pi^\mp} \;=\; \frac{1}{2}\left(\frac{U_+^-}{U_+^+} \,+\, \frac{U_-^-}{U_-^+}\right) .$$

To extract an estimate for the CKM angle α, the twelve real parameters describing the magnitudes and phases of the six decay amplitudes A_+, A_-, A_0, $\overline{A}_+$, $\overline{A}_+$ and $\overline{A}_0$ were estimated from a χ^2-minimization, taking into account the fitted values of the parameters U and I and their correlation matrix. The advantage of performing the time-dependent Dalitz plot fit in terms of the parameters U and I rather than fitting directly the magnitudes and phases of the six decay amplitudes is that uncertainties on the U and I are closer to Gaussian distributed than those on the parameters that describe the amplitudes. This makes it more straightforward to combine measurements from different experiments in terms of the parameters .

The constraints on the CKM angle α that were derived from these analyses are shown in Figure 5.99 below. A simulation study performed as part of the BaBar analysis indicated that the results of these fits for α should not be regarded as reliable given the size of the currently available event samples. Nevertheless, the results of the two analyses are commonly used together with those from $\pi^+\pi^-$ and $\rho^+\rho^-$ isospin to derive combined constraints on the value of α.

5.4.4 Measurements in $B^0 \to (a_1\pi)^0$ decays

Combining the decay modes $B^0 \to a_1^\pm\pi^\mp$, $B^0 \to a_1^0\pi^0$ and their charge conjugates, and reconstructing the a_1 mesons in the decay chain $a_1 \to \rho\pi$ followed by $\rho \to \pi\pi$, there are six decay modes that all result in the same final state, $\pi^+\pi^-\pi^0\pi^0$. However, in contrast to the case of decays to $\pi^+\pi^-\pi^0$ via $\rho\pi$ intermediate states discussed above, there is no region in phase space in which the $a_1^\pm$ and a_1^0 resonance bands overlap and therefore no interference of the different decay modes occurs that would allow to extract the relative phases between the different amplitudes. Instead, measurements follow an approach suggested in Ref. [412]. An effective *CP* violating phase $\alpha_{\rm eff} = \alpha + \Delta\alpha$ can be extracted from a combined measurement of the time-dependent decay rates for the four decay modes $B^0 \to a_1^-\pi^+$, $\overline{B}^0 \to a_1^+\pi^-$, $B^0 \to a_1^+\pi^-$ and $\overline{B}^0 \to a_1^-\pi^+$. As illustrated in Figure 5.79, the spectator d or $\overline{d}$ quark of the decaying neutral B meson becomes part of the a_1 meson in the first two decay modes while it becomes part of the pion in the last two decay modes. The decay-time dependent probability for an initial B^0 meson ($q = +1$) or an initial $\overline{B}^0$ meson ($q = -1$) to decay into the final states $a_1^\pm\pi^\mp$ is given by

$$\begin{aligned} f_q^{a_1^\pm\pi^\mp}(\Delta t) \;&=\; (1 \,\pm\, A_{a_1\pi})\,\frac{e^{-\Delta t/\tau_B}}{8\tau_B} \;\times\; \{\, 1 \,+ \\ &\qquad q\cdot(S_{a_1\pi} \,\pm\, \Delta S_{a_1\pi})\cdot\sin(\Delta m_d\,\Delta t) \;-\; q\cdot(C_{a_1\pi} \,\pm\, \Delta C_{a_1\pi})\cdot\cos(\Delta m_d\,\Delta t)\,\} \,. \end{aligned}$$

As usual, the parameter $C_{a_1\pi}$ describes the flavour-dependent direct *CP* violating asymmetry and the parameter $S_{a_1\pi}$ describes the mixing-induced *CP* violating asymmetry related to the weak phase $\alpha_{\rm eff}$. Extra terms enter because the $a_1^\pm(1260)$ is a spin-1 vector meson and the final state $a_1^\pm\pi^\mp$ is not a *CP* eigenstate. The parameter $A_{a_1\pi}$ describes the time-integrated

direct *CP* asymmetry, summed over the two initial B meson flavours. The parameter $\Delta S_{a_1\pi}$ is related to the relative strong phase between the processes in which the spectator quark becomes part of the a_1 meson and the processses in which it becomes part of the pion, while the parameter $\Delta C_{a_1\pi}$ describes the decay rate asymmetry between these two types of processes. The *CP* violating weak phase $\alpha_{\rm eff}$ can be determined as

$$\alpha_{\rm eff} \;=\; \frac{1}{4}\left\{ \arcsin\left(\frac{S_{a_1\pi} + \Delta S_{a_1\pi}}{\sqrt{1 - (C_{a_1\pi} + \Delta C_{a_1\pi})^2}}\right) \;+\; \arcsin\left(\frac{S_{a_1\pi} - \Delta S_{a_1\pi}}{\sqrt{1 - (C_{a_1\pi} - \Delta C_{a_1\pi})^2}}\right)\right\} .$$

The Belle collaboration published a measurement [413] of $\alpha_{\rm eff}$ in decays $B^0 \to a_1^\pm\pi^\mp$ based on on their full data set, corresponding to 772 million produced $B\overline{B}$ pairs, while the BaBar collaboration published a measurement [414] based on a data set corresponding to about 384 million produced $B\overline{B}$ pairs.

Both analyses required four tracks that had to fulfill loose requirements on their impact parameter with respect to the e^+e^- interaction point and that passed particle identification criteria to suppress kaon, proton and electron candidates. Assuming that the $a_1^\pm$ decay to $\pi^+\pi^-\pi^\pm$ is dominated by the intermediate state $\rho^0\pi^\pm$, a neutral dipion combination with an invariant mass above the K^0_S mass was required. This was combined with a third pion to form an $a_1^\pm$ candidate and a fourth pion to form B^0 candidates. The usual event selection based on the beam-energy substituted invariant mass, $m_{\rm ES}$, the energy imbalance, ΔE, and a combination of event shape variables was appplied. To supress combinatorial background, candidates were rejected for which the cosine of the opening angle between the momentum of the B candidate in the rest frame of the $a_1^\pm$ candidate and the momentum of the bachelor pion produced in the decay $a_1^\pm \to \rho^0\pi^\pm$ was close to ± 1. Appropriate vetoes on the invariant masses of combinations of two or three of the final-state particles were applied to remove peaking backgrounds from B-meson decays involving $D \to K\pi$, $D \to K\pi\pi$, $J/\psi \to \mu^+\mu^-$ and $K^0_S \to \pi^+\pi^-$. The decay vertex of the signal B candidate was reconstructed from a fit to the four final-state tracks, the decay vertex of the opposite-side B meson was estimated from a fit to the remaining tracks in the event, and the decay-time difference Δt was determined in the usual manner from the distance between the two decay vertices and the boost of the $\Upsilon(4S)$ rest frame in the laboratory system. The standard BaBar and Belle flavour tagging algorithms were applied to derive the initial flavour of the signal B candidate and to sort event candidates into categories according to the quality of the tagging information.

The parameters $A_{a_1\pi}$, $S_{a_1\pi}$, $C_{a_1\pi}$, $\Delta S_{a_1\pi}$ and $\Delta C_{a_1\pi}$ were extracted in the BaBar analysis from a simultaneous unbinned maximum likelihood fits to $m_{\rm ES}$, ΔE, a Fisher discriminant combining event-shape variables, the three-pion invariant mass, the helicity angle of the $a_1^\pm$ candidate, and Δt. The helicity angle, defined as the angle between the normal to the decay plane of the 3π decay plane and the flight direction of the bachelor pion from the B candidate, was included in the fit as it provided separation against B-meson decays to four pions via the $a_2^\pm(1320)\pi^\mp$ intermediate state. The likelihood function employed in the BaBar analysis contained separate terms for signal, for continuum background from non-$B\overline{B}$ events, for $B\overline{B}$ decays to charmed and charmless final states, for non-resonant $B^0 \to \rho\pi\pi$ decays and for the decay mode $B^0 \to a_2^\pm(1320)\pi^\mp$. The likelihood function employed in the Belle analysis contained separate terms for correctly reconstructed signal, for misreconstructed signal, for non-$B\overline{B}$ continuum background, background from decays of neutral and charged B mesons to charmed and charmless final states, and for five specific peaking backgrounds. Here, a first fit to ΔE, a Fisher discriminant combining event-shape variables, the three-pion invariant mass, and the helicity angle was performed to determine the signal and background fractions in the event sample and these were then fixed in a second fit to the Δt distribution to extract the parameters describing the decay-time distribution.

The results for $A_{a_1\pi}$ and $C_{a_1\pi}$ obtained by BaBar and those obtained by Belle were compatible with each other and with zero, while a discrepancy corresponding to 3.2 Gaussian standard

Table 5.2: Averages for α as determined from combinations of direct measurements by the BaBar and Belle collaborations, the CKMfitter [3] and UTFit [211] groups, compared to the results of Standard Model fits of CKM parameters, excluding direct measurements of α. The values quoted by the CKMfitter group include results presented up to the CKM2014 conference in the beginning of September 2014, those quoted by the UTfit group include results presented up to the ICHEP2014 conference in the beginning of July 2014.

	BaBar/Belle [112]	CKMfitter [3]	UTFit [211]
direct	$(88 \pm 5)^\circ$	$(87.7^{+3.5}_{-3.3})^\circ$	$(90.7 \pm 7.0)^\circ$
CKM fit	-	$(91.5^{+4.2}_{-1.3})^\circ$	$(87.2 \pm 3.9)^\circ$

deviations exists between two measurements of $S_{a_1\pi}$. The BaBar analysis resulted in

$$S_{a_1\pi} \;=\; 0.37 \pm 0.21\,(\text{stat}) \pm 0.07\,(\text{syst})$$

while the Belle analysis yielded

$$S_{a_1\pi} \;=\; -0.51 \pm 0.14\,(\text{stat}) \pm 0.08\,(\text{syst})\ .$$

The quoted uncertainties on all measured parameters were dominated by the statistical uncertainty. Systematic uncertainties were dominated by possible *CP* violating effects in the background components and, in the case of the BaBar analysis, by effects related to the parametrization of the likelihood functions. The value of α_{eff} can be extracted from this analysis up to a four-fold ambiguity. One of the solutions quoted by BaBar, $\alpha_{\text{eff}} = (78.6 \pm 7.3)^\circ$ is compatible with the Standard Model value of α, while the closest of the four solutions quoted by Belle is $\alpha_{\text{eff}} = (107.3 \pm 6.6 \pm 4.8)^\circ$.

5.4.5 Constraints on the angle α

The BaBar and Belle collaborations have jointly published [112] combined constraints on the angle α derived from their latest measurements. The combination was formed by extracting for each of the individual analyses a χ^2 profile as a function of the assumed value of the angle α. The different χ^2 profiles were then added up and translated into a profile of the confidence level, $1 - \text{C.L.}$, where peaks at $1 - \text{C.L.} = 1$ correspond to the favoured solutions for α, while regions with $1 - \text{C.L.} < a$ are excluded at confidence level a relative to the favoured solution. The results are shown in Figure 5.99 in terms of $1 - \text{C.L.}$.

The combined result of $B \to \pi\pi$ isospin analyses clearly reflects the inherent eight-fold ambiguity in the determination of α. The combination of the $B \to \rho\rho$ isospin analyses shows the two-fold ambiguity due to the symmetry of $\sin(2\alpha)$, while the four-fold ambiguity that results from the relative orientation of the isospin triangles is not visible here. Due to the large difference in the branching fractions for the decays $B^0 \to \rho^0\rho^0$ and $B^\pm \to \rho^\pm\rho^0$ on the one hand and the decay $B^0 \to \rho^0\rho^0$ on the other hand, the triangles are squashed and the four solutions too close to each other to be resolved at the current precision of the measurements. This measurement currently provides the most precise determination of α. The time-dependent Dalitz plot analysis of $B \to (\rho\pi)^0$ decays does not allow significant constraints on the value of α at the current level of statistics but is expected by the authors of Ref. [112] to dominate the precision of the measurement when sufficiently large data samples become available. Constraints from the $B \to a_1\pi$ analyses were not included in these averages since uncertainties related to the underlying theoretical assumption of SU(3) flavour symmetry were deemed to be difficult to estimate. The result of the overall combination is quoted as

$$\alpha \;=\; (88 \pm 5)^\circ\ .$$

Results quoted by the CKMfitter and UTfit groups are summarized in Table 5.2.

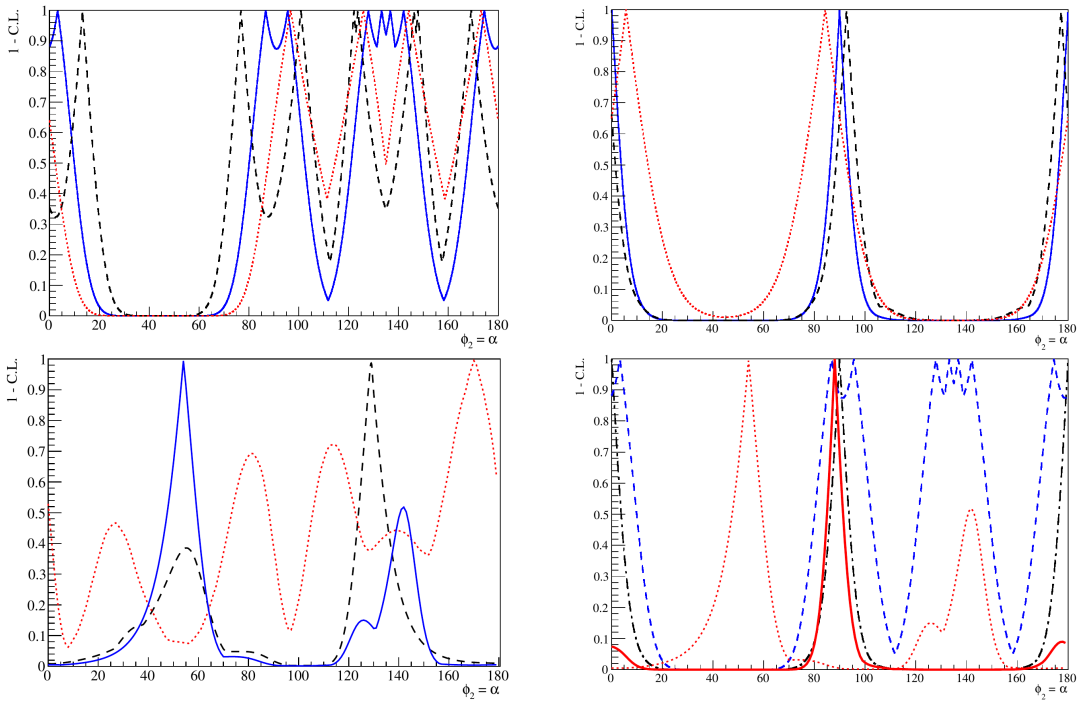

Figure 5.99: Profiles of $1 - \text{C.L.}$ as a function of the assumed value of the CKM angle α for BaBar and Belle combinations of (top left) isospin analyses of $B \to \pi\pi$ decays, (top right) isospin analyses of $B \to \rho\rho$ decays, (bottom left) time-dependent Dalitz plot analysis of $B \to (\rho\pi)^0$ decays and (bottom right) the overall combination of all three types of analyses. In the upper panels and the lower left panel, blue solid curves show the combined results, dashed black curves show the BaBar-only result and dotted red curves show the Belle-only results. In the lower right panel, the solid red curve shows the overall combination, the dashed blue line shows the combined result of the $\pi\pi$ isospin analysis, the dash-dotted black line shows the combined result of the $\rho\rho$ isospin analysis and the dotted red line shows the combined result of the time-dependent $(\rho\pi)^0$ Dalitz plot analysis (from [112])

5.5 The CKM angle γ

The angle γ between the base of the Unitarity Triangle and the side connecting the origin of the complex plane to the apex of the triangle is defined by

$$\gamma \equiv \arg\left(-\frac{V_{ud}V_{ub}^*}{V_{cd}V_{cb}^*}\right)$$

and is the currently least precisely measured parameter of the Unitarity Triangle. Including results presented up to the CKM2014 conference in the beginning of September 2014, the CKMfitter group [3] quotes the world average from direct measurements as $\gamma = (73.2^{+6.3}_{-7.0})^\circ$. The UTfit group [211], using direct measurements available by the ICHEP2014 conference in the beginning of July 2014, quotes $\gamma = (68.4 \pm 7.5)^\circ$.

A theoretically clean determination of the angle γ can be derived from measurements of the ratios and charge asymmetries of time integrated decay rates in pure tree decays $B^\pm \to DK^\pm$, where D denotes a D^0 or $\overline{D}^0$ meson. As shown by the Feynman diagrams in Figure 5.100, B^+ mesons can decay to $\overline{D}^0 K^+$ via an external tree process and to $D^0 K^+$ via an internal tree process, and vice versa for B^- decays. If the neutral D meson is reconstructed in a final state $[f]_\text{D}$ that is accessible from D^0 decays as well as $\overline{D}^0$ decays, the two decay paths illustrated in Figure 5.101 form two interfering amplitudes leading to the same final state. The two amplitudes have different weak and strong phases and can therefore generate *CP* violating effects as discussed in Section 3.3. In particular, the weak phase between the two amplitudes is given by the phase between V_{ub} and V_{cb}, i.e the angle γ. Adopting a phase convention in

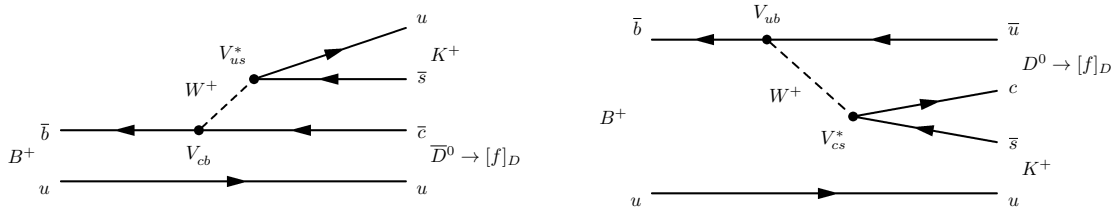

Figure 5.100: Feynman diagrams for (left) the colour-allowed, external tree decay $B^+ \to \overline{D}^0 K^+$ and (right) the colour-suppressed, internal tree decay $B^+ \to D^0 K^-$.

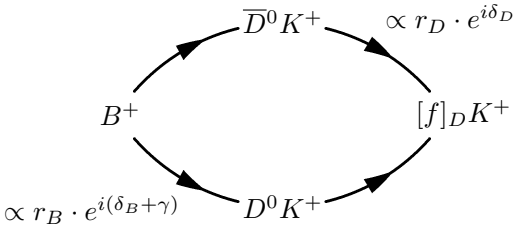

Figure 5.101: Illustration of the phases and the ratios of magnitudes between the interfering amplitudes in tree decays $B^+ \to DK^+ \to [f]_{\rm D} K^+$. See the text for further explanations.

which the decay amplitudes $A_B \equiv A(B^+ \to \overline{D}^0 K^+)$ and $A_D \equiv D^0 \to [f]_{\rm D} K^+$ are real and following the notation of Figure 5.101, where δ_B and δ_D denote the strong phases between the respective decay amplitudes and r_B and r_D their relative magnitudes, the decay rate for the decay $B^+ \to [f]_{\rm D} K^+$ is given by

$$\begin{aligned}
\Gamma(B^+ \to [f]_{\rm D} K^+) &= \left| A_B \cdot r_D A_D \, e^{i\delta_D} + r_B A_B \, e^{i(\delta_B+\gamma)} \cdot A_D \right|^2 \\
&= A_B^2 A_D^2 \, r_D^2 + A_B^2 A_D^2 r_B^2 + A_B^2 A_D^2 r_B r_D \left(e^{i(\delta_B+\delta_D+\gamma)} + e^{-i(\delta_B+\delta_D+\gamma)} \right) \\
&= A_B^2 A_D^2 \left(r_D^2 + r_B^2 + 2\, r_B r_D \cos\left(\delta_B + \delta_D + \gamma\right) \right)
\end{aligned}$$

The unknown parameters r_B, δ_B, r_D and δ_D can be extracted simultaneously with γ by combining measurements in decays to different final states $[f]_{\rm D}$ as discussed below. Since these decays do not involve any loop diagrams, the extracted value for γ should not be affected by possible contributions from New Physics.

In practice, however, these measurements are challenging. Colour suppression of the internal tree amplitude in combination with the ratio of the magnitudes of the involved CKM elements implies that the $B^+ \to D^0 K^+$ decay amplitude is suppressed by a factor $r_B \approx\approx 0.1$ compared to the amplitude for the decay $B^+ \to \overline{D}^0 K^+$. The large difference in magnitude between the two amplitudes limits possible interference effects and therefore the sensitivity to the weak phase γ. Moreover, branching fractions for the interesting decay modes are small, making it difficult to collect large event samples. The measurements involve decays to purely hadronic final states, which are difficult to trigger, and excellent K/π separation capability is required to suppress backgrounds from the more than ten times more abundant decays $B^+ \to D\pi^+$. In principle, decays $B^+ \to D\pi^+$ are in fact open to a similar treatment as discussed here for $B^+ \to DK^+$, but interference effects and possible *CP* violating asymmetries are expected to be even smaller in these decay modes since the suppression of the internal tree decay due to the magnitudes of the involved CKM matrix elements is significantly stronger in this case, $(|V_{ub}|\,|V_{cd}|)/(|V_{cb}|\,|V_{ud}|) \propto \lambda^2$ with the Wolfenstein parameter $\lambda \approx 0.23$. Nevertheless, measurements at LHCb actually start to be sensitive to *CP* violating effects in these decay modes, as discussed further below in this section.

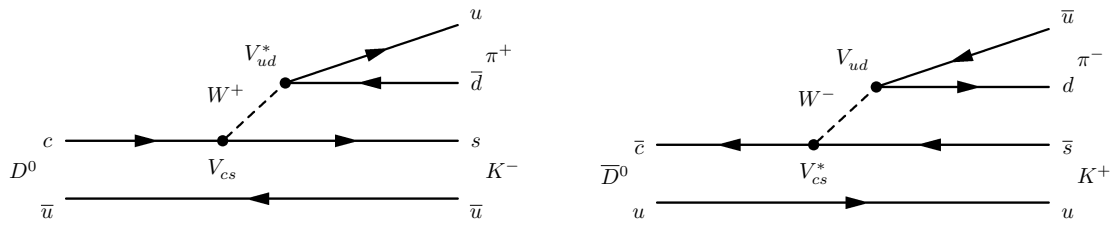

Figure 5.102: Feynman diagrams for the Cabibbo-allowed decays (left) $D^0 \to K^-\pi^+$ and (right) $\overline{D}^0 \to K^+\pi^-$.

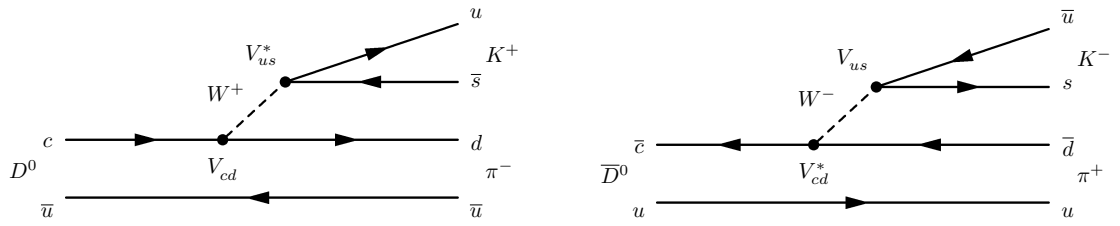

Figure 5.103: Feynman diagrams for the doubly Cabibbo-suppressed decays (left) $D^0 \to K^+\pi^-$ and (right) $\overline{D}^0 \to K^-\pi^+$ that are employed in ADS analyses of the decay chain $B^+ \to [f]_{\rm D}K^+$. The decay amplitudes are suppressed compared to the Cabibbo-allowed processes shown in Figure 5.102 by the ratio of the involved CKM matrix elements, $(|V_{cd}||V_{us}|)/(|V_{cs}||V_{ud}|) \propto \lambda^2$, with the Wolfenstein parameter $\lambda \approx 0.23$.

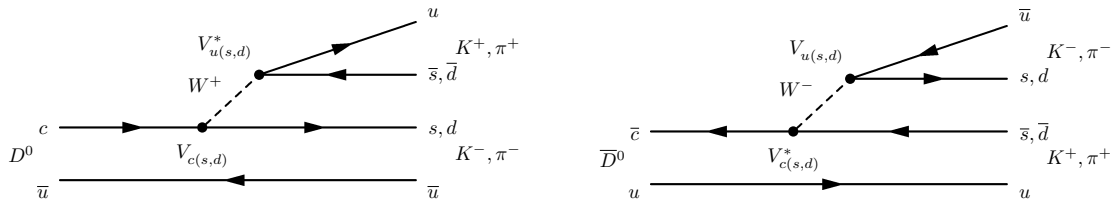

Figure 5.104: Feynman diagrams for the decays of (left) D^0 mesons and (right) $\overline{D}^0$ mesons to the *CP* eigenstates K^+K^- or $\pi^+\pi^-$ that are employed in GLW analyses of the decay chain $B^+ \to [f]_{\rm D}K^+$.

Three general approaches have been proposed to extract the weak phase γ, using different combinations of final states $[f]_{\rm D}$. They are usually referred to as the GLW, ADS and GGSZ methods after the names of the theoreticians who proposed them. The GGSZ method is also known as the Dalitz-plot method.

The GLW method [415, 416] exploits decays of the neutral D mesons to *CP* eigenstates such as $[K^+K^-]_{\rm D}$ shown in Figure 5.104, in addition to the Cabibbo-favoured decay modes shown in Figure 5.102. Angular momentum conservation implies that K^+K^- pairs from decays of neutral D mesons are produced with relative angular momentum $L = 0$ and therefore in a *CP* even state. The decay $B^+ \to [K^+K^-]_{\rm D}K^+$ then proceeds via an intermediate state $D^0_{CP+}K^+$, where D^0_{CP+} denotes the *CP* even eigenstate in the $D^0\overline{D}^0$ system,

$$|\, D^0_{CP+}\,\rangle \;\equiv\; \frac{1}{2}\Big(\,|\, D^0\,\rangle \;+\; |\,\overline{D}^0\,\rangle\,\Big)\;.$$

This definition leads to a relation between the three complex decay amplitudes,

$$\sqrt{2}\cdot A\,(B^+ \to D^0_{CP+}K^+) \;=\; A\,(B^+ \to D^0K^+) \;+\; A\,(B^+ \to \overline{D}^0K^+)\;,$$

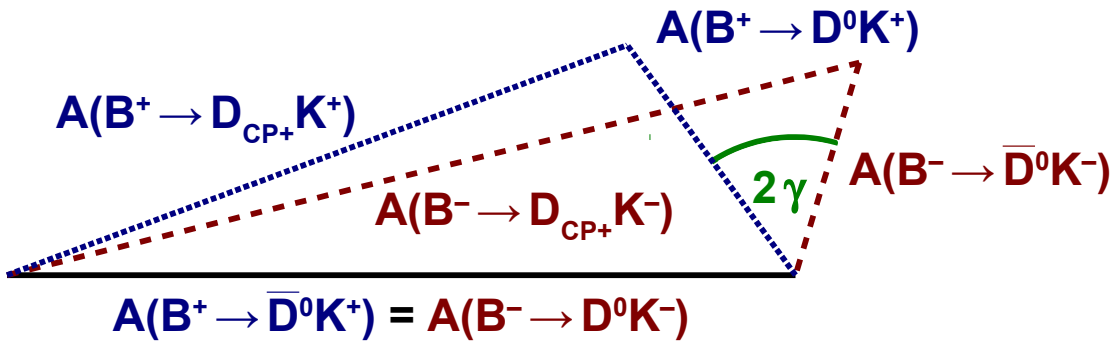

Figure 5.105: Illustration of the triangular relations in the complex plane that are exploited in the GLW method to extract the CKM angle γ from measurements of the decay rates for $B^{\pm} \to [f_{CP}]_{\rm D} K^{\pm}$ to CP eigenstates f_{CP}. See the text for further explanations.

and similarly for the charge-conjugated modes

$$\sqrt{2} \cdot A\left(B^- \to D^0_{CP+} K^-\right) \;=\; A\left(B^- \to \overline{D}^0 K^-\right) \;+\; A\left(B^- \to D^0 K^-\right) \,.$$

These relations are often represented as two triangles in the complex plane as illustrated in Figure 5.105, where again a phase convention is adopted in which the decay amplitude for the external tree decays is real. The two triangles then share a common base and the weak phase γ is given by the angle between the two sides representing the amplitudes of the internal tree decays. In principle, the two triangles could be constructed and the angle γ extracted by measuring the length of each side via the decay rate of the respective process. However, there is a number of caveats. Firstly, there is an inherent four-fold ambiguity in the determination of γ due to the four possible relative orientations of the two triangles, flipping the one horizontally or vertically with respect to the other. Secondly, the small value of r_B implies that the triangles are squashed. The sides representing the amplitudes of the internal tree decays are much shorter than the others, limiting the sensitivity to γ. Thirdly, the lengths of only two of the three sides of each triangle can actually be measured. The decay rate for the process $B^+ \to D^0_{CP+} K^+$ can be measured via D decays to CP-even eigenstates such as $[K^+K^-]_{\rm D}$, as discussed above. The decay rate for the process $B^+ \to \overline{D}^0 K^+$ can be measured through the final state $[K^+\pi^-]_{\rm D} K^+$. The decay to this final state via the intermediate state $D^0 K^+$ is suppressed in both steps of the decay chain and is therefore negligibly small. The inital decay $B^+ \to D^0 K^+$ is suppressed by the value of r_B and the subsequent decay $D^0 \to K^+\pi^-$ is doubly Cabibbo suppressed. The problem is in determining the decay rate for the process $B^+ \to D^0 K^+$, which cannot be measured in a similar manner. The decay to the final state $[K^-\pi^+]_{\rm D} K^+$ via the intermediate state $\overline{D}^0 K^+$ is suppressed by the ratio of the D decay amplitudes, but because of the smallness of r_B the decay via the intermediate state $D^0 K^+$ is suppressed as well. The two suppression factors turn out to be of the same order of magnitude, such that the decay is expected to proceed with similar rate via each of the two intermediate states. As a consequence, only two experimental observables can be derived from the triangle relationships, which alone is not sufficient to extract γ. Two additional observables can be constructed using similar arguments for D meson decays to CP odd final states, such as $[K^0_S\pi^0]_{\rm D}$. The $K^0_S\pi^0$ pair is again produced with relative angular momentum $L = 0$, but the final state is CP odd due to the internal quantum numbers of the π^0 meson.

The four experimental observables are conveniently defined as ratios and relative asymmetries of decay rates, since systematic uncertainties related to the luminosity determination and to reconstruction and selection efficiencies partially cancel in the ratios. The four observables

are defined as

$$R_{CP\pm} \equiv \frac{\Gamma\left(B^- \to D^0_{CP\pm} K^-\right) + \Gamma\left(B^+ \to D^0_{CP\pm} K^+\right)}{1/2\left(\Gamma\left(B^- \to D^0 K^-\right) + \Gamma\left(B^+ \to \overline{D}^0 K^+\right)\right)}$$

and

$$A_{CP\pm} \equiv \frac{\Gamma\left(B^- \to D^0_{CP\pm} K^-\right) - \Gamma\left(B^+ \to D^0_{CP\pm} K^+\right)}{\Gamma\left(B^- \to D^0_{CP\pm} K^-\right)\} + \Gamma\left(B^+ \to D^0_{CP\pm} K^+\right)} \; .$$

With $r_D = 1$ for decays to CP eigenstats, $\delta_D = 0$ for decays to CP even eigenstates and $\delta_D = \pi$ for decays to CP odd eigenstates, these observables are given in terms of the unknown parameters r_B, δ_B and γ by

$$\begin{aligned} R_{CP\pm} &= 1/2 \cdot \left\{\left(1 + r_B^2 + 2\, r_B \cos\left(\delta_B - \gamma\right)\right) + \left(1 + r_B^2 + 2\, r_B \cos\left(\delta_B + \gamma\right)\right)\right\} \\ &= 1 + r_B^2 \pm 2\, r_B \cos\delta_B \cos\gamma \end{aligned}$$

$$\begin{aligned} A_{CP\pm} &= \frac{\left(1 + r_B^2 \pm 2\, r_B \cos\left(\delta_B - \gamma\right)\right) - \left(1 + r_B^2 \pm 2\, r_B \cos\left(\delta_B + \gamma\right)\right)}{\left(1 + r_B^2 \pm 2\, r_B \cos\left(\delta_B - \gamma\right)\right) + \left(1 + r_B^2 \pm 2\, r_B \cos\left(\delta_B + \gamma\right)\right)} \\ &= \pm \frac{2\, r_B \sin\delta_B \sin\gamma}{1 + r_B^2 \pm 2\, r_B \cos\delta_B \cos\gamma} \\ &= \pm 2\, r_B \sin\delta_B \sin\gamma \,/\, R_{CP\pm} \; , \end{aligned}$$

where the trigonometric relations

$$\cos(\delta_B - \gamma) - \cos(\delta_B + \gamma) = 2 \sin\delta_B \sin\gamma$$

and

$$\cos(\delta_B - \gamma) + \cos(\delta_B + \gamma) = 2 \cos\delta_B \cos\gamma$$

have been employed. From the final result it is obvious that

$$A_{CP+}\, R_{CP+} = A_{CP-}\, R_{CP-} \; ,$$

leaving three independent observables to determine the three unkown parameters r_B, δ_B and γ.

The remaining challenge in the GLW approach is the limited sensitivity to γ due to the smallness of r_B. The idea of the ADS method [417, 418] is to overcome this limitation by studying asymmetries in the suppressed modes, $B^+ \to [K^-\pi^+]_{\rm D} K^+$ and $B^- \to [K^+\pi^-]_{\rm D} K^-$. As discussed above, the decay $B^+ \to [K^-\pi^+]_{\rm D} K^+$ via the intermediate state $B^+ \to \overline{D}^0 K^+$ is suppressed by the ratio of the D decay amplitudes while the decay via the intermediate state $D^0 K^+$ is suppressed by the smallness of r_B, and vice versa for the charge-conjugated decay $B^- \to [K^+\pi^-]_{\rm D} K^-$. The two suppression factors being of the same order of magnitude, the two interfering amplitudes are of similar size and interference effects can be large. These considerations give rise to two additional observables that are again defined as a ratio and a relative asymmetry,

$$R_{\rm ADS} \equiv \frac{\Gamma(B^- \to [K^+\pi^-]_D K^-) + \Gamma(B^+ \to [K^-\pi^+]_D K^+)}{\Gamma(B^- \to [K^-\pi^+]_D K^-) + \Gamma(B^+ \to [K^+\pi^-]_D K^+)}$$

and

$$A_{\rm ADS} \equiv \frac{\Gamma(B^- \to [K^+\pi^-]_D K^-) - \Gamma(B^+ \to [K^-\pi^+]_D K^+)}{\Gamma(B^- \to [K^+\pi^-]_D K^-) + \Gamma(B^+ \to [K^-\pi^+]_D K^+)}$$

and are given by

$$\begin{aligned} R_{\rm ADS} &= r_B^2 + r_D^2 + 2\, r_B r_D \cos\left(\delta_B + \delta_D\right) \cos\gamma \\ A_{\rm ADS} &= 2\, r_B r_D \sin\left(\delta_B + \delta_D\right) \sin\gamma \,/\, R_{\rm ADS} \end{aligned}$$

The two additional unknowns, the strong phase δ_D between the two D decay amplitudes and the ratio r_D of their magnitudes, have to be either determined as part of the analysis or have to be fixed from external measurements. The challenge in measuring the ADS observables is the small branching fraction, of the order of 5×10^{-8}, for these suppressed decay modes.

The sensitivity to γ does not only depend on the ratio of the magnitudes of the two interfering amplitudes, but also on the value of the a priori unknown strong phase differences. As can been seen from the expressions for the GLW and ADS observables above, a value of γ can be extracted even in the case of vanishing strong phases, but the sensitivity of the measurement improves if the strong phases are large. The idea of the GGSZ or Dalitz-plot method [419, 420] is to enhance the sensitivity to γ by exploiting interference patterns in the phase space of D decays to self-conjugate three-body final states that are accessible through both D^0 and $\overline{D}^0$ decays. Naively speaking, each phase-space point in the Dalitz plot can be regarded as a quasi two-body decay for which the same arguments apply as for the GLW and ADS modes discussed above and if regions of phase space exist in which strong phases are large, these regions will give enhanced sensiticity to γ. Measurements of the Dalitz plot structure in D decays, for example at CLEO-c, have in fact shown rich resonance structures, implying that large interference are possible. An attractive final state for such studies is $[K^0_S\pi^+\pi^-]_{\rm D}$. As illustrated in Figure 5.106, the decay to this final state is Cabibbo allowed for both D^0 and $\overline{D}^0$ mesons and since it contains only charged final-state particles if the K^0_S is reconstructed in its decay to a pair of charged pions.

The concept of Dalitz-plot analyses has already been briefly discussed in Section 5.3 in the context of measurements of the CP violating phase $\sin 2\beta_{\rm eff}$ in the decay $B^0 \to \phi K^0_S$. Defining the two Dalitz variables as the squared invariant masses of the $K^0_S\pi^+$ pair and the $K^0_S\pi^-$ pair,

$$\begin{aligned} s_+ &\equiv m^2(\pi^+, K^0_S) \\ s_- &\equiv m^2(\pi^-, K^0_S) \ , \end{aligned}$$

the $D^0 \to K^0_S\pi^+\pi^-$ decay amplitude as a function of these variables can be written as

$$A_{D^0}(s_+, s_-) \ \equiv \ A_{+-}\, e^{i\delta_{+-}} \ ,$$

where the real parameters A_{+-} and δ_{+-} describe the magnitude and strong phase of the decay amplitude as a function of the position (s_+, s_-) in the Dalitz plot. Since the D^0 meson and therefore the final state have spin 0, the decay amplitude for the charge-conjugated process $\overline{D}^0 \to K^0_S\pi^+\pi^-$ is obtained by simply swapping the two Dalitz-plots variables,

$$A_{\overline{D}^0}(s_+, s_-) \ = \ A_{D^0}(s_-, s_+) \ = \ A_{-+}\, e^{i\delta_{-+}} \ .$$

Effects due to mixing and CP violation in the $D^0\overline{D}^0$ system are known to be small and are neglected here, but can be taken into account in a more complete analysis, as discussed for example in Ref. [419]. Adopting again a phase convention in which the decay amplitude for

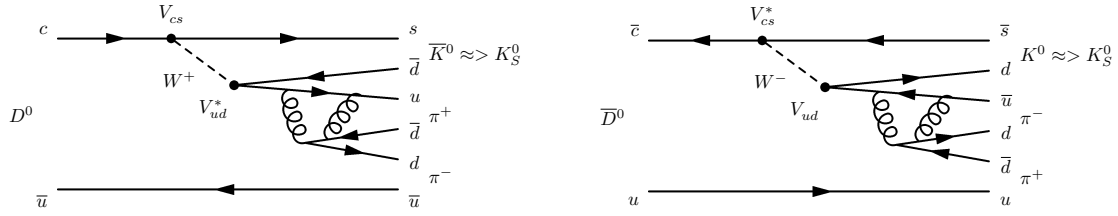

Figure 5.106: Feynman diagrams for the decays of (left) D^0 mesons and (right) $\overline{D}^0$ mesons to the final state $K^0_S\pi^+\pi^-$ that is employed in GGSZ/Dalitz-plot analyses of the decay chain $B^+ \to [K^0_S\pi^+\pi^-]_{\rm D}K^+$.

the decay $B^+ \to \overline{D}^0 K^+$ is real, and writing

$$\begin{aligned} A(B^+ \to \overline{D}^0 K^+) &\equiv A_B \\ A(B^+ \to D^0 K^+) &\equiv r_B A_B \, e^{i(\delta_B + \gamma)} \, , \end{aligned}$$

the decay amplitude for the full decay chain $B^+ \to [K^0_S \pi^+ \pi^-]_{\rm D} K^+$ is

$$A_{B^+}(s_+, s_-) \;=\; A_B \cdot A_{-+} \, e^{\delta_{-+}} \;+\; r_B A_B \, e^{i(\delta_B + \gamma)} \cdot A_{+-} \, e^{i\delta_{+-}}$$

and the differential decay rate for this process is given by

$$\begin{aligned} \frac{d\Gamma_{B^+}}{ds_+ ds_-} &= A_B^2 A_{-+}^2 \;+\; r_B^2 A_B^2 A_{+-}^2 \;+\; 2\, r_B A_B \, A_{-+} A_{+-} \, {\rm Re}\left\{ e^{i\,(\delta_{-+} + \delta_{+-})} \cdot e^{-i\,(\delta_B - \gamma)} \right\} \\ &= A_B^2 A_{-+}^2 \;+\; r_B^2 A_B^2 A_{+-}^2 \;+\; 2\, r_B A_B A_{-+} A_{+-} \;\cdot \\ &\qquad \left\{ \cos\left(\delta_{-+} - \delta_{+-}\right) \cos\left(\delta_B + \gamma\right) \;+\; \sin\left(\delta_{-+} - \delta_{+-}\right) \sin\left(\delta_B + \gamma\right) \right\} . \end{aligned}$$

For the charge-conjugated process,

$$\begin{aligned} \frac{d\Gamma_{B^-}}{ds_+ ds_-} &= A_B^2 A_{+-}^2 \;+\; r_B^2 A_B^2 A_{-+}^2 \;+\; 2\, r_B A_B A_{+-} A_{-+} \;\cdot \\ &\qquad \left\{ \cos\left(\delta_{+-} - \delta_{-+}\right) \cos\left(\delta_B - \gamma\right) \;+\; \sin\left(\delta_{+-} - \delta_{-+}\right) \sin\left(\delta_B - \gamma\right) \right\} \end{aligned}$$

and the difference between the Dalitz-plot distributions for decays of positive and negative B mesons provides sensitivity to the angle γ. However, the extraction of γ from these measurements requires knowledge of the magnitude and strong phase of the D^0 decay amplitude as a function of the Dalitz plot variables. Two approaches have been employed to extract this information from measurements. In model-dependent approaches, the $D^0 \to K^0_S \pi^+ \pi^-$ decay amplitude is parametrized by an analytical function that models known intermediate resonances as well as non-resonant components. The parameters of this model, including the magnitudes and strong phases of the amplitude, are then extracted from a fit to measured differential decay rates. Measurements of the differential decay rate were performed at BaBar and Belle. To distinguish between D^0 decays and $\overline{D}^0$ decays, event samples were used in which the neutral D mesons were produced via $D^{*+} \to D^0 \pi^+$ or $D^{*-} \to \overline{D}^0 \pi^-$ and the charge of the low-momentum pion was used to tag them as D^0 or $\overline{D}^0$.

A weakness of model-dependent analyses is the difficulty to quantify the systematic uncertainties that are related to the choice of the amplitude model. In model-independent analyses, such uncertainties are avoided by extracting the relevant parameters of the D^0 decay amplitude directly from measurements. This is achieved by performing a binned analysis in the Dalitz-plot variables. The Dalitz plot is divided into $2N$ regions i, that are defined symmetric around the line $s_+ = s_-$, i.e. under the exchange $s_+ \leftrightarrow s_-$. It is convenient to label the regions from 1 to N for $s_+ > s_-$ and from -1 to $-N$ for the corresponding region with $s_+ < s_-$. The binning leads to a loss in statistical precision of the measurement, since information on the variation of the strong phase within each of the regions is lost. This loss can be minimized by optimizing the number of regions and the definition of their shapes, taking into account the number of selected events and their distribution across the Dalitz plot as well as the expected variation of the strong phases across the Dalitz plot. A not optimal binning will increase the statistical uncertainty but it will not bias the result of the measurement. A concrete example of the binning employed in model-independent Dalitz-plot analyses in Belle and LHCb is shown in Figure 5.107. Averaging the D decay amplitude over region i and defining the coefficients

$$c_i \;\equiv\; \frac{\int_i A_{+-} A_{-+} \cos\left(\delta_{+-} - \delta_{-+}\right) ds_+ ds_-}{\sqrt{\int_i A_{+-}^2 \, ds_+ ds_- \;\cdot\; \int_i A_{+-}^2 \, ds_+ ds_-}} \, ,$$

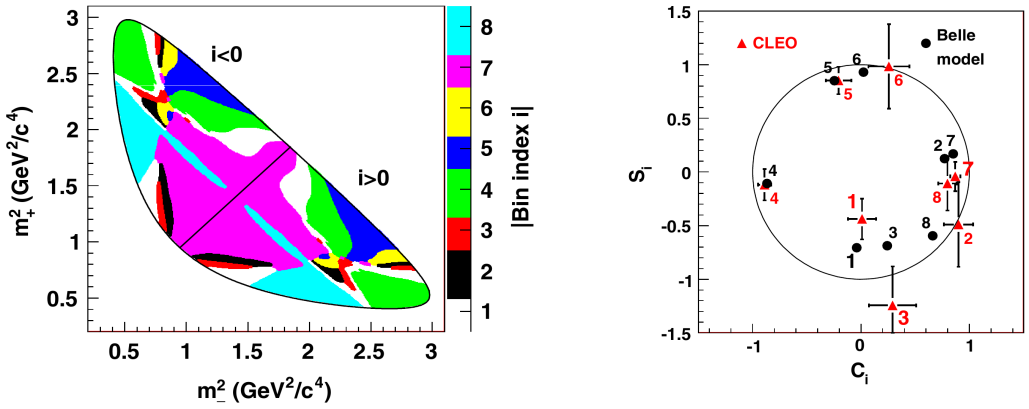

Figure 5.107: The left panel illustrates the definition of the sixteen Dalitz-plot regions employed in model-independent GGSZ/Dalitz-plot analyses of $B^+ \to [K^0_S\pi^+\pi^-]_{\rm D}K^+$ decays by the Belle and LHCb collaborations. The Dalitz-plot variables are denoted here as $m^2_- \equiv m^2(K^0_S\pi^-)$ and $m^2_+ \equiv m^2(K^0_S\pi^+)$. The regions for $m^2_+ > m^2_-$ are assigned negative indices and those for $m^2_+ < m^2_-$ are assigned positive indices. In the panel on the right, red triangles indicate the values of the parameters c_i and s_i in each of the bins as measured by CLEO-c while black dots indicate the corresponding values as calculated by integrating the isobar model obtained in the latest model-dependent Dalitz-plot analysis by the Belle collaboration. Reasonable agreement is found within the uncertainties of the measurement (from [421]).

$$s_i \equiv \frac{\int_i A_{+-}A_{-+}\sin(\delta_{+-}-\delta_{-+})\,ds_+ds_-}{\sqrt{\int_i A^2_{+-}\,ds_+ds_- \cdot \int_i A^2_{+-}\,ds_+ds_-}}$$

and

$$K_i \equiv \int_i A^2_{+-}\,ds_+ds_- \ ,$$

the expected number of $B^+ \to [K^0_S\pi^+\pi^-]_{\rm D}K^+$ events in region i is given by

$$N^+_i = h_{B^+}\left\{K_{-i} + r_B^2K_i + 2\sqrt{K_iK_{-i}}\,[c_ir_B\cos(\delta_B+\gamma) - s_ir_B\sin(\delta_B+\gamma)]\right\}$$

and the expected number of $B^- \to [K^0_S\pi^+\pi^-]_{\rm D}K^-$ events in this region is

$$N^-_i = h_{B^-}\left\{K_i + r_B^2K_{-i} + 2\sqrt{K_iK_{-i}}\,(c_ir_B\cos(\delta_B-\gamma) + s_ir_B\sin(\delta_B-\gamma))\right\} \ .$$

All parameters in these two equations can in principle be determined from a fit to the binned Dalitz-plot distributions for the $B^+ \to [K^0_S\pi^+\pi^-]_{\rm D}K^+$ and $B^- \to [K^0_S\pi^+\pi^-]_{\rm D}K^-$ candidates. Given the size of the currently available event samples, it is, however, advantageous to fix the coefficients K_i, c_i and s_i from independent measurements. The coefficients K_i can be measured via decay rates of flavour-specific D^0 decays, while measurements of c_i and s_i have been performed at CLEO-c [422]. CLEO-c was a e^+e^- charm factory that evolved from the symmetric $B\overline{B}$ factory, CLEO, at the e^+e^- collider CESR at Cornell. Operating the collider at a center-of-mass energy of 3.77 GeV, corresponding to the mass of the $\Psi(3770)$ resonance, large numbers of $D^0\overline{D}^0$ pairs were produced via the process $e^+e^- \to \Psi(3770) \to D^0\overline{D}^0$. Similar to the case of $B^0\overline{B}^0$ pairs from decays of the $\Upsilon(4S)$ resonance, the $D^0\overline{D}^0$ pairs were produced in a quantum-correlated state. This quantum entanglement allowed to extract the parameters c_i and s_i using a double-tagged method. One sample of events was collected in which both D mesons were reconstructed in the signal decay $K^0\pi^+\pi^-$. In this sample, the number of events where one D meson falls into the Dalitz-plot region i and the second D meson falls into region j is

$$M_{ij} = K_iK_{-j} + K_{-i}K_j - 2\sqrt{K_iK_jK_{-i}K_j}(c_ic_j + s_is_j) \ .$$

In a second sample of events, on D meson was reconstructed in the signal decay and the second D meson was reconstructed in a decay to a *CP* eigenstate, such as K^+K^-. Due to the quantum entanglement, the signal-side D meson then also decays as a *CP* eigenstate, its decay amplitude is given by $1/\sqrt{2}(A_{D^0} \pm A_{\overline{D}^0})$, and the number of events falling into bin i is

$$M_i \;=\; K_i \;+\; K_{-i} \pm 2\sqrt{K_i K_{-i}} \cdot c_i \;.$$

The combination of the two measurements allows to determine the coefficients c_i and s_i up to a two-fold ambiguity, which is due to a simultaneous reversal of the signs of all s_i. This ambiguity is resolved by a comparison with the results of model-dependent analyses of the strong phases.

In both model-dependent and model-independent GGSZ/Dalitz-plot analyses, fits to the Dalitz-plot variables are usually performed in terms of the Cartesian parameters

$$\begin{aligned} x_\pm &\equiv r_B \cos(\Delta_B \pm \gamma) \\ y_\pm &\equiv r_B \sin(\Delta_B \pm \gamma) \end{aligned}$$

to avoid potential biases on the fit results from the fact that the value of r_B is known to be small and bound to be positive. Moreover, the resulting uncertainties on $x_\pm$ and $y_\pm$ are closer to Gaussian distributed than those on r_B and γ, making it more straightforward to combine results from different measurements. The values of r_B and γ, and their uncertainties, are extracted by error propagation taking into account the correlation between $x_\pm$ and $y_\pm$. Analyses based on the GGSZ/Dalitz-plot method have so far provided the most stringent constraints on γ. However, systematic uncertainties related to the determination of the D decay parameters across the Dalitz plot will ultimately limit the precision that can be achieved using this approach, while the precision of results from combined GLW and ADS analyses is expected to continue to improve with increasing statistics.

All approaches discussed so far rely on the interference of tree decay amplitudes $B^\pm \to [f]_D K^\pm$ via intermediate D^0 and $\overline{D}^0$ mesons. An alternative approach to extract the CKM angle γ is via the measurement of the time-dependent *CP* asymmetry in the decay $B_s^0 \to D_s^\pm K^\pm$. The *CP* violating phase in this decay is given by $\gamma - 2\beta_s$, where β_s is the complex phase in B_s^0-$\overline{B}_s^0$ mixing, which is predicted in the Standard Model to be close to zero with good precision. Measurements of time-dependent *CP* violating asymmetries in the $B_s^0\overline{B}_s^0$ system will be described in the next chapter.

Measurements of the GLW observables, $A_{CP\pm}$ and $R_{CP\pm}$, in the decay $B^\pm \to DK^\pm$ have been published by the BaBar [423–425] and Belle [426] collaborations. The published Belle analysis was based on about 35% of their data collected at the $\Upsilon(4S)$ resonance and its results are not competitive with the most recent measurement published by the BaBar collaboration. Results from an updated Belle analysis using their full data set collected at the $\Upsilon(4S)$ resonance have been quoted in Ref. [427], but the corresponding analysis has not been published. The CDF [428] and LHCb [429] collaborations published measurements of the GLW observables A_{CP+} and R_{CP+} for D decays to *CP* even final states, where the CDF measurement is not competitive with the results published by the other three collaborations. Measurements of GLW observables have also been performed in other decay modes. The BaBar collaboration published measurements in the decays $B^\pm \to D^*K^\pm$ with $D^* \to D\pi^0$ or $D^* \to D\gamma$ [430,431] and in the decay $B^\pm \to DK^{*\pm}$ with $K^{*\pm} \to K^0_S\pi^\pm$ [432,433]. The Belle collaboration published a measurement in the decay mode $B^\pm \to D^*K^\pm$ with $D^* \to D\pi^0$ [426] and quoted updated results in Ref. [427]. Measurements of GLW observables in the decay $B^0 \to DK^{*0}$ with $K^{*0} \to K^+\pi^-$ have been published by the BaBar [434] and LHCb [435] collaborations.

Measurements of the ADS observables $R_{\rm ADS}$ and $A_{\rm ADS}$ in the decay $B^\pm \to DK^\pm$ with $D \to K^\pm\pi^\mp$ have been published by the BaBar [436,437], Belle [438], CDF [439] and LHCb [429] collaborations. The BaBar collaboration has also published measurements of these parameters in the decays $B^\pm \to D^*K^\pm$ with $D^* \to D\pi^0$ or $D^* \to D\gamma$ [436, 437] and $B^\pm \to DK^{*\pm}$ with

$K^{*\pm} \to K^0_S\pi^\pm$ [433,440]. The Belle collaboration quoted results for ADS parameters in the decay $B^\pm \to D^*K^\pm$ in Ref. [427], but did not publish the corresponding analysis. Measurements of ADS parameters have also been performed in $B^\pm \to DK^\pm$ with D decays to three- and four-body final states. The BaBar collaboration published a measurement in $D \to K^\mp\pi^\pm\pi^0$ [441, 442], while the LHCb collaboration published a measurement in $D \to K^\mp\pi^\pm\pi^+\pi^-$ [443]. Finally, measurements of ADS parameters in the decay mode $B^0 \to DK^{*0}$ with $K^{*0} \to K^+\pi^-$ have been published by the Belle [444] and LHCb [435] collaborations.

Model-dependent GGSZ/Dalitz-plot analyses in the decay $B^\pm \to DK^\pm$ with $D \to K^0_S\pi^+\pi^-$ were pioneered by the Belle collaboration [420,445,446] and have been pursued at BaBar [447–449] and LHCb [450]. The quoted BaBar and Belle publications also contained measurements in the decay modes $B^\pm \to D^*K^\pm$ with $D^* \to D\pi^0$ or $D^* \to D\gamma$ and in the decay mode $B^\pm \to DK^{*\pm}$ with $K^{*\pm} \to K^\pm\pi^0$, while the quoted BaBar and LHCb publications also included Dalitz-plot analyses of D decays to $K^0_SK^+K^-$. The BaBar collaboration also published model-dependent Dalitz-plot analyses in $B^\pm \to DK^\pm$ with D decays to the Cabibbo-suppressed final state $\pi^+\pi^-\pi^0$ [451] and in neutral B-meson decays $B^0 \to DK^{*0}$ with $K^{*0} \to K^+\pi^-$ and $D \to K^0_S\pi^+\pi^-$ [452].

Model-independent Dalitz-plot analyses in the decay $B^\pm \to DK^\pm$ with $D \to K^0_S\pi^+\pi^-$ were published by the Belle [421] and LHCb [453,454] collaboration, where Ref. [454] also contained a measurement in D decays to K^+K^-. The LHCb collaboration also published an analysis of charge asymmetries in the decay $B^\pm \to DK^\pm$ with $D \to K^0_SK^\pm\pi^\mp$ [455].

In the remainder of this section, selected GLW and ADS analyses from the B factories and LHCb will be described first, followed by model-dependent and model-independent GGSZ/Dalitz-plot analyses and a short discussion of the resulting constraints on the CKM phase γ.

5.5.1 Measurements of GLW observables

The most precise published measurements of GLW observables to date are those by the BaBar and LHCb collaborations in the decay $B^\pm \to DK^\pm$. The two analyses will be described here.

The latest BaBar measurement [425] of GLW observables in the decay $B^\pm \to DK^\pm$ is based on their full data set. Candidates were reconstructed in the *CP* even final states $[K^+K^-]_{\rm D}$ and $[\pi^+\pi^-]_{\rm D}$ and in the *CP* odd final states $[K^0_S\pi^0]_{\rm D}$ with $K^0_S \to \pi^+\pi^-$, $[K^0_S\phi]_{\rm D}$ with $\phi \to K^+K^-$ and $[K^0_S\omega]_{\rm D}$ with $\omega \to \pi^+\pi^-\pi^0$. The effect of *CP* violation in the $K^0\overline{K}^0$ system was neglected by assuming the K^0_S to be a purely *CP* even state. A geometric fit was performed to constrain the D daughter particles to a common vertex and candidates with a low χ^2 probability of this fit were rejected. Particle identification criteria as described in Section 4.1 were applied to distinguish between final-state kaons and pions. To reject backgrounds from random combinations of particles, a cut was applied on the opening angles between the flight directions of the D daughter particles in the rest frame of the D candidate and the flight direction of the D candidate in the rest frame of the B candidate. The cosine of this opening angle is strongly peaked at ±1 for random combinations of final-state particles, while it follows a flat distribution for signal. The invariant-mass distribution of D candidates is shown in Figure 5.108. Selected D candidates were combined with an additional track to form $B^\pm \to D\pi^\pm$ and $B^\pm \to DK^\pm$ candidates. In the case of the flavour-specific final state $[K\pi]_{\rm D}$, the charge of the accompanying kaon or pion was required to be opposite that of the kaon from the decay of the D candidate. The B candidate had to pass requirements on the two kinematic variables introduced in Section 4.1, namely its beam-energy substituted invariant mass, $m_{\rm ES}$, and the energy imbalance, ΔE. Event shape variables, combined into a Fisher discriminant, were employed to reject continuum background from non-$B\overline{B}$ events. The values of the GLW observables $R_{CP\pm}$ and $A_{CP\pm}$ were extracted from a simultaneous maximum likelihood fit to the measured distributions of $m_{\rm ES}$, ΔE and the Fisher discriminant for the selected signal candidates. The signal sample was divided into 24 categories for the two possible charges of the $B^\pm$ candidate, for

the six final states $[f]_{\rm D}$ considered in the analysis, and for $D\pi^\pm$ and $DK^\pm$ candidates. The kaon/pion identification criteria that were applied on the prompt hadron from the $B^\pm$ decay were tuned on collision data to yield a 2% probability for misidentifying a true pion for a kaon. The corresponding kaon identification efficiency was determined to be 77% from samples of simulated events. The likelihood fit function contained separate terms for $B^\pm \to DK^\pm$ and $B^\pm \to D\pi^\pm$ signal components, for irreducible backgrounds from charmless $B^\pm$ decays to the same final state particles as the signal, for other $B\overline{B}$ backgrounds, and for continuum background from non-$B\overline{B}$ events. The fraction of irreducible background was estimated from sidebands in the invariant-mass distribution of reconstructed D candidates and was fixed in the final fit. The GLW parameters were fixed in the fit to be identical for all *CP* even final states and for all *CP* odd final states. To reduce systematic uncertainties related to the knowledge of D branching fractions and differences in the reconstruction efficiencies for different final states, the GLW parameters $R_{CP\pm}$ were determined via the double ratio

$$R_{CP\pm} \;=\; \frac{\Gamma(B^+ \to D_{CP\pm}K^+) + \Gamma(B^- \to D_{CP\pm}K^-)}{\Gamma(B^+ \to D_{CP\pm}\pi^+) + \Gamma(B^- \to D_{CP\pm}\pi^-)} \;\times\; \frac{\Gamma(B^+ \to D^0\pi^+) + \Gamma(B^- \to \overline{D}^0\pi^-)}{\Gamma(B^+ \to D^0K^+) + \Gamma(B^- \to \overline{D}^0K^-)} \,.$$

The underlying assumption

$$R_{CP\pm}(B^\pm \to D\pi^\pm) \;\equiv\; \frac{\Gamma(B^+ \to D_{CP\pm}\pi^+) + \Gamma(B^- \to D_{CP\pm}\pi^-)}{\Gamma(B^+ \to D^0\pi^+) + \Gamma(B^- \to \overline{D}^0\pi^-)} \;=\; 1$$

neglects *CP* violating effects in the decay mode $B^\pm \to D\pi^\pm$ and a systematic uncertainty was assigned to take this approximation into account. As discussed in the introduction to this section, the assumption is valid to good approximation due to the small value of r_B in this decay mode. The result of the fit to the $m_{\rm ES}$ distributions for $B^\pm \to DK^\pm$ candidates is shown in Figure 5.109. In the calculation of $m_{\rm ES}$ and ΔE, the pion mass hypothesis was applied to the bachelor particle from the $B^\pm$ decay. For true $B^\pm \to DK^\pm$ decays, this leads to a shift in the calculated value of ΔE that depends on the momentum of the kaon. An event-by-event correction was applied to the fit function for the $B^\pm \to DK^\pm$ component to compensate for this effect. All other parameters used in the fit to describe the $m_{\rm ES}$ and ΔE distributions for the signal component were set to be identical for the $B^\pm \to DK^\pm$ and $B^\pm \to D\pi^\pm$ components. In this manner, the the parameters describing the signal shapes were determined with good precision from the large sample of $B^\pm \to D\pi^\pm$ candidates. The results obtained for the four GLW parameters are listed in Figure 5.111 together with those from other GLW analyses. The precision of the measurements was limited by statistical uncertainties. Leading contributions to the systematic uncertainties on the ratios R_{CP+} and R_{CP+} were found to be the uncertainty assigned for the assumption $R^\pi_{CP\pm} = 1$, effects related to the correction of the wrongly calculated value of ΔE for $B^\pm \to DK^\pm$ events, and possible biases from fixed parameters in the likelihood function. The systematic uncertainty on the asymmetries A_{CP+} and A_{CP-} was found to be dominated by effects related to the understanding of irreducible backgrounds, charge asymmetries in detection and particle identification efficiencies and again to the correction of the ΔE value for $B^\pm \to DK^\pm$ events.

The LHCb collaboration published [429] a simultaneous measurement of the GLW observables R_{CP+} and A_{CP+} and the ADS observables $R_{\rm ADS}$ and $A_{\rm ADS}$ in $B^\pm \to DK^\pm$ and $B^\pm \to D\pi^\pm$ decays, based on their 2011 data set corresponding to an integrated luminosity of 1 fb^{-1} collected in pp collisions at a center-of-mass energy of 7 TeV. Neutral D meson candidates were formed from two tracks with transverse momentum $p_{\rm T} > 0.25$ GeV/c that fulfilled kaon or pion identification criteria. A third track was added to form $B^\pm$ candidates. This last track was required to have transverse momentum $p_{\rm T} > 0.5$ GeV and momentum $5 < p < 100$ GeV to ensure good kaon/pion separation. The decay vertices of the $B^\pm$ and D candidates were determined from a kinematic fit constraining the mass of the D candidate to the nominal mass of the D^0 meson. The selection of $B^\pm$ candidates was based on a multivariate classifier,

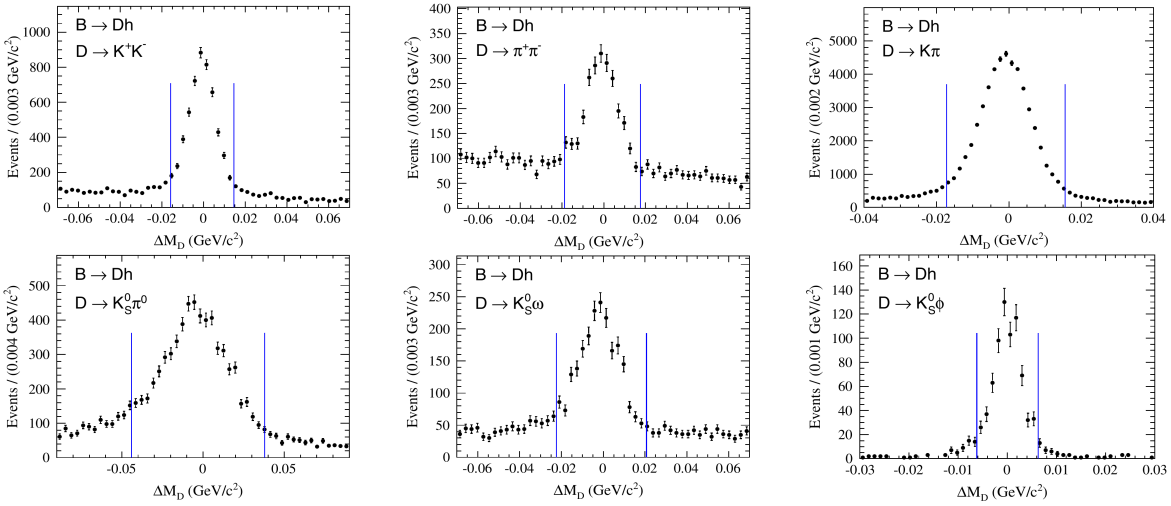

Figure 5.108: Invariant-mass distributions of D meson candidates reconstructed in the CP even final states K^+K^- and $\pi^+\pi^-$, the CP odd final states $K^0_S\pi^0$,$K^0_S\omega$ and $K^0_S\phi$, and the flavour-specific final state $K^\pm\pi^\pm$, as obtained in the BaBar measurement of GLW observables in the decay $B^\pm \to DK^\pm$. Vertical lines indicate the cuts that were applied to select candidates for the further analysis (from [425]).

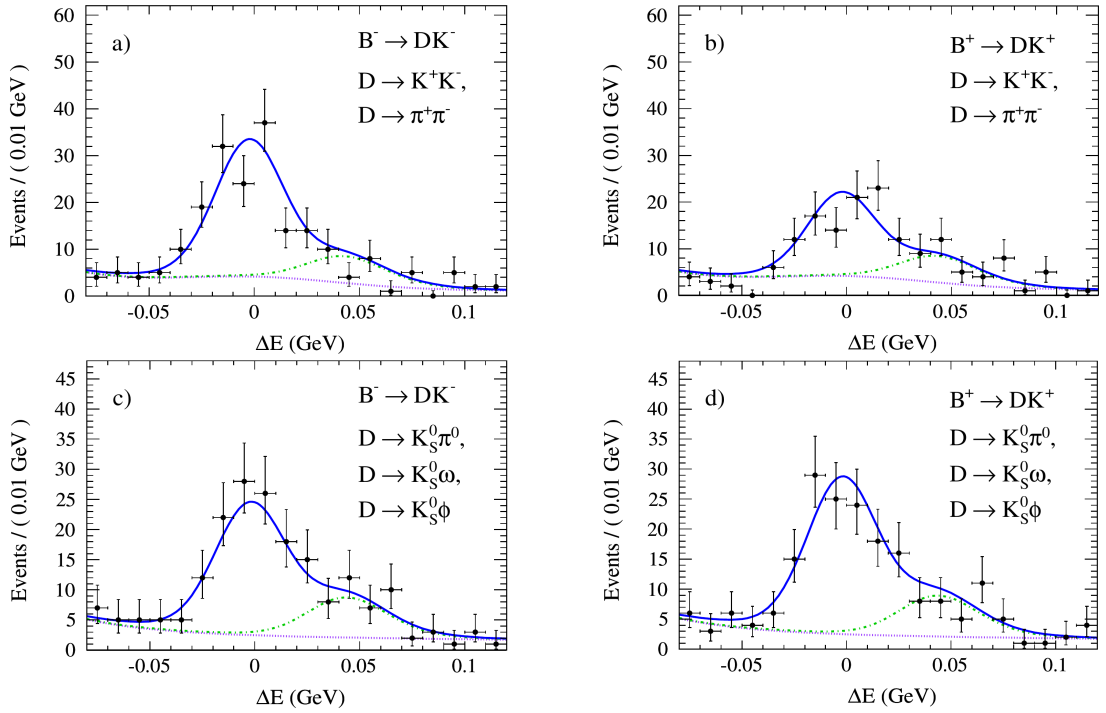

Figure 5.109: Measured ΔE distributions for selected (top left) $B^- \to D_{CP+}K^-$, (top right) $B^+ \to D_{CP+}K^+$, (bottom left) $B^- \to D_{CP-}K^-$ and (bottom right) $B^+ \to D_{CP-}K^+$ candidates from the BaBar measurement of GLW observables in the decay $B^\pm \to DK^\pm$. The results of the maximum likelihood fit to the data are superimposed, where the dash-dotted green line indicates the remaining $B^\pm \to D\pi^\pm$ component and the dotted purple line indicates the sum of all other background components. The shapes of the functions describing the $B^\pm \to DK^\pm$ and $B^\pm \to D\pi^\pm$ components were determined by simultaneously fitting the much larger $B^\pm \to D\pi^\pm$ sample (from [425]).

implemented as a Boosted Decision Tree algorithm. The algorithm used as input parameters the transverse momenta of the final state particles, the D and the $B^{\pm}$ candidate and their impact parameters with respect to the reconstructed pp collision vertex, the decay times, flight distances and vertex reconstruction quality of the D and $B^{\pm}$ candidates, and the opening angle between the reconstructed momentum vector of the $B^{\pm}$ candidate and the line connecting the pp collision vertex with its reconstructed decay vertex. Additional background suppression was achieved by means of an isolation variable, defined as $(p_{\mathrm{T}}(B) - \sum p_{\mathrm{T}})/(p_{\mathrm{T}}(B) + \sum p_{\mathrm{T}})$, where $\sum p_{\mathrm{T}}$ is the scalar sum of the transverse momenta of all reconstructed tracks in a cone around the momentum vector of the $B^{\pm}$ candidate, excluding the final state particles assigned to the $B^{\pm}$ candidate itself. Furthermore, a significant displacement of the reconstructed decay vertex of the D candidate from the reconstructed decay vertex of the $B^{\pm}$ candidate vertex was required to suppress background from charmless decays of B mesons and cross-feed where the prompt kaon or pion from the $B^{\pm}$ decay is swapped with one of the D decay products. Finally, vetoes on the invariant masses of different combinations of final-state particles were applied to suppress specific backgrounds. Candidates were vetoed if the invariant mass of the prompt particle from the decay of the $B^{\pm}$ candidate and the oppositely charged particle from the decay of the D candidate yielded an invariant mass compatible with J/ψ mass when the muon mass hypothesis was applied to both these particles. To suppresses cross-feed from Cabibbo-favoured to Cabibbo suppressed D decay modes, candidates were vetoed if the invariant mass of the $K\pi$ pair from the decay of the D candidate was compatible with the mass of the D^0 meson also when the kaon and pion mass hypotheses were swapped. The GLW and ADS observables were extracted from a binned maximum likelihood fit to the invariant-mass distributions of selected candidates in a total of 16 event categories, namely $B^+ \to DK^+$, $B^- \to DK^-$, $B^+ \to D\pi^+$ and $B^- \to D\pi^-$ decays followed by D decays to the two CP eigenstates, the favoured and the suppressed flavour-specific final states. The invariant-mass distributions measured in the decays to the CP eigenstates and in the favoured flavour-specific decay modes are shown in Figure 5.110. The results for the suppressed modes are shown in the discussion of ADS analyses below. The likelihood functions contained terms for correctly reconstructed $B^{\pm} \to DK^{\pm}$ signal and correctly reconstructed $B^{\pm} \to D\pi^{\pm}$ signal, for true $B^{\pm} \to D\pi^{\pm}$ events misidentified as $B^{\pm} \to DK^{\pm}$ and true $B^{\pm} \to DK^{\pm}$ events misidentified as $B^{\pm} \to D\pi^{\pm}$, for backgrounds from partially reconstructed decays of B mesons to final states including a D meson, and for combinatorial background. The parameters describing the shapes of these components were defined to be identical for the four D decay modes and were therefore precisely determined from the abundant favoured flavour-specific modes. Moreover, the ratio of the parameters describing the widths of the signals for correctly reconstructed $B^{\pm} \to DK^{\pm}$ events and correctly reconstructed $B^{\pm} \to D\pi^{\pm}$ events were also fixed in the fit. Two additional components were included in the likelihood function for the $[K^+K^-]_{\mathrm{D}}$ sample to describe backgrounds from $\Lambda_b^0 \to \Lambda_c^+ K^-$ and $\Lambda_b^0 \to \Lambda_c^+ \pi^-$ decays. The performance of the kaon/pion identification was estimated from a large control sample of $D^{*\pm} \to [\pi^{\pm}K^{\mp}]_{\mathrm{D}}\pi^{\pm}$ events, where the charge of the low-momentum pion from the D^* decay unambiguously identifies the identities of the kaon and the pion from the decay of the D meson. The probability to misidentify a true prompt pion from the $B^{\pm}$ decay for a kaon was estimated to be 3.8% for an 87.6% efficiency to correctly identify a true kaon. The results obtained for the GLW observables are listed in Figure 5.111, the results for the ADS observable will be discussed below. The precision of the measurement was limited by statistical uncertainties. The value of R_{CP+} was calculated via a double ratio in the same manner as described for the BaBar analysis above, and systematic uncertainty from the underlying assumption of vanishing CP violation in the decay $B^{\pm} \to D\pi^{\pm}$ was found to dominate the systematic uncertainty on R_{CP+}, together with the understanding of the kaon/pion identification performance and possible bias from fixing the relative width of the $B^{\pm} \to DK^{\pm}$ and $B^{\pm} \to D\pi^{\pm}$ signals in the fits to the invariant-mass distributions. The systematic uncertainty on A_{CP+} was found to be dominated by the understanding of possible charge asymmetries in reconstruction and particle identification efficiencies.

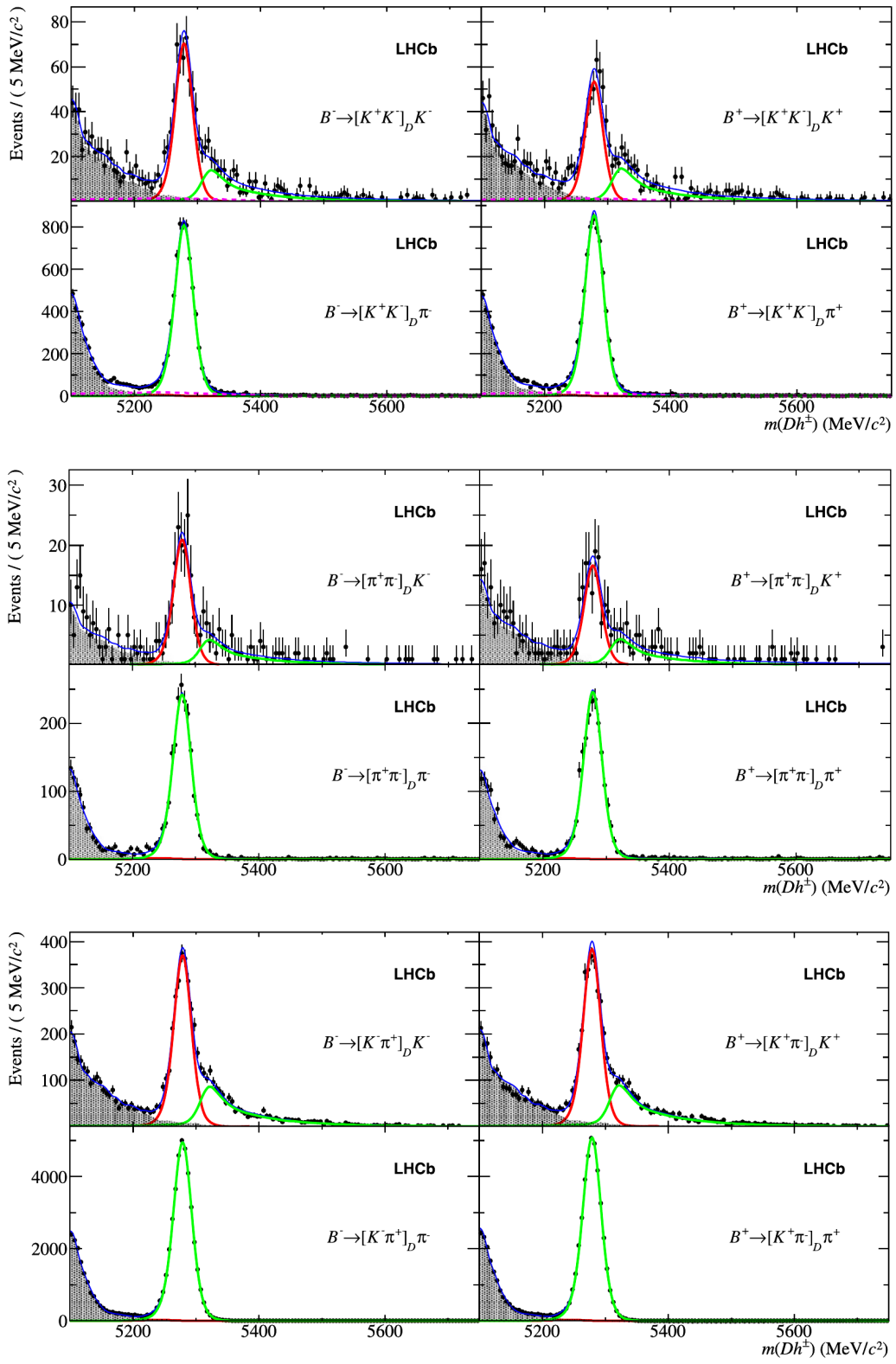

Figure 5.110: Invariant-mass distributions for selected $B^- \to [f]_{\rm D} K^-$, $B^+ \to [f]_{\rm D} K^+$, $B^- \to [f]_{\rm D} \pi^-$ and $B^+ \to [f]_{\rm D} \pi^+$ candidates reconstructed in the (top panels) *CP*-even final state $[K^+K^-]_{\rm D}$, the (middle panels) *CP*-even final state $[\pi^+\pi^-]_{\rm D}$ and the (bottom panels) favoured flavour-specific final states $[K^-\pi^+]_{\rm D}$ resp. $[K^+\pi^-]_{\rm D}$, from the LHCb measurement of GLW observables in these decay modes. The result of the maximum likelihood fit to the data is superimposed, where dark red lines indicate the $B^\pm \to DK^\pm$ component, light green lines indicate the $B^\pm \to D\pi^\pm$ component and shaded areas indicate the background component from partially reconstructed B-meson decays. The effect of the *CP* asymmetry in $B^\pm \to [K^+K^-]_{\rm D} K^\pm$ and $B^\pm \to [\pi^+\pi^-]_{\rm D} K^\pm$ is visible as a difference in signal yields between B^+ and B^- decays. As expected, *CP* violating effects in $B^\pm \to [K^+K^-]_{\rm D} \pi^\pm$ and $B^\pm \to [\pi^+\pi^-]_{\rm D} \pi^\pm$ are too small to be visible (from [429]).

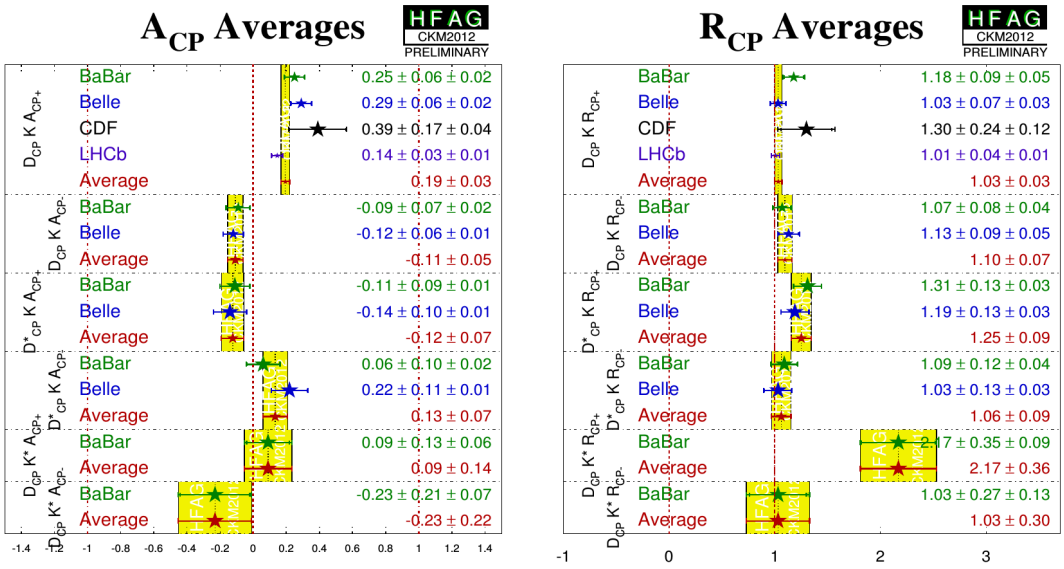

Figure 5.111: Measurements of the GLW observables, A_{CP} and R_{CP} in the decay modes $B^{\pm} \to DK^{\pm}$, $B^{\pm} \to D^{*}K^{\pm}$ and $B^{\pm} \to DK^{*\pm}$ and their respective averages, as compiled by the Heavy Flavour Averaging Group, including results available by the beginning of September 2014 (from [2]).

The latest measurements of GLW observables are summarized in Figure 5.111. The constraints on the CKM angle γ that have been derived from these measurements are discussed in the final part of this section.

5.5.2 Measurements of ADS observables

Both the BaBar [437] and the Belle [438] collaborations published measurements of ADS observables in the decay $B^{\pm} \to DK^{\pm}$ based on their full data sets collected at the $\Upsilon(4S)$ resonance. The related decay $B^{\pm} \to D\pi^{\pm}$ was employed as a control channel. Neutral D candidates were formed by a pair of oppositely charged kaon and pion candidates, where kaon/pion identification criteria were tuned to yield an efficiency of 85% for correctly identifying a true kaon and a probability of a few % to misidentify a true pion for a kaon. To suppress cross-feed from Cabibbo-favoured to Cabibbo suppressed D decay modes, candidates were vetoed if the invariant mass of the $K\pi$ pair was compatible with the mass of the D^0 meson also when the kaon and pion mass hypotheses were swapped. A kinematic fit constraining the invariant mass of the D candidate to the nominal mass of the D^0 meson was performed on the selected candidates. The D candidate was then combined with a charged kaon or pion to form $B^{\pm} \to DK^{\pm}$ and $B^{\pm} \to D\pi^{\pm}$ candidates. To suppress background from $B^{\pm} \to [K^{+}K^{-}]_{\mathrm{D}}\pi^{\pm}$ decays in which the $K^{\mp}\pi^{\pm}$ combination accidentally form an invariant mass close to the mass of the D^0 meson, $B^{\pm} \to [K^{\mp}\pi^{\pm}]_{\mathrm{D}}K^{\pm}$ candidates were rejected if the invariant mass of the $K^{\pm}K^{\mp}$ pair was compatible with the mass of the D^0 meson. The selection of signal candidates was based on the beam-energy substituted invariant mass of the $B^{\pm}$ candidate and its energy imbalance, and on a multivariate classifier combining event-shape variables and topological information of the event. In the case of the Belle analysis, also the standard flavour tagging algorithm was applied and its response included as an input to the multivariate classifier, since flavour tags of good quality signal B-meson decay products and therefore provide separation against non-$B\overline{B}$ background. Eight decay categories, namely the suppressed and allowed decays of B^{+} and B^{-} candidates to $DK^{\pm}$ and to $\pi^{\pm}$, were defined and the signal yields in each of these categories were determined from a simultaneous maximum-likelihood fit to the measured distributions of m_{ES}, ΔE and the multivariate classifier in BaBar, and to ΔE and the multivariate classifier in Belle. The likelihood function contained terms for signal, for peaking

$B\overline{B}$ backgrounds, for combinatorial $B\overline{B}$ background and for background from non-$B\overline{B}$ events. A significant background component in the $B^\pm \to DK^\pm$ samples was due to $B^\pm \to D\pi^\pm$ decays in which the prompt pion from the $B^\pm$ decay was misidentified as a kaon. The fraction of this background was fixed in the Belle analysis using an estimate of the pion misidentification probability determined from the samples of favoured modes in collision data. In the BaBar analysis, the fraction of this background was determined from samples of simulated events. Other sources of peaking backgrounds are charmless decays $B^\pm \to K^+K^-\pi^\pm$, in which the $K\pi$ pair is not produced via a D resonance, as well as remaining cross-feed from the favoured decay modes and from $B^\pm \to [K^+K^-]_{\rm D}\pi^\pm$ decays, which fail the mass vetoes described above. The fractions of these backgrounds were estimated from samples of simulated events in the BaBar analysis and from sidebands in the invariant-mass distributions of D candidates in the Belle analysis. Results were found to be compatible with zero. These backgrounds were therefore ignored in the analysis and a systematic uncertainty was assigned for this approximation. The $m_{\rm ES}$ distributions for the favoured and suppressed $B^\pm \to DK^\pm$ decay modes obtained in the BaBar analysis are shown in Figure 5.112 and the ΔE distributions for the suppressed $B^\pm \to DK^\pm$ decay modes obtained in the Belle analysis are shown in Figure 5.113. A hint for the suppressed decay mode $B^\pm \to [\pi^+K^-]_{\rm D}K^\pm$ with a significance corresponding to 2.1 Gaussian standard deviations was found in the BaBar analysis, while the Belle analysis found evidence for a signal corresponding to 4.1 Gaussian standard deviations. Separating the samples into $B^+ \to [\pi^+K^-]_{\rm D}K^+$ and $B^- \to [\pi^-K^+]_{\rm D}K^-$, both analyses found a large asymmetry in event yields between the two charge-conjugated decays. The obtained results for the ADS observables are listed in Figure 5.115. Given the low event yields, it is not surprising that the precision on the ADS observables was found to be limited by statistical uncertainties. Systematic uncertainties were found in both analyses to be dominated by the understanding of peaking backgrounds in the sample of suppressed decays.

The LHCb analysis of GLW and ADS observables [429] in the decay $B^\pm \to DK^\pm$ has been described above. The obtained invariant-mass distributions for the suppressed decay modes $B^+ \to [\pi^+K^-]_{\rm D}K^+$ and $B^- \to [\pi^-K^+]_{\rm D}K^-$ are shown in Figure 5.114. Combining the B^+ and B^- samples, a signal for the suppressed mode with a significance corresponding to 10.0 Gaussian standard deviations is found, making this the first observation of the decay mode with more than the canonical five standard deviations. Evidence for a non-vanishing *CP* asymmetry is found with a significance corresponding to 4.0 Gaussian standard deviations. The results of the measurement in terms of the ADS observables are listed in Figure 5.115.

The LHCb collaboration has also performed a measurement of ADS observables using four-body D decays $B^\pm \to [\pi^\pm K^\mp \pi^+\pi^-]_{\rm D}K^\pm$ [443], resulting in the first observation of ths decay mode, with a significance of the signal corresponding to 5.1 Gaussian standard deviations. A hint for a non-vanishing *CP* asymmetry was found with a significance corresponding to about two Gaussian standard deviations.

The latest measurements of ADS observables are summarized in Figure 5.115. The constraints on the CKM angle γ that have been derived from these measurements are discussed in the final part of this section.

5.5.3 Model-dependent GGSZ/Dalitz-plot analyses

The BaBar collaboration published a model-dependent GGSZ/Dalitz-plot analysis of the decay mode $B^\pm \to [K^0_S\pi^+\pi^-]_{\rm D}K^\pm$ using their full data set [449], while the latest analysis published by the Belle collaboration [446] was based on a data set corresponding to about 85% of the total integrated luminosity collected at the $\Upsilon(4S)$ resonance. In both analyses, K^0_S candidates were formed by combining two oppositely charged tracks from a common vertex that was required to be significantly displaced from the nominal e^+e^- interaction region. The K^0_S candidate was combined with another two oppositely charged pions to form D candidates. The $D^0 \to K^0_S\pi^+\pi^-$ decay amplitude was described by a coherent sum of two-body resonances and a non-resonant

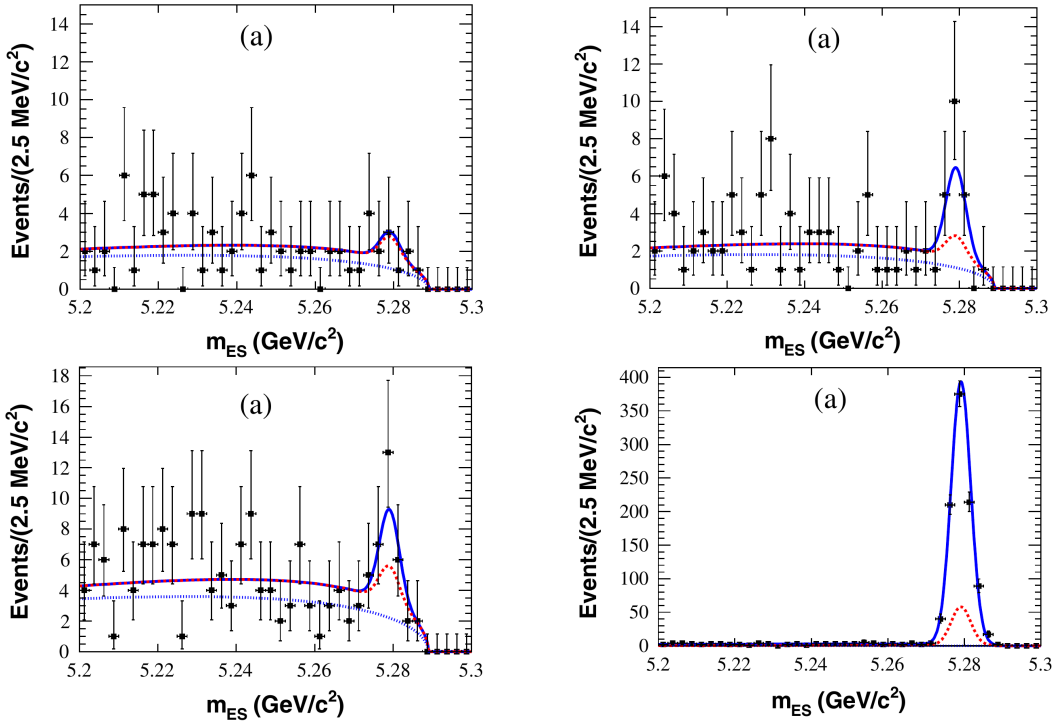

Figure 5.112: Measured distributions of the beam-energy substituted invariant mass for selected candidates in (top left) the suppressed decay mode $B^+ \to [\pi^\pm K^\mp]_{\rm D} K^+$, (top right) the charge-conjugated suppressed decay mode $B^- \to [\pi^\pm K^\mp]_{\rm D} K^-$, (bottom left) their sum, and (bottom right) the favoured modes $B^\pm \to [K^\pm \pi^\mp]_{\rm D} K^\pm$, from the latest BaBar measurement of the ADS observables $A_{\rm ADS}$ and $R_{\rm ADS}$ in these decay modes. The result of the maximum likelihood fit to the data is superimposed, where dotted lines indicate the non-$B\overline{B}$ background component and dashed lines indicate the sum of all background components (from [437]).

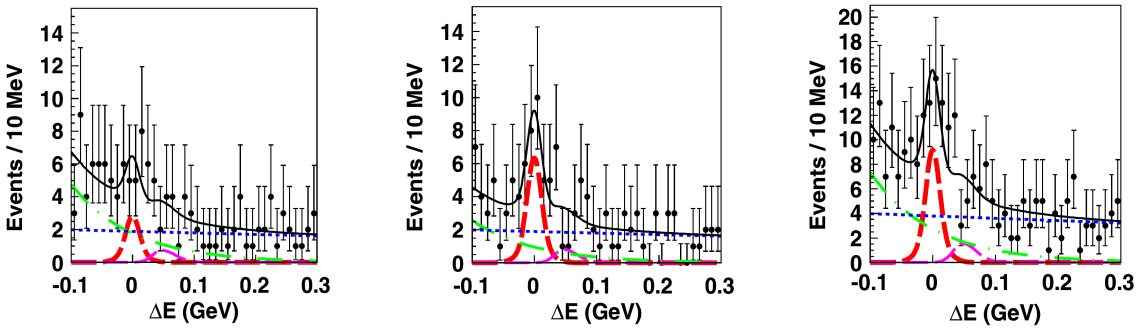

Figure 5.113: Measured ΔE distributions for selected candidates in (left) the suppressed decay mode $B^+ \to [\pi^\pm K^\mp]_{\rm D} K^+$, (middle) the charge-conjugated suppressed decay mode $B^- \to [\pi^\pm K^\mp]_{\rm D} K^-$, and (right) their sum, from the latest Belle measurement of the ADS observables $A_{\rm ADS}$ and $R_{\rm ADS}$ in these decay modes. The result of the maximum likelihood fit to the data is superimposed, where thick, red dashed lines indicate the signal component, thin, magenta dashed lines indicate the background component from misidentified $B^+ \to [\pi^\pm K^\mp]_{\rm D} \pi^\pm$, green dash-dotted lines indicate the component due to other $B\overline{B}$ background and blue dotted lines indicate the non-$B\overline{B}$ background component (from [438]).

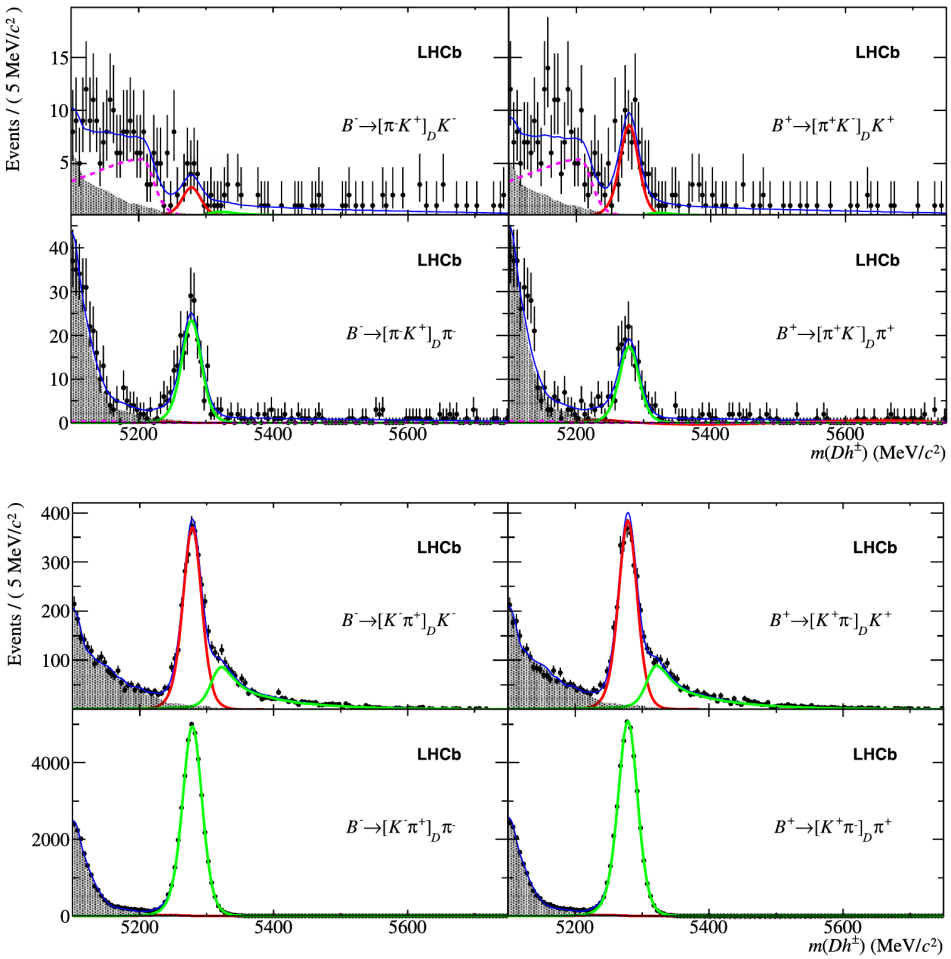

Figure 5.114: Invariant-mass distributions for selected $B^-\to[f]_{\rm D}K^-$, $B^+\to[f]_{\rm D}K^+$, $B^-\to[f]_{\rm D}\pi^-$ and $B^+\to[f]_{\rm D}\pi^+$ candidates reconstructed in the (top panels) suppressed and (bottom panels) favoured flavour-specific final states, from the LHCb measurement of ADS observables in these decay modes. The result of the maximum likelihood fit to the data is superimposed, where dark red lines indicate the $B^\pm\to[f]_{\rm D}K^\pm$ component, light green lines indicate the $B^\pm\to[f]_{\rm D}\pi^\pm$ component, dashed magenta lines indicate the background component from partially reconstructed $B^0_s\to\overline{D}^0K^-\pi^+$ and $\overline{B}^0_s\to D^0K^+\pi^-$ decays and shaded areas indicate the background component from other partially reconstructed B-meson decays (from [429]).

amplitude as

$$f(s_+,s-) \;=\; a_{\rm NR}e^{i\xi_{\rm NR}} \;+\; \sum a_k e^{i\xi_k}A_k(s_+,s_+)\;,$$

where $a_{\rm NR}$ is the magnitude and $\xi_{\rm NR}$ the phase of the non-resonant amplitude, a_k and ξ_k are the magnitude and phase of the k^{th} resonant amplitude, and $A_k(s_+,s_+)$ is the matrix element that describes the dynamics of this decay amplitude. The BaBar amplitude model included eight resonant components for $K^*(892)^+\pi^-$, $K^*(1680)^+\pi^-$, $K^*_2(1410)^+\pi^-$, $K^*(892)^-\pi^+$, $K^*_2(1410)^-\pi^+$, $K^0_S\rho(770)$, $K^0_S\omega(782)$ and $K^0_Sf_2(1270)$. A detailed description of the parametrizations of the matrix elements for each of these resonant amplitudes is given in Ref. [448]. The Belle amplitude model included an additional ten resonant components for $K^*(1410)^\pm\pi^\mp$, $K^*(1680)^\pm\pi^\mp$, $K^0_Sf_0(980)$, $K^0_Sf_0(1370)$, $K^0_S\rho(1450)$, $K^0_S\sigma_1$, and $K^0_S\sigma_2$. The magnitudes and phases of the amplitudes were extracted from fits to the Dalitz-plot distributions for samples of flavour-tagged $D^0\to K^0_S\pi^+\pi^-$ and $\overline{D}^0\to K^0_S\pi^+\pi^-$ decays. These samples were obtained from $D^{*\pm}\to D\pi^\pm$ decays in which the charge of the low-momentum pion from the decay of the D^* meson tags the flavour of the accompanying D meson as a D^0 or $\overline{D}^0$. Large samples of such decays were available since $D^{*\pm}$ mesons were copiously produced at

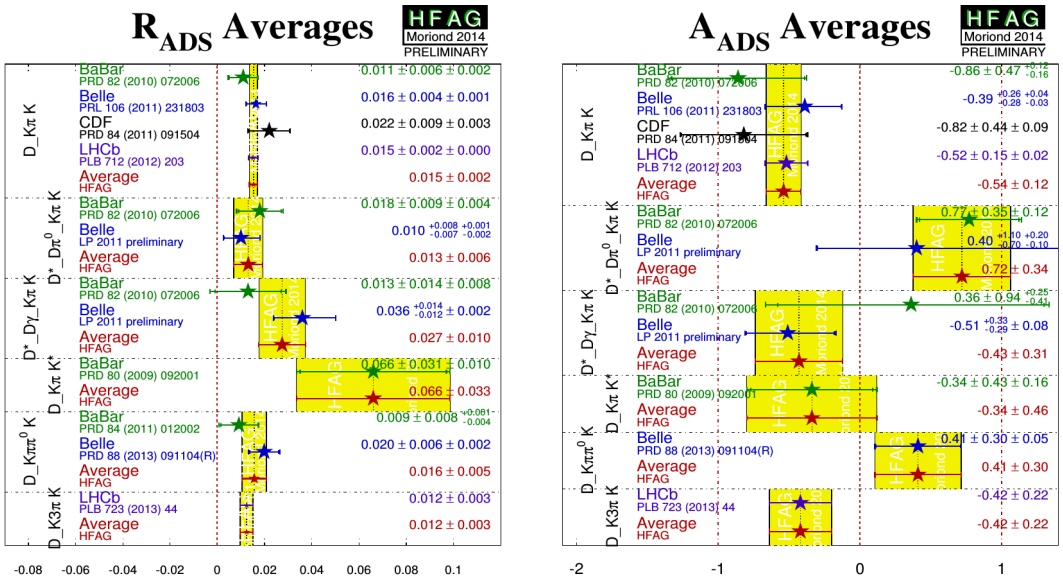

Figure 5.115: Measurements of ADS observables $A_{\rm ADS}$ and $R_{\rm ADS}$ in the decay modes $B^\pm \to DK^\pm$, $B^\pm \to D^*K^\pm$ and $B^\pm \to DK^{*\pm}$ and their respective averages, as compiled by the Heavy Flavour Averaging Group including results available by the beginning of September 2014 (from [2]).

the B factories via the continuum process $e^+e^- \to c\bar{c}$. The measured Dalitz-plot distribution for the flavour-tagged sample from the Belle analysis is shown in Figure 5.116 together with the result of the amplitude fit. In both the Belle and the BaBar analyses, the fits took into account efficiency variations and variations of backgrounds across the Dalitz plot as well as the finite momentum resolution of the measurement. Efficiency variations were estimated from simulation. For the GGSZ analysis itself, $B^\pm \to [K^0_S\pi^+\pi^-]_{\rm D}K^\pm$ candidates where selected by combining a neutral D candidate with a track identified as a charged kaon. As usual, the selection of $B^\pm$ candidates was based on the beam-energy substituted invariant mass, $m_{\rm ES}$, and the energy imbalance, ΔE, and event-shape variables were employed to suppress non-$B\overline{B}$ background. The measured $m_{\rm ES}$ and ΔE distributions from the two analyses are shown in Figures 5.118 and 5.119, respectively. The resulting Dalitz-plot distributions for B^+ and B^- candidates are shown in Figure 5.121. The Cartesian observables, $x_\pm$ and $y_\pm$, were extracted from maximum likelihood fits to $m_{\rm ES}$, ΔE, the event-shape variables, and the Dalitz-plot variables for the selected B^+ and B^- samples. The fit functions contained components for the signal component, for background from $B^\pm \to D\pi^\pm$ decays in which the prompt pion from the decay of the $B^\pm$ meson is misidentified as a kaon, for other $B\overline{B}$ background, and for non-$B\overline{B}$ background. In the Belle analysis, the non-$B\overline{B}$ background component was further split into separate contributions from events with and without charm. The obtained results for the observables $x_\pm$ and $y_\pm$ are listed in Figure 5.122. The precision of the measurements was limited by statistical uncertainties. Leading experimental systematic uncertainties were related to the understanding of background shapes derived from samples of simulated events, the relative background fractions, and the understanding of efficiency variations across the Dalitz plot. Systematic uncertainties related to the amplitude model were not quoted for the observables $x_\pm$ and $y_\pm$, but they dominated the systematic uncertainties quoted for the values of γ and r_B that were derived from these measurements.

The LHCb collaboration published a model-dependent GGSZ/Dalitz-plot analysis based on their 2011 data set, corresponding to an integrated luminosity of 1 fb^{-1} collected in pp collisions at a center-of-mass energy of 7 TeV. The decay mode $B^\pm \to [K^0_S\pi^+\pi^-]_{\rm D}\pi^\pm$ was employed as a control channel to measure acceptance and efficiency variations across the phase space. This decay mode has a similar topology but higher branching fraction than the signal mode and

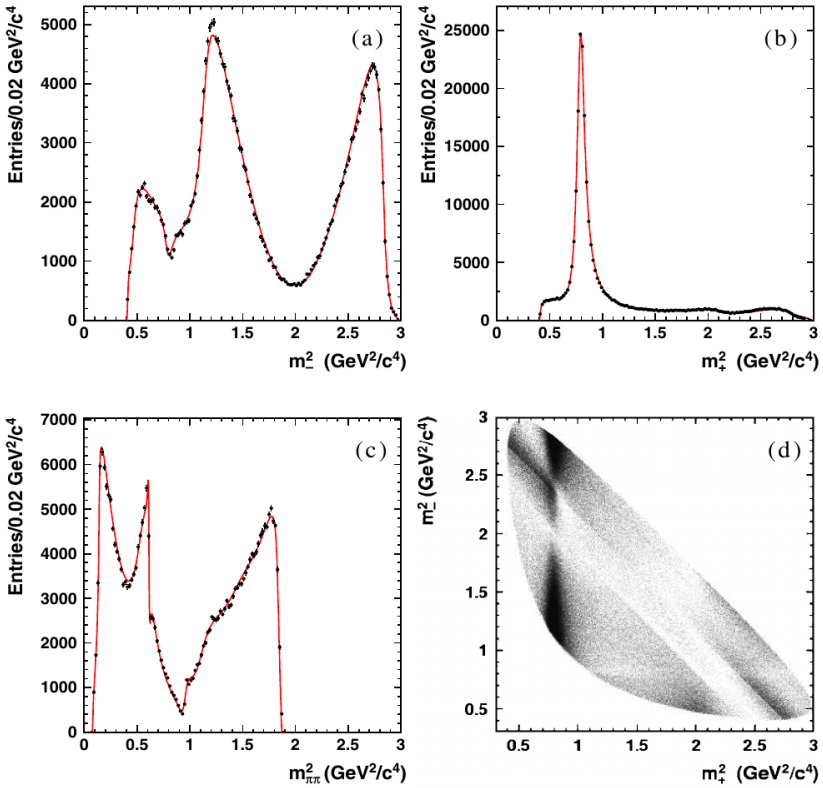

Figure 5.116: Distributions of the squared invariant masses for (top left) $K^0_S\pi^-$, (top right) $K^0_S\pi^+$ and (bottom left) $\pi^+\pi^-$ pairs and (bottom right) the resulting Dalitz-plot for the $D^{*-} \to [K^0_S\pi^+\pi^-]_D\pi^-$ sample from which the parameters of the isobar model for the model-dependent GGSZ/Dalitz-plot analyses in Belle was derived. The result of the fit to the data is superimposed in the invariant-mass projections (from [445]).

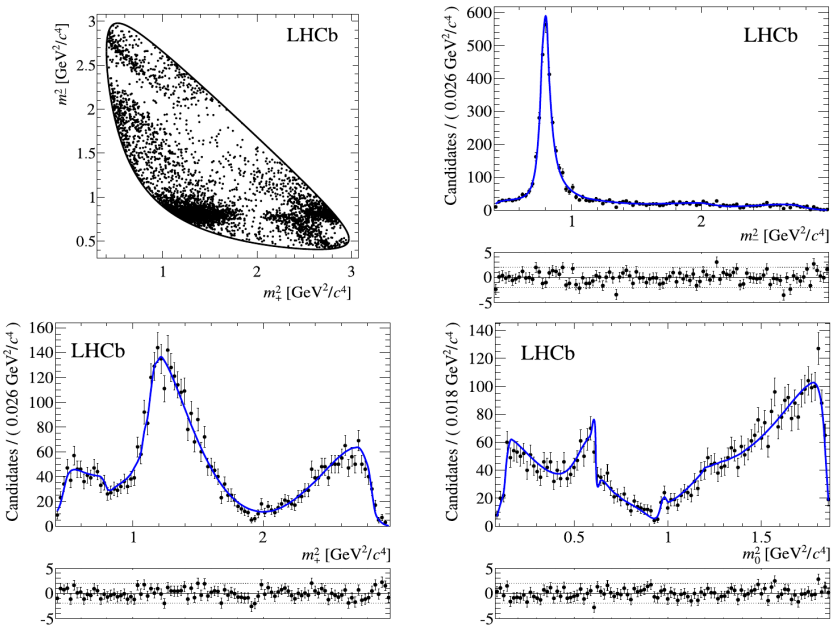

Figure 5.117: Dalitz-plot distribution and projections of the squared invariant masses and distributions of the squared invariant masses of $K^0_S\pi^-$, $K^0_S\pi^+$ and $\pi^+\pi^-$ pairs for selected $B^- \to [K^0_S\pi^+\pi^-]_D\pi^-$ candidates from which the parameters of the amplitude model for the model-dependent GGSZ/Dalitz-plot analysis in LHCb was derived. The result of the fit of the BaBar amplitude model to the data is superimposed in the invariant-mass projections (from [450]).

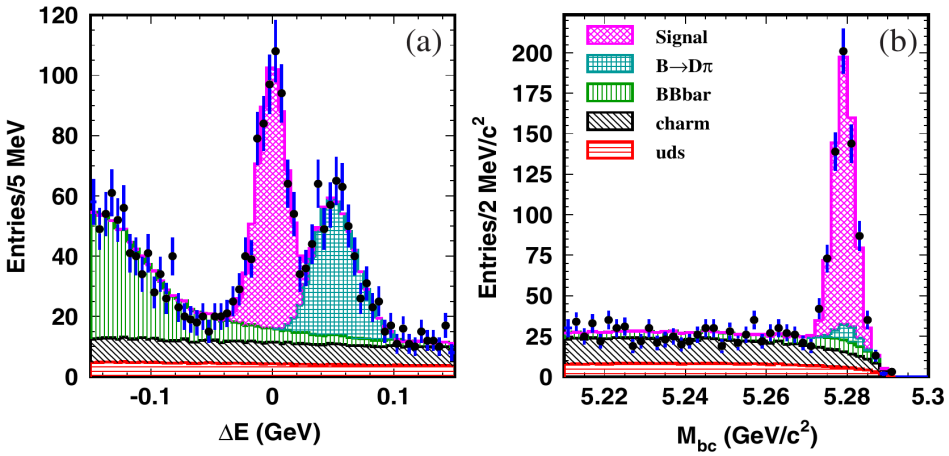

Figure 5.118: Measured distribution of (left) the energy imbalance and (right) the beam-energy substituted invariant mass for selected $B^\pm \to [K^0_S\pi^+\pi^-]_D K^\pm$ candidates from the latest model-dependent GGSZ/Dalitz-plot analysis in Belle. The results of the maximum-likelihood fit to the data are superimposed, where shaded areas indicate the different signal and background components as denoted in the plot legend (from [446]).

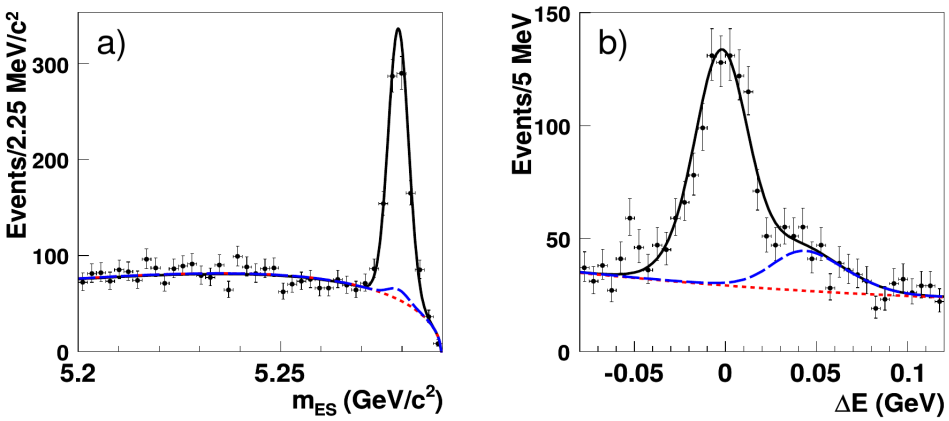

Figure 5.119: Measured distribution of (left) the beam-energy substituted invariant mass and (right) the energy imbalance for selected $B^\pm \to [K^0_S\pi^+\pi^-]_D K^\pm$ candidates from the latest model-dependent GGSZ/Dalitz-plot analysis in BaBar. The results of the maximum-likelihood fit to the data are superimposed, where dashed blue lines indicate the background component from misidentified $B^\pm \to D\pi^\pm$ candidates and red dotted lines indicate the sum of all other background components (from [449]).

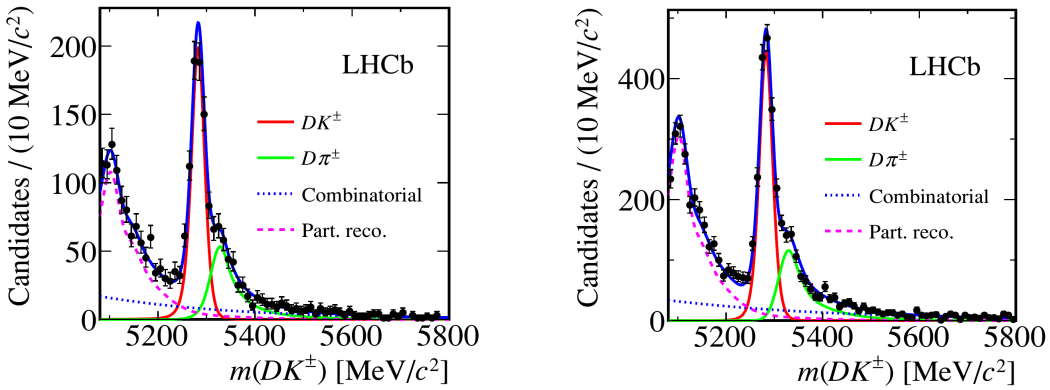

Figure 5.120: Invariant-mass distributions for selected $B^\pm \to [K^0_S\pi^+\pi^-]_D K^\pm$ candidates reconstructed using (left) "long" and (right) "downstream" K^0_S candidates from the model-independent GGSZ/Dalitz-plot analysis in LHCb. The result of the maximum-likelihood fit to the data is superimposed, with the different fit components indicated as denoted in the plot legend (from [454]).

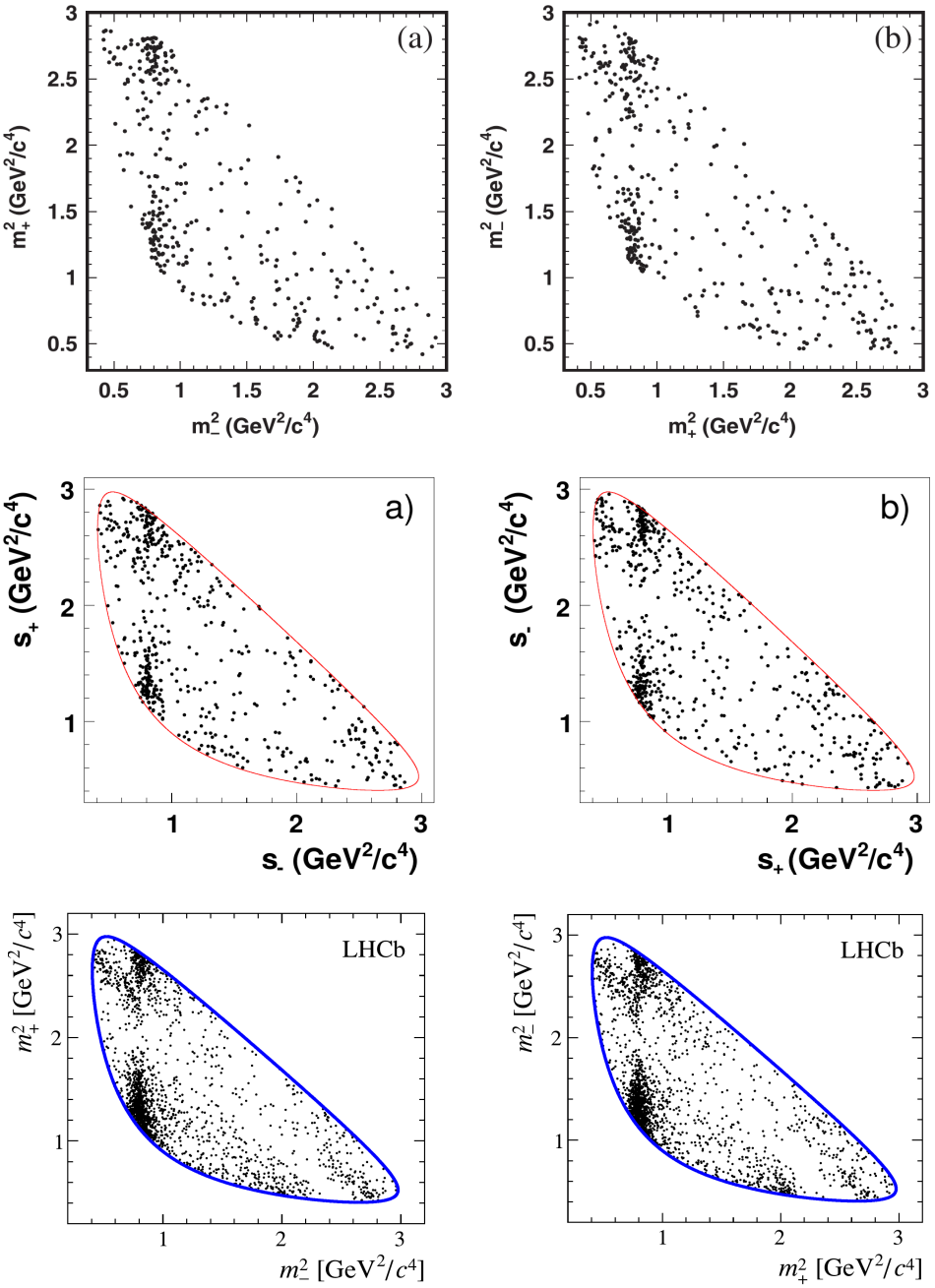

Figure 5.121: Dalitz-plot distributions for selected (left) $B^+ \to [K^0_S\pi^+\pi^-]_D K^+$ and (right) $B^- \to [K^0_S\pi^+\pi^-]_D K^-$ candidates from (top) the latest Belle model-dependent analysis based on about 85% of the full Belle data set, (middle) the latest BaBar model-dependent analysis based on the full BaBar data set and (bottom) the LHCb model-independent analysis based on the combined run I data set (from [446, 449, 454]).

CP violating effects are expected to be small compared to the precision that the measurement could aim for. Two types of $K^0_S \to \pi^+\pi^-$ candidates were employed in the analysis: for "long" candidates, the tracks of both final-state pions were reconstructed using information from the vertex locator, while for "downstream" candidates no information from the vertex locator was used in the reconstruction of these tracks. "Downstream" candidates are typically due to K^0_S mesons that decay outside the acceptance of the vertex locator. They are less precisely reconstructed than "long" K^0_S candidates, leading to worse vertex and invariant mass resolutions. Selected K^0_S candidate were combined with a pair of oppositely charged tracks to form neutral D candidates and these were combined with another track that was required to have good associated particle identification information to form $B^\pm \to [K^0_S\pi^+\pi^-]_{\rm D}K^\pm$ signal candidates or $B^\pm \to [K^0_S\pi^+\pi^-]_{\rm D}\pi^\pm$ candidates for the control sample. The selection of candidates for both samples was based on kinematic and topological properties of the decay chain, such as the impact parameters of the final-state particles with respect to the reconstructed *pp* collision vertex, the invariant masses of the $B^\pm$, D and K^0_S candidates, their reconstructed momentum vectors and the displacement of their reconstructed decay vertices. The decay vertex of the K^0_S candidate was required to be well separated from the decay vertex of the D candidate, which in turn was required to be downstream of the $B^\pm$ vertex. The $B^\pm$ vertex had to be well separated from *pp* collision vertex. Moreover, the reconstructed momentum vectors of the K^0_S and $B^\pm$ candidates were required to have a small opening angle with respect to the lines connecting the *pp* collision vertex and the respective decay vertices. To improve the resolution on the measurement of Dalitz-plot variables, a kinematic fit was performed on the selected candidates, constraining the invariant masses of the K^0_S and D candidates to the known masses of the K^0_S meson and the D^0 meson and constraining the $B^\pm$ momentum vector to point back to the *pp* collision vertex. Possible background contributions in the sample of selected candidates were estimated from samples of simulated events. The dominating background contributions were found to be due to $B^\pm \to [K^0_S\pi^+\pi^-]_{\rm D}\pi^\pm$ decays in which the prompt pion from the decay of the $B^\pm$ meson was misidentified as a kaon, and partially reconstructed decays including a true $D \to K^0_S\pi^+\pi^-$ decay, such as $B^\pm \to D^*K^\pm$ followed by $D^* \to D\pi^0$ or $D^* \to D\gamma$, where the slow pion or the photon escapes detection, or $B^0 \to DK^{*0}$, $B^0_s \to DK^{*0}$ or $B^\pm \to D\rho^\pm$, where a kaon or pion from the decay of the K^{*0} or $\rho^\pm$ escaped detection. The fraction of these backgrounds was estimated from a maximum likelihood fit to the invariant-mass distributions of the selected candidates. This fit was performed separately for the samples reconstructed using "long" and "downstream" K^0_S candidates to account for the different invariant-mass resolutions in the two samples. The fraction of $B^\pm \to D\pi^\pm$ background relative to the signal yield was fixed in the fits using the known ratio of the branching fractions for the two decay modes and measured kaon/pion identification efficiencies and misidentification probabilities. The kaon/pion identification performance was measured from collision data employing large samples of $D^{*\pm} \to [K^\mp\pi^\pm]_{\rm D}\pi^\pm$ decays, in which the true identity of the two daughter particles from the D decay is given by the charge of the accompanying prompt low-momentum pion from the decay of the D^* meson. The signal and background fractions determined from the fit to the invariant-mass distributions were then fixed in the fit to the Dalitz-plot distributions to extract the Cartesian observables $x_\pm$ and $y_\pm$. The Dalitz-plot fit used the BaBar amplitude model as measured in [456] and the $B^\pm \to [K^0_S\pi^+\pi^-]_{\rm D}\pi^\pm$ sample was employed to estimate efficiency variations across the Dalitz plot. The results obtained for $x_\pm$ and $y_\pm$ are listed in Figure 5.122. The precision of the measurement was limited by statistical uncertainties. Leading contributions to the systematic uncertainty were found to be due to the understanding of the fraction of combinatorial background in the selected candidate sample, efficiency variations across the Dalitz plot and a small bias in the fit results that was observed in simulated experiments.

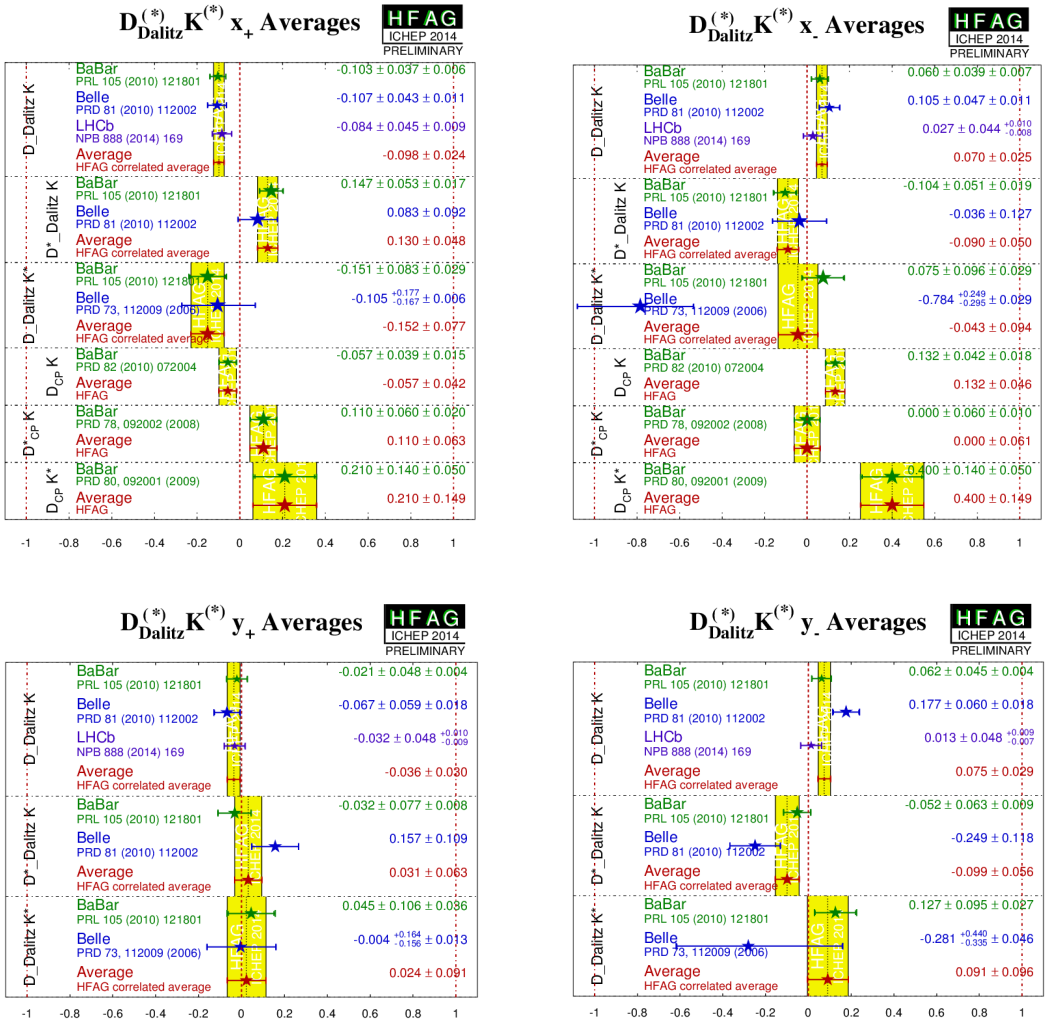

Figure 5.122: Measurements of the Cartesian observables $x_\pm$ and $y_\pm$ as obtained in model-dependent GGSZ/Dalitz-plot analyses in the decay modes $B^\pm \to [K^0_S\pi^+\pi^-]_D K^\pm$, $B^\pm \to D^* K^\pm$ and $B^\pm \to D K^{*\pm}$ and their respective averages, as compiled by the Heavy Flavour Averaging Group (from [2]).

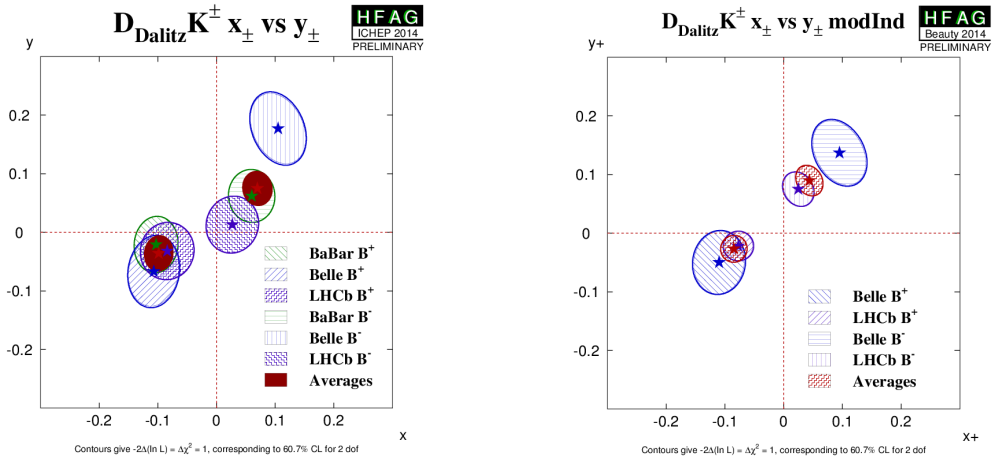

Figure 5.123: Confidence-regions in the $x_\pm$ and $y_\pm$ plane from (left) model dependent and (right) model independent GGSZ/Dalitz-plot analyses in the decay mode $B^\pm \to [K^0_S\pi^+\pi^-]_D K^\pm$, and their respective averages, as compiled by the Heavy Flavour Averaging Group (from [2]).

5.5.4 Model-independent GGSZ/Dalitz-plot analyses

Model-independent GGSZ/Dalitz-plot analyses in the decay mode $B^\pm \to [K^0_S\pi^+\pi^-]_{\rm D}K^\pm$ have been published by the Belle [421] and LHCb [454] collaborations.

The Belle analysis [421] was based on their full data set collected at the $\Upsilon(4S)$ resonance and employed the Dalitz-plot binning shown in Figure 5.107. The values of the coefficients s_i and c_i were taken from the already mentioned CLEO-c measurement [422]. The coefficients K_i were measured using large samples of flavour-tagged $D^0 \to K^0_S\pi^+\pi^-$ and $\overline{D}^0 \to K^0_S\pi^+\pi^-$ candidates, which were obtained from $D^{*\pm} \to D\pi^\pm$ decays in which the charge of the low-momentum pion from the decay of the D^* meson tags the flavour of the accompanying D meson as a D^0 or $\overline{D}^0$. The selection of K^0_S candidates and neutral D candidates was similar to that described for the model-dependent analyses described above. A clean sample of $D^{*\pm} \to D\pi^\pm$ candidates was selected based on the invariant mass of the D candidate and the difference between the invariant masses of the D^* candidate and the D candidate. The selection of $B^\pm \to DK^\pm$ candidates was based on the beam-energy substituted invariant mass, $m_{\rm ES}$, and the energy imbalance, ΔE, of the $B^\pm$ candidate and two event-shape variables. The values of the Cartesian coordinates $x_\pm$ and $y_\pm$ were extracted from a combined four-dimensional maximum likelihood fit to these four selection variables. The likelihood function contained terms for the signal component, for a background component from $B^\pm \to [K^0_S\pi^+\pi^-]_{\rm D}\pi^\pm$ decays in which the prompt pion from the decay of the $B^\pm$ meson was misidentified as a kaon, for peaking backgrounds from other decays of B mesons, which were found to be dominated by $B^\pm \to D^*\pi^\pm$ decays in which the pion or photon from the decay $D^* \to D\pi$ or $D^* \to D\gamma$ escaped detection, for combinatorial background from $B\overline{B}$ events and for combinatorial background from non-$B\overline{B}$ events. The total signal yield was found to be 55% larger than that obtained in the model-dependent GGSZ/Dalitz-plot analysis described above. An increase in event yields by about 17% is expected due to the use of a larger data set in this analysis, the remainder was attributed to improvements in track reconstruction algorithms. Reconstruction efficiencies and efficiency variations as a function of the Dalitz-plot variables cancel in the determination of $x_\pm$ and $y_\pm$ as long as the efficiency variations are identical for the signal sample and for the samples employed in the calculation of the coefficients K_i, s_i and c_i. In the case of the parameters K_i, this was achieved to good approximation by selecting the sample of $D^{*\pm} \to D\pi^\pm$ candidates such that the average momentum of the D candidates in this sample matched that in the signal sample. In the case of the coefficients s_i and c_i, the Belle efficiency profile measured in the model-dependent analysis described above was employed to apply appropriate corrections to the values published by CLEO-c. The results of this measurement in terms of the parameters $x_\pm$ and $y_\pm$ are shown in Figure 5.123. Again, the precision of the measurement is limited by statistical uncertainty. The largest contributions to the systematic uncertainties are due to the knowledge of the coefficients s_i and c_i, the modeling of the signal component in the likelihood fit, and the understanding of the $B\overline{B}$ background contamination in the selected signal sample. The combined systematic uncertainties quoted for $x_\pm$ and $y_\pm$ are about 50% larger than the experimental systematic uncertainties quoted for the model-dependent analysis described above. However, the systematic uncertainties quoted for the model-dependent analysis did not include the uncertainty due to the model dependence.

The model-independent LHCb analysis [454] was based on the combined run-I data set, consisting of a total integrated luminosity of 3 fb^{-1} collected in pp collisions at center-of-mass energies of 7 TeV and 8 TeV. The same Dalitz-plot binning scheme was employed as in the Belle analysis described in the previous paragraph, and the values of the coefficients s_i and c_i were also taken from the CLEO-c measurement [422]. The values of the coefficients K_i were measured using a large sample of flavour-tagged $D^0 \to K^0_S\pi^+\pi^-$ and $\overline{D}^0 \to K^0_S\pi^+\pi^-$ candidates produced via semileptonic decays $B \to D^{*\pm}\mu^\mp\nu_\mu$ with $D^{*\pm} \to D\pi^\pm$. The flavour of the neutral D meson is tagged here both by the charge of the muon from the decay of the B meson and by the charge of the low-momentum pion from the decay of the D^* meson. The selection of

$B^\pm \to [K^0_S\pi^+\pi^-]_{\rm D}K^\pm$ signal candidates and a $B^\pm \to [K^0_S\pi^+\pi^-]_{\rm D}\pi^\pm$ control sample was based on similar topological and kinematic variables as those employed in the model-dependent LHCb analysis described above. To further improve the discrimination power, several of these variables were combined here into a multivariate classifier using a Boosted Decision Tree algorithm. Selection criteria for the flavour-tagged sample from semileptonic decays of B mesons were chosen to be as similar as possible to those for the signal candidates to mimimize differences in the respective efficiency profiles as a function of the Dalitz-plot variables. All samples included "long" K^0_S candidates and "downstream" K^0_S candidates as defined in the description of the model-dependent analysis above. The signal yields in the flavour-tagged sample were determined for each Dalitz-plot region from a combined fit to the distributions of the invariant mass of the selected D candidates and of the difference between the invariant masses of the D^* candidate and the D candidate. The two distributions are shown in Figure 5.120 together with the result of the fit. The $B^\pm \to [K^0_S\pi^+\pi^-]_{\rm D}K^\pm$ signal yields were extracted from a combined maximum likelihood fit to the invariant-mass distributions for the selected $B^\pm \to [K^0_S\pi^+\pi^-]_{\rm D}K^\pm$ and $B^\pm \to [K^0_S\pi^+\pi^-]_{\rm D}\pi^\pm$ candidates. The likelihood function contained terms for the signal component, for a background component from $B^\pm \to D\pi^\pm$ decays in which the prompt pion from the decay of the $B^\pm$ meson was misidentified as a kaon, a background component for partially reconstructed decays of B mesons and a component for combinatorial background from random combinations of tracks. The fraction of background from misidentified $B^\pm \to D\pi^\pm$ decays was fixed in the fit to a value calculated from the signal yields measured in the $B^\pm \to D\pi^\pm$ sample and the kaon/pion identification efficiencies and misidentification probabilities. Like in the model-dependent analysis, the kaon/pion identification performance was determined from collision data using large samples of flavour-specific $D^{*\pm} \to [\pi^\pm K^\mp]_{\rm D}\pi^\pm$ decays. The probability to misidentify a true pion from the decay $B^\pm \to D\pi^\pm$ for a kaon was estimated to be 4% for an efficiency of 86% to correctly identify a true kaon from the decay $B^\pm \to DK^\pm$. The fit was performed in a first step to the full data sample, integrated over the Dalitz-plot variables, to determine the parameters of the likelihood function. To extract the Cartesian observables $x_\pm$ and $y_\pm$, the fit was then repeated separately for each of the Dalitz-plot regions, with the parameters of the likelihood functions fixed to the values obtained in the global fit. As discussed in the previous paragraph, the effect of reconstruction efficiencies cancels in the determination of $x_\pm$ and $y_\pm$ only if efficiency variations as a function of the Dalitz-plot variables are identical for the signal sample and for the event samples that were employed to determine the coefficients K_i, s_i and c_i. Differences between the efficiency profiles for the signal sample and the semileptonic sample that was employed to calculate the coefficients K_i were corrected using samples of simulated events. The possible effect of corrections to the s_i and c_i coefficients published by CLEO-c was checked using samples of simulated events, generated according to the BaBar amplitude model that had also been employed in the model-dependent LHCb analysis. No significant effect was observed and therefore no correction was applied, but a systematic uncertainty was assigned. The results of this measurement in terms of the parameters $x_\pm$ and $y_\pm$ are shown in Figure 5.123. Again, the precision of the measurement is limited by statistical uncertainty. The largest contributions to the systematic uncertainties are due to the correction of the efficiency profile in the case of the observables $x_\pm$ and by the knowledge of the coefficients s_i and c_i in the case of the observables $y_\pm$.

The results of model-dependent and model-independent measurements are strongly correlated since they are based on the same data and use similar reconstruction algorithms. They can therefore not be combined to derive constraints on the angle γ.

5.5.5 Constraints on the angle γ

The BaBar [457], Belle [427] and LHCb [458, 459] collaborations have each published constraints on the CKM angle γ from combinations of their latest measurements of GLW, ADS and GGSZ/Dalitz-plot observables. BaBar include in their average measurements in $B^\pm \to DK^\pm$,

$B^\pm \to D^* K^\pm$ and $B^\pm \to D K^{*\pm}$. Belle include results from $B^\pm \to D K^\pm$ and $B^\pm \to D^* K^\pm$. The Belle combination uses the result of their model-dependent GGSZ/Dalitz-plot analysis. The latest LHCb combination includes GLW, ADS and GGSZ/Dalitz-plot observables from $B^\pm \to D K^\pm$, including their measurements in $D \to K^\pm \pi^\mp \pi^+ \pi^-$ and $D \to K^0_S K^\pm \pi^\mp$, ADS and GLW observables from $B^0 \to D K^{*0}$ and their measurement of $\gamma - 2\beta_s$ from the time-dependent *CP* asymmetry in the decay $B^0_s \to D^\pm_s K^\mp$. The GGSZ/Dalitz-plot result from the model-independent measurement was used in this case. The BaBar and Belle averages neglected possible biases from $D^0 - \overline{D}^0$ mixing and *CP* violating effects in the $D^0 \overline{D}^0$ system, while the LHCb combination corrected for these effects using the world average values of the $D^0 - \overline{D}^0$ mixing parameters and *CP* violating asymmetries.

The BaBar and Belle collaborations also published a joint combination [112] while combinations of results from all three experiments have been performed by the CKMfitter [3] and UTfit [211] groups. The results are summarized in Table 5.3.

To conclude the survey of the Unitarity Triangle, Figure 5.126 shows the determination of its apex using only measurements of the three angles, as compiled by the CKMfitter group [3].

Table 5.3: Averages for γ as determined from various combinations of direct measurements and from Standard Model fits of CKM parameters, excluding direct measurements of γ, as prepared by the CKMfitter [3] and UTFit [211] groups. The values quoted by the CKMfitter group include results presented up to the CKM2014 conference in the beginning of September 2014, values quoted by the UTfit group include results presented up to the ICHEP2014 conference in the beginning of July 2014.

	BaBar [457]	Belle [427]	LHCb [459]	CKMfitter [3]	UTFit [211]
direct	$(69^{+17}_{-16}))^\circ$	$(68^{+15}_{-14})^\circ$	$(73^{+\ 9}_{-10})^\circ$	$(73.2^{+6.3}_{-7.0})^\circ$	$(68.4 \pm 7.5)^\circ$
CKM fit	-	-	-	$(66.9^{+1.0}_{-3.7})^\circ$	$(69.5 \pm 3.9)^\circ$

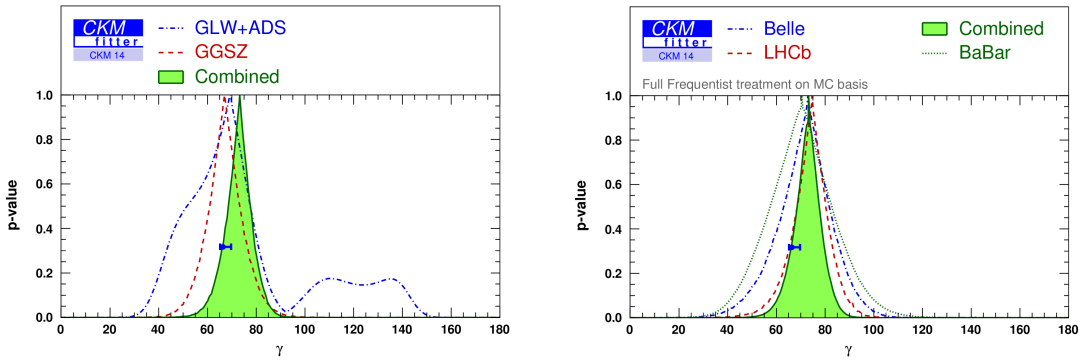

Figure 5.124: (from [3]).

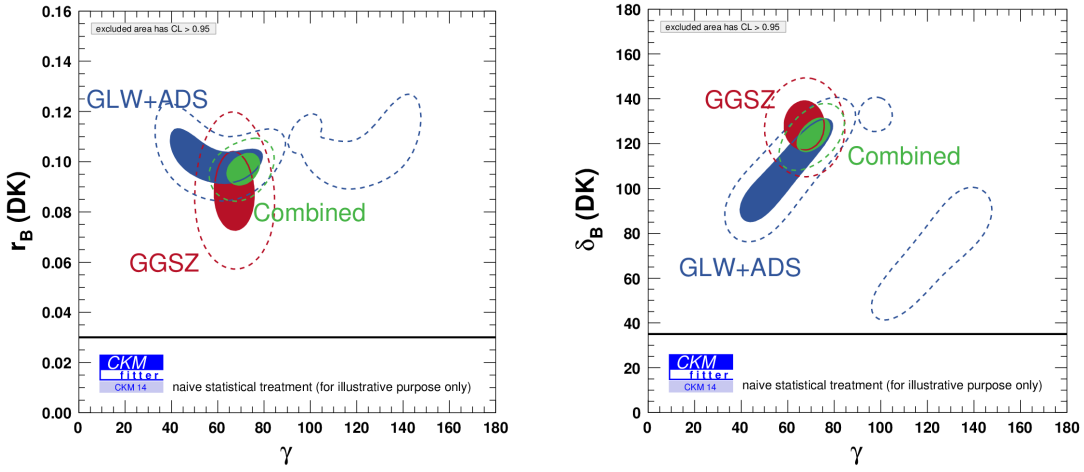

Figure 5.125: (from [3]).

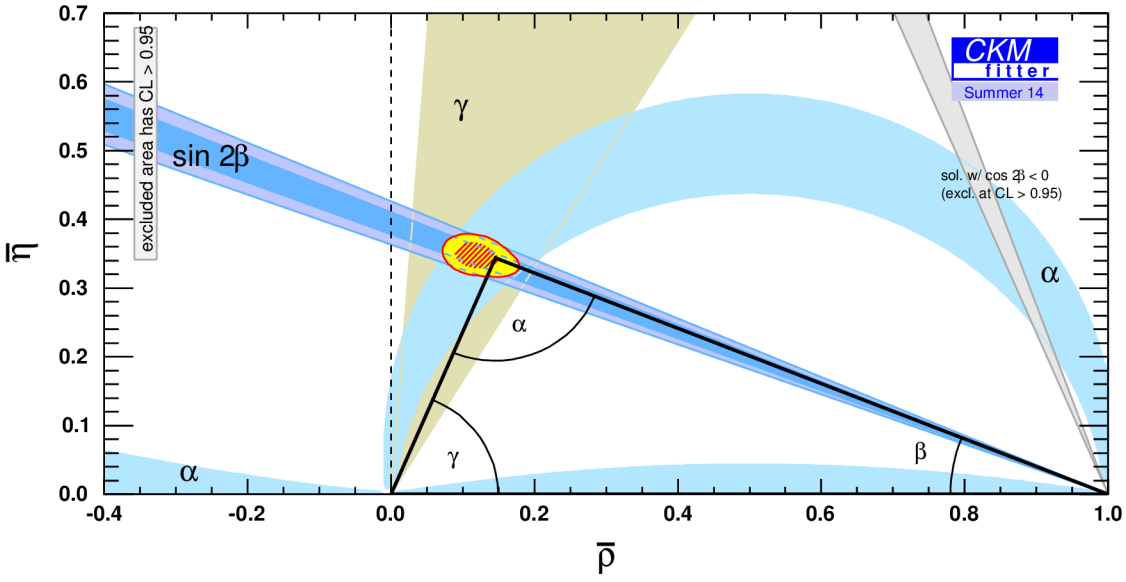

Figure 5.126: (from [3]).

Chapter 6

Showdown: Challenging the Standard Model in $B_s^0 - \overline{B}_s^0$ Mixing and Rare B Decays

> It was beauty killed the beast.
>
> — Carl Denham

The consistent picture that emerges from the survey of the Unitarity Triangle described in the previous chapter have established the CKM mechanism of the Standard Model as the dominant source of *CP* violation in the quark sector. The main focus of the experimental effort in heavy-quark flavour physics is now to perform precision measurements of observables that provide good sensitivity to possible subdominant contributions from physics beyond the Standard Model.

Of particular interest for such searches are observables in flavour-changing processes that involve loop diagrams, such as penguin decay diagrams or the box diagrams mediating particle-antiparticle mixing. Additional, heavy particles that are predicted in most extensions of the Standard Model can appear in such processes as virtual particles inside the loops and can lead to deviations in the values of observables from their Standard Model predictions. The sensitivity to such additional contributions is best in processes that are strongly suppressed in the Standard Model and in observables that the Standard Model predicts to be close to zero with good precision. Four examples of such processes and observables will be discussed in this chapter.

The *CP* violating phase ϕ_s in the decay mode $B_s^0 \to J/\psi\phi$ is to good approximation equal, in the Standard Model, to the complex phase of the $B_s^0 - \overline{B}_s^0$ mixing amplitude and both are related to the small angle in one of the squashed unitarity triangles. Standard Model fits lead to an estimate of only -2° for the *CP* violating phases. The phenomenology of the decay $B_s^0 \to J/\psi\phi$ is similar to that of the "golden" decay mode $B^0 \to J/\psi K_S^0$ that was employed to measure the angle β of the Unitarity Triangle as described in Section 5.3. The measurement of the *CP* violating phase in $B_s^0 \to J/\psi\phi$ presents addditional challenges due to the fact that the $J/\psi\phi$ pair is not produced in a *CP* eigenstate and that the decay-width difference, $\Delta\Gamma_s$, between the two mass eigenstates in the $B^0\overline{B}^0$ system is not negligibly small. Moreover, the measurement requires the ability to resolve the rapid $B_s^0 - \overline{B}_s^0$ oscillations. Measurements of ϕ_s were performed by the CDF and D0 collaborations at the Tevatron and are now being pursued at the LHC, where the most precise results have been reported by the LHCb collaboration.

The semileptonic asymmetry $a_{\rm sl}^s$ measures the magnitude of *CP* violation in $B_s^0 - \overline{B}_s^0$ mixing and is predicted to be as small as 2×10^{-5} in the Standard Model. It is defined as the relative difference between the rate of $\overline{B}_s^0$ mesons to decay into positive leptons and the rate of B_s^0 mesons to decay into negative leptons. Both processes can occur only if the B_s^0 or

$\overline{B}^0_s$ meson had mixed into its antiparticle at the time of its decay. A non-zero value of the asymmetry implies that the mixing process is not symmetric and that *CP* is therefore violated in the mixing. The semileptonic asymmetry $a^d_{\rm sl}$ in the $B^0\overline{B}^0$ system is defined in the same manner and is predicted to have a value of about 4×10^{-4} in the Standard Model. One way to measure semileptonic asymmetries is via the so-called same-sign dilepton charge asymmetry, which exploits the fact that associated production leads to the creation of a $b\bar{b}$ pair. Looking at events in which the created b and $\bar{b}$ hadron both decayed semileptonically, the observation of a pair of positive leptons implies that the b quark must have hadronized into a $\overline{B}^0$ or $\overline{B}^0_s$ meson and that this must then have mixed into its antiparticle at the time of its decay. Likewise, the observation of a pair of negative leptons implies that an initial B^0 or B^0_s meson had mixed into its antiparticle when it decayed. The relative difference in the rates of positive and negative same-sign dilepton events measures $a^d_{\rm sl}$ at the B factories, where no B^0_s and $\overline{B}^0_s$ mesons are produced, and a linear combination of $a^d_{\rm sl}$ and $a^s_{\rm sl}$ at hadron colliders. The D0 collaboration published measurements of the same-sign dimuon charge asymmetry that indicate a significant deviation from Standard Model predictions. Since direct measurements of $a^d_{\rm sl}$ yielded values that were in good agreement with the Standard Model prediction, it was speculated that the result of the D0 measurement could be an indication for a possible sign of contributions from New Physics in $B^0_s - \overline{B}^0_s$ mixing. Direct measurements of $a^s_{\rm sl}$ at D0 and LHCb agree with the Standard Model prediction but are also compatible within their precision with the same-sign dimuon charge asymmetry measured by the D0 collaboration.

Decays that involve a flavour-changing neutral current $b \to s$ or $b \to d$ transition are forbidden at tree level by the GIM mechanism discussed in Section 2.6 and can proceed only via loop diagrams. As these processes are suppressed in the Standard Model, branching fractions and other observables in such decays can be significantly affected by possible contributions from New Physics. A key measurement is that of the branching fraction of the very rare decays $B^0_s \to \mu^+\mu^-$ and $B^0 \to \mu^+\mu^-$. These processes are not only flavour-changing neutral current decays, but they are further suppressed by helicity violation due to the $V - A$ character of the weak interaction. Their branching fractions are predicted to be of the order of 3×10^{-9} and 1×10^{-10}, respectively, in the Standard Model and are sensitive to New Physics. The first observation of the decay $B^0_s \to \mu^+\mu^-$ has recently been reported by the CMS and LHCb collaborations and the measured branching fraction is in good agreement with the Standard Model prediction, putting severe constraints on the parameter space for models of New Physics. First evidence for the decay $B^0 \to \mu^+\mu^-$ has also been found but uncertainties on the measurement of its branching fraction are significant.

The rare decay $B^0 \to K^{*0}\mu^+\mu^-$ is a flavour-changing neutral current process that is mediated via electroweak penguin diagrams. This decay has been widely studied because angular distributions of the final-state particles in this decay give rise to a number of observables that exhibit good sensitivity to possible contributions from New Physics. Measurements of such observables have been performed at BaBar, Belle and CDF and more recently at ATLAS and CMS, but the most precise results stem from measurements at LHCb. Results are in general in good agreement with Standard Model predictions, except for an intriguing devation that was found in one of the angular observables. This observation has stirred some interest in the theory community but on its own provides too weak a signature to make serious claims regarding possible New Physics contributions. The published LHCb result is based on the data set collected in 2011, an analysis of the full run I data set is still pending.

In the next sections, measurements of the phase ϕ_s in $B^0_s \to J/\psi\phi$ will be described first, followed by a disussion of measurements of the semileptonic asymmetries $a^d_{\rm sl}$ and $a^s_{\rm sl}$, the measurement of the $B^0_s \to \mu^+\mu^-$ branching fraction and the search for the decay $B^0 \to \mu^+\mu^-$ and, finally, the measurement of angular observables in the rare decay $B^0 \to K^{*0}\mu^+\mu^-$.

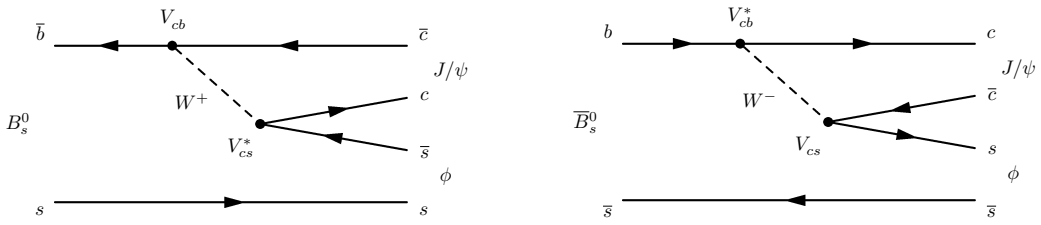

Figure 6.1: Dominating tree diagrams for the decays (left) $B_s^0 \to J/\psi\phi$ and (right) $\overline{B}_s^0 \to J/\psi\phi$.

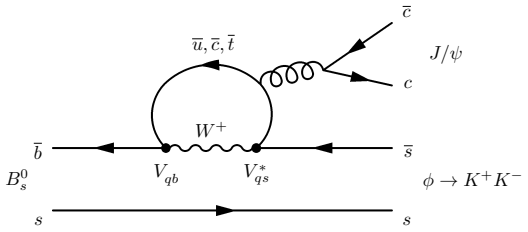

Figure 6.2: Leading penguin diagrams for the decay $B_s^0 \to J/\psi\phi$. Note the similarity in both the tree diagrams shown above and the penguin diagrams shown here with the corresponding diagrams for the decay $B_s \to J/\psi K_S^0$ discussed in Section 5.3. The only change is that of the spectator quark from a down to a strange quark.

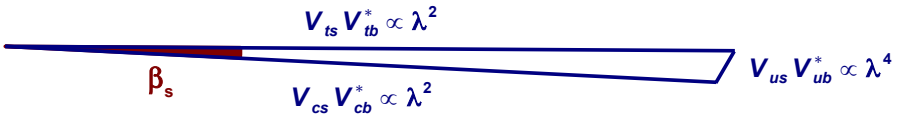

Figure 6.3: Illustration of the squashed unitarity triangle defined by the relation $V_{us}V_{ub}^* + V_{ts}V_{tb}^* + V_{cs}V_{cb}^* = 0$.

6.1 The *CP* violating phase ϕ_s

A time-dependent *CP* asymmetry in the decay $B_s^0 \to J/\psi\phi$ can be caused by the interference of mixing and decay as described in Section 3.3. The final state $J/\psi\phi$ can be reached through decays of B_s^0 mesons and of $\overline{B}_s^0$ mesons, where the decay amplitudes are dominated by the tree diagrams shown in Figure 6.1. Neglecting subdominant penguin decay amplitudes, the relative weak phase between the direct decay $B_s^0 \to J/\psi\phi$ and the decay after mixing, $B_s^0 \to \overline{B}_s^0 \to J/\psi\phi$, is then given by

$$\phi_s \equiv \lambda_{J/\psi\phi} = -\left(\frac{q}{p}\right)_{B_s^0} \cdot \left(\frac{\overline{A}_{J/\psi\phi}}{A_{J/\psi\phi}}\right) = -\left(\frac{V_{ts}V_{tb}^*}{V_{ts}^*V_{tb}}\right) \cdot \left(\frac{V_{cb}V_{cs}^*}{V_{cb}^*V_{cs}}\right) = -2 \cdot \arg\left(\frac{V_{ts}V_{tb}^*}{V_{cb}^*V_{cs}}\right) .$$

The phase

$$\beta_s \equiv \arg\left(\frac{V_{ts}V_{tb}^*}{V_{cs}V_{cb}^*}\right)$$

also describes one of the angles in the unitarity triangle that follows from applying the unitarity condition to the second and third rows of the CKM matrix,

$$V_{us}V_{ub}^* + V_{ts}V_{tb}^* + V_{cs}V_{cb}^* = 0 .$$

The first term on the left side of the equation is proportional to λ^4, while the other two terms are proportional to λ^2 in terms of the Wolfenstein parameter $\lambda \approx 0.23$. The triangle is therefore squashed and, as illustrated in Figure 6.3, the angle β_s is small. A global CKM fit, performed

by the CKMfitter group [3] in autumn 2014, yields the Standard Model prediction

$$\beta_s \;=\; 0.01826\,^{+\,0.00059}_{-\,0.00064}\ \text{rad}\ .$$

By extention, the *CP* violating phase in the decay $B_s^0 \to J/\psi\phi$, $\phi_s = -2\beta_s$, is expected to be small in the Standard Model. Finally, to good approximation, β_s is also equal to the weak *CP* violating phase of the $B_s^0 - \overline{B}_s^0$ mixing amplitude. As discussed in Section 3.3, the *CP* violating phase in mixing is given by the relative weak phase between the dispersive part, M_{12}, and the absorptive part, Γ_{12}, of the mixing amplitude, which in the $B_s^0\overline{B}_s^0$ system are dominated by the box diagrams with internal top quarks and the box diagrams with internal charm quarks, respectively. The relative weak phase between M_{12} and Γ_{12} is then

$$\arg\left(\frac{M_{12}}{\Gamma_{12}}\right) \;=\; \arg\left(\frac{V_{ts}V_{tb}^*}{V_{cb}^*V_{cs}}\right) \;=\; \beta_s\ .$$

It is therefore often stated in the literature that the *CP* violating phase in the decay $B_s^0 \to J/\psi\phi$ measures the $B_s^0 - \overline{B}_s^0$ mixing phase. This statement is, however, true only up to approximations that the $B_s^0 \to J/\psi\phi$ decay amplitude receives no contributions with weak phase different from that of the tree amplitude and that the dispersive and absorptive parts of the $B_s^0 - \overline{B}_s^0$ mixing amplitude receive no contributions with weak phases different from those of the top and charm loops, respectively. In practice, these approximations are fulfilled to good precision in the Standard Model, but can be violated if New Physics contribute to the $B_s^0 \to J/\psi\phi$ decay amplitude or in $B_s^0 - \overline{B}_s^0$ mixing.

The fact that the Standard Model decay amplitude for the decay $B_s^0 \to J/\psi\phi$ is dominated by the phase of the tree amplitude can be demonstrated in the same manner as for the decay $B^0 \to J/\psi K_S^0$ discussed in Section 5.3. The leading Standard Model penguin diagrams for the decay $B_s^0 \to J/\psi\phi$ are shown in Figure 6.2. Denoting with T, P_t, P_c, and P_u the amplitudes of the tree process and the penguin processes with intermediate top, charm and up quarks, respectively, and exploiting one of the unitarity conditions of the CKM matrix to substitute

$$V_{tb}^*V_{ts} \;=\; -V_{cb}^*V_{cs} \;-\; V_{ub}^*V_{us}$$

the decay amplitude can be expressed as

$$\begin{aligned} A_{J/\psi\phi} \;&=\; (T + P_c)\cdot(V_{cb}^*V_{cs}) \;+\; P_u\cdot(V_{ub}^*V_{us}) \;+\; P_t\cdot(V_{tb}^*V_{ts}) \\ &=\; (T + P_c - P_t)\cdot(V_{cb}^*V_{cs}) \;+\; (P_u - P_t)\cdot(V_{ub}^*V_{us}) \end{aligned}$$

and the term proportional to the phase of $V_{cb}^*V_{cs}$ is suppressed by the ratio of the magnitudes of the CKM elements,

$$\frac{|V_{ub}^*V_{us}|}{|V_{cb}^*V_{cs}|} \;\propto\; \frac{\lambda^4}{\lambda^2} \;=\; \lambda^2\,,$$

with, again, the Wolfenstein parameter $\lambda \approx 0.23$.

The good sensitivity to possible New Physics contributions in $B_s^0 - \overline{B}_s^0$ mixing, combined with a reasonably large visible branching fraction,

$$\text{BF}\,(B_s^0 \to J/\psi\phi)\;\times\;\text{BF}\,(J/\psi \to \mu^+\mu^-)\;\times\;\text{BF}\,(\phi \to K^+K^-)\;\approx\;3\times10^{-5}\ ,$$

and the clear event signature of two oppositely charged muons from a J/ψ decay and two oppositely charged kaons from the same decay vertex, make the measurement of the *CP* violating phase ϕ_s in the decay $B_s^0 \to J/\psi\phi$ a benchmark analysis for the study of *CP* violating effects in the $B_s^0\overline{B}_s^0$ system. However, the measurement poses a few additional challenges compared to the "golden" decay mode $B^0 \to J/\psi K_S^0$ that allowed the B factories to establish *CP* violation in the $B^0\overline{B}^0$ system and to perform precision measurements of the CKM angle $\sin(2\beta)$.

Firstly, of course, B_s^0 mesons are not produced at the $\Upsilon(4S)$ resonance and the B_s^0 production rate in hadron collisions is about a factor of four lower than that for B^0 mesons. The measurement of the decay-time dependent *CP* asymmetry requires the ability to resolve the rapid $B_s^0-\overline{B}_s^0$ oscillations, i.e. the decay-time resolution of the experiment plays an important role in the measurement. The decay width difference, $\Delta\Gamma_s$, between the two mass eigenstates in the $B_s^0\overline{B}_s^0$ system is not negligibly small and has to be extracted from the measurement simultaneously with the phase ϕ_s. Finally, the final state $J/\psi\phi$ is not a *CP* eigenstate and a decay-time dependent angular analysis has to be performed to statistically separate the *CP* even and *CP* odd components. The decay $B_s^0 \to J/\psi\phi$ is a decay of a pseudoscalar particle with spin $J = 0$ to two vector particles with spin $J = 1$. Angular momentum conservation in the decay allows the $J/\psi\phi$ pair to be produced with relative angular momentum $L = 0, 1$ or 2. The states with $L = 0$ and $L = 2$ are *CP* even, while the state with $L = 1$ is *CP* odd. In addition, there can be a non-resonant S-wave component of K^+K^- pairs with relative angular momentum $L_{KK} = 0$, which happen to have an invariant mass close to the mass of the ϕ meson but which were not produced via an intermediate ϕ resonance. In this case, the relative angular momentum between the K^+K^- pair and the J/ψ meson has to be $L = 1$ and the final state is *CP* odd.

The angular analysis is conveniently performed in the so-called transversity basis, that was already introduced in Section 5.3 in the context of a time-dependent angular analysis of the decay mode $B^0 \to J/\psi K^{*0}$. In this basis, the resonant decay amplitude is decomposed in terms of linear polarization states of the two vector mesons relative to their direction of motion, i.e. relative to the $B_s^0 \to J/\psi\phi$ decay axis in the rest frame of the decaying B_s^0 meson. The amplitude A_0 describes the state in which the two vector mesons are polarized longitudinally along the decay axis, while the amplitudes $A_\parallel$ and $A_\perp$ describe the states of parallel and orthogonal polarization in the plane perpendicular to the decay axis. Each of the three polarization states has a well-defined *CP* symmetry: the amplitudes A_0 and $A_\parallel$ are *CP* even and the amplitude $A_\perp$ is *CP* odd. The three transversity angles, $\omega \equiv (\psi_T, \theta_T, \phi_T)$, employed in most analyses are defined in Figure 6.4. In the latest LHCb analyses, the decay amplitudes are instead expressed in terms of the helicity angles $(\cos\theta_K, \cos\theta_\mu, \varphi_h)$, defined in Figure 6.5. The reason for this is that the helicity angles were found to be better suited for background and acceptance corrections in view of the forward geometry of the LHCb detector. The helicity amplitudes, h_0, h_+ and h_-, are related to the transversity amplitudes by

$$h_0 \;=\; A_0 \quad ; \quad h_+ \;=\; \frac{1}{\sqrt{2}}\,(A_\parallel + A_\perp) \quad ; \quad h_- \;=\; \frac{1}{\sqrt{2}}\,(A_\parallel - A_\perp)\;.$$

A full derivation of the time-dependent decay rate in terms of the transversity amplitudes is given in Ref. [460]. Neglecting effects of *CP* violation in $B_s^0-\overline{B}_s^0$ mixing, which are expected and measured to be negligibly small compared to the current precision of measurements of ϕ_s, the differential decay rate as a function of the decay time and the decay angles can be written as

$$\begin{aligned}\frac{d^4\Gamma\,(B_s^0 \to J/\psi\phi)}{dt\,d\omega} \;\propto\; \sum_{k=1}^{10} \Big\{ N_k\, f_k(\omega) \;\times\; e^{-\overline{\Gamma}_s t}\;\big[\\ a_k \cosh\left(\tfrac{\Delta\Gamma_s}{2}\,t\right) \,+\, b_k \sinh\left(\tfrac{\Delta\Gamma_s}{2}\,t\right) \\ +\; q\,\{\, c_k \cos\left(\Delta m_s t\right) \,+\, d_k \sin\left(\Delta m_s t\right)\,\}\;\big]\;\Big\}\;,\end{aligned}$$

where $q = +1$ for an initial B_s^0 meson and $q = -1$ for an initial $\overline{B}_s^0$ meson, $\overline{\Gamma}_s$ is the average decay width in the $B_s^0\overline{B}_s^0$ system and Δm_s is the $B_s^0-\overline{B}_s^0$ oscillation frequency. The coefficients N_k are given by the magnitudes, $|A_0|$, $|A_\parallel|$, $|A_\perp|$ and $|A_S|$, of the four polarization amplitudes at time $t = 0$, the dependence on the decay angles is contained in the functions $f_k(\omega)$, and the coefficients a_k, b_k, c_k and d_k contain information on the the *CP* violating phase ϕ_s and

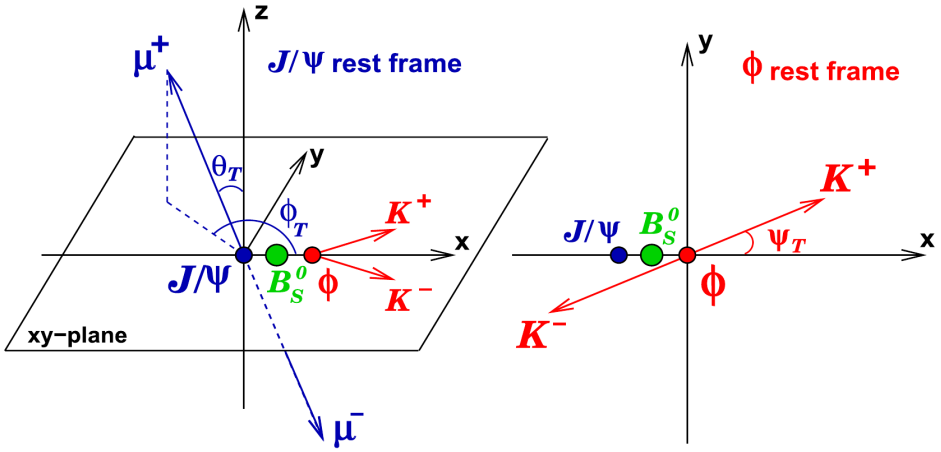

Figure 6.4: Definition of the transversity angles $(\psi_T, \theta_T, \phi_T)$ as employed in most time-dependent angular analyses of the decay $B_s^0 \to J/\psi\phi$: the angle ψ_T is measured between the K^+ momentum vector and the direction opposite to the B_s^0 momentum vector in the rest frame of the ϕ meson, while θ_T and ϕ_T are the polar and azimuthal angles of the positive lepton in a coordinate system defined by the K^+K^- decay plane and the direction of the B_s^0 momentum vector in the rest frame of the J/ψ meson (from [163]).

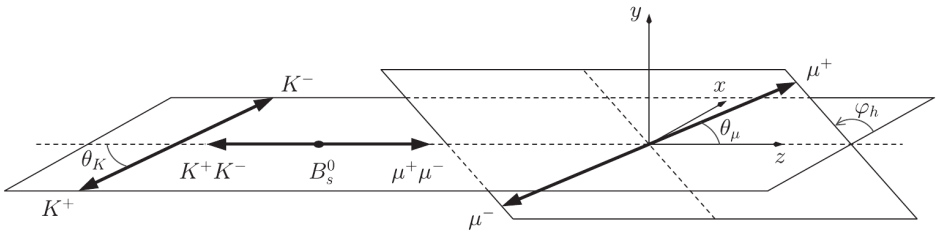

Figure 6.5: Definition of the helicity angles $(\theta_K, \theta_\mu, \varphi_h)$ employed in recent angular analyses of the decay $B_s^0 \to J/\psi\phi$ by the LHCb collaboration: the angle θ_K is measured between the K^+ momentum vector and the direction opposite to the B_s^0 momentum vector in the rest frame of the K^+K^- pair, the angle θ_μ is measured between the μ^+ momentum vector and the direction opposite to the B momentum vector in the rest frame of the $\mu^+\mu^-$ pair, and φ_h is the angle between the K^+K^- and $\mu^+\mu^-$ decay planes (from [204]).

the strong phases δ_0, $\delta_\parallel$, $\delta_\perp$ and δ_S. The expressions for the angular functions $f_k(\omega)$ are given in Table 6.1 both in terms of the transversity angles and in terms of the helicity angles. The expressions in terms of transversity angles are similar to those listed in Section 5.3 for the angular analysis in the decay mode $B^0 \to J/\psi K^{*0}$. Explicit expressions for the coefficents N_k, a_k, b_k, c_k and d_k are given in Table 6.2, where

$$A \equiv \frac{1-|\lambda_{J/\psi\phi}|^2}{1+|\lambda_{J/\psi\phi}|^2} \quad ; \quad S \equiv -\frac{2\,|\lambda_{J/\psi\phi}|\,\sin\phi_s}{1+|\lambda_{J/\psi\phi}|^2} \quad ; \quad D \equiv -\frac{2\,|\lambda_{J/\psi\phi}|\,\cos\phi_s}{1+|\lambda_{J/\psi\phi}|^2} \; .$$

Neglecting direct *CP* violation in the decay, which could be caused by interference with the subdominant penguin amplitudes but is expected to be small, $|\lambda_{J/\psi\phi}| = 1$ and

$$A \;=\; 0 \quad ; \quad S \;=\; -\sin\phi_s \quad ; \quad D \;=\; -\cos\phi_s \; .$$

This approximation is made in most analyses, while the latest analyses by the LHCb collaboration include measurements of $|\lambda_{J/\psi\phi}|$.

Due to the finite decay-width difference, $\Delta\Gamma_s$, the terms proportional to $\cosh\left(\frac{\Delta\Gamma_s}{2}\,t\right)$ and $\sinh\left(\frac{\Delta\Gamma_s}{2}\,t\right)$ allow to extract information on the *CP* phase ϕ_s from the untagged differential decay rate, without the need to distinguish between initial B_s^0 mesons and initial $\overline{B}_s^0$ mesons.

Table 6.1: Compilation of the angular functions $f_k(\omega)$ in the terms of the transversity angles $(\psi_T, \theta_T, \phi_T)$, and in terms of the helicity angles $(\theta_K, \theta_\mu, \varphi_h)$ employed in the latest LHCb analysis of the decay $B_s^0 \to J/\psi K^+K^-$.

k	transversity angles $(\psi_T, \theta_T, \phi_T)$	helicity angles $(\theta_K, \theta_\mu, \varphi_h)$
1	$2\cos^2\psi_T\,(1\,-\,\sin^2\theta_T\,\cos^2\phi_T)$	$2\cos^2\theta_K\,\sin^2\theta_\mu$
2	$\sin^2\psi_T\,(1-\sin^2\theta_T\,\cos^2\phi_T)$	$\sin^2\theta_K\,(1-\sin^2\theta_\mu\,\cos^2\varphi_h)$
3	$\sin^2\psi_T\,\sin^2\theta_T$	$\sin^2\theta_K\,(1-\sin^2\theta_\mu\,\sin^2\varphi_h)$
4	$-\sin^2\psi_T\,\sin(2\theta_T)\,\sin\phi_T$	$\sin^2\theta_K\,\sin^2\theta_\mu\,\sin(2\varphi_\mu)$
5	$\frac{1}{2}\sqrt{2}\,\sin(2\psi_T)\,\sin^2\theta_T\sin(2\phi_T)$	$\frac{1}{2}\sqrt{2}\,\sin(2\theta_K)\,\sin(2\theta_\mu)\,\cos\varphi_h$
6	$\frac{1}{2}\sqrt{2}\,\sin(2\psi_T)\,\sin(2\theta_T)\cos\phi_T$	$-\frac{1}{2}\sqrt{2}\,\sin(2\theta_K)\,\sin(2\theta_\mu)\,\sin\varphi_h$
7	$\frac{2}{3}\,(1\,-\,\sin^2\theta_T\,\cos^2\phi_T)$	$\frac{2}{3}\,\sin^2\theta_\mu$
8	$-\frac{1}{3}\sqrt{6}\,\sin\psi_T\,\sin^2\theta_T\,\sin(2\phi_T)$	$\frac{1}{3}\sqrt{6}\,\sin\theta_K\,\sin(2\theta_\mu)\,\cos\varphi_h$
9	$\frac{1}{3}\sqrt{6}\,\sin\psi_T\,\sin(2\theta_T)\,\cos\phi_T$	$-\frac{1}{3}\sqrt{6}\,\sin\theta_K\,\sin(2\theta_\mu)\,\sin\varphi_h$
10	$\frac{4}{3}\sqrt{3}\,\cos\psi_T\,(1\,-\,\sin^2\theta_T\,\cos^2\phi_T)$	$\frac{4}{3}\sqrt{3}\,\cos\theta_K\sin^2\theta_\mu$

Table 6.2: Compilation of the coefficients N_k, a_k, b_k, c_k and d_k that appear in the description of the differential $B_s^0 \to J/\psi\phi$ decay rate as a function of the decay time and decay angles.

k	N_k	a_k	b_k	c_k	d_k
1	$\lvert A_0\rvert^2$	1	D	C	$-S$
2	$\lvert A_\parallel\rvert^2$	1	D	C	$-S$
3	$\lvert A_\perp\rvert^2$	1	$-D$	C	S
4	$\lvert A_\parallel\rvert\lvert A_\perp\rvert$	$C\sin(\delta_\perp-\delta_\parallel)$	$S\cos(\delta_\perp-\delta_\parallel)$	$\sin(\delta_\perp-\delta_\parallel)$	$D\cos(\delta_\perp-\delta_\parallel)$
5	$\lvert A_0\rvert\lvert A_\parallel\rvert$	$\cos(\delta_\parallel-\delta_0)$	$D\cos(\delta_\parallel-\delta_0)$	$C\cos(\delta_\parallel-\delta_0)$	$-S\cos(\delta_\parallel-\delta_0)$
6	$\lvert A_0\rvert\lvert A_\perp\rvert$	$C\sin(\delta_\perp-\delta_0)$	$S\cos(\delta_\perp-\delta_0)$	$\sin(\delta_\perp-\delta_0)$	$D\cos(\delta_\perp-\delta_0)$
7	$\lvert A_S\rvert^2$	1	$-D$	C	S
8	$\lvert A_S\rvert\lvert A_\parallel\rvert$	$C\cos(\delta_\parallel-\delta_S)$	$S\sin(\delta_\parallel-\delta_S)$	$\cos(\delta_\parallel-\delta_S)$	$D\cos(\delta_\parallel-\delta_S)$
9	$\lvert A_S\rvert\lvert A_\perp\rvert$	$\sin(\delta_\perp-\delta_S)$	$-D\sin(\delta_\perp-\delta_S)$	$C\sin(\delta_\perp-\delta_S)$	$S\sin(\delta_\perp-\delta_S)$
10	$\lvert A_S\rvert\lvert A_\perp\rvert$	$C\cos(\delta_0-\delta_S)$	$S\sin(\delta_0-\delta_S)$	$\cos(\delta_0-\delta_S)$	$D\sin(\delta_0-\delta_S)$

Better sensitivity to ϕ_s is, however, provided by flavour-tagged analyses, which give access to the terms proportional to $\pm\cos(\Delta m_s t)$ and $\pm\sin(\Delta m_s t)$.

The expression of the differential decay rate is invariant under the simultaneous transformation

$$\left(\phi_s, \Delta\Gamma_s, \delta_0, \delta_\parallel, \delta_\perp, \delta_S\right) \;\leftrightarrow\; \left(\pi-\phi_s, -\Delta\Gamma_s, -\delta_0, -\delta_\parallel, \pi-\delta_\perp, -\delta_S\right)\;,$$

leading to a two-fold ambiguity in the determination of ϕ_s and $\Delta\Gamma_s$. This ambiguity has been resolved by a measurement at LHCb of the evolution of the relative strong phase between the S-wave amplitude and the P-wave amplitudes as a function of the K^+K^- invariant mass in the region of the J/ψ resonance. The approach is similar to that of the BaBar measurement in the decay $B^0 \to J/\psi K^{*0}$, described in Section 5.3, which allowed to resolve a sign ambiguity in the determination of the angle β of the Unitarity Triangle.

The LHCb collaboration performed measurements of ϕ_s also in the decay mode $B_s^0 \to J/\psi\pi^+\pi^-$. The branching fractions for this decay is smaller than that for the decay $B_s^0 \to J/\psi\phi$, but no angular analysis is required, here, because the final state is an almost pure CP eigenstate.

Measurements of ϕ_s and $\Delta\Gamma_s$ in the decay modes $B_s^0 \to J/\psi\phi$ and $B_s^0 \to J/\psi K^+K^-$ will

be described next, followed by short descriptions of the analysis of strong phases in this decay mode and of the measurement of ϕ_s in the decay mode $B_s^0 \to J/\psi\pi^+\pi^-$. The section concludes with a short summary of the resulting constraints on ϕ_s.

6.1.1 Measurements in $B_s^0 \to J/\psi\phi$ and $B_s^0 \to J/\psi K^+K^-$

Measurements of ϕ_s and $\Delta\Gamma_s$ in the decay $B_s^0 \to J/\psi\phi$ with $J/\psi \to \mu^+\mu^-$ and $\phi \to K^+K^-$ have been performed at the CDF [163, 164, 461, 462] and D0 [165, 463, 464] experiments at the Tevatron and by the ATLAS [465, 466], CMS [467] LHCb [204, 206, 468] experiments at the LHC. Early measurements at the Tevatron [461–464] seemed to hint at a possible discrepancy with the Standard Model prediction for ϕ_s, but the deviation was not confirmed by the later measurements, which are in good agreement with Standard Model expectations. The CDF collaboration published a final analysis [164] based on the full CDF II data sample, corresponding to an integrated luminosity of 9.6 fb^{-1}, while the latest analysis published by the D0 collaboration [165] was based on a partial data set corresponding to an integrated luminosity of 8 fb^{-1}. The latest measurement published by the ATLAS collaboration was based on their data collected in 2011, corresponding to an integrated luminosity of 4.9 fb^{-1}. The LHCb collaboration recently published a measurement [206] based on their full run-I data set corresponding to 3 fb^{-1} collected at pp collision energies of 7 TeV in 2011 and 8 TeV in 2012. The CMS collaboration presented preliminary results [467] based a data set corresponding to an integrated luminosity of 20 fb^{-1}, collected in 2011 and the first half of 2012.

All measurements followed a similar general approach. Event selections at the trigger level were based on the signature of one or two muons with significant transverse momentum. In the case of CDF, CMS and LHCb, the invariant mass of the muon pair was also employed in the trigger decision. The CMS trigger required furthermore that the muon pair originated from a common vertex and that this vertex was significantly displaced from the reconstructed pp interaction vertex. The LHCb trigger required either an opposite-charge muon pair with large invariant mass or a single muon candidate with high transverse momentum and with large impact parameter with respect to the reconstructed pp interaction vertex.

The offline selections required two oppositely charged muons compatible with originating from a common vertex and with an invariant mass compatible with the known mass of the J/ψ meson, and two additional, oppositely charged, tracks compatible with originating from the same vertex. In the CDF and LHCb analyses, kaon identification requirements were applied on these two tracks, while the D0, ATLAS and CMS detectors do not provide adequate kaon identification capability and all tracks that were not identified as muons were considered here. In all analyses, a kinematic fit was performed, constraining the four tracks to a common vertex and the invariant mass of the dimuon pair to the mass of the J/ψ meson. Selection requirements were applied on the quality of this fit and on kinematic properties of the final state particles and the B_s^0 candidate. In the CDF and D0 analyses, discriminating variables were combined into multi-variate classifiers, employing an artificial neural network algorithm in the case of the CDF analysis and Boosted Decision Tree algorithms in the case of the DO analysis. In the CMS analysis, the reconstructed proper decay length of the B_s^0 candidate was required to be larger than 200 μm in order to avoid possible biases due to the decay-time dependent acceptance of the trigger condition. In the CDF, D0, ATLAS and CMS analyses, the invariant mass of the kaon pair was required to be within a window of about ± 10 MeV/c^2 around the known mass of the ϕ meson, while the LHCb analysis made use of kaon pairs in a wider invariant-mass window, from 990 MeV/c^2 to 1050 MeV/c^2.

The physics observables of interest were extracted from multidimensional maximum likelihood fits using as input variables the reconstructed invariant mass and decay time or decay length of the signal candidates, the estimated uncertainty on the decay time or decay length measurement, the measured decay angles of the final-state particles, the response of flavour tagging algorithms, and the estimated flavour mistag probability. The analyses at CDF and

ATLAS included in addition the estimated uncertainty on the invariant-mass reconstruction as an input variable to the fit. The different inputs to the fit are described in the following.

The measured invariant-mass distributions of the selected B_s^0 candidates from all five analyses are shown in Figure 6.6, together with the results of the maximum likelihood fits. The mass distribution of the signal component was described by a Gaussian function in the D0 analysis and by the sum of three Gaussian functions with common mean in the CMS analysis. The CDF and ATLAS analyses employ a Gaussian probability density function with standard deviations derived on an event-by-event basis from the estimated uncertainty on the reconstructed invariant mass. The LHCb analysis, finally, employs a modified Gaussian function [469] to take into account the effects of final-state radiation and event-to-event fluctuations in the uncertainty on the measured invariant mass. The background component is dominated by combinatorial background and its invariant-mass distribution was modelled by linear, quadratic or exponential functions. A specific background source are $B^0 \to J/\psi K^{*0}$ and $B^0 \to J/\psi K^+\pi^-$ decays in which the final-state pion is misidentified as a kaon. This background component was included in the ATLAS analysis with a fraction and with shapes determined from simulated samples of events. In the LHCb analysis, this background was dealt with by injecting an appropriate fraction of simulated events into the data sample and assigning these events a negative weight in the fit. The numbers of $B_s^0 \to J/\psi K^+K^-$ signal candidates as extracted from the maximum likelihood fits to collision data are listed in Table 6.3.

In the LHCb analysis, the results of the fit to the $J/\psi K^+K^-$ invariant mass spectrum were employed to derive a probability for each $J/\psi K^+K^-$ candidate to belong to the signal or background component. Based on these probabilities, appropriate positive or negative weights were then assigned to each candidate in the maximum likelihood fit to the remaining input variables, such that the background component was effectively subtracted statistically and did not need to be modelled in that fit. The method is known by the ugly name of ${}_sPlot$ and was first described in Ref. [470]. The ${}_sPlot$ technique is based on the assumption that the variables employed in the maximum likelihood fit are uncorrelated with the variable from which the weights are derived. Simulation studies demonstrated that this assumption is fulfilled to good approximation for the $J/\psi K^+K^-$ invariant mass and the decay-time, flavour tagging and angular variables used in the maximum likelihood fit. A systematic uncertainty was assigned.

The decay time of the B_s^0 candidate was calculated in the CDF, D0, ATLAS and CMS analyses as $t = m_{B_s^0} L_{xy} \,/\, p_{\rm T}$, where $m_{B_s^0}$ is the nominal mass of the B_s^0 meson, L_{xy} is the measured distance between the reconstructed decay vertex of the B_s^0 candidate and the associated $p\overline{p}$ or pp interaction vertex, projected onto the reconstructed momentum vector of the B_s^0 candidate in the plane transverse to the beam axis, and $p_{\rm T}$ is the magnitude of that momentum vector. In the LHCb analysis, the decay time was calculated from a kinematic fit of the full decay chain of the signal candidate, constraining the momentum vector of the B_s^0 candidate to point back to the associated pp interaction vertex. The uncertainty on the decay-time measurement is not negligibly small compared to the $B_s^0 - \overline{B}_s^0$ oscillation period of $2\pi/\Delta m_s \approx 350$ fs and therefore leads to a dilution of the oscillation amplitude. A precise modelling of the decay time resolution is therefore essential in order to extract the *CP* violating phase ϕ_s from the observed time-dependent asymmetry. In all analyses, the decay time resolution was modelled by a Gaussian probability density function, or the sum of two Gaussian probability density functions, with standard deviations that were derived on an event-by-event basis from the estimated uncertainty on the reconstructed decay time. A constant correction factor was applied to the estimated uncertainty to compensate for imperfections in the reconstruction. This correction factor was determined from samples of simulated events in the case of the D0 and CMS analyses. In the CDF and ATLAS analyses, it was a free parameter in the maximum likelihood fit to the data. In the LHCb analysis, it was determined from collision data, employing large samples of fake $J/\psi K^+K^-$ candidates formed by a prompt J/ψ meson and two kaons produced directly in the pp collision. The true decay time for these candidates

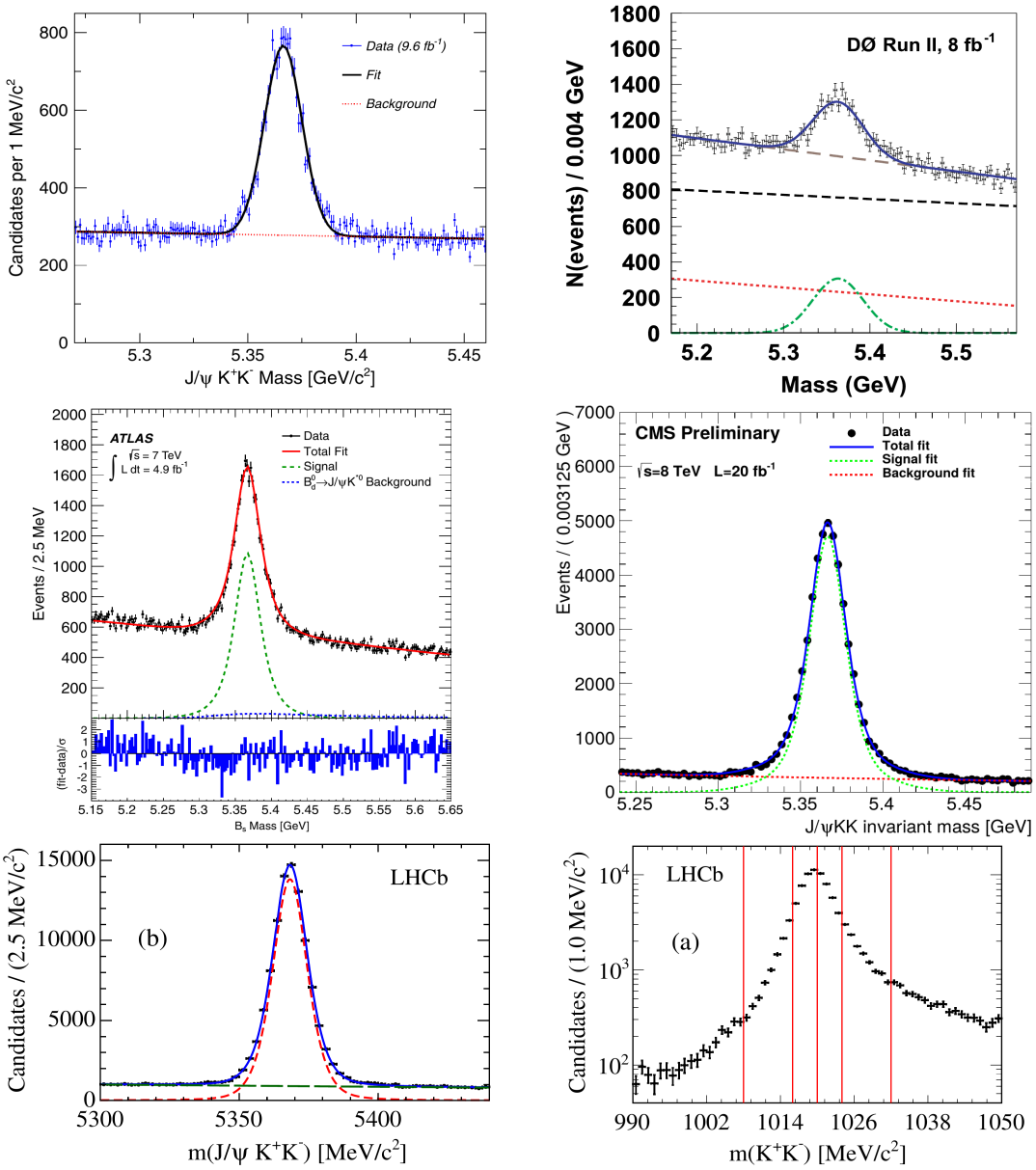

Figure 6.6: Measured $J/\psi K^+K^-$ invariant-mass distributions for selected candidates from the latest (top left) CDF, (top right) D0, (middle left) ATLAS, (middle right) CMS and (bottom left) LHCb measurements of the *CP* violating phase ϕ_s in the decay $B_s^0 \to J/\psi K^+K^-$. The bottom right panel shows the measured invariant-mass distribution of the K^+K^- pairs as obtained in the LHCb measurement, where vertical lines indicate boundaries of mass bins employed in the analysis. In all other panels, the results of the maximum-likelihood fit to the data are superimposed, indicating the signal and background components as assigned by the respective fits. Note the different scales on the mass axes that make the signal distributions look similarly wide. (from [164, 165, 206, 466, 467]).

Table 6.3: Number of signal candidates, combined tagging power, and average decay-time resolution quoted for the latest CDF, D0, ATLAS, CMS and LHCb measurements of ϕ_s in the decays $B_s^0 \to J/\psi\phi$, respectively $B_s^0 \to J/\psi K^+K^-$.

	signal candidates	tagging power	decay-time resolution
CDF [164]	11'000	(1.39±0.05)%(OS) (3.5±1.4)%(SS)	90 fs
D0 [165]	6'500	$\approx 3\%$	
ATLAS [466]	22'500	$(1.45 \pm 0.05)\%$	
CMS [467]	49'000	$(0.97 \pm 0,03)\%$	
LHCb [206]	96'000	$(3.73 \pm 0.15)\%$	46 fs

is zero and the distribution of the measured decay times gives a good estimate for the true decay-time resolution. The decay-time distribution for background candidates was described in the CDF, D0 and ATLAS analyses by the sum of a δ-function or a narrow Gaussian function for the prompt background component due to random combinations of particles produced directly in the $p\overline{p}$ or pp collision, an exponential function for negative decay times to model badly reconstructed events and two falling exponential functions for positive decay times to model badly reconstructed events and backgrounds from decays of long-lived particles. In the CMS analysis, the prompt background component was rejected by an explicit cut on the decay time¿ Two exponential functions were employed, here, to model backgrounds at positive decay times. In all cases, the functions modelling the background distributions were convolved with a resolution function in a similar manner as the signal model.

Flavour tagging algorithms were employed in all analyses to distinguish between candidates that were initially produced as B_s^0 meson and candidates that were initially produced as $\overline{B}_s^0$ mesons. Flavour tagging at CDF and D0 and at LHCb has been discussed in Sections 4.3 and 4.4. The CDF analysis used a combination of opposite-side lepton and jet charge tagging algorithms and a same-side kaon tagging algorithm, while the D0 analysis employed a combination of opposite-side lepton and vertex charge algorithms and the LHCb analysis used opposite-side lepton, kaon and vertex charge algorithms and a same-side kaon tagging algorithm. Flavour tagging in the ATLAS analysis was based on a combination of opposite-side muon and jet-charge tagging algorithms and the CMS analysis relied on opposite-side muon and electron tagging algorithms. In the ATLAS analysis, the performance of the muon tagging algorithm was enhanced by considering not only the charge of the muon itself but also the sum of the charges of other particles in a cone around the direction of flight of the muon. All tagging algorithms returned in addition to a tagging decision also an event-by-event estimate of the probability for this decision to be wrong. A precise calibration of this mistag probability is essential as wrong tags lead to a dilution of the measured $B_s^0 - \overline{B}_s^0$ oscillation amplitude and therefore affect the measurement of ϕ_s. The combined opposite-side tagging algorithms were calibrated in all analyses, except that by the D0 collaboration, using large samples of decays $B^\pm \to J/\psi K^\pm$, in which the charge of the final-state kaon reveals the true identify of the decaying B meson. In the D0 analsis, the calibration of the tagging algorithm was performed by a measurement of the amplitude of the $B^0 - \overline{B}^0$ flavour oscillation signal in a sample of semileptonic decays $B^0 \to D^{*\mp}\ell^\pm X$. The measured amplitude should be ± 1, if the dilution due to flavour tagging and finite decay-time resolution of the experiment is correctly accounted for. The calibration of the same-side kaon tagging algorithms employed in the CDF and LHCb analyses has to be performed using samples of B_s^0 decays, since the performance of the algorithms relies on the properties of the hadronization process that leads to a B_s^0 meson. In both cases, the calibration was performed by measuring the amplitude of the $B_s^0 - \overline{B}_s^0$ flavour oscillation signal in flavour-specific decays $B_s^0 \to D_s^\mp \pi^\pm$. In CDF, no such

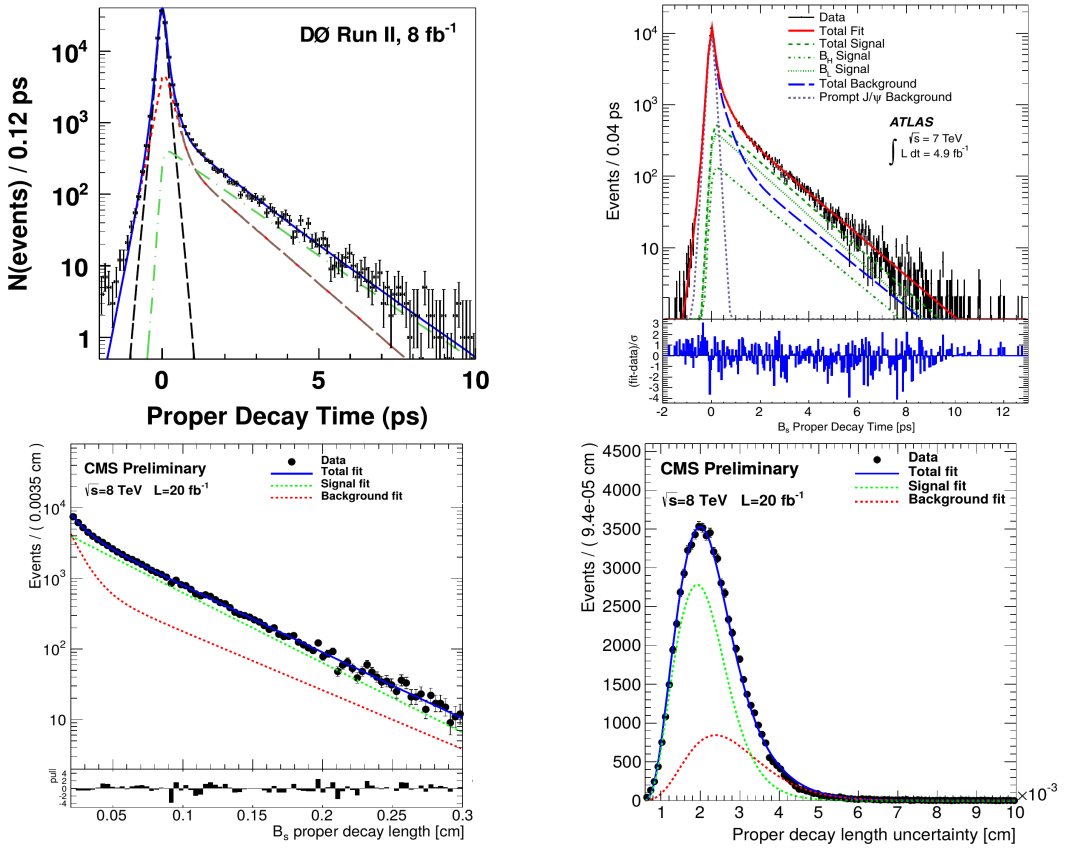

Figure 6.7: Measured decay-time or decay-length distributions for selected candidates from the latest (top left) D0, (top right) ATLAS and (bottom left) CMS measurements of the *CP* violating phase ϕ_s in the decay $B_s^0 \to J/\psi K^+K^-$. The bottom right panel shows the distribution of the estimated decay-length uncertainties from the CMS measurement. Note that a cut on the decay length was imposed in the CMS analysis, rejecting the prompt component that is prominent in the distributions from the D0 and ATLAS measurements. Projections of the maximum likelihood fit to the data are superimposed. In the upper left panel, the dash-dotted green line indicates the signal component, the long-dashed black line indicates the prompt background component and the short-dashed red line indicates the non-prompt background component. For the other panels, legends are shown inside the plots. The CDF collaboration did not publish a decay-time distribution from their final analysis, the corresponding results from the latest LHCb analysis are shown in Figure 6.8 (from [165, 466, 467]).

calibration sample was available for the later part of the data taking period since the increasing instantaneous luminosity led to low trigger efficiencies for B-meson decays to purely hadronic final states. The same-side tagging algorithm was therefore only applied for the first part of the data sample, corresponding to an instantaneous luminosity of 5.2 fb^{-1}. The effect of the flavour-tagging performance on the statistical precision of the measurement is given by the tagging power, $D = \varepsilon_{\text{tag}}(1 - 2\omega_{\text{tag}})$, where ε_{tag} is the fraction of signal candidates for which a flavour tagging decision can be assigned and ω_{tag} is the fraction of flavour tagging decisions that are wrong. The values of the combined tagging power measured in each of the analyses are summarized in Table 6.3.

Finally, the angular distributions of background components were modelled in the D0, CDF, ATLAS and CMS analyses by Legendre polynomials, sinusoidal functions or other empirical functions. In the case of the CDF analysis, the parameters describing the shape of these functions were fixed from a fit to candidates in the side-bands of the $J/\psi K^+K^-$ invariant-mass distribution. They were treated as free parameters in the maximum likelihood fit to the data in the case of the D0, ATLAS and CMS analyses. Acceptance and reconstruction efficiencies as a function of the decay angles were determined in all analyses from samples of

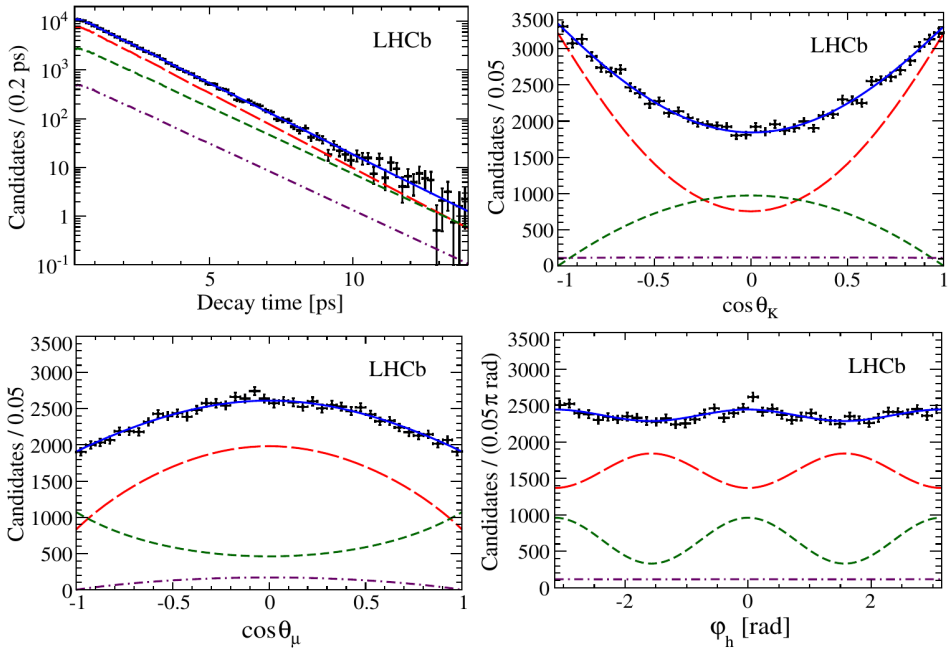

Figure 6.8: Measured distributions in decay time and helicity angles for the signal component in the latest LHCb measurement of the *CP* violating phase ϕ_s in the decay $B_s^0 \to J/\psi K^+K^-$. Projections of the maximum likelihood fit to the data are superimposed, where solid blue lines indicate the full signal contribution, long-dashed red lines indicate the *CP*-even *P*-wave component, short-dashed green lines indicate the *CP*-odd *P*-wave component and dash-dotted purple lines indicate the *S*-wave component, which is also *CP*-odd. The difference in lifetime between the *CP* even and *CP* odd components are clearly visible in the decay time projection (from [206]).

simulated events.

Some results of the maximum likelihood fits to the data are shown in Figures 6.7 and 6.8. In all analyses, fit parameters included the main observables of interest, namely the *CP* violating phase ϕ_s and the decay-width difference $\Delta\Gamma_s$, as well as the average decay width or lifetime, $\overline{\Gamma}_s \equiv 1/c\tau_s$, in the $B_s^0\overline{B}_s^0$ system, magnitudes and phases of the strong decay amplitudes. In the CDF, D0, ATLAS and CMS analyses, the value of the $B_s^0 - \overline{B}_s^0$ oscillation frequency, Δm_s, was fixed using external input. In the LHCb analysis, Δm_s was treated as a free parameter in the fit and the result

$$\Delta m_s \;=\; 17.711\,^{+0.055}_{-0.057}\,(\text{stat}) \;\pm\; 0.011\,(\text{syst})\;\text{ps}^{-1}$$

is compatible with that obtained in the dedicated LHCb measurement of Δm_s in the decay $B_s^0 \to D_s^-\pi^+$, discussed in Section 5.1. The LHCb analysis also included the parameter $|\lambda_{J/\psi\phi}|$ as a free fit parameter. The result,

$$|\lambda_{J/\psi\phi}| \;=\; 0.964 \;\pm\; 0.019\,(\text{stat}) \;\pm\; 0.007\,(\text{syst})\;,$$

is compatible with no significant direct *CP* violation in the decay. Finally, the LHCb analysis also yielded the most precise result for the *CP* violating phase to date, namely

$$\phi_s \;=\; 0.058 \;\pm\; 0.049\,(\text{stat}) \;\pm\; 0.006\,(\text{syst})\;\;\text{rad}\;.$$

The quoted systematic uncertainty was found to be dominated by effects related to the knowledge of the angular acceptance, the modelling of the decay-time resolution, the correction for the small $B^0 \to J/\psi K^{*0}$ background contamination, and to the assumption, inherent in the applied ${}_s$Plot technique, that the fit variables are uncorrelated with the invariant mass of the $J/\psi K^+K^-$ candidate. The results of all measurements in terms of ϕ_s, and $\Delta\Gamma_s$ are compared

in Figure 6.12. Due to the limited sizes of the signal samples, the CDF and D0 analyses found that the results of the maximum likelihood fits to their data were affected by biases that depended on the true values of the fit parameters themselves. Confidence regions in the $(\phi_s, \Delta\Gamma_s)$ plane were therefore extracted using many samples of simulated "toy experiments", in which the values of these parameters were varied over a wide region. Due to this approach, statistical and systematic uncertainties were not quoted separately for these measurements. In the ATLAS and CMS analyses, the precision on ϕ_s was found to be limited by statistical uncertainties. Leading systematic uncertainties were found to be related to the modelling of the angular acceptance in both analyses, to the understanding of the tagging performance and the fraction of $B^0 \to J/\psi K^{*0}$ background in the ATLAS analysis, and to possible biases from neglecting the possibility of direct *CP* violation and other model assumptions in the CMS analysis.

6.1.2 Resolving the ambiguity in the determination of ϕ_s and $\Delta\Gamma_s$

As discussed in the introduction to this section, the time-dependent differential $B_s^0 \to J/\psi K^+K^-$ decay rate is invariant under the simultaneous transformation

$$\left(\phi_s, \Delta\Gamma_s, \delta_0, \delta_\parallel, \delta_\perp, \delta_S\right) \leftrightarrow \left(\pi - \phi_s, -\Delta\Gamma_s, -\delta_0, -\delta_\parallel, \pi - \delta_\perp, -\delta_S\right) ,$$

leading to a two-fold ambiguity in the determination of the *CP* violating phase, ϕ_s, and the sign of the decay-width difference, $\Delta\Gamma_s$, in the $B_s^0\overline{B}_s^0$ system. This ambiguity was resolved by an LHCb measurement [471] that investigated the evolution of the strong phases δ_0, $\delta_\parallel$, $\delta_\perp$ and δ_S as a function of the K^+K^- invariant mass in the region around the $\phi \to K^+K^-$ resonance. A similar analysis of strong phases in the decay mode $B^0 \to J/\psi K^{*0}$ with $K^{*0} \to K^+\pi^-$ had allowed the BaBar collaboration [374] to break a two-fold ambiguity in the determination of the CKM angle β. The BaBar measurement is described here in Section 5.3.

The total $B_s^0 \to J/\psi K^+K^-$ decay rate in the region of the ϕ resonance is a coherent sum of a resonant P-wave contribution, in which the K^+K^- pair is produced via an intermediate ϕ meson and with relative angular momentum $L_{KK} = 1$, and a non-resonant S-wave contribution, in which the K^+K^- pair is produced with relative angular momentum $L_{KK} = 0$. A time-dependent angular analysis of the decay allows to extract the magnitudes and relative strong phases of the different amplitudes, up to the mentioned two-fold ambiguity. The ambiguity can be broken by performing the analysis in bins of the K^+K^- mass across the resonance and studying the evolution of the difference between the strong phases of the P-wave and S-wave amplitudes. The strong phases of the P-wave amplitudes, δ_0, $\delta_\parallel$ and $\delta_\perp$, are expected to exhibit a large positive shift as they go through a resonance at the mass of the ϕ meson, while the phase of the non-resonant S-wave amplitude, δ_S, is expected to evolve only slowly as a function of the $K\pi$ invariant mass in this region. The difference between the phase of the S-wave and the phase of any of the P-waves, e.g. $\delta_S - \delta_\perp$, is therefore expected to undergo a large negative shift at the mass of the resonance. Measuring the sign of this phase shift in data allows to distinguish between the solutions with $\delta_\perp$ and $\pi - \delta_\perp$ and thereby break the ambiguity.

The LHCb measurement was based on a data set corresponding to an integrated luminosity of 0.37 fb^{-1} collected in the first half of 2011. The selection of $B_s^0 \to J/\psi K^+K^-$ candidates was based on similar criteria as in the ϕ_s measurement described above. Candidates with a reconstructed decay time below 0.3 ps were discarded to eliminate the large component of prompt combinatorial background from random combinations of J/ψ mesons and charged particles from the pp interaction point. The ${}_sPlot$ technique, using the invariant mass of the selected $J/\psi K^+K^-$ candidates as a discriminating variable, was again employed to statistically subtract the background component in the maximum likelihood fit to the decay-time, flavour-tagging, and angular variables. The decay-time resolution was modelled in the fit by a sum

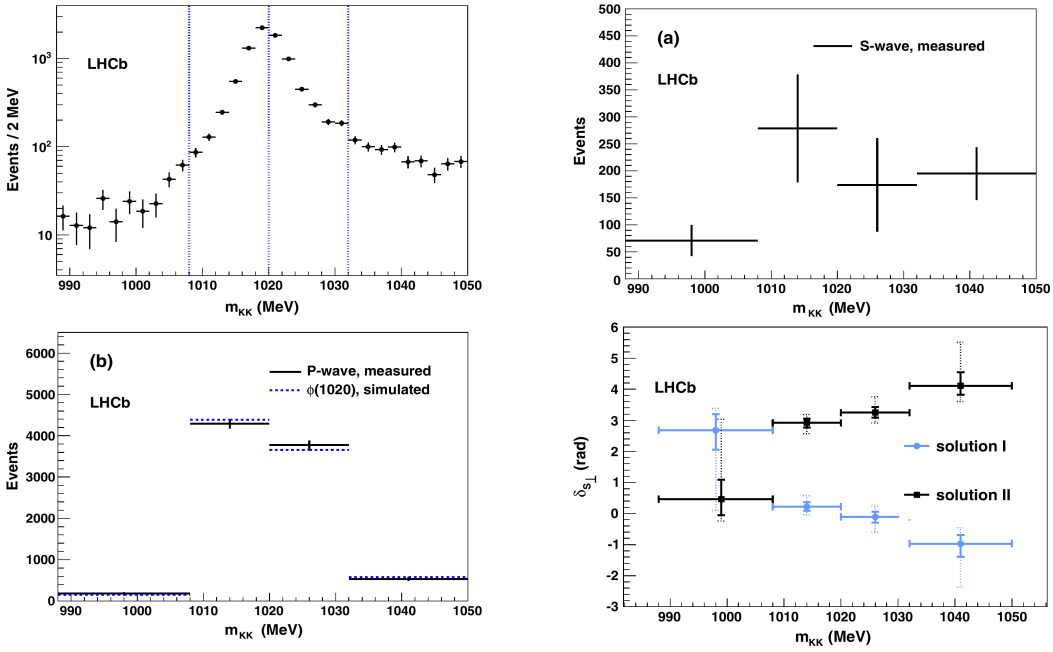

Figure 6.9: Results of the LHCb analysis of strong phases in the decay $B_s^0 \to J/\psi K^+K^-$: (top left) invariant-mass distribution of K^+K^- pairs for the selected $B_s^0 \to J/\psi K^+K^-$ candidates, where vertical lines indicate the boundaries of the four invariant-mass bins for which the strong phases were determined; (top right) number of candidates in each bin that the fit assigned to the S-wave component; (bottom left) number of candidates in each bin that the fit assigned to the P-wave components; and (bottom right) difference $\delta_S - \delta_\perp$ between the strong phases of the S-wave amplitude and one of the P-wave amplitudes. The two ambiguous solutions are shown, where solution I shows the expected negative trend. This is the solution that corresponds to a positive value of $\Delta\Gamma_s$ and a value of ϕ_s close to zero as predicted by the Standard Model (from [471]).

of three Gaussian functions with parameters derived from a fit to fake $J/\psi K^+K^-$ candidates formed by prompt J/ψ mesons and pairs of kaons produced in the pp interaction. Flavour tagging was based on a combination of opposite-side lepton, kaon and vertex charge algorithms and the estimated mistag probability returned by the algorithm was calibrated on flavour-specific B meson decays. The same-side kaon tagging algorithm employed in later analyses had not yet been commissioned at the time of this measurement. Also untagged events, for which the initial flavour of the B_s^0 meson could not be derived, where included in the fit, since they provide sensitivity to the B_s^0 lifetime and decay amplitudes. The fit was performed in four bins of the K^+K^- invariant mass between 988 and 1050 MeV/c^2 as illustrated in Figure 6.9. The CP violating phase, ϕ_s, the decay width difference, $\Delta\Gamma_s$, and the relative magnitudes and strong phases of the decay amplitudes in each of the four bins, were free parameters in the fit. It was assumed in the fit that the three P-wave amplitudes exhibit the same dependence on the invariant mass of the K^+K^- pair.

The number of candidates assigned to the S-wave component is similar in each of the four mass bins, in agreement with the expected constant S-wave contribution across the four mass bins. The distribution of the number of candidates assigned to the P-wave component peaks as expected at the mass of the ϕ meson and agrees well with that extracted from a sample of simulated $B_s^0 \to J/\psi\phi$ events. The average value of the phase difference $\delta_S - \delta_\perp$ for each of the four bins shows a clear trend across the four bins. The significance of this trend was estimated to correspond to 4.7 Gaussian standard deviations by performing a maximum likelihood fit of a straight line to the four data points and calculating the increase in the log likelihood value when the slope of the line was fixed to zero. The solution that shows the expected negative trend is that with positive value of $\Delta\Gamma_s$ and with ϕ_s close to zero as expected in the Standard

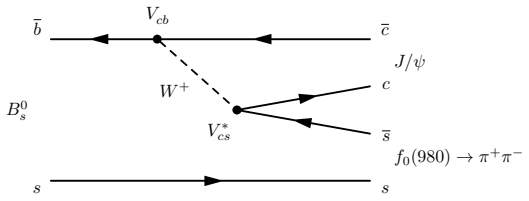

Figure 6.10: Tree diagram for the decay $B_s^0 \to J/\psi f_0(980)$, followed by $f_0(980) \to \pi^+\pi^-$.

Model. This result implies that the lighter of the two mass eigenstates in the $B_s^0\overline{B}_s^0$ system is almost aligned with the *CP* even eigenstate and decays faster than the heavier of the two mass eigenstates.

The result of this analysis was confirmed as part of an LHCb measurement of ϕ_s based on the full 2011 data set [204], corresponding to an integrated luminosity of 1 fb^{-1}.

6.1.3 Measurements in $B_s^0 \to J/\psi\pi^+\pi^-$

The decay $B_s^0 \to J/\psi f_0(980)$ followed by $f_0(980) \to \pi^+\pi^-$ was suggested in Ref. [472] as a promising alternative for measuring the *CP* violating phase ϕ_s. The $f_0(980)$ meson is a scalar particle that is expected to contain a significant $s\overline{s}$ component. Its mass lies just below the K^+K^- threshold and it therefore decays predominantly to a pair of pions, but its coupling to K^+K^- has been demomstrated by Dalitz-plot analyses of the decays $B^\pm \to K^\pm K^+K^-$ at BaBar [473, 474] and $J/\psi \to \phi K^+K^-$ at BES [475]. The decay is expected to ve dominated by the tree process illustrated in Figure 6.10 and involves the same CKM phases as the decay $B_s^0 \to J/\psi\phi$ discussed above.

The branching fraction for this decay is about a factor of five smaller than that for the decay $B_s^0 \to J/\psi\phi$. However, since the $f_0(980)$ meson is a scalar particle with internal spin $J = 0$, the relative angular momentum between the J/ψ and the $f_0(980)$ is fixed to $L = 1$. The final state the therefore produced in a pure *CP*-odd eigenstate and no angular analysis is required to separate different *CP* components.

The first measurement of ϕ_s in this decay mode by the LHCb collaboration [476] was based on a data set corresponding to an integrated luminosity of 0.41 fb^{-1}, collected in 2010 and first half of 2011 and found a result compatible with that from the $B_s^0 \to J/\psi\phi$ analysis, albeit with larger statistical uncertainty. Dalitz-plot analyses of the decay $B_s^0 \to J/\psi\pi^+\pi^-$ by the LHCb collaboration [477] then showed that the decay to this final state could be well described by a combination of resonant $s\overline{s}$ components, in particular the $f_0(980)$, $f_0(1370)$, and $f_2(1270)$, with a possible non-resonant S-wave contribution of about 8%. More than 90% of the ammplitude were attributed to were attributed to processes that produce the $\pi^+\pi^-$ pair with relative angular momentum $L_{\pi\pi} = 0$ and therefore yield a *CP* odd final state. A small fraction of the amplitude, attributed to the $f_2(1270)$ resonance, produces $\pi^+\pi^-$ pairs with relative angular momentum $L = 2$ and can lead to a *CP* odd final state if the $f_2(1270)$ and J/ψ resonances are produced in a state with transverse relative polarization. However, the fit indicated that this contribution is small and that the *CP* odd component of the final state is larger than 97.7% at 95% confidence level.

A subsequent LHCb measurement of ϕ_s in this decay mode [478], based on the full 2011 data set corresponding to an integrated luminosity of 1 fb^{-1}, extended the analysis to include $\pi^+\pi^-$ pairs with an invariant masses in the range from 775 to 1550 MeV/c^2. The possible small *CP* even component was neglected and no angular analysis was performed. The decay-time

dependent decay rate is then simply given by

$$\frac{d\Gamma_q\,(B_s^0 \to J/\psi\pi^+\pi^-)}{dt} \;\propto\; e^{-\overline{\Gamma}_s t}\,\{\cosh(\Delta\Gamma_s\,t/2) \;+\; \cos\phi_s\cdot\sinh(\Delta\Gamma_s\,t/2) \;+\; q\;\cdot\;\sin\phi_s\cdot\sin(\Delta m_s t)\}\;,$$

where again $q = +1$ for an initial B_s^0 meson and $q = -1$ for an initial $\overline{B}_s^0$ meson. As noted before, the untagged decay rate,

$$\frac{d\Gamma\,(B_s^0 \to J/\psi\pi^+\pi^-)}{dt} \;\propto\; 2\,e^{-\overline{\Gamma}_s t}\,\{\cosh(\Delta\Gamma_s\,t/2) \;+\; \cos\phi_s\cdot\sinh(\Delta\Gamma_s\,t/2)\}$$

also provides some sensitivity to ϕ_s via the non-zero value of the decay-width difference, $\Delta\Gamma_s$. Untagged signal candidates were therefore included in the analysis. The values of the average decay width, $\overline{\Gamma}_s$, the decay width difference, $\Delta\Gamma_s$, and the $B_s^0-\overline{B}_s^0$ oscillation frequency, Δm_s, were constrained to their values measured in other LHCb analyses. The statistical uncertainty on the measurement of ϕ_s was about a factor of two larger than that obtained in the $B_s^0 \to J/\psi\phi$ analysis. The two central values were compatible with each other. The result of a combined analysis using both decay modes was published in Ref. [204].

The most recent LHCb analysis of $\phi_s$in the decay mode $B_s^0 \to J/\psi\pi^+\pi^-$ [205] was based on the full run I data set, corresponding to an integrated luminosity of 3 fb^{-1}. In view of the increased size of the available data sample, a full time-dependent angular analysis was performed, avoiding the need to rely on the assumption of a purely *CP* odd final state. The differential decay rate was measured as a function of the decay-time, the three decay angles, and the invariant mass of the $\pi^+\pi^-$ pair. Neglecting the effect of *CP* violation in $B_s^0-\overline{B}_s^0$ mixing, which is known to be small compared to the precision this measurement aimed for,

$$\frac{d\Gamma_q\,(B_s^0 \to J/\psi\pi^+\pi^-)}{dt\,dm_{\pi\pi}\,d\omega} \;\propto\; e^{-\overline{\Gamma}_s t}\times\left\{\frac{|A_f|^2+|\overline{A}_f|^2}{2}\,\cosh\left(\tfrac{\Delta\Gamma_s}{2}\,t\right) \;-\; \mathrm{Re}\left(\phi_s\,A_f^*\,\overline{A}_f\right)\sinh\left(\tfrac{\Delta\Gamma_s}{2}\,t\right) + q\left(\frac{|A_f|^2-|\overline{A}_f|^2}{2}\,\cos(\Delta m_s\,t) \;-\; \mathrm{Im}\left(\phi_s\,A_f^*\,\overline{A}_f\right)\sin(\Delta m_s\,t)\right)\right\}\;,$$

where $q = +1$ for an initial B_s^0 meson and $q = -1$ for an initial $\overline{B}_s^0$ meson. The amplitudes A_f and $\overline{A}_f$ describe the dynamics of the decay and contain the dependence on $m_{\pi\pi}$ and on the decay angles ω. They were parametrized in a similar fashion to other Dalitz-plot analyses described in Section 5.5. Explicit expressions have been derived in Ref. [479].

The decay-time resolution was modelled in the fit to the data by the sum of three Gaussian probability density functions with standard deviations derived on an event-by-event basis from the estimated measurement uncertainty returned by the reconstruction algorithm. A constant offset and scale factors were applied to these estimates to take into account the effects of an imperfect understanding of the measurement uncertainties. This offset and the scale factors were derived from collision data using samples of fake $B_s^0 \to J/\psi\pi^+\pi^-$ candidates formed by combining prompt J/ψ candidates and two charged pions produced in the primary pp interaction. The dependence of the acceptance on the decay-time was modelled by an empirical function

$$\varepsilon(t) \;=\; \frac{\alpha\cdot(t-t_0)^n}{1+\alpha\cdot(t-t_0)^n} \;\times\; (1+\beta_1 t+\beta_2 t^2)\;,$$

where the first term describes the efficiency loss at small decay times due to trigger and selection requirements and the second term describes efficiency loss at large decay times due to detector acceptance and deteriorating track reconstruction efficiency. The parameters α, n, β_1 and β_2 were determined from collision data using a control sample of $B^0 \to J/\psi K^{*0}$ events with $K^{*0} \to K^\pm\pi^\mp$. A small difference in the decay-time dependence of the acceptance between this control channel and the signal mode $B_s^0 \to J/\psi\pi^+\pi^-$ was estimated and corrected for using

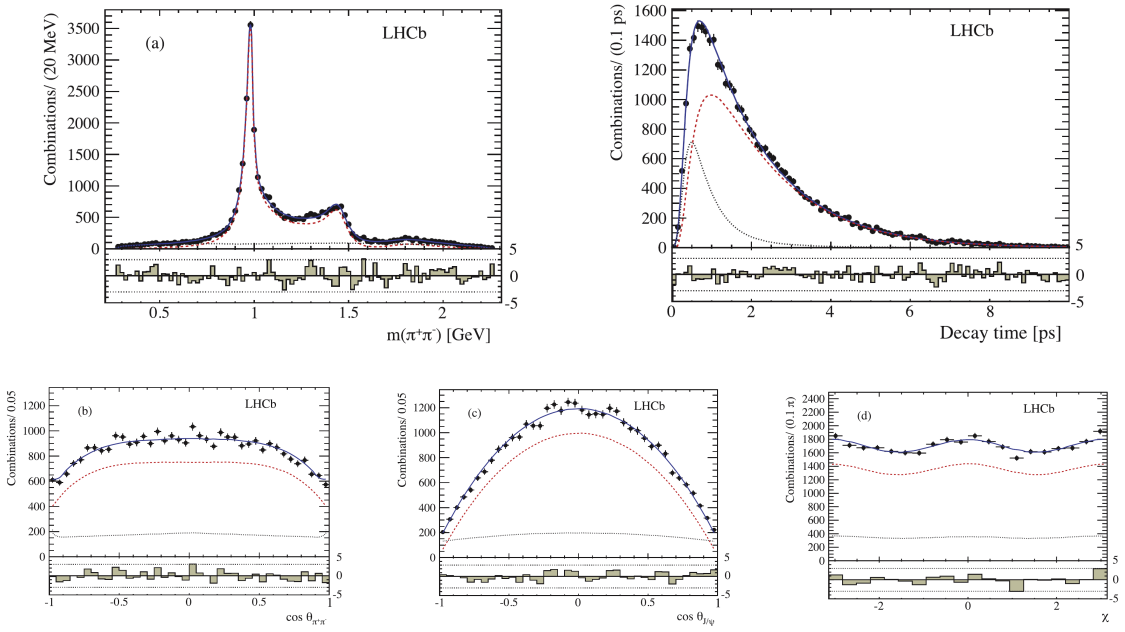

Figure 6.11: Measured distributions of (top left) the invariant mass of the $\pi^+\pi^-$ pair, (top right) the decay time and (bottom) the three helicity angles for selected candidates from the latest LHCb measurement of the *CP* violating phase ϕ_s in the decay $B_s^0 \to J/\psi\pi^+\pi^-$. The results of the maximum-likelihood fit to the data are superimposed, where red dashed lines indicate the signal component and black dotted lines indicate the background component (from [205]).

samples of simulated events. The initial flavour of the B_s^0 or $\overline{B}_s^0$ meson was derived from the usual combination of opposite-side and same-side kaon tagging algorithms. The estimated event-by-event mistag probability returned by the tagging algorithm was calibrated in the usual manner on collision data, using flavour-specific control channels in the case of the opposite-side tagging algorithms and by fitting the $B_s^0 - \overline{B}_s^0$ oscillation amplitude in $B_s^0 \to D_s^{\pm}\pi^{\mp}$ in the case of the same-side kaon tagging algorithm. The angular acceptance was corrected using samples of simulated events. Following the results of the earlier time-integrates analysis [477], the amplitude model was described by a coherent sum of five interfering amplitudes from intermediate $f_0(980)$, $f_0(1500)$, $f_0(1790)$, $f_2(1270)$ and $f_2'(1270)$ resonances. As a cross check, an additional S-wave contribution was implemented and the effect on the result was found to be small. The results of the fit to the measured $\pi^+\pi^-$ invariant-mass distribution and the measured distributions in decay time and decay angles are shown in Figure 6.11. The values of $\overline{\Gamma}_s$, $\Delta\Gamma_s$ and Δm_s were constrained to their values found in other LHCb analyses [204, 248], but $|\lambda_{J/\psi\pi\pi}|$ was a free parameter in the fit, allowing for a non-zero asymmetry from direct *CP* violation in the decay. The obtained results

$$|\lambda_{J/\psi\pi\pi}| \;=\; 0.89 \,\pm\, 0.05\,(\text{stat}) \,\pm\, 0.01\,(\text{syst})$$

and

$$\phi_s \;=\; 0.070 \,\pm\, 0.068\,(\text{stat}) \,\pm\, 0.008\,(\text{syst}) \;\text{rad}\;,$$

are compatible with those obtained in the analysis of the decay mode $B_s^0 \to J/\psi K^+K^-$. The systematic uncertainty on this measurement was found to be dominated by effects related to the resonance model and to a potential bias due to a possible $B_s^0 - \overline{B}_s^0$ production asymmetry in pp collisions. A measurement of this asymmetry has in the meantime been performed by the LHCb collaboration [480] and no significant asymmetry was found Within the precision of the measurement of about 2%.

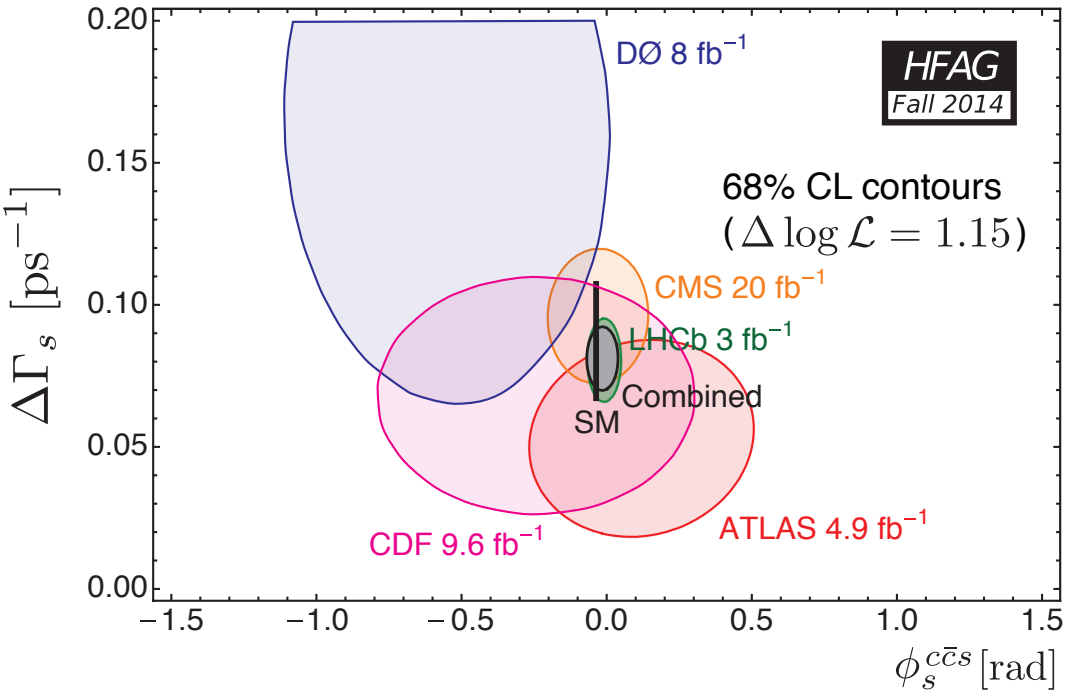

Figure 6.12: Constraints on the decay-width difference $\Delta\Gamma_s$ and the *CP* violating phase ϕ_s as compiled by the Heavy Flavour Averaging Group at the end of summer 2014 (from [2]).

6.1.4 Constraints on ϕ_s and $\Delta\Gamma_s$

Constraints on ϕ_s, and $\Delta\Gamma_s$ from the latest measurements at CDF, D0, ATLAS, CMS and LHCb are shown in Figure 6.12. Only one of the two ambiguous solutions $(\phi_s, \Delta\Gamma_s) \leftrightarrow (\pi - \phi_s, -\Delta\Gamma_s)$ is shown, according to the result of the analysis of strong phases in $B^0_s \to J/\psi K^+K^-$, that excluded the second solution with a significance corresponding to 4.7 Gaussian standard deviations.

Combining the results available at the end of summer 2014, the Heavy Flavour Averaging Group [2] quote a world average of

$$\phi_s \;=\; -0.015 \,\pm\, 0.035 \;\text{rad}$$

which is in good agreement with, but still significantly less precise than, the Standard Model expectation [3],

$$\phi_s \;=\; -2\beta_s \;=\; -0.0365\,^{+0.0012}_{-0.0013} \;\text{rad}\;.$$

It should be noted, however, that the quoted uncertainty on the Standard Model expectation does not contain uncertainties related to the possible effects of subdominant decay amplitudes with different CKM phases from the dominant tree amplitude. As an example, generic decay topologies contributing to the decay $B^0_s \to J/\psi f_0(980)$ are illustrated in Figure 6.13, taken from Ref. [481]. A better understanding of such subdominant contributions becomes increasingly important as the precision of measurements improves.

6.2 The semileptonic asymmetries $a^s_{\rm sl}$ and $a^d_{\rm sl}$

The magnitude of the *CP* violating asymmetry in $B^0_s - \overline{B}^0_s$ or $B^0 - \overline{B}^0$ mixing can be measured via the rate asymmetries in decays to flavour-specific final states f. The final state f is called flavour specific if it can be reached via the decay of a B^0 meson, but not via the decay of a $\overline{B}^0$ meson. The charge-conjugated final state $\overline{f}$ can then be reached by the decay of a $\overline{B}^0$ meson, but not by that of a B^0 meson. The decay of an initial B^0 meson to the final state $\overline{f}$ can still

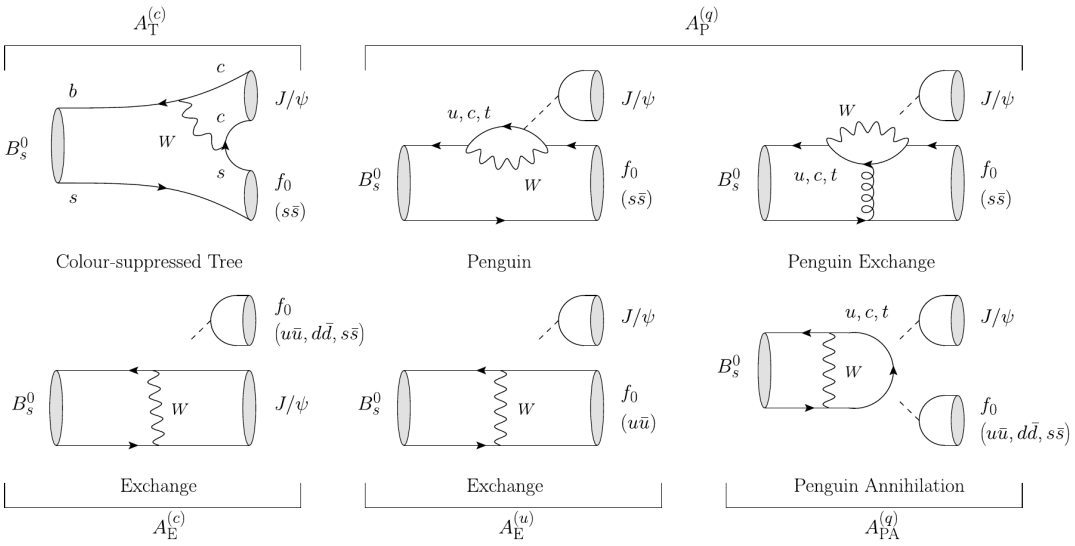

Figure 6.13: Illustration of decay topologies contributing to the decay $B_s^0 \to J/\psi f_0(980) \to J/\psi\pi^+\pi^-$ (from [481]).

occur, but only via mixing, i.e. via the process $B^0 \to \overline{B}^0 \to \overline{f}$. Likewise, the decay of an initial $\overline{B}^0$ meson to the final state f can occur via the mixing process $\overline{B}^0 \to B^0 \to f$ and only via this process. The flavour-specific charge asymmetry

$$a_{\rm fs}^d \;\equiv\; \frac{\Gamma\left(\overline{B}^0 \to B^0 \to f\right) \,-\, \Gamma\left(B^0 \to \overline{B}^0 \to \overline{f}\right)}{\Gamma\left(\overline{B}^0 \to B^0 \to f\right) \,+\, \Gamma\left(B^0 \to \overline{B}^0 \to \overline{f}\right)}$$

measures the relative difference in the mixing probabilities $B^0 \to \overline{B}^0$ and $\overline{B}^0 \to B^0$ and a non-zero value of this asymmetry implies that *CP* symmetry is violated in $B^0 - \overline{B}^0$ mixing. Likewise, the flavour-specific charge asymmetry

$$a_{\rm fs}^s \;\equiv\; \frac{\Gamma\left(\overline{B}_s^0 \to B_s^0 \to f\right) \,-\, \Gamma\left(B_s^0 \to \overline{B}_s^0 \to \overline{f}\right)}{\Gamma\left(\overline{B}_s^0 \to B_s^0 \to f\right) \,+\, \Gamma\left(B_s^0 \to \overline{B}_s^0 \to \overline{f}\right)}$$

measures the *CP* violating asymmetry in $B_s^0 - \overline{B}_s^0$ mixing. Semileptonic decays are particularly well suited for these measurements. They are flavour specific, since the conservation of electric charge ensures that b quarks can only decay to positive leptons and $\overline{b}$ quarks can only decay to negative leptons. Moreover, they are pure tree decays, excluding the possibility of a direct *CP* violation in the decay. The flavour-specific asymmetries measured in semileptonic decays are also called semileptonic charge asymmetries and are abbreviated by $a_{\rm sl}^d$ and $a_{\rm sl}^s$ for the $B^0\overline{B}^0$ and $B_s^0\overline{B}_s^0$ systems, respectively.

The phenomenology of particle-antiparticle mixing in the neutral meson systems has been discussed in Sections 3.1 and 3.3. The relevant points will be repeated here for convenience, taking again the $B^0\overline{B}^0$ system as an example. The same formalism applies for the $B_s^0\overline{B}_s^0$ system. The time-dependent probabilities for the mixing transitions $B^0 \to \overline{B}^0$ and $\overline{B}^0 \to B^0$ are given by

$$P_{B^0\to\overline{B}^0}(t) \;=\; \frac{1}{2}\left|\frac{q}{p}\right|^2 e^{-\overline{\Gamma}_d\, t}\left\{\cosh\left(\frac{\Delta\Gamma_d}{2}\,t\right) \,-\, \cos\left(\Delta m_d\, t\right)\right\}$$

and

$$P_{\overline{B}^0\to B^0}(t) \;=\; \frac{1}{2}\left|\frac{p}{q}\right|^2 e^{-\overline{\Gamma}_d\, t}\left\{\cosh\left(\frac{\Delta\Gamma_d}{2}\,t\right) \,-\, \cos\left(\Delta m_d\, t\right)\right\}\,,$$

where $\overline{\Gamma}_d$ is the average decay width, $\Delta\Gamma_d$ the decay width difference and Δm_d the mass difference between the two mass eigenstates in the $B^0\overline{B}^0$ system, and q and p define the two

mass eigenstates in terms of the flavour eigenstates,

$$|\,B_{L,H}\,\rangle \;=\; p\,|\,B^0\,\rangle \,\pm\, q\,|\,\overline{B}^0\,\rangle\;.$$

The two mixing probabilities differ, and *CP* symmetry is violated in mixing, if

$$\left|\frac{q}{p}\right| \;\neq\; 1\,,$$

i.e. when the two mass eigenstates are not aligned with the *CP* eigenstates

$$|\,B_{CP\pm}\,\rangle \;=\; \frac{1}{\sqrt{2}}\left(|\,B^0\,\rangle \,\pm\, |\,\overline{B}^0\,\rangle\right)\;.$$

The flavour-specific charge asymmetry is given in terms of the mixing probabilities by

$$\begin{aligned} a^{\rm d}_{\rm fs} \;&=\; \frac{P_{\overline{B}^0\to B^0}(t) \,-\, P_{B^0\to\overline{B}^0}(t)}{P_{\overline{B}^0\to B^0}(t) \,+\, P_{B^0\to\overline{B}^0}(t)} \\ &=\; \frac{|p/q|^2 \,-\, |q/p|^2}{|p/q|^2 \,+\, |q/p|^2} \;=\; \frac{1 \,-\, |q/p|^4}{1 \,+\, |q/p|^4}\quad, \end{aligned}$$

and does not depend on the decay time.

The creation of a *CP* violating asymmetry in any process requires the interference of two contributing amplitudes with different complex phase. In the case of mixing,

$$\frac{q}{p} \;=\; -\sqrt{\frac{M^*_{12} - i\frac{\Gamma^*_{12}}{2}}{M_{12} - i\frac{\Gamma_{12}}{2}}} \tag{6.1}$$

and it is a relative phase

$$\phi_d \;\equiv\; \arg\left(-\frac{M_{12}}{\Gamma_{12}}\right)$$

between the dispersive part, M_{12}, and the absorptive part, Γ_{12}, of the mixing amplitude that can lead to $|q/p| \neq 1$.

The observables, Δm_d, $\Delta\Gamma_d$ and $a^d_{\rm fs}$ are related to the mixing amplitudes via

$$\begin{aligned} \Delta m_d \;&\approx\; 2\,|M_{12}| \\ \Delta\Gamma_d \;&\approx\; 2\,|\Gamma_{12}|\,\cos\phi_d \\ a^d_{\rm fs} \;&=\; \tfrac{|\Gamma_{12}|}{|M_{12}|}\,\sin\phi_d \;\approx\; \frac{\Delta\Gamma_d}{\Delta m_d}\,\tan\phi_d\quad. \end{aligned}$$

The required phase ϕ_d is accommodated in the Standard Model, where the dispersive part of the $B^0\overline{B}^0$ mixing amplitude is dominated by box diagrams with intermediate top quarks while its absorptive part is dominated by box diagrams with charm quarks. The complex phase between the two amplitudes is given by the weak phases of the involved CKM elements,

$$\phi_d \;=\; 2\,\arg\left(\frac{V_{td}V^*_{tb}}{V_{cd}V^*_{cb}}\right)\;.$$

The same formalism applies in the $B^0_s\overline{B}^0_s$ system, where

$$a^s_{\rm fs} \;\approx\; \frac{\Delta\Gamma_s}{\Delta m_s}\,\tan\phi_s$$

and the weak phase of the mixing amplitude is in the Standard Model given by

$$\phi_s \;=\; -2\beta_s \;\equiv\; 2\,\arg\left(\frac{V_{ts}V^*_{tb}}{V_{cs}V^*_{cb}}\right)\;.$$

As discussed in the previous section, β_s is the small angle in one of the squashed unitarity triangles. As also pointed out in the previous section, the *CP* violating phase ϕ_s in $B_s^0 - \overline{B}_s^0$ mixing should not be confused with the mixing-induced *CP* violating phase in the decay $B_s^0 \to J/\psi\phi$, which is also denoted as ϕ_s. Both are equivalent to $-2\beta_s$ only up to the approximations of neglecting subdominant contributions to the $B_s^0 - \overline{B}_s^0$ mixing amplitude and the $B_s^0 \to J/\psi\phi$ decay amplitude and they can be affected differently by possible contributions from New Physics.

While the Standard Model accommodates *CP* violating phases in the $B^0 - \overline{B}^0$ and $B_s^0 - \overline{B}_s^0$ mixing amplitudes, the resulting *CP* violating asymmetries are expected to be very small, because the box diagrams with intermediate top quarks dominate strongly over those with intermediate charm quarks. The dispersive part of the mixing amplitude therefore dominates strongly over the absorptive part, and the interference effects that are necessary to create an asymmetry are restricted to be small. Estimates for the Standard Model values of the flavour-specific asymmetries have been quoted [482] as

$$\begin{aligned} a_{\rm fs}^d &= (-4.1 \pm 0.6) \times 10^{-4} \\ a_{\rm fs}^s &= (1.9 \pm 0.3) \times 10^{-5} \ , \end{aligned}$$

while the latest Standard Model fit by the CKMfitter group, taking into account measurements available by September 2014, but excluding direct measurements of $a_{\rm sl}^d$ and $a_{\rm sl}^s$, yielded

$$\begin{aligned} a_{\rm fs}^d \equiv a_{\rm sl}^d &= (-6.5\,^{+1.8}_{-1.9}) \times 10^{-4} \\ a_{\rm fs}^s \equiv a_{\rm sl}^s &= (2.9 \pm 0.8) \times 10^{-5} \ . \end{aligned}$$

The smallness of the asymmetries predicted by the Standard Model, combined with the fact that mixing proceeds through loop processes, make measurements of flavour-specific asymmetries a sensitive probe for possible contributions from New Physics.

The main challenges for measurements of $a_{\rm sl}^d$ and $a_{\rm sl}^s$ are on the one hand the need to accumulate large event samples to reach the best possible statistical precision and on the other hand the need to understand and correct for artificial asymmetries due to backgrounds, detection and reconstruction effects.

Two approaches have been followed in recent measurements at the B factories, at D0 and at LHCb. The first of these is to measure the asymmetry in the rate of like-sign dilepton pairs,

$$A_{\rm sl} \equiv \frac{\Gamma(\ell^+\ell^+) - \Gamma(\ell^-\ell^-)}{\Gamma(\ell^+\ell^+) + \Gamma(\ell^-\ell^-)} \ .$$

If one of the two leptons is due to the semileptonic decay of a b hadron and the other lepton is due to the semileptonic decay of the pair-produced $\overline{b}$ hadron, the observation of two leptons of the same charge sign implies that either the b hadron or the $\overline{b}$ hadron had mixed into its antiparticle at the time of its decay. Measuring different rates of positive and negative dilepton pairs implies that *CP* is violated in the mixing. At the B factories, mixing can appear only in the $B^0\overline{B}^0$ system and $A_{\rm sl}$ is therefore measures directly the semileptonic asymmetry $a_{\rm sl}^d$. At hadron colliders, mixing in both the $B^0\overline{B}^0$ and $B_s^0\overline{B}_s^0$ systems has to be considered and $A_{\rm sl}$ measures a linear combination of $a_{\rm sl}^d$ and $a_{\rm sl}^s$. The advantage of this approach is the large event yields, the main drawback is in the large backgrounds from other sources of charged leptons and possible asymmetries in these backgrounds.

Clean samples of semileptonic decays can be obtained by reconstructing the $D^{(*)\mp}$ or $D_s^{\mp}$ meson that is usually produced together with the charged lepton. However, the small branching fractions for charm decays to specific final states lead to a large loss in event yields if this charmed meson has to be fully reconstructed in any given final state. The BaBar collaboration published a measurement in which the charmed meson itself was not reconstructed but its presence was implied by the signature of a low-momenum pion from the decay $D^{*\pm} \to D\pi^{\pm}$. This low-momentum pion was required to be of opposite charge to that of the charged lepton

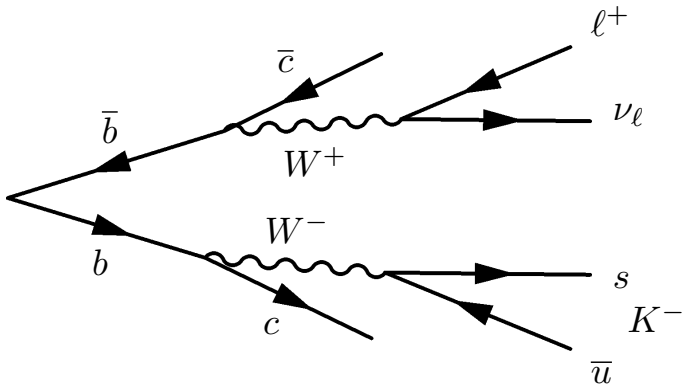

Figure 6.14: Illustration of use of kaon tagging in the BaBar measurement of the semileptonic asymmetry. Without mixing, the lepton on the signal side and the kaon on the tagging side carry opposite charge. Selecting events

as appropriate for semileptonic decay to $D^{*\mp}\ell^{\pm}X$ followed by $D^{*\mp} \to D\pi^{\mp}$. Flavour-specific information from the decay of the accompanying B meson in the event has to be employed to assign the initial flavours of the B^0 and $\overline{B}^0$ meson pair and thereby isolate the semileptonic decays that proceeded via mixing. This was done in the BaBar measurement by searching for charged kaons from the decay of the accompanying B meson. As discussed in Section 4.1, B^0 mesons decay predominantly to positive kaons while $\overline{B}^0$ mesons decay predominantly to negative leptons. As illustrated in Figure 6.14, the combination of a lepton and kaon of the same charge sign indicates a mixed event. The BaBar measurement is described in more detail below.

A similar approach does not seem feasible at hadron colliders due to the less clean event signatures and the lower flavour tagging efficiency. The approach chosen in measurements of $a^d_{\rm sl}$ and $a^s_{\rm sl}$ published by the D0 and LHCb collaborations is to fully reconstruct the charmed meson in the semileptonic decay but to not tag the initial flavour of the decaying B^0 or B^0_s meson. Taking this time the $B^0_s\overline{B}^0_s$ system as an example, the time-dependent decay rate to $D^+_s\ell^-$ pairs is then proportional to the sum of the mixing probabilities

$$P_{B^0_s\to\overline{B}^0_s}(t) \,+\, P_{\overline{B}^0_s\to\overline{B}^0_s}(t) \;=\; \frac{1}{2}\,e^{-\overline{\Gamma}_s\,t}\,\left\{\left(1+\left|\frac{q}{p}\right|^2_s\right)\,\cosh\left(\frac{\Delta\Gamma_s}{2}\,t\right)\,+\,\left(1-\left|\frac{q}{p}\right|^2_s\right)\,\cos\left(\Delta m_s\,t\right)\right\}$$

or, using

$$a^s_{\rm sl} \;=\; \frac{1\,-\,|q/p|^4_s}{1\,+\,|q/p|^4_s} \quad\Leftrightarrow\quad \left|\frac{q}{p}\right|^4_s \;=\; \frac{1\,-\,a^s_{\rm sl}}{1\,+\,a^s_{\rm sl}}$$

and the approximation

$$\left|\frac{q}{p}\right|^2_s \;=\; \sqrt{\frac{1-a^s_{\rm sl}}{1+a^s_{\rm sl}}} \;=\; \sqrt{\frac{(\,1-a^s_{\rm sl}\,)^2}{1-(\,a^s_{\rm sl}\,)^2}} \;\approx\; 1-a^s_{\rm sl}\;,$$

the time-dependent decay rates to $D^{\mp}_s\ell^{\pm}$ pairs are

$$\frac{d\Gamma\,(D^{\mp}_s\ell^{\pm})}{dt} \;\propto\; e^{-\overline{\Gamma}_s\,t}\,\left\{\left(1\pm\,\frac{a^s_{\rm sl}}{2}\right)\,\cosh\left(\frac{\Delta\Gamma_s}{2}\,t\right)\,\mp\,\frac{a^s_{\rm sl}}{2}\,\cos\left(\Delta m_s\,t\right)\right\}\;.$$

Finally, the decay-rate asymmetry becomes

$$\frac{\frac{d\Gamma}{dt}\,(D^-_s\ell^+)\,-\,\frac{d\Gamma}{dt}\,(D^+_s\ell^-)}{\frac{d\Gamma}{dt}\,(D^-_s\ell^+)\,+\,\frac{d\Gamma}{dt}\,(D^+_s\ell^-)} \;=\; \frac{a^s_{\rm sl}}{2}\;-\;\frac{a^s_{\rm sl}}{2}\,\frac{\cos\left(\Delta m_s\,t\right)}{\cosh\left(\Delta\Gamma_s\,t/2\right)}\;.$$

The same results apply of course for decays to $D^{(*)\mp}\ell^{\pm}$ pairs in the $B^0\overline{B}^0$ system, except that the decay-width difference $\Delta\Gamma_d$ is negligibly small and the final equations simplify to

$$\frac{d\Gamma\left(D^{(*)\mp}\ell^{\pm}\right)}{dt} \propto e^{-\overline{\Gamma}_d t}\left\{1 \pm \frac{a^d_{\rm sl}}{2} \mp \frac{a^d_{\rm sl}}{2}\cos\left(\Delta m_d t\right)\right\} .$$

and

$$\frac{\frac{d\Gamma}{dt}\left(D^{(*)-}\ell^{+}\right) - \frac{d\Gamma}{dt}\left(D^{(*)+}\ell^{-}\right)}{\frac{d\Gamma}{dt}\left(D^{(*)-}\ell^{+}\right) + \frac{d\Gamma}{dt}\left(D^{(*)+}\ell^{-}\right)} = \frac{a^d_{\rm sl}}{2} - \frac{a^d_{\rm sl}}{2}\cos\left(\Delta m_d t\right) .$$

Measurements of $a^d_{\rm sl}$ have been performed at LEP, CLEO, the Tevatron, BaBar and Belle, and LHCb. All measurements are compatible with a vanishingly small *CP* violating asymmetry in $B^0-\overline{B}^0$ mixing and are in good agreement with Standard Model predictions. The most precise results stem from recent measurements at BaBar, D0and LHCb.

The D0 collaboration published several measurements of the same-sign dilepton charge asymmetry that indicate a significant deviation from the Standard Model prediction. The effect persisted with increasing size of the analysed data sample and despite the inclusion in the analysis of additional sources of potential background asymmetries. As discussed above, the same-sign dilepton charge asymmetry measures a linear combination of $a^d_{\rm sl}$ and $a^s_{\rm sl}$ and in view of the good agreement between measurements and Standard Model predictions in the $B^0\overline{B}^0$ system it has been speculated that the observed deviation could be an indication for contributions from New Physics in $B^0_s-\overline{B}^0_s$ mixing.

Direct measurements of $a^s_{\rm sl}$ have recently been performed at D0 and LHCb. In particular the LHCb result agrees well with the Standard Model prediction of a very small asymmetry. Within their precision, both results are also compatible with the large same-sign dilepton asymmetry measured at D0.

The most recent measurements of $a^d_{\rm sl}$ will be described next, followed by the new measurements of $a^s_{\rm sl}$ and the D0 measurement of the same-sign dilepton charge asymmetry. The section will conclude with a brief summary.

6.2.1 Measurements of $a^d_{\rm sl}$

Measurements of the semileptonic charge asymmetry in the $B^0\overline{B}^0$ system have been published by the ALEPH and OPAL collaborations at LEP [218, 483], by the CLEO collaboration [213, 484, 485] and the CDF I [486] collaboration, and by the BaBar [487–492], Belle [493], D0 [494] and LHCb [495] collaborations. All measurements are compatible with a vanishingly small *CP* violating asymmetry in $B^0-\overline{B}^0$ mixing and are in good agreement with Standard Model predictions. The most precise results stem from the recent measurements at BaBar, D0 and LHCb.

One of the recently published measurements [491] by the BaBar collaboration has already been mentioned in the introduction to this section. This measurement was based on the full data set collected at the $\Upsilon(4S)$ resonance and employed the combination of a charged lepton with an oppositely charged low pion to imply a semileptonic decay to $D^{*\mp}\ell^{\pm}X$ followed by $D^{*\mp}\to D\pi^{\mp}$. In addition to this $\ell^{\pm}\pi^{\mp}$ pair, the presence of a charged kaon was required in the remainder of the event.

If this kaon was produced in the decay of the second B meson in the event, the sign of its charge contains information on the initial flavour of the signal B meson, and therefore allows to distinguish between mixed and unmixed signal candidates as illustrated in Figure 6.14 above. Such kaons will be referred to as K_T. However, charged kaons can also be produced in the decay of the signal B meson itself, for example in the decay of the D meson. Such kaons, referred to as K_R in the following, do not contain any information on the initial flavour or mixing state of the signal B meson but can be employed to extract detection asymmetries from

data. COnsidering only the signature of the semileptonic decay, the measured time-integrated asymmetry is given by

$$A_{\rm raw} \equiv \frac{N(\ell^+) - N(\ell^-)}{N(\ell^+) + N(\ell^-)} = a_\ell + a^d_{\rm sl}\,\chi_d \ ,$$

where a_ℓ is a charge asymmetry due to differences in detection efficiency for positive and negative leptons, and χ_d is the time-inegrated mixing probabiliy in the $B^0\overline{B}^0$ system. A signal-side kaon does not add any information but leads to an additional term due to the charge asymmetry, a_K, in the kaon detection efficiency,

$$A_R \equiv \frac{N(\ell^+K^+_R) - N(\ell^-K^-_R)}{N(\ell^+K^+_R) + N(\ell^-K^-_R)} = a_\ell + a_K + a^d_{\rm sl}\,\chi_d \ .$$

The combination with a charged kaon from the tagging side allows o separate mixed and unmixed events and, neglecting for now the effect of wrong tags, the measured raw asymmetry becomes

$$A_{\rm T} \equiv \frac{N(\ell^+K^+_T) - N(\ell^-K^-_T)}{N(\ell^+K^+_T) + N(\ell^-K^-_T)} = a_\ell + a_K + a^d_{\rm sl} \ .$$

The combination of these measurements allows to extract $a^d_{\rm sl}$ together with a_ℓ and a_K. The reconstructed trajectories of the lepton candidate and the low-momentum pion candidate were required to be compatible with the two particles originating from a common decay vertex. The momentum of the $D^{*\mp}$ candidate was estimated from the measured momentum of the low-momentum pion, which is produced almost at rest in the rest frame of the $D^{*\mp}$, due to the small amount of energy that is released in the decay $D^{*\mp} \to D\pi^\mp$. The mass of the missing neutrino from the semileptonic decay was then estimated as $m^2_\nu \equiv (E_{\rm beam} - E_{D^*} - E_\ell)^2 - (\vec{p}_{D^*}\vec{p}_\ell)^2$, where $E_{\rm beam}$ is the precisely known beam energy in the rest frame of the e^+e^- collision and $\vec{p}_\ell$ is the reconstructed momentum vector of the lepton candidate. The value of m^2_ν defined in this manner should be close to zero for signal candidates and can assume arbitrary values for background. The measured m^2_ν distribution is shown in Figure 6.15 together with the estimated signal and background contributions. The contribution from non-$B\overline{B}$ continuum was estimated from collision data collected at a centre-of-mass energy below the $\Upsilon(4S)$ resonance. The combinatorial background from $B\overline{B}$ events was determined from the fit to the m^2_ν distribution. The $D^{*\mp} \to D\pi^\mp$ signal component contains a fraction of events from processes of the type $B \to D^{*\mp}X\ell^\pm\nu_\ell$. This component is labelled D^{**} in the figure. A fraction of this type of events will be due the decay of non-oscillating $B^\pm$ mesons and this fraction was fixed in the fit 66% assuming conservation of isospin. The remaining backgrounds were estimated from samples of simulated events. Kaon candidates were selected by applying particle identification criteria that were tuned to yield a probability of 3% to misidentify a true pion for a kaon, for an efficiency of 85% to correctly identify a true kaon. Two discriminating variables were employed to distinguish between K_T and K_R candidates, namely the cosine of the opening angle between the reconstructed momentum vectors of the charged lepton and the kaon, $\cos\theta_{\ell K}$, and the distance along the beam axis between the position of the $\ell^\pm\pi^\mp$ vertex and the point of origin of the kaon candidate. The latter was estimated as the point of closest approach of the kaon trajectory to the beam axis. The distance between these two positions was translated into a decay time difference Δt using the Lorentz boost of the $\Upsilon(4S)$ rest frame in the laboratory system. The sample of selected signal candidates was split into the four lepton categories, $e^\pm$ and $\mu^\pm$, and eight tagging categories, $e^\pm K^\pm$, $e^\pm K^\mp$, $\mu^\pm K^\pm$ and $\mu^\pm K^\mp$. The candidates in each category were then binned according to their measured values of $\cos\theta_{\ell K}$, Δt, the estimated uncertainty on Δt, and the momentum of the kaon candidate. The measurement of $a^d_{\rm sl}$ was extracted from a combined four-dimensional fit to these binned distributions. The

signal components in bin j of the same-sign categories were parametrized as

$$\begin{aligned} G_{\ell^+K^+}(j) &= (1+a_\ell)\,(1+a_K)\,\times\,\Big\{ \\ &\quad (1-f_{K_R}^{++})\,\Big[\,(1-\omega_T^+)\,G_{B^0B^0}(j)\,+\,\omega_T^-\,G_{B^0\overline{B}^0}(j)\,\Big] \\ &\quad +\,f_{K_R}^{++}\,(1-\omega_R^+)\,G_{K_R}(j)\,(1+\chi_d\,a_{\rm sl}^d)\,\Big\} \end{aligned}$$

and as

$$\begin{aligned} G_{\ell^-K^-}(j) &= (1-a_\ell)\,(1-a_K)\,\times\,\Big\{ \\ &\quad (1-f_{K_R}^{--})\,\Big[\,(1-\omega_T^-)\,G_{\overline{B}^0\overline{B}^0}(j)\,+\,\omega_T^+\,G_{\overline{B}^0B^0}(j)\,\Big] \\ &\quad +\,f_{K_R}^{--}\,(1-\omega_R^-)\,G_{K_R}(j)\,(1-\chi_d\,a_{\rm sl}^d)\,\Big\}\ , \end{aligned}$$

where $f_{K_R}^{\pm\pm}$ describes the fractions of K_R kaons in each sample as a function of the momentum of the kaon candidate, while $\omega_T^\pm$ and $\omega_R^\pm$ describe the mistag fractions for K_T and K_R candidates, respectively. The function G_{K_R} describes the decay-time evolution for $\ell^\pm K_R^\pm$ candidates and its shape was derived from a subsample of the selected events enriched in such candidates. The functions $G_{B^0B^0}$, $G_{B^0\overline{B}^0}$, $G_{\overline{B}^0B^0}$ and $G_{\overline{B}^0\overline{B}^0}$ describe the decay-time evolution for $\ell^\pm K_T^\pm$ candidates. They were parametrized by convolving the theoretical equations that describe the time evolution of $B^0\overline{B}^0$ mixing with a decay-time resolution function. The theoretical equations were expanded, as prescribed in Ref. [496], to include the small effect of interference between Cabibbo-favoured and doubly Cabibbo suppressed decays on the tagging side. The decay-time resolution was described by a combination of several Gaussian functions convolved with an exponential function to take into consideration the finite lifetime of intermediate charmed mesons. The fit functions contained a total of 168 parameters, including $a_{\rm sl}^d$ and the detection asymmetries a_ℓ and a_K, that were determined from the fit to the data. Possible biases due to the fit procedure were investigated using samples of simulated events and were found to be negligible. The result of the measurement is listed in Table 6.4. Its precision was found to be limited by systematic uncertainties related to the understanding of the composition of the sample of selected candidates.

The BaBar collaboration recently submitted for publication a measurement of $a_{\rm sl}^d$ that uses same-sign dilepton pairs and is based on the full data set collected at the $\Upsilon(4S)$ resonance [492]. Signal candidates were selected by requiring the two tracks with the highest and the second highest reconstructed momentum in the event to be identified as an electron or as a muon. Event-shape variables were employed to reduce background from non-$B\overline{B}$ continuum events. To suppress backgrounds further, selection criteria were applied on the values of the momenta and particle identification information for the two lepton candidates, their invariant mass, the opening angle between the two tracks and the distance between their points of closest approach to the beam axis. Lepton candidates that gave an invariant mass compatible with the mass of the J/ψ resonance or with being due to a photon conversion were rejected. Several of these selection criteria were combined into a multivariate classifier. The two lepton candidates were ordered by the magnitudes of their reconstructed momenta and a total of sixteen event categories were defined according to the charge sign and flavour of each of the two candidates: e^+e^+, $\mu^+\mu^+$, $e^+\mu^+$, and μ^+e^+, the same four categories for negative same-sign dilepton pairs, and another eight categories for pairs of opposite-sign dilepton candidates. In each category, the background component due to non-$B\overline{B}$ continuum events was subtracted using collision data collected at a centre-of-mass energy below the $\Upsilon(4S)$ resonance. The remaining number of candidates after this background subtraction in each of the eight same-sign event categories was parametrized as

$$N_{\ell_1\ell_2}^{\pm\pm}\ \equiv\ \frac{1}{2}N_{\ell_1\ell_2}^0\,(1+R_{\ell_1\ell_2}^{\pm\pm}\left[\,1\pm A_{\ell_1}\pm A_{\ell_2}\pm\frac{1+(c_{\ell_1\ell_2}^{\pm\pm}-w_{\ell_1\ell_2}^{\pm\pm})\,R_{\ell_1\ell_2}^{\pm\pm}}{1+R_{\ell_1\ell_2}^{\pm\pm}}\ a_{\rm sl}^d\right]\chi_{\ell_1\ell_2}\ ,$$

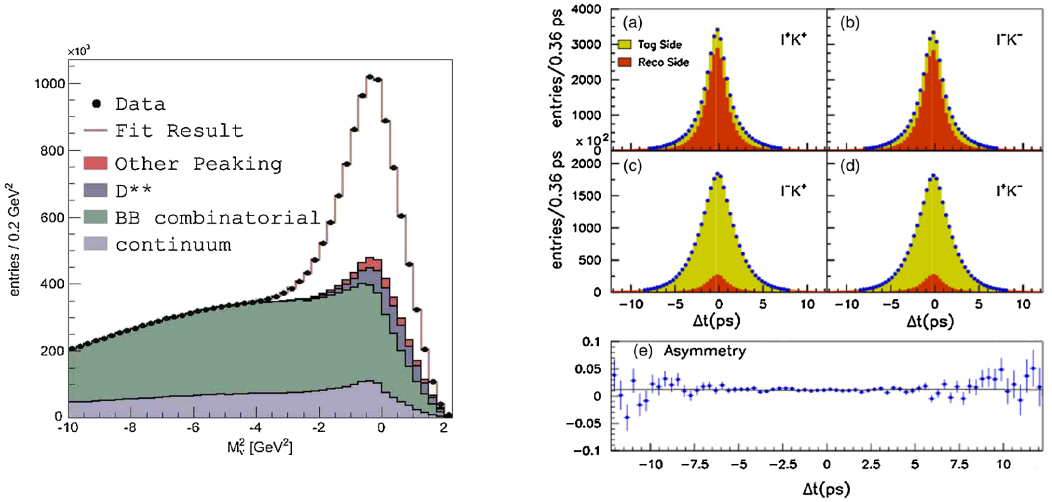

Figure 6.15: Results of the BaBar measurement of $a_{\rm sl}^d$ employing partially reconstructed $D^{*\mp}$ candidates and kaon tagging. The panel on the left shows the distribution of the estimated neutrino mass that was employed to determine the composition of the candidate sample; the results of the fit are superimposed as described by the plot legend. The panels on the right show Δt distributions for different tagging categories, after subtraction of the non-$B\overline{B}$ background component, as well as the resulting raw asymmetry between ℓ^+K^+ and ℓ^-K^- candidates; "Tag Side" and "Reco Side" refer to ℓK_T and ℓK_R candidates, respectively (from [491]).

where $N^0_{\ell_1\ell_2}$ is a normalization factor, A_{ℓ_1} and A_{ℓ_2} are the charge asymmetries in the detection efficiencies for the higher- and lower-momentum lepton candidate, respectively, R is the yield ratio between the remaining $B\overline{B}$ background and the signal component for this event category, c and w are the probabilities for a background event in this category to accidentally yield the correct, respectively wrong, charge sign assignment, and $\chi_{\ell_1\ell_2}$ is the effective time-integrated mixing probability, including acceptance effects. The number of candidates in each of the eight opposite-sign event categories was parametrized as

$$N^{\pm\mp}_{\ell_1\ell_2} \equiv \frac{1}{2} N^0_{\ell_1\ell_2} \left(1 + R^{\pm\mp}_{\ell_1\ell_2}\right) \left[1 \pm A_{\ell_1} \mp A_{\ell_2}\right] \left(1 - \chi_{\ell_1\ell_2} + r_B\right) ,$$

where r_B is the ratio between the number of charged and neutral $B\overline{B}$ meson pairs. The parameters R, c and w are different for each of the sixteen event categories and were determined from samples of simulated events, while the four parameters A_{μ_1}, A_{μ_2}, A_{e_1} and A_{e_2}, the four parameters $N^0_{\ell_1\ell_2}$ and the four parameters $\chi_{\ell_1\ell_2}$ are shared between the different charge assignments and were determined simultaneously with $a_{\rm sl}^d$ from a fit to the measured numbers of events in each of the sixteen categories. An additional constraint was obtained from measuring the charge asymmetry in a sample of events in which only a single charged lepton was required, such that a total of 17 observables were available to determine the thirteen unknown parameters. The result of the measurement is listed in Table 6.4. Its precision is limited by the statistical uncertainty, which is about a factor of two larger than that of the tagged analysis, which was based on the same data set. The quoted systematic uncertainty, on the other hand, is almost a factor of two smaller, here. It was found to be dominated by effects related to possible biases from the simulation and to uncertainties in the determination of the lepton misidentification probabilities.

The measurement of $a_{\rm sl}^d$ published by the D0 collaboration [494] is based on the full run-II data set, corresponding to an integrated luminosity of 10.4 fb^{-1}. Signal candidates were selected in the semileptonic decays of neutral B mesons to $D^{\mp}\mu^{\pm}X$ with $D^{\mp} \to K^{\pm}\pi^{\mp}\pi^{\mp}$ and to $D^{*\mp}\mu^{\pm}X$ with $D^{*\mp} \to D\pi^{\mp}$ and $D \to K^{\pm}\pi^{\mp}$. No attempt was made to tag the initial flavour of the neutral B meson. The trigger selection for both samples was based on a combination

of single and dimuon triggers that did not impose requirements on the impact parameter of the muon candidates. The offline selections required a well identified muon and three tracks with appropriate charge assignments and a topology compatible with the respective decay chain. Combinations of thirteen, respectively 22 discriminating variables were employed in the selections, including the transverse momenta of the final-state particles, their angular separation and a variable measuring their track isolation, the quality of vertex fits for D, D^*, and B decay vertices and the displacement of these vertices, as well as the invariant masses of the D and B candidates and, in the case of the decay to $D^{*\mp}\mu^{\pm}X$, the difference between the invariant masses of the $D^{*\mp}$ candidate and the D candidate. Invariant-mass distributions for the selected candidates in the two samples are shown in Figure 6.16 together with the results of a fit to extract the signal yields. The measured raw charge asymmetries are

$$A_{\rm raw} \;\equiv\; \frac{N(D^{(*)-}\mu^+) - N(D^{(*)+}\mu^-)}{N(D^{(*)-}\mu^+) - N(D^{(*)+}\mu^-)} \;=\; A_D \;+\; f_{\rm osc} \times a^d_{\rm sl}\;,$$

where A_D describes the charge asymmetry due to differences in trigger and detection efficiencies and $f_{\rm osc}$ is the fraction of the selected $D^{(*)}\mu$ pairs that are actually due to decays of neutral B mesons after mixing. The detection asymmetry a_D was estimated from collision data as described below, while $f_{\rm osc}$ was determined from samples of simulated events, taking into account contributions from the decays of unmixed B^0 and $\overline{B}^0$ mesons and $B^{\pm}$, B^0_s and $\overline{B}^0_s$ mesons, as well as $D^{(*)\mp}$ mesons from associated $c\overline{c}$ production. Since the $B^0-\overline{B}^0$ oscillation frequency and the B^0 decay width are of similar size, the fraction of neutral B mesons that have undergone mixing at the time of their decay varies significantly as a function of the decay time. The sensitivity of the measurement to $a^d_{\rm sl}$ can therefore be improved by performing a decay-time dependent measurement, despite the fact that the value of $a^d_{\rm sl}$ itself is decay-time independent. In this measurement, the decay time of the neutral B meson was estimated as

$$t \;\approx\; \frac{L_{xy}\, m_B}{p_{\rm T}(D^{(*)}\mu)}\;,$$

where m_B is the mass of the B^0 meson, $p_{\rm T}(D^{(*)}\mu)$ is the reconstructed transverse momentum of the $D^{\mp}\mu^{\pm}$ or $D^{*\mp}\mu^{\pm}$ pair, and L_{xy} is the measured distance between the $p\overline{p}$ interaction vertex and the decay vertex of the B candidate, projected onto the direction of the transverse momentum vector. The precision of this estimate is limited by the missing momentum of the undetected neutrino and therefore the measurement was performed only in six bins of the proper decay length, ct, between -0.1 cm and 0.6 cm. Negative decay lengths can be measured due to resolution effects. The first two of these bins, around $ct = 0$ cm, have negligible contribution from decays after mixing and served as control regions for the determination of the detection asymmetry. The raw asymmetry in each decay-length bin was determined by performing separate fits to the difference and the sum of the invariant-mass distributions for the $D^{(*)-}\mu^+$ and $D^{(*)+}\mu^-$ candidates in this bin. Examples of these fits are shown in Figure 6.16. Possible charge asymmetries related to the geometry and performance of the detector were reduced by reversing the polarity of the spectrometer magnets in regular intervals. Moreover, selected candidates were appropriately weighted in this analysis to compensate for differences in the sizes of the data sets collected with the different magnet polarities. Assuming that remaining detection-related charge asymmetries were small and that second-order effects could therefore be neglected, the detection asymmetry was decomposed into the contributions for each of the four final-state particles as

$$A_D \;\approx\; A_\mu \;+\; A_K \;-\; 2\,A_\pi\;,$$

where the kaon charge asymmetry is expected to dominate due to the different hadronic interaction cross sections for positive and negative kaons in the material of the detector. Negative

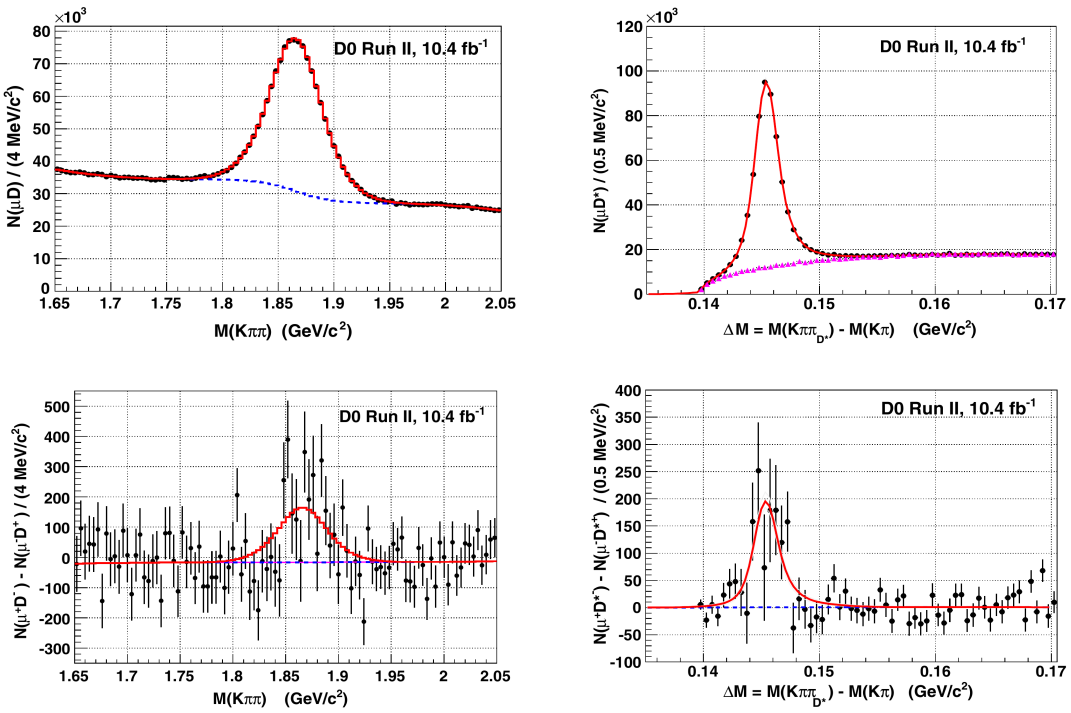

Figure 6.16: Distributions of (left) the invariant mass of $D^{\mp}$ candidates in the $D^{\mp}\mu^{\pm}$ sample and (right) the difference between the invariant masses of the $D^{*\mp}$ and D candidates in the $D^{*\mp}\mu^{\pm}$ sample employed in the D0measurement of $a_{\rm sl}^d$. The upper panels show the distribution for the full selected samples, while the lower panels show the difference between the distributions for $D^{(*)-}\mu^+$ and $D^{(*)+}\mu^-$ candidates in the fifth of the six decay-length bins employed in the analysis. In all four panels, the results of the fit to the data is superimposed, where dashed lines or magenta triangles indicate the background components (from [494]).

kaons contain a $\overline{u}$ quark that can undergo annihilation with u quarks in the detector material, while there is no equivalent process for positive kaons. A larger fraction of negative kaons is therefore expected to be lost due to hadronic interactions, resulting in a lower reconstruction efficiency than for positive kaons. The size of this effect was estimated from collision data using samples of $K^{*0} \to K^+\pi^-$ and $\overline{K}^{*0} \to K^-\pi^+$ candidates. An overall positive kaon asymmetry of about 1% was indeed found, in agreement with expectation. A possible charge asymmetry for pion candidates can be due to different track reconstruction efficiencies for positive and negative particles, but was expected to be largely compensated for by the regular reversal of the magnetic field. The effect was studied in collision data using control samples of $K_S^0 \to \pi^+\pi^-$ and $K^{*\pm} \to K_S^0\pi^{\pm}$ candidates and was indeed found to be negligibly small. Finally, the muon-detection charge asymmetry was studied using samples of $J/\psi \to \mu^+\mu^-$ candidates. A small but significant effect was observed and corrected for. The complete analysis was performed separately for the two decay modes and the four decay-length bins. The eight results were compatible with each other within their uncertainties and a weighted average, using the sum of the squares of the statistical and systematic uncertainties as weights, was calculated to obtain the final result shown in Table 6.4. The precision of this measurement was found to be limited by the statistical uncertainty. The quoted systematic uncertainty was estimated by performing a large number of simulated experiments in which all input parameters were varied within their estimated uncertainties. No individual contributions were therefore quoted.

The recently published measurement of $a_{\rm sl}^d$ by the LHCb collaboration [495] is based on the combined run I data set, corresponding to an integrated luminosity of 3 fb^{-1}. The analysis used the same decay signatures as the D0 measurement described above, namely decays of neutral B mesons to $D^{\mp}\mu^+X$ with $D^{\mp} \to K^{\pm}\pi^{\mp}\pi^{\mp}$ and $D^{*\mp}\mu^+X$ with $D^{*\mp} \to D\pi^{\mp}$ and

$D \to K^{\pm}\pi^{\mp}$. Also here, no attempt was made to tag the initial flavour of the neutral B meson. Signal candidates were selected at the trigger level by requiring a muon with large transverse momentum and a significant impact parameter with respect to the reconstructed pp interaction vertex and a second reconstructed track that was consistent with the generic topology of a b hadron decay when combined with the muon. The offline selection required four tracks that were well identified as muon, kaon and pions by the particle identification systems and did not point back to any reconstructed pp interaction vertex. Further selection requirements exploited the topology and kinematics of the decay, requiring well reconstructed D, D^*, and B-meson decay vertices, cutting on the reconstructed decay time of the D meson candidate and its impact parameter with respect to the pp interaction vertex, on the invariant mass of the $D_s\mu$ candidate and, in the case of the $D^{*\mp}\mu^+$ sample, on the difference between the invariant masses of the $D^{*\mp}$ candidate and the D candidate. The decay time of the B meson candidate was estimated as

$$t \;=\; \langle k \rangle \;\times\; m_B \,\frac{L}{p(D^{(*)}\mu)}$$

where m_B is the known mass of the B^0 meson, $p(D^{(*)}\mu)$ is the reconstructed momentum of the $D^{\mp}\mu^{\pm}$ or $D^{*\mp}\mu^{\pm}$ pair and L is the decay length of the B meson candidate, calculated as the distance between the pp interaction vertex and the $D^{(*)}\mu$ vertex. The factor $\langle k \rangle$ is a function of the invariant mass of the $D^{\mp}\mu^{\pm}$ or $D^{*\mp}\mu^{\pm}$ pair and was included to apply an average correction for the missing momentum of the undetected final-state particles. It was determined by calculating the ratio k between the reconstructed momentum of the $D^{(*)}\mu$ pair and the true momentum of the decaying B meson in samples of simulated events and fitting a second-order polynomial to the observed distribution as a function of the invariant mass of the $D^{(*)}\mu$ pair. The distribution of $k/\langle k \rangle$ is employed to model the decay-time resolution in the fit to the collision data. The value of $a^d_{\rm sl}$ was extracted from a two-dimensional fit to the binned distributions of the reconstructed B-meson decay time and the invariant mass of charm-meson candidate. The fit model included contributions for the signal component, for combinatorial background and for a background component from decays of $B^{\pm}$ mesons to $D^{*\mp}\mu^{\pm}X^{\pm}$ final states. Since it is difficult to distinguish this background from the signal, its fraction was determined from simulated samples of events and fixed in the fit to the data. The decay-time distribution for the signal component was described as

$$N_{D^{(*)\mp}\ell^{\pm}}(t) \;\propto\; e^{-\Gamma_d\, t} \left\{ 1 \,\pm\, A_D \,\pm\, \frac{a^d_{\rm sl}}{2} \,\mp\, \left(A_P \,+\, \frac{a^d_{\rm sl}}{2} \right) \cos\left(\Delta m_d\, t\right) \right\} ,$$

convolved with the decay-time resolution function discussed above. The parameter A_D describes the charge asymmetry due to differences in trigger and detection efficiencies and A_P describes a possible small charge asymmetry in the production rates of B^0 and $\overline{B}^0$ mesons in pp collisions. The value of A_P was a free parameter in the fit to the data, while the detection asymmetry A_D was estimated from collision data using independent control samples. To reduce detector-related asymmetries, also in the LHCb experiment the polarity of the spectrometer magnet was reversed in regular intervals during the data taking periods, and similar sizes of data sets were collected for each of the two polarities. To estimate the remaining detection asymmetry, the final-state kaon was paired together with the lower-$p_{\rm T}$ pion and the final-state muon was paired together with the higher-$p_{\rm T}$ pion. The charge asymmetry for the $K^{\pm}\pi^{\mp}$ pair was estimated from samples of prompt $D^{\mp} \to K^{\pm}\pi^{\mp}\pi^{\mp}$ candidates and $D^{\mp} \to K^0\pi^{-}$ candidates with $K^0 \to \pi^+\pi^-$. The same particle-identification requirements were applied to the final-state particles as in the signal sample and candidates in the control sample were assigned weights such that the weighted momentum and pseudorapidity distributions of the final-state particles reproduced those of the kaon and pion in the signal sample. The effect of a possible $D^{\pm}$ production asymmetry was cancelled out by combining the measurements in the two different decay modes. As expected, the largest effect was found in the kaon reconstruction

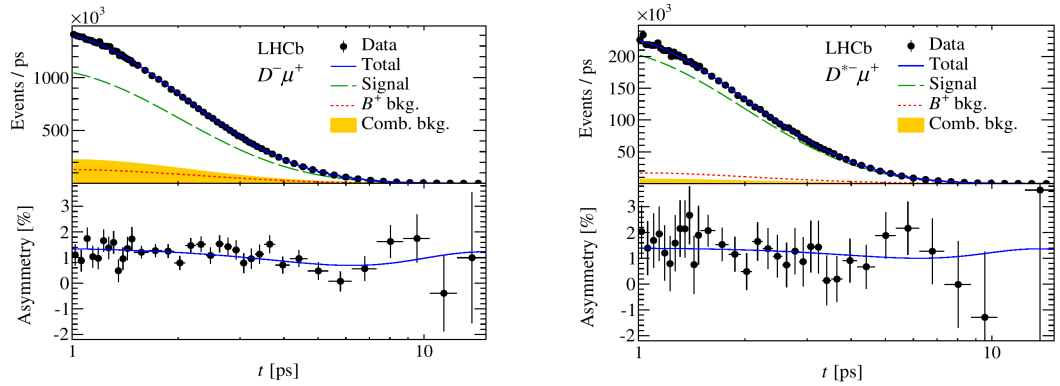

Figure 6.17: Decay-time distributions and raw asymmetries as a function of the decay time for selected (left) $D^{\mp}\mu^{\pm}$ and (right) $D^{*\mp}\mu^{\pm}$ candidates from the LHCb measurement of $a_{\rm sl}^d$. The results of the fit to the data are superimposed, indicating signal and background components as described in the plot legends. Note that the observed raw asymmetry is dominated by the detection asymmetry for positive and negative kaons (from [495]).

efficiency, where the difference in hadronic interactions in the detector material caused a charge asymmetry of about 1 %. A possible charge asymmetry in the track reconstrucion efficiency for the $\mu^{\pm}\pi^{\mp}$ pair was essentially eliminated by assigning appropriate weights to each signal candidate such that the distributions in transverse momentum and pseudorapidity for the two particles were effectively equalized. This weighting caused an effective loss of 40% in statistical precision but made the two oppositely charged particles appear almost symmetric to the tracking system. The charge asymmetry caused by the particle identification requirements applied in the selection of the high-$p_{\rm T}$ pion were determined from an unbiased control sample of $D^{*\mp} \to D\pi^{\mp}$ candidates with $D \to K^{\mp}\pi^{\pm}$. Again, candidates in the control sample were assigned appropriate weights such that the transverse-momentum and pseudorapidity distribution of the pions matched those in the signal sample. The charge asymmetry due to muon trigger and identification requirements was estimated from a sample of appropriately weighted $J/\psi \to \mu^+\mu^-$ decays, which had been selected without imposing any trigger or identification requirements on one of the two muons. In the fit for $a_{\rm sl}^d$, the decay-time distribution and the detection asymmetries for the $B^{\pm}$ background component were treated in the same way as for the signal component, except that the oscillatory term in the decay-time dependence was set to zero. The $B^{\pm}$ production asymmetry was fixed to its value found in the dedicated LHCb measurement. The time-dependence of the combinatorial background component was again described by the same way as for the signal component, except that the value of $a_{\rm sl}^d$ was in this case set to zero. A possible production asymmetry was considered as a free parameter in the fit. The fit was performed separately for the two magnet polarities, for the data sets collected in 2011 and 2012, and for the $D^{*\mp}\mu^{\pm}$ and $D^{\mp}\mu^{\pm}$ samples. Appropriatetly weighted averages were calculated to determine the final result. The result of the $a_{\rm sl}^d$ measurement is listed in Table 6.4 below. Its precision was found to be limited by the systematic uncertainty, where the dominant contribution was due to the measurement of the detection asymmetries, which in turn was limited by the size of the available control samples. The second largest contribution to the quoted systematic uncertainty was due to the current knowledge of the B^+/B^- production asymmetry. The $B^0/\overline{B}^0$ production asymmetries were measured to be $A_P(7\text{ TeV}) = (-0.66 \pm 0.26\,(\text{stat}) \pm 0.22\,(\text{syst}))\,\%$ in the data set collected at a pp collision energy of 7 TeV in 2011 and $A_P(8\text{ TeV}) = (-0.48 \pm 0.15\,(\text{stat}) \pm 0.17\,(\text{syst}))\,\%$ in the data set collected at a pp collision energy of 8 TeV in 2012. The results are consistent with each other and compatible with the result of a dedicated measurement by the LHCb collaboration [480] of this production asymmetry at 7 TeV collision energy.

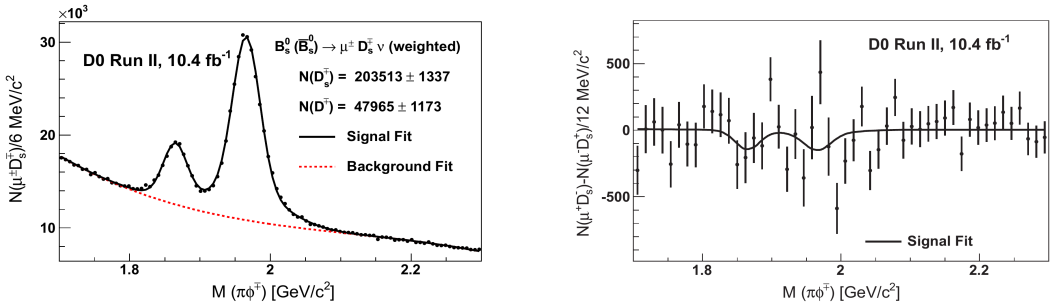

Figure 6.18: (Left) sum and (right) differences of the time-integrated invariant mass distributions for $K^+K^-\pi^-$ and $K^+K^-\pi^+$ candidates from the D0 measurement of $a^s_{\rm sl}$ in decay modes $B^0_s \to D^\mp_s \mu^\pm X$ (from [499]).

6.2.2 Measurements of $a^s_{\rm sl}$

Measurements of the semileptonic asymmetry in decays of $B^0_s\overline{B}^0_s$ system have been published by the D0 [497–499] and LHCb [500] collaborations. An early measurement by the CDF collaboration [486], based on data collected during run I of the Tevatron is not competitive with these more recent results.

The most recent measurement by the D0 collaboration [499] was based on the full run-II data set, corresponding to an integrated luminosity of 10.4 fb^{-1}, and employed the decay mode $B^0_s \to D^\mp_s \mu^\pm X$ with $D^\mp_s \to \phi\pi^\mp$ and $\phi \to K^+K^-$. Again, no attempt was made to reconstruct the initial flavour of the B^0_s or $\overline{B}^0_s$ meson. The trigger selection was based on a combination of single and dimuon triggers that did not impose requirements on the impact parameter of the muon candidates. The offline selection required a well identified muon candidate, two oppositely charged tracks that under the kaon mass hypothesis yielded an invariant mass compatible with the known mass of the ϕ meson, and a third track of opposite charge to that of the muon candidate. To form a $D^\mp_s$ candidate, the three tracks were required to be compatible with originating from a common vertex, which had to be displaced from the reconstructed $p\overline{p}$ interaction vertex. To form a B^0_s or $\overline{B}^0_s$ candidate, the reconstructed $D^\mp_s$ candidate and the muon candidate had to be compatible with originating from a common vertex, which also had to be displaced from the $p\overline{p}$ interaction vertex. Further selection requirements were applied on the transverse momentum of the K^+K^- pair, the helicity angle between the $K^\pm$ and $D^\mp_s$ momentum vectors, the quality of the $D^\mp_s$ vertex fit, the invariant mass and the isolation of the $D^\mp_s\mu^\pm$ candidate, and the angles between the reconstructed momentum vectors of the $D^\mp_s$ and $B^0_s/\overline{B}^0_s$ candidates and the lines connecting the $p\overline{p}$ interaction vertex with the corresponding decay vertices. Due to the fast flavour oscillation in the $B^0_s\overline{B}^0_s$ system, no gain can be expected from a time-dependent analysis in this case and the asymmetry was therefore extracted from a fit to the sum and differences of the time-integrated invariant mass distributions for $K^+K^-\pi^-$ and $K^+K^-\pi^+$ candidates as shown in Figure 6.18. The fit considered contributions from the signal component, a background component due to the Cabibbo-suppressed decay $D^\mp \to K^\pm\pi^\mp\pi^\mp$, and combinatorial background from random combinations of tracks. Assuming that the individual asymmetries are small and that second-order effects can be neglected, the charge asymmetry for the signal component was expressed as

$$A_{\rm raw} \equiv \frac{N(D^-_s\mu^+) - N(D^+_s\mu^-)}{N(D^-_s\mu^+) + N(D^+_s\mu^-)} = A_{\rm track} + A_{KK} + A_\mu + f_{\rm osc} \times a^d_{\rm sl}\,,$$

where $A_{\rm track}$, A_{KK} and A_μ describe possible asymmetries in the track reconstruction, kaon and muon detection efficiencies for positive and negative particles, while $f_{\rm osc}$ describes the fraction of $D^\mp_s\mu^\pm$ pairs that were actually due to decays of B^0_s or $\overline{B}^0_s$ mesons after mixing. Separate asymmetry parameters were allowed for the $D^\mp$ and combinatorial background components.

The value of $f_{\rm osc}$ was determined from samples of simulated events, taking into account contributions from decays of mixed and unmixed B^0_s or$\overline{B}^0_s$ mesons and from $B^\pm$, B^0 and $\overline{B}^0$ mesons, as well as prompt $D^\mp_s$ mesons from associated $c\bar{c}$ production. Charge asymmetries related to the geometry and performance of the detector could again be expected to be small due to the regular reversal of the polarity of the spectrometer magnets. The remaining track reconstruction asymmetry was estimated from control samples of $K^0_S \to \pi^+\pi^-$ and $K^{*\pm} \to K^0_S\pi^\pm$ candidates in the same manner as in the measurement of $a^d_{\rm sl}$ described above, and again the effect was found to be negligible. The asymmetry in the reconstruction efficiency of negative and positive kaons, which dominated the raw charge asymmetry in the case of the $a^d_{\rm sl}$ measurement described above, is suppressed here since the final state K^+K^- is charge symmetric. However, a small asymmetry remains due to the fact that the momentum distributions of the negative and positive kaon from the decay of the ϕ meson are not identical. The effect was estimated using a control sample of $K^{*0} \to K^+\pi^-$ and $\overline{K}^{*0} \to K^-\pi^+$ candidates. The muon trigger and identification asymmetry was studied in a control sample of $J/\psi \to \mu^+\mu^-$ candidates, as a function of the transverse momentum and the pseudorapidity of the muons. The total detection asymmetry was found to be $A_{\rm track} + A_{KK} + A_\mu = (0.13 \pm 0.06\,\%$. The result for $a^s_{\rm sl}$ is shown in Figure 6.22 below. The precision of the measurement was found to be limited by the statistical uncertainty, where the quoted systematic uncertainty included the contribution from the measurement of the detection asymmetry and a contribution of similar size due to the fitting procedure.

The only measurement of $a^s_{\rm sl}$ so far published by the LHCb collaboration [500] was based on the data set collected in 2011, corresponding to an integrated luminosity of 1 fb^{-1}. A measurement making use of the full run I data set has not been published yet.

The analysis was based on the time-integrated charge asymmetry in the decay mode $B^0_s \to D^\mp_s\mu^\pm X$ with $D^\mp_s \to \phi\pi^\mp$ and $\phi \to K^+K^-$, where and no attempt was made to tag the initial flavour of the B^0_s or$\overline{B}^0_s$ meson. Signal candidates were selected at the trigger level by requiring a muon with large transverse momentum and either one or two additional tracks that were consistent with the generic topology of a b hadron decay when combined with the muon, or a pair of tracks consistent with a $\phi \to K^+K^-$ decay. The offline selection again exploited the topology of the decay chain. The muon candidate as well as the three other tracks used in forming the candidate were required to be incompatible with originating from the reconstructed pp interaction vertex. Two of the tracks had to be identified as oppositely charged kaons and had to yield an invariant mass compatible with the mass of the ϕ meson. To form a $D^\mp_s$ candidate, the three tracks were required to be compatible with originating from a common vertex that was significantly displaced from the pp interaction vertex. A further requirement was placed on the sum of the transverse momenta of the three particles. To form a B^0_s or $\overline{B}^0_s$ candidate, the $D^\mp_s$ candidate and the muon had to be compatible with originating from a common vertex that was required to be downstream of the pp interaction vertex. The reconstructed momentum vectors of the $B^0_s/\overline{B}^0_s$ candidate and the $D^\mp_s$ candidate had to be roughly aligned with the lines connecting the pp interaction vertex and the $D^\mp_s\mu^\pm$ and $K^+K^-\pi^\mp$ vertices, respectively. Finally, a loose cut was applied on the invariant mass of the $B^0_s/\overline{B}^0_s$ candidate. The $D^-_s\mu^+$ and $D^+_s\mu^-$ event yields, $N(D^-_s\mu^+)$ and $N(D^+_s\mu^-)$, were extracted from separate fits to the $K^+K^-\pi^-$ and $K^+K^-\pi^+$ invariant mass distributions as shown in Figure 6.19. As mentioned above, the polarity of the LHCb dipole magnet was reversed regularly during data taking to average out possible charge asymmetries due to detector geometry or performance. The complete analysis was performed separately for the two data sets collected with different magnet polarity and the measured values for $a^s_{\rm sl}$ were averaged to obtain a final measurement.

The measured charge asymmetry was defined as

$$A_{\rm meas} \;\equiv\; \frac{N(D^-_s\mu^+) \;-\; N(D^+_s\mu^-) \;\times\; \varepsilon(\mu^+)/\varepsilon(\mu^-)}{N(D^-_s\mu^+) \;+\; N(D^+_s\mu^-) \;\times\; \varepsilon(\mu^+)/\varepsilon(\mu^-)} \;-\; A_{\rm track} \;-\; A_{\rm bkg}\;,$$

where $\varepsilon(\mu^+)/\varepsilon(\mu^-)$ describes the ratio of muon trigger and identification efficiencies, $A_{\rm track}$ is

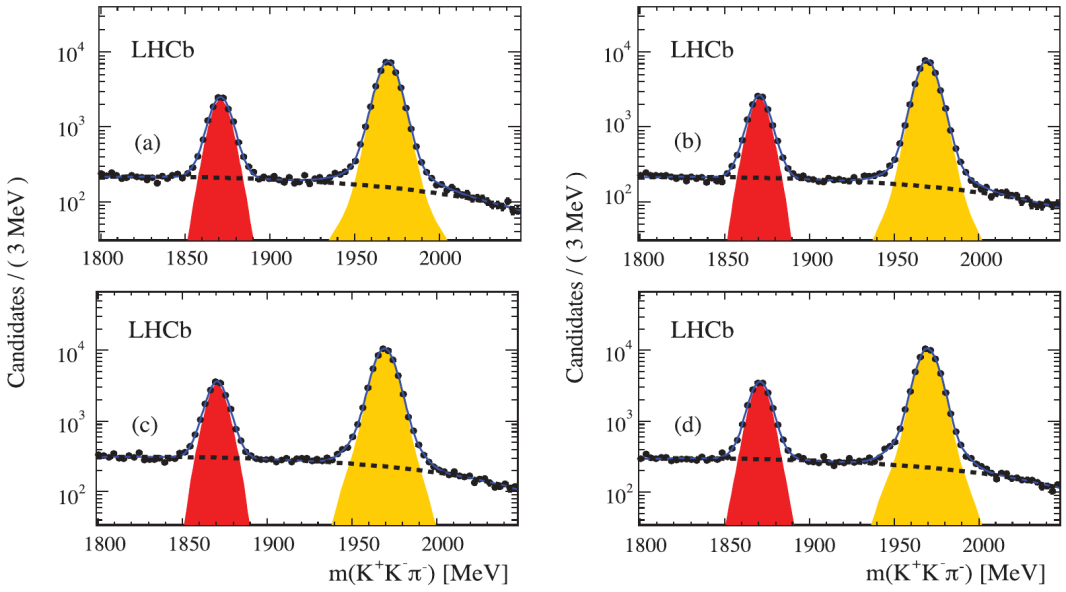

Figure 6.19: Distributions of (left) the $K^+K^-\pi^+$ invariant mass for selected $K^+K^-\pi^+\mu^-$ candidates and (right) the $K^+K^-\pi^-$ invariant mass for selected $K^+K^-\pi^-\mu^+$ candidates from the LHCb measurement of $a^s_{\rm sl}$. The upper and lower panels show the distributions for data collected with the two polarities of the LHCb spectrometer magnet. The results of the fit to the data are superimposed, where the light, yellow shaded areas indicate the signal component, the dark, red shaded areas indicate the background component from $D^\mp \to K^+K^-\pi^\mp$ decays and dashed lines indicate the component due to combinatorial background. The axis label for the panels on the left is wrong (from [500]).

the charge asymmetry due to a difference in track reconstruction efficiencies for positive and negative particles, and $A_{\rm bkg}$ is a charge asymmetry induced by $D_s^\mp\mu^\pm$ background contributions. The time-integrated charge asymmetry defined in this way is related to $a^s_{\rm sl}$ as

$$A_{\rm meas} \;=\; \frac{a^s_{\rm sl}}{2} \;+\; \left(A_P \;-\; \frac{a^s_{\rm sl}}{2} \right) \;\times\; \frac{\int_0^\infty e^{-\overline{\Gamma}_s t}\,\cos\left(\Delta m_s\, t\right)\epsilon(t)\,dt}{\int_0^\infty e^{-\overline{\Gamma}_s t}\,\cosh(\Delta\Gamma_s\, t/2)\,\epsilon(t)\,dt}\;,$$

where A_P is the $B^0_s - \overline{B}^0_s$ production asymmetry in pp collisions, which has been shown in an independent measurement by the LHCb collaboration [480] to be no larger than a few percent. This small initial asymmetry is further diluted by the rapid $B^0_s - \overline{B}^0_s$ oscillation. Taking into account the known values of the average decay width $\overline{\Gamma}_s$, the mass difference Δm_s and the decay-width difference $\Delta\Gamma_s$ in the $B^0_s\overline{B}^0_s$ system as well as the decay-time acceptance $\epsilon(t)$ of the LHCb experiment, the ratio of the two time integrals on the right-hand side of the equation evaluates to approximately 0.2 %. The effect of the production asymmetry is therefore no larger than a few times 10^4, which is negligible compared to the precision that the measurement of $a^s_{\rm sl}$ aimed for. Therefore, for the purpose of this measurement,

$$A_{\rm meas} \;=\; \frac{a^s_{\rm sl}}{2}\;.$$

The ratio of trigger and muon identification efficiencies, $\varepsilon(\mu^+)/\varepsilon(\mu^-)$, was determined from collision data employing control samples of $J/\psi\mu^+\mu^-$ candidates and a control sample of $D^\mp\mu^\pm$ candidates with $D^\mp \to K^\pm\pi^\mp\pi^\mp$, which was selected by employing similar trigger requirements as those used in the selection of the signal candidates. To avoid possible biases due to different momentum distributions or spatial distributions of the muons in the control and signal samples, the analysis was performed in three-dimensional bins of the muon momentum and two spatial coordinates. As a cross check, two different binning schemes were employed to describe the spatial distribution of the muons: one based on a Cartesian coordinate system,

which is better matched to the detector geometry, and one based on transverse momentum and azimuthal angle, which is more closely related to the properties of the particles. The charge asymmetry $A_{\rm track}$, related to track reconstruction efficiencies, was estimated from collision data employing control samples of $D^{*\mp} \to D\pi^{\mp}$ candidates with $D^0 \to K^-\pi^+\pi^+(\pi^-)$ and $D^0 \to K^+\pi^-\pi^-(\pi^+)$. The clear event signature allowed to extract clean samples of candidates without explicitly reconstructing the $(\pi^{\mp})$, allowing to measure the track reconstruction efficiencies for these particles. The effect of the different interaction cross sections of negative and positive kaons in the detector material was estimated from a comparison of $D^{\pm} \to K^{\mp}\pi^+\pi^-$ and $D_s^+ \to K^0_S\pi^+$ control samples. Efficiency differences largely cancel in the reconstruction of the $\pi^{\mp}\mu^{\pm}$ and K^+K^- pairs and the remaining asymmetry was indeed found to be small, $A_{\rm track} = (0.02 \pm 0.13)\,\%$. Three sources of backgrounds were considered that could cause an asymmetry $A_{\rm bkg}$. These were combinations of a true $D_s^{\mp}$ meson from a b hadron decay with a misidentified muon, $D_s^{\mp}$ mesons produced in decays of a b hadron to a $D_s^{\mp}$ meson and a second charmed hadron, followed by a semileptonic decay of this charmed hadron, and prompt $D_s^{\mp}$ mesons from associated $c\bar{c}$ production. All these contributions were found to be small and the resulting background asymmetry was estimated to be $A_{\rm bkg} = (0.05 \pm 0.05)\,\%$. A possible asymmetry due to backgrounds without a true $D_s^{\mp}$ candidate had been eliminated statistically by fitting separately the invariant mass distributions for $D_s^-\mu^+$ and $D_s^+\mu^-$ candidates. The final result of the measurement was calculated by performing the weighted average of the results obtained in bins of the muon momentum and spatial coordinates and by averaging the asymmetries measured for the two magnet polarities. The result is shown in Figure 6.22 below, where the statistical uncertainty is slightly larger than the quoted systematic uncertainty. The latter was dominated by the uncertainty in the determination of the small charge asymmetry related to track reconstruction efficiencies.

6.2.3 Measurement of the same-sign dimuon charge asymmetry

The D0 collaboration published several analyses of the same-sign dimuon charge asymmetry [501–504]. The latest of these measurements was based on the full run-II data set, corresponding to an integrated luminosity of 10.4 fb^{-1}. Samples of 6×10^6 same-sign dimuon pairs and 2×10^9 inclusive single muon candidates were collected using inclusive and dimuon triggers, respectively. Muon candidates were required to have matching track segments reconstructed in the central tracking system and the muon system. The inclusive muon sample was employed as a control channel to estimate background fractions and charge asymmetries that were then employed for the actual measurement in the same-sign dimuon sample. To take into account variations in the background fractions and asymmetries due to kinematic properties of the particles, the analysis was performed in bins of the transverse momentum and pseudorapidity of the candidates. Moreover, the analysis was performed separately for three regions in the impact parameter of the reconstructed track with respect to the reconstructed $p\bar{p}$ interaction vertex. Due to the significant lifetime of b hadrons, the subsamples with larger track impact parameter are expected to contain larger fractions of true muons from b hadron decays.

The raw charge asymmetry in bin i of the inclusive muon sample is

$$a^i_{\rm raw} \;\equiv\; \frac{n_i^+ - n_i^-}{n_i^+ + n_i^-} \;=\; a^i_{CP} \,+\, a^i_{\rm bkg}\;,$$

where n_i^+ and n_i^- are the numbers of reconstructed positive and negative muon candidates in this bin, a^i_{CP} is the charge asymmetry due to CP violating effects and $a^i_{\rm bkg}$ describes the charge asymmetry due to different reconstruction efficiencies for positive and negative muons and different background contaminations in the positive and negative samples. The asymmetries a^i_{CP} are expected to be negligibly small in the inclusive muon sample and their measurement provides a cross check for the understanding of the background asymmetries. These can be

parametrized as

$$a^i_{\rm bkg} \;=\; (1 - f^i_K - f^i_\pi - f^i_p)\, a^i_\mu \;+\; f^i_K a^i_K \;+\; f^i_\pi a^i_\pi \;+\; f^i_p a^i_p \;,$$

where f^i_K, f^i_π and f^i_p are the fractions of muon candidates in bin i that are due to misidentified kaons, pions and protons, rspectively, a^i_K, a^i_π and a^i_p are the charge asymmetries in these backgrounds, and a^i_μ is the charge asymmetry in the identification of true muons. All these parameters were determined from collision data using various control samples. The largest background asymmetry is expected from misidentified kaons, where positive kaons have a smaller interaction cross section in the detector material than negative kaons and decays in flight $K^+ \to \mu^+\nu_\mu$ are therefore more likely than decays in flight $K^- \to \mu^-\overline{\nu}_\mu$. Two algorithms were employed to estimate this asymmetry. The first of these was based on samples of $K^{*0} \to K^+\pi^-$ and $\overline{K}^{*0} \to K^-\pi^+$ candidates in combination with samples of K^0_S and $K^{*\pm} \to K^0_S\pi^\pm$ candidates with $K^0_S \to \pi^+\pi^-$. The fraction of $K^{*0} \to K^+\pi^-$ and $\overline{K}^{*0} \to K^-\pi^+$ candidates, in which the kaon is wrongly identified as a muon can be measured and is related to f^i_K via

$$f^i_{K^{*0}} \;=\; \varepsilon^i_0 \cdot R^i_{K^{*0}} \cdot f^i_K \;,$$

where $R^i_{K^{*0}}$ is the fraction of all produced charged kaons that is due to decays of K^{*0} mesons, while ε^i_0 is the efficiency for reconstructing the accompanying pion under the condition that the misidentified kaon has already been reconstructed. The number of selected $K^{*\pm} \to K^0_S\pi^\pm$ candidates is related to the total number of selected K^0_S candidates as

$$N^i(K^{*\pm} \to K^0_S\pi^\pm) \;=\; \varepsilon^i_c \cdot R^i_{K^{*\pm}} \cdot N^i(K^0_S) \;,$$

where $R^i_{K^{*\pm}}$ is the fraction of all produced K^0_S mesons that is due to $K^{*\pm}$ decays, while ε^i_c is the efficiency for reconstructing the accompanying pion under the condition that the K^0_S meson has already been reconstructed. The selection criteria that were applied to collect the two control samples were symmetrized as much as possible, including the requirement that one of the two charged pions from the decay of the K^0_S decay had to be identified wrongly as a muon. The assumption was then made that the efficiencies for reconstructing the accompanying pion were identical in the two samples. Exploiting isospin invariance between the charged and neutral kaon systems, it was further assumed that the fraction of $K^\pm$ from K^{*0} decays and the fraction of K^0_S from $K^{*\pm}$ decays were equal. Putting these two assumptions together,

$$\varepsilon^i_0 \cdot R^i_{K^{*0}} \;=\; \varepsilon^i_c \cdot R^i_{K^{*\pm}} \;=\; \frac{N^i(K^{*\pm} \to K^0_S\pi^\pm)}{N^i(K^0_S)}$$

and the fraction f^i_K could be calculated as

$$f^i_K \;=\; \frac{N^i(K^0_S)}{N(K^{*\pm} \to K^0_S\pi^\pm)} \;\cdot\; f^i_{K^{*0}} \;.$$

The second method exploited the fact that the track segment reconstructed in the main tracking system tends to measure the trajectory of the kaon before its decay in flight, while the track segment in the muon system measures the trajectory of the muon after the decay. Since the muon is emitted under a finite angle with respect to the flight direction of the decaying kaon, the track angle measured in the muon system should deviate from that measured in the main tracking system. The difference between the two track angles therefore provides a discriminating variable that should allow to distinguish on a statistical basis between true muons and muons from decays in flight. A second such discriminating variable is the difference between the momenta measured in the main tracking system and in the muon system. As the neutrino carries away part of the energy of the decaying kaon, the momentum measured in the muon system should be lower than that measured in the main tracking system. The distributions

of these two variables for true and misidentified muons were measured using control samples of $D \to K^{\mp}\mu^{\pm}\nu$ candidates on the one hand and $\phi \to K^+K^-$ and $K^0_S \to \pi^+\pi^-$ candidates on the other hand. The shapes of the distributions measured in these control samples were then employed in a fit to the distributions measured in the inclusive muon sample in order to estimate the fraction of misidentified muons in this sample. The results of the two methods were roughly consistent with each other and the observed differences were assigned as a systematic uncertainty for the determination of the f^i_K. The fractions f^i_π were derived from f^i_K as

$$f^i_\pi \;\equiv\; \frac{P^i(\pi \to \mu)}{P^i(K \to \mu)} \cdot \frac{n^i_\pi}{n^i_K} \cdot f^i_K \;,$$

where $P^i(\pi \to \mu)$ and $P^i(K \to \mu)$ are the probabilities for misidentifying a true pion or kaon for a muon, while n^i_π and n^i_K are the mean multiplicities of charged pions and kaons in bin i of the inclusive muon sample. The multiplicities were determined from samples of simulated events, while the misidentification probabilities was determined from data as

$$\frac{P^i(\pi \to \mu)}{P^i(K \to \mu)} \;\equiv\; \frac{N^i_\mu(K^0_S \to \pi^{\pm}\pi^{\mp})/N^i(K^0_S \to \pi^{\pm}\pi^{\mp})}{N^i_\mu(\phi \to K^{\pm}K^{\mp})/N^i(\phi \to K^{\pm}K^{\mp})}$$

where $N^i(K^0_S \to \pi^{\pm}\pi^{\mp})$ and $N^i(\phi \to K^+K^-)$ are the total numbers of reconstructed $K^0_S \to \pi^{\pm}\pi^{\mp}$ and $\phi \to K^+K^-$ candidates with a pion or kaon falling into bin i, while $N^i_\mu(K^0_S \to \pi^{\pm}\pi^{\mp})$ and $N^i_\mu(\phi \to K^+K^-)$ are the numbers of such candidates in which this pion or kaon was wrongly identified as a muon. The fraction f^i_p was derived from f^i_K in the same manner using the fractions of $\Lambda \to p\pi^-$ and $\overline{\Lambda} \to \overline{p}\pi^+$ candidates in which the proton or antiproton was wrongly identified as a muon. Finally, it was concluded that the inclusive muon sample contained 16% of misidentified kaons, 30% of misidentified pions, 0.5% of misidentified protons and about 53% of true muons.

The charge asymmetries a^i_K were determined from control samples of $K^{*0}/\overline{K}^{*0} \to K^{\pm}\pi^{\mp}$ and $\phi \to K^+K^-$ candidates in which either the positive or the negative kaon was wrongly identified as a muon. The asymmetries a^i_π was determined in the same manner from a control sample of $K^0_S \to \pi^+\pi^-$ candidates and the asymmetries a^i_p were determined from control samples of $\Lambda \to p\pi^-$ and $\overline{\Lambda} \to \overline{p}\pi^+$ candidates. All asymmetries were determined from the collected data and therefore included effects from trigger, selection and reconstruction asymmetries. The muon identification asymmetries a^i_μ, finally, were determined from samples of $J/\psi \to \mu^+\mu^-$ candidates that had been selected without imposing requirements on muon identification criteria. The charge asymmetry due to different track reconstruction efficiencies for positive and negative muon candidates was assumed to be negligible, based on the results of previous studies. Track reconstruction asymmetries cancel to first order due to the regular reversal of magnet field polarities during data taking.

Comparisons of the estimated background asymmetries $a^i_{\rm bkg}$ and the measured raw charge asymmetries $a^i_{\rm raw}$ in all transverse-momentum and pseudorapidity bins and all three impact-parameter ranges are shown in Figure 6.20. They are in good agreement with each other as expected for a vanishing *CP* asymmetry in the inclusive muon sample. Forming the weighted average over all bins,

$$a_{CP} \;\equiv\; \sum_i \left\{ \frac{n^+_i + n^-_i}{\sum_i (n^+_i + n^-_i)} \left(a^i_{\rm raw} \;-\; a^i_{\rm bkg}\right) \right\} \;=\; (\,-0.032 \,\pm\, 0.042\,(\text{stat}) \,\pm\, 0.061\,(\text{syst})\,)\,\% \;.$$

In the same-sign dimuon sample, the raw asymmetry for candidates with one muon in bin i and the second muon in bin j is

$$A^{ij}_{\rm raw} \;\equiv\; \frac{N^{++}_{ij} - N^{--}_{ij}}{N^{++}_{ij} + N^{--}_{ij}} \;,$$

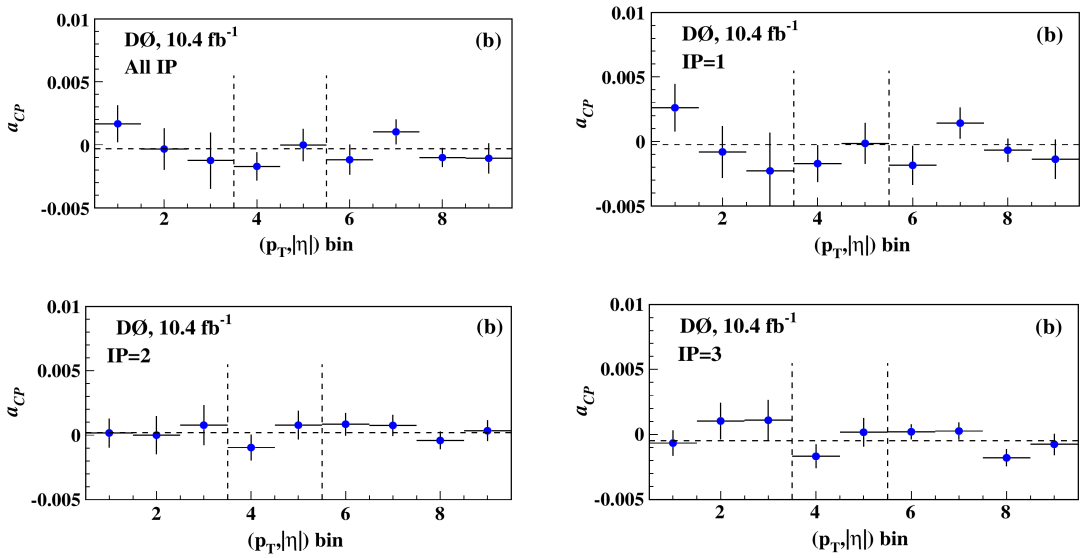

Figure 6.20: Values of the asymmetry $a^i_{CP} \equiv a_{\rm raw} - a_{\rm bkg}$ as calculated in the nine bins in transverse momentum and pseudorapidity for (top left) all candidates in the inclusive muon sample, and for candidates in (top right) the inner, (bottom left) the intermediate, and (bottom right) the outer impact-parameter region employed in the latest D0 analysis. Horizontal dashed lines indicated the weighted averages, while vertical dashed lines separate between bins corresponding to different pseudorapidity regions (from [504]).

where the numbers of positive and negative same-sign dilepton pairs can be expressed as

$$N^{\pm\pm}_{ij} \;=\; \frac{1}{2}\,(N^{++}_{ij} + N^{--}_{ij}) \;\cdot\; (1 \pm A^{ij}_{CP})\,(1 \pm a^i_{\rm bkg})\,(1 \pm a^j_{\rm bkg}) \;.$$

Here, A^{ij}_{CP} describes the charge asymmetry due to *CP* violating effects for this subsample of candidates and $a^i_{\rm bkg}$ and $a^j_{\rm bkg}$ are the background asymmetries for the muon candidates in bin i and bin j, respectively. These background asymmetries were determined in the same manner as in the analysis of the inclusive muon sample. For bin i,

$$a^i_{\rm bkg} \;\equiv\; (1 - F^i_k - F^i_\pi - F^i_p)\,a^i_\mu \;+\; F^i_k\,a^i_k \;+\; F^i_\pi\,a^i_\pi \;+\; F^i_p\,a^i_p \;,$$

where the values for the charge asymmetries a^i_k, a^i_π, a^i_p, a^i_μ were taken from the analysis of the inclusive muon sample and the fractions F^i_k, F^i_π and F^i_p of misidentified muons from kaons, pions and protons were re-calculated for the dimuon sample using the same methods as described above. The number of positive and negative muon candidates in bin i are

$$N^\pm_i \;=\; N^{\pm\pm}_{ii} + \sum_j N^{\pm\pm}_{ij} \;,$$

where the term $N^{\pm\pm}_{ii}$ appears inside and outside the sum to take into account that it describes the case where two muon candidates fall into bin i. The raw charge asymmetry for muon candidates in bin i is then

$$A^i_{\rm raw} \;\equiv\; \frac{N^+_i - N^-_i}{N^+_i + N^-_i} \;=\; \frac{(N^{++}_{ii} - N^{--}_{ii}) \;+\; \sum_j (N^{++}_{ij} - N^{--}_{ij})}{(N^{++}_{ii} + N^{--}_{ii}) \;+\; \sum_j (N^{++}_{ij} + N^{--}_{ij})}$$

and the contribution to this asymmetry due to *CP* violation is

$$A^i_{CP} \;=\; \frac{(N^{++}_{ii} + N^{--}_{ii})\,A^{ii}_{CP} \;+\; \sum_j \left\{(N^{++}_{ij} + N^{--}_{ij})\,A^{ij}_{CP}\right\}}{(N^{++}_{ii} + N^{--}_{ii}) \;+\; \sum_j (N^{++}_{ij} + N^{--}_{ij})}$$

The total *CP* asymmetry, calculated as the weighted average of the terms A^i_{CP},

$$A_{CP} \equiv \sum_i \left\{ \frac{N_i^+ + N_i^-}{\sum_i (N_i^+ + N_i^-)} A^i_{CP} \right\} = (-0.235 \pm 0.064\,(\text{stat}) \pm 0.055\,(\text{syst}))\,\%$$

was found to deviate significantly from zero. The only source of systematic uncertainties discussed in the publication is that on the determination of the background fractions, f_K, f_π and f_p.

The asymmetries a_{CP} and A_{CP} were by construction determined as asymmetries over all muon candidates contained in the inclusive muon and same-sign dimuon samples, respectively. However, a fraction of these candidates are backgrounds from misidentified kaons, pions and protons. The charge asymmetries due to misidentified muons were corrected for as described above. However, their presence in the samples of candidates leads to a dilution of the observed *CP* asymmetry that needs to be compensated for. To this end, the measured asymmetries were expressed as

$$a_{CP} = a_S f_S$$

and

$$A_{CP} = F_{SS} A_S + F_{SL} a_s \,,$$

where a_S and A_S are the *CP* asymmetries considering only true muons. The factor f_S is the fraction of true muons in the inclusive muon sample, while F_{SL} and F_{SS} are the fractions of candidates with one and two true muons, respectively, in the same-sign dimuon sample. The values of these factors were calculated from the background fractions f_K, f_π, f_p, F_K, F_π and F_p, with additional input from samples of simulated events. Note that it was implicitly assumed, here, that the sources of misidentified muons themselves do not contribute to a *CP* asymmetry.

Two Standard-Model sources of *CP* violation were considered in the latest D0 publication. The first of these is mixing in the $B^0\overline{B}^0$ and $B^0_s\overline{B}^0_s$ systems, which leads to a combined semileptonic asymmetry

$$A^b_{sl} \approx 0.58\, a^d_{\rm sl} + 0.42\, a^s_{\rm sl} \,,$$

where the factors 0.58 and 0.42 take into account the fragmentation fractions for a b or $\overline{b}$ quark to hadronize into a neutral or strange B meson as well as the mixing parameters in the $B^0\overline{B}^0$ and $B^0_s\overline{B}^0_s$ systems. The expected contributions to the observed asymmetries are

$$a_s = c_b\, A^b_{sl}$$

and

$$A_s = C_b\, A^b_{sl} \,,$$

where the dilution factors c_b and C_b correct for the fact that only a fraction of all true muons are actually due to decays of neutral or strange B mesons after mixing, The two factors were determined from samples of simulated events and found to be $c_b = 6.3\%$ and $C_b = 52\%$ on average. Both factors increased as expected from the inner to the outer impact-parameter region considered in the analysis. The second source of *CP* violation was first pointed out in Ref. [505]. It is due to decays of neutral B mesons to flavour-symmetric final $c\bar{c}d\bar{d}$ states such as $D^{(*)\pm}D^{(*)\mp}$, followed by a semileptonic decay of one of the charmed mesons. As illustrated in Figure 6.21, this final state can be reached from decays of B^0 mesons as well as from decays of $\overline{B}^0$ mesons. A *CP* violating asymmetry can therefore be caused by the interference of mixing and decay. This source of *CP* violation does not contribute to a_s, since the final state $D^{(*)\pm}D^{(*)\mp}$ is charge-symmetric and semileptonic decays of $D^{(*)\pm}$ mesons and $D^{(*)\mp}$ mesons are equally probable. In combination with a semileptonic decay of the opposite-side b hadron, however, a difference in the probabilities of initial B^0 mesons and initial $\overline{B}^0$ mesons to decay to this final state does cause a charge asymmetry in the same-sign dilepton sample. Estimates for the possible size of this effect were made in Ref. [505] as well as in the latest D0 publication, and

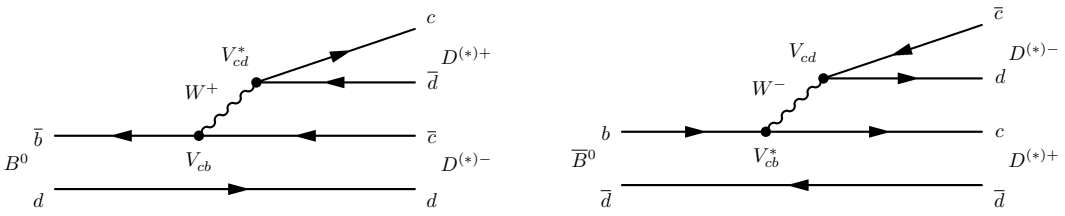

Figure 6.21: Illustration of the external tree decays (left) $B^0 \to D^{(*)+}D^{(*)-}$ and (right) $\overline{B}^0 \to D^{(*)+}D^{(*)-}$.

Table 6.4: Results of the most recent measurements of the semileptonic charge asymmetry, $a_{\rm sl}^d$, in $B^0\overline{B}^0$ mixing.

BaBar ($\pi_{D^*}^{\mp}\ell^{\pm}$) [491]	$(0.06 \pm 0.17\,(\text{stat}) \,^{+}_{-}\, ^{0.38}_{0.32}\,(\text{syst}))\%$
BaBar ($\ell^{\pm}\ell^{\pm}$) [492]	$(-0.39 \pm 0.35\,(\text{stat}) \pm 0.19\,(\text{syst}))\%$
D0 [494]	$(0.68 \pm 0.45\,(\text{stat}) \pm 0.14\,(\text{syst}))\%$
LHCb [495]	$(-0.02 \pm 0.19\,(\text{stat}) \pm 0.30\,(\text{syst}))\%$

both found it to be a factor of four to five larger than the asymmetry expected from mixing. The equivalent process exists also for decays of strange B mesons to final states such as $D_s^{\pm}D_s^{\mp}$, but the generated *CP* violating asymmetry is expected to be negligibly small in the Standard Model. Taking into account the two described Standard Model sources of *CP* violation, the D0 collaboration find a discrepancy between their measurement and the expected asymmetry at the level of 3.6 Gaussian standard deviations.

6.2.4 Comparison of results

Constraints on the semileptonic asymmetries $a_{\rm sl}^d$ and $a_{\rm sl}^s$, dominated by the latest measurements at BaBar, D0 and LHCb described above, are shown in Figure 6.22. Direct measurements of the semileptonic asymmetry $a_{\rm sl}^d$ in the $B^0\overline{B}^0$ system are in excellent agreement with the Standard Model prediction, while the D0 measurement of the same-sign dimuon charge asymmetry, which is sensitive to a linear combination of $a_{\rm sl}^d$ and $a_{\rm sl}^s$, shows a significant deviation. Direct measurements of the semileptonic asymmetry $a_{\rm sl}^s$ in the $B_s^0\overline{B}_s^0$ system agree with the Standard Model prediction, but are also compatible within their precision with the anomalous same-sign dimuon charge asymmetry claimed by the D0 collaboration. An LHCb measurement of $a_{\rm sl}^s$ using the full run I data set is pending.

6.3 The branching fraction of the very rare decay $B_s^0 \to \mu^+\mu^-$

Decays of B^0 and B_s^0 mesons to pairs of charged leptons are strongly suppressed in the Standard Model. Firstly, they involve a flavour-changing neutral current $b \to s$ or $b \to d$ transition and can therefore proceed only via suppressed loop diagrams, such as those shown in Figure 6.23. Moreover, these decays are also helicity suppressed. Neutral and strange B mesons are pseudoscalar particles with internal spin $J = 0$ and the conservation of angular momentum in the decay forces the lepton-antilepton pair to be produced with spins pointing into opposite directions. On the other hand, conservation of momentum in the rest frame of the decaying B meson forces the lepton-antilepton pair to be produced with momenta pointing in opposite directions. The decay therefore produces a lepton and an antilepton of same helicity, which is suppressed by the $V - A$ nature of the weak interaction. A possible scalar coupling due to penguin diagrams with an intermediate Standard-Model Higgs boson exists but is strongly

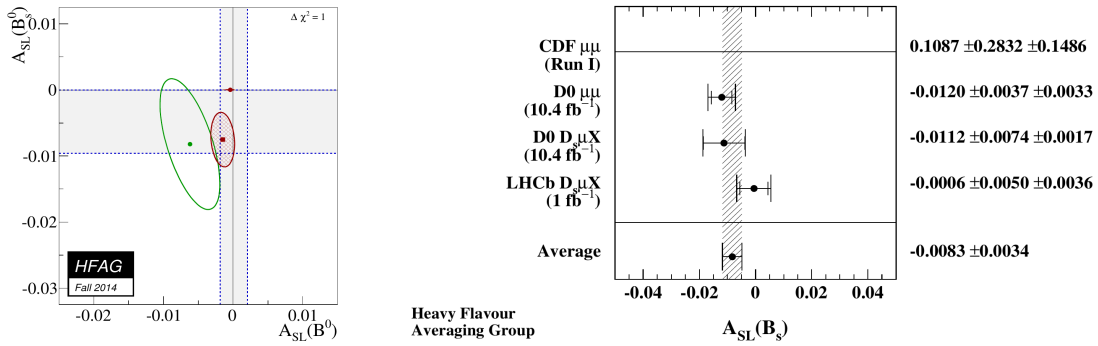

Figure 6.22: Comparison of measurements of the semileptonic asymmetries in the $B^0\overline{B}^0$ and $B_s^0\overline{B}_s^0$ systems, denoted here as $A_{\rm SL}(B^0)$ and $A_{\rm SL}(B_s^0)$, respectively, as compiled by the Heavy Flavour Averaging Group from results available by the beginning of September 2014. In the left panel, shaded vertical and horizontal bands indicate allowed regions from direct measurements of $a_{\rm sl}^d$ and $a_{\rm sl}^s$, respectively, while the green ellipse indicates constraints from the D0 measrement of the same-sign dilepton asymmetry and the red ellipse indicates the result of a fit to all measurements. The Standard Model prediction with its uncertainty is indicated by the red dot close to $(0, 0)$. The panel on the right shows a compilation of measurements of $a_{\rm sl}^s$, where the error bars of the CDF I measurement stretch across about ten times the width of the shown range (from [2]).

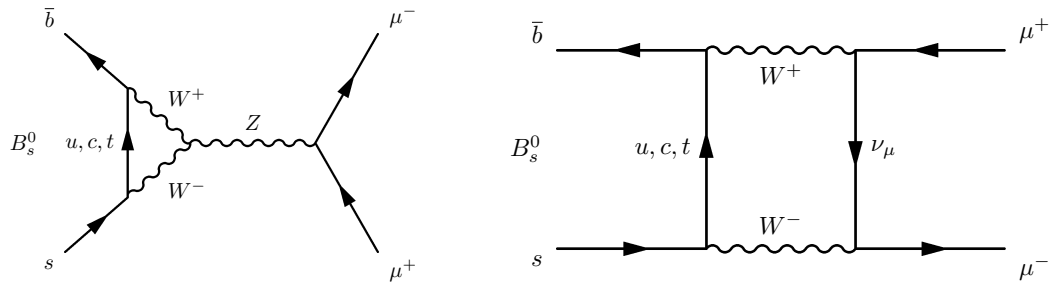

Figure 6.23: Illustration of Standard Model processes that mediate the very rare decay $B_s^0 \to \mu^+\mu^-$ via (left) penguin or (right) box diagrams.

suppressed by a factor m_B^2/m_W^2, where m_B and m_W are the mass of the decaying B meson and the mass of the W boson, respectively. The helicity suppression scales with the square of the mass of the final-state leptons and is therefore strongest for decays to e^+e^- pairs and least strong for decays to $\tau^+\tau^-$ pairs. Since the reconstruction of τ leptons presents experimental challenges, it is the decays to pairs of muons that offer the best chances of observing these decays and putting to the test Standard Model predictions of their branching fractions. These branching fractions can be significantly affected in many proposed extentions of the Standard Model, in particular in models with an extended Higgs sector such as supersymmetric models [506–513], but also in models introducing leptoquarks [514] or extra dimensions [515, 516]. As an example, a possible decay diagram involving charged and neutral Higgs bosons is shown in Figure 6.24. A significant enhancement of the branching fraction is expected in the Minimal Supersymmetric Standard Model (MSSM) if the ratio, $\tan\beta$, of the vacuum expectation values of the two predicted Higgs boson doublets is large [517–521]. In general, interference effects can, however, also lead to a further suppression of the branching fraction compared to the Standard Model prediction [522, 523].

Predictions of the branching fraction are based on Heavy-Quark Effective Field Theories using local Operator Product Expansion (OPE). A detailed and comprehensible description of the technique can be found in Ref. [524]. Heavy-Quark Effective Field Theories exploit the fact that the strong coupling constant is still reasonably small at the mass scale of the b quark, allowing short-distance effects to be calculated perturbatively. Choosing an appropriate fac-

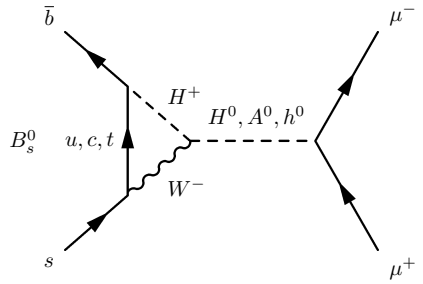

Figure 6.24: Example of a possible loop process that could contribute to the $B_s^0 \to \mu^+\mu^-$ and $B^0 \to \mu^+\mu^-$ decay amplitudes in extentions of the Standard Model with charged and neutral Higgs bosons. Note, that the helicity suppression inherent in the Standard Model is bypassed here due to the scalar nature of the intermediate Higgs boson.

Table 6.5: The six electroweak penguin operators that could play a role in the decays $B_s^0 \to \mu^+\mu^-$ and $B^0 \to \mu^+\mu^-$. In the Standard Model, only Q_{10} contributes significantly to the decay amplitude, while extentions of the Standard Model can also allow contributions from Q'_{10}, the scalar operators Q_S and Q'_S and the pseudoscalar operators Q_P and Q'_P.

$Q_{10} \equiv \frac{e^2}{g^2}\left(\overline{s}\,\gamma_\mu(\frac{1-\gamma_5}{2})\,b\right)\left(\overline{\ell}\,\gamma^\mu\gamma_5\,\ell\right)$	$Q'_{10} \equiv \frac{e^2}{g^2}\left(\overline{s}\,\gamma_\mu(\frac{1+\gamma_5}{2})\,b\right)\left(\overline{\ell}\,\gamma^\mu\gamma_5\,\ell\right)$
$Q_S \equiv \frac{e^2}{16\pi^2}\,m_b\left(\overline{s}\,(\frac{1+\gamma_5}{2})\,b\right)\left(\overline{\ell}\,\ell\right)$	$Q'_S \equiv \frac{e^2}{16\pi^2}\,m_b\left(\overline{s}\,(\frac{1-\gamma_5}{2})\,b\right)\left(\overline{\ell}\,\ell\right)$
$Q_P \equiv \frac{e^2}{16\pi^2}\,m_b\left(\overline{s}\,(\frac{1+\gamma_5}{2})\,b\right)\left(\overline{\ell}\,\gamma_5\,\ell\right)$	$Q'_P \equiv \frac{e^2}{16\pi^2}\,m_b\left(\overline{s}\,(\frac{1-\gamma_5}{2})\,b\right)\left(\overline{\ell}\,\gamma_5\,\ell\right)$

torization scale, μ, typically taken to be of the order of a few GeV, an effective Hamiltonian, $H_{\rm eff}$, is defined in which these perturbative short-distance effects are factorized out from the low-energy long distance effects that have to be determined using non-perturbative methods. Following a proof by Wilson and Zimmermann [525], this effective Hamiltonian can be expanded into a set of local, renormalized operators $Q_i(\mu)$ and complex-valued effective coupling constants $C_i(\mu)$,

$$H_{\rm eff} \;=\; \frac{G_F}{\sqrt{2}} \sum_i \left\{ V^i_{\rm CKM}\, C_i(\mu) \times Q_i(\mu) \right\} \;,$$

where G_F is the Fermi coupling constant and $V^i_{\rm CKM}$ describes the CKM matrix elements involved in the process. The coefficients $C_i(\mu)$, called Wilson coefficients, contain the short-distance dynamics due to effects above the chosen factorization scale μ, while the operators $Q_i(\mu)$ contain the low-energy, long distance effects. In analogy to the Fermi theory of muon decay, the operators can be regarded as four-fermion interaction vertices and the Wilson coefficients as the respective effective coupling constants. The amplitude for a given process $M \to f$ is then given by integrating over the effective operators, i.e.

$$A(M \to f) \;=\; \langle\, f\,|H_{\rm eff}|\,M\,\rangle \;=\; \frac{G_F}{\sqrt{2}} \sum_i \left\{ V^i_{\rm CKM}\, C_i(\mu) \times \langle\, f\,|Q_i(\mu)|\,M\,\rangle \right\} \;.$$

The six electroweak penguin operators that could in principle play a role in the decays $B_s^0 \to \mu^+\mu^-$ and $B^0 \to \mu^+\mu^-$ are listed in Table 6.5. Due to the $V-A$ character of the weak interaction, the only significant contribution in the Standard Model is due to the axial-vector coupling C_{10}, leading to the prediction for the branching fraction

$$\mathrm{BF}\,(B_s^0 \to \mu^+\mu^-) \;=\; \frac{G_F}{\pi}\;|V^*_{tb}V_{ts}|^2\;|C_{10}|^2 \;\times\; \left(\frac{\alpha_{\rm em}}{4\pi\,\sin^2\theta_W}\right)^2 \tau_{B_s^0}\, f^2_{B_s^0}\, m_{B_s^0}\, m^2_\mu \sqrt{1-\frac{4m^2_\mu}{m^2_{B_s^0}}}\;,$$

where $\alpha_{\rm em}$ is the electromagnetic coupling constant and θ_W the Weinberg angle of the electroweak interaction, $\tau_{B_s^0}$ and $m_{B_s^0}$ are the lifetime and mass of the decaying B_s^0 meson and m_μ is the mass of the muon. Long-distance QCD effects are contained in the decay constant $f_{B_s^0}^2$, which has to be calculated in Lattice QCD [526] and dominates the uncertainty on the prediction of the cross section [527]. The prediction for the decay $B^0 \to \mu^+\mu^-$ is obtained by replacing the appropriate CKM matrix elements as well as the mass, lifetime and decay constant for the B^0 meson. The magnitude of the Wilson coefficient, $|C_{10}|$, is given at leading order by the Inami-Lim function [109]

$$Y_0(x) \;=\; \frac{x}{8}\left(\frac{4-x}{1-x} + \frac{3x}{(1-x)^2}\,\ln x\right)\;,$$

where $x = m_t^2(\mu)/m_W$, reflecting the fact that the loop diagrams with internal top quarks dominate. As pointed out in Ref. [528], the estimates as defined above yield the *CP* averaged branching fractions evaluated for time $t = 0$ and, in the case of the decay $B_s^0 \to \mu^+\mu^-$, this estimate needs to be scaled by a correction factor

$$\frac{1}{1 - \Delta\Gamma_s/(2\overline{\Gamma}_s)}$$

in order to compare it with the time-integrated decay rate that is measured in experiments. In the case of the decay $B^0 \to \mu^+\mu^-$ no such correction is needed due to the vanishingly small value of the decay width difference, $\Delta\Gamma_d$, in the $B^0\overline{B}^0$ system. Including this scale factor in the estimate for the decay $B_s^0 \to \mu^+\mu^-$, the latest Standard Model predictions are [529]

$$\mathrm{BF}\,(B_s^0 \to \mu^+\mu^-) \;=\; (\,3.66 \,\pm\, 0.23\,) \times 10^{-9}$$

and

$$\mathrm{BF}\,(B^0 \to \mu^+\mu^-) \;=\; (\,1.06 \,\pm\, 0.09\,) \times 10^{-10}\;.$$

The first search for the decay $B^0 \to \mu^+\mu^-$ was reported in 1984 by the CLEO collaboration [530] and resulted in an upper limit on its branching fraction of 0.02% at 90% confidence level. Subsequent searches for the decay $B^0 \to \mu^+\mu^-$ were performed at CLEO [531, 532], Argus [533], Belle [534] and BaBar [535, 536], while searches for $B^0 \to \mu^+\mu^-$ and $B_s^0 \to \mu^+\mu^-$ were performed at UA1 [537], L3 [538], CDF I [539, 540], CDF II [541–545] and D0 [546–549], and at ATLAS [550], CMS [551] and LHCb [552–554]. The first evidence for the decay $B_s^0 \to \mu^+\mu^-$ with a significance corresponding to more than three Gaussian standard deviations was reported by the LHCb collaboration [555] in 2012, followed by measurements of its branching fractions by the LHCb [556] and CMS [557] collaborations. A combination of the latest LHCb and CMS measurements [558] resulted in the first observation of the decay $B_s^0 \to \mu^+\mu^-$ with a significance exceeding five Gaussian standard deviations. The measured branching fraction is in good agreement with the Standard Model prediction, leading to stringent constraints on the allowed parameter space for proposed extentions to the Standard Model.

The LHCb measurement [556] was based on the full run I data set, corresponding to an integrated luminosity of 3 fb^{-1}. A sample of signal candidates was collected by a combination of single-muon and dimuon triggers, followed by a loose offline selection that required two well identified and oppositely charged muon candidates, which fulfilled requirements on their momenta and transverse momenta, had significant impact parameters with respect to any reconstructed *pp* interaction vertex, and were compatible with originating from a common vertex that was displaced from the *pp* interaction vertices. The sample of selected candidates was then split into subsamples of different signal sensitivity according to the response of a multivariate classifier that combined a total of twelve discriminating variables related to the topology and kinematic properties of the decay. These variables included the reconstructed transverse momentum and decay time of the B meson candidate and its impact parameter

with respect to the associated pp interaction vertex, two variables related to the isolation of the B meson candidate and the two muon candidates, and several variables related to the decay angles of the muon candidates. The response of this multivariate classifier was calibrated on collision data using candidates from the dimuon invariant mass sidebands as a proxy for background and an ensemble of charmless two-body B^0 and B_s^0 decays to $K^{\pm}\pi^{\mp}$, $\pi^+\pi^-$ and K^+K^- as a proxy for the signal component. The masses of muons, pions and kaons all being small compared to the mass of the decaying B_s^0 or B^0 meson, the topology and kinematic properties of these charmless two-body decays of B mesons are similar to those of the signal decays. Possible biases due to the different trigger and particle identification requirements applied in the selections of the signal and calibration samples were corrected for using additional control samples. The method is described in detail in Ref. [559].

The $B_s^0 \to \mu^+\mu^-$ and $B^0 \to \mu^+\mu^-$ signal yields in each of the subsamples defined by the response of the multivariate classifier were then determined from a simultaneous fits to the invariant-mass distribution of the muon pairs. The expected shape of the invariant mass distribution for the signal components was described in this fit to the data by modified Gaussian functions with power-law tails to describe radiative tails and a small fraction of poorly reconstructed candidates. The parameters describing these power-law tails were determined from simulated signal events, while the parameters describing the Gaussian functions were determined from collision data employing samples of charmless two-body B^0 and B_s^0 decays and dimuon decays of charmonium and bottomonium resonances. The measured invariant-mass distributions for these control samples are shown in Figures 6.25 and 6.26. The means of the two Gaussian functions were determined directly from a combined fit to the four invariant-mass distributions of the charmless two-body decays. The width of the signal distributions in these control samples, however, cannot be used directly as an estimate for the expected signal width in $B_s^0 \to \mu^+\mu^-$ and $B^0 \to \mu^+\mu^-$. If tight particle identification criteria are applied to obtain clean samples of π^+K^-, $K^+\pi^-$, $\pi^+\pi^-$ and K^+K^- candidates, the momentum-dependence of the particle-identification performance will lead to a bias on the momentum distribution of the selected candidates, the invariant-mass resolution and the width of the observed signal. If loose particle identification criteria are applied, misidentified pions and kaons will cause cross-feed between the four final states, resulting in a broadening of the signal distribution. The method that was employed to correct for these biases and determine the expected width of the signal distribution for $B_s^0 \to \mu^+\mu^-$ and $B^0 \to \mu^+\mu^-$ decays is again described in detail in Ref. [559]. To cross-check the results of this method, a second approach was developed in Ref. [559] to determine the expected width of the signal at the B^0 and B_s^0 masses by interpolating between the measured widths of the $J/\psi \to \mu^+\mu^-$ and $\psi(2s) \to \mu^+\mu^-$ signals at lower mass and the $\Upsilon(1S)$, $\Upsilon(2S)$ and $\Upsilon(3S) \to \mu^+\mu^-$ signals at higher masses. The interpolation used a power-law function to describe the invariant-mass resolution as a function of the invariant mass. The validity of this model in the invariant-mass range of interest was verified using simulated samples of $pp \to \mu^+\mu^- X$ Drell-Yan events. Both approaches yielded compatible results, estimating the width of the $B_s^0 \to \mu^+\mu^-$ signal to be about 23 MeV/c^2. The two results were averaged to fix the width of the Gaussian function employed in the fit to the data.

The dominant source of background in the sample of selected candidates were combinations of two muons from events in which both the b hadron and the $\bar{b}$ hadron decayed semileptonically and, as illustrated in Figure 6.28, the trajectories of the two produced muons happened to be compatible with coming from a common vertex. This component was described in the fits to the invariant-mass distributions by falling exponential functions. In addition to the signal components and the component for combinatorial background, the fit function contained components for charmless two-body B^0 and B_s^0 decays in which both final-state kaons or pions were misidentified as muons, for $B^0 \to \pi^-\mu^+\nu_\mu$ and $B_s^0 \to K^-\mu^+\nu_\mu$ decays in which the pion or kaon was misidentified as a muon and for $B \to \pi\mu^+\mu^-$ decays in which the pion escaped detection. The latter two sources of background yield invariant dimuon masses below the B^0 and $B_s^0 \to \mu^+\mu^-$ signals, but their inclusion in the fit is important as it affects the fraction

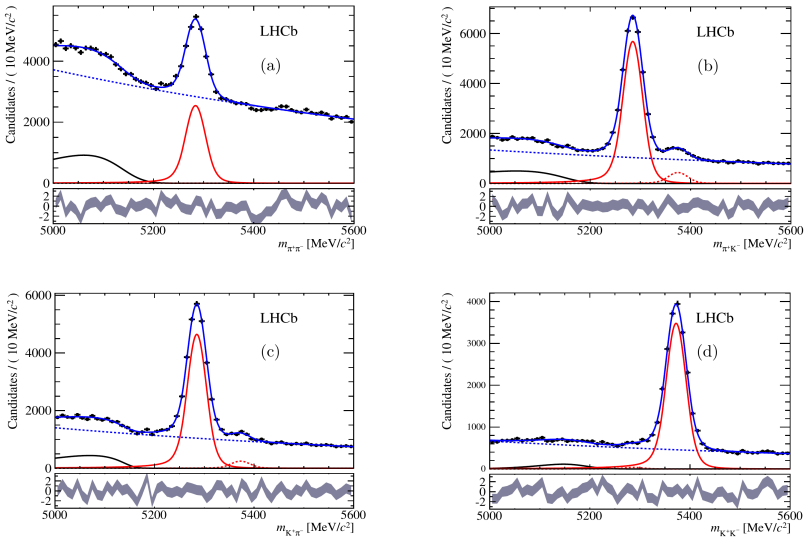

Figure 6.25: Measured invariant-mass distributions for (top left) $\pi^+\pi^-$, (top right) π^+K^-, (bottom left) $K^+\pi^-$ and (bottom right) K^+K^- candidates in the control sample of charmless two-body decays of B mesons employed to determine the signal shape in the LHCb analysis of the very rare decays $B_s^0 \to \mu^+\mu^-$ and $B^0 \to \mu^+\mu^-$. The results of a fit to the data are superimposed, where solid and dashed red lines indicate dominant and subdominant B^0 and B_s^0 signal components, respectively, dashed blue lines indicate the component from combinatorial background and black solid lines indicate the component from partially reconstructed backgrounds (from [559])

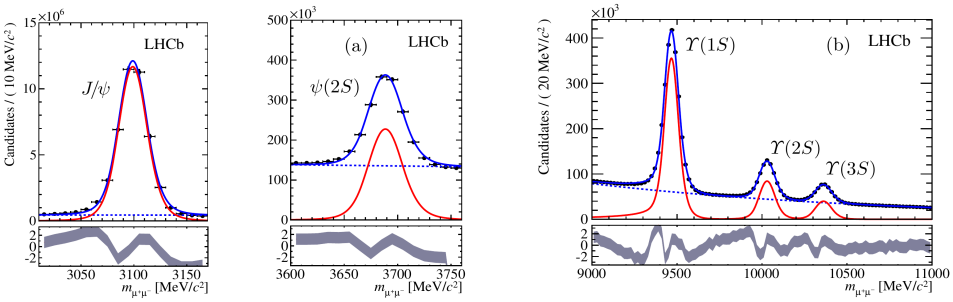

Figure 6.26: Measured invariant-mass distributions of dimuon pairs in the vicinity of the masses of the (left) J/ψ, (middle) $\psi(2s)$ and (right) $\Upsilon(1S)$, $\Upsilon(2S)$ and $\Upsilon(3S)$ resonances (from [559])

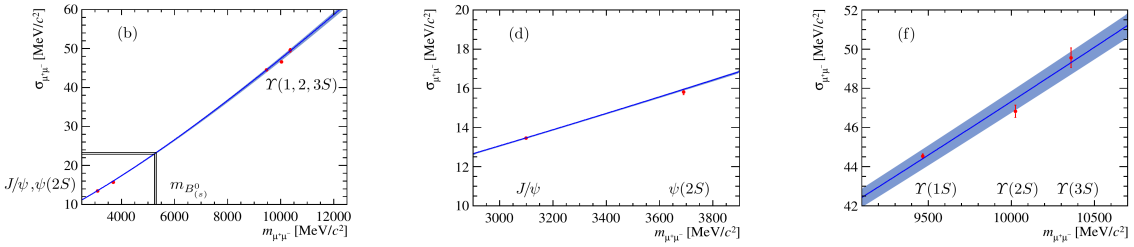

Figure 6.27: Interpolation of the dimuon invariant-mass resolution fitting a power-law function to the values extracted from the analysis of the charmonium resonances shown in Figure 6.26 above. The panel on the left shows the full mass range, indicating the masses of the B^0 and B_s^0 mesons, while the middle and right panels show the same interpolation in the restricted mass ranges around the charmonium and bottomonium resonances, respectively. Blue lines indicate the result of the interpolation, blue shaded areas its statistical uncertainty (from [559])

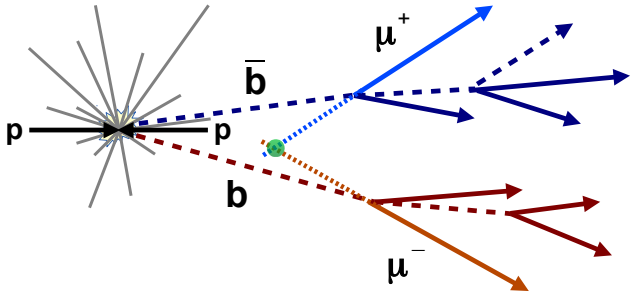

Figure 6.28: Illustration of the dominant source of background in the search for the very rare decays $B^0 \to \mu^+\mu^-$ and $B_s^0 \to \mu^+\mu^-$: both b hadrons produced in the event decay semileptonically and two oppositely charged muons are produced which accidentally point back to a common vertex that is displaced from the pp interaction vertex.

of the yield that the fit assigns to combinatorial background underneath the signals. The shapes of the invariant-mass distributions for these sources of background were determined from simulation. Their expected yields were estimated from the known branching fractions of the decays and from measured misidentifications probabilities. and then constrained to these estimates in fit to the data. The result of the fit to candidates with high signal sensitivity according to the response of the multivariate classifier is shown in Figure 6.29. Summed over the full range of the multivariate classifier response, an excess of $B_s^0 \to \mu^+\mu^-$ candidates over the no-signal hypothesis was observed with a significance corresponding to 4.0 Gaussian standard deviations. A smaller and not significant excess was found for $B^0 \to \mu^+\mu^-$. To avoid systematic uncertainties related to the knowledge of the $b\bar{b}$ production cross section and the determination of the integrated luminosity, and to reduce uncertainties related to the determination of trigger, reconstruction and selection efficiencies, the extracted event yield was converted into a cross section measurement using appropriately chosen normalization channels with well known branching fractions. The branching fraction was expressed as

$$\mathrm{BF}\,(B_s^0 \to \mu^+\mu^-) \;\equiv\; \mathrm{BF}_{\mathrm{norm}}\,\frac{f_{\mathrm{norm}}}{f_s}\,\frac{\epsilon_{\mathrm{norm}}}{\epsilon_{B_s^0\to\mu^+\mu^-}}\,\frac{N_{B_s^0\to\mu^+\mu^-}}{N_{\mathrm{norm}}} \;\equiv\; \alpha_{\mathrm{norm}} \times N_{B_s^0\to\mu^+\mu^-}\;,$$

where $\mathrm{BF}_{\mathrm{norm}}$ is the known branching fraction of the normalization channel, the fragmentation fractions f_s and f_{norm} describe the probabilities for a b or $\bar{b}$ quark to hadronize into strange, neutral or charged B mesons, $\epsilon_{B_s^0\to\mu^+\mu^-}$ and ϵ_{norm} describe the combined trigger, reconstruction and selection efficiencies for $B_s^0 \to \mu^+\mu^-$ candidates and for candidates in the normalization channels, respectively, and $N_{B_s^0\to\mu^+\mu^-}$ and N_{norm} are the measured signal yields in the two samples. Trigger, track reconstruction and particle identification efficiencies were determined from collision data, while the ratio of acceptance and selection efficiencies were determined from samples of simulated events. The ratio of fragmentation fractions, $f_s/(f_u + f_d)$, was taken from an independent LHCb measurement [138, 560] and it was assumed that $f_u = f_d$. The two decay modes $B^0/\overline{B}^0 \to K^\pm\pi^\mp$ and $B^\pm \to J/\psi K^\pm$ with $J/\psi \to \mu^+\mu^-$ were chosen as normalization channels. The first of these has a very similar decay topology to the signal decays, leading to similar acceptance and reconstruction efficiencies, but its selection relied on different trigger algorithms and particle identification criteria than that for the signal decays. The decay $B^\pm \to J/\psi K^\pm$ with $J/\psi \to \mu^+\mu^-$ has an extra final-state track compared to the signal decays, but can be selected using similar trigger and particle-identification requirements. The normalization factors α_{norm} derived from the two normalization channels were found to be in good agreement with each other. Despite the lack of a clear signal, a branching fraction measurement was derived in the same manner for the decay $B^0 \to \mu^+\mu^-$ and the results of the

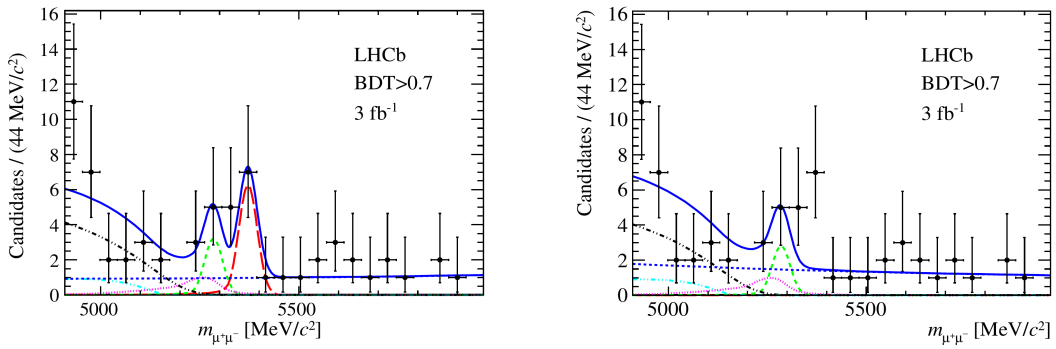

Figure 6.29: Measured invariant-mass distribution for signal-like $\mu^+\mu^-$ candidates, with an assigned value of the multivariate classifier of BDT > 0.7, from the LHCb measurement of the decays $B_s^0 \to \mu^+\mu^-$ and $B^0 \to \mu^+\mu^-$. The results of the simultaneous fit to candidates in all BDT bins is superimposed, where red long-dashed line indicates the $B_s^0 \to \mu^+\mu^-$ signal component, green dashed lines indicate the $B^0 \to \mu^+\mu^-$ signal component, blue dashed lines the component from combinatorial background, magenta dotted lines the background component from misidentified charmless two-body decays of B mesons, blue dot-dashed lines the background component from $B \to \pi\mu^+\mu^-$ and black dot-dashed lines the background component from $B^0 \to \pi^-\mu^+\nu_\mu$, and $B_s^0 \to K^-\mu^+\nu_\mu$. The panel on the left shows the result of the full fit, while the panel on the right shows the result of a fit in which the $B_s^0 \to \mu^+\mu^-$ signal component was removed from the fit function to illustrate the deterioration in agreement with the data (from [556]).

two measurements were quoted as

$$\begin{aligned} \mathrm{BF}\,(B_s^0 \to \mu^+\mu^-) &= (\,2.9\,^{+1.1}_{-1.0}\,(\mathrm{stat})\,^{+0.3}_{-0.1}\,(\mathrm{syst})\,) \times 10^{-9} \\ \mathrm{BF}\,(B^0 \to \mu^+\mu^-) &= (\,3.7\,^{+2.4}_{-2.1}\,(\mathrm{stat})\,^{+0.6}_{-0.4}\,(\mathrm{syst})\,) \times 10^{-10}\ . \end{aligned}$$

The statistical uncertainty on the measurement was obtained by fitting the data with all nuisance parameters fixed to their nominal values. The fit was then repeated adding Gaussian constraints for all nuisance parameters, including the normalization factor α_{norm}, with the standard deviations of these constraints set to the estimated uncertainty on the nuisance parameter. This second fit will result in a larger uncertainty on the branching fraction measurement and the difference in quadrature between this uncertainty and the statistical uncertainty as determined in the first fit was assigned as the systematic uncertainty.

The CMS analysis was based on a data set corresponding to an integrated luminosity of 25 fb^{-1}, about 80% of which were collected at a pp collision energy of 8 TeV in the year 2012, while the remaining 20% were collected at a collision energy of 7 TeV in the year 2011. The trigger required two muon candidates that fulfilled requirements on their transverse momentum and invariant mass and were compatible with originating from a common vertex. In the offline selection, tight muon identification requirements were applied on the two candidates and the fraction of misidentified hadrons was further reduced by means of a multivariate classifier that combined kinematic properties of the candidates with information on track reconstruction quality and information from muon detectors. A second multivariate classifier employed to suppress background, combining a total of up to twelve discriminating variables, including the distance of closest approach of the two muon candidates, the quality of the dimuon vertex fit and two variables related to its displacement from the associated pp interaction vertex, the transverse momentum and pseudorapidity of the dimuon candidate and the impact parameter of its reconstructed momentum vector with respect to the associated pp interaction vertex, the opening angle between the momentum vector of the dimuon candidate and the line connecting the pp interaction vertex with the dimuon vertex, and four variables related to the isolation of the two muon candidates and of the combined dimuon candidate.

The selection was applied separately for candidates with both muons pointing into central region of the detector and candidates for which at least one muon pointed into the forward or

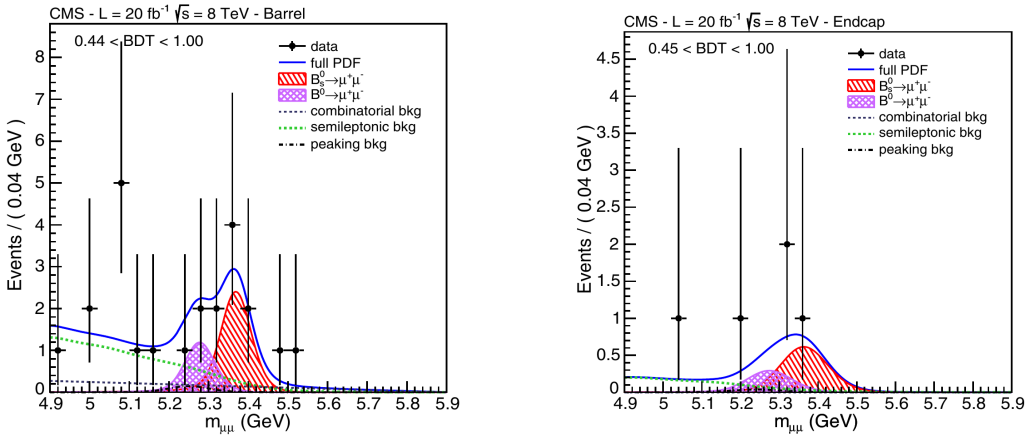

Figure 6.30: Measured invariant-mass distribution for signal-like $\mu^+\mu^-$ candidates with an assigned value of the multivariate classifier $b > 0.44$ and (left) both muon candidates in the central region of the detector or (right) at least one of the two muon candidates in the forward or backward region of the detector, from the CMS measurement of the decays $B_s^0 \to \mu^+\mu^-$ and $B^0 \to \mu^+\mu^-$. The results of the fits to the full data samples are superimposed with signal and background fractions indicated as listed in the plot legend (from [557]).

backward region. This separation was done to take into account the superior reconstruction quality in the central region of the CMS detector. For example, according to simulation studies, the dimuon invariant-mass resolution deteriorates from 32 MeV/c^2 for $B_s^0 \to \mu^+\mu^-$ candidates pointing into the central region of the detector to 75 MeV/c^2 for $B_s^0 \to \mu^+\mu^-$ candidates pointing into the forward and backward regions. Similar to the LHCb analysis described above, the event sample was further split into several categories according to the response of the multivariate classifier. Finally, a simultaneous fit to a total of twelve categories of candidates was performed to extract the $B_s^0 \to \mu^+\mu^-$ and $B^0 \to \mu^+\mu^-$ signal yields. The signal components and a background component for misidentified charmless two-body decays of B mesons were described in the fit by Gaussian functions with power-law tails. All parameters of these functions were derived from an analysis of simulated events. In addition, the fit function contained a component for combinatorial background, which was modelled by first-order polynomials, and backgrounds from misidentified semileptonic b hadron decays to $\pi^\mp\mu^\pm\nu_\mu$, $K^\mp\mu^\pm\nu_\mu$, $\pi^\pm\mu^+\mu^-$, $K^\pm\mu^+\mu^-$, $\overline{p}\mu^+\nu_\mu$ and $p\mu^-\overline{\nu}_\mu$. These background components were also estimated from samples of simulated events. The result of the fit for the event category with the highest signal sensitivity according to the response of the multivariate classifier is shown in Figure 6.30. Combining all twelve categories, an excess of $B_s^0 \to \mu^+\mu^-$ candidates over the background-only hypothesis was found with a significance corresponding to 4.3 Gaussian standard deviations. No significant excess of $B^0 \to \mu^+\mu^-$ candidtaes was found. Similar to the LHCb measurement, the decay mode $B^\pm \to J/\psi K^\pm$ with $J/\psi \to \mu^+\mu^-$ was employed as normalization channel to convert the signal yields into a measurement of the branching fraction. All efficiencies were determined from simulated events and the LHCb measurement of the ratio of fragmentation fractions [138, 560] was employed. The CMS experiment probes $b\bar{b}$ production in a different range of pseudorapidity and transverse momentum from the LHCb experiment and the fragmentation fractions could depend on these variables. A possible dependence was investigated using a control sample of $B_s^0 \to J/\psi K^+K^-$ candidates, but no significant effect was found. Also the CMS collaboration decided to derive a branching fraction for the decay $B^0 \to \mu^+\mu^-$ despite the absence of a significant signal. The results of the two measurements were quoted as

$$\begin{aligned} \mathrm{BF}\,(B_s^0 \to \mu^+\mu^-) &= (3.0\,^{+1.0}_{-0.9}) \times 10^{-9} \\ \mathrm{BF}\,(B^0 \to \mu^+\mu^-) &= (3.5\,^{+2.1}_{-1.8}) \times 10^{-10}\,, \end{aligned}$$

The quoted uncertainties include statistical and systematic unertainties. Sources of systematic

were the knowledge of the hadron-to-muon misidentification probability and the knowledge of branching fractions and normalization of the peaking background component in the fit to the data. They were included in the fit as Gaussian constraints, with the standard deviations of these constraints set to the value of the estimated uncertainty.

The two measurements were combined [558], resulting in the first observation of the decay $B_s^0 \to \mu^+\mu^-$ with a significance exceeding five Gaussian standard deviations. First evidence for the decay $B^0 \to \mu^+\mu^-$ was also claimed with a significance corresponding to three Gaussian standard deviations. The measured branching fractions were reported as

$$\mathrm{BF}\,(B_s^0 \to \mu^+\mu^-) \;=\; (\,2.8\,^{+\,0.7}_{-\,0.6}\,) \times 10^{-9}$$

and

$$\mathrm{BF}\,(B^0 \to \mu^+\mu^-) \;=\; (\,3.9\,^{+\,1.6}_{-\,1.4}\,) \times 10^{-10}\;,$$

where quoted uncertainties include statistical and systematic contributions and are dominated in both cases by the statistical uncertainty. In the case of the decay $B_s^0 \to \mu^+\mu^-$, the result is in good agreement with the Standard Model prediction and puts severe constraints on the allowed parameter space for many extentions of the Standard Model. In the case of the decay $B^0 \to \mu^+\mu^-$, the reported central value of the measurement is somewhat higher than the Standard Model prediction but the uncertainty is large.

The next goal for measurements in these decay modes will be to determine the ratio of their two branching fractions. This ratio provides an even more stringent test of the Standard Model and proposed extensions with minimal flavour violation [561]. A log-likelihood profile as a function of this ratio as obtained by the combination of the current LHCb and CMS measurements is shown in Figure 6.33. The result is compatible with the Standard Model prediction within 2.3 Gaussian standard deviations.

6.4 Angular observables in the rare decay $B^0 \to K^{*0}\mu^+\mu^-$

The decay $B^0 \to K^{*0}\mu^+\mu^-$ is due to the flavour-changing neutral current process $b \to s\mu^+\mu^-$ and can occur in the Standard Model only via loop processes as illustrated in Figure 6.34. First evidence for this decay was found by the BaBar collaboration [562] and the first observation with a significance exceedigng five Gaussian standard deviations was reported by the Belle [563] collaboration soon after. The 2014 edition of the Review of Particle Physics [1] quotes the branching fraction as

$$\mathrm{BF}\,(B^0 \to K^{*0}\mu^+\mu^-) \;=\; (\,1.05 \,\pm\, 0.10\,) \;\times\; 10^{-6}\;.$$

The main interest in studying this decay mode lies in the fact that the angular distribution of the final-state particles is sensitive to the interference between different short-distance contributions in the decay amplitude. A number of observables can be constructed from the angular distribution that exhibit good sensitivity to possible contributions from physics beyond the Standard Model.

With $K^{*0} \to K^+\pi^-$, the decay is characterized by a total of four final-state particles and can be fully described by four parameters. These are usually defined as the squared momentum transfer, q^2, to the $\mu^+\mu^-$ pair, which also defines its invariant mass, and three helicity angles, θ_K, θ_ℓ and ϕ. A definition of the helicity angles is shown in Figure 6.36 but different conventions have been used in literature. In measurements, the angle θ_ℓ is often defined with respect to the positive muon for the decay $B^0 \to K^{*0}\mu^+\mu^-$ and with respect to the negative muon in the charge-conjugated decay $\overline{B}^0 \to \overline{K}^{*0}\mu^+\mu^-$, while theory papers usually employ a convention in which θ_ℓ is defined with respect to the postive muon in both cases. A similar confusion exists regarding the definition of the angle ϕ between the two decay planes. These different conventions lead to swaps in the sign of some of the observables.

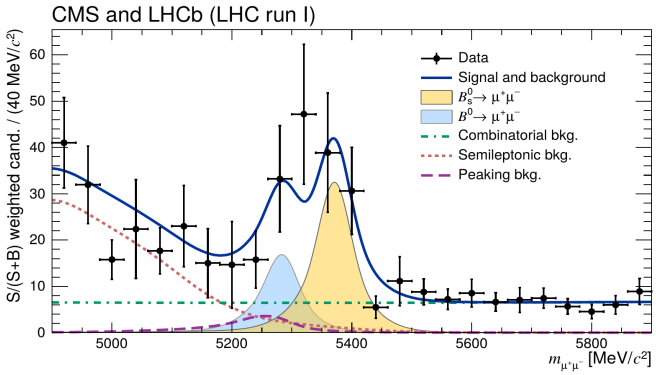

Figure 6.31: Weighted invariant-mass distribution for all $\mu^+\mu^-$ candidates from the combined LHCb and CMS measurements of the decays $B_s^0 \to \mu^+\mu^-$ and $B^0 \to \mu^+\mu^-$. Each candidate was weighted with the average signal fraction, $S/(S+B)$, for the category to which it belonged. The result of the fit to the data is superimposed with signal and background fractions indicated as listed in the plot legend (from [558]).

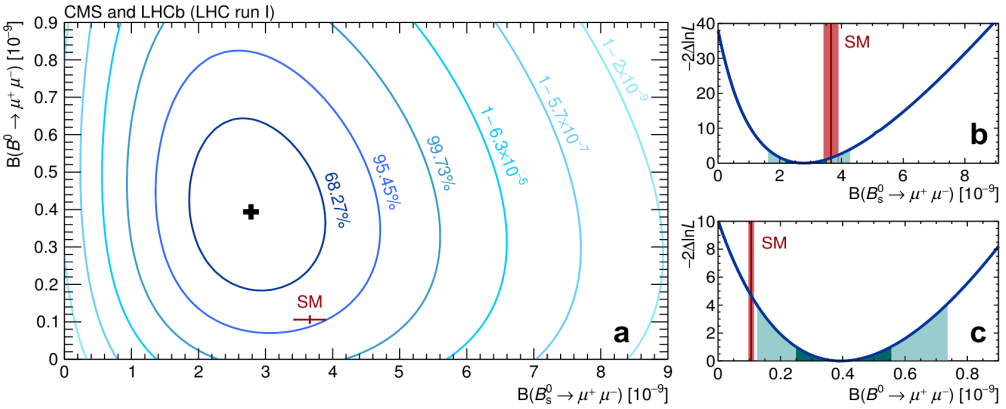

Figure 6.32: Measured invariant-mass distribution for signal-like $\mu^+\mu^-$ candidates in (Results of the combined fit to the run I LHCb and CMS measurements of the $B_s^0 \to \mu^+\mu^-$ and $B^0 \to \mu^+\mu^-$ branching fractions. The panel on the left shows curves of constant likelihood in the BF $(B_s^0 \to \mu^+\mu^-)$–BF $(PBz \to \mu^+\mu^-)$ plane, while the two panels on the right show the projections onto the two axes. Here, dark and light shaded areas indicate the confidence intervals corresponding to one and two Gaussian standard deviations, respectively. The red cross in the left panel and the vertical red bars in the panels on the right indicate the values predicted in the Standard Model with their uncertainties [558]).

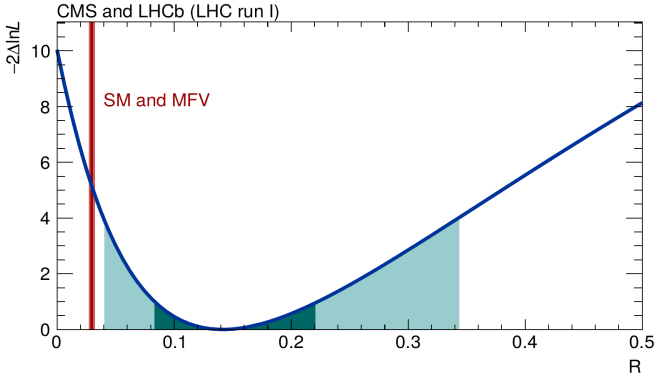

Figure 6.33: Log-likelihood as a function of the assumed value of the branching fraction ratio $R \equiv$ BF $(B^0 \to \mu^+\mu^-)$/BF $(B_s^0 \to \mu^+\mu^-)$ as obtained from a combined fit to the run I LHCb and CMS data. Dark and light shaded areas indicate the confidence intervals for R corresponding to one and two Gaussian standard deviations, respectively. The vertical red bar indicates the value of R predicted in the Standard Model and in extentions of the Standard Model with minimum flavour violation (from [558]).

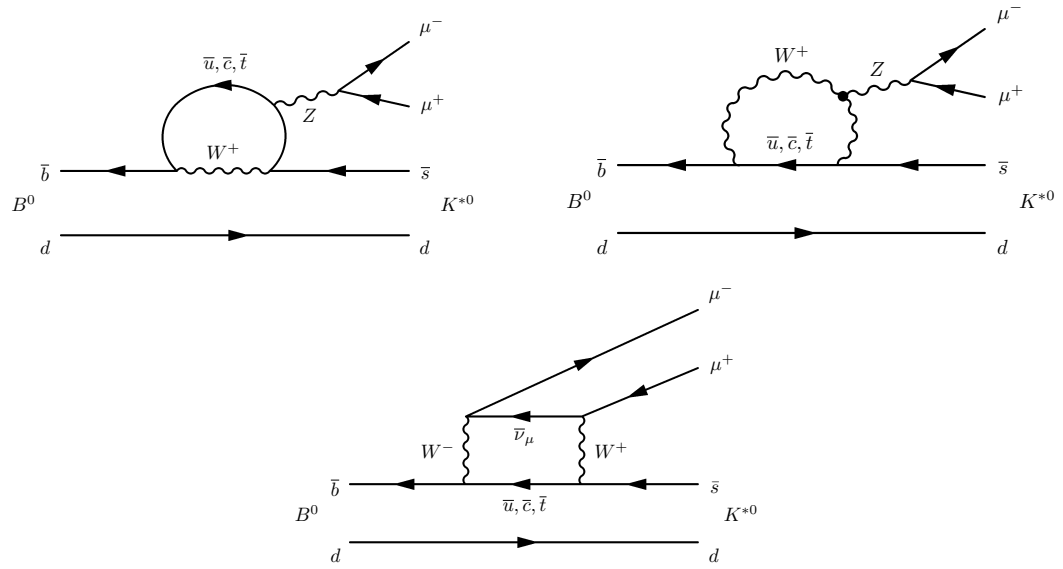

Figure 6.34: Illustration of Standard Model processes that mediate the rare decay $B^0 \to K^{*0}\mu^+\mu^-$ via (top left and right) penguin or (bottom) box diagrams.

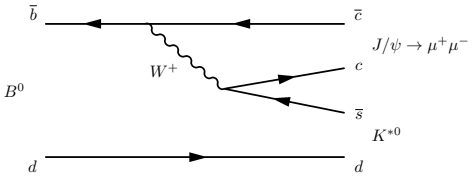

Figure 6.35: Illustration of the tree process that dominates the decay amplitude to the final state $K^{*0}\mu^+\mu^-$ for values of the squared momentum transfer q^2 corresponding to the masses of the charmonium resonances, J/ψ and $\psi(2s)$.

At values of the dimuon invariant mass, q^2 corresponding to the charmonium resonances, the tree decays $B^0 \to J/\psi K^{*0}$ and $B^0 \to \psi(2s)K^{*0}$ with J/ψ and $\psi(2s) \to \mu^+\mu^-$, as illustrated in Figure 6.35, constitute an overwhelming irreducible background. The corresponding ranges in q^2 therefore have to be excluded from analyses. At values of q^2 above the $\psi(2s)$ resonance, the decay amplitude could be affected by possible broad charmonium resonances, though it has been argued that these effects on the angular observables could cancel [565] if they are integrated over a sufficiently large q^2 range. In general, theory predictions are regarded to be most reliable for values of q^2 between 1 GeV$^2/c^2$ and 6 GeV$^2/c^2$ and most analyses concentrate on this range. Calculations are performed using Operator Product Expansion as already discussed in the previous section. The decay rate is expressed as

$$A(B^0 \to K^{*0}\mu^+\mu^-) \;=\; \frac{G_F}{\sqrt{2}} \sum_i \left\{ V^i_{\rm CKM}\, C_i \;\times\; \langle\, K^{*0}\mu^+\mu^- \,|Q_i|\, B^0 \,\rangle \right\} \;,$$

where the twelve operators Q_i listed in Table 6.6 can in principle contribute to the $K^{*0} \to K^+\pi^-$ decay amplitude. In the Standard Model, only the operators Q_7, Q_9 and Q_{10} are relevant. Possible contributions from physics beyond the Standard Model could modify the values of the Wilson coefficients C_i with respect to their Standard Model predictions. The precision of these predictions is limited by low-energy long distance effects involved in the $B^0 \to K^{*0}$ transition. These are parametrized as hadronic form factors that have to be calculated using non-perturbative methods. At the high end of the q^2 spectrum, they are best obtained from Lattice-QCD calculations [566, 567], while at values of q^2 below the charmonium resonances they are calculated using light-cone sum rules [274,568]. The uncertainties on these calculations

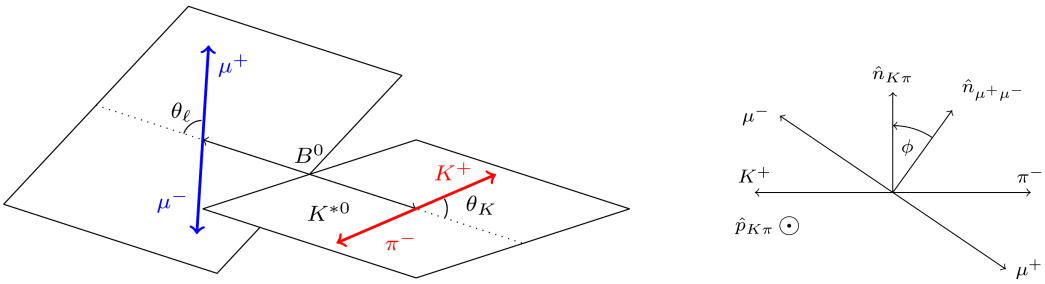

Figure 6.36: Definition of the helicity angles (left) θ_ℓ and θ_K and (right) ϕ as employed in the LHCb analysis of angular observables in the decay $B^0 \to K^{*0}\mu^+\mu^-$. For the charge-conjugated process $\overline{B}^0 \to \overline{K}^{*0}\mu^-\mu^+$, the angles θ_ℓ and θ_K are defined with respect to the negative muon and kaon, respectively, and the angle ϕ changes its direction (from [564]). Different conventions are used in literature. The angle θ_ℓ, for example, is often defined with respect to the positive muon for the B^0 decay and with respect to the negative muon for $\overline{B}^0$ decays. These different conventions lead to changes in the definitions of the sign for some observables.

Table 6.6: The twelve operators that could in principle play a role in the decay $B^0 \to K^{*0}\mu^+\mu^-$. In the Standard Model, only Q_7, Q_9 and Q_{10} contribute significantly to the decay amplitude.

$Q_7 \equiv \frac{e}{g^2}\, m_B \left(\overline{s}\,\sigma_{\mu\nu}(\frac{1+\gamma_5}{2})\,b\right) F^{\mu\nu}$	$Q'_7 \equiv \frac{e}{g^2}\, m_b \left(\overline{s}\,\sigma_{\mu\nu}(\frac{1-\gamma_5}{2})\,b\right) F^{\mu\nu}$
$Q_8 \equiv \frac{1}{g}\, m_b \left(\overline{s}\,\sigma_{\mu\nu} T^\alpha(\frac{1+\gamma_5}{2})\,b\right) G^{\mu\nu\,\alpha}$	$Q'_8 \equiv \frac{1}{g}\, m_b \left(\overline{s}\,\sigma_{\mu\nu} T^\alpha(\frac{1-\gamma_5}{2})\,b\right) G^{\mu\nu\,\alpha}$
$Q_9 \equiv \frac{e^2}{g^2} \left(\overline{s}\,\gamma_\mu(\frac{1-\gamma_5}{2})\,b\right) \left(\overline{\ell}\,\gamma^\mu\,\ell\right)$	$Q'_9 \equiv \frac{e^2}{g^2} \left(\overline{s}\,\gamma_\mu(\frac{1+\gamma_5}{2})\,b\right) \left(\overline{\ell}\,\gamma^\mu\gamma_5\,\ell\right)$
$Q_{10} \equiv \frac{e^2}{g^2} \left(\overline{s}\,\gamma_\mu(\frac{1-\gamma_5}{2})\,b\right) \left(\overline{\ell}\,\gamma^\mu\gamma_5\,\ell\right)$	$Q'_{10} \equiv \frac{e^2}{g^2} \left(\overline{s}\,\gamma_\mu(\frac{1+\gamma_5}{2})\,b\right) \left(\overline{\ell}\,\gamma^\mu\gamma_5\,\ell\right)$
$Q_S \equiv \frac{e^2}{16\pi^2}\, m_b \left(\overline{s}\,(\frac{1+\gamma_5}{2})\,b\right) \left(\overline{\ell}\,\ell\right)$	$Q'_S \equiv \frac{e^2}{16\pi^2}\, m_b \left(\overline{s}\,(\frac{1-\gamma_5}{2})\,b\right) \left(\overline{\ell}\,\ell\right)$
$Q_P \equiv \frac{e^2}{16\pi^2}\, m_b \left(\overline{s}\,(\frac{1+\gamma_5}{2})\,b\right) \left(\overline{\ell}\,\gamma_5\,\ell\right)$	$Q'_P \equiv \frac{e^2}{16\pi^2}\, m_b \left(\overline{s}\,(\frac{1-\gamma_5}{2})\,b\right) \left(\overline{\ell}\,\gamma_5\,\ell\right)$

are significant. The precision of predictions and therefore the sensitivity to possible effects from physics beyond the Standard Model can be improved by constructing observables from the angular distributions that are independent of these form factors at leading order. Various such observables have been proposed in literature and some have actually been measured. Examples with be discussed below.

Factorizing the dependence on q^2 and on the helicity angles, the differential decay rate can be expressed as

$$\frac{d^4\Gamma\,(B^0 \to K^{*0}\mu^+\mu^-)}{dq^2\, d\cos\theta_\ell\, d\cos\theta_K\, d\phi} = \frac{9}{32\pi} \sum_k \Big\{ I_k(q^2) \times f_k(\cos\theta_\ell, \cos\theta_K, \phi) \Big\}$$

where all dependence on the helicity angles is contained in the functions $f_k(\cos\theta_\ell, \cos\theta_K, \varphi_h)$ and the coefficients $I_k(q^2)$ contain the information on the Wilson coefficients. In the approximation of vanishing lepton mass, these coefficients can be expressed in terms of six transversity amplitudes, $A^{L,R}_{0,\|,\perp}$, where the indices 0, $\|$, and $\perp$ refer to the polarization state of the K^{*0} meson while the indices L and R describe the chirality state of the lepton current. For finite lepton masses, a seventh amplitude, A_t has to be taken into account and an eighth amplitude, A_S, enters if in addition the possibility of scalar contributions to the decay amplitude is taken into consideration. The effects of these additional amplitudes are suppressed by a factor m_ℓ^2/q^2 and can be neglected within the considered range of q^2 and the current precision of measurements. Explicit expressions for the angular coefficients I_k and functions f_k in the approximation of vanishing lepton mass are given in Table 6.7. Full expressions taking into account the finite

Table 6.7: Compilation of the angular coefficients I_k and function $f_k(\theta_K, \theta_\ell, \phi)$ as employed in analyses of angular distributions in the decay $B^0 \to K^{*0}\mu^+\mu^-$. The angular coefficients are quoted here for the approximation of a vanishingly small mass of the lepton. The coefficient I_6^c assumes a non-zero value if this assumption is dropped.

k	$I_k(q^2)$	$f_k(\theta_K, \theta_\ell, \phi)$
1^s	$\frac{3}{4}\left(\lvert A_\perp^L\rvert^2 + \lvert A_\perp^R\rvert^2 + \lvert A_\parallel^L\rvert^2 + \lvert A_\parallel^R\rvert^2\right)$	$\sin^2\theta_K$
1^c	$\lvert A_0^L\rvert^2 + \lvert A_0^R\rvert^2$	$\cos^2\theta_K$
2^s	$\frac{1}{4}\left(\lvert A_\perp^L\rvert^2 + \lvert A_\perp^R\rvert^2 + \lvert A_\parallel^L\rvert^2 + \lvert A_\parallel^R\rvert^2\right)$	$\sin^2\theta_K \cos(2\theta_\ell)$
2^c	$-\left(\lvert A_0^L\rvert^2 + \lvert A_0^R\rvert^2\right)$	$\cos^2\theta_K \cos(2\theta_\ell)$
3	$\frac{1}{2}\left(\lvert A_\perp^L\rvert^2 + \lvert A_\perp^R\rvert^2 - (\lvert A_\parallel^L\rvert^2 + \lvert A_\parallel^R\rvert^2)\right)$	$\sin^2\theta_K \sin^2\theta_\ell \cos(2\phi)$
4	$\frac{1}{\sqrt{2}}\,\mathrm{Re}\left(A_0^L A_\parallel^{L*} + A_0^R A_\parallel^{R*}\right)$	$\sin(2\theta_K)\sin(2\theta_\ell)\cos\phi$
5	$\sqrt{2}\,\mathrm{Re}\left(A_0^L A_\perp^{L*}) - A_0^R A_\perp^{R*}\right)$	$\sin(2\theta_K)\sin\theta_\ell\cos\phi$
6^s	$2\,\mathrm{Re}\left(A_\parallel^L A_\perp^{L*} - A_\parallel^R A_\perp^{R*}\right)$	$\sin^2\theta_K \cos\theta_\ell$
6^c	0	$\cos^2\theta_K \cos\theta_\ell$
7	$\sqrt{2}\,\mathrm{Im}\left(A_0^L A_\perp^{L*} - A_0^R A_\perp^{R*}\right)$	$\sin(2\theta_K)\sin\theta_\ell\sin\phi$
8	$\frac{1}{\sqrt{2}}\,\mathrm{Im}\left(A_0^L A_\parallel^{L*} + A_0^R A_\parallel^{R*}\right)$	$\sin(2\theta_K)\sin(2\theta_\ell)\sin\phi$
9	$2\,\mathrm{Im}\left(A_\parallel^L A_\perp^{L*} + A_\parallel^R A_\perp^{R*}\right)$	$\sin^2\theta_K \sin^2\theta_\ell \sin(2\phi)$

lepton masses can be found for example in Ref. [569]. The dependence of the decay amplitude on the Wilson coefficients is contained in the transversity amplitudes. Explicit expressions for the transversity amplitudes in terms of the Wilson coefficients can also be found in [569].

Note that the decay angles are expressed in terms of the helicity basis, while the decay amplitudes are expressed in terms of the transversity basis. The relationship between these two bases has already been discussed in Section 6.1. As a reminder, the transversity amplitudes are related to the helicity amplitudes, h_0, h_+ and h_-, as

$$A_0 \;=\; h_0 \quad ; \quad A_\parallel \;=\; \frac{1}{\sqrt{2}}\,(h_+ + h_-) \quad ; \quad A_\perp \;=\; \frac{1}{\sqrt{2}}\,(h_+ - h_-)\;.$$

Taking into account also the charge-conjugated process $\overline{B}^0 \to \overline{K}^{*0}\mu^+\mu^-$, the sum of the two decay rates is given by

$$\frac{d^4\Gamma\,(B^0 \to K^{*0}\mu^+\mu^- + \overline{B}^0 \to \overline{K}^{*0}\mu^+\mu^-)}{dq^2\,d\cos\theta_\ell\,d\cos\theta_K\,d\phi} \;=\; \frac{9}{32\pi}\sum_k \left\{\, S_k(q^2) \,\times\, f_k(\cos\theta_\ell, \cos\theta_K, \phi)\,\right\}\;,$$

where

$$S_k(q^2) \;\equiv\; I_k(q^2) + \overline{I}_k(q^2)$$

and the coefficients $\overline{I}_k$ are obtained from the I_k by reversing the signs of all weak phases in the decay amplitudes. A second set of observables,

$$A_k(q^2) \;\equiv\; I_k(q^2) - \overline{I}_k(q^2)\;,$$

is provided by the difference between the two decay rates. The angular coefficients $I_k(q^2)$ and $\overline{I}_k(q^2)$, $S_k(q^2)$ and $A_k(q^2)$ are observables that can be extrated from the measured angular distributions. However, they suffer from significant theory uncertainties due to the dependence of the decay amplitudes on hadronic form factors. This theory uncertainty can be significantly reduced by forming combinations and ratios of the angular coefficients in which the form factors

cancel at first order. An example is the forward-backward asymmetry, $A_{FB}(q^2)$, of the emitted muon with respect to the flight direction of the decaying B^0 meson in the rest frame of the dimuon system, i.e. the asymmetry between the number of decays for which $\cos\theta_\ell > 0$ and the number of decays for which $\cos\theta_\ell < 0$. In terms of the coefficients I_k, it is given by

$$A_{FB} \;=\; -\frac{3}{2}\,\frac{2I_6^s + I_6^c}{3I_1^c + 6I_1^s - I_2^c - 2I_2^s} \;=\; -\frac{3I_6^s}{4(I_1^c + 4I_2^s)}\;,$$

where the second equality holds in the limit of vanishing mass of the lepton. In the Standard Model, the value of $A_{FB}(q^2)$ is expected to cross from negative to positive values at around $q^2 = 4\ \mathrm{GeV}^2/c^2$. Form-factor uncertainties cancel at the location of this zero-crossing point and the measurement of its position as a function of q^2 can therefore provide a sensitive test of the Standard Model prediction [570]. However, this cancellation of the form-factor dependence occurs in the case of $A_{FB}(q^2)$ only in the vicinity of the zero-crossing point. Other observables have been proposed and studied in literature in which the form-factor dependencies cancel to first order over a wider range in q^2. A compilation of such observables is given in Table 6.8.

The six complex transversity amplitudes give rise to twelve real parameters, which are reflected in the twelve coefficients I_k. However, these twelve parameters are not independent from each other. In the approximation of vanishing mass of the lepton, there exist four relationships, reducing the number of independent observables to eight. Three of these relations are obvious from the expressions in Table 6.7,

$$I_1^s = 3I_2^s \;\;;\;\; I_1^c = -I_2^c \;\;;\;\; I_6^c = 0\;,$$

while the fourth one is less obvious and was first identified in Ref. [576] from an analysis of continuous infinitesimal symmetries in the angular distributions. An "optimal set" of eight independent observables that fully describe the decay amplitude in the approximation of vanishing mass of the lepton has been proposed in Ref. [577] as

$$\left\{ d\Gamma/dq^2 \;;\; A_{FB} \;;\; P_1 \equiv A_T^{(2)} \;;\; P_2 \equiv \frac{1}{2}A_T^{(\mathrm{re})} \;;\; P_3 \equiv -\frac{1}{2}A_T^{(\mathrm{im})} \;;\; P_4' \;;\; P_5' \;;\; P_6' \right\}\;.$$

Hadronic form factors cancel at leading order over the full q^2 range of interest in all these observables except $d\Gamma/dq^2$ and A_{FB}.

Measurements of the angular observables

Measurements of angular observables have been performed at Belle [578, 579], BaBar [580, 581] and CDF [582, 583] and more recently at CMS [584] and LHCb [564, 585]. The ATLAS collaboration presented a preliminary result from such an analysis [586] that has, however, not been published since 2013.

The latest analysis published by the Belle collaboration [579] was based on about 85% of their full data set collected at the $\Upsilon(4S)$ resonance. A total of 246 signal candidates were extracted and employed to measure the differential branching fraction, the forward-backward asymmetry, A_{FB}, and the longitudinal polarization fraction F_L in three bins of q^2 below the J/ψ resonance, one bin in between the J/ψ and $\psi(2s)$ resonances and two bins above the $\psi(2s)$ resonance. The latest measurement by the BaBar collaboration [581] was based on 64 signal candidates extracted from about 80% of their full data set collected at the $\Upsilon(4S)$ resonance. These were employed to measure A_{FB} and F_L in two wide bins of q^2, one below and one above the J/ψ resonance. Finally, the CDF collaboration published a measurement of A_{FB} and F_L as well as $A_T^{(2)}$ and A_T^{im}, based on 165 signal candidates extracted from a data set corresponding to an integrated luminosity of 6.8 fb^{-1}. The CDF measurement was performed in the same bins of q^2 that had been employed in the Belle analysis. In view of the limited statistics, the observables were extracted in all cases from single-differential decay rates in one

Table 6.8: Compilation of angular observables proposed for measurements in the decay $B^0 \to K^{*0}\mu^+\mu^-$ and their definitions in terms of transversity amplitudes and/or angular coefficients I_k or S_k. The differential branching fraction, $d\Gamma/dq^2$, the lepton forward-backward asymmetry, A_{FB}, and the K^{*0} polarization fractions F_L and $F_T = (1-F_L)$ exhibit sensitivity to hadronic form factors, while these cancel to first order in the remaining observables.

Observable	Amplitudes	I_k or S_k
$d\Gamma/dq^2$	$\lvert A_0^L\rvert^2 + \lvert A_0^R\rvert^2 + \lvert A_\parallel^L\rvert^2 + \lvert A_\parallel^R\rvert^2 + \lvert A_\perp^L\rvert^2 + \lvert A_\perp^R\rvert^2$	$\frac{1}{4}(3I_1^c + 6I_1^s - I_2^c - 2I_2^s)$
A_{FB}	$\frac{3}{2}\frac{\mathrm{Re}\,(A_\parallel^L A_\perp^{L*} - A_\parallel^R A_\perp^{R*})}{\lvert A_0^L\rvert^2+\lvert A_0^R\rvert^2+\lvert A_\parallel^L\rvert^2+\lvert A_\parallel^R\rvert^2+\lvert A_\perp^L\rvert^2+\lvert A_\perp^R\rvert^2}$	$-\frac{3}{2}\frac{2I_6^s+I_6^c}{3I_1^c+6I_1^s-I_2^c-2I_2^s}$
F_L	$\frac{\lvert A_0^L\rvert^2+\lvert A_0^R\rvert^2}{\lvert A_0^L\rvert^2+\lvert A_0^R\rvert^2+\lvert A_\parallel^L\rvert^2+\lvert A_\parallel^R\rvert^2+\lvert A_\perp^L\rvert^2+\lvert A_\perp^R\rvert^2}$	$\frac{I_2^c}{4I_2^s-I_2^c}$
F_T	$\frac{\lvert A_\parallel^L\rvert^2+\lvert A_\parallel^R\rvert^2+\lvert A_\perp^L\rvert^2+\lvert A_\perp^R\rvert^2}{\lvert A_0^L\rvert^2+\lvert A_0^R\rvert^2+\lvert A_\parallel^L\rvert^2+\lvert A_\parallel^R\rvert^2+\lvert A_\perp^L\rvert^2+\lvert A_\perp^R\rvert^2}$	$\frac{2(2I_2^s-I_2^c)}{4I_2^s-I_2^c}$
$A_T^{(2)}$ [571]	$\frac{\lvert A_\perp^L\rvert^2+\lvert A_\perp^R\rvert^2-\lvert A_\parallel^L\rvert^2+\lvert A_\parallel^R\rvert^2}{\lvert A_\perp^L\rvert^2+\lvert A_\perp^R\rvert^2+\lvert A_\parallel^L\rvert^2+\lvert A_\parallel^R\rvert^2}$	$\frac{I_3}{2I_2^s}$
$A_T^{(3)}$ [572]	$\frac{\lvert A_0^L A_\parallel^{L*} + A_0^{R*} A_\parallel^R\rvert}{\sqrt{(\lvert A_0^L\rvert^2+\lvert A_0^R\rvert^2)(\lvert A_\perp^L\rvert^2+\lvert A_\perp^R\rvert^2)}}$	$\sqrt{\frac{4(I_4)^2+(I_7)^2}{-2I_2^c(2I_2^s+I_3)}}$
$A_T^{(4)}$ [572]	$\frac{\lvert A_0^L A_\perp^{L*} - A_0^{R*} A_\perp^R\rvert}{\lvert A_0^{L*} A_\parallel^L + A_0^R A_\parallel^{R*}\rvert}$	$\sqrt{\frac{(I_5)^2+4(I_8)^2}{4(I_4)^2+(I_7)^2}}$
$A_T^{(\mathrm{im})}$ [573]	$\frac{2\,\mathrm{Im}\,(A_\parallel^L A_\perp^{L*} + A_\parallel^R A_\perp^{R*})}{\lvert A_\perp^L\rvert^2+\lvert A_\perp^R\rvert^2+\lvert A_\parallel^L\rvert^2+\lvert A_\parallel^R\rvert^2}$	$\frac{I_9}{2I_2^s}$
$A_T^{(\mathrm{re})}$ [573]	$\frac{2\,\mathrm{Re}\,(A_\parallel^L A_\perp^{L*} - A_\parallel^R A_\perp^{R*})}{\lvert A_\perp^L\rvert^2+\lvert A_\perp^R\rvert^2+\lvert A_\parallel^L\rvert^2+\lvert A_\parallel^R\rvert^2}$	$\frac{I_6^s}{4I_2^s}$
$H_T^{(1)}$ [574]	$\frac{\mathrm{Re}\,(A_0^L A_\parallel^{L*} + A_0^{R*} A_\parallel^R)}{\sqrt{(\lvert A_0^L\rvert^2+\lvert A_0^R\rvert^2)(\lvert A_\parallel^L\rvert^2+\lvert A_\parallel^R\rvert^2)}}$	$\frac{\sqrt{2}I_4}{\sqrt{-2I_2^c(2I_2^s-I_3)}}$
$H_T^{(2)}$ [574]	$\frac{\mathrm{Re}\,(A_0^L A_\perp^{L*} + A_0^{R*} A_\perp^R)}{\sqrt{(\lvert A_0^L\rvert^2+\lvert A_0^R\rvert^2)(\lvert A_\perp^L\rvert^2+\lvert A_\perp^R\rvert^2)}}$	$\frac{I_5}{\sqrt{-2I_2^c(2I_2^s+I_3)}}$
$H_T^{(3)}$ [574]	$\frac{\mathrm{Re}\,(A_\parallel^L A_\perp^{L*} + A_\parallel^{R*} A_\perp^R)}{\sqrt{(\lvert A_\parallel^L\rvert^2+\lvert A_\parallel^R\rvert^2)(\lvert A_\perp^L\rvert^2+\lvert A_\perp^R\rvert^2)}}$	$\frac{I_6}{2\sqrt{(2I_2^s)^2-I_3}}$
P_4' [575]		$\frac{S_4}{\sqrt{-S_2^c S_2^s}}$
P_5' [575]		$\frac{S_5}{2\sqrt{-S_2^c S_2^s}}$
P_6' [575]		$-\frac{S_7}{2\sqrt{-S_2^c S_2^s}}$
P_8' [575]		$-\frac{S_8}{2\sqrt{-S_2^c S_2^s}}$

of the helicity angles, i.e. by integrating over the other two decay angles. The single-differential cross sections are then

$$\begin{aligned}
\frac{d\Gamma}{d\cos\theta_K} &= \tfrac{3}{2}\,F_L\,\cos^2\theta_K \,+\, \tfrac{3}{4}\,(1-F_L)\,(1-\cos^2\theta_K) \\
\frac{d\Gamma}{d\cos\theta_\ell} &= \tfrac{3}{4}\,F_L\,(1-\cos^2\theta_\ell) \,+\, \tfrac{3}{8}\,(1-F_L)\,(1+\cos^2\theta_\ell) \,+\, A_{FB}\,\cos\theta_\ell \\
\frac{d\Gamma}{d\phi} &= \tfrac{1}{2\pi}\,\left[1 \,+\, \tfrac{1}{2}(1-F_L)\,A_T^{(2)}\,\cos(2\phi) \,+\, A_T^{\rm im}\,\sin(2\phi)\right] \,.
\end{aligned}$$

The CMS collaboration performed a measurement of $d\Gamma/dq^2$, F_L and A_{FB} based on their 2011 data set, corresponding to an integrated luminosity of 5.2 fb^{-1} [584]. The analysis was again performed in the same q^2 bins as used in the Belle analysis, except that a lower cut at $q^2 > 1$ GeV$^2/c^4$ was employed in the lowest q^2 bin. Distributions of the $K^\pm\pi^\mp\mu^+\mu^-$ invariant mass of selected candidates is shown in Figure 6.37. The angular observables were extracted from a three-dimensional fit to the measured invariant mass, $\cos\theta_K$ and $\cos\theta_\ell$ of the selected candidates, i.e. integrating over the angle ϕ. Summed over all q^2 bins, the fit assigned a total of about 415 candidates to the $B^0 \to K^{*0}\mu^+\mu^-$ signal component. The differential cross section was expressed as

$$\begin{aligned}
\frac{1}{\Gamma}\frac{d^3\Gamma\,(B^0\to K^{*0}\mu^+\mu^-)}{dq^2\,d\cos\theta_\ell\,d\cos\theta_K} &= \frac{9}{16}\,\times\Big\{\,\tfrac{2}{3}F_S \,+\, (\tfrac{4}{3}A_S\cos\theta_K)\,(1-\cos^2\theta_\ell)) \,+\, (1-F_S)\,\times\Big[\\
&\quad + 2F_L\,(1-\cos^2\theta_K)(1-\cos^2\theta_\ell)) \\
&\quad + \tfrac{1}{2}\,(1-F_L)\,(1-\cos^2\theta_K)\,(1+\cos^2\theta_\ell)) \\
&\quad \,+\, \tfrac{4}{3}\,A_{FB}\,(1-\cos^2\theta_K)\,\cos\theta_\ell\Big]\Big\} \,,
\end{aligned}$$

where the additional parameters F_S and A_S were introduced to describe the effect of a possible S-wave contribution from $K^+\pi^-$ pairs with relative angular momentum $L_{K\pi} = 0$, that were not produced via an intermediate K^{*0} resonance. The parameter F_S describes the fraction of this S-wave amplitude and the asymmetry A_S is caused by its interference with the longitudinallly polarized K^{*0} decay amplitude. The two parameters were found to be $F_S = 0.01 \pm 0.01$ and $A_S = -0.10 \pm 0.01$ in a fit to the control channel $B^0 \to J/\psi K^{*0}$ and were fixed to these values in the fits to the signal candidates. The results of the fits are shown in Figure 6.38 and were found to be in good agreement with Standard Model predictions, which were extracted from Ref. [587].

The most precise and comprehensive measurements of angular observables to date were presented in two publications by the LHCb collaboration. Both these publications were based on a sample of about 900 $B^0 \to K^{*0}\mu^+\mu^-$ and $\overline{B}^0 \to \overline{K}^{*0}\mu^+\mu^-$ candidates that were extracted from the 2011 data set, corresponding to an integrated luminosity of 1 fb^{-1}. The first publication [564] described a measurement of the differential branching fraction as well as the simultaneous determination of four angular observables from a fit to the differential decay rate as a function of all three helicity angles in bins of q^2. Again, the same six q^2 bins were employed as in the Belle analysis mentioned above. A transformation in the angle ϕ,

$$\phi \;\to\; \hat{\phi} \;=\; \begin{cases} \phi + \pi & \text{if } \phi < 0 \\ \phi & \text{otherwise} \end{cases}$$

was employed to effectively cancel all observables proportional to $\cos\phi$ or $\sin\phi$. From the expressions in Table 6.7 it can be seen that this eliminates the coefficients I_4, I_5, I_7 and I_8. The remaining four independent observables were chosen as F_L, A_{FB}, S_3 and A_9 and the

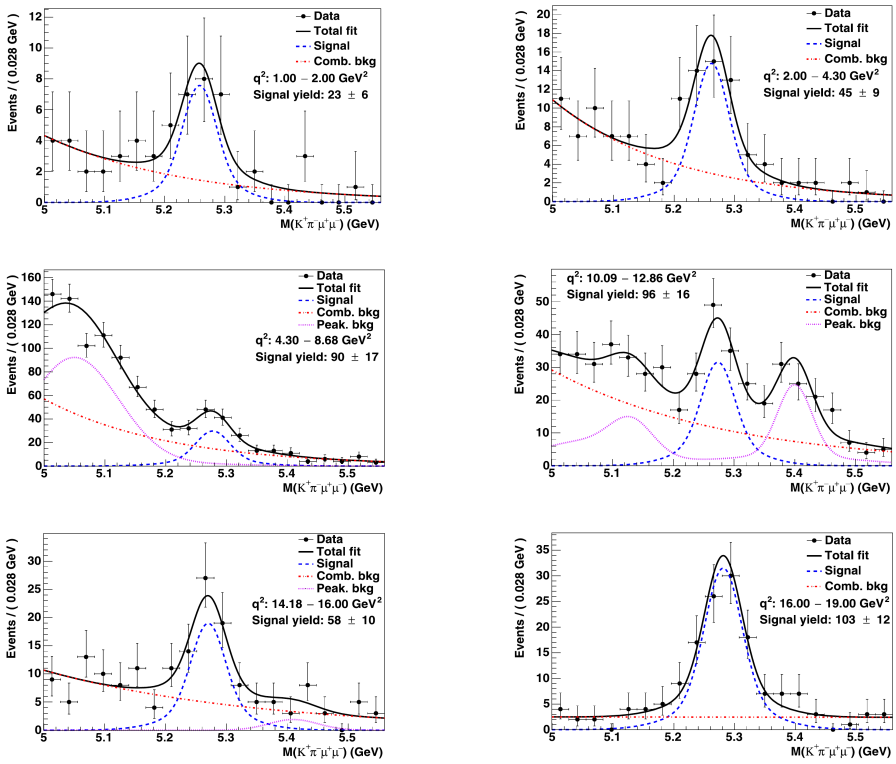

Figure 6.37: Measured distributions of the $K^{\pm}\pi^{\mp}\mu^+\mu^-$ invariant mass in six q^2 bins as obtained in the CMS analysis of angular observables in the decay $B^0 \to K^{*0}\mu^+\mu^-$. The q^2 ranges for each bin are indicated in the legend of each panel. The result of the fit to the data is superimposed as explained in the legends, where "Comb.bkg." refers to the component of combinatorial background from random combinations of final-state particles and "Peak.bkg." refers to backgrounds from $B^0 \to J/\psi K^{*0}$ and $B^0 \to \psi(2s)K^{*0}$ decays that fail to be removed by the veto on the dimuon invariant mass (from [584]).

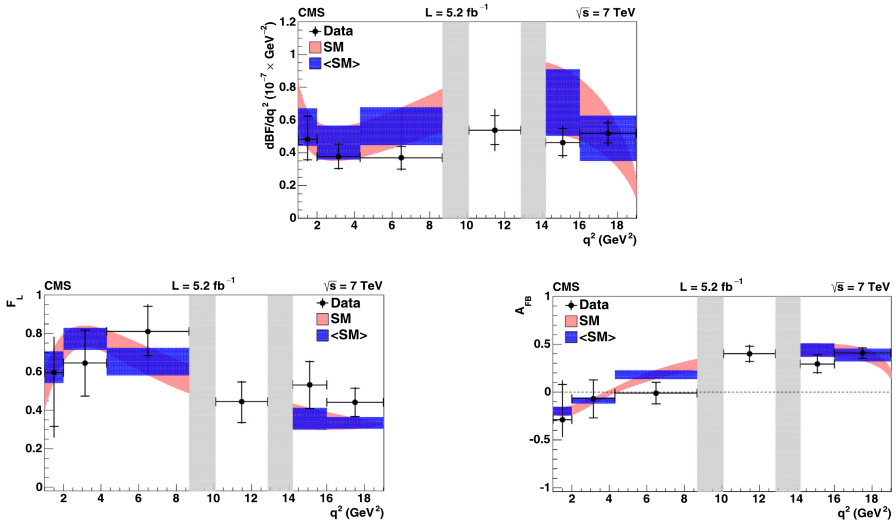

Figure 6.38: Results of the fit for (top) the differential branching fraction, $d\Gamma/dq^2$, (bottom left) the longitudinal polarization fraction, F_L, and (bottom right) the forward-backward asymmetry, A_{FB}, in six q^2 bins as obtained in the CMS analysis of angular observables in the decay $B^0 \to K^{*0}\mu^+\mu^-$. Standard Model predictions extracted from Ref. [587] are superimposed, where light shaded bands indicate the prediction with its uncertainty and dark blue rectangles show the same prediction averaged over the corresponding q^2 bin. The two gaps between the third, fourth and fifth q^2 bins correspond to the regions of the J/ψ and $\psi(2s)$ resonances that were excluded from the analysis. No attempt was made to calculate a Standard Model prediction for the bin in between the J/ψ and $\psi(2s)$ resonances (from [584]).

differential decay rate was expressed as

$$\begin{aligned}\frac{1}{d\Gamma/dq^2}\frac{d^4\Gamma\left(B^0\to K^{*0}\mu^+\mu^-\right)}{dq^2\,d\cos\theta_\ell\,d\cos\theta_K\,d\hat{\phi}} &= \frac{9}{16\pi}\times\Big\{F_L\,\cos^2\theta_K \\ &+\tfrac{3}{4}\left(1-F_L\right)\left(1-\cos^2\theta_K\right) \\ &-F_L\,\cos^2\theta_K\left(2\,\cos^2\theta_\ell\right)-1\big) \\ &+\tfrac{1}{4}\left(1-F_L\right)\left(1-\cos^2\theta_K\right)\left(2\,\cos^2\theta_\ell\right)-1\big) \\ &+S_3\left(1-\cos^2\theta_K\right)\left(1-\cos^2\theta_\ell\right)\,\cos\left(2\hat{\phi}\right) \\ &+\tfrac{34}{3}\,A_{FB}\left(1-\cos^2\theta_K\right)\,\cos\theta_\ell \\ &+\;A_9\left(1-\cos^2\theta_K\right)\left(1-\cos^2\theta_\ell\right)\,\sin\left(2\hat{\phi}\right)\Big\}\;.\end{aligned}$$

Two alternative fits were performed to the same data set. In one of these fits, the observables A_{FB} and S_3 were replaced by the theoretically clean observables $A_T^{(\mathrm{re})}$, $A_T^{(2)}$ using the relations

$$\begin{aligned}A_{FB} &= \tfrac{3}{4}\left(1-F_L\right)A_T^{(\mathrm{re})} \\ S_3 &= \tfrac{1}{2}\left(1-F_L\right)A_T^{(2)}\;,\end{aligned}$$

and in the third fit, the sign convention for the angle $\hat{\phi}$ was reversed in order to measure the *CP* averaged observable S_9 instead of the asymmetry A_9. Due to a small value of the strong phase between the two transverse decay amplitudes $A_\perp$ and $A_\parallel$, the value of S_9 is expected to be close to zero over the full range of q^2 in the Standard Model and most of its extentions. The measurement of S_9 can therefore serve as a cross check of the measurement technique.

Signal candidates were selected at the trigger level by requiring first at least one muon candidate with transverse momentum above a certain threshold, then a reconstructed track with transverse momentum above another threshold and significant impact parameter with respect to the reconstructed *pp* interaction vertex and finally two tracks that formed a displaced vertex. The offline selection was based on particle identification requirements for the muon, kaon and pion candidates and their impact parameters with respect to the *pp* interaction vertex, the invariant mass of the kaon/pion pair and that of the B^0 candidate, the fit quality of the B^0 decay vertex and its displacement from the *pp* interaction vertex, and the impact parameter of the B^0 candidate with respect to the *pp* interaction vertex and the angle between the B momentum vector and the line connecting the *pp* interaction vertex and the decay vertex of the B^0 candidate. Several of these variables were combined in multivariate classifier. This multivariate classifier was trained on collision data employing a large sample of $B^0\to J/\psi K^{*0}$ candidates as a proxy for signal and candidates from the upper sideband of the $K^+\pi^-\mu^+\mu^-$ invariant-mass distribution as a proxy for background. Care was taken in the selection of the discriminating variables to minimize possible biases on the q^2 distribution and angular distributions of the selected candidates. For example, no requirements were made in the offline selection on the transverse momenta of the muon candidates as such requirements would lead to strong biases on the distribution in $\cos\theta_\ell$ at low values of q^2.

The two-dimensional distribution of the invariant mass of the B^0 candidate versus the dimuon invariant mass for the selected candidates is shown in Figure 6.40, indicating the regions in dimuon invariant mass that were vetoed to reject the large background from $B^0\to J/\psi K^{*0}$ decays. Appropriate invariant-mass vetoes were also applied to reject possible peaking backgrounds from $B^0\to J/\psi K^{*0}$ decays in which the kaon or pion were misidentified and swapped with one of the final-state muons, from decays $B_s^0\to\phi\mu^+\mu^-$ with $\phi\to K^+K^-$ or $\Lambda_b\to\Lambda^*(1520)\mu^+\mu^-$ with $\Lambda^*(1520)\to pK^-$ in which a kaon or the proton were misidentified as a pion, and finally

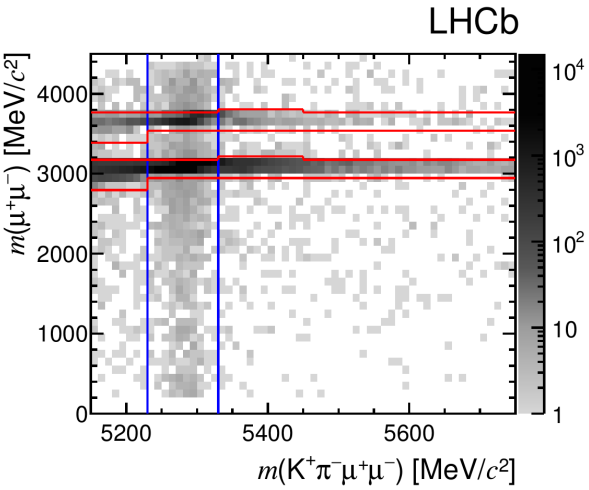

Figure 6.39: Distribution of the invariant mass of the dimuon pair versus the the $K^\pm\pi^\mp\mu^+\mu^-$ invariant mass, from the LHCb analysis of angular observables in the decay $B^0 \to K^{*0}\mu^+\mu^-$. Horizontal lines indicate the dimuon mass bands that were vetoed to remove the background from $B^0 \to J/\psi K^{*0}$ and $B^0 \to \psi(2s)K^{*0}$ decays, while vertical lines indicate the signal window around the nominal B^0 mass (from [564]).

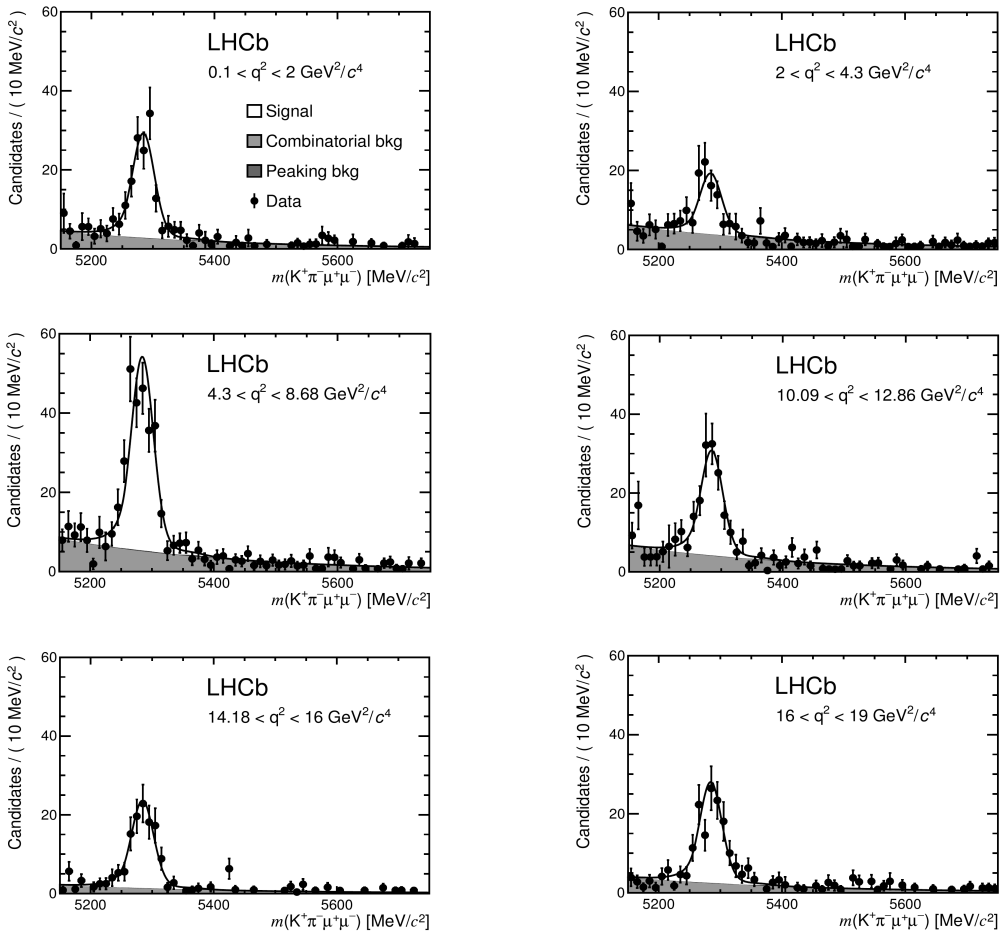

Figure 6.40: Measured distributions of the $K^\pm\pi^\mp\mu^+\mu^-$ invariant mass in six q^2 bins as obtained in the LHCb analysis of angular observables in the decay $B^0 \to K^{*0}\mu^+\mu^-$. The q^2 ranges for each bin are indicated in the legend of each panel. The result of the fit to the data is superimposed, where grey shaded areas indicate the component assigned to combinatorial background. Peaking backgrounds are negligible after the dimuon invariant-mass vetoes described in the main text. Candidates were weighted with the inverse of the assigned efficiency as described in the text (from [564]).

from combinations of a true decay $B^+ \to K^+\mu^+\mu^-$ with a random kaon from the decay of the other b hadron in the event. The effects of detector acceptance and selection efficiencies as a function of $\cos\theta_\ell$, $\cos\theta_K$ and ϕ were estimated in fine bins of q^2 using large samples of simulated events. These effects were corrected for in the analysis by weighting each selected candidate with the inverse of the efficiency $\epsilon(\cos\theta_\ell, \cos\theta_K, \phi) \equiv \epsilon(\cos\theta_\ell) \times \epsilon(\cos\theta_K) \times \epsilon(\phi)$, i.e. it was assumed that the efficiencies in the three angular variables factorize. The validity of this assumption was verified in the sample of simulated events. The differential branching fraction $d\Gamma/dq^2$ was determined by fits to the invariant-mass distribution of the B^0 candidates in each of the q^2 bins. The signal component was modelled in these fits by the sum of two modified Gaussian distributions with power-law tails to model radiative tails. The parameters of this function were determined from collision data employing the large signal of $B^0 \to J/\psi K^{*0}$ candidates. In addition to the signal component, the fit function contained contributions for combinatorial background and for peaking backgrounds from $B_s^0 \to K^{*0}\mu^+\mu^-$ decays and from misidentified $B_s^0 \to \phi\mu^+\mu^-$ and $B^0 \to J/\psi K^{*0}$ decays that ecaped the invariant-mass vetoes described above. The combinatorial background component was described by an exponential function, the $B_s^0 \to K^{*0}\mu^+\mu^-$ component by the same functional form as the signal component, and the other two peaking backgrounds with empirical shapes derived from samples of simulated events. To reduce systematic uncertainties, the differential branching fraction was measured relative to that of the decay $B_s^0 \to J/\psi K^{*0}$ as

$$\begin{aligned}\frac{d\,\mathrm{BF}\,(B^0 \to K^{*0}\mu^+\mu^-)}{dq^2} \;\equiv\; & \frac{1}{\Delta q^2}\,\frac{N_{B^0\to K^{*0}\mu^+\mu^-}}{N_{B^0\to J/\psi K^{*0}}}\,\frac{\epsilon_{B^0\to J/\psi K^{*0}}}{\epsilon_{B^0\to K^{*0}\mu^+\mu^-}} \times \\ & \times\, \mathrm{BF}\,(B^0 \to J/\psi K^{*0}) \;\times\; \mathrm{BF}\,(J/\psi \to \mu^+\mu^-)\end{aligned}$$

The angular observables were determined by a simultaneous fit to the invariant mass of the B^0 candidates and the three decay angles. The angular distribution for the background component was modelled in this fit by a product of three second-order Chebychev polynomials. The underlying assumption that the angular distribution of the background can be factorized into three individual components was validated on collision data employing candidates from the upper sideband of the $K^+\pi^-\mu^+\mu^-$ invariant-mass distribution. The results of the fit to the data are shown in Figure 6.41 together with Standard-Model predictions extracted from Ref. [588]. Good agreement was found in all observables. The measured values in the lowest q^2 bin, corresponding to $0 < q^2 < 2\ \mathrm{GeV}^2/c^2$, were corrected for the effect of the finite mass of the muon, which had hitherto been neglected and causes a correction factor

$$\frac{1 - 4m_\mu^2/q^2}{1 + 2m_\mu^2/q^2} \quad \text{or} \quad \frac{\sqrt{1 - 4m_\mu^2/q^2}}{1 + 2m_\mu^2/q^2}$$

on the angular coefficients I_k. The effect of a possible S-wave contribution from $K^+\pi^-$ pairs with relative angular momentum $L_{K\pi} = 0$ was tested by including the additional term

$$\frac{2}{3}\,F_S\,(1 - \cos^2\theta_\ell) \;+\; \frac{4}{3}\,A_S\,\cos\theta_K\,(1 - \cos^2\theta_\ell)$$

in the fit to the data. The S-wave fraction F_S was determined from this fit to be smaller than 7% at a confidence level of 68% and was not further considered in the nominal fit. A systematic uncertainty was assigned to the final results to take this approximation into account. Additional systematic uncertainties were assigned to cover possible biases due to the modelling of the angular efficiency. Other sources of systematic uncertainties, such as production and detection asymmetries were studied but found to have a negligible effect. Finally, the angular fit was also applied to the $B^0 \to J/\psi K^{*0}$ control sample and the results were found to be in good agreement with expectations.

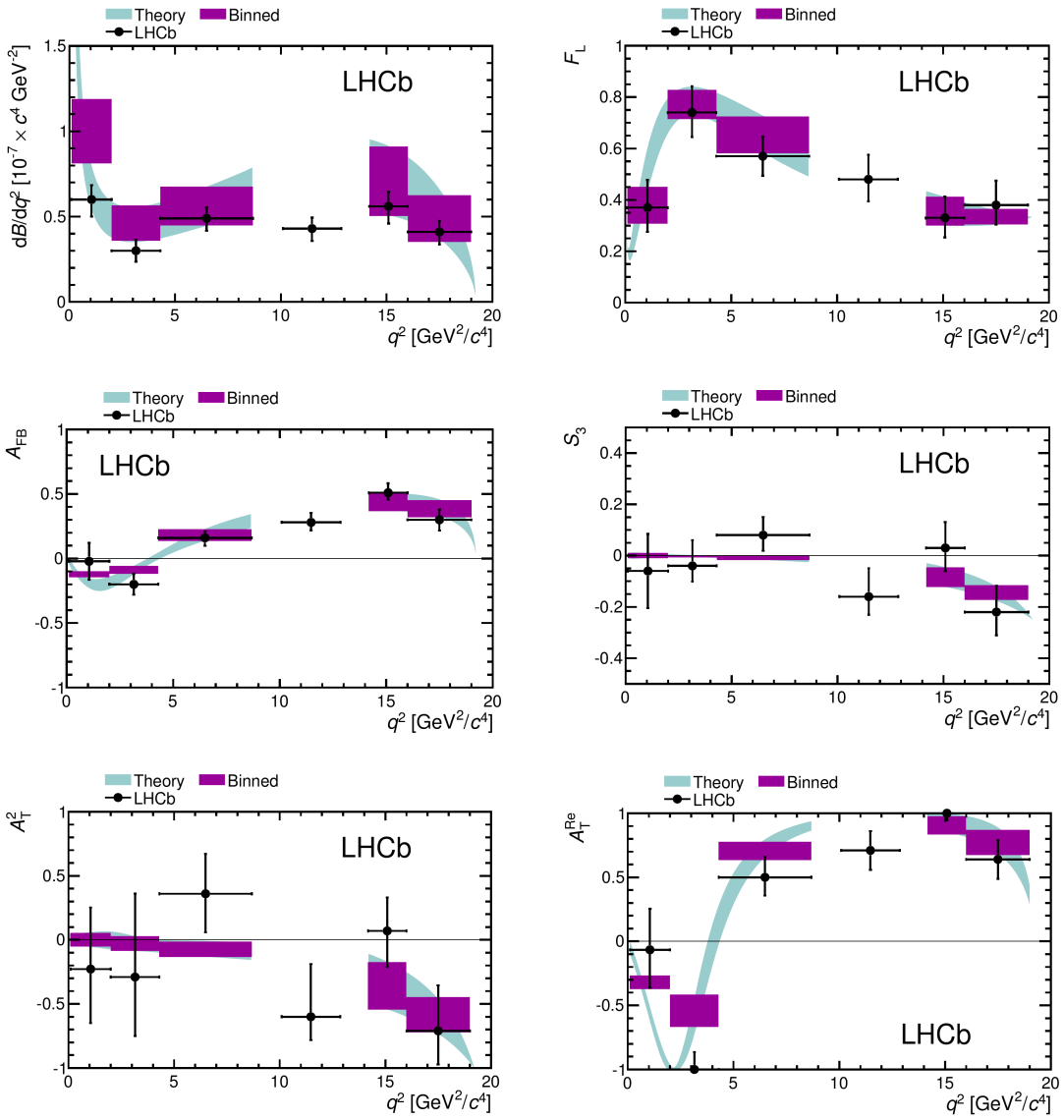

Figure 6.41: Measurements of (top left) $d\Gamma/dq^2$, (top right) F_L, (middle left) A_{FB}, (middle right) S_3, (bottom left) $A_T^{(2)}$ and (bottom right) $A_T^{\rm re}$ in six bins of the squared momentum transfer, q^2, as obtained in the LHCb measurement of angular observables in the decay $B^0 \to K^{*0}\mu^+\mu^-$ and $\overline{B}^0 \to \overline{K}^{*0}\mu^+\mu^-$. Standard Model predictions are superimposed, where light shaded bands indicate the prediction with its uncertainty and dark purple rectangles show the same prediction averaged over the corresponding q^2 bin. The two gaps between the third, fourth and fifth q^2 bins correspond to the regions of the J/ψ and $\psi(2s)$ resonances that were excluded from the analysis. No attempt was made to calculate a Standard Model prediction for the bin in between the J/ψ and $\psi(2s)$ resonances. The results for the asymmetry A_9 were found to be compatible with the expectation of vanishing asymmetry in all q^2 bins and are not shown here (from [564]).

The final result of this analysis was a measurement of the zero-crossing point, q_0^2, of the foward-backward asymmetry $A_{FB}(q^2)$. As mentioned above, uncertainties due to hadronic form-factors largely cancel in the calculation of this zero-crossing point and its position can therefore be predicted with good precision. Different calculations [589–591] lead to predictions between 4 and 4.3 GeV^2/c^4, with quoted uncertainties between 5 and 10%. The LHCb measurement was performed by fitting third-order polynomials to the measured q^2 distributions for candidates with $\cos\theta_\ell > 0$ and separately for candidates with $\cos\theta_\ell < 0$. The position of the zero-crossing point was then estimated by calculating the difference of the two polynomials and dividing it by their sum. The result of the measurement,

$$q_0^2 \;=\; (\,4.9 \,\pm\, 0.9\,)\ \mathrm{GeV}^2/c^4 \ ,$$

agrees with the Standard Model prediction within its uncertainty.

In the second publication based on the 2011 data set [585], the LHCb collaboration presented a first measurement of the form-factor independent observables P_4', P_5', P_6' and P_8'. The analysis was based on the same selection of signal candidates and used the same binning in q^2 as that described in the previous paragraphs. Moreover, correction for the effects of angular acceptance and selection efficiencies and the treatment of background components in the fit were also implemented in the same manner. The angular distribution was describedd in terms of the new observables as

$$\begin{aligned}
\frac{1}{d\Gamma/dq^2}\frac{d^4\Gamma\,(B^0\to K^{*0}\mu^+\mu^-)}{dq^2\,d\cos\theta_\ell\,d\cos\theta_K\,d\hat{\phi}} \;=\; & \frac{9}{32\pi}\times\Big\{\tfrac{3}{4}\,(1-F_L)\,\sin^2\theta_K \,+\, F_L\,\cos^2\theta_K \\
& +\tfrac{1}{4}\,(1-F_L)\,\sin^2\theta_K\,\cos\left(2\theta_\ell\right) \,-\, F_L\cos^2\theta_K\,\cos\left(2\theta_\ell\right) \\
& +\tfrac{1}{2}\,(1-F_L)\,A_T^{(2)}\,\sin^2\theta_K\,\sin^2\theta_\ell\,\cos\left(2\phi\right) \\
& +\sqrt{F_L(1-F_L)}\,P_4'\,\sin\left(2\theta_K\right)\,\sin\left(2\theta_\ell\right)\,\cos\phi \\
& +\sqrt{F_L(1-F_L)}\,P_5'\,\sin\left(2\theta_K\right)\,\sin\theta_\ell\,\cos\phi \\
& +(1-F_L)\,A_T^{\mathrm{re}}\,\sin^2\theta_K\,\cos\theta_\ell \\
& +\sqrt{F_L(1-F_L)}\,P_6'\,\sin\left(2\theta_K\right)\,\sin\theta_\ell\,\sin\phi \\
& +\sqrt{F_L\,(1-F_L)}\,P_8'\,\sin\left(2\theta_K\right)\,\sin\left(2\theta_\ell\right)\,\sin\phi \\
& \,+\, A_9\,\sin^2\theta_K\,\sin^2\theta_\ell\sin\left(2\phi\right)\Big\}
\end{aligned}$$

and the sets of angular transformations listed in Table 6.9 were applied to reduce the number of parameters in the fits for each of the new observables. A careful inspection of the expression above will show that each of these sets of transformations preserves the first five terms on the right-hand side of the equation plus the term sensitive to the observable P_k' in question, while it cancels all other terms. The remaining expressions therefore depend only on F_L, $A_T^{(2)}$ and the observable P_k'. Each of the P_k' was determined from an independent fit to the invariant mass distribtution and the angular distributions in terms of the appropriate set of transformed angles. The values of F_L and $A_T^{(2)}$ were treated as free parameters in the fit and the fitted values agreed in all cases with those found in the earlier analysis. The results of the fits for P_4' and P_5' are shown in Figure 6.42. The results for P_6' and P_8' were found to be close to zero in all q^2 bins as expected due to the small value of the strong phase difference between the relevant decay amplitudes. All results as well as a detailed description of the analysis and the treatment of systematic uncertainties can be found in Ref. [592]. In general the results were found to be in good agreement with Standard Model predictions, with the exception of the fit for the observable P_5' in the bin $4.30 < q^2 < 8.68\ \mathrm{GeV}^2/c^4$, which yielded a result

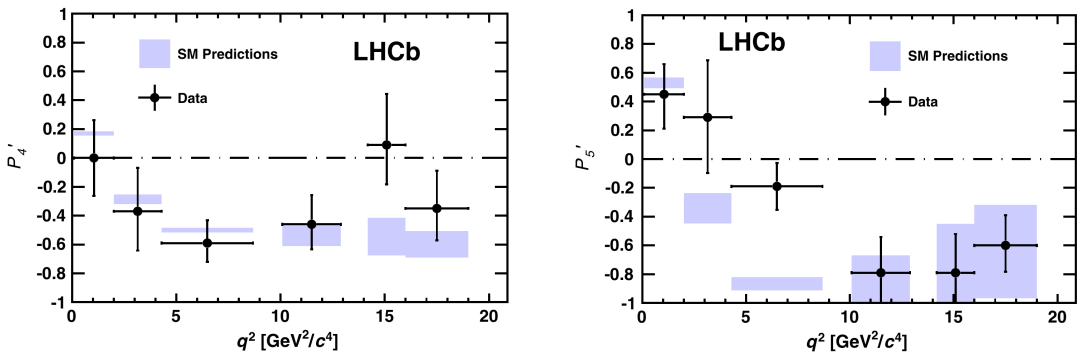

Figure 6.42: Measurements of the angular observables (left) P_4' and (right) P_5' in six bins of the squared momentum transfer, q^2, as obtained in the LHCb measurement of these angular observables in the decay $B^0 \to K^{*0}\mu^+\mu^-$ and $\overline{B}^0 \to \overline{K}^{*0}\mu^+\mu^-$. Standard Model predictions are indicated by the shaded rectangles. A significant deviation between measurement and predction is apparent in the third q^2 bin for the observable P_5' (from [585]).

that deviated significantly from expectations. Comparing in particular to the prediction from Ref. [577], the discrepancy in this bin was estimated to correspond to 3.7 Gaussian standard deviations. This result has triggered some interest in the theory community, where it has become known as "the $B \to K^*\mu^+\mu^-$ anomaly". For example, it has been shown in Ref. [593] that a modification of the Wilson coefficient C_9 with respect to its Standard Model value can reduce this discrepancy and lead at the same time to a better agreement between prediction and measurement also in other observables. It has been shown that the discrepancy could be explained by the existence of a hypothetical Z' boson [594, 595]. On the other hand, it has also been argued that uncertainties related to non-factorizable QCD power corrections, could be larger [596] than estimated in Ref. [593] or that the effect could be due to previously not considered charm-loop effects [597]. In Ref. [598], a number of proposals have been made for measurements of complementary observables that could shed more light on the issue. While these discussions are ongoing, an LHCb measurement of the angular observables in the decay $B^0 \to K^{*0}\mu^+\mu^-$ is at the moment still pending[1].

[1]Preliminary results from the analysis of the full run I data set have been presented [599] at the 2015 Moriond conference in La Thuile. They confirm the results of the published analysis and the discrepancy with current Standard Model predictions in the observable P_5'.

Table 6.9: Sets of angular transformations that were applied in the fits for the LHCb analysis of angular observables in the decay $B^0 \to K^{*0}\mu^+\mu^-$ to fit for each of the observables P_4', P_5', P_6' and P_8'.

P_4'		P_5'	
$\phi \to -\phi$	for $\phi < 0$	$\phi \to -\phi$	for $\phi < 0$
$\phi \to \pi - \phi$	for $\theta_\ell > \pi/2$	$\theta_\ell \to \pi - \theta_\ell$	for $\theta_\ell > \pi/2$
$\theta_\ell \to \pi - \theta_\ell$	for $\theta_\ell > \pi/2$		
P_6'		**P_8'**	
$\phi \to \pi - \phi$	for $\phi > \pi/2$	$\phi \to \pi - \phi$	for $\phi > \pi/2$
$\phi \to -\pi - \phi$	for $\theta_\ell < -\pi/2$	$\phi \to -\pi - \phi$	for $\theta_\ell < -\pi/2$
$\theta_\ell \to \pi - \theta_\ell$	for $\theta_\ell > \pi/2$	$\theta_K \to \pi - \theta_K$	for $\theta_\ell > \pi/2$
		$\theta_\ell \to \pi - \theta_\ell$	for $\theta_\ell > \pi/2$

Chapter 7

Epilogue: Preparing for the Next Challenge

> It is pertinent to remember that the great steps are always made by those who don't work on the most fashionable subject.
>
> — Alvaro de Rújula as quoted in: Gary Taubes, Nobel Dreams, Random House Inc, New York, 1986.

As shown in the previous two Chapters, we have witnessed over the last abou fifteen years an immense progress in the understanding of heavy quark flavour physics, thanks to the great success of the two B factories, important contributions from the two Tevatron experiments and, more recently, the impressive results coming out of the first two years of LHCb data taking. Tensions have been Despite a few tensions and discrepancies, which will require further studies, the overall picture that emerges from these measurements is that the Standard Model in general and the Cabibbo-Kobayashi-Maskawa model of flavour-changing quark interactions in particular stand tall. The overconstraint determination of the parameters that describe the CKM Unitarity Triangle results in a consistent picture and has established the CKM mechanism as the dominant source of CP violation in the quark sector. The current precision of these measurements constrains possible contributions from physics beyond the Standard Model to the level of 10-20%. Measurements of CP violating observables in $B_s^0 - \overline{B}_s^0$ mixing and of observables in rare decays of B^0 and B_s^0 mesons are in general in good agreement with Standard Model predictions and put severe constraints on the parameter space of proposed extentions to the Standard Model.

The main goal for the LHCb experiment and for future experiments studying flavour-changing interactions of heavy-quarks will be to improve on the precision of the existing measurements and thereby extend the sensitivity to possible sub-dominant contributions from physics beyond the Standard Model. Obvious topics that come to mind today include

- in consistency checks of the Unitarity Triangle parameters, to further improve the precision in measurements of the angle γ (Section 5.5) and to resolve inconsistencies regarding the length of the side R_u (Section 5.2);
- in measurements of CP violating observables in the $B_s^0\overline{B}_s^0$ system, to resolve the question of the D0 claim for an anomalous same-sign dimuon charge asymmetry Section 6.2;
- in measurements of observables in rare decays of b hadrons, to measure the branching fraction of the rare decay $B^0 \to \mu^+\mu^-$ and to investigate the perceived "$B^0 \to K^{*0}\mu^+\mu^-$ anomaly";

but the field is large and who knows what tomorrow's "fashionable" observable is going to be.

The precision of most measurements has so far been limited by statistical uncertainties and leading systematic uncertainties are often limited by the size of the available data samples in control channels. Therefore, significant improvements can be expected from the analysis of larger data samples. However, with the exception of the semileptonic asymmetry $a^s_{\rm sl}$ and angular observables in the decay $B^0 \to K^{*0}\mu^+\mu^-$ where LHCb measurements using the full run I data set are still pending[1], no significant new input from experiments should be expected for a couple of years. The two B factories as well as the Tevatron have been terminated and most analyses of key observables published by the BaBar, Belle, CDF and D0 collaborations have already been based on the complete or almost complete collected data samples. The LHC has been shut down for maintenance and consolidation work of more than two years now. The restart of the LHC is imminent in spring 2015, but it is going to take the LHCb collaboration a few years to collect and digest a data set that will correspond to a significant increase of the already analaysed data.

In the longer term, the prospect for improved measurements looks promising. The LHCb collaboration expects to collect an integrated luminosity of 5 fb^{-1} during the three years of LHC operation foreseen from 2015 till 2018. Taking into account the expected increase in the $b\bar{b}$ production cross section due to the higher LHC collision energy and envisaged improvements in the operation of the software trigger [600], this should allow to treble the available data samples for key observables. In parallel, the LHCb collaboration works on a comprehensive upgrade of the detector that would permit to operate at a five times higher instantaneous luminosity, and with significantly increased trigger efficiencies for crucial decay modes to fully hadronic final states. The stated goal of the LHCb upgrade effort is to accumulate an integrated luminosity of 50 fb^{-1} over a data taking period of 10 years. The physics case of the LHCb upgrade has been explored in Ref. [601]. Expected statistical uncertainties on key observables are reproduced here in Table 7.1. Technical aspects of the upgrade are described in a series of Technical Design Reports [602–606].

At the same time, a next generation B factory, Belle II, aiming for a 40 times higher instantaneous luminosity than that achieved at KEKB, is under construction at KEK. The planning foresees to start commissioning in 2015 and to collect integrated luminosities of 10 ab^{-1} by 2019 and 50 ab^{-1} by 2023. For comparison, the data sample collected by the Belle experiment corresponds to 1 ab^{-1}. The Belle upgrade project is described in detail in Ref. [607] and its physics potential has been explored in Ref. [608]. A summary of the expected sensitivities to various observables is reproduced here in Table 7.2.

The physics programmes for Belle II and the LHCb upgrade continue to build on the respective strengths of the two approaches, where the main advantage for LHCb lies in the access to observables in all b hadron systems, while the cleaner environment in e^+e^- collisions will give Belle II access to final states with photons and missing particles and the potential to perform inclusive measurements.

A word of caution before the final conclusion. In view of the high level of statistical accuracy that Belle II and the LHCb upgrade aim for, the careful study and understanding of systematic effects will become a more and more important issue. While the statistical treatment of the data has seen significant improvements over the last years, with dedicated workshops being organized on the topic, the approach to systematic uncertainties seems less well under control. A concerted effort to establish guidelines and quality standards might be desirable.

And, of course, it will be interesting to see how well the currently stated precision of theory predictions will prevail when challenged by more and more precise measurements. But, it is precisely this interaction between theory and experiment that defines the beauty of this field. If more and more precise measurements lead to significant and robust deviations from Standard

[1]Preliminary results of an angular analysis of the decay $B^0 \to K^{*0}\mu^+\mu^-$ employing the full run I data set have been presented at the Moriond 2015 conference. They are compatible with the results of the published analysis and confirm a tension with Standard Model predictions.

Model predictions, they give us a glimpse of physics beyond the Standard Model. The pattern of the observed deviations might even allow to put constraints on the dynamics of the New Physics at work. If no significant deviations are found, precise measurements by challenging theory predictions will contribute to a better understanding of the more subtle aspects of the dynamics at work within the Standard Model.

Enough to do, then. Let's get back to work.

Table 7.1: Expected statistical sensitivities of LHCb measurements in key observables, from the analysis of the full run I data set corresponding to an integrated luminosity of 3 fb^{-1}, at the end of LHC run II in 2018, assuming an additional 5 fb^{-1} will be collected, and for an integrated luminosity of 50 fb^{-1} collected with an upgraded detector and trigger. Note that these estimates do not include systematic uncertainties, which will not be negligible in all cases (from [609]).

Type	Observable	LHC Run 1	LHCb 2018	**LHCb upgrade**	Theory
B_s^0 mixing	$\phi_s(B_s^0 \to J/\psi\,\phi)$ (rad)	0.05	0.025	**0.009**	~ 0.003
	$\phi_s(B_s^0 \to J/\psi\ f_0(980))$ (rad)	0.09	0.05	**0.016**	~ 0.01
	$A_{\rm sl}(B_s^0)$ (10^{-3})	2.8	1.4	**0.5**	0.03
Gluonic	$\phi_s^{\rm eff}(B_s^0 \to \phi\phi)$ (rad)	0.18	0.12	**0.026**	0.02
penguin	$\phi_s^{\rm eff}(B_s^0 \to K^{*0}\bar{K}^{*0})$ (rad)	0.19	0.13	**0.029**	< 0.02
	$2\beta^{\rm eff}(B^0 \to \phi K_S^0)$ (rad)	0.30	0.20	**0.04**	0.02
Right-handed	$\phi_s^{\rm eff}(B_s^0 \to \phi\gamma)$	0.20	0.13	**0.030**	< 0.01
currents	$\tau^{\rm eff}(B_s^0 \to \phi\gamma)/\tau_{B_s^0}$	5%	3.2%	**0.8%**	0.2 %
Electroweak	$S_3(B^0 \to K^{*0}\mu^+\mu^-; 1 < q^2 < 6\,{\rm GeV}^2/c^4)$	0.04	0.020	**0.007**	0.02
penguin	$q_0^2\,A_{\rm FB}(B^0 \to K^{*0}\mu^+\mu^-)$	10%	5%	**1.9%**	$\sim 7\%$
	$A_{\rm I}(K\mu^+\mu^-; 1 < q^2 < 6\,{\rm GeV}^2/c^4)$	0.14	0.07	**0.024**	~ 0.02
	$\mathcal{B}(B^+ \to \pi^+\mu^+\mu^-)/\mathcal{B}(B^+ \to K^+\mu^+\mu^-)$	14%	7%	**2.4%**	$\sim 10\%$
Higgs	$\mathcal{B}(B_s^0 \to \mu^+\mu^-)$ (10^{-9})	1.0	0.5	**0.19**	0.3
penguin	$\mathcal{B}(B^0 \to \mu^+\mu^-)/\mathcal{B}(B_s^0 \to \mu^+\mu^-)$	220%	110%	**40%**	$\sim 5\,\%$
Unitarity	$\gamma(B \to D^{(*)}K^{(*)})$	7°	4°	**1.1°**	negligible
triangle	$\gamma(B_s^0 \to D_s^\mp K^\pm)$	17°	11°	**2.4°**	negligible
angles	$\beta(B^0 \to J/\psi\,K_S^0)$	1.7°	0.8°	**0.31°**	negligible
Charm	$A_\Gamma(D^0 \to K^+K^-)$ (10^{-4})	3.4	2.2	**0.5**	–
CP violation	ΔA_{CP} (10^{-3})	0.8	0.5	**0.12**	–

Table 7.2: Comparison of current precision of Belle measurements and expected sensitivities for Belle II (reproduced from [607]).

Observable	Belle 2006 ($\sim$0.5 ab^{-1})	Belle II/SuperKEKB (5 ab^{-1})	(50 ab^{-1})
Hadronic $b \to s$ transitions			
$\Delta\mathcal{S}_{\phi K^0}$	0.22	0.073	0.029
$\Delta\mathcal{S}_{\eta' K^0}$	0.11	0.038	0.020
$\Delta\mathcal{S}_{K^0_S K^0_S K^0_S}$	0.33	0.105	0.037
$\Delta\mathcal{A}_{\pi^0 K^0_S}$	0.15	0.072	0.042
$\mathcal{A}_{\phi\phi K+}$	0.17	0.05	0.014
$\phi_1^{eff}(\phi K_S)$ Dalitz		3.3°	1.5°
Radiative/electroweak $b \to s$ transitions			
$\mathcal{S}_{K^0_S\pi^0\gamma}$	0.32	0.10	0.03
$\mathcal{B}(B \to X_s\gamma)$	13%	7%	6%
$A_{CP}(B \to X_s\gamma)$	0.058	0.01	0.005
C_9 from $A_{FB}(B \to K^*\ell^+\ell^-)$	-	11%	4%
C_{10} from $A_{FB}(B \to K^*\ell^+\ell^-)$	-	13%	4%
C_7/C_9 from $A_{FB}(B \to K^*\ell^+\ell^-)$	-		5%
R_K		0.07	0.02
$\mathcal{B}(B^+ \to K^+\nu\nu)$	†† $< 3\,\mathcal{B}_{\rm SM}$		30%
$\mathcal{B}(B^0 \to K^{*0}\nu\bar{\nu})$	†† $< 40\,\mathcal{B}_{\rm SM}$		35%
Radiative/electroweak $b \to d$ transitions			
$\mathcal{S}_{\rho\gamma}$	-	0.3	0.15
$\mathcal{B}(B \to X_d\gamma)$	-	24% (syst.)	
Leptonic/semileptonic B decays			
$\mathcal{B}(B^+ \to \tau^+\nu)$	3.5σ	10%	3%
$\mathcal{B}(B^+ \to \mu^+\nu)$	†† $< 2.4\mathcal{B}_{\rm SM}$	4.3 ab^{-1} for 5σ discovery	
$\mathcal{B}(B^+ \to D\tau\nu)$	-	8%	3%
$\mathcal{B}(B^0 \to D\tau\nu)$	-	30%	10%
LFV in τ decays (U.L. at 90% C.L.)			
$\mathcal{B}(\tau \to \mu\gamma)$ [10^{-9}]	45	10	5
$\mathcal{B}(\tau \to \mu\eta)$ [10^{-9}]	65	5	2
$\mathcal{B}(\tau \to \mu\mu\mu)$ [10^{-9}]	21	3	1
Unitarity triangle parameters			
$\sin 2\phi_1$	0.026	0.016	0.012
ϕ_2 ($\pi\pi$)	11°	10°	3°
ϕ_2 ($\rho\pi$)	$68° < \phi_2 < 95°$	3°	1.5°
ϕ_2 ($\rho\rho$)	$62° < \phi_2 < 107°$	3°	1.5°
ϕ_2 (combined)		2°	$\lesssim 1°$
ϕ_3 ($D^{(*)}K^{(*)}$) (Dalitz mod. ind.)	20°	7°	2°
ϕ_3 ($DK^{(*)}$) (ADS+GLW)	-	16°	5°
ϕ_3 ($D^{(*)}\pi$)	-	18°	6°
ϕ_3 (combined)		6°	1.5°
$\lvert V_{ub}\rvert$ (inclusive)	6%	5%	3%
$\lvert V_{ub}\rvert$ (exclusive)	15%	12% (LQCD)	5% (LQCD)
$\bar{\rho}$	20.0%		3.4%
$\bar{\eta}$	15.7%		1.7%
Charm physics			
D mixing parameters			
x	0.25%	0.12%	0.09%
y	0.16%	0.10%	0.05%
$\delta_{K\pi}$	10°	6°	4°
$\lvert q/p\rvert$	0.16	0.1	0.05
ϕ	0.13 rad	0.08 rad	0.05 rad
A_D	2.4%	1%	0.3%
New particles[N]			
$\gamma\gamma \to Z(3930) \to D\bar{D}^*$		$> 3\sigma$	
$B \to KX(3872)(\to D^0\bar{D}^{*0})$		400 events	
$B \to KX(3872)(\to J/\psi\pi^+\pi^-)$		1250 events	
$B \to KZ^+(4430)(\to \psi'\pi^+)$		1000 events	
$e^+e^- \to \gamma_{\rm ISR}Y(4260)(\to J/\psi\pi^+\pi^-)$		3000 events	
Electroweak parameters		($\sim$10 ab^{-1})	
$\sin^2\Theta_W$	-	3×10^{-4}	

Bibliography

[1] Particle Data Group, K. Olive *et al.*, *Review of Particle Physics*, Chin. Phys. **C38** (2014) 090001.

[2] Heavy Flavor Averaging Group (HFAG), Y. Amhis *et al.*, *Averages of b-hadron, c-hadron, and τ-lepton properties as of summer 2014*, `arXiv:1412.7515`.

[3] CKMfitter Group, J. Charles *et al.*, *CP violation and the CKM matrix: assessing the impact of the asymmetric B factories*, Eur. Phys. J. **C41** (2005) 1-131, `arXiv:hep-ph/0406184`.

[4] V. Gribov and B. Pontecorvo, *Neutrino astronomy and lepton charge*, Phys. Lett. **B28** (1969) 493.

[5] B. Schwingenheuer, *Status and prospects of searches for neutrinoless double beta decay*, Annalen Phys. **525** (2013) 269-280, `arXiv:1210.7432`.

[6] A. Hoecker, *Charged-lepton flavour physics*, Pramana **79** (2012) 1141-1167, `arXiv:1201.5093`.

[7] L. Wolfenstein, *Parametrization of the Kobayashi-Maskawa Matrix*, Phys. Rev. Lett. **51** (1983) 1945.

[8] M. Artuso, E. Barberio, and S. Stone, *B meson decays*, PMC Phys. **A3** (2009) 3, `arXiv:0902.3743`.

[9] C. Jarlskog, *Commutator of the Quark Mass Matrices in the Standard Electroweak Model and a Measure of Maximal CP Violation*, Phys. Rev. Lett. **55** (1985) 1039.

[10] W. Heisenberg, *On the structure of atomic nuclei*, Z. Phys. **77** (1932) 1-11.

[11] E. Wigner, *On the consequences of the symmetry of the nuclear Hamiltonian on the spectroscopy of nuclei*, Phys. Rev. **51** (1937) 106-119.

[12] G. Rochester and C. Butler, *Evidence for the existence of new unstable elementary particles*, Nature **160** (1947) 855-857.

[13] A. Pais, *Some remarks on the V-particles*, Phys. Rev. **86** (1952) 663-672.

[14] M. Gell-Mann, *Isotopic spin and new unstable particles*, Phys. Rev. **92** (1953) 833-834.

[15] T. Nakano and K. Nishijima, *Charge independence for V-particles*, Prog. Theor. Phys. **10** (1953) 581-582.

[16] K. Nishijima, *Charge independence theory of V-particles*, Prog. Theor. Phys. **13** (1955) 285-304.

[17] T. Lee and C.-N. Yang, *Question of parity conservation in weak interactions*, Phys. Rev. **104** (1956) 254-258.

[18] C. Wu *et al.*, *Experimental test of parity conservation in beta decay*, Phys. Rev. **105** (1957) 1413-1414.

[19] R. Garwin, L. Lederman, and M. Weinrich, *Observations of the failure of conservation of parity and charge conjugation in meson decays: the magnetic moment of the free muon*, Phys. Rev. **105** (1957) 1415-1417.

[20] J. Friedman and V. Telegdi, *Nuclear emulsion evidence for parity nonconservation in the decay chain* $\pi^+ \to \mu^+ \to e^+$, Phys. Rev. **106** (1957) 1290-1293.

[21] A. Salam, *On parity conservation and neutrino mass*, Nuovo Cim. **5** (1957) 299-301.

[22] L. Landau, *On the conservation laws for weak interactions*, Nucl. Phys. **3** (1957) 127-131.

[23] T. Lee and C.-N. Yang, *Parity nonconservation and a two-component theory of the neutrino*, Phys. Rev. **105** (1957) 1671-1675.

[24] R. Feynman and M. Gell-Mann, *Theory of Fermi interaction*, Phys. Rev. **109** (1958) 193-198.

[25] N. Cabibbo, *Unitary symmetry and leptonic decays*, Phys. Rev. Lett. **10** (1963) 531-533.

[26] L. Okun and B. Pontecorvo, *Some remarks on slow processes of transformation of elementary particles*, Zh. Eksp. Teor. Fiz. **32** (1957) 1587-1588.

[27] R. P. Feynman, R. B. Leighton, and M. I. Sands, Addison-Wesley Publishing Co., Inc., Reading, Massachusetts, 1963.

[28] M. Gell-Mann and A. Pais, *Behavior of neutral particles under charge conjugation*, Phys. Rev. **97** (1955) 1387-1389.

[29] T. Lee, R. Oehme, and C.-N. Yang, *Remarks on possible noninvariance under time reversal and charge conjugation*, Phys. Rev. **106** (1957) 340-345.

[30] K. Lande *et al.*, *Observation of long-lived neutral V particles*, Phys. Rev. **103** (1956) 1901-1904.

[31] A. Pais and O. Piccioni, *Note on the decay and absorption of the* Θ^0, Phys. Rev. **100** (1955) 1487-1489.

[32] F. Muller *et al.*, *Regeneration and mass difference of neutral K mesons*, Phys. Rev. Lett. **4** (1960) 418-421.

[33] R. Good *et al.*, *Regeneration of neutral K mesons and their mass difference*, Phys. Rev. **124** (1961) 1223-1239.

[34] J. Christenson, J. Cronin, V. Fitch, and R. Turlay, *Evidence for the* 2π *decay of the* K_2^0 *meson*, Phys. Rev. Lett. **13** (1964) 138-140.

[35] V. Fitch, R. Roth, J. Russ, and W. Vernon, *Evidence for constructive interference between coherently regenerated and CP-nonconserving amplitudes*, Phys. Rev. Lett. **15** (1965) 73-76.

[36] V. Fitch, R. Roth, J. Russ, and W. Vernon, *Studies of* $K_2^0 \to \pi^+\pi^-$ *decay and interference*, Phys. Rev. **164** (1967) 1711-1721.

[37] J.-M. Gaillard *et al.*, *Measurement of the decay of the long-lived neutral K meson into two neutral pions*, Phys. Rev. Lett. **18** (1967) 20-25.

[38] J. W. Cronin, P. F. Kunz, W. S. Risk, and P. C. Wheeler, *Measurement of the decay rate of* $K_2^0 \to \pi^0 + \pi^0$, Phys. Rev. Lett. **18** (1967) 25-29.

[39] S. Bennett *et al.*, *Measurement of the charge asymmetry in the decay* $K_L^0 \to \pi^\pm + e^\mp + \nu$, Phys. Rev. Lett. **19** (1967) 993-997.

[40] D. E. Dorfan *et al.*, *Charge asymmetry in the muonic decay of the* K_2^0, Phys. Rev. Lett. **19** (1967) 987-993.

[41] A. Sakharov, *Violation of CP invariance, C asymmetry, and baryon asymmetry of the universe*, Pisma Zh. Eksp. Teor. Fiz. **5** (1967) 32-35.

[42] M. Gell-Mann, *A schematic model of baryons and mesons*, Phys. Lett. **8** (1964) 214-215.

[43] G. Zweig, *An* $SU(3)$ *model for strong interaction symmetry and its breaking. Version 2*, CERN-TH-412, NP-14146, PRINT-64-170.

[44] M. Gell-Mann, *The eightfold way: a theory of strong interaction symmetry*, CTSL-20, TID-12608.

[45] Y. Ne'eman, *Derivation of strong interactions from a gauge invariance*, Nucl. Phys. **26** (1961) 222-229.

[46] S. Glashow, J. Iliopoulos, and L. Maiani, *Weak interactions with lepton-hadron symmetry*, Phys. Rev. **D2** (1970) 1285-1292.

[47] S. Glashow, *Partial symmetries of weak interactions*, Nucl. Phys. **22** (1961) 579-588.

[48] S. Weinberg, *Physical processes in a convergent theory of the weak and electromagnetic interactions*, Phys. Rev. Lett. **27** (1971) 1688-1691.

[49] M. Kobayashi and T. Maskawa, *CP violation in the renormalizable theory of weak interaction*, Prog. Theor. Phys. **49** (1973) 652-657.

[50] E598 collaboration, J. Aubert *et al.*, *Experimental observation of a heavy particle* J, Phys. Rev. Lett. **33** (1974) 1404-1406.

[51] SLAC-SP-017 collaboration, J. Augustin *et al.*, *Discovery of a narrow resonance in* e^+e^- *annihilation*, Phys. Rev. Lett. **33** (1974) 1406-1408.

[52] A. Boyarski *et al.*, *The quantum numbers and decay widths of the* $\psi(3095)$, Phys. Rev. Lett. **34** (1975) 1357.

[53] C. Bacci *et al.*, *Preliminary result of Frascati (ADONE) on the nature of a new 3.1* GeV *particle produced in* e^+e^- *annihilation*, Phys. Rev. Lett. **33** (1974) 1408.

[54] DASP collaboration, W. Braunschweig *et al.*, *A measurement of large-angle* e^+e^- *scattering at the 3100* MeV *resonance*, Phys. Lett. **B53** (1974) 393.

[55] G. Abrams *et al.*, *The discovery of a second narrow resonance in* e^+e^- *annihilation*, Phys. Rev. Lett. **33** (1974) 1453-1455.

[56] T. Appelquist and H. D. Politzer, *Orthocharmonium and* e^+e^- *annihilation*, Phys. Rev. Lett. **34** (1975) 43.

[57] T. Appelquist, A. De Rujula, H. D. Politzer, and S. Glashow, *Charmonium spectroscopy*, Phys. Rev. Lett. **34** (1975) 365.

[58] E. Eichten *et al.*, *The spectrum of charmonium*, Phys. Rev. Lett. **34** (1975) 369-372.

[59] I. Peruzzi *et al.*, *Observation of a narrow charged state at 1876* MeV/c^2 *decaying to an exotic combination of* $K\pi\pi$, Phys. Rev. Lett. **37** (1976) 569-571.

[60] S. Herb *et al.*, *Observation of a dimuon resonance at 9.5* GeV *in 400-GeV proton-nucleus collisions*, Phys. Rev. Lett. **39** (1977) 252-255.

[61] E. Eichten and K. Gottfried, *Heavy quarks in* e^+e^- *annihilation*, Phys. Lett. **B66** (1977) 286.

[62] W. R. Innes *et al.*, *Observation of structure in the* Υ *region*, Phys. Rev. Lett. **39** (1977) 1240.

[63] K. Ueno *et al.*, *Evidence for the* Υ'' *and a search for new narrow resonances*, Phys. Rev. Lett. **42** (1979) 486-489.

[64] CLEO collaboration, D. Andrews *et al.*, *Observation of a fourth Upsilon state in* e^+e^- *annihilations*, Phys. Rev. Lett. **45** (1980) 219.

[65] CLEO collaboration, S. Behrends *et al.*, *Observation of exclusive decay modes of B-flavored mesons*, Phys. Rev. Lett. **50** (1983) 881-884.

[66] C. Darden *et al.*, *Evidence for a narrow resonance at 10.01* GeV *in electron-positron annihilations*, Phys. Lett. **B78** (1978) 364.

[67] J. Bienlein *et al.*, *Observation of a narrow resonance at 10.02* GeV *in* e^+e^- *annihilations*, Phys. Lett. **B78** (1978) 360-363.

[68] C. Darden *et al.*, *Observation of a narrow resonance at 9.46* GeV *in electron-positron annihilations*, Phys. Lett. **B76** (1978) 246.

[69] Pluto collaboration, C. Berger *et al.*, *Observation of a narrow resonance formed in* e^+e^- *annihilation at 9.46* GeV, Phys. Lett. **B76** (1978) 243-245.

[70] CLEO collaboration, C. Bebek *et al.*, *Evidence for new flavor production at the* $\Upsilon(4S)$, Phys. Rev. Lett. **46** (1981) 84.

[71] CDF collaboration, F. Abe *et al.*, *Observation of top quark production in* $\overline{p}p$ *collisions*, Phys. Rev. Lett. **74** (1995) 2626-2631, `arXiv:hep-ex/9503002`.

[72] D0 collaboration, S. Abachi *et al.*, *Observation of the top quark*, Phys. Rev. Lett. **74** (1995) 2632-2637, `arXiv:hep-ex/9503003`.

[73] ARGUS COLLABORATION, H. Albrecht *et al.*, *Observation of* $B^0-\overline{B}^0$ *mixing*, Phys. Lett. **B192** (1987) 245.

[74] G. Lubkin, *UA1 at CERN says it has candidates for sixth quark, top*, Phys. Today **37N8** (1984) 17-18.

[75] CLEO collaboration, A. Jawahery, $B^0-\overline{B}^0$ *mixing and rare decays of B mesons.*, .

[76] T. Wu and C.-N. Yang, *Phenomenological analysis of violation of CP invariance in decay of* K^0 *and* $\overline{K}^0$, Phys. Rev. Lett. **13** (1964) 380-385.

[77] L. Wolfenstein, *Violation of CP invariance and the possibility of very weak interactions*, Phys. Rev. Lett. **13** (1964) 562-564.

[78] T. Lee and C. Wu, *Weak interactions: decays of neutral K mesons*, Ann. Rev. Nucl. Part. Sci. **16** (1966) 511-590.

[79] M. Sozzi, *On the direct CP violation parameter ε'*, Eur. Phys. J. **C36** (2004) 37-42, arXiv:hep-ph/0401176.

[80] A. J. Buras, M. Jamin, and M. E. Lautenbacher, *A 1996 analysis of the CP violating ratio ε'/ε*, Phys. Lett. **B389** (1996) 749-756, arXiv:hep-ph/9608365.

[81] D. Bartlett *et al.*, *$K_2^0 \to 2\pi^0$ decay rate*, Phys. Rev. Lett. **21** (1968) 558-561.

[82] I. Budagov *et al.*, *A measurement of the branching ratio of the CP violating decay mode $K_L^0 \to 2\ \pi^0$*, Phys. Lett. **B28** (1968) 215-219.

[83] J. Gaillard *et al.*, *The decay of long-lived neutral kaons into two neutral pions*, Nuovo Cim. **A59** (1969) 453-489.

[84] R. Cence *et al.*, *Measurement of the branching ratio $K_L^0 \to 2\pi^0/K_L^0 \to 3\pi^0$*, Phys. Rev. Lett. **22** (1969) 1210-1214.

[85] M. Banner, J. Cronin, J. Liu, and J. Pilcher, *Experimental study of the decay $K_L^0 \to \pi^0\pi^0$ and other rare decay modes*, Phys. Rev. **188** (1969) 2033-2059.

[86] I. Budagov *et al.*, *Measurement of the branching ratio of the CP-violating decay mode $K_L^0 \to 2\pi^0$*, Phys. Rev. **D2** (1970) 815-827.

[87] V. Barmin *et al.*, *Measurement of the decay probability $K_L^0 \to 2\pi^0$*, Phys. Lett. **B33** (1970) 377-380.

[88] M. Holder *et al.*, *On the decay $K_L^0 \to \pi^0\pi^0$*, Phys. Lett. **B40** (1972) 141-146.

[89] M. Banner *et al.*, *Measurement of η^{00}/η^{+-}*, Phys. Rev. Lett. **28** (1972) 1597-1601.

[90] J. Christenson *et al.*, *Measurement of the phase and magnitude of η^{00}*, Phys. Rev. Lett. **43** (1979) 1209.

[91] J. Black *et al.*, *Measurement of the CP nonconservation parameter ε'/ε*, Phys. Rev. Lett. **54** (1985) 1628-1630.

[92] R. Bernstein *et al.*, *Measurement of ε'/ε in the neutral kaon system*, Phys. Rev. Lett. **54** (1985) 1631-1634.

[93] M. Woods *et al.*, *First result on a new measurement of ε'/ε in the neutral kaon system*, Phys. Rev. Lett. **60** (1988) 1695.

[94] NA31 collaboration, H. Burkhardt *et al.*, *First evidence for direct CP violation*, Phys. Lett. **B206** (1988) 169.

[95] NA31 collaboration, G. Barr *et al.*, *A new measurement of direct CP violation in the neutral kaon system*, Phys. Lett. **B317** (1993) 233-242.

[96] L. Gibbons *et al.*, *Measurement of the CP violation parameter* Re *$(\varepsilon'/\varepsilon)$*, Phys. Rev. Lett. **70** (1993) 1203-1206.

[97] NA48 collaboration, A. Lai *et al.*, *A precise measurement of the direct CP violation parameter* Re *$(\varepsilon'/\varepsilon)$*, Eur. Phys. J. **C22** (2001) 231-254, arXiv:hep-ex/0110019.

[98] KTeV collaboration, A. Alavi-Harati *et al.*, *Measurements of direct CP violation, CPT symmetry, and other parameters in the neutral kaon system*, Phys. Rev. **D67** (2003) 012005, arXiv:hep-ex/0208007.

[99] NA48 collaboration, V. Fanti *et al.*, *The beam and detector for the NA48 neutral kaon CP violations experiment at CERN*, Nucl. Instrum. Meth. **A574** (2007) 433-471.

[100] N. Doble, L. Gatignon, and P. Grafstrom, *A novel application of bent crystal channeling to the production of simultaneous particle beams*, Nucl. Instrum. Meth. **B119** (1996) 181-191.

[101] KTeV collaboration, A. Alavi-Harati *et al.*, *Observation of direct CP violation in $K_{(S,L)} \to \pi\pi$ decays*, Phys. Rev. Lett. **83** (1999) 22-27, arXiv:hep-ex/9905060.

[102] NA48 collaboration, V. Fanti *et al.*, *A new measurement of direct CP violation in two pion decays of the neutral kaon*, Phys. Lett. **B465** (1999) 335-348, arXiv:hep-ex/9909022.

[103] NA48 collaboration, J. Batley *et al.*, *A precision measurement of direct CP violation in the decay of neutral kaons into two pions*, Phys. Lett. **B544** (2002) 97-112, arXiv:hep-ex/0208009.

[104] KTeV collaboration, E. Abouzaid *et al.*, *Precise measurements of direct CP violation, CPT symmetry, and other parameters in the neutral kaon system*, Phys. Rev. **D83** (2011) 092001, arXiv:1011.0127.

[105] BaBar collaboration, B. Aubert *et al.*, *Observation of CP violation in the B^0 meson system*, Phys. Rev. Lett. **87** (2001) 091801, arXiv:hep-ex/0107013.

[106] Belle collaboration, K. Abe *et al.*, *Observation of large CP violation in the neutral B meson system*, Phys. Rev. Lett. **87** (2001) 091802, arXiv:hep-ex/0107061.

[107] V. Weisskopf and E. P. Wigner, *Calculation of the natural brightness of spectral lines on the basis of Dirac's theory*, Z. Phys. **63** (1930) 54-73.

[108] V. Weisskopf and E. Wigner, *Over the natural line width in the radiation of the harmonius oscillator*, Z. Phys. **65** (1930) 18-29.

[109] T. Inami and C. Lim, *Effects of superheavy quarks and leptons in low-energy weak processes $K_L^0 \to \mu\overline{\mu}$, $K^+ \to \pi^+\nu\overline{\nu}$ and $K^0 \leftrightarrow \overline{K}^0$*, Prog. Theor. Phys. **65** (1981) 297.

[110] H. Quinn, *B physics and CP violation*, arXiv:hep-ph/0111177.

[111] BaBar collaboration, B. Aubert *et al.*, *Measurement of the $e^+e^- \to b\bar{b}$ cross section between $\sqrt{s}$ = 10.54-GeV and 11.20-GeV*, Phys. Rev. Lett. **102** (2009) 012001, arXiv:0809.4120.

[112] BaBar collaboration, Belle collaboration, A. Bevan *et al.*, *The Physics of the B Factories*, Eur. Phys. J. **C74** (2014), no. 11 3026, arXiv:1406.6311.

[113] BaBar collaboration, B. Aubert *et al.*, *The BaBar detector*, Nucl. Instrum. Meth. **A479** (2002) 1-116, arXiv:hep-ex/0105044.

[114] A. Abashian *et al.*, *The Belle detector*, Nucl. Instrum. Meth. **A479** (2002) 117-232.

[115] Z. Natkaniec *et al.*, *Status of the Belle silicon vertex detector*, Nucl. Instrum. Meth. **A560** (2006) 1-4.

[116] R. Abe *et al.*, *The new beampipe for the Belle experiment*, Nucl. Instrum. Meth. **A535** (2004) 558-561.

[117] L. Landau, *On the energy loss of fast particles by ionization*, J. Phys. (USSR) **8** (1944) 201-205.

[118] BABAR, B. Aubert *et al.*, *The BABAR detector: upgrades, operation and performance*, Nucl. Instrum. Meth. **A729** (2013) 615-701, `arXiv:1305.3560`.

[119] BaBar-DIRC collaboration, I. Adam *et al.*, *The DIRC particle identification system for the BaBar experiment*, Nucl. Instrum. Meth. **A538** (2005) 281-357.

[120] G. Moliere, *Theory of the scattering of fast charged particles. 2. Repeated and multiple scattering*, Z. Naturforsch. **A3** (1948) 78-97.

[121] H. Bethe, *Moliere's theory of multiple scattering*, Phys. Rev. **89** (1953) 1256-1266.

[122] F. Anulli *et al.*, *Performance of 2nd Generation BaBar Resistive Plate Chambers*, Nucl. Instrum. Meth. **A552** (2005) 276-291.

[123] BaBar LST collaboration, M. Andreotti, *A barrel IFR instrumented with limited streamer tubes for BABAR experiment*, SLAC-PUB-12205.

[124] Belle collaboration, Y. Ushiroda *et al.*, *Development of the central trigger system for the BELLE detector at the KEK B factory*, Nucl. Instrum. Meth. **A438** (1999) 460-471.

[125] B. Cheon *et al.*, *Electromagnetic calorimeter trigger at Belle*, Nucl. Instrum. Meth. **A494** (2002) 548-554.

[126] T. G. Dietterich and G. Bakiri, *Solving multiclass learning problems via Error-Correcting Output Codes*, Journal of Artificial Intelligence Research **2** (1994) 263-286.

[127] R. Kalman, *A new approach to linear filtering and prediction problems*, J. Fluids. Eng. **82(1)** (1960) 35-45.

[128] R. Fruhwirth, *Application of Kalman filtering to track and vertex fitting*, Nucl. Instrum. Meth. **A262** (1987) 444-450.

[129] G. C. Fox and S. Wolfram, *Observables for the analysis of event shapes in e^+e^- annihilation and other processes*, Phys. Rev. Lett. **41** (1978) 1581.

[130] R. A. Fisher, *The use of multiple measurements in taxonomic problems*, Annals Eugen. **7** (1936) 179-188.

[131] BaBar collaboration, B. Aubert *et al.*, *Improved measurement of CP asymmetries in $B^0 \to c\bar{c}K^{*0}$ decays*, Phys. Rev. Lett. **94** (2005) 161803, `arXiv:hep-ex/0408127`.

[132] BELLE collaboration, K. Abe *et al.*, *Improved measurement of CP-violation parameters $\sin(2\phi_1)$ and $|\Lambda|$, B meson lifetimes, and $B^0-\overline{B}^0$ mixing parameter Δm_d*, Phys. Rev. **D71** (2005) 072003, `arXiv:hep-ex/0408111`.

[133] ARGUS collaboration, H. Albrecht *et al.*, *Kaons in flavour tagged B decays*, Z. Phys. **C62** (1994) 371-382.

[134] Belle collaboration, H. Kakuno *et al.*, *Neutral B flavor tagging for the measurement of mixing induced CP violation at Belle*, Nucl. Instrum. Meth. **A533** (2004) 516-531, `arXiv:hep-ex/0403022`.

[135] J. M. Campbell, J. Huston, and W. Stirling, *Hard interactions of quarks and gluons: a primer for LHC physics*, Rept. Prog. Phys. **70** (2007) 89, `arXiv:hep-ph/0611148`.

[136] E. Norrbin and T. Sjostrand, *Production and hadronization of heavy quarks*, Eur. Phys. J. **C17** (2000) 137-161, arXiv:hep-ph/0005110.

[137] T. Sjostrand, S. Mrenna, and P. Z. Skands, *A brief introduction to PYTHIA 8.1*, Comput. Phys. Commun. **178** (2008) 852-867, arXiv:0710.3820.

[138] LHCb, R. Aaij *et al.*, *Measurement of the fragmentation fraction ratio f_s/f_d and its dependence on B meson kinematics*, JHEP **1304** (2013) 001, arXiv:1301.5286.

[139] CDF collaboration, T. Aaltonen *et al.*, *Operational experience, improvements, and performance of the CDF Run II Silicon Vertex Detector*, Nucl. Instrum. Meth. **A729** (2013) 153-181, arXiv:1301.3180.

[140] D0 collaboration, V. Abazov *et al.*, *The upgraded D0 detector*, Nucl. Instrum. Meth. **A565** (2006) 463-537, arXiv:physics/0507191.

[141] K. Anikeev *et al.*, *B physics at the Tevatron: Run II and beyond*, arXiv:hep-ph/0201071.

[142] A. Kulyavtsev *et al.*, *Proposal for an experiment to measure mixing, CP violation and rare decays in charm and beauty particle decays at the Fermilab Collider - BTeV*, FERMILAB-PROPOSAL-0918.

[143] G. Borissov, *B-physics results from Tevatron*, Int. J. Mod. Phys. **A28** (2013) 1330007, arXiv:1304.2173.

[144] CDF collaboration, R. Blair *et al.*, *The CDF-II detector: Technical Design Report*, FERMILAB-DESIGN-1996-01, FERMILAB-PUB-96-390-E.

[145] M. J. Morello, *Measurements of CP asymmetries and branching fractions of two-body charmless decays of B^0 and B_s^0 mesons*, FERMILAB-THESIS-2007-57.

[146] A. A. Affolder *et al.*, *Construction report of the intermediate silicon layers (ISL) ladders*, Nucl. Instrum. Meth. **A461** (2001) 216-218.

[147] CDF collaboration, R. Oldeman, *Performance of CDF for B physics*, eConf **C0304052** (2003) FO005, arXiv:hep-ex/0307027.

[148] CDF collaboration, T. Nelson, *The CDF layer 00 detector*, Int. J. Mod. Phys. **A16S1C** (2001) 1091-1093.

[149] CDF collaboration, C. S. Hill, *Initial experience with the CDF layer 00 silicon detector*, Nucl. Instrum. Meth. **A511** (2003) 118-120.

[150] D0 collaboration, R. Angstadt *et al.*, *The layer 0 inner silicon detector of the D0 experiment*, Nucl. Instrum. Meth. **A622** (2010) 298-310, arXiv:0911.2522.

[151] *http://garfield.web.cern.ch/garfield/*, .

[152] CDF collaboration, A. A. Affolder *et al.*, *CDF central outer tracker*, Nucl. Instrum. Meth. **A526** (2004) 249-299.

[153] D0 collaboration, D. Smirnov *et al.*, *Status of the D0 fiber tracker and preshower detectors*, D0-5683.

[154] A. Bross *et al.*, *Characterization and performance of visible light photon counters (VLPCs) for the upgraded D0 detector at the Fermilab Tevatron*, Nucl. Instrum. Meth. **A477** (2002) 172-178.

[155] CDF collaboration, A. Annovi, *CDF: B physics performance and trigger - operational experience*, Nucl. Phys. Proc. Suppl. **170** (2007) 283-287.

[156] E. J. Thomson *et al.*, *Online track processor for the CDF upgrade*, IEEE Trans. Nucl. Sci. **49** (2002) 1063-1070.

[157] CDF collaboration, B. Ashmanskas *et al.*, *The CDF silicon vertex trigger*, Nucl. Instrum. Meth. **A518** (2004) 532-536, `arXiv:physics/0306169`.

[158] D0 collaboration, D. Bauer, *B physics and triggers at D0: operational experience*, Nucl. Phys. Proc. Suppl. **170** (2007) 288-291.

[159] T. Adams *et al.*, *The D0 Run II impact parameter trigger*, Nucl. Instrum. Meth. A (2007) `arXiv:physics/0701195`.

[160] CDF collaboration, S. Cabrera *et al.*, *The CDF-II time-of-flight detector*, Nucl. Instrum. Meth. **A494** (2002) 416-423.

[161] CDF collaboration, A. Abulencia *et al.*, *Observation of $B^0_{(s)} \to K^+K^-$ and measurements of branching fractions of charmless two-body decays of B^0 and B^0_s mesons in $\overline{p}p$ collisions at $\sqrt{s} = 1.96$ TeV*, Phys. Rev. Lett. **97** (2006) 211802, `arXiv:hep-ex/0607021`.

[162] CDF collaboration, T. Aaltonen *et al.*, *Measurements of direct CP violating asymmetries in charmless decays of strange bottom mesons and bottom baryons*, Phys. Rev. Lett. **106** (2011) 181802, `arXiv:1103.5762`.

[163] CDF collaboration, T. Aaltonen *et al.*, *Measurement of the CP-violating phase $\beta_s^{J/\psi\phi}$ in $B^0_s \to J/\psi\phi$ decays with the CDF II detector*, Phys. Rev. **D85** (2012) 072002, `arXiv:1112.1726`.

[164] CDF collaboration, T. Aaltonen *et al.*, *Measurement of the bottom-strange meson mixing phase in the full CDF data set*, Phys. Rev. Lett. **109** (2012) 171802, `arXiv:1208.2967`.

[165] D0 collaboration, V. M. Abazov *et al.*, *Measurement of the CP-violating phase $\phi_s^{J/\psi\phi}$ using the flavor-tagged decay $B^0_s \to J/\psi\phi$ in 8 fb^{-1} of $p\overline{p}$ collisions*, Phys. Rev. **D85** (2012) 032006, `arXiv:1109.3166`.

[166] R. Field and R. Feynman, *A parametrization of the properties of quark jets*, Nucl. Phys. **B136** (1978) 1.

[167] G. C. Blazey *et al.*, *Run II jet physics*, `arXiv:hep-ex/0005012`.

[168] D0 collaboration, V. Abazov *et al.*, *Measurement of B_d mixing using opposite-side flavor tagging*, Phys. Rev. **D74** (2006) 112002, `arXiv:hep-ex/0609034`.

[169] A. Asner *et al.*, *ECFA-CERN Workshop on large hadron collider in the LEP tunnel, Lausanne and CERN, Geneva, Switzerland, 21-27 March 1984: Proceedings.1.*, CERN-84-10-V-1, ECFA-84-85, CERN-YELLOW-84-10-V-1.

[170] R. Barbieri, *Why is this energy range so interesting, in: ECFA-CERN workshop on large hadron collider in the LEP tunnel, Lausanne and CERN Geneva, Switzerland, 21-27 March 1984: Proceedings.2*, CERN-84-10-V-2.

[171] G. Jarlskog and D. Rein, *ECFA Large Hadron Collider workshop, Aachen, Germany, 4-9 October 1990: Proceedings.2.*, CERN-90-10-V-2.

[172] COBEX collaboration, S. Erhan *et al.*, *Letter of Intent for a dedicated collider beauty experiment at the Large Hadron Collider at CERN*, CERN/LHCC 93-50, LHCC/I6.

[173] GAJET collaboration, R. Arnold *et al.*, *Letter of Intent: Study of CP violation in B-meson decays using an internal gas jet target at LHC*, CERN/LHCC 93-54, LHCC/I7.

[174] LHB collaboration, K. Kirseboom *et al.*, *Letter of Intent: Measurement of CP violation in B-meson decays with an extracted LHC beam*, CERN/LHCC 93-45, LHCC/I5.

[175] LHCC, *Recommendations of the LHC committee: dedicated B experiments*, CERN/LHCC 94-26, LHCC/M-6.

[176] LHC-B collaboration, *LHC-B: A dedicated LHC collider beauty experiment for precision measurements of CP-violation. Letter of Intent*, CERN-LHCC-95-05.

[177] LHCb collaboration, S. Amato *et al.*, *LHCb Technical Proposal*, CERN-LHCC-98-04, CERN-LHCC-P-4.

[178] LHCb collaboration, J. Alves, A. Augusto *et al.*, *The LHCb detector at the LHC*, JINST **3** (2008) S08005.

[179] R. Hierck, *Optimisation of the LHCb detector*, LHCb-2003-114, CERN-LHCb-2003-114, CERN-THESIS-2003-041.

[180] LHC-B collaboration, *LHCb magnet: Technical Design Report*, CERN-LHCC-2000-007.

[181] HERA-B Inner Tracker collaboration, Y. Bagaturia *et al.*, *Studies of aging and HV break down problems during development and operation of MSGC and GEM detectors for the inner tracking system of HERA-B*, Nucl. Instrum. Meth. **A490** (2002) 223, arXiv:hep-ex/0204011.

[182] CMS collaboration, *The CMS tracker: addendum to the Technical Design Report*, CERN-LHCC-2000-016.

[183] LHCb collaboration, *LHCb Technical Design Report: reoptimized detector design and performance*, CERN-LHCC-2003-030.

[184] R. Mankel, *A concurrent track evolution algorithm for pattern recognition in the HERA-B main tracking system*, Nucl. Instrum. Meth. **A395** (1997) 169-184.

[185] R. Mankel and A. Spiridonov, *The concurrent track evolution algorithm: extension for track finding in the inhomogeneous magnetic field of the HERA-B spectrometer*, Nucl. Instrum. Meth. **A426** (1999) 268-282, arXiv:hep-ex/9809021.

[186] H. Dijkstra *et al.*, *The use of the TT1 tracking station in the Level-1 trigger*, LHCb-2002-045, CERN-LHCb-2002-045.

[187] M. Brice, *Assembling the last module of the vertex locator for LHCb*, photo, Mar, 2007.

[188] R. Aaij *et al.*, *Performance of the LHCb Vertex Locator*, JINST **9** (2014) 09007, arXiv:1405.7808.

[189] H. Voss, *LHCb IT assembly*, photo, Apr, 2008.

[190] LHCb Outer Tracker group, R. Arink *et al.*, *Performance of the LHCb Outer Tracker*, JINST **9** (2014) 01002, arXiv:1311.3893.

[191] LHCb collaboration, R. Aaij *et al.*, *Measurement of the track reconstruction efficiency at LHCb*, arXiv:1408.1251.

[192] M. De Cian, *Track reconstruction efficiency and analysis of $B^0 \to K^{*0}\mu^+\mu^-$ at the LHCb experiment*, CERN-THESIS-2013-145.

[193] J. van Tilburg, *Track simulation and reconstruction in LHCb*, CERN-THESIS-2005-040.

[194] LHCb, R. Aaij *et al.*, *LHCb detector performance*, arXiv:1412.6352.

[195] LHCb collaboration, R. Aaij *et al.*, *Measurement of Upsilon production in pp collisions at* $\sqrt{s} = 7$ TeV, Eur. Phys. J. **C72** (2012) 2025, arXiv:1202.6579.

[196] CMS collaboration, S. Chatrchyan *et al.*, *Measurement of the* $\Upsilon(1S), \Upsilon(2S)$*, and* $\Upsilon(3S)$ *cross sections in pp collisions at* $\sqrt{s} = 7$ TeV, Phys. Lett. **B727** (2013) 101-125, arXiv:1303.5900.

[197] ATLAS collaboration, G. Aad *et al.*, *Measurement of Upsilon production in 7* TeV *pp collisions at ATLAS*, Phys. Rev. **D87** (2013), no. 5 052004, arXiv:1211.7255.

[198] R. Aaij *et al.*, *The LHCb trigger and its performance in 2011*, JINST **8** (2013) P04022, arXiv:1211.3055.

[199] LHCb HLT Group, J. Albrecht, V. Gligorov, G. Raven, and S. Tolk, *Performance of the LHCb High Level Trigger in 2012*, J. Phys. Conf. Ser. **513** (2014) 012001, arXiv:1310.8544.

[200] LHCb collaboration, *LHCb: RICH Technical Design Report*, CERN-LHCC-2000-037.

[201] LHCb RICH Group, M. Adinolfi *et al.*, *Performance of the LHCb RICH detector at the LHC*, Eur. Phys. J. **C73** (2013) 2431, arXiv:1211.6759.

[202] LHCb collaboration, R. Aaij *et al.*, *Opposite-side flavour tagging of B mesons at the LHCb experiment*, Eur. Phys. J. **C72** (2012) 2022, arXiv:1202.4979.

[203] LHCb collaboration, *Optimization and calibration of the same-side kaon tagging algorithm using hadronic* B_s^0 *decays in 2011 data*, LHCb-CONF-2012-033, CERN-LHCb-CONF-2012-033.

[204] LHCb collaboration, R. Aaij *et al.*, *Measurement of CP violation and the* B_s^0 *meson decay width difference with* $B_s^0 \to J/\psi K^+K^-$ *and* $B_s^0 \to J/\psi\pi^+\pi^-$ *decays*, Phys. Rev. **D87** (2013), no. 11 112010, arXiv:1304.2600.

[205] LHCb collaboration, R. Aaij *et al.*, *Measurement of the CP-violating phase* ϕ_s *in* $\overline{B}_s^0 \to J/\psi\pi^+\pi^-$ *decays*, Phys. Lett. **B736** (2014) 186, arXiv:1405.4140.

[206] LHCb collaboration, R. Aaij *et al.*, *Precision measurement of CP violation in* $B_s^0 \to J/\psi K^+K^-$ *decays*, arXiv:1411.3104.

[207] LHCb collaboration, R. Aaij *et al.*, *Measurement of CP violation in* $B_s^0 \to \phi\phi$ *decays*, Phys. Rev. **D90** (2014) 052011, arXiv:1407.2222.

[208] LHCb collaboration, R. Aaij *et al.*, *Measurement of CP asymmetry in* $B_s^0 \to D_s^{\mp}K^{\pm}$ *decays*, JHEP **1411** (2014) 060, arXiv:1407.6127.

[209] LHCb collaboration, R. Aaij *et al.*, *Measurement of the CP-violating phase* ϕ_s *in* $\overline{B}_s^0 \to D_s^+D_s^-$ *decays*, Phys. Rev. Lett. **113** (2014), no. 21 211801, arXiv:1409.4619.

[210] LHCb collaboration, R. Aaij *et al.*, *Measurement of the CP-violating phase* β *in* $B^0 \to J/\psi\pi^+\pi^-$ *decays and limits on penguin effects*, arXiv:1411.1634.

[211] UTfit collaboration, M. Bona *et al.*, *The Unitarity Triangle fit in the Standard Model and hadronic parameters from Lattice QCD: a reappraisal after the measurements of* Δm_s *and* BF $(B \to \tau\nu_\tau)$, JHEP **0610** (2006) 081, arXiv:hep-ph/0606167.

[212] ARGUS collaboration, H. Albrecht *et al.*, *A study of* $\overline{B}^0 \to D^{*+}\ell^-\overline{\nu}_\ell$ *and* $B^0-\overline{B}^0$ *mixing using partial* D^{*+} *reconstruction*, Phys. Lett. **B324** (1994) 249-254.

[213] CLEO collaboration, B. Behrens *et al.*, *Precise measurement of* $B^0-\overline{B}^0$ *mixing parameters at the* $\Upsilon(4S)$, Phys. Lett. **B490** (2000) 36-44, arXiv:hep-ex/0005013.

[214] ALEPH collaboration, D. Buskulic *et al.*, *Improved measurement of the* $B^0_d-\overline{B}^0_d$ *oscillation frequency*, Z. Phys. **C75** (1997) 397-407.

[215] DELPHI collaboration, P. Abreu *et al.*, *Measurement of* $B^0_d-\overline{B}^0_d$ *oscillations*, Z. Phys. **C76** (1997) 579-598.

[216] L3 collaboration, M. Acciarri *et al.*, *Measurement of the* $B^0_d-\overline{B}^0_d$ *oscillation frequency*, Eur. Phys. J. **C5** (1998) 195-203.

[217] OPAL collaboration, G. Alexander *et al.*, *A measurement of the* B^0_d *oscillation frequency using leptons and* $D^{*\pm}$ *mesons*, Z. Phys. **C72** (1996) 377-388.

[218] OPAL collaboration, K. Ackerstaff *et al.*, *A study of B meson oscillations using hadronic* Z^0 *decays containing leptons*, Z. Phys. **C76** (1997) 401-415, arXiv:hep-ex/9707009.

[219] OPAL collaboration, K. Ackerstaff *et al.*, *An Updated study of B meson oscillations using dilepton events*, Z. Phys. **C76** (1997) 417-423, arXiv:hep-ex/9707010.

[220] OPAL collaboration, G. Abbiendi *et al.*, *Measurement of the* B^0 *lifetime and oscillation frequency using* $B^0 \to D^{*+}\ell^-\overline{\nu}_\ell$ *decays*, Phys. Lett. **B493** (2000) 266-280, arXiv:hep-ex/0010013.

[221] SLD collaboration, K. Abe *et al.*, *A search for time dependent* $B^0_{(s)}-\overline{B}^0_{(s)}$ *oscillations using exclusively reconstructed* $D^{(*)\pm}$ *mesons*, Phys. Rev. **D66** (2002) 032009, arXiv:hep-ex/0207048.

[222] SLD collaboration, K. Abe *et al.*, *Search for time dependent* $B^0_{(s)}-\overline{B}^0_{(s)}$ *oscillations using a vertex charge dipole technique*, Phys. Rev. **D67** (2003) 012006, arXiv:hep-ex/0209002.

[223] CDF collaboration, F. Abe *et al.*, *Measurement of the* $B^0-\overline{B}^0$ *oscillation frequency using* πB *meson charge-flavor correlations in* $p\overline{p}$ *collisions at* $\sqrt{s} = 1.8$ TeV, Phys. Rev. Lett. **80** (1998) 2057-2062, arXiv:hep-ex/9712004.

[224] CDF collaboration, F. Abe *et al.*, *Measurement of the* $B^0-\overline{B}^0$ *flavor oscillation frequency and study of same side flavor tagging of B mesons in* $p\overline{p}$ *collisions*, Phys. Rev. **D59** (1999) 032001, arXiv:hep-ex/9806026.

[225] CDF collaboration, T. Affolder *et al.*, *Measurement of the* $B^0-\overline{B}^0$ *oscillation frequency using* $\ell^- D^{*+}$ *pairs and lepton flavor tags*, Phys. Rev. **D60** (1999) 112004, arXiv:hep-ex/9907053.

[226] CDF collaboration, F. Abe *et al.*, *Measurement of the* $B^0-\overline{B}^0$ *oscillation frequency using dimuon data in* $p\overline{p}$ *collisions at* $\sqrt{s} = 1.8$ TeV, Phys. Rev. **D60** (1999) 051101.

[227] ALEPH collaboration, R. Barate *et al.*, *Study of* B^0_s *oscillations and lifetime using fully reconstructed* D_s*-decays*, Eur. Phys. J. **C4** (1998) 367-385.

[228] ALEPH collaboration, R. Barate *et al.*, *Search for* B^0_s *oscillations using inclusive lepton events*, Eur. Phys. J. **C7** (1999) 553-569, arXiv:hep-ex/9811018.

[229] ALEPH collaboration, A. Heister *et al.*, *Improved search for $B_s^0-\overline{B}_s^0$ scillations*, Eur. Phys. J. **C29** (2003) 143-170.

[230] DELPHI collaboration, P. Abreu *et al.*, *Study of $B_s^0-\overline{B}_s^0$ oscillations and B_s^0 lifetimes using hadronic decays of B_s^0 mesons*, Eur. Phys. J. **C18** (2000) 229-252, arXiv:hep-ex/0105077.

[231] DELPHI collaboration, P. Abreu *et al.*, *Measurement of the B_s^0 lifetime and study of $B_s^0-\overline{B}_s^0$ oscillations using $D_s\ell$ events*, Eur. Phys. J. **C16** (2000) 555, arXiv:hep-ex/0107077.

[232] OPAL collaboration, G. Abbiendi *et al.*, *A study of B_s^0 meson oscillation using hadronic Z^0 decays containing leptons*, Eur. Phys. J. **C11** (1999) 587-598, arXiv:hep-ex/9907061.

[233] OPAL collaboration, G. Abbiendi *et al.*, *A study of B_s^0 meson oscillation using D_s-lepton correlations*, Eur. Phys. J. **C19** (2001) 241-256, arXiv:hep-ex/0011052.

[234] SLD collaboration, K. Abe *et al.*, *Time dependent $B_s^0-\overline{B}_s^0$ mixing using inclusive and semileptonic B decays at SLD*, SLAC-PUB-8225.

[235] CDF collaboration, F. Abe *et al.*, *A search for $B_s^0-\overline{B}_s^0$ oscillations using the semileptonic decay $B_s^0 \to \phi\ell^+ X\nu$*, Phys. Rev. Lett. **82** (1999) 3576-3580.

[236] BaBar collaboration, B. Aubert *et al.*, *Measurement of $B^0-\overline{B}^0$ flavor oscillations in hadronic B^0 decays*, Phys. Rev. Lett. **88** (2002) 221802, arXiv:hep-ex/0112044.

[237] BaBar collaboration, B. Aubert *et al.*, *Measurement of the $B^0-\overline{B}^0$ oscillation frequency with inclusive dilepton events*, Phys. Rev. Lett. **88** (2002) 221803, arXiv:hep-ex/0112045.

[238] BaBar collaboration, B. Aubert *et al.*, *Simultaneous measurement of the B^0 meson lifetime and mixing frequency with $B^0 \to D^{*-}\ell^+\nu_\ell$ decays*, Phys. Rev. **D67** (2003) 072002, arXiv:hep-ex/0212017.

[239] BaBar collaboration, B. Aubert *et al.*, *Measurement of the B^0 lifetime and the $B^0-\overline{B}^0$ oscillation frequency using partially reconstructed $B^0 \to D^{*+}\ell^-\overline{\nu}_\ell$ decays*, Phys. Rev. **D73** (2006) 012004, arXiv:hep-ex/0507054.

[240] Belle collaboration, N. Hastings *et al.*, *Studies of $B^0-\overline{B}^0$ mixing properties with inclusive dilepton events*, Phys. Rev. **D67** (2003) 052004, arXiv:hep-ex/0212033.

[241] Belle collaboration, K. Hara *et al.*, *Measurement of the $B^0-\overline{B}^0$ mixing parameter Δm_d using semileptonic B^0 decays*, Phys. Rev. Lett. **89** (2002) 251803, arXiv:hep-ex/0207045.

[242] Belle collaboration, T. Tomura *et al.*, *Measurement of the oscillation frequency for $B^0-\overline{B}^0$ mixing using hadronic B^0 decays*, Phys. Lett. **B542** (2002) 207-215, arXiv:hep-ex/0207022.

[243] LHCb collaboration, R. Aaij *et al.*, *Measurement of the $B^0-\overline{B}^0$ oscillation frequency Δm_d with the decays $B^0 \to D^-\pi^+$ and $B^0 \to J/\psi K^{*0}$*, Phys. Lett. **B719** (2013) 318-325, arXiv:1210.6750.

[244] LHCb collaboration, R. Aaij *et al.*, *Observation of $B_s^0-\overline{B}_s^0$ mixing and measurement of mixing frequencies using semileptonic B decays*, Eur. Phys. J. **C73** (2013), no. 12 2655, arXiv:1308.1302.

[245] CDF collaboration, A. Abulencia *et al.*, *Observation of $B_s^0-\overline{B}_s^0$ oscillations*, Phys. Rev. Lett. **97** (2006) 242003, arXiv:hep-ex/0609040.

[246] CDF collaboration, A. Abulencia *et al.*, *Measurement of the $B_s^0-\overline{B}_s^0$ oscillation frequency*, Phys. Rev. Lett. **97** (2006) 062003, arXiv:hep-ex/0606027.

[247] LHCb collaboration, R. Aaij *et al.*, *Measurement of the $B_s^0-\overline{B}_s^0$ oscillation frequency Δm_s in $B_s^0 \to D_s^-(3)\pi$ decays*, Phys. Lett. **B709** (2012) 177-184, arXiv:1112.4311.

[248] LHCb collaboration, R. Aaij *et al.*, *Precision measurement of the $B_s^0-\overline{B}_s^0$ oscillation frequency with the decay $B_s^0 \to D_s^-\pi^+$*, New J. Phys. **15** (2013) 053021, arXiv:1304.4741.

[249] BaBar, J. Lees *et al.*, *Time-integrated luminosity recorded by the BaBar detector at the PEP-II e^+e^- collider*, Nucl. Instrum. Meth. **A726** (2013) 203-213, arXiv:1301.2703.

[250] H. Tajima *et al.*, *Proper time resolution function for measurement of time evolution of B mesons at the KEK-B factory*, Nucl. Instrum. Meth. **A533** (2004) 370-386, arXiv:hep-ex/0301026.

[251] D0 collaboration, V. Abazov *et al.*, *First direct two-sided bound on the B_s^0 oscillation frequency*, Phys. Rev. Lett. **97** (2006) 021802, arXiv:hep-ex/0603029.

[252] H. Moser and A. Roussarie, *Mathematical methods for $B-\overline{B}$ oscillation analyses*, Nucl. Instrum. Meth. **A384** (1997) 491-505.

[253] Belle collaboration, N. Satoyama *et al.*, *A search for the rare leptonic decays $B^+ \to \mu^+\nu_\mu$ and $B^+ \to e^+\nu_e$*, Phys. Lett. **B647** (2007) 67-73, arXiv:hep-ex/0611045.

[254] BaBar collaboration, B. Aubert *et al.*, *Search for the rare leptonic decays $B^+ \to \ell^+\nu_\ell$ (ℓ=e,μ)*, Phys. Rev. **D79** (2009) 091101, arXiv:0903.1220.

[255] Belle collaboration, W. Dungel *et al.*, *Measurement of the form factors of the decay $B^0 \to D^{*-}\ell^+\nu$ and determination of the CKM matrix element $|V_{cb}|$*, Phys. Rev. **D82** (2010) 112007, arXiv:1010.5620.

[256] ARGUS Collaboration, H. Albrecht *et al.*, *Investigation of the decays $\overline{B}^0 \to D^{*+}\ell\overline{\nu}$ and $\overline{B} \to D^{**}\ell\overline{\nu}$*, Z. Phys. **C57** (1993) 533-540.

[257] ALEPH, D. Buskulic *et al.*, *A measurement of the $|V_{cb}|$ from $\overline{B}^0 \to D^{*+}\ell^-\overline{\nu}_\ell$*, Phys. Lett. **B359** (1995) 236-248.

[258] ALEPH collaboration, D. Buskulic *et al.*, *Measurements of $|V_{cb}|$, form-factors and branching fractions in the decays $\overline{B}^0 \to D^{*+}\ell^-\overline{\nu}_\ell$ and $\overline{B}^0 \to D^+\ell^-\overline{\nu}_\ell$*, Phys. Lett. **B395** (1997) 373-387.

[259] DELPHI collaboration, J. Abdallah *et al.*, *Measurement of $|V_{cb}|$ using the semileptonic decay $\overline{B}^0 \to D^{*+}\ell^-\overline{\nu}_\ell$*, Eur. Phys. J. **C33** (2004) 213-232, arXiv:hep-ex/0401023.

[260] DELPHI collaboration, P. Abreu *et al.*, *Measurement of V_{cb} from the decay process $\overline{B}^0 \to D^{*+}\ell^-\overline{\nu}_\ell$*, Phys. Lett. **B510** (2001) 55-74, arXiv:hep-ex/0104026.

[261] OPAL, K. Ackerstaff *et al.*, *A measurement of $|V_{cb}|$ using $\overline{B}^0 \to D^{*+}\ell^-\overline{\nu}_\ell$ decays*, Phys. Lett. **B395** (1997) 128-140.

[262] OPAL collaboration, G. Abbiendi *et al.*, *Measurement of $|V_{cb}|$ using $\overline{B}^0 \to D^{*+}\ell^-\overline{\nu}_\ell$ decays*, Phys. Lett. **B482** (2000) 15-30, arXiv:hep-ex/0003013.

[263] CLEO collaboration, N. Adam *et al.*, *Determination of the $\overline{B} \to D^* \ell \overline{\nu}$ decay width and $|V_{cb}|$*, Phys. Rev. **D67** (2003) 032001, arXiv:hep-ex/0210040.

[264] CLEO collaboration, J. E. Bartelt *et al.*, *Measurement of the $B \to D \ell \nu$ branching fractions and form-factor*, Phys. Rev. Lett. **82** (1999) 3746, arXiv:hep-ex/9811042.

[265] BaBar, B. Aubert *et al.*, *Measurement of the $\overline{B}^0 \to D^{*+} \ell^- \overline{\nu}_\ell$ decay rate and $|V_{cb}|$*, Phys. Rev. **D71** (2005) 051502, arXiv:hep-ex/0408027.

[266] BaBar collaboration, B. Aubert *et al.*, *Determination of the form-factors for the decay $B^0 \to D^{*-} \ell^+ \nu_\ell$ and of the CKM matrix element $|V_{cb}|$*, Phys. Rev. **D77** (2008) 032002, arXiv:0705.4008.

[267] Belle, K. Abe *et al.*, *Determination of $|V_{cb}|$ using the semileptonic decay $\overline{B}^0 \to D^{*+} e^- \overline{\nu}_{\rm e}$*, Phys. Lett. **B526** (2002) 247-257, arXiv:hep-ex/0111060.

[268] BaBar collaboration, B. Aubert *et al.*, *Measurement of the decay $B^- \to D^{*0} e^- \overline{\nu}_{\rm e}$*, Phys. Rev. Lett. **100** (2008) 231803, arXiv:0712.3493.

[269] Belle collaboration, K. Abe *et al.*, *Measurement of $\mathcal{B}(\overline{B}^0 \to D^+ \ell^- \overline{\nu})$ and determination of $|V_{cb}|$*, Phys. Lett. **B526** (2002) 258-268, arXiv:hep-ex/0111082.

[270] BaBar collaboration, B. Aubert *et al.*, *Measurement of $|V_{cb}|$ and the form-factor slope in $\overline{B} \to D \ell^- \overline{\nu}$ decays in events tagged by a fully reconstructed B meson*, Phys. Rev. Lett. **104** (2010) 011802, arXiv:0904.4063.

[271] BaBar collaboration, B. Aubert *et al.*, *Measurements of the semileptonic decays $\overline{B} \to D \ell \overline{\nu}$ and $\overline{B} \to D^* \ell \overline{\nu}$ using a global fit to $DX \ell \overline{\nu}$ final states*, Phys. Rev. **D79** (2009) 012002, arXiv:0809.0828.

[272] E. Dalgic *et al.*, *B meson semileptonic form-factors from unquenched lattice QCD*, Phys. Rev. **D73** (2006) 074502, arXiv:hep-lat/0601021.

[273] J. A. Bailey *et al.*, *The $B \to \pi \ell \nu$ semileptonic form factor from three-flavor lattice QCD: a model-independent determination of $|V_{ub}|$*, Phys. Rev. **D79** (2009) 054507, arXiv:0811.3640.

[274] P. Ball and R. Zwicky, *New results on $B \to \pi$, K, η decay formfactors from light-cone sum rules*, Phys. Rev. **D71** (2005) 014015, arXiv:hep-ph/0406232.

[275] CLEO, S. Athar *et al.*, *Study of the q^2 dependence of $B \to \pi \ell \nu$ and $B \to \rho(\omega) \ell \nu$ decay and extraction of $|V_{ub}|$*, Phys. Rev. **D68** (2003) 072003, arXiv:hep-ex/0304019.

[276] CLEO, R. Gray *et al.*, *A study of exclusive charmless semileptonic B decays and extraction of $|V_{ub}|$ at CLEO*, Phys. Rev. **D76** (2007) 012007, arXiv:hep-ex/0703042.

[277] CLEO collaboration, N. Adam *et al.*, *A study of exclusive charmless semileptonic B decay and $|V_{ub}|$*, Phys. Rev. Lett. **99** (2007) 041802, arXiv:hep-ex/0703041.

[278] BaBar, B. Aubert *et al.*, *Study of $B \to \pi \ell \nu$ and $B \to \rho \ell \nu$ decays and determination of $|V_{ub}|$*, Phys. Rev. **D72** (2005) 051102, arXiv:hep-ex/0507003.

[279] BaBar collaboration, B. Aubert *et al.*, *Measurement of the $B \to \pi \ell \nu$ branching fraction and determination of $|V_{ub}|$ with tagged B mesons*, Phys. Rev. Lett. **97** (2006) 211801, arXiv:hep-ex/0607089.

[280] BaBar collaboration, B. Aubert *et al.*, *Measurement of the $B^0 \to \pi^- \ell^+ \nu$ form-factor shape and branching fraction, and determination of $|V_{ub}|$ with a loose neutrino reconstruction technique*, Phys. Rev. Lett. **98** (2007) 091801, arXiv:hep-ex/0612020.

[281] BaBar collaboration, B. Aubert *et al.*, *Measurements of $B \to \{\pi, \eta, \eta'\} \ell \nu_\ell$ branching fractions and determination of $|V_{ub}|$ with semileptonically tagged B esons*, Phys. Rev. Lett. **101** (2008) 081801, arXiv:0805.2408.

[282] BaBar collaboration, P. del Amo Sanchez *et al.*, *Study of $B \to \pi \ell \nu$ and $B \to \rho \ell \nu$ decays and determination of $|V_{ub}|$*, Phys. Rev. **D83** (2011) 032007, arXiv:1005.3288.

[283] BaBar collaboration, P. del Amo Sanchez *et al.*, *Measurement of the $B^0 \to \pi^- \ell^+ \nu$ and $B^+ \to \eta^{(\prime)} \ell^+ \nu$ branching fractions, the $B^0 \to \pi^- \ell^+ \nu$ and $B^+ \to \eta \ell^+ \nu$ form-factor shapes, and determination of $|V_{ub}|$*, Phys. Rev. **D83** (2011) 052011, arXiv:1010.0987.

[284] BaBar collaboration, J. Lees *et al.*, *Branching fraction and form-factor shape measurements of exclusive charmless semileptonic B decays, and determination of $|V_{ub}|$*, Phys. Rev. **D86** (2012) 092004, arXiv:1208.1253.

[285] Belle collaboration, T. Hokuue *et al.*, *Measurements of branching fractions and q^2 distributions for $B \to \pi \ell \nu$ and $B \to \rho \ell \nu$ decays with $B \to D^{(*)} \ell \nu$ decay tagging*, Phys. Lett. **B648** (2007) 139-148, arXiv:hep-ex/0604024.

[286] BELLE collaboration, H. Ha *et al.*, *Measurement of the decay $B^0 \to \pi^- \ell^+ \nu$ and determination of $|V_{ub}|$*, Phys. Rev. **D83** (2011) 071101, arXiv:1012.0090.

[287] Belle collaboration, A. Sibidanov *et al.*, *Study of exclusive $B \to X_u \ell \nu$ decays and extraction of $|V_{ub}|$ using full reconstruction tagging at the Belle experiment*, Phys. Rev. **D88** (2013), no. 3 032005, arXiv:1306.2781.

[288] A. Khodjamirian, T. Mannel, N. Offen, and Y.-M. Wang, *$B \to \pi \ell \nu_\ell$ width and $|V_{ub}|$ from QCD Light-Cone Sum Rules*, Phys. Rev. **D83** (2011) 094031, arXiv:1103.2655.

[289] A. Bharucha, *Two-loop corrections to the $B \to \pi$ form factor from QCD sum rules on the light-cone and $|V_{ub}|$*, JHEP **1205** (2012) 092, arXiv:1203.1359.

[290] I. I. Bigi, N. Uraltsev, and A. Vainshtein, *Nonperturbative corrections to inclusive beauty and charm decays: QCD versus phenomenological models*, Phys. Lett. **B293** (1992) 430-436, arXiv:hep-ph/9207214.

[291] A. V. Manohar and M. B. Wise, *Inclusive semileptonic B and polarized Λ_b decays from QCD*, Phys. Rev. **D49** (1994) 1310-1329, arXiv:hep-ph/9308246.

[292] I. I. Bigi, M. A. Shifman, N. Uraltsev, and A. I. Vainshtein, *QCD predictions for lepton spectra in inclusive heavy flavor decays*, Phys. Rev. Lett. **71** (1993) 496-499, arXiv:hep-ph/9304225.

[293] K. G. Wilson, *Nonlagrangian models of current algebra*, Phys. Rev. **179** (1969) 1499-1512.

[294] I. I. Bigi, M. A. Shifman, N. Uraltsev, and A. I. Vainshtein, *Sum rules for heavy flavor transitions in the SV limit*, Phys. Rev. **D52** (1995) 196-235, arXiv:hep-ph/9405410.

[295] O. Buchmuller and H. Flacher, *Fit to moment from $B \to X_c \ell \overline{\nu}$ and $B \to X_s \gamma$ decays using heavy quark expansions in the kinetic scheme*, Phys. Rev. **D73** (2006) 073008, arXiv:hep-ph/0507253.

[296] A. H. Hoang, Z. Ligeti, and A. V. Manohar, *B decays in the Υ expansion*, Phys. Rev. **D59** (1999) 074017, arXiv:hep-ph/9811239.

[297] CLEO collaboration, S. Csorna *et al.*, *Moments of the B meson inclusive semileptonic decay rate using neutrino reconstruction*, Phys. Rev. **D70** (2004) 032002, arXiv:hep-ex/0403052.

[298] CDF collaboration, D. Acosta *et al.*, *Measurement of the moments of the hadronic invariant mass distribution in semileptonic B decays*, Phys. Rev. **D71** (2005) 051103, arXiv:hep-ex/0502003.

[299] DELPHI collaboration, J. Abdallah *et al.*, *Determination of heavy quark non-perturbative parameters from spectral moments in semileptonic B decays*, Eur. Phys. J. **C45** (2006) 35-59, arXiv:hep-ex/0510024.

[300] BaBar collaboration, B. Aubert *et al.*, *Measurements of moments of the hadronic mass distribution in semileptonic B decays*, Phys. Rev. **D69** (2004) 111103, arXiv:hep-ex/0403031.

[301] BaBar collaboration, B. Aubert *et al.*, *Measurement and interpretation of moments in inclusive semileptonic decays $\overline{B} \to X_c \ell^- \overline{\nu}$*, Phys. Rev. **D81** (2010) 032003, arXiv:0908.0415.

[302] BELLE collaboration, C. Schwanda *et al.*, *Moments of the hadronic invariant mass spectrum in $B \to X_c \ell \nu$ decays at Belle*, Phys. Rev. **D75** (2007) 032005, arXiv:hep-ex/0611044.

[303] CLEO collaboration, A. Mahmood *et al.*, *Measurement of the B-meson inclusive semileptonic branching fraction and electron energy moments*, Phys. Rev. **D70** (2004) 032003, arXiv:hep-ex/0403053.

[304] BaBar collaboration, B. Aubert *et al.*, *Measurement of the electron energy spectrum and its moments in inclusive $B \to X e \nu$ decays*, Phys. Rev. **D69** (2004) 111104, arXiv:hep-ex/0403030.

[305] Belle collaboration, P. Urquijo *et al.*, *Moments of the electron energy spectrum and partial branching fraction of $B \to X_c e \nu$ decays at Belle*, Phys. Rev. **D75** (2007) 032001, arXiv:hep-ex/0610012.

[306] CLEO collaboration, S. Chen *et al.*, *Branching fraction and photon energy spectrum for $b \to s\gamma$*, Phys. Rev. Lett. **87** (2001) 251807, arXiv:hep-ex/0108032.

[307] BaBar collaboration, B. Aubert *et al.*, *Measurements of the $B \to X_s \gamma$ branching fraction and photon spectrum from a sum of exclusive final states*, Phys. Rev. **D72** (2005) 052004, arXiv:hep-ex/0508004.

[308] BaBar collaboration, B. Aubert *et al.*, *Measurement of the branching fraction and photon energy moments of $B \to X_s \gamma$ and A_{CP} ($B \to X_{s+d}\gamma$)*, Phys. Rev. Lett. **97** (2006) 171803, arXiv:hep-ex/0607071.

[309] Belle collaboration, C. Schwanda *et al.*, *Measurement of the moments of the photon energy spectrum in $B \to X_s \gamma$ decays and determination of $|V_{cb}|$ and $m(b)$ at Belle*, Phys. Rev. **D78** (2008) 032016, arXiv:0803.2158.

[310] Belle collaboration, A. Limosani *et al.*, *Measurement of inclusive radiative B-meson decays with a photon energy threshold of 1.7* GeV, Phys. Rev. Lett. **103** (2009) 241801, arXiv:0907.1384.

[311] BaBar collaboration, B. Aubert *et al.*, *Measurement of the $B \to X_s\gamma$ branching fraction and photon energy spectrum using the recoil method*, Phys. Rev. **D77** (2008) 051103, arXiv:0711.4889.

[312] Belle collaboration, P. Koppenburg *et al.*, *An inclusive measurement of the photon energy spectrum in $b \to s\gamma$ decays*, Phys. Rev. Lett. **93** (2004) 061803, arXiv:hep-ex/0403004.

[313] BaBar collaboration, B. Aubert *et al.*, *Determination of the branching fraction for $B \to X_c\ell\nu$ decays and of $|V_{cb}|$ from hadronic mass and lepton energy moments*, Phys. Rev. Lett. **93** (2004) 011803, arXiv:hep-ex/0404017.

[314] M. Battaglia *et al.*, *Heavy quark parameters and $|V_{cb}|$ from spectral moments in semileptonic B decays*, eConf **C0304052** (2003) WG102, arXiv:hep-ph/0210319.

[315] C. W. Bauer *et al.*, *Global analysis of inclusive B decays*, Phys. Rev. **D70** (2004) 094017, arXiv:hep-ph/0408002.

[316] ALEPH collaboration, R. Barate *et al.*, *Determination of $|V_{ub}|$ from the measurement of the inclusive charmless semileptonic branching ratio of b hadrons*, Eur. Phys. J. **C6** (1999) 555-574.

[317] L3 collaboration, M. Acciarri *et al.*, *Measurement of the inclusive charmless semileptonic branching fraction of beauty hadrons and a determination of $|V_{ub}|$ at LEP*, Phys. Lett. **B436** (1998) 174-186.

[318] OPAL collaboration, G. Abbiendi *et al.*, *Measurement of $|V_{ub}|$ using b hadron semileptonic decay*, Eur. Phys. J. **C21** (2001) 399-410, arXiv:hep-ex/0107016.

[319] DELPHI collaboration, P. Abreu *et al.*, *Determination of $|V_{ub}|/|V_{cb}|$ with DELPHI at LEP*, Phys. Lett. **B478** (2000) 14-30, arXiv:hep-ex/0105054.

[320] CLEO collaboration, A. Bornheim *et al.*, *Improved measurement of $|V_{ub}|$ with inclusive semileptonic B decays*, Phys. Rev. Lett. **88** (2002) 231803, arXiv:hep-ex/0202019.

[321] BaBar collaboration, B. Aubert *et al.*, *Measurement of the inclusive electron spectrum in charmless semileptonic B decays near the kinematic endpoint and determination of $|V_{ub}|$*, Phys. Rev. **D73** (2006) 012006, arXiv:hep-ex/0509040.

[322] BaBar collaboration, B. Aubert *et al.*, *Determination of $|V_{ub}|$ from measurements of the electron and neutrino momenta in inclusive semileptonic B decays*, Phys. Rev. Lett. **95** (2005) 111801, arXiv:hep-ex/0506036.

[323] BaBar collaboration, B. Aubert *et al.*, *Determinations of $|V_{ub}|$ from inclusive semileptonic B decays with reduced model dependence*, Phys. Rev. Lett. **96** (2006) 221801, arXiv:hep-ex/0601046.

[324] BaBar, B. Aubert *et al.*, *Measurements of partial branching fractions for $\overline{B} \to X_u\ell\overline{\nu}_\ell$ and determination of $|V_{ub}|$*, Phys. Rev. Lett. **100** (2008) 171802, arXiv:0708.3702.

[325] BaBar collaboration, J. Lees *et al.*, *Study of $\overline{B} \to X_u\ell\overline{\nu}$ decays in $B\overline{B}$ events tagged by a fully reconstructed B-meson decay and determination of $|V_{ub}|$*, Phys. Rev. **D86** (2012) 032004, arXiv:1112.0702.

[326] BELLE collaboration, H. Kakuno *et al.*, *Measurement of $|V_{ub}|$ using inclusive $B \to X_u\ell\nu$ decays with a novel X_u reconstruction method*, Phys. Rev. Lett. **92** (2004) 101801, arXiv:hep-ex/0311048.

[327] Belle collaboration, A. Limosani *et al.*, *Measurement of inclusive charmless semileptonic B-meson decays at the endpoint of the electron momentum spectrum*, Phys. Lett. **B621** (2005) 28-40, arXiv:hep-ex/0504046.

[328] Belle collaboration, I. Bizjak *et al.*, *Determination of $|V_{ub}|$ from measurements of the inclusive charmless semileptonic partial rates of B mesons using full reconstruction tags*, Phys. Rev. Lett. **95** (2005) 241801, arXiv:hep-ex/0505088.

[329] Belle collaboration, P. Urquijo *et al.*, *Measurement of $|V_{ub}|$ from inclusive charmless semileptonic B decays*, Phys. Rev. Lett. **104** (2010) 021801, arXiv:0907.0379.

[330] Heavy Flavor Averaging Group, Y. Amhis *et al.*, *Averages of b-hadron, c-hadron, and τ-lepton properties as of early 2012*, arXiv:1207.1158.

[331] U. Aglietti, F. Di Lodovico, G. Ferrera, and G. Ricciardi, *Inclusive measure of $|V_{ub}|$ with the analytic coupling model*, Eur. Phys. J. **C59** (2009) 831-840, arXiv:0711.0860.

[332] U. Aglietti, G. Ferrera, and G. Ricciardi, *Semi-inclusive B decays and a model for soft-gluon effects*, Nucl. Phys. **B768** (2007) 85-115, arXiv:hep-ph/0608047.

[333] J. R. Andersen and E. Gardi, *Inclusive spectra in charmless semileptonic B decays by dressed gluon exponentiation*, JHEP **0601** (2006) 097, arXiv:hep-ph/0509360.

[334] E. Gardi, *On the determination of $|V_{ub}|$ from inclusive semileptonic B decays*, arXiv:0806.4524.

[335] C. W. Bauer, Z. Ligeti, and M. E. Luke, *Precision determination of $|V_{ub}|$ from inclusive decays*, Phys. Rev. **D64** (2001) 113004, arXiv:hep-ph/0107074.

[336] P. Gambino, P. Giordano, G. Ossola, and N. Uraltsev, *Inclusive semileptonic B decays and the determination of $|V_{ub}|$*, JHEP **0710** (2007) 058, arXiv:0707.2493.

[337] B. O. Lange, M. Neubert, and G. Paz, *Theory of charmless inclusive B decays and the extraction of V_{ub}*, Phys. Rev. **D72** (2005) 073006, arXiv:hep-ph/0504071.

[338] Fermilab Lattice collaboration, MILC collaboration, A. Bazavov *et al.*, *B and D meson decay constants from three-flavor lattice QCD*, Phys. Rev. **D85** (2012) 114506, arXiv:1112.3051.

[339] ETM collaboration, N. Carrasco *et al.*, *B-physics from $N_f = 2$ tmQCD: the Standard Model and beyond*, JHEP **1403** (2014) 016, arXiv:1308.1851.

[340] C. McNeile *et al.*, *High-precision f_{B_s} and HQET from relativistic Lattice QCD*, Phys. Rev. **D85** (2012) 031503, arXiv:1110.4510.

[341] H. Na *et al.*, *The B and B_s^0 meson decay constants from Lattice QCD*, Phys. Rev. **D86** (2012) 034506, arXiv:1202.4914.

[342] HPQCD collaboration, R. Dowdall *et al.*, *B-meson decay constants from improved lattice nonrelativistic QCD with physical u, d, s, and c quarks*, Phys. Rev. Lett. **110** (2013), no. 22 222003, arXiv:1302.2644.

[343] Belle collaboration, K. Ikado *et al.*, *Evidence of the purely leptonic decay $B^- \to \tau^- \overline{\nu}_\tau$*, Phys. Rev. Lett. **97** (2006) 251802, arXiv:hep-ex/0604018.

[344] BaBar collaboration, B. Aubert *et al.*, *A search for $B^+ \to \tau^+ \nu_\tau$ with hadronic B tags*, Phys. Rev. **D77** (2008) 011107, arXiv:0708.2260.

[345] BaBar collaboration, B. Aubert *et al.*, *A search for* $B^+ \to \tau^+\nu_\tau$, Phys. Rev. **D76** (2007) 052002, arXiv:0705.1820.

[346] BaBar collaboration, B. Aubert *et al.*, *A Search for* $B^+ \to \ell^+\nu_\ell$ *recoiling against* $B^- \to D^0\ell^-\overline{\nu}_\ell X$, Phys. Rev. **D81** (2010) 051101, arXiv:0912.2453.

[347] BaBar collaboration, J. Lees *et al.*, *Evidence of* $B \to \tau\nu_\tau$ *decays with hadronic* B *tags*, Phys. Rev. **D88** (2013) 031102, arXiv:1207.0698.

[348] Belle collaboration, K. Hara *et al.*, *Evidence for* $B^- \to \tau^-\overline{\nu}_\tau$ *with a semileptonic tagging method*, Phys. Rev. **D82** (2010) 071101, arXiv:1006.4201.

[349] Belle collaboration, I. Adachi *et al.*, *Evidence for* $B^- \to \tau^-\overline{\nu}_\tau$ *with a hadronic tagging method using the full data sample of Belle*, Phys. Rev. Lett. **110** (2013), no. 13 131801, arXiv:1208.4678.

[350] Belle collaboration, A. Abdesselam *et al.*, *Measurement of the branching fraction of* $B^+ \to \tau^+\nu_\tau$ *decays with the semileptonic tagging method and the full Belle data sample*, arXiv:1409.5269.

[351] M. Feindt *et al.*, *A hierarchical NeuroBayes-based algorithm for full reconstruction of B mesons at B factories*, Nucl. Instrum. Meth. **A654** (2011) 432-440, arXiv:1102.3876.

[352] LHCb, R. Aaij *et al.*, *Determination of the quark coupling strength* $|V_{ub}|$ *using baryonic decays*, arXiv:1504.0156.

[353] M. Beneke, *Corrections to* $\sin(2\beta)$ *from CP asymmetries in* $B^0 \to \pi^0,\rho^0,\eta,\eta',\omega,\phi)K_S^0$ *decays*, Phys. Lett. **B620** (2005) 143-150, arXiv:hep-ph/0505075.

[354] H.-Y. Cheng, C.-K. Chua, and A. Soni, *Effects of final-state interactions on mixing-induced CP violation in penguin-dominated B decays*, Phys. Rev. **D72** (2005) 014006, arXiv:hep-ph/0502235.

[355] H.-n. Li and S. Mishima, *Penguin-dominated* $B \to PV$ *decays in NLO perturbative QCD*, Phys. Rev. **D74** (2006) 094020, arXiv:hep-ph/0608277.

[356] OPAL collaboration, K. Ackerstaff *et al.*, *Investigation of CP violation in* $B^0 \to J/\psi K_S^0$ *decays at LEP*, Eur. Phys. J. **C5** (1998) 379-388, arXiv:hep-ex/9801022.

[357] ALEPH collaboration, R. Barate *et al.*, *Study of the CP asymmetry of* $B^0 \to J/\psi K_S^0$ *decays in ALEPH*, Phys. Lett. **B492** (2000) 259-274, arXiv:hep-ex/0009058.

[358] CDF collaboration, T. Affolder *et al.*, *A measurement of* $\sin(2\beta)$ *from* $B \to J/\psi K_S^0$ *with the CDF detector*, Phys. Rev. **D61** (2000) 072005, arXiv:hep-ex/9909003.

[359] BaBar collaboration, B. Aubert *et al.*, *Measurement of CP violating asymmetries in* B^0 *decays to CP eigenstates*, Phys. Rev. Lett. **86** (2001) 2515-2522, arXiv:hep-ex/0102030.

[360] BELLE collaboration, A. Abashian *et al.*, *Measurement of the CP violation parameter* $\sin(2\phi_1)$ *in* B_d^0 *meson decays*, Phys. Rev. Lett. **86** (2001) 2509-2514, arXiv:hep-ex/0102018.

[361] BaBar collaboration, B. Aubert *et al.*, *A study of time dependent CP-violating asymmetries and flavor oscillations in neutral B decays at the* $\Upsilon(4S)$, Phys. Rev. **D66** (2002) 032003, arXiv:hep-ex/0201020.

[362] BaBar collaboration, B. Aubert *et al.*, *Measurement of the CP-violating asymmetry amplitude* $\sin(2\beta)$, Phys. Rev. Lett. **89** (2002) 201802, arXiv:hep-ex/0207042.

[363] BaBar collaboration, B. Aubert *et al.*, *Improved measurement of CP violation in neutral B decays to* $c\bar{c}s$, Phys. Rev. Lett. **99** (2007) 171803, arXiv:hep-ex/0703021.

[364] Belle collaboration, K. Abe *et al.*, *Improved measurement of mixing induced CP violation in the neutral B meson system*, Phys. Rev. **D66** (2002) 071102, arXiv:hep-ex/0208025.

[365] Belle collaboration, K.-F. Chen *et al.*, *Observation of time-dependent CP violation in* $B^0 \to \eta' K^0$ *decays and improved measurements of CP asymmetries in* $B^0 \to \phi K^0$, $K^0_S K^0_S$ *and* $B^0 \to J/\psi K^0$ *decays*, Phys. Rev. Lett. **98** (2007) 031802, arXiv:hep-ex/0608039.

[366] Belle collaboration, H. Sahoo *et al.*, *Measurements of time-dependent CP violation in* $B^0 \to \psi(2s) K^0_S$ *decays*, Phys. Rev. **D77** (2008) 091103, arXiv:0708.2604.

[367] BaBar collaboration, B. Aubert *et al.*, *Measurement of time-dependent CP asymmetry in* $B^0 \to c\bar{c}K^{(*)0}$ *decays*, Phys. Rev. **D79** (2009) 072009, arXiv:0902.1708.

[368] I. Adachi *et al.*, *Precise measurement of the CP violation parameter* $\sin(2\phi_1)$ *in* $B^0 \to (c\bar{c})K^0$ *decays*, Phys. Rev. Lett. **108** (2012) 171802, arXiv:1201.4643.

[369] BaBar collaboration, B. Aubert *et al.*, *Measurement of* $\sin(2\beta)$ *using hadronic* J/ψ *decays*, Phys. Rev. **D69** (2004) 052001, arXiv:hep-ex/0309039.

[370] LHCb collaboration, R. Aaij *et al.*, *Measurement of the time-dependent CP asymmetry in* $B^0 \to J/\psi K^0_S$ *decays*, Phys. Lett. **B721** (2013) 24-31, arXiv:1211.6093.

[371] LHCb collaboration, R. Aaij *et al.*, *First evidence of direct CP violation in charmless two-body decays of* B^0_s *mesons*, Phys. Rev. Lett. **108** (2012) 201601, arXiv:1202.6251.

[372] LHCb collaboration, *Measurement of time-dependent CP violation in charmless two-body B decays*, LHCb-CONF-2012-007, CERN-LHCb-CONF-2012-007.

[373] LHCb, R. Aaij *et al.*, *Measurement of CP violation in* $B^0 \to J/\psi K^0_S$ *decays*, arXiv:1503.0708.

[374] BaBar collaboration, B. Aubert *et al.*, *Ambiguity-free measurement of* $\cos(2\beta)$*: time-integrated and time-dependent angular analyses of* $B \to J/\psi K\pi$, Phys. Rev. **D71** (2005) 032005, arXiv:hep-ex/0411016.

[375] S. T'Jampens, *Study of CP symmetry violation in the charmonium-*$K^*(892)$ *channel by a complete time dependent angular analysis (BaBar experiment)*, SLAC-R-836.

[376] R. Dalitz, *On the analysis of tau-meson data and the nature of the tau-meson*, Phil. Mag. **44** (1953) 1068-1080.

[377] R. Dalitz, *Decay of tau mesons of known charge*, Phys. Rev. **94** (1954) 1046-1051.

[378] BELLE collaboration, Y. Nakahama *et al.*, *Measurement of CP violating asymmetries in* $B^0 \to K^+K^-K^0_S$ *decays with a time-dependent Dalitz approach*, Phys. Rev. **D82** (2010) 073011, arXiv:1007.3848.

[379] BaBar collaboration, J. Lees *et al.*, *Study of CP violation in Dalitz-plot analyses of* $B^0 \to K^+K^-K^0_S$, $B^+ \to K^+K^-K^+$, *and* $B^+ \to K^0_S K^0_S K^+$, Phys. Rev. **D85** (2012) 112010, arXiv:1201.5897.

[380] S. M. Flatte, *Coupled-channel analysis of the $\pi\eta$ and $K\overline{K}$ systems near $K\overline{K}$ threshold*, Phys. Lett. **B63** (1976) 224.

[381] M. Gronau and D. London, *Isospin analysis of CP asymmetries in B decays*, Phys. Rev. Lett. **65** (1990) 3381-3384.

[382] H. J. Lipkin, Y. Nir, H. R. Quinn, and A. Snyder, *Penguin trapping with isospin analysis and CP asymmetries in B decays*, Phys. Rev. **D44** (1991) 1454-1460.

[383] M. Gronau, *Elimination of penguin contributions to CP asymmetries in B decays through isospin analysis*, Phys. Lett. **B265** (1991) 389-394.

[384] Babar collaboration, B. Aubert *et al.*, *A study of $B^0 \to \rho^+\rho^-$ decays and constraints on the CKM angle α*, Phys. Rev. **D76** (2007) 052007, arXiv:0705.2157.

[385] Belle collaboration, A. Somov *et al.*, *Measurement of the branching fraction, polarization, and CP asymmetry for $B^0 \to \rho^+\rho^-$ decays, and determination of the CKM phase ϕ_2*, Phys. Rev. Lett. **96** (2006) 171801, arXiv:hep-ex/0601024.

[386] A. E. Snyder and H. R. Quinn, *Measuring CP asymmetry in $B \to \rho\pi$ decays without ambiguities*, Phys. Rev. **D48** (1993) 2139-2144.

[387] BaBar collaboration, B. Aubert *et al.*, *Measurement of CP-violating asymmetries in $(\rho\pi)^0$ using a time-dependent Dalitz plot analysis*, Phys. Rev. **D76** (2007) 012004, arXiv:hep-ex/0703008.

[388] BaBar, J. Lees *et al.*, *Measurement of CP-violating asymmetries in $B^0 \to (\rho\pi)^0$ decays using a time-dependent Dalitz plot analysis*, Phys. Rev. **D88** (2013), no. 1 012003, arXiv:1304.3503.

[389] BaBar collaboration, B. Aubert *et al.*, *Measurements of branching fractions and CP-violating asymmetries in $B^0 \to \pi^+\pi^-$, $K^+\pi^-$, K^+K^- decays*, Phys. Rev. Lett. **89** (2002) 281802, arXiv:hep-ex/0207055.

[390] BaBar collaboration, B. Aubert *et al.*, *Branching fractions and CP asymmetries in $B^0 \to \pi^0\pi^0$, $B^+ \to \pi^+\pi^0$ and $B^+ \to K^+\pi^0$ decays and isospin analysis of the $B \to \pi\pi$ system*, Phys. Rev. Lett. **94** (2005) 181802, arXiv:hep-ex/0412037.

[391] BaBar collaboration, B. Aubert *et al.*, *Improved measurements of CP-violating asymmetry amplitudes in $B^0 \to \pi^+\pi^-$ decays*, Phys. Rev. Lett. **95** (2005) 151803, arXiv:hep-ex/0501071.

[392] BaBar collaboration, B. Aubert *et al.*, *Improved measurements of the branching fractions for $B^0 \to \pi^+\pi^-$ and $B^0 \to K^+\pi^-$, and a search for $B^0 \to K^+K^-$*, Phys. Rev. **D75** (2007) 012008, arXiv:hep-ex/0608003.

[393] BaBar collaboration, B. Aubert *et al.*, *Observation of CP violation in $B^0 \to K^+\pi^-$ and $B^0 \to \pi^+\pi^-$*, Phys. Rev. Lett. **99** (2007) 021603, arXiv:hep-ex/0703016.

[394] BaBar collaboration, B. Aubert *et al.*, *Study of $B^0 \to \pi^0\pi^0$, $B^\pm \to \pi^\pm\pi^0$ and $B^\pm \to K^\pm\pi^0$ decays, and isospin analysis of $B \to \pi\pi$ decays*, Phys. Rev. **D76** (2007) 091102, arXiv:0707.2798.

[395] BaBar collaboration, J. Lees *et al.*, *Measurement of CP asymmetries and branching fractions in charmless two-body B-meson decays to pions and kaons*, Phys. Rev. **D87** (2013), no. 5 052009, arXiv:1206.3525.

[396] Belle collaboration, K. Abe *et al.*, *Observation of $B^0 \to \pi^0\pi^0$*, Phys. Rev. Lett. **94** (2005) 181803, arXiv:hep-ex/0408101.

[397] Belle collaboration, K. Abe *et al.*, *Improved evidence for direct CP violation in $B^0 \to \pi^+\pi^-$ decays and model-independent constraints on ϕ_2*, Phys. Rev. Lett. **95** (2005) 101801, arXiv:hep-ex/0502035.

[398] Belle collaboration, H. Ishino *et al.*, *Observation of direct CP violation in $B^0 \to \pi^+\pi^-$ decays and model-independent constraints on ϕ_2*, Phys. Rev. Lett. **98** (2007) 211801, arXiv:hep-ex/0608035.

[399] Y.-T. Duh *et al.*, *Measurements of branching fractions and direct CP asymmetries for $B \to K\pi$, $B \to \pi\pi$ and $B \to KK$ decays*, Phys. Rev. **D87** (2013) 031103, arXiv:1210.1348.

[400] Belle collaboration, I. Adachi *et al.*, *Measurement of the CP violation parameters in $B^0 \to \pi^+\pi^-$ decays*, Phys. Rev. **D88** (2013), no. 9 092003, arXiv:1302.0551.

[401] LHCb, R. Aaij *et al.*, *First measurement of time-dependent CP violation in $B_s^0 \to K^+K^-$ decays*, JHEP **1310** (2013) 183, arXiv:1308.1428.

[402] BaBar collaboration, B. Aubert *et al.*, *Study of the decay $B^0(\overline{B}^0) \to \rho^+\rho^-$, and constraints on the CKM angle α*, Phys. Rev. Lett. **93** (2004) 231801, arXiv:hep-ex/0404029.

[403] BaBar collaboration, B. Aubert *et al.*, *Improved measurement of the CKM angle alpha using $B^0 \to \rho^+\rho^-$ decays*, Phys. Rev. Lett. **95** (2005) 041805, arXiv:hep-ex/0503049.

[404] BaBar collaboration, B. Aubert *et al.*, *Evidence for $B^0 \to \rho^0\rho^0$ decay and implications for the CKM angle α*, Phys. Rev. Lett. **98** (2007) 111801, arXiv:hep-ex/0612021.

[405] BaBar collaboration, B. Aubert *et al.*, *Measurement of the branching fraction, polarization, and CP asymmetries in $B^0 \to \rho^0\rho^0$ decay, and implications for the CKM angle α*, Phys. Rev. **D78** (2008) 071104, arXiv:0807.4977.

[406] BaBar collaboration, B. Aubert *et al.*, *Measurements of branching fraction, polarization, and charge asymmetry of $B^\pm \to \rho^\pm\rho^0$ and a search for $B^\pm \to \rho^\pm f_0(980)$*, Phys. Rev. Lett. **97** (2006) 261801, arXiv:hep-ex/0607092.

[407] Belle collaboration, A. Somov *et al.*, *Improved measurement of CP-violating parameters in $B^0 \to \rho^+\rho^-$ decays*, Phys. Rev. **D76** (2007) 011104, arXiv:hep-ex/0702009.

[408] Belle collaboration, I. Adachi *et al.*, *Study of $B^0 \to \rho^0\rho^0$ decays, implications for the CKM angle ϕ_2 and search for other four pion final states*, Phys. Rev. **D89** (2014), no. 11 072008, arXiv:1212.4015.

[409] BELLE collaboration, J. Zhang *et al.*, *Observation of $B^+ \to \rho^+\rho^0$*, Phys. Rev. Lett. **91** (2003) 221801, arXiv:hep-ex/0306007.

[410] Belle collaboration, C. Wang *et al.*, *Study of $B^0 \to \rho^\pm\pi^\mp$ time-dependent CP violation at Belle*, Phys. Rev. Lett. **94** (2005) 121801, arXiv:hep-ex/0408003.

[411] Belle collaboration, A. Kusaka *et al.*, *Measurement of CP asymmetry in a time-dependent Dalitz analysis of $B^0 \to (\rho\pi)^0$ and a constraint on the CKM angle ϕ_2*, Phys. Rev. Lett. **98** (2007) 221602, arXiv:hep-ex/0701015.

[412] M. Gronau and J. Zupan, *Weak phase α from $B^0 \to a_1^\pm(1260)\pi^\mp$*, Phys. Rev. **D73** (2006) 057502, arXiv:hep-ph/0512148.

[413] BELLE collaboration, J. Dalseno *et al.*, *Measurement of branching fraction and first evidence of CP Violation in* $B^0 \to a_1^{\pm}(1260)\pi^{\mp}$ *decays*, Phys. Rev. **D86** (2012) 092012, arXiv:1205.5957.

[414] BaBar collaboration, B. Aubert *et al.*, *Measurements of CP-violating asymmetries in* $B^0 \to a_1^{\pm}(1260)\pi^{\mp}$ *decays*, Phys. Rev. Lett. **98** (2007) 181803, arXiv:hep-ex/0612050.

[415] M. Gronau and D. London, *How to determine all the angles of the unitarity triangle from* $B_d^0 \to DK_S^0$ *and* $B_s^0 \to D\phi$, Phys. Lett. **B253** (1991) 483-488.

[416] M. Gronau and D. Wyler, *On determining a weak phase from CP asymmetries in charged B decays*, Phys. Lett. **B265** (1991) 172-176.

[417] D. Atwood, I. Dunietz, and A. Soni, *Enhanced CP violation with* $B \to KD^0(\overline{D}^0)$ *modes and extraction of the CKM angle* γ, Phys. Rev. Lett. **78** (1997) 3257-3260, arXiv:hep-ph/9612433.

[418] D. Atwood, I. Dunietz, and A. Soni, *Improved methods for observing CP violation in* $B^{\pm} \to KD$ *and measuring the CKM phase* γ, Phys. Rev. **D63** (2001) 036005, arXiv:hep-ph/0008090.

[419] A. Giri, Y. Grossman, A. Soffer, and J. Zupan, *Determining* γ *using* $B^+ \to DK^{\pm}$ *with multibody D decays*, Phys. Rev. **D68** (2003) 054018, arXiv:hep-ph/0303187.

[420] Belle collaboration, A. Poluektov *et al.*, *Measurement of* ϕ_3 *with Dalitz plot analysis of* $B^{\pm} \to D^{(*)}K^{\pm}$ *decay*, Phys. Rev. **D70** (2004) 072003, arXiv:hep-ex/0406067.

[421] Belle collaboration, H. Aihara *et al.*, *First measurement of* ϕ_3 *with a model-independent Dalitz-plot analysis of* $B \to DK$, $D \to K_S^0\pi\pi$ *decay*, Phys. Rev. **D85** (2012) 112014, arXiv:1204.6561.

[422] CLEO collaboration, J. Libby *et al.*, *Model-independent determination of the strong-phase difference between* D^0 *and* $\overline{D} \to K_{S,L}^0 h^+h^-$ *(h=*π*,K) and its impact on the measurement of the CKM angle* $\gamma\phi_3$, Phys. Rev. **D82** (2010) 112006, arXiv:1010.2817.

[423] BaBar collaboration, B. Aubert *et al.*, *Measurements of the branching fractions and CP-asymmetries of* $B^- \to D_{CP}^0 K$ *decays*, Phys. Rev. **D73** (2006) 051105, arXiv:hep-ex/0512067.

[424] BaBar collaboration, B. Aubert *et al.*, *Measurement of CP observables in* $B^{\pm} \to D_{CP}^0 K^{\pm}$ *decays*, Phys. Rev. **D77** (2008) 111102, arXiv:0802.4052.

[425] BaBar collaboration, P. del Amo Sanchez *et al.*, *Measurement of CP observables in* $B^{\pm} \to D_{CP}K^{\pm}$ *decays and constraints on the CKM angle* γ, Phys. Rev. **D82** (2010) 072004, arXiv:1007.0504.

[426] BELLE collaboration, K. Abe *et al.*, *Study of* $B^{\pm} \to D_{CP}K^{\pm}$ *and* ${D^*}_{CP}K^{\pm}$ *decays*, Phys. Rev. **D73** (2006) 051106, arXiv:hep-ex/0601032.

[427] Belle collaboration, K. Trabelsi, *Study of direct CP in charmed B decays and measurement of the CKM angle* γ *at Belle*, arXiv:1301.2033.

[428] CDF collaboration, T. Aaltonen *et al.*, *Measurements of branching fraction ratios and CP asymmetries in* $B^{\pm} \to D_{CP}K^{\pm}$ *decays in hadron collisions*, Phys. Rev. **D81** (2010) 031105, arXiv:0911.0425.

[429] LHCb collaboration, R. Aaij *et al.*, *Observation of CP violation in* $B^+ \to DK^+$ *decays*, Phys. Lett. **B712** (2012) 203-212, arXiv:1203.3662.

[430] BaBar collaboration, B. Aubert *et al.*, *Measurement of the ratio* $\mathrm{BF}\,(B^- \to D^{*0}K^-)/\mathrm{BF}\,(B^- \to D^{*0}\pi^-)$ *and of the CP asymmetry of* $B^- \to D^{*0}_{CP+}K^-$ *decays*, Phys. Rev. **D71** (2005) 031102, arXiv:hep-ex/0411091.

[431] BaBar collaboration, B. Aubert *et al.*, *Measurement of ratios of branching fractions and CP-violating asymmetries of* $B^\pm \to D^{(*)}K^\pm$ *decays*, Phys. Rev. **D78** (2008) 092002, arXiv:0807.2408.

[432] BaBar collaboration, B. Aubert *et al.*, *Measurement of CP asymmetries for the decays* $B^\pm \to D^0_{CP}K^{*\pm}$, Phys. Rev. **D72** (2005) 071103, arXiv:hep-ex/0507002.

[433] BaBar collaboration, B. Aubert *et al.*, *Measurement of CP violation observables and parameters for the decays* $B^\pm \to DK^{*\pm}$, Phys. Rev. **D80** (2009) 092001, arXiv:0909.3981.

[434] BaBar collaboration, B. Aubert *et al.*, *Search for* $b \to u$ *transitions in* $B^0 \to D^0K^{*0}$ *decays*, Phys. Rev. **D80** (2009) 031102, arXiv:0904.2112.

[435] LHCb collaboration, R. Aaij *et al.*, *Measurement of CP violation parameters in* $B^0 \to DK^{*0}$ *decays*, Phys. Rev. **D90** (2014), no. 11 112002, arXiv:1407.8136.

[436] BaBar collaboration, B. Aubert *et al.*, *Search for* $b \to u$ *transitions in* $B^- \to D^0K^-$ *and* $B^- \to D^{*0}K^-$, Phys. Rev. **D72** (2005) 032004, arXiv:hep-ex/0504047.

[437] Babar collaboration, P. del Amo Sanchez *et al.*, *Search for* $b \to u$ *transitions in* $B^- \to DK^-$ *and* D^*K^- *decays*, Phys. Rev. **D82** (2010) 072006, arXiv:1006.4241.

[438] Belle collaboration, Y. Horii *et al.*, *Evidence for the suppressed decay* $B^- \to DK^-$, $D \to K^+\pi^-$, Phys. Rev. Lett. **106** (2011) 231803, arXiv:1103.5951.

[439] CDF collaboration, T. Aaltonen *et al.*, *Measurements of branching fraction ratios and CP-asymmetries in suppressed* $B^- \to D(\to K^+\pi^-)K^-$ *and* $B^- \to D(\to K^+\pi^-)\pi^-$ *decays*, Phys. Rev. **D84** (2011) 091504, arXiv:1108.5765.

[440] BaBar collaboration, B. Aubert *et al.*, *A study of* $b \to c$ *and* $b \to u$ *interference in the decay* $B^- \to [K^+\pi^-]_{\mathrm{D}}K^{*-}$, Phys. Rev. **D72** (2005) 071104, arXiv:hep-ex/0508001.

[441] BaBar collaboration, B. Aubert *et al.*, *Search for* $b \to u$ *transitions in* $B^- \to [K^+\pi^-\pi^0]_{\mathrm{D}}K^-$, Phys. Rev. **D76** (2007) 111101, arXiv:0708.0182.

[442] BaBar collaboration, J. Lees *et al.*, *Search for* $b \to u$ *transitions in* $B^\pm \to [K^\mp\pi^\pm\pi^0]_{\mathrm{D}}K^\pm$ *decays*, Phys. Rev. **D84** (2011) 012002, arXiv:1104.4472.

[443] LHCb collaboration, R. Aaij *et al.*, *Observation of the suppressed ADS modes* $B^\pm \to [\pi^\pm K^\mp\pi^+\pi^-]_{\mathrm{D}}K^\pm$ *and* $B^\pm \to [\pi^\pm K^\mp\pi^+\pi^-]_{\mathrm{D}}\pi^\pm$, Phys. Lett. **B723** (2013) 44-53, arXiv:1303.4646.

[444] Belle collaboration, K. Negishi *et al.*, *Search for the decay* $B^0 \to DK^{*0}$ *followed by* $D \to K^-\pi^+$, Phys. Rev. **D86** (2012) 011101, arXiv:1205.0422.

[445] Belle collaboration, A. Poluektov *et al.*, *Measurement of* ϕ_3 *with Dalitz plot analysis of* $B^+ \to D^{(*)}K^{(*)+}$ *decay*, Phys. Rev. **D73** (2006) 112009, arXiv:hep-ex/0604054.

[446] Belle collaboration, A. Poluektov *et al.*, *Evidence for direct CP violation in the decay* $B \to D^{(*)}K$, $D \to K^0_S\pi^+\pi^-$ *and measurement of the CKM phase* ϕ_3, Phys. Rev. **D81** (2010) 112002, arXiv:1003.3360.

[447] BaBar collaboration, B. Aubert *et al.*, *Measurement of γ in $B^{\mp} \to D^{(*)}K^{\mp}$ decays with a Dalitz analysis of $D \to K^0_S\pi^-\pi^+$*, Phys. Rev. Lett. **95** (2005) 121802, arXiv:hep-ex/0504039.

[448] BaBar collaboration, B. Aubert *et al.*, *Improved measurement of the CKM angle γ in $B^{\mp} \to D^{(*)}K^{(*)\mp}$ decays with a Dalitz plot analysis of D decays to $K^0_S\pi^+\pi^-$ and $K^0_SK^+K^-$*, Phys. Rev. **D78** (2008) 034023, arXiv:0804.2089.

[449] BaBar collaboration, P. del Amo Sanchez *et al.*, *Evidence for direct CP violation in the measurement of the Cabibbo-Kobayashi-Maskawa angle γ with $B^{\mp} \to D^{(*)}K^{(*)\mp}$ decays*, Phys. Rev. Lett. **105** (2010) 121801, arXiv:1005.1096.

[450] LHCb collaboration, R. Aaij *et al.*, *Measurement of CP violation and constraints on the CKM angle γ in $B^{\pm} \to DK^{\pm}$ with $D \to K^0_S\pi^+\pi^-$ decays*, Nucl. Phys. **B888** (2014) 169-193, arXiv:1407.6211.

[451] BaBar collaboration, B. Aubert *et al.*, *Measurement of CP violation parameters with a Dalitz plot analysis of $B^{\pm} \to D(\pi^+\pi^-\pi^0)K^{\pm}$*, Phys. Rev. Lett. **99** (2007) 251801, arXiv:hep-ex/0703037.

[452] BaBar collaboration, B. Aubert *et al.*, *Constraints on the CKM angle γ in $B^0 \to \overline{D}^0(D^0)K^{*0}$ with a Dalitz analysis of $D^0 \to K^0_S\pi^+\pi^-$*, Phys. Rev. **D79** (2009) 072003, arXiv:0805.2001.

[453] LHCb collaboration, R. Aaij *et al.*, *A model-independent Dalitz plot analysis of $B^{\pm} \to DK^{\pm}$ with $D \to K^0_Sh^+h^-$ (h=π,K) decays and constraints on the CKM angle γ*, Phys. Lett. **B718** (2012) 43-55, arXiv:1209.5869.

[454] LHCb collaboration, R. Aaij *et al.*, *Measurement of the CKM angle γ using $B^{\pm} \to DK^{\pm}$ with $D \to K^0_S\pi^+\pi^-$, $K^0_SK^+K^-$ decays*, JHEP **1410** (2014) 97, arXiv:1408.2748.

[455] LHCb collaboration, R. Aaij *et al.*, *A study of CP violation in $B^{\pm} \to DK^{\pm}$ and $B^{\pm} \to D\pi^{\pm}$ decays with $D \to K^0_SK^{\pm}\pi^{\mp}$ final states*, Phys. Lett. **B733** (2014) 36-45, arXiv:1402.2982.

[456] BaBar collaboration, P. del Amo Sanchez *et al.*, *Measurement of $D^0\overline{D}^0$ mixing parameters using $D^0 \to K^0_S\pi^+\pi^-$ and $D^0 \to K^0_SK^+K^-$ decays*, Phys. Rev. Lett. **105** (2010) 081803, arXiv:1004.5053.

[457] BaBar, J. Lees *et al.*, *Observation of direct CP violation in the measurement of the Cabibbo-Kobayashi-Maskawa angle γ with $B^{\pm} \to D^{(*)}K^{*\pm}$ decays*, Phys. Rev. **D87** (2013), no. 5 052015, arXiv:1301.1029.

[458] LHCb collaboration, R. Aaij *et al.*, *Measurement of the CKM angle γ from a combination of $B^{\pm} \to Dh^{\pm}$ analyses*, Phys. Lett. **B726** (2013) 151-163, arXiv:1305.2050.

[459] LHCb collaboration, *Measurement of the CKM angle γ using $B^{\pm} \to DK^{\pm}$ with $D \to K^0_S\pi^+\pi^-$, $K^0_SK^+K^-$ decays*, LHCB-CONF-2014-004.

[460] A. S. Dighe, I. Dunietz, and R. Fleischer, *Extracting CKM phases and $B^0_s - \overline{B}^0_s$ mixing parameters from angular distributions of nonleptonic B decays*, Eur. Phys. J. **C6** (1999) 647-662, arXiv:hep-ph/9804253.

[461] CDF collaboration, T. Aaltonen *et al.*, *Measurement of lifetime and decay-width difference in $B^0_s \to J/\psi\phi$ decays*, Phys. Rev. Lett. **100** (2008) 121803, arXiv:0712.2348.

[462] CDF collaboration, T. Aaltonen *et al.*, *First flavor-tagged determination of bounds on mixing-induced CP violation in $B_s^0 \to J/\psi\phi$ decays*, Phys. Rev. Lett. **100** (2008) 161802, arXiv:0712.2397.

[463] D0 collaboration, V. Abazov *et al.*, *Lifetime difference and CP-violating phase in the B_s^0 system*, Phys. Rev. Lett. **98** (2007) 121801, arXiv:hep-ex/0701012.

[464] D0 collaboration, V. Abazov *et al.*, *Measurement of B_s^0 mixing parameters from the flavor-tagged decay $B_s^0 \to J/\psi\phi$*, Phys. Rev. Lett. **101** (2008) 241801, arXiv:0802.2255.

[465] ATLAS collaboration, G. Aad *et al.*, *Time-dependent angular analysis of the decay $B_s^0 \to J/\psi\phi$ and extraction of $\Delta\Gamma_s$ and the CP-violating weak phase ϕ_s by ATLAS*, JHEP **1212** (2012) 072, arXiv:1208.0572.

[466] ATLAS collaboration, G. Aad *et al.*, *Flavor tagged time-dependent angular analysis of the $B_s^0 \to J/\psi\phi$ decay and extraction of $\Delta\Gamma_s$ and the weak phase ϕ_s in ATLAS*, Phys. Rev. **D90** (2014), no. 5 052007, arXiv:1407.1796.

[467] CMS collaboration, *Measurement of the CP-violating weak phase ϕ_s and the decay width difference $\Delta\Gamma_s$ using the $B_s^0 \to J/\psi\phi(1020)$ decay channel*, CMS-PAS-BPH-13-012.

[468] LHCb collaboration, R. Aaij *et al.*, *Measurement of the CP-violating phase ϕ_s in the decay $B_s^0 \to J/\psi\phi$*, Phys. Rev. Lett. **108** (2012) 101803, arXiv:1112.3183.

[469] D. Martinez Santos and F. Dupertuis, *Mass distributions marginalized over per-event errors*, Nucl. Instrum. Meth. **A764** (2014) 150-155, arXiv:1312.5000.

[470] M. Pivk and F. R. Le Diberder, *SPlot: A statistical tool to unfold data distributions*, Nucl. Instrum. Meth. **A555** (2005) 356-369, arXiv:physics/0402083.

[471] LHCb collaboration, R. Aaij *et al.*, *Determination of the sign of the decay width difference in the B_s^0 system*, Phys. Rev. Lett. **108** (2012) 241801, arXiv:1202.4717.

[472] S. Stone and L. Zhang, *S-waves and the measurement of CP violating phases in B_s decays*, Phys. Rev. **D79** (2009) 074024, arXiv:0812.2832.

[473] BaBar collaboration, B. Aubert *et al.*, *Dalitz-plot analysis of the decays $B^\pm \to K^\pm\pi^\mp\pi^\pm$*, Phys. Rev. **D72** (2005) 072003, arXiv:hep-ex/0507004.

[474] BaBar collaboration, B. Aubert *et al.*, *Dalitz plot analysis of the decay $B^\pm \to K^\pm K^\pm K^\mp$*, Phys. Rev. **D74** (2006) 032003, arXiv:hep-ex/0605003.

[475] BES collaboration, M. Ablikim *et al.*, *Resonances in $J/\psi \to \phi\pi^+\pi^-$ and ϕK^+K^-*, Phys. Lett. **B607** (2005) 243-253, arXiv:hep-ex/0411001.

[476] LHCb collaboration, R. Aaij *et al.*, *Measurement of the CP violating phase ϕ_s in $\overline{B}_s^0 \to J/\psi f_0(980)$*, Phys. Lett. **B707** (2012) 497-505, arXiv:1112.3056.

[477] LHCb collaboration, R. Aaij *et al.*, *Analysis of the resonant components in $B_s^0 \to J/\psi\pi^+\pi^-$*, Phys. Rev. **D86** (2012) 052006, arXiv:1204.5643.

[478] LHCb collaboration, R. Aaij *et al.*, *Measurement of the CP-violating phase ϕ_s in $\overline{B}_s^0 \to J/\psi\pi^+\pi^-$ decays*, Phys. Lett. **B713** (2012) 378-386, arXiv:1204.5675.

[479] L. Zhang and S. Stone, *Time-dependent Dalitz-plot formalism for $B_q \to J/\psi h^+h^-$*, Phys. Lett. **B719** (2013) 383-387, arXiv:1212.6434.

[480] LHCb collaboration, R. Aaij *et al.*, *Measurement of the $\overline{B}^0 - B^0$ and $\overline{B}^0_s - B^0_s$ production asymmetries in pp collisions at $\sqrt{s} = 7$ TeV*, Phys. Lett. **B739** (2014) 218-228, arXiv:1408.0275.

[481] R. Fleischer, R. Knegjens, and G. Ricciardi, *Anatomy of $B^0_{(s)} \to J/\psi f_0(980)$*, Eur. Phys. J. **C71** (2011) 1832, arXiv:1109.1112.

[482] A. Lenz and U. Nierste, *Numerical updates of lifetimes and mixing parameters of B mesons*, arXiv:1102.4274.

[483] ALEPH collaboration, R. Barate *et al.*, *Investigation of inclusive CP asymmetries in B^0 decays*, Eur. Phys. J. **C20** (2001) 431-443.

[484] CLEO collaboration, J. E. Bartelt *et al.*, *Two measurements of $B^0 - \overline{B}^0$ mixing*, Phys. Rev. Lett. **71** (1993) 1680-1684.

[485] CLEO collaboration, D. Jaffe *et al.*, *Bounds on the CP asymmetry in like sign dileptons from $B^0\overline{B}^0$ meson decays*, Phys. Rev. Lett. **86** (2001) 5000-5003, arXiv:hep-ex/0101006.

[486] CDF collaboration, F. Abe *et al.*, *Measurement of $b\bar{b}$ production correlations, $B^0\overline{B}^0$ mixing, and a limit on $\varepsilon(B)$ in $p\overline{p}$ collisions at $\sqrt{s} = 1.8$ TeV*, Phys. Rev. **D55** (1997) 2546-2558.

[487] BaBar collaboration, B. Aubert *et al.*, *Search for T and CP violation in $B^0 - \overline{B}^0$ mixing with inclusive dilepton events*, Phys. Rev. Lett. **88** (2002) 231801, arXiv:hep-ex/0202041.

[488] BaBar collaboration, B. Aubert *et al.*, *Limits on the decay-rate difference of neutral B mesons and on CP, T, and CPT violation in $B^0 - \overline{B}^0$ oscillations*, Phys. Rev. Lett. **92** (2004) 181801, arXiv:hep-ex/0311037.

[489] BaBar collaboration, B. Aubert *et al.*, *Limits on the decay rate difference of neutral B mesons and on CP, T, and CPT violation in $B^0 - \overline{B}^0$ oscillations*, Phys. Rev. **D70** (2004) 012007, arXiv:hep-ex/0403002.

[490] BaBar collaboration, B. Aubert *et al.*, *Search for T, CP and CPT violation in $B^0 - \overline{B}^0$ mixing with inclusive dilepton events*, Phys. Rev. Lett. **96** (2006) 251802, arXiv:hep-ex/0603053.

[491] BaBar collaboration, J. Lees *et al.*, *Search for CP violation in $B^0 - \overline{B}^0$ mixing using partial reconstruction of $B^0 \to D^{(*)-} X \ell^+ \nu_\ell$ and a kaon tag*, Phys. Rev. Lett. **111** (2013), no. 10 101802, arXiv:1305.1575.

[492] The BABAR collaboration, J. Lees *et al.*, *Study of CP asymmetry in $B^0 - \overline{B}^0$ mixing with inclusive dilepton events*, arXiv:1411.1842.

[493] Belle collaboration, E. Nakano *et al.*, *Charge asymmetry of same-sign dileptons in $B^0 - \overline{B}^0$ mixing*, Phys. Rev. **D73** (2006) 112002, arXiv:hep-ex/0505017.

[494] D0 collaboration, V. M. Abazov *et al.*, *Measurement of the semileptonic charge asymmetry in B^0 meson mixing with the D0 detector*, Phys. Rev. **D86** (2012) 072009, arXiv:1208.5813.

[495] LHCb collaboration, R. Aaij *et al.*, *Measurement of the semileptonic CP asymmetry in $B^0 - \overline{B}^0$ mixing*, Phys. Rev. Lett. **114** (2015) 041601, arXiv:1409.8586.

[496] O. Long, M. Baak, R. N. Cahn, and D. P. Kirkby, *Impact of tag side interference on time dependent CP asymmetry measurements using coherent $B^0\overline{B}^0$ pairs*, Phys. Rev. **D68** (2003) 034010, arXiv:hep-ex/0303030.

[497] D0 collaboration, V. Abazov *et al.*, *Measurement of the charge asymmetry in semileptonic B_s decays*, Phys. Rev. Lett. **98** (2007) 151801, arXiv:hep-ex/0701007.

[498] D0 collaboration, V. Abazov *et al.*, *Search for CP violation in $B_s^0 \to \mu^+ D_s^- X$ decays in $p\overline{p}$ collisions at $\sqrt{s} = 1.96$ TeV*, Phys. Rev. **D82** (2010) 012003, arXiv:0904.3907.

[499] D0 collaboration, V. Abazov *et al.*, *Measurement of the semileptonic charge asymmetry using $B_s^0 \to D_s \mu X$ decays*, Phys. Rev. Lett. **110** (2013) 011801, arXiv:1207.1769.

[500] LHCb collaboration, R. Aaij *et al.*, *Measurement of the flavour-specific CP-violating asymmetry $a_{\rm sl}^s$ in B_s^0 decays*, Phys. Lett. **B728** (2014) 607-615, arXiv:1308.1048.

[501] D0 collaboration, V. Abazov *et al.*, *Measurement of the CP-violation parameter of B^0 mixing and decay with $p\overline{p} \to \mu\mu X$ data*, Phys. Rev. **D74** (2006) 092001, arXiv:hep-ex/0609014.

[502] D0 collaboration, V. M. Abazov *et al.*, *Evidence for an anomalous like-sign dimuon charge asymmetry*, Phys. Rev. **D82** (2010) 032001, arXiv:1005.2757.

[503] D0 collaboration, V. M. Abazov *et al.*, *Measurement of the anomalous like-sign dimuon charge asymmetry with 9 fb^{-1} of $p\overline{p}$ collisions*, Phys. Rev. **D84** (2011) 052007, arXiv:1106.6308.

[504] D0 collaboration, V. M. Abazov *et al.*, *Study of CP-violating charge asymmetries of single muons and like-sign dimuons in $p\overline{p}$ collisions*, Phys. Rev. **D89** (2014), no. 1 012002, arXiv:1310.0447.

[505] G. Borissov and B. Hoeneisen, *Understanding the like-sign dimuon charge asymmetry in $p\overline{p}$ collisions*, Phys. Rev. **D87** (2013), no. 7 074020, arXiv:1303.0175.

[506] K. Babu and C. F. Kolda, *Higgs mediated $B^0 \to \mu^+\mu^-$ in minimal supersymmetry*, Phys. Rev. Lett. **84** (2000) 228-231, arXiv:hep-ph/9909476.

[507] C. Bobeth, T. Ewerth, F. Kruger, and J. Urban, *Analysis of neutral Higgs boson contributions to the decays $\overline{B}_s \to \ell^+\ell^-$ and $\overline{B} \to K\ell^+\ell^-$*, Phys. Rev. **D64** (2001) 074014, arXiv:hep-ph/0104284.

[508] A. Dedes, H. K. Dreiner, and U. Nierste, *Correlation of $B_s \to \mu^+\mu^-$ and $(g-2)(\mu)$ in minimal supergravity*, Phys. Rev. Lett. **87** (2001) 251804, arXiv:hep-ph/0108037.

[509] R. L. Arnowitt, B. Dutta, T. Kamon, and M. Tanaka, *Detection of $B_s \to \mu^+\mu^-$ at the Tevatron run II and constraints on the SUSY parameter space*, Phys. Lett. **B538** (2002) 121-129, arXiv:hep-ph/0203069.

[510] S. Baek, P. Ko, and W. Y. Song, *Implications on SUSY breaking mediation mechanisms from observing $B_s \to \mu^+\mu^-$ and the muon $(g-2)$*, Phys. Rev. Lett. **89** (2002) 271801, arXiv:hep-ph/0205259.

[511] S. Baek, Y. G. Kim, and P. Ko, *Neutralino dark matter scattering and $B_s \to \mu^+\mu^-$ in SUSY models*, JHEP **0502** (2005) 067, arXiv:hep-ph/0406033.

[512] J. R. Ellis, K. A. Olive, Y. Santoso, and V. C. Spanos, *On $B_s \to \mu^+\mu^-$ and cold dark matter scattering in the MSSM with non-universal Higgs masses*, JHEP **0605** (2006) 063, arXiv:hep-ph/0603136.

[513] I. Gogoladze, R. Khalid, Y. Mimura, and Q. Shafi, *Direct and indirect detection and LHC signals of Bino-Higgsino Dark Matter*, Phys. Rev. **D83** (2011) 095007, arXiv:1012.1613.

[514] S. Davidson and S. Descotes-Genon, *Minimal flavour violation for leptoquarks*, JHEP **1011** (2010) 073, arXiv:1009.1998.

[515] M. Blanke *et al.*, *Rare K and B decays in a warped extra dimension with custodial protection*, JHEP **0903** (2009) 108, arXiv:0812.3803.

[516] M. Bauer, S. Casagrande, U. Haisch, and M. Neubert, *Flavor physics in the Randall-Sundrum model: II. tree-level weak-interaction processes*, JHEP **1009** (2010) 017, arXiv:0912.1625.

[517] C.-S. Huang, W. Liao, and Q.-S. Yan, *The promising process to distinguish supersymmetric models with large* $\tan\beta$ *from the Standard Model:* $B \to X_s \mu^+ \mu^-$, Phys. Rev. **D59** (1999) 011701, arXiv:hep-ph/9803460.

[518] C. Hamzaoui, M. Pospelov, and M. Toharia, *Higgs mediated FCNC in supersymmetric models with large* $\tan\beta$, Phys. Rev. **D59** (1999) 095005, arXiv:hep-ph/9807350.

[519] S. R. Choudhury and N. Gaur, *Dileptonic decay of* B_s *meson in SUSY models with large* $\tan\beta$, Phys. Lett. **B451** (1999) 86-92, arXiv:hep-ph/9810307.

[520] S. R. Choudhury, A. S. Cornell, N. Gaur, and G. C. Joshi, *Signatures of new physics in dileptonic B-decays*, Int. J. Mod. Phys. **A21** (2006) 2617-2634, arXiv:hep-ph/0504193.

[521] J. Parry, *Lepton flavor violating Higgs boson decays,* $\tau \to \mu\gamma$ *and* $B_s \to \mu^+\mu^-$ *in the constrained MSSM+NR with large* $\tan\beta$, Nucl. Phys. **B760** (2007) 38-63, arXiv:hep-ph/0510305.

[522] J. R. Ellis, J. S. Lee, and A. Pilaftsis, *B-meson observables in the maximally CP-violating MSSM with minimal flavour violation*, Phys. Rev. **D76** (2007) 115011, arXiv:0708.2079.

[523] C. Beskidt *et al.*, *Constraints from the decay* $B_s^0 \to \mu^+\mu^-$ *and LHC limits on Supersymmetry*, Phys. Lett. **B705** (2011) 493-497, arXiv:1109.6775.

[524] G. Buchalla, A. J. Buras, and M. E. Lautenbacher, *Weak decays beyond leading logarithms*, Rev. Mod. Phys. **68** (1996) 1125-1144, arXiv:hep-ph/9512380.

[525] K. Wilson and W. Zimmermann, *Operator product expansions and composite field operators in the general framework of quantum field theory*, Commun. Math. Phys. **24** (1972) 87-106.

[526] S. Aoki *et al.*, *Review of lattice results concerning low-energy particle physics*, Eur. Phys. J. **C74** (2014), no. 9 2890, arXiv:1310.8555.

[527] A. J. Buras, J. Girrbach, D. Guadagnoli, and G. Isidori, *On the Standard Model prediction for* $\mathcal{B}(B_{s,d} \to \mu^+\mu^-)$, Eur. Phys. J. **C72** (2012) 2172, arXiv:1208.0934.

[528] K. De Bruyn *et al.*, *Probing New Physics via the* $B_s^0 \to \mu^+\mu^-$ *effective lifetime*, Phys. Rev. Lett. **109** (2012) 041801, arXiv:1204.1737.

[529] C. Bobeth *et al.*, $B_{s,d} \to \ell^+\ell^-$ *in the Standard Model with reduced theoretical uncertainty*, Phys. Rev. Lett. **112** (2014) 101801, arXiv:1311.0903.

[530] CLEO collaboration, R. Giles *et al.*, *Two-body decays of B mesons*, Phys. Rev. **D30** (1984) 2279.

[531] CLEO collaboration, R. Ammar *et al.*, *Search for B^0 decays to two charged leptons*, Phys. Rev. **D49** (1994) 5701-5704.

[532] CLEO collaboration, T. Bergfeld *et al.*, *Search for decays of B^0 mesons into pairs of leptons: $B^0 \to e^+e^-$, $B^0 \to \mu^+\mu^-$ and $B^0 \to e^\pm\mu^\mp$*, Phys. Rev. **D62** (2000) 091102, arXiv:hep-ex/0007042.

[533] ARGUS collaboration, H. Albrecht *et al.*, *B meson decays into charmonium states*, Phys. Lett. **B199** (1987) 451.

[534] BELLE collaboration, M. Chang *et al.*, *Search for $B^0 \to \ell^+\ell^-$ at BELLE*, Phys. Rev. **D68** (2003) 111101, arXiv:hep-ex/0309069.

[535] BaBar collaboration, B. Aubert *et al.*, *Search for decays of B^0 mesons into pairs of charged leptons: $B^0 \to e^+e^-$, $B^0 \to \mu^+\mu^-$, $B^0 \to e^\pm\mu^\mp$*, Phys. Rev. Lett. **94** (2005) 221803, arXiv:hep-ex/0408096.

[536] BaBar collaboration, B. Aubert *et al.*, *Search for decays of B^0 mesons into e^+e^-, $\mu^+\mu^-$, and $e^\pm\mu^\mp$ final states*, Phys. Rev. **D77** (2008) 032007, arXiv:0712.1516.

[537] UA1 collaboration, C. Albajar *et al.*, *A search for rare B meson decays at the CERN $Sp\overline{p}S$ collider*, Phys. Lett. **B262** (1991) 163-170.

[538] L3 collaboration, M. Acciarri *et al.*, *Search for neutral B meson decays to two charged leptons*, Phys. Lett. **B391** (1997) 474-480.

[539] CDF collaboration, F. Abe *et al.*, *Search for flavor changing neutral current B meson decays in $p\overline{p}$ collisions at $\sqrt{s} = 1.8$ TeV*, Phys. Rev. Lett. **76** (1996) 4675-4680.

[540] CDF collaboration, F. Abe *et al.*, *Search for the decays $B_d^0 \to \mu^+\mu^-$ and $B_s^0 \to \mu^+\mu^-$ in $p\overline{p}$ collisions at $\sqrt{s} = 1.8$ TeV*, Phys. Rev. **D57** (1998) 3811-3816.

[541] CDF collaboration, D. Acousta *et al.*, *Search for $B_s^0 \to \mu^+\mu^-$ and $B_d^0 \to \mu^+\mu^-$ decays in $p\overline{p}$ collisions at $\sqrt{s} = 1.96$ TeV*, Phys. Rev. Lett. **93** (2004) 032001, arXiv:hep-ex/0403032.

[542] CDF collaboration, A. Abulencia *et al.*, *Search for $B_s \to \mu^+\mu^-$ and $B_d \to \mu^+\mu^-$ decays in $p\overline{p}$ collisions with CDF II*, Phys. Rev. Lett. **95** (2005) 221805, arXiv:hep-ex/0508036.

[543] CDF collaboration, T. Aaltonen *et al.*, *Search for $B_s^0 \to \mu^+\mu^-$ and $B_d^0 \to \mu^+\mu^-$ decays with 2 fb^{-1} of $p\overline{p}$ collisions*, Phys. Rev. Lett. **100** (2008) 101802, arXiv:0712.1708.

[544] CDF collaboration, T. Aaltonen *et al.*, *Search for $B_s^0 \to \mu^+\mu^-$ and $B^0 \to \mu^+\mu^-$ decays with CDF II*, Phys. Rev. Lett. **107** (2011) 191801, arXiv:1107.2304.

[545] CDF collaboration, T. Aaltonen *et al.*, *Search for $B_s^0 \to \mu^+\mu^-$ and $B^0 \to \mu^+\mu^-$ decays with the full CDF run II data set*, Phys. Rev. **D87** (2013), no. 7 072003, arXiv:1301.7048.

[546] D0 collaboration, V. Abazov *et al.*, *A search for the flavor-changing neutral current decay $B_s^0 \to \mu^+\mu^-$ in $p\overline{p}$ collisions at $\sqrt{s} = 1.96$ TeV with the D0 detector*, Phys. Rev. Lett. **94** (2005) 071802, arXiv:hep-ex/0410039.

[547] D0 collaboration, V. Abazov *et al.*, *Search for $B_s \to \mu^+\mu^-$ at D0*, Phys. Rev. **D76** (2007) 092001, arXiv:0707.3997.

[548] D0 collaboration, V. M. Abazov *et al.*, *Search for the rare decay $B_s^0 \to \mu^+\mu^-$*, Phys. Lett. **B693** (2010) 539-544, arXiv:1006.3469.

[549] D0 collaboration, V. M. Abazov *et al.*, *Search for the rare decay $B_s \to \mu\mu$*, Phys. Rev. **D87** (2013), no. 7 072006, arXiv:1301.4507.

[550] ATLAS collaboration, G. Aad *et al.*, *Search for the decay $B_s^0 \to \mu\mu$ with the ATLAS detector*, Phys. Lett. **B713** (2012) 387-407, arXiv:1204.0735.

[551] CMS collaboration, S. Chatrchyan *et al.*, *Search for $B_s^0 \to \mu^+\mu^-$ and $B^0 \to \mu^+\mu^-$ decays*, JHEP **1204** (2012) 033, arXiv:1203.3976.

[552] LHCb collaboration, R. Aaij *et al.*, *Search for the rare decays $B_s^0 \to \mu^+\mu^-$ and $B^0 \to \mu^+\mu^-$*, Phys. Lett. **B699** (2011) 330-340, arXiv:1103.2465.

[553] LHCb collaboration, R. Aaij *et al.*, *Search for the rare decays $B_s^0 \to \mu^+\mu^-$ and $B^0 \to \mu^+\mu^-$*, Phys. Lett. **B708** (2012) 55-67, arXiv:1112.1600.

[554] LHCb collaboration, R. Aaij *et al.*, *Strong constraints on the rare decays $B_s^0 \to \mu^+\mu^-$ and $B^0 \to \mu^+\mu^-$*, Phys. Rev. Lett. **108** (2012) 231801, arXiv:1203.4493.

[555] LHCb collaboration, R. Aaij *et al.*, *First evidence for the decay $B_s^0 \to \mu^+\mu^-$*, Phys. Rev. Lett. **110** (2013), no. 2 021801, arXiv:1211.2674.

[556] LHCb collaboration, R. Aaij *et al.*, *Measurement of the $B_s^0 \to \mu^+\mu^-$ branching fraction and search for $B^0 \to \mu^+\mu^-$ decays at the LHCb experiment*, Phys. Rev. Lett. **111** (2013) 101805, arXiv:1307.5024.

[557] CMS collaboration, S. Chatrchyan *et al.*, *Measurement of the $B_s^0 \to \mu^+\mu^-$ branching fraction and search for $B^0 \to \mu^+\mu^-$ with the CMS Experiment*, Phys. Rev. Lett. **111** (2013) 101804, arXiv:1307.5025.

[558] CMS collaboration, LHCb collaboration, V. Khachatryan *et al.*, *Observation of the rare $B_s^0 \to \mu^+\mu^-$ decay from the combined analysis of CMS and LHCb data*, arXiv:1411.4413.

[559] C. Elsasser, *The rare decays $B_{(s)}^0 \to \mu^+\mu^-$ and Z boson production at LHCb and radiation damage in its Silicon Tracker*, CERN-THESIS-2015-xxx.

[560] LHCb collaboration, *Updated average f_s/f_d b-hadron production fraction ratio for 7 TeV pp collisions*, LHCb-CONF-2013-011, CERN-LHCb-CONF-2013-011.

[561] A. J. Buras, *Relations between $\Delta m_{(s,d)}$ and $B_{(s,d)} \to \mu\overline{\mu}$ in models with minimal flavor violation*, Phys. Lett. **B566** (2003) 115-119, arXiv:hep-ph/0303060.

[562] BaBar collaboration, B. Aubert *et al.*, *Evidence for the rare decay $B \to K^*\ell^+\ell^-$ and measurement of the $B \to K\ell^+\ell^-$ branching fraction*, Phys. Rev. Lett. **91** (2003) 221802, arXiv:hep-ex/0308042.

[563] Belle collaboration, A. Ishikawa *et al.*, *Observation of $B \to K^*\ell^+\ell^-$*, Phys. Rev. Lett. **91** (2003) 261601, arXiv:hep-ex/0308044.

[564] LHCb collaboration, R. Aaij *et al.*, *Differential branching fraction and angular analysis of the decay $B^0 \to K^{*0}\mu^+\mu^-$*, JHEP **1308** (2013) 131, arXiv:1304.6325.

[565] M. Beylich, G. Buchalla, and T. Feldmann, *Theory of $B \to K^{(*)}\ell^+\ell^-$ decays at high q^2: OPE and quark-hadron duality*, Eur. Phys. J. **C71** (2011) 1635, arXiv:1101.5118.

[566] HPQCD collaboration, C. Bouchard *et al.*, *Rare decay $B \to K\ell^+\ell^-$ form factors from lattice QCD*, Phys. Rev. **D88** (2013), no. 5 054509, arXiv:1306.2384.

[567] R. R. Horgan, Z. Liu, S. Meinel, and M. Wingate, *Lattice QCD calculation of form factors describing the rare decays $B \to K^* \ell^+ \ell^-$ and $B_s \to \phi \ell^+ \ell^-$*, Phys. Rev. **D89** (2014), no. 9 094501, arXiv:1310.3722.

[568] P. Ball and R. Zwicky, *$B_{d,s} \to \rho$, ω, K^*, ϕ decay form-factors from light-cone sum rules revisited*, Phys. Rev. **D71** (2005) 014029, arXiv:hep-ph/0412079.

[569] W. Altmannshofer *et al.*, *Symmetries and asymmetries of $B \to K^* \mu^+ \mu^-$ decays in the Standard Model and beyond*, JHEP **0901** (2009) 019, arXiv:0811.1214.

[570] A. Ali, P. Ball, L. Handoko, and G. Hiller, *A comparative study of the decays $B \to K, K^* \ell^+ \ell^-$ in standard model and supersymmetric theories*, Phys. Rev. **D61** (2000) 074024, arXiv:hep-ph/9910221.

[571] F. Kruger and J. Matias, *Probing new physics via the transverse amplitudes of $B^0 \to K^{*0} (\to K^- \pi^+) \ell^+ \ell^-$ at large recoil*, Phys. Rev. **D71** (2005) 094009, arXiv:hep-ph/0502060.

[572] U. Egede *et al.*, *New observables in the decay mode $\overline{B} \to \overline{K}^{*0} \ell^+ \ell^-$*, JHEP **0811** (2008) 032, arXiv:0807.2589.

[573] D. Becirevic and E. Schneider, *On transverse asymmetries in $B \to K^* \ell^+ \ell^-$*, Nucl. Phys. **B854** (2012) 321-339, arXiv:1106.3283.

[574] C. Bobeth, G. Hiller, and D. van Dyk, *The benefits of $\overline{B} \to \overline{K}^* \ell^+ \ell^-$ decays at low recoil*, JHEP **1007** (2010) 098, arXiv:1006.5013.

[575] S. Descotes-Genon, J. Matias, M. Ramon, and J. Virto, *Implications from clean observables for the binned analysis of $B \to K^* \mu^+ \mu^-$ at large recoil*, JHEP **1301** (2013) 048, arXiv:1207.2753.

[576] U. Egede *et al.*, *New physics reach of the decay mode $\overline{B} \to \overline{K}^{*0} \ell^+ \ell^-$*, JHEP **1010** (2010) 056, arXiv:1005.0571.

[577] S. Descotes-Genon, T. Hurth, J. Matias, and J. Virto, *Optimizing the basis of $B \to K^{*0} \ell^+ \ell^-$ observables in the full kinematic range*, JHEP **1305** (2013) 137, arXiv:1303.5794.

[578] Belle collaboration, A. Ishikawa *et al.*, *Measurement of forward-backward asymmetry and Wilson coefficients in $B \to K^* \ell^+ \ell^-$*, Phys. Rev. Lett. **96** (2006) 251801, arXiv:hep-ex/0603018.

[579] BELLE collaboration, J.-T. Wei *et al.*, *Measurement of the differential branching fraction and forward-backword asymmetry for $B \to K^* \ell^+ \ell^-$*, Phys. Rev. Lett. **103** (2009) 171801, arXiv:0904.0770.

[580] BaBar collaboration, B. Aubert *et al.*, *Measurements of branching fractions, rate asymmetries, and angular distributions in the rare decays $B \to K \ell^+ \ell^-$ and $B \to K^* \ell^+ \ell^-$*, Phys. Rev. **D73** (2006) 092001, arXiv:hep-ex/0604007.

[581] BaBar collaboration, B. Aubert *et al.*, *Angular distributions in the decays $B \to K^* \ell^+ \ell^-$*, Phys. Rev. **D79** (2009) 031102, arXiv:0804.4412.

[582] CDF collaboration, T. Aaltonen *et al.*, *Measurement of the forward-backward asymmetry in the $B \to K^{(*)} \mu^+ \mu^-$ decay and first observation of the $B_s^0 \to \phi \mu^+ \mu^-$ decay*, Phys. Rev. Lett. **106** (2011) 161801, arXiv:1101.1028.

[583] CDF collaboration, T. Aaltonen *et al.*, *Measurements of the angular distributions in the decays $B \to K^{(*)}\mu^+\mu^-$ at CDF*, Phys. Rev. Lett. **108** (2012) 081807, arXiv:1108.0695.

[584] CMS collaboration, S. Chatrchyan *et al.*, *Angular analysis and branching fraction measurement of the decay $B^0 \to K^{*0}\mu^+\mu^-$*, Phys. Lett. **B727** (2013) 77-100, arXiv:1308.3409.

[585] LHCb collaboration, R. Aaij *et al.*, *Measurement of form-factor-independent observables in the decay $B^0 \to K^{*0}\mu^+\mu^-$*, Phys. Rev. Lett. **111** (2013), no. 19 191801, arXiv:1308.1707.

[586] ATLAS collaboration, *Angular analysis of $B_d \to K^{*0}\mu^+\mu^-$ with the ATLAS experiment*, ATLAS-CONF-2013-038, ATLAS-COM-CONF-2013-043.

[587] C. Bobeth, G. Hiller, and D. van Dyk, *General analysis of $\overline{B} \to \overline{K}^{(*)}\ell^+\ell^-$ decays at low recoil*, Phys. Rev. **D87** (2013), no. 3 034016, arXiv:1212.2321.

[588] C. Bobeth, G. Hiller, and D. van Dyk, *More benefits of semileptonic rare B decays at low recoil: CP violation*, JHEP **1107** (2011) 067, arXiv:1105.0376.

[589] M. Beneke, T. Feldmann, and D. Seidel, *Exclusive radiative and electroweak $b \to d$ and $b \to s$ penguin decays at NLO*, Eur. Phys. J. **C41** (2005) 173-188, arXiv:hep-ph/0412400.

[590] A. Ali, G. Kramer, and G.-h. Zhu, *$B \to K^*\ell^+\ell^-$ decay in soft-collinear effective theory*, Eur. Phys. J. **C47** (2006) 625-641, arXiv:hep-ph/0601034.

[591] C. Bobeth, G. Hiller, D. van Dyk, and C. Wacker, *The decay $B \to K\ell^+\ell^-$ at low hadronic recoil and model-independent $\Delta B = 1$ constraints*, JHEP **1201** (2012) 107, arXiv:1111.2558.

[592] M. De Cian, *Track reconstruction efficiency and analysis of $B^0 \to K^{*0}\mu^+\mu^-$ at the LHCb experiment*, CERN-THESIS-2013-145.

[593] S. Descotes-Genon, J. Matias, and J. Virto, *Understanding the $B \to K^*\mu^+\mu^-$ anomaly*, Phys. Rev. **D88** (2013), no. 7 074002, arXiv:1307.5683.

[594] R. Gauld, F. Goertz, and U. Haisch, *An explicit Z'-boson explanation of the $B \to K^*\mu^+\mu^-$ anomaly*, JHEP **1401** (2014) 069, arXiv:1310.1082.

[595] W. Altmannshofer, S. Gori, M. Pospelov, and I. Yavin, *Quark flavor transitions in $L_\mu - L_\tau$ models*, Phys. Rev. **D89** (2014), no. 9 095033, arXiv:1403.1269.

[596] F. Beaujean, C. Bobeth, and D. van Dyk, *Comprehensive Bayesian analysis of rare (semi)leptonic and radiative B decays*, Eur. Phys. J. **C74** (2014), no. 6 2897, arXiv:1310.2478.

[597] J. Lyon and R. Zwicky, *Resonances gone topsy turvy - the charm of QCD or new physics in $b \to s\ell^+\ell^-$?*, arXiv:1406.0566.

[598] S. Descotes-Genon, L. Hofer, J. Matias, and J. Virto, *On the impact of power corrections in the prediction of $B \to K^*\mu^+\mu^-$ observables*, JHEP **1412** (2014) 125, arXiv:1407.8526.

[599] LHCb collaboration, *Angular analysis of the $B^0 \to K^{*0}\mu^+\mu^-$ decay*, CERN-LHCb-CONF-2015-002, LHCb-CONF-2015-002.

[600] T. Head, *The LHCb trigger system*, JINST **9** (2014) C09015.

[601] LHCb collaboration, R. Aaij *et al.*, *Implications of LHCb measurements and future prospects*, Eur. Phys. J. **C73** (2013) 2373, arXiv:1208.3355.

[602] LHCb collaboration, *Framework TDR for the LHCb Upgrade: Technical Design Report*, CERN-LHCC-2012-007, LHCB-TDR-012.

[603] LHCb collaboration, *LHCb VELO Upgrade Technical Design Report*, CERN-LHCC-2013-021, LHCB-TDR-013.

[604] LHCb collaboration, *LHCb PID Upgrade Technical Design Report*, CERN-LHCC-2013-022, LHCB-TDR-014.

[605] LHCb collaboration, *LHCb Tracker Upgrade Technical Design Report*, CERN-LHCC-2014-001, LHCB-TDR-015.

[606] LHCb collaboration, *LHCb Trigger and Online Technical Design Report*, CERN-LHCC-2014-00X, LHCB-TDR-016.

[607] Belle-II collaboration, T. Abe *et al.*, *Belle II Technical Design Report*, arXiv:1011.0352.

[608] T. Aushev *et al.*, *Physics at Super B Factory*, arXiv:1002.5012.

[609] LHCb collaboration, *Updated sensitivity projections for the LHCb Upgrade*, CERN-LHCb-PUB-2013-015, LHCb-PUB-2013-015.